The Effects of Clay Content on the Behavior of Mudstones and Siltstones

A dissertation submitted by

Mark R. Zablocki

in partial fulfillment of the requirements for the degree of

Doctor of Philosophy

in

Civil and Environmental Engineering

May 2025

© 2025, Mark R. Zablocki

Adviser: Dr. John T. Germaine

Abstract

Understanding the fabric controls of soils is important to understanding the mechanical behavior of soil. Historically soils have been categorized as grain supported (sands) or clay supported. A laboratory program to systematically characterize the engineering properties with variations of clay content is presented. The laboratory program is conducted on resedimented soil specimens, created from mixtures of mass controlled fractions of Gulf of Mexico Eugene Island Clay a natural high plasticity clay and Min-U-Sil 40 a manufactured quartz silt. Specimen clay content ranges in 10% clay by mass increments from 0% clay pure Min-U-Sil 40 to 63% clay the natural clay content of the Gulf of Mexico Eugene Island powder. The laboratory program includes constant rate of strain compression testing to a 90 MPa vertical stress to characterize compression and permeability behavior. Constant rate of strain testing with integral shear wave and pressure wave measurements to a maximum stress of 30 MPa to characterize the dynamic behavior of the soils. K0 consolidated triaxial compression shear testing at two effective stress level 1 MPa and 10 MPa to characterize the strength behavior. Soil compressibility monotonically increases with increasing clay content at low stresses and increases with decreasing clay content at higher stresses. Soil permeability decreases monotonically with increasing clay. The lateral stress ratio at rest K0 increases with increasing clay content and increasing stress. The dynamic properties of soil are largely dependent on the density and compressibility of the soil. The shear strength and effective friction angle monotonically decrease with increasing clay content. The importance of the dependence of soil properties on clay content is demonstrated through estimation of engineering parameters based on in situ measurements at International Ocean Drilling Program Expedition 308 Site U1324 evaluations of soil compressibility models, permeability models, shear modulus correlations, and estimation of the fracture gradient.

Acknowledgements

I would like to acknowledge and thank Dr. Germaine, who served as advisor for this work and mentored me during my time at Tufts. Without Dr. Germaine's guidance, knowledge, dedication, and patience, this work could not have been completed. I appreciate the past near decade at Tufts and my opportunity to work under Dr. Germaine. I could not have found a better situation for continuing my education than being at the Tufts Advanced Geomaterials Laboratory under Dr. Germaine's guidance.

I would like to thank my committee, Dr. Richard Plumb, Dr. Julia Reece, and Dr. Luis Dorfmann. I appreciate their varied backgrounds, specialties, and insights. I appreciate the industry knowledge and passion for the field geology of Dr. Plumb. The expertise and academic rigor of Dr. Reece. The intuitive knowledge and attention to detail of Dr. Dorfmann.

I would like to thank Dr. Peter Flemings and Dr. Maria Nikolinakou and the rest of the University of Texas, GeoFluids faculty members, students, and staff. Thank you for allowing me to present my research in the GeoFluids meetings. Working with UT GeoFluids group exposed me to world class scientists and industry leaders and the real world application of my work. I cherish the rare opportunity to work with a group of experts to advance the state of the art. I appreciate Dr. Fleming's vision and candor, and Dr. Nikolinakou's technical expertise. The UT GeoFluids group is special, and I am proud to have been a member of it.

I would like to thank Valerie and Edward Zablocki for encouraging me and providing so much support during my time at Tufts. I would also like to thank Matt and Siobhan Zablocki, for their patience and grace. I would not have been able to complete my studies if you had not been there to push me or pick up my slack as needed.

I would like to apologize to and thank Julia Bel, Cassidy Zablocki, Orin Zablocki, and Tu Bel my family who have supported me through this selfish act. I have disappeared for countless weekends to work on this dissertation robbing you of a husband, father, and friend. In return I have received love, compassion, and companionship. A written thank you is not sufficient; my hope is that my time away fades into a distant memory as we head into the future together. I love you all dearly.

Contents

CHAPTER 1. Introduction 1

1-1 Background 1

1-2 Thesis Scope and Objectives 2

1-3 Organization of the Thesis 2

CHAPTER 2. Review of Engineering Parameters and Behavioral Trends of Grain Supported and Clay Supported Soils 5

2-1 Introduction 5

2.1. Compression of Soils 6

Lateral Stress Ratio, K, K_0 and K_0 Compression 15

2.2. Permeability of Soils 20

2.3. Dynamic Properties of Soils 24

2.4. Mechanical Strength Properties of Soils 32

2.5. Summary 41

CHAPTER 3. Experimental Testing Equipment and Procedures 73

3-1 Introduction 73

3-2 Specimen Creation Methods 74

Resedimentation (Slurry Sedimentation) Process 74

Undercompaction Process 78

3-3 Laboratory Testing Equipment 81

Introduction 81

Electronic Laboratory Instrumentation 82

Displacement Transducers 82

Load and Pressure Transducers 83

Pressure-Volume Actuators (PVA) 85

Central Data Acquisition System (DAQ) 85

Computer Control System 86

Automated High Stress Constant Rate of Strain Test Apparatus 87

Automated Tall Constant Rate of Strain Test Apparatus 89

Automated Stress Path Triaxial Cell 91
3-4 Laboratory Testing Methods 93
Introduction 93
Index Property Tests 93
Constant Rate of Strain (CRS) Compression Tests 96
Constant Head Permeability Testing 102
Constant Head Permeability Testing with Backpressure 103
Triaxial Consolidation/Shear Test Methods 104
CHAPTER 4. Characterization of the Study Materials 118
4-1 Introduction 118
4-2 Geologic Origin of Parent Materials 118
Gulf of Mexico Eugene Island (GoM_EI) 118
Min-U-Sil 40 119
4-3 Index Testing and Soil Classification 119
Particle Size Distributions 119
Specific Gravity 120
Atterberg Limits 120
Classification of the Study Soils 121
4-4 Imaging of Study Soil Mixtures 121
Imaging of Triaxial Test Specimens 121
CHAPTER 5. Compression And Permeability Test Results 135
5.1. Introduction 135
5.2. Compression of the Silt and Clay Mixtures 136
Experimental Results 136
High Stress CRS Compression Behavior 136
Compressibility of the Silt Clay Mixtures 139
Compressibility of the Silt Clay Mixtures and Material Packing 140
5.3. Compression Curve Corrections 143
Introduction 143
Tall Constant Rate of Strain Sidewall Friction Correction 144
Excess Pore Pressure Correction Due to Fast Axial Strain Rate in Triaxial Tests 147
5.4. Permeability of the Silt and Clay Mixtures 149

5.5. Coefficient of Consolidation and Uniaxial Grain Compressibility, M_v 151
CHAPTER 6. Vertical Velocity Measurements of Silt-Clay Mixtures 192
6-1 Introduction 192
6-2 Waveform Processing and Velocity Calculation 192
Uncertainty in the Velocity Measurements 197
6-3 Velocity Measurements 199
6-4 Dynamic Elastic Parameters 200
6-5 Discussion 202
Dynamic Elastic Moduli of the Silt Clay Mixtures 205
Modeling of Soil Wave Velocity by Lithology and Effective Stress 206
Comparison of Modeled Velocities 207
CHAPTER 7. Undrained Shear Results 249
7-1 Introduction 249
7-2 Undrained Strength Properties and Shear Behavior 250
Undrained Strength Properties 0% Clay Mixtures 250
Undrained Strength Properties 10% Clay Mixtures 254
Undrained Strength Properties 20% Clay Mixtures 256
Undrained Strength Properties 30% Clay Mixtures 258
Undrained Strength Properties 40% Clay Mixtures 260
Undrained Strength Properties 50% Clay Mixtures 261
Undrained Strength Properties 60% Clay Mixtures 262
Undrained Strength Properties RGoM_EI 264
7-3 Trends in Strength Parameters 265
Introduction 265
Maximum Shear Strength of the Silt and Clay Mixtures 265
Friction Angle of the Silt and Clay Mixtures 268
Axial Strain During Shearing 269
CHAPTER 8. Evaluation of Clay Dependency on Engineering Parameters and Soil Behavior 290
8-1 Introduction 290
8-2 Influence of Clay Particles on Soil Structure 290
8-3 Influence of Clay Particles on Soil Compression 298
8-4 Influence of Clay Particles on K_0 Compression 299

8-5 Influence of Clay Particles on Permeability 302
8-6 Influence of Clay Particles on Dynamic Elastic Properties 304
8-7 Influence of Clay Particles on Strength Properties 308
8-8 Conclusion and Significant Findings 310
CHAPTER 9. Evaluation of Clay Dependent Soil Parameter Correlations 335
9-1 Introduction 335
9-2 Evaluating Clay Content 335
9-3 Soil Compressibility and Clay Content 336
9-4 Permeability and Clay Content 343
Permeability and Porosity 343
Permeability and Stress 352
9-5 Dynamic Properties and Clay Content 353
9-6 Strength Properties and Clay Content 358
CHAPTER 10. Conclusion and Recommendations 395
10-1 Overview 395
10-2 Key Findings and Developments 395
10-3 Recommendations for Future Work 399
Works Cited 400

Table of Appendices

Appendix A – Shear Wave Processing Matlab code

Appendix B - Pressure Wave Processing Matlab code

Table of Tables

Table 4-1: Summary of Atterberg Limits and Specific Gravity Testing 124
Table 5-1: Summary of High Stress CRS Tests 153
Table 5-2: Summary of Tall CRS Tests 154
Table 5-3: Summary of Consolidation Phase of Triaxial Tests 155
Table 6-1: Summary of test conditions during velocity measurements for CRS1652. 209
Table 6-2: Summary of test conditions during velocity measurements for CRS1700. 210
Table 6-3: Summary of test conditions during velocity measurements for CRS1663. 211
Table 6-4: Summary of test conditions during velocity measurements for CRS1678. 212
Table 6-5: Summary of test conditions during velocity measurements for CRS1632. 213
Table 6-6: Summary of test conditions during velocity measurements for CRS1698. 214
Table 6-7: Summary of test conditions during velocity measurements for CRS1638. 215
Table 6-8: Summary of test conditions during velocity measurements for CRS1688. 216
Table 6-9: Summary of test conditions during velocity measurements for CRS1633. 217
Table 6-10: Summary of test conditions during velocity measurements for CRS1693. 218
Table 6-11: Summary of test conditions during velocity measurements for CRS1646. 219
Table 6-12: Summary of test conditions during velocity measurements for CRS1679. 220
Table 6-13: Summary of test conditions during velocity measurements for CRS1629. 221
Table 6-14: Summary of test conditions during velocity measurements for CRS1672. 222
Table 6-15: Summary of P wave power equation fits for TCRS tests. 223
Table 6-16: Summary of S wave power equation fits for TCRS tests. 223
Table 7-1: Summary of Triaxial Test Shear Phase Results 271
Table 8-1: Percentage of Minerals in GoM_EI powder based on X-Ray Powder Diffraction 313
Table 8-2: Estimated Elastic Parameters for the Clay Mixtures Based on a Weighted Average of the Elastic Parameters of the Constituent Minerals 313
Table 8-3: Volumes used to Determine V_{grain} and Strength Parameters from 1 MPa tests. 314
Table 8-4: Volumes used to Determine V_{grain} and Strength Parameters from 10 MPa tests. 314
Table 9-1: Summary of Statistical Evaluation of Clay Content Dependency on Compressibility 362
Table 9-2: Compression Indices and Reference Densities for Modeling High Stress CRS test Results 362
Table 9-3: Summary of Statistical Evaluation of Clay Content Dependency on Porosity and Permeability 362
Table 9-4: Summary of G_{max} Correlations Evaluated with TCRS Results 362
Table 9-5: Summary of G_{max} Correlations Fitting Parameters and 363

Table of Figures

Figure 2-1: Classification of soils by particle size from sand to clay within the Unified Soil Classification System (USCS). 43
Figure 2-2: Classification of fine-grained soils and fine-grained soil fractions from the Atterberg Limits within the USCS adopted from ASTM D2487..... 43
Figure 2-3: Stress-Strain relationship in cyclic loading at small strains in dry sand adopted from Hicher (1996). Each cycle is centered around the origin and a shifted representation is presented to distinguish individual cycles. The elastic recoverable strain limit is shown at a strain of $1.5X10^{-5}$. 44
Figure 2-4: Pre-failure behavior of a normally consolidated, K_0 consolidated resedimented Boston blue clay consolidated to a vertical effective stress of about 03. MPa. Figure 2-2 a) -c) are stress–strain curves in 0–0.0005, 0–0.005, and 0.05% axial strain ranges; d) is a comparison of strains measured by two linear variable differential transducers in the 0–0.05% strain range; and e) is the stiffness degradation curve for the tested specimen. 44
Figure 2-5: Stress-Strain relationship in cyclic loading at small strains in saturated clays adopted from Hicher (1996). Each cycle is centered around the origin and a shifted representation is presented to distinguish individual cycles. The hysteretic nature of the cyclic loads indicates the non-recoverable nature of the strains. 45
Figure 2-6: Published measurements of Young's modulus from specimen-mounted small-strain measurements Santagata (1998) and CK_0UC triaxial test results Abdulhadi (2009), Casey (2014) are compared to the velocity-derived Young's modulus Marjanovic (2016). Adopted from Marjanovic (2016). 45
Figure 2-7: Porosity gradient by burial depth obtained by mapping the measured porosity of well cuttings by depth adopted from Hedberg (1926). Curve A represents the data from the porosity measurements. Curve B represents the theoretical porosity calculated based on 50% porosity as mud and 8% porosity at an 8,000 ft burial depth and an increase in density with burial depth. Curve C is an adjustment to curve A to remove irregularities within the measurements using considerations from curve B. 46
Figure 2-8: A logarithmic model for sediment porosity as a function of burial depth, using the equation $n = n0e - bx$. Where n is the porosity, $n0$ is the average surficial porosity, e is the natural logarithm, b is a constant and x is the depth of burial. Adopted from Athy (1930). 46
Figure 2-9: Geological mechanisms for pressurized zones in excess of hydrostatic pressures within the Gulf of Mexico adopted from Dickinson (1953). The shaded facies represent permeable sands while the unshaded facies represent impermeable shales. 47
Figure 2-10: Ranges of probable earth stress for lithostatic pressures and hydrostatic pressures based on variations in mineral density and water density of distilled water to brine containing 100,000 ppm dissolved solids adapted from McCulloh (1967)..... 48
Figure 2-11: Total porosities of sedimentary rocks versus depth derived empirically from laboratory measurements of more than 4,000 samples of conventional cores from the Los Angeles and Ventura basins of California, other scattered localities in the United States, and the Po basin of Italy. Adopted from McCulloh (1967). 49

Figure 2-12: Variation of shale bulk densities with depth in sedimentary basins. 1 = methane-saturated clastic sedimentary rock (probable minimum density) McCulloh (1967); 2 = mudstone- Po Valley Basin, Italy Storer (1959); 3 = average Gulf Coast shale densities; values derived from geophysical data Dickinson (1953); 4 = average Gulf Coast shale densities derived from density logs and formation samples Eaton (1969); 5 = Motatan-1 - Maracaibo Basin, Venezuela Dallmus (1958); 6 = Gorgeteg No.1 - Hungary; calculated wet density values Skeels (1943); 7= Pennsylvanian and Permian dry shale density values, Oklahoma and Texas; Athy's adjusted curve Dallmus (1958); 8 = Las Ollas-1 - eastern Venezuela Dallmus (1958). Figure 2-10 is adopted from Rieke and Chilingar (1974). 50
Figure 2-13: Comparison of the compression of reconstituted clay specimens (Series II) to intact clay specimens to a 100 MPa stress adopted from Finnegan (2020). The intact specimen is significantly denser at lower effective stresses than the reconstituted specimens, but at high effective stresses the compression behavior converges. The difference at low effective stresses is attributed to the stress history of the intact specimens which is not present in the reconstituted specimens. The convergence of the behavior at high stresses is attributed to the intrinsic compression discussed within Burland (1990). 51
Figure 2-14: A comparison of the compression behavior of resedimented silts and clays up to a 100 MPa effective stress level adopted from Casey (2014). 51
Figure 2-15: Comparison of the compression of various sand and clays adopted from Hedberg (1926). . 52
Figure 2-16: Compression curves of two London clay specimens with different clay fractions adopted from Dewhurst, et al. (1998). 52
Figure 2-17: Compression curves of seven sand and Kaolinite clay mixtures from one dimension compression testing on the mixture adopted from Monkul and Ozden (2007). The FC percentage shown represent the added Kaolinite clay content by mass. 53
Figure 2-18: Compression curves of six amended resedimented clay and silt mixtures from uniaxial constant-rate-of-strain consolidation tests adopted from Reece (2021). All samples were consolidated to a maximum vertical effective stress of 20 MPa. 53
Figure 2-19: Mohr's circles at failure under one dimensional loading adopted from Federico and Elia (2009). The dashed circles and line represent the state of stress at maximum stress and the mobilized friction angle. The solid circle and line represent the state of stress at the friction failure envelope. 54
Figure 2-20: Different determinations of least principal stress from pore pressure (curve $P_{P)}$ and vertical stress data (curve S_V) for a well in the Gulf of Mexico. **Curve a** from Zoback and Healy (1984) method, **curve b** is Breckels and van Eekelen (1982), **curve c** is from Hubbert and Willis (1957) utilizing a modified empirical coefficient of 0.5, **curve d** is based on Holbrook, Maggiori et al. (1993), and **curve e** is from Eaton (1969), the figure is adopted from Zoback (2007). 55
Figure 2-21: Observed relationship between the normally consolidated K_0 and sin of the effective friction angle for various soil types adopted from Mayne and Kulhawy (1982). 56
Figure 2-22: Variations of K_0 by fines content and relative density adopted from Lee, Lee and Park (2014). 56
Figure 2-23: Measured relationship between K_0 and relative density of sand specimens adopted from Li, et al. (2023). 57
Figure 2-24: Permeability of clay and shale from laboratory tests plotted versus porosity and showing clay fraction and geologic setting adopted from Neuzil (2019). The hydraulic conductivity scale is for

aqueous fluids at room temperature. Data from various studies as presented in Neuzil (2019). The dashed lines indicate minimum and maximum theoretical permeabilities from the log permeability linear porosity relationship presented within Bekins, Mcaffrey and Dreiss (1995). 57
Figure 2-25: Ranges in hydraulic conductivity and permeability for various geologic materials adopted from Freeze and (Cherry 1979). 58
Figure 2-26: Permeability of clay and silt mixtures by porosity from a model (continuous lines) and direct measurements (data points) adopted from Yang & Aplin, (2010). The clay contents range to the corresponding colored model result and data points are presented in the key. 58
Figure 2-27: Ranges in permeability by hydraulic conductivity for resedimented mudrocks adapted from Casey (2014). 59
Figure 2-28: Effect of uniform confining pressure on the compressional velocity through a dry, saturated, and partially saturated Berea Sandstone specimens adapted from Wyllie, Gregory and Gardner (1956). 59
Figure 2-29: Wave velocities normal to the bedding plane by quartz content and depositional environment for the Longmaxi Shale Formation at 30 MPa confining stress adapted from Deng, et al. (2021). The green points are measurements on samples formed in a shallow water depositional environment and the red points are measurements on samples formed in a deep-water depositional environment. The green points show a trend in decreasing velocity with increasing quartz content while the red points have no discernable trends. 60
Figure 2-30: Wave velocities by brine saturation for Ottawa Sand specimens, where K is a parameter that estimates the interaction between the soil grains and pore fluid adapted from Domenico (1977). The plot indicates the significant effect saturation has on compressional wave velocities and the relatively negligible effect on shear wave velocities. 60
Figure 2-31: Variations in S wave velocity (top) and P wave velocity in saturated sands of varying particle size, and angularity adopted from Prasad and Meissner (1992). The S wave velocities are unaffected by grain size and angularity. The P wave velocities decrease with decreasing particle size and increasing particle angularity. 61
Figure 2-32: Change in contact radius by pressure Contact Radius Models of soils with different mean grain sizes adopted from Prasad and Meissner (1992). (a) R = 110 µm, (b) R = 150 µm, (c) R = 225 µm, (d) R = 275 µm. The number on each curve denotes the initial contact radius taken for the curve's calculation. 61
Figure 2-33: Variations in S wave velocity (top) and P wave velocity in a saturated sand specimen consisting of 65% by mass 0.295 mm to 0.35 mm quartz sand grains and 35% by mass 0.053 to 0.088 quartz sand grains as adapted from Zimmer, et al. (2007). The specimen was subjected to seven load unload pressure cycles up to a maximum stress of 20 MPa and velocity measurements were conducted during both the loading and unloading portions of the test. The color code represents the effective stresses, modeled measurements for the modified Reuss average model (solid), modified Hashin-Shtrikman average model (dotted), and Hardin and Blandford empirical model (dashed) are also shown as discussed within Zimmer, et al. (2007). 62
Figure 2-34: The effect of burial depth on p wave velocity in mixtures of Ottawa Sand and Smectite clay from D.-H. Han (1986). 63

Figure 2-35: Diagrammatic spectrum of sand and clay mixtures and critical clay-content adapted from (Marion, Nur, Yin, & Han, 1992), c is the clay content by volume and ϕ_s is the porosity of the sand grains. 63
Figure 2-36: Left: Porosity by specimen clay content at the indicated confining stress level. Right: P Wave velocity by clay content at the indicated confining stress level. For both plots the numbers represent the measured data and the lines represent modeled fits to the data. Both plots are adapted from Yin (1992). 64
Figure 2-37: Velocity measurements by vertical effective stress for dry and brine saturated synthetic mixtures of Smectite and Kaolinite clay adapted from Mondol, Bjorlykke, et al. (2007). Left: P-wave velocities, Right: S-Wave velocities. 65
Figure 2-38: P-wave and S-wave velocity measurements by vertical effective stress for various intact, reconstituted and resedimented sand and clay specimens adapted from Marjanovic (2016). Left: P-wave velocities, Right: S-Wave velocities. 65
Figure 2-39: P-wave and S-wave velocity measurements by vertical effective stress for resedimented clay specimens adapted from Ranjpour (2020). Left: P-wave velocities, Right: S-Wave velocities. 66
Figure 2-40: Defining stress in a particulate system as adapted from Lambe and Whitman (1969). The normal macroscopic stress is defined as force N dived by the area of the plane, and the macroscopic shear components acting on the plane are the shear forces T_x and T_y divided by the area of the plane. . 66
Figure 2-41: Stresses at failure, relationship of Mohr circle at failure, the Mohr-Coulomb failure criteria, and the theoretical failure plane as adapted from Lambe and Whitman (1969). 67
Figure 2-42: State parameter from tests performed on Kogyuk 350/2 sand from Been and Jefferies (1985). The positive state parameter indicate contractive behavior towards the Steady State Line and the negative state parameter indicates dilative behavior towards the steady state line during shearing. 67
Figure 2-43: The effect of pore pressure on the undrained stress path as quantified by the A parameter adapted from Lambe and Whitman (1969). 68
Figure 2-44: Normalized shear stress to effective consolidation stress by shear strain for three Maine organic clay specimens as an example of Normalized Soil Parameter concept adapted from Ladd and Foott (1974) 68
Figure 2-45: Compressive strength of mudrocks by clay content over varying confining pressures adapted from Jizba (1991) 69
Figure 2-46: Clay content effects on the linear Mohr-Coulomb failure envelopes for shaley sandstones and shales adapted from Jizba (1991). 69
Figure 2-47: Unconfined Compressive Strength (UCS) for Travis Peak samples by grain contacts adapted from Plumb, Herron and Olsen (1992). The grain contacts were evaluated by petrographic analyses of thin sections from the tested lithofacies. 70
Figure 2-48: Clay content effects on stress paths and shear behavior of sand and clay mixtures adapted from Georgiannou, Burland and Hight (1990). CC is the clay content by mass and the specimens were subjected to CK_0UC triaxial testing. 70
Figure 2-49: Stress strain plots for clay and sand mixtures consolidated to a 200 kPa effective stress and sheared in a CK_0DC triaxial test adapted from Prakasha and Chandrasekaran (2005). 71

Figure 2-50: CIUC test stress paths on mixtures of Kaolinite clay and Ottawa Sand adapted from Simpson and Evans (2016). Where f is the clay content by mass and M is the slope of the critical state line. 71
Figure 2-51: Critical state friction angle by clay fraction from Simpson and Evans (2016). The critical state friction angle at 30% clay may be higher than anticipated due to difficulties in maintaining a consistent specimen density with the dry tamped method employed. 72
Figure 2-52: Interpreted Mohr-Coulomb failure envelopes for CIDC triaxial tests adapted from Shen, et al. (2021). FC indicates the clay content between 0% and 40% clay by mass. 72
Figure 3-1: Left: bulk Gulf of Mexico Eugene Island Powder. Right: Min-U-Sil 40 in bowl and 35 g/L sea salt solution in beaker 109
Figure 3-2: Using a stand mixer to blend the GoM_EI and MUS powders with a saline solution to create a stable slurry for use in resedimentation 109
Figure 3-3: Evacuating the tempered slurry within a vacuum chamber prior to placement in a consolidometer 110
Figure 3-4: Placement of evacuated slurry in a consolidometer by a tremie tube and funnel 110
Figure 3-5: Typical consolidometer and weight hanger setup used during resedimentation 111
Figure 3-6: Triaxial specimen trimming equipment. Bottom: wire saw and straight razor. Right: guide for trimming diameter and aluminum confine jacket for trimming ends. Left: jug for trimming perpendicular ends. 111
Figure 3-7: Constant Rate of Strain trimming equipment. Top: vertical trimming stand sized for the CRS confining ring. Bottom: dental tool to remove excess material 112
Figure 3-8: Brass base assembly and acrylic rod with adjustable brass collar used for undercompaction method to make 0% clay content specimens 113
Figure 3-9: Tufts electronic data acquisitions system. Top: personal computer to access system. Below: HP3497A A/D converter above multiplexer 113
Figure 3-10: Tufts high stress CRS testing apparatus 114
Figure 3-11: Tufts tall CRS testing apparatus and test setup 114
Figure 3-12: Schematic Diagram of Components for a Typical Tufts Automated Triaxial Test Apparatus adapted from Santagata (1998) 114
Figure 3-13: Tufts low stress triaxial testing apparatus, rated for an internal fluid pressure of 1 MPa 115
Figure 3-14: Tufts medium stress triaxial testing apparatus, rated for an internal fluid pressure of 10 MPa 115
Figure 3-15: Casagrande cup used for determinations of the liquid limit 116
Figure 3-16: Fall cone apparatus used for determinations of the liquid limit 116
Figure 3-17: Head loss due to the high stress CRS equipment modified for permeability testing with a back pressure at three axial stress ranges, <1 MPa stress (blue line), 1 to 10 MPa stress orange line, and >10 MPa stress black line. 117
Figure 4-1: Index map showing Eugene Island Block 330 oilfield, consisting of block 125
Figure 4-2: Generalized geologic cross section of the Eugene Island 330 block minibasin. Sediments from well A-12 and A-20ST were used in the resedimentation experiments. The cored interval is represented by a solid green line. Adapted from (Alexander & Flemings, 1995) 125

Figure 4-3: Reported properties of Min-U-Sil 40 by the manufacturer US Silica adapted from (US Silica, 2017). The red box indicates grain sized distribution for Min-U-Sil 40 measured with the SediGraph method..... 126
Figure 4-4: Comparison of particle size distribution of Gulf of Mexico Eugene Island (red line and points) to Min-U-Sil 40 (black line and points), measured through timed sedimentation testing. GoM_EI measurements adapted from (Casey, 2014), and MUS measurements adapted from (Schneider, 2011) 126
Figure 4-5: Grain size distribution testing results from four timed sedimentation hydrometer tests on Min-U-Sil 40. The TAG lab hydrometer testing number is provided in the key to the plot..... 127
Figure 4-6: Determinations of the specific gravity of each 10% clay content increment of the silt and clay mixtures. 127
Figure 4-7: Plot of plasticity index by liquid limit indicating the results of the Atterberg Limit tests performed on the mixtures of GoM_EI and MUS. The fall cone method determinations are represented by square points and the Casagrande cup method is represented by the circular points. 128
Figure 4-8: Cross polarized images of the top and bottom of TX1388 a 10% clay low stress (1 MPa) triaxial specimen thin section. The red arrow denotes the direction of the top of the specimen..... 128
Figure 4-9: Cross polarized images of the top and bottom of TX1353 a 20% clay low stress (1 MPa) triaxial specimen thin section. The red arrow denotes the direction of the top of the specimen..... 129
Figure 4-10: Cross polarized images of the top and bottom of TX1390 a 30% clay low stress (1 MPa) triaxial specimen thin section. The red arrow denotes the direction of the top of the specimen..... 129
Figure 4-11: Cross polarized images of the top and bottom of TX1355 a 40% clay low stress (1 MPa) triaxial specimen thin section. The red arrow denotes the direction of the top of the specimen..... 129
Figure 4-12: Cross polarized images of the top and bottom of TX1385 a 50% clay low stress (1 MPa) triaxial specimen thin section. The red arrow denotes the direction of the top of the specimen..... 130
Figure 4-13: Cross polarized images of the top and bottom of TX1350 a 60% clay low stress (1 MPa) triaxial specimen thin section. The red arrow denotes the direction of the top of the specimen..... 130
Figure 4-14: Cross polarized images of the top and bottom of TX1363 a RGoM_EI low stress (1 MPa) triaxial specimen thin section. The red arrow denotes the direction of the top of the specimen..... 130
Figure 4-15: SEM image at 1000x magnification of CRS1622 a 10% clay specimen consolidated to a 90 MPa effective stress..... 131
Figure 4-16: SEM image at 1000x magnification of CRS1619 a 20% clay specimen consolidated to a 90 MPa effective stress..... 131
Figure 4-17: SEM image at 998x magnification of CRS1616 a 30% clay specimen consolidated to a 90 MPa effective stress..... 132
Figure 4-18: SEM image at 1000x magnification of CRS1617 a 40% clay specimen consolidated to a 90 MPa effective stress..... 132
Figure 4-19: SEM image at 1000x magnification of CRS1582 a 50% clay specimen consolidated to a 90 MPa effective stress..... 133
Figure 4-20: SEM image at 1000x magnification of CRS1550 a 60% clay specimen consolidated to a 90 MPa effective stress..... 133
Figure 4-21: SEM image at 1000x magnification of CRS1584 a RGoM_EI specimen consolidated to a 90 MPa effective stress..... 134

Figure 5-1: Upper limit, lower limit, and average compression curves for 0% clay specimens. Limits and average from high stress CRS tests CRS1571, CRS1584, and CRS1620. 158
Figure 5-2: Upper limit, lower limit, and average compression curves for 10% clay specimens. Limits and average from high stress CRS tests CRS1591, and CRS1682. 159
Figure 5-3: Upper limit, lower limit, and average compression curves for 20% clay specimens. Limits and average from high stress CRS tests CRS1608, CRS1619, and CRS1630. 160
Figure 5-4: Upper limit, lower limit, and average compression curves for 30% clay specimens. Limits and average from high stress CRS tests CRS1616, and CRS1621. 161
Figure 5-5: Upper limit, lower limit, and average compression curves for 40% clay specimens. Limits and average from high stress CRS tests CRS1585, and CRS1593. 162
Figure 5-6: Upper limit, lower limit, and average compression curves for 50% clay specimens. Limits and average from high stress CRS tests CRS1585, and CRS1593. 163
Figure 5-7: Upper limit, lower limit, and average compression curves for 60% clay specimens. Limits and average from high stress CRS tests CRS1572, and CRS1592. 164
Figure 5-8: Upper limit, lower limit, and average compression curves for RGoM_EI specimens. Limits and average from high stress CRS tests CRS1581, CRS1594, and CRS1618. 165
Figure 5-9: Average compression curves from high stress CRS measurements. The bounds for compression behavior of the different silt and clay mixtures are presented in Figure 5.1 through Figure 5.8. 166
Figure 5-10: Upper limit, lower limit, and average compression curves for 10% clay specimens. Limits and average from Tall CRS tests CRS1652, and CRS1700. 167
Figure 5-11: Upper limit, lower limit, and average compression curves for 20% clay specimens. Limits and average from Tall CRS tests CRS1663, and CRS1678. 168
Figure 5-12: Upper limit, lower limit, and average compression curves for 30% clay specimens. Limits and average from Tall CRS tests CRS1632, and CRS1698. 169
Figure 5-13: Upper limit, lower limit, and average compression curves for 40% clay specimens. Limits and average from Tall CRS tests CRS1638, and CRS1688. 170
Figure 5-14: Upper limit, lower limit, and average compression curves for 50% clay specimens. Limits and average from Tall CRS tests CRS1633, and CRS1693. 171
Figure 5-15: Upper limit, lower limit, and average compression curves for 60% clay specimens. Limits and average from Tall CRS tests CRS1646, and CRS1679. 172
Figure 5-16: Upper limit, lower limit, and average compression curves for RGoM_EI clay specimens. Limits and average from Tall CRS tests CRS1629, and CRS1672. 173
Figure 5-17: Average compression curves from tall CRS measurements. The bounds for compression behavior of the different silt and clay mixtures are presented in Figure 4.10 through Figure 4.16. 174
Figure 5-18: Upper limit, lower limit, and average compression curves for 0% clay specimens. Limits and averages from 1 MPa and 10 MPa triaxial test consolidation phases. 175
Figure 5-19: Upper limit, lower limit, and average compression curves for 10% clay specimens. Limits and averages from 1 MPa and 10 MPa triaxial test consolidation phases. 176
Figure 5-20: Upper limit, lower limit, and average compression curves for 20% clay specimens. Limits and averages from 1 MPa and 10 MPa triaxial test consolidation phases. 177

Figure 5-21: Upper limit, lower limit, and average compression curves for 30% clay specimens. Limits and averages from 1 MPa and 10 MPa triaxial test consolidation phases. 178
Figure 5-22: Upper limit, lower limit, and average compression curves for 40% clay specimens. Limits and averages from 1 MPa and 10 MPa triaxial test consolidation phases. 179
Figure 5-23: Upper limit, lower limit, and average compression curves for 50% clay specimens. Limits and averages from 1 MPa and 10 MPa triaxial test consolidation phases. 180
Figure 5-24: Upper limit, lower limit, and average compression curves for 60% clay specimens. Limits and averages from 1 MPa and 10 MPa triaxial test consolidation phases. 181
Figure 5-25: Upper limit, lower limit, and average compression curves for RGoM_EI specimens. Limits and averages from 1 MPa and 10 MPa triaxial test consolidation phases. 182
Figure 5-26: Upper limit, lower limit, and average compression curves for RGoM_EI specimens. Limits and averages from 1 MPa and 10 MPa triaxial test consolidation phases. 183
Figure 5-27: Coefficient of Compression (a_v) determined from the indicated axial effective stress from a 1 MPa reference stress in the high stress CRS apparatus. 184
Figure 5-28: Coefficient of Compression (a_v) determined from the indicated axial effective stress from a 1 MPa reference stress in the tall CRS apparatus. 184
Figure 5-29: Soil fabrics due to crystalline grain (silts and sands) and clay (shale) packing adapted from (Marion, Nur, Yin, & Han, 1992). ϕ_S represents the critical clay content at which the sand porosity is completely filled with clay particles and is the transition point between grain supported and clay supported soil fabrics. 185
Figure 5-30: Average void ratio/porosity from the high stress CRS tests of each studied mixture at a 1 MPa Vertical Stress. The red X indicates the interpreted critical clay fraction. 186
Figure 5-31: Average void ratio/porosity from the high stress CRS tests of each studied mixture at a 1 MPa, 2 MPa, 5 MPa ,10 MPa, 15 MPa, 20 MPa, 30 MPa, 40 MPa, and 50 MPa Vertical Stress. The red X indicates the interpreted critical clay fraction. 186
Figure 5-32: Comparison of the applied axial effective stress against the axial effective stress at the midpoint of the specimen corrected for sidewall friction forces in tall CRS test CRS1652 a 90% silt material. 187
Figure 5-33: Comparison of the applied axial effective stress against the distributed axial effective stress corrected for sidewall friction forces in tall CRS test CRS1652 a 90% silt material. 187
Figure 5-34: Comparison of the uncorrected compression curve against the compression curve corrected for sidewall friction forces in tall CRS test CRS1652 a 90% silt material. 188
Figure 5-35: Comparison of the measured effective stress compression curve and the effective stress compression curve corrected for excess pore pressures during consolidation of specimen TX1484, a RGoM_EI specimen. 188
Figure 5-36: Average permeability presented by porosity for each test clay content as measured through constant head testing or constant rate of strain tests. 189
Figure 5-37: Average permeability (k) presented by axial effective stress level for each test clay content as measured through constant head testing or CRS tests. Solid lines indicate a log-log linear regression. 189

Figure 5-38: Average coefficient of consolidation (C_v) presented by axial effective stress level for each test clay content as measured through high stress CRS tests. Solid lines indicate a log-log linear regression..... 190
Figure 5-39: Average uniaxial compressibility of soil grains (M_v) presented by axial effective stress level for each test clay content as measured through high stress CRS tests. Solid lines indicate a log-log linear regression..... 190
Figure 5-40: Top log-log linear regression of uniaxial grain compressibility by effective axial stress for each studied soil clay content. Middle log-log linear regression of permeability by effective axial stress for each studied soil clay content. Bottom log-log linear regression of coefficient of consolidation by effective axial stress for each studied soil clay content from the high stress CRS tests..... 191
Figure 6-1: AIC selected P-wave arrival time for 25 MPa stress level of test CRS1672 a RGoM_EI specimen. The red line indicates the arrival time select by the automated method..... 224
Figure 6-2: AIC series for P-wave arrival time selection for 25 MPa stress level of test CRS1672 a RGoM_EI specimen. The red line indicates the global minimum of the AIC series that corresponds to the automated selected arrival time..... 224
Figure 6-3: Comparison of S-waves collected at a 5 MPa effective stress level and a 25 MPa effective stress level during TCRS test CRS 1672 performed on a RGoM_EI test specimen. 225
Figure 6-4: Example comparison of relative percent difference in wave velocity for S wave measured at 5 MPa in CRS1688 a 60% clay specimen. The frequency represents the cutoff frequency input for each filter, the cutoff frequency was incremented as discussed in Section 6.2. The presented difference in velocity is the percent difference between the calculated velocity with the associated cutoff frequency and filter combination relative to the calculated velocity without filtering..... 225
Figure 6-5: Comparison of processed and unprocessed S-waves collected at a 5 MPa stress level of CRS1688 a 60% clay specimen. The processed S wave has been subjected to a moving average interval of 11 points and a 7 kHz high pass filter. 226
Figure 6-6: Determination of inherent delay in the system when measuring P Waves. The delay was selected as the Y intercept of a linear fit through the dummy measurements and determined to be 0.00000211 seconds. 226
Figure 6-7: Determination of inherent delay in the system when measuring S Waves. The delay was selected as the Y intercept of a linear fit through the dummy measurements and determined to be 0.00000121 seconds. 227
Figure 6-8: Measured P wave velocity by axial effective stress for 10% clay specimens. 228
Figure 6-9: Measured S wave velocity by axial effective stress for 10% clay specimens. 228
Figure 6-10: Measured P wave velocity by axial effective stress for 20% clay specimens. 229
Figure 6-11: Measured S wave velocity by axial effective stress for 20% clay specimens. 229
Figure 6-12: Measured P wave velocity by axial effective stress for 30% clay specimens. 230
Figure 6-13: Measured P wave velocity by axial effective stress for 30% clay specimens. 230
Figure 6-14: Measured P wave velocity by axial effective stress for 40% clay specimens. 231
Figure 6-15: Measured P wave velocity by axial effective stress for 40% clay specimens. 231
Figure 6-16: Measured P wave velocity by axial effective stress for 50% clay specimens. 232
Figure 6-17: Measured P wave velocity by axial effective stress for 50% clay specimens. 232
Figure 6-18: Measured P wave velocity by axial effective stress for 60% clay specimens. 233

Figure 6-19: Measured P wave velocity by axial effective stress for 60% clay specimens. 233
Figure 6-20: Measured P wave velocity by axial effective stress for RGoM_EI specimens. 234
Figure 6-21: Measured P wave velocity by axial effective stress RGoM_EI specimens. 234
Figure 6-22: Measured P wave velocity by axial effective stress for all studied silt-clay mixtures. 235
Figure 6-23: Measured S wave velocity by axial effective stress for all studied silt-clay mixtures 235
Figure 6-24: Calculated shear modulus (G) by axial effective stress for all studied silt-clay mixtures..... 236
Figure 6-25: Calculated constrained modulus (M) by axial effective stress for all studied silt-clay mixtures. 236
Figure 6-26: Calculated bulk modulus (K) by axial effective stress for all studied silt-clay mixtures. 237
Figure 6-27: Calculated Young's modulus (E) by axial effective stress for all studied silt-clay mixtures. 237
Figure 6-28: Calculated Lame's first parameter (λ) by axial effective stress for all studied silt-clay mixtures. 238
Figure 6-29: Calculated Poisson ratio (ν) by axial effective stress for all studied silt-clay mixtures. 238
Figure 6-30: Calculated shear modulus (G) by bulk soil density for all studied silt-clay mixtures. 239
Figure 6-31: Calculated constrained modulus (M) by bulk soil density for all studied silt-clay mixtures. 239
Figure 6-32: Calculated bulk modulus (K) by bulk soil density for all studied silt-clay mixtures. 240
Figure 6-33: Calculated Young's modulus (E) by bulk soil density for all studied silt-clay mixtures. 240
Figure 6-34: Calculated Lame's first parameter λ) by bulk soil density for all studied silt-clay mixtures. 241
Figure 6-35: Calculated Poisson's ratio (ν) by bulk soil density for all studied silt-clay mixtures. 241
Figure 6-36: Average measured P wave velocity in Tall CRS tests by clay content (% clay of specimen mass) at 6 effective stress levels ,1 MPa, 5 MPa, 10 MPa, 15 MPa, 20 MPa, and 25 MPa as indicated in the plot. 242
Figure 6-37: Average measured S wave velocity in Tall CRS tests by clay content (% clay of specimen mass) at 6 effective stress levels ,1 MPa, 5 MPa, 10 MPa, 15 MPa, 20 MPa, and 25 MPa as indicated in the plot. 242
Figure 6-38: Comparison of P-waves collected at a 5 MPa effective stress level and a 25 MPa effective stress level during TCRS test CRS 1672 performed on a RGoM_EI test specimen. 243
Figure 6-39: Comparison of P-waves collected at a 5 MPa effective stress level and a 25 MPa effective stress level during TCRS test CRS 1700 performed on a 10% clay test specimen. 243
Figure 6-40: Comparison of S-waves collected at a 5 MPa effective stress level and a 25 MPa effective stress level during TCRS test CRS 1672 performed on a RGoM_EI test specimen. 244
Figure 6-41: Comparison of S-waves collected at a 5 MPa effective stress level and a 25 MPa effective stress level during TCRS test CRS 1700 performed on a 10% clay test specimen. 244
Figure 6-42: Ratio of the P wave velocity to the S wave velocity at each velocity measurement stress from 1 to 30 MPa, for the tested silt and clay mixtures. 245
Figure 6-43: P wave velocity power equation A parameter by specimen clay content. A parameter from power equation fits for P wave measurements from individual TCRS tests were averaged over clay contents and plotted by clay content. The 30% clay specimens A parameter were not average instead CRS1698s value was used for a better fit. The data was fit linearly in segments to capture observed trends. The linear fit equations shown can be used to provide the A parameter for P waves as a function of clay content. 246

Figure 6-44: P wave velocity power equation B parameter by specimen clay content. B parameter from power equation fits for individual TCRS tests were averaged over clay content and plotted by clay content. The data was fit linearly to capture observed trends. The linear fit equations shown can be used to provide the B parameter for P waves as a function of clay content..... 246
Figure 6-45: S wave velocity power equation A parameter by specimen clay content. A parameter from power equation fits for S wave measurements from individual TCRS tests were averaged over clay contents and plotted by clay content. The data was fit with a second order polynomial to capture observed trends. The linear fit equations shown can be used to provide the A parameter for S waves as a function of clay content. 247
Figure 6-46: S wave velocity power equation B parameter by specimen clay content. B parameter from power equation fits for individual TCRS tests were averaged over clay content and plotted by clay content. The data was fit linearly to capture observed trends. The linear fit equations shown can be used to provide the B parameter for S waves as a function of clay content. 247
Figure 6-47: P wave velocity power models, fit using Equation 6.10 to laboratory measurements published within Marjanovic 2016, Ranjpour 2020, and this study. The fitting parameters are provided within the legend on the plot. 248
Figure 6-48: S wave velocity power models, fit using Equation 6.10 to laboratory measurements published within Ranjpour 2020, and this study. The fitting parameters are provided within the legend on the plot..... 248
Figure 7-1: Normalized shear stress by axial strain from undrained shear phase of triaxial tests performed on 0% clay content specimens, at two consolidation stress levels 1 MPa and 10 MPa. The red crosses indicate maximum shear stress and the green crosses indicate maximum effective friction angle. 274
Figure 7-2: Example K_0 consolidated undrained compression triaxial test stress path from test TX1475 a 50% clay specimen. K_0 consolidation performed between points A and B (blue points), where the measured K_0 value is σ'_1/σ'_3 at point B. Undrained compression shearing stress path is presented as points B to C (red points). The maximum shear stress is labeled q_{Max}, and the corresponding effective friction angle (α') is represented as the solid line through the origin and q_{Max}. The maximum measured effective friction angle is indicated by the ϕ'_{Max} and the corresponding effective friction angle (α') is represented as the dashed line through the origin and ϕ'_{Max}. The p-q space friction angle (α') is related to the Mohr-Coulomb friction angle (ϕ') by $Sin\phi' = Tan(\alpha')$. 274
Figure 7-3: Normalized shear stress (q) by normalized average effective stress (p') from undrained shear phase of triaxial tests performed on 0% clay content specimens, at two consolidation stress levels 1 MPa and 10 MPa. The red crosses indicate maximum shear stress and the green crosses indicate maximum effective friction angle. 275
Figure 7-4: Normalized shear induced pore pressures from undrained shear phase of triaxial tests performed on 0% clay content specimens, at two consolidation stress levels 1 MPa and 10 MPa..... 275
Figure 7-5: Normalized shear stress by axial strain from undrained shear phase of triaxial tests performed on 10% clay content specimens, at two consolidation stress levels 1 MPa and 10 MPa. The red crosses indicate maximum shear stress and the green crosses indicate maximum effective friction angle..... 276

Figure 7-6: Normalized shear stress (q) by normalized average effective stress (p') from undrained shear phase of triaxial tests performed on 10% clay content specimens, at two consolidation stress levels 1 MPa and 10 MPa. The red crosses indicate maximum shear stress and the green crosses indicate maximum effective friction angle. 276
Figure 7-7: Normalized shear induced pore pressures from undrained shear phase of triaxial tests performed on 10% clay content specimens, at two consolidation stress levels 1 MPa and 10 MPa..... 277
Figure 7-8: Normalized shear stress by axial strain from undrained shear phase of triaxial tests performed on 20% clay content specimens, at two consolidation stress levels 1 MPa and 10 MPa. The red crosses indicate maximum shear stress and the green crosses indicate maximum effective friction angle. 277
Figure 7-9: Normalized shear stress (q) by normalized average effective stress (p') from undrained shear phase of triaxial tests performed on 20% clay content specimens, at two consolidation stress levels 1 MPa and 10 MPa. The red crosses indicate maximum shear stress and the green crosses indicate maximum effective friction angle. 278
Figure 7-10: Normalized shear induced pore pressures from undrained shear phase of triaxial tests performed on 20% clay content specimens, at two consolidation stress levels 1 MPa and 10 MPa..... 278
Figure 7-11: Normalized shear stress by axial strain from undrained shear phase of triaxial tests performed on 30% clay content specimens, at two consolidation stress levels 1 MPa and 10 MPa. The red crosses indicate maximum shear stress and the green crosses indicate maximum effective friction angle. 279
Figure 7-12: Normalized shear stress (q) by normalized average effective stress (p') from undrained shear phase of triaxial tests performed on 30% clay content specimens, at two consolidation stress levels 1 MPa and 10 MPa. The red crosses indicate maximum shear stress and the green crosses indicate maximum effective friction angle. 279
Figure 7-13: Normalized shear induced pore pressures from undrained shear phase of triaxial tests performed on 30% clay content specimens, at two consolidation stress levels 1 MPa and 10 MPa..... 280
Figure 7-14: Normalized shear stress by axial strain from undrained shear phase of triaxial tests performed on 40% clay content specimens, at two consolidation stress levels 1 MPa and 10 MPa. The red crosses indicate maximum shear stress and the green crosses indicate maximum effective friction angle. 280
Figure 7-15: Normalized shear stress (q) by normalized effective average effective stress (p') from undrained shear phase of triaxial tests performed on 40% clay content specimens, at two consolidation stress levels 1 MPa and 10 MPa. The red crosses indicate maximum shear stress and the green crosses indicate maximum effective friction angle. 281
Figure 7-16: Normalized shear induced pore pressures from undrained shear phase of triaxial tests performed on 40% clay content specimens, at two consolidation stress levels 1 MPa and 10 MPa..... 281
Figure 7-17: Normalized shear stress by axial strain from undrained shear phase of triaxial tests performed on 50% clay content specimens, at two consolidation stress levels 1 MPa and 10 MPa. The red crosses indicate maximum shear stress and the green crosses indicate maximum effective friction angle. 282
Figure 7-18: Normalized shear stress (q) by normalized average effective stress (p') from undrained shear phase of triaxial tests performed on 50% clay content specimens, at two consolidation stress

levels 1 MPa and 10 MPa. The red crosses indicate maximum shear stress and the green crosses indicate maximum effective friction angle. 282
Figure 7-19: Normalized shear induced pore pressures from undrained shear phase of triaxial tests performed on 50% clay content specimens, at two consolidation stress levels 1 MPa and 10 MPa..... 283
Figure 7-20: Normalized shear stress by axial strain from undrained shear phase of triaxial tests performed on 60% clay content specimens, at two consolidation stress levels 1 MPa and 10 MPa. The red crosses indicate maximum shear stress and the green crosses indicate maximum effective friction angle. 283
Figure 7-21: Normalized shear stress (q) by normalized average effective stress (p') from undrained shear phase of triaxial tests performed on 60% clay content specimens, at two consolidation stress levels 1 MPa and 10 MPa. The red crosses indicate maximum shear stress and the green crosses indicate maximum effective friction angle. 284
Figure 7-22: Normalized shear induced pore pressures from undrained shear phase of triaxial tests performed on 60% clay content specimens, at two consolidation stress levels 1 MPa and 10 MPa..... 284
Figure 7-23: Normalized shear stress by axial strain from undrained shear phase of triaxial tests performed on RGoM_EI specimens, at two consolidation stress levels 1 MPa and 10 MPa. The red crosses indicate maximum shear stress and the green crosses indicate maximum effective friction angle. 285
Figure 7-24: Normalized shear stress (q) by normalized average effective stress (p') from undrained shear phase of triaxial tests performed on RGoM_EI specimens, at two consolidation stress levels 1 MPa and 10 MPa. The red crosses indicate maximum shear stress and the green crosses indicate maximum effective friction angle. 285
Figure 7-25: Normalized shear induced pore pressures from undrained shear phase of triaxial tests performed on RGoM_EI specimens, at two consolidation stress levels 1 MPa and 10 MPa. 286
Figure 7-26: Average maximum normalized shear stress by specimen clay content from undrained shear phase of triaxial tests at two consolidation stress levels 1 MPa and 10 MPa. The range in measured values are shown in the error bars, blue for 1 MPa and red for 10 MPa tests..... 286
Figure 7-27: Average and range of triaxial specimen initial wet density prior to triaxial testing by specimen clay content by mass. The lines provide the range of specimen densities, the blue circles are the average specimen density for the 1 MPa tests and the red diamonds are the average specimen density for the 10 MPa tests. 287
Figure 7-28: Average effective friction angle by specimen clay content measured at the maximum shear stress at two stress levels 1 MPa and 10 MPa. The range in measured values are shown in the error bars, blue for 1 MPa and red for 10 MPa tests..... 287
Figure 7-29: Average maximum effective friction angle by specimen clay content measured during the undrained triaxial shear phase at two stress levels 1 MPa and 10 MPa. The range in measured values are shown in the error bars, blue for 1 MPa and red for 10 MPa tests. 288
Figure 7-30: Average axial strain at maximum shear stress measure by specimen clay content from undrained shear phase of triaxial tests at two consolidation stress levels 1 MPa and 10 MPa. The 0% clay, 10% clay and 20% clay materials were not K_0 consolidated and instead were anisotropically consolidated along a predetermined computer controlled stress path with K value assumed to be K_0. These materials

are not shown due to the difference in consolidation. The range in measured values are shown in the error bars, blue for 1 MPa and red for 10 MPa tests. 288
Figure 7-31: Average axial strain corresponding with the maximum measured friction angle by specimen clay content from undrained shear phase of triaxial tests at two consolidation stress levels 1 MPa and 10 MPa. The range in measured values are shown in the error bars, blue for 1 MPa and red for 10 MPa tests. 289
Figure 8-1: High stress CRS compression curves used to evaluate clay content effects on soil compressibility (Figure 5-9 reproduced) 315
Figure 8-2: Average void ratio/porosity from the high stress CRS tests of each studied mixture at a 1 MPa, 2 MPa, 5 MPa ,10 MPa, 15 MPa, 20 MPa, 30 MPa, 40 MPa, and 50 MPa Vertical Stress. The red X indicates the interpreted critical clay fraction. 315
Figure 8-3: Flow chart for evaluating grain supported vs. clays supported or transitional material from Thevanayagam, Shenthan, Mohan, & Liang (2002) 316
Figure 8-4: Void ratio by specimen clay content from High Stress CRS test at 1 MPA stress level. Three determinations for the threshold fines content are provided. The estimated minimum density by experimental analyses. An analytical minimum as the intersection of the theoretical minimum coarse grained and theoretical minimum fine grained void ratios per the Lade, Liggio Jr., & Yamamuro (1998) equations. And a semi-analytical analysis per the Rahman, Lo, & Gnanendran (2009) equation. 316
Figure 8-5: Void ratio by specimen clay content from High Stress CRS test at 10 MPA stress level. Two determinations for the threshold fines content are provided. The estimated minimum density by experimental analyses. An analytical minimum as the intersection of the theoretical minimum coarse grained and theoretical minimum fine grained void ratios per the Lade, Liggio Jr., & Yamamuro (1998) equations. 317
Figure 8-6: Void ratio by specimen clay content from High Stress CRS test at 50 MPA stress level. Two determinations for the threshold fines content are provided. The estimated minimum density by experimental analyses. An analytical minimum as the intersection of the theoretical minimum coarse grained and theoretical minimum fine grained void ratios per the Lade, Liggio Jr., & Yamamuro (1998) equations. 317
Figure 8-7: Theoretical and measured minimum void ratio for non-plastic fines in sand from Hang, Wu, Cheng, Li, & Chen (2024) 318
Figure 8-8: Variation in $F_{C\ max}$ by Coefficient of Uniformity for the fines using Equation 8.10 Hang, Wu, Cheng, Li, & Chen (2024). $FC_{in\text{-}max}$ varies between 49.9% and 95.4%, decreasing with and increasing C_u^f. 318
Figure 8-9: Void ratio by specimen clay content from High Stress CRS test at a 1 MPA stress level. Estimates of $FC_{in\ min}$, FC_{th} and $FC_{in\ max}$ are provided to illustrate the different Cases for grain supported or fines supported materials. 319
Figure 8-10: Void ratio by specimen clay content from High Stress CRS test at a 50 MPA stress level. Estimates of $FC_{in\ min}$, FC_{th} and $FC_{in\ max}$ are provided to illustrate the different Cases for grain supported or fines supported materials. 319
Figure 8-11: Variation in the compression ratio (CR) by specimen clay content. The blue points present CR between 0.5 to 1 MPA, the red points present CR between 1 to 50 MPa, and the green present CR between 50 to 90 MPa. 320

Figure 8-12: K_0 measurements during the triaxial consolidation stage for the RGoM_EI specimens. 320
Figure 8-13: K_0 values by specimen clay content measured during consolidation phase of the triaxial tests. The black points present the average K_0 at a 1 MPa stress level with corresponding gray error bars for the minimum and maximum K_0 values. The red points present the average K_0 at a 10 MPa stress level with corresponding blue error bars for the minimum and maximum K_0 values. 321
Figure 8-14: Lateral stress ratio at rest (K_0) by maximum friction angles measured during shearing. The dashed line represents the Jaky (1944) correlation, and the Solid line represents the Federico (2008) correlation. 321
Figure 8-15: Mohr's circles of stress for K_0 condition (mobilized friction angle) and failure friction angle from (Federico, 2021). 322
Figure 8-16: Example calculation of mobilized friction angle at maximum consolidation stress from triaxial consolidation phase. The mobilized friction angle (α' mob.) is the angle from the origin through the maximum consolidation stress (Point B) represented by the solid line. The effective failure angle is the dashed line from the origin through Point C. The stress path presents is TX1475 a 50% clay material. 322
Figure 8-17: Measured mobilized friction angle during consolidation phase by maximum friction angle measured during shear phase. The black line indicates the 0.618 mobilization ratio in Equation 8.16 from (Federico, 2021) for reference. The red line provides the best fit linear correlation of a slope of 0.513 from the triaxial tests. 323
Figure 8-18: K_0 values by specimen clay content measured during the consolidation phase of the triaxial tests and predicted using Equation 8.16. The open points represent the predicted values using Equation 8.16. 323
Figure 8-19: Permeability by porosity measured during high stress CRS testing. 324
Figure 8-20: Permeability by specimen clay content at equivalent porosities of 0.4, 0.35, 0.3, and 0.25. 324
Figure 8-21: Permeability by vertical effective stress measured during high stress CRS testing. 325
Figure 8-22: Shear wave velocity by pressure wave velocity from the TCRS tests. Three shear wave velocity correlations are presented from Castagna, Batzle, & Eastwood (1985), Han (1986), and Brocher (2005). 325
Figure 8-23: Average specimen density by clay content based on phase relations and measured volumetric strain at 6 axial stress from the TCRS tests. 326
Figure 8-24: Average S wave velocity and P wave velocity by clay content from the TCRS tests. 326
Figure 8-25: Hashin-Shtrikman bounds and average for the bulk modulus of the silt-clay mixtures tested; calculated from the mixture bulk modulus and shear modulus provided in Table 8-3 327
Figure 8-26: Hashin-Shtrikman upper bounds for the shear modulus of the silt-clay mixtures tested; calculated from the mixture bulk modulus and shear modulus provided in Table 8-3 327
Figure 8-27: Bulk modulus and shear modulus for 10% clay mixtures calculated from wave measurements from Tall CRS testing. The Hashin-Shtrikman bounds, and average are calculated from the mixture bulk modulus and shear modulus provided in Table 8-3. 328
Figure 8-28: Bulk modulus and shear modulus for 20% clay mixtures calculated from wave measurements from Tall CRS testing. The Hashin-Shtrikman bounds, and average are calculated from the mixture bulk modulus and shear modulus provided in Table 8-3. 328

Figure 8-29: Bulk modulus and shear modulus for 30% clay mixtures calculated from wave measurements from Tall CRS testing. The Hashin-Shtrikman bounds, and average are calculated from the mixture bulk modulus and shear modulus provided in Table 8-3. 329
Figure 8-30: Bulk modulus and shear modulus for 40% clay mixtures calculated from wave measurements from Tall CRS testing. The Hashin-Shtrikman bounds, and average are calculated from the mixture bulk modulus and shear modulus provided in Table 8-3. 329
Figure 8-31: Bulk modulus and shear modulus for 50% clay mixtures calculated from wave measurements from Tall CRS testing. The Hashin-Shtrikman bounds, and average are calculated from the mixture bulk modulus and shear modulus provided in Table 8-3. 330
Figure 8-32: Bulk modulus and shear modulus for 60% clay mixtures calculated from wave measurements from Tall CRS testing. The Hashin-Shtrikman bounds, and average are calculated from the mixture bulk modulus and shear modulus provided in Table 8-3. 330
Figure 8-33: Bulk modulus and shear modulus for RGoM_EI clay mixtures calculated from wave measurements from Tall CRS testing. The Hashin-Shtrikman bounds, and average are calculated from the mixture bulk modulus and shear modulus provided in Table 8-3. 331
Figure 8-34: Bulk Modulus by axial effective stress (Figure 6-26). 331
Figure 8-35: Shear modulus by axial effective stress (Figure 6-24). 332
Figure 8-36: Average axial strain corresponding with the measured maximum shear stress by specimen clay content from undrained shear phase of triaxial tests at two consolidation stress levels 1 MPa and 10 MPa. (Figure 7-28). 332
Figure 8-37: Average normalized shear strength by specimen clay content measured during the shear phase of the triaxial tests. The black points present the average q/σ'_V at a 1 MPa stress level with corresponding gray error bars for the minimum and maximum q/σ'_V values. The red points present the average q/σ'_V at a 10 MPa stress level with corresponding blue error bars for the minimum and maximum q/σ'_V values. 333
Figure 8-38: Average effective friction angle by specimen clay content measured during the shear phase of the triaxial tests. The black points present the average ϕ' at a 1 MPa stress level with corresponding gray error bars for the minimum and maximum ϕ' values. The red points present the average ϕ' at a 10 MPa stress level with corresponding blue error bars for the minimum and maximum ϕ' values. 333
Figure 8-39: Effective friction angle by V_{grain} (1-(Porosity+V_{clay})). The open symbols are the 1 MPa tests and the closed symbols are the 10 MPa tests. 334
Figure 9-1: High stress CRS compression curves used to evaluate clay content effects on soil compressibility (Figure 5-9 reproduced) 364
Figure 9-2: High Stress CRS compression curves (solid lines) fit with a log linear σ'_V and void ratio model (dashed lines). 364
Figure 9-3: High Stress CRS compression curves (solid lines) fit with a log linear σ'_V and porosity model (dashed lines). 365
Figure 9-4: Plot of reference void ratio at σ'_V of 0.5 MPa as a function of clay content used in the compression models. The top (blue) equation corresponds to method 1 where the clay size fraction of Min-U-Sil is not accounted in the clay content. The middle equation (orange) includes the clay sized particles of Min-U-Sil material in the clay content determination. The bottom equation (grey) accounts for mineralogical clay content as discussed in Section 9-2. 365

Figure 9-5: Plot of calibrated compression index (C_C) as a function of clay content used in the compression models. The top (blue) equation corresponds to method 1 where the clay size fraction of Min-U-Sil is not accounted in the clay content. The middle equation (orange) includes the clay sized particles of the added Min-U-Sil material in the clay content determination. The bottom equation (grey) accounts for mineralogical clay content as discussed in Section 9-2. 366
Figure 9-6: Plot of reference porosity at σ'_V of 0.5 MPa as a function of clay content used in the compression models. The top (blue) equation corresponds to method 1 where the clay size fraction of Min-U-Sil is not accounted in the clay content. The middle equation (orange) includes the clay sized particles of the added Min-U-Sil material in the clay content determination. The bottom equation (grey) accounts for mineralogical clay content as discussed in Section 9-2. 366
Figure 9-7: Plot of calibrated compression index ($C_{C\phi}$) as a function of clay content used in the compression models. The top (blue) equation corresponds to method 1 where the clay size fraction of Min-U-Sil is not accounted in the clay content. The middle equation (orange) includes the clay sized particles of the added Min-U-Sil material in the clay content determination. The bottom equation (grey) accounts for mineralogical clay content as discussed in Section 9-2. 367
Figure 9-8: Evaluation of the 0% clay High Stress CRS compression curve by the six clay content dependent compression models. The solid black line is the 0% clay test compression curve. The solid colored lines represent the void ratio model of Equation 9.2, also denoted as e. The dashed colored lines represent the porosity model of Equation 9.3, also denoted as n. The colors denote the method used to determine clay content where blue corresponds to method 1, orange to method 2 and grey to method 3 as detailed within section 9-2. 367
Figure 9-9: Evaluation of the 30% clay High Stress CRS compression curve by the six clay content dependent compression models. The solid green line is the 30% clay test compression curve. The solid colored lines represent the void ratio model of Equation 9.2, also denoted as e. The dashed colored lines represent the porosity model of Equation 9.3, also denoted as n. The colors denote the method used to determine clay content where blue corresponds to method 1, orange to method 2 and grey to method 3 as detailed within section 9-2 368
Figure 9-10: Evaluation of the RGoM_EI clay High Stress CRS compression curve by the six clay content dependent compression models. The solid red line is the RGoM_EI clay test compression curve. The solid colored lines represent the void ratio model of Equation 9.2, also denoted as e. The dashed colored lines represent the porosity model of Equation 9.3, also denoted as n. The colors denote the method used to determine clay content where blue corresponds to method 1, orange to method 2 and grey to method 3 as detailed within section 9-2 368
Figure 9-11: Borehole caliper measurements, and bulk density by depth below mudline in feet, from adnVISION logging while drilling measurements at IODP expedition 308 site U1324. The blue caliper data points indicate measurements less than 10 inches in diameter, the orange caliper points are greater than 10 inches and have been removed from the data processing. Porosity and bulk density are from adnVISION logging while drilling measurements (orange) and moisture and shipboard density testing (green) Flemings, Behrmann, & John (2006). Clay content from laboratory testing presented in Sawyer, Jacoby, Flemings, & Germaine (2008). 369
Figure 9-12: Compression models using the slope and density intercept at 1 MPa from Table 9-2 for the high stress CRS tests. 369

Figure 9-13: Pressure at IODP Expedition 308 Site U1324. Lithostatic pressure from integrating the bulk density measurements on core samples. Hydrostatic pressure for reference. Pore pressure measurements from Long, Flemings, Dugan, Germaine, & Ferrell (2008). Pore pressure gradient considered in calculations fit to pore pressure measurements. 370
Figure 9-14: Left , porosity from moisture and shipboard density testing (blue) Flemings, Behrmann, & John (2006) and clay content from laboratory testing Sawyer, Jacoby, Flemings, & Germaine (2008). Right estimated vertical effective stress from integrating bulk density measurements and Equations 9.4 and 9.5 for RGoM_EI clay (red), Min-U-Sil 40 (black), and a variable clay content based on the compression models presented in Figure 9-13 (blue). 371
Figure 9-15: Permeability by porosity from High Stress CRS experiments. 372
Figure 9-16: Permeability by porosity measurements from High Stress CRS measurements, solid lines indicate the geometric mean permeability by porosity model from Reece (2021). 372
Figure 9-17: Permeability by porosity measurements from High Stress CRS measurements, solid lines indicate the shifted geometric mean permeability by porosity model from Reece (2021). The model has been shifted to omit 0% clay and use 10% clay data is the lower bound clay content. 373
Figure 9-18: Values of $\log_{10}(k_{0.5})$ adopted from Casey (2014) plotted against liquid limit. 373
Figure 9-19: Values of γ from Casey (2014) plotted against liquid limit. 374
Figure 9-20: Permeability by porosity measurements from High Stress CRS measurements, solid lines indicate modeled permeability as function of the Liquid Limit from Casey (2014). 374
Figure 9-21: Permeability by porosity measurements from High Stress CRS measurements, solid lines indicate modeled permeability as function of clay fraction and void ratio from Yang & Aplin (2010). The clay fraction for the model is calculated using method 1, classifying clay by particle size considering the clay particle of RGoM_EI only. 375
Figure 9-22: Permeability by porosity measurements from High Stress CRS measurements, solid lines indicate modeled permeability as function of clay fraction and void ratio from Yang & Aplin (2010). The clay fraction for the model is calculated using method 2, classifying clay by particle size considering both the clay particles of Min-U-Sil and RGoM_EI. 375
Figure 9-23: Permeability by porosity measurements from High Stress CRS measurements, solid lines indicate modeled permeability as function of clay fraction and void ratio from Yang & Aplin (2010). The clay fraction for the model in Figure 9-16 was calculated using method 3, classifying clay by mineralogy and considering the mineralogical clay fraction of RGoM_EI. 376
Figure 9-24: Permeability by vertical effective stress from High Stress CRS testing. 376
Figure 9-25: Regression lines for the critical state friction angle experimental data presented in Casey (2014) Figure 6-52. The regression lines are of the form $\phi'_{cs} = A(0.001\sigma'_V\ [MPa])^B$. Figures 9-26 and 9-27 provide the correlations for A and B respectively. 377
Figure 9-26: Correlation between the parameter A and liquid limit for the critical state friction angle regressions in Figure 9-21 from Casey (2014). 377
Figure 9-27: Correlation between the parameter B and liquid limit for the critical state friction angle regressions in Figure 9-21 from Casey (2014). 378
Figure 9-28: Measured small strain shear modulus G_{max}, normalized to the correlation void ratio function by effective stress state parameter. Orange line represents the power of the test data to evaluate the n value in Equation 9.13. 378

Figure 9-29: Small strain shear modulus G_{max} computed by shear wave velocity and density, by the stress components of Equation 9.13. The void ratio function is from Kim & Novak (1981) and the data are linearly fit to determine S for Equation 9.13. 379
Figure 9-30: The product of the average S fitting value and void ratio function by void ratio for the three empirical correlations compared. The average S fitting values are the average of the values presented in Table 9-5 for the reference stress of 1 atmosphere 0.1013 MPa. 379
Figure 9-31: S fitting parameter for an atmospheric reference stress by clay content (left) and by liquid limit (right) for the Kim & Novak (1981) correlation. 380
Figure 9-32: n fitting parameter for an atmospheric reference stress by clay content (left) and by liquid limit (right) for the Kim & Novak (1981) correlation. 380
Figure 9-33: S fitting parameter for an atmospheric reference stress by clay content (left) and by liquid limit (right) for the Shibuya & Tanaka (1996) correlation. 381
Figure 9-34: n fitting parameter for an atmospheric reference stress by clay content (left) and by liquid limit (right) for the Shibuya & Tanaka (1996) correlation. 381
Figure 9-35: S fitting parameter for an atmospheric reference stress by clay content (left) and by liquid limit (right) for the Shibuya, Hwang, & Mitachi, (1997) correlation. 382
Figure 9-36: n fitting parameter for an atmospheric reference stress by clay content (left) and by liquid limit (right) for the Shibuya, Hwang, & Mitachi (1997) correlation. 382
Figure 9-37: Measured G_{max} (data points) by Axial Effective Stress Shibuya & Tanaka (1996), Shibuya, Hwang, & Mitachi, (1997) or Mean Effective Stress Kim & Novak (1981), with the corresponding fit empirical correlations for TCRS 1652 a 10% clay mixture. 383
Figure 9-38: Measured G_{max} (data points) by Axial Effective Stress Shibuya & Tanaka (1996), Shibuya, Hwang, & Mitachi (1997) or Mean Effective Stress Kim & Novak (1981), with the corresponding fit empirical correlations for TCRS 1632 a 30% clay mixture. 383
Figure 9-39: Measured G_{max} (data points) by Axial Effective Stress Shibuya & Tanaka (1996), Shibuya, Hwang, & Mitachi (1997) or Mean Effective Stress Kim & Novak, (1981), with the corresponding fit empirical correlations for TCRS 1693 a 50% clay mixture. 384
Figure 9-40: Measured G_{max} (data points) by Axial Effective Stress Shibuya & Tanaka (1996), Shibuya, Hwang, & Mitachi, (1997) or Mean Effective Stress Kim & Novak, (1981), with the corresponding fit empirical correlations for TCRS 1672 a RGoM_EI specimen. 384
Figure 9-41: Borehole caliper and shear wave velocity from wireline measurements, and bulk density by depth below mudline in feet from logging while drilling measurements, at IODP expedition 308 site U1324. The blue caliper data points indicate measurements less than 10 inches in diameter, the orange caliper points are greater than 10 inches and have been removed from the data processing. 385
Figure 9-42: Lithostatic stress, hydrostatic stress and void ratio by depth below mudline from IODP expedition 308 site U1324. The lithostatic stress was calculated by integrating the logging while drilling density logs. Porosity is from logging while drilling neutron porosity measurements. 386
Figure 9-43: Shear modulus at site U1324 calculated from wireline dipole sonic imager velocity logs and logging while drilling density logs. 387
Figure 9-44: Linear best fit lines correlating the S and n parameters for the Shibuya & Tanaka (1996) void ratio function of equation 9.13 by specimen clay content. 387

Figure 9-45: Shear modulus calculated from bulk density and wave velocity (left) and shear modulus estimated by the void ratio from Equation 9.13 by Kim & Novak (1981), Shibuya & Tanaka (1996), Shibuya, Hwang, & Mitachi (1997), and a modified version of Shibuya & Tanaka (1996) by depth below mudline. The modified version of the Shibuya & Tanaka (1996) void ratio expression adjusts the S and n fitting parameters based on clay content per the linear best fit lines provided in Figure 9-43. The coefficient of determination (R^2) is provided on the right plot. 388
Figure 9-46: Clay content by depth below mudline in feet from Sawyer, Jacoby, Flemings, & Germaine (2008). Shear modulus calculated from bulk density from logging while drilling measurements and wave velocity from dipole sonic imager wireline measurements. An estimated shear modulus using the modified version of Shibuya & Tanaka (1996) by depth below mudline is shown for comparison to the calculated shear modules from density and velocity measurements. The modified version of the Shibuya & Tanaka (1996) void ratio expression adjusts the S and n fitting parameters based on clay content per linear best fit lines provided in Figure 9-44. 389
Figure 9-47: Poisson's ratio by pressure wave velocity from the TCRS tests. Two correlations are presented from calculating Poisson's ratio from the estimated shear wave using the Castagna, Batzle, & Eastwood (1985) V_P-V_S relationship, and a correlation presented in Brocher (2005). 390
Figure 9-48: Lateral stress ratio (K_0) as a function of the dynamic Poisson's ratio solid line and as a function effective friction angle using the Federico (2021) equation discussed in Chapter 8. 390
Figure 9-49: Borehole caliper wireline measurements, lithostatic stress from integrating density measurements on core samples, and pore pressure calibrated to pore pressure measurements presented in Figure 9-13 by depth below mudline at IODP expedition 308 site U1324. The blue caliper data points indicate measurements less than 10 inches in diameter, the orange caliper points are greater than 10 inches and have been removed from the data processing. 391
Figure 9-50: Clay content by depth below mudline in feet from Sawyer, Jacoby, Flemings, & Germaine (2008). Shear wave velocity, and pressure wave velocity by depth below mudline from dipole sonic imager wireline measurements at Site U1324. The measurements are filtered to remove measurements from a borehole diameter exceeding 10 inches. 392
Figure 9-51: Effective friction angle from clay content, Poisson's ratio calculated from velocity wireline measurements, and lateral stress ratio from effective friction angle using Equation 8.16 and from Poisson's ratio using Equation 9.15 at Site U1324. The calculations are filtered to remove measurements from a borehole diameter exceeding 10 inches. 393
Figure 9-52: Lithostatic stress, least horizontal stress (σ_h) by the lateral stress ratio from friction angle and Poisson's Ratio, and hydrostatic stress by depth, filtered to exclude measurements from a borehole exceeding 10 inches in diameter. 394

CHAPTER 1. Introduction

1-1 Background

Geotechnical engineers separate soil behaviors into two classifications for fabric control of the mechanical properties, granular soils (sands and gravels) and cohesive soils (silts and clays). Both soil classifications display unique behaviors to their supporting mechanism, that serve as the basis for separating the materials. Within the natural world soils are typically comprised of a multitude of particle sizes and minerals representing intermediary mixtures of grain supported and clay supported (cohesive) soils. Despite the prevalence in nature, variations in material properties due to small changes in lithology is not typically accounted for in engineering parameters due to a limited understanding of how to quantify these effects. Soil lithology, specifically the clay content of soil, is thought to play a significant role in the mechanical properties of soil.

This thesis details a laboratory program performed to investigate the mechanical properties of lithology controlled granular soils and cohesive soils. The work focuses on lithology controlled mixtures created by a parent offshore sediment; Gulf of Mexico Eugene Island (GoM_EI) clay, collected offshore of Louisiana, USA during the 1990s as document in Stump, (1998). The GoM_EI clay is amended with a manufactured quartz silt product Min-U-Sil 40, for lithology control. Resedimentation techniques are used in the laboratory program to create reproducible, homogenous test specimens to investigate the systematic variation of soil behavior with variations in the clay fraction. Min-U-Sil 40, a crushed quartz material by US Silica, was admixed with RGoM_EI to lower the clay fraction and to be the grains for grain supported behaviors. Specimens with clay mass fractions between 0% and 63% clay were subjected to geotechnical laboratory testing. The laboratory program investigated the variation in mechanical properties with variation in clay content by measuring the compressibility and permeability of the silt-clay mixtures up to stresses of 90+ MPa, the dynamic properties of the mixtures by shear wave and

pressure wave velocity measurements to an effective stress of up to 30 MPa, and the mechanical strength properties by K_0 consolidated undrained compression shear testing at effective pre-shear stresses of 1 MPa and 10 MPa.

The overall goal of this work is to advance the understanding of soil behavior for mixed silt and clay soils. The research aims to present the effects of clay content on soil engineering parameters within the framework of stress dependent behaviors for fine-grained soils.

1-2 Thesis Scope and Objectives

The goal of this dissertation is to gain insights into the influence of clay content on the mechanical properties of silt and clay mixtures. The overall intent of this research is to characterize the behaviors of the silt and clay mixtures to provide a basis of reference for the sensitivity of engineering parameters to clay content. This objective is achieved through a geotechnical laboratory testing program performed on resedimented specimens with clay mass fractions ranging from 0% to 63% (natural clay content of GoM_EI). The results of the experiments are discussed relative to the behaviors of weakly cemented mudrocks similar to those observed in offshore drilling in the Gulf of Mexico.

1-3 Organization of the Thesis

This thesis is organized into ten chapters.

Chapter Two presents a literature review providing context and progression of research into the mechanical properties and engineering parameters for soils of differing lithology. The intent of the chapter is to establish a baseline knowledge in which to discuss experimental results from the laboratory program. Chapter Two presents common engineering parameters used to model both grains supported, and clay supported soil types, and discusses the unique material behaviors and engineering parameters for both soil fabrics.

Chapter Three presents the equipment and testing procedure used within the geotechnical laboratory testing program. Chapter Three includes the creation of the lithology controlled specimens, through resedimentation methods from a bulk clay powder, or the undercompaction method for a granular soil. The procedures for index testing performed to classify the lithology-controlled soil mixtures. The control systems, hardware, software, measurement instrumentation, and any modifications necessary to run the laboratory tests. Specific test procedures for the laboratory tests and pertinent calculations for determining the test results.

Chapter Four presents a brief geologic review of the Gulf of Mexico Eugene Island Clay serving as the parent clay material for the lithology controlled specimens. Chapter Four includes classification of the soil mixtures by the index testing results of the and evaluation of the soil fabric through micrography.

Chapter Five discusses the compressibility and permeability measurements from the laboratory testing program. Chapter Five includes experimental compression results up to a 90 MPa vertical effective stress, trends in material compressibility with clay content and a discussion on the packing of the coarse and fine grained particles. Corrections to the compression behavior due to experimental methods, and the permeability measurements of the lithology controlled specimens to a 90 MPa effective vertical stress.

Chapter Six discusses wave velocity measurements from the tall Constant Rate of Strain (CRS) testing and the corresponding isotropic elastic parameters in the silt and clay mixtures. Chapter Six includes a discussion on processing the waveforms from the velocity measurements including sensitivity of the arrival time to digital filters and data averaging, the automation of the P wave arrival time selection, and the method of selecting the S wave arrival time. Velocity measurements at 1 MPa effective stress increments up to a vertical effective stress of 30 MPa and the corresponding isotropic

elastic parameters are included in Chapter Six. Also included is a discussion on wave velocity models for the silt and clay mixtures and a comparison of the wave velocity measurements to previous studies.

Chapter Seven discusses the strength properties and associated engineering parameters from the laboratory triaxial shear testing. Chapter Seven includes the undrained shear results on the mixtures consolidated to a 1 MPa and 10 MPa pre-shear vertical effective stress. Chapter Seven presents trends in the strength properties by clay content including the maximum shear stress, the effective friction angle, and the strain to both maximum shear stress and maximum effective friction angle.

Chapter Eight presents interpretations of the effects of clay content on the mechanical behaviors and engineering properties of silts and clays as an analog of grain supported and clay supported materials. Chapter Eight includes the application of binary mixture theory to the compression test results for evaluation of the soil packing, determination of the controlling fabric, determination of important fines content limits and the general applicability of binary mixture theory to a high plasticity fines material. Chapter Eight provides interpretations on the effects of specimen clay content on the compressibility, permeability, wave velocities and dynamic properties, and strength properties of the silt clay mixtures.

Chapter Nine present applications of the laboratory testing program results through examples of the effects of clay content on soil material behavior. Chapter Nine presents statistical evaluations of common geotechnical engineering and geology compression, permeability, and correlated small strain shear modulus (G_{Max}) models. Chapter nine includes example field applications for consideration of clay content in the determination of effective stress, estimated G_{Max}, and fracture gradient in an offshore well.

Chapter Ten provides a summary of the results and main conclusions and recommendations for future research.

CHAPTER 2. Review of Engineering Parameters and Behavioral Trends of Grain Supported and Clay Supported Soils

2-1 Introduction

This chapter provides background information based on a review of existing literature for grain and clay mixtures. Generalized behaviors of compressibility, permeability, dynamic mechanical properties, and strength parameters are discussed including observations of trends in the engineering properties by clay content. A brief description on the classification of grain (clastic) and clays and the differences between the fields of geotechnical engineering and geology in classifying and characterizing these materials is provided. The remainder of this chapter is split into four sections each discussing a distinct engineering parameter. Section 2.2 discusses compression (elastic and plastic), Section 2.3 discusses permeability, Section 2.4 discusses the dynamic mechanical properties of soils, and Section 2.5 discusses the mechanical strength properties of soils under static conditions. Each section provides commentary on previous research that has been significant in developing the authors understanding of the behavior of soil through the studied engineering parameter. The intent of this chapter is to provide sufficient background information for understanding to the importance of the experimental program performed for this study.

In the field of geotechnical engineering the classification of soils is commonly performed within the Unified Soil Classification System (USCS) as outlined in ASTM D2487, “Standard Practice for Classification of Soils for Engineering Purposes.” Coarse grained soils are defined by particle size distribution as having a majority of particle sizes greater than 0.075 mm. Figure 2-1 provides a classification plot of soil type by soil particles size per the USCS from clay sized particles up to sand sized (gravel particle sizes are not included in the Figure). Fine grained soils are defined in engineering practice by particle size distribution as having most particles sized less than 0.075 mm. In engineering practice, clays and silts are

differentiated by particle size, where a silt is within the range of 0.075 mm to 0.002 mm and a clay is any particle less than 0.002 mm. Behavior of the soils is classified by an index test referred to as the Atterberg Limits. The Atterberg limits measure the water content at which the fine-grained soils behave plasticly (Plastic Limit), and as a fluid (Liquid Limit). Figure 2-2 provides a typical plot used to classify fine-grained soils by the Atterberg Limits into clays and silts of high or low plasticity as adopted from ASTM D2487.

Geologists classify silts and clays by mineralogy or particle size depending on the application of the classification. Silts are clastic, small particles of broken pieces of older rocks, the same crystalline structures that comprise sands and gravels. Clay minerals are complex aluminum silicates that are defined by the elemental composition of their crystalline structure that is generally composed of two basic units' silica tetrahedron and alumina octahedron. These units combine to make larger sheets which combine into various clay minerals that are differentiated by the order of the sheets or substituted elements as explained further in section 2.5.

2.1. Compression of Soils

The compressibility of soils has been a long-standing topic for study due to the risk settlements impose on earth supported structures, the importance of understanding soil stress states for well drilling, and for estimating consolidation driven pore pressure overpressures. Compression of soil can be separated into four broad categories. Elastic compression of the load carrying soil particles (soil matrix), which is typically considered an instantaneous change due to changes in loading. Plastic deformation of the soil through rearrangement of particles typically through the expulsion of water of saturated soils, or through the reorientation or breakage of grains under changes in loading. The second mechanism is commonly referred to as consolidation for fine grained soils and is time dependent and dependent on the permeability of the soil being loaded. The third mechanism is secondary compression, volume

changes that occur in saturated soils at constant effective stress. The fourth mechanism is shearing failure of the material due to loading in excess of the soils shear strength. This section will provide a literature review of elastic and consolidation-based deformations, secondary compression was not explicitly measured during this laboratory study and therefore will not be discussed. Shear based deformation will be discussed in Section 2.5 which discussed the mechanical strength literature.

Elastic compression is characterized through the application of elastic theory by considering soil as an elastic medium and estimating deformations using elastic parameters. Elastic deformation indicates that the deformations are reversible, which has been found to only occur at very small strain amplitudes less than 10^{-5} in dry granular soils under static loading as found in Hicher (1996) and shown in Figure 2-3 or to strain amplitudes less than 10^{-7} under dynamic loading as shown by Prasad and Meissner (1992). Granular soils were also found to have nonlinear elastic behavior within the recoverable strain range as Young's modulus (E) is dependent on the mean effective stress. For clay supported soils a linear range of deformation behavior is found to occur at small strain amplitudes less than $5X10^{-4}$, but the strains are not recoverable and therefore not elastic as indicated in Santagata, Germaine, and Ladd (2005) and shown in Figure 2-4. Cyclic testing of saturated clays indicates the plastic deformation of clay happens at small strains as shown in Figure 2-5 from Hicher (1996). Due to the very small strains, specialty equipment is required to accurately measure the "elastic" behavior of soils mechanically. Alternative dynamic moduli measurement techniques have been developed to measure the stiffness of the soil at very small strain amplitudes. These techniques include the resonant column apparatus, dynamic measurement through wave propagation, and various others. Comparison of the elastic moduli measured through mechanical loading apparatus adapted to measure sufficiently small strains, to measurements of the elastic moduli through dynamic techniques indicate fairly good agreement between the methods. This agreement is limited to measurements where strain amplitudes are similar Hicher (1996), Marjanovic (2016). Figure 2-6 presents a comparison of the determination of the Young's

Modulus from mechanical measurements and dynamics measurements of like soils adopted from Marjanovic (2016). Variations of “elastic” deformation by changes in soil composition is best characterized by variations of elastic parameters by soil composition. Section 2.4 provides a literature review on dynamic measurements of soil and the effects of soil composition to estimated elastic parameters.

Inelastic compressibility of sediments is a significant topic in both geology and geotechnical engineering, due to inelastic behavior of soil and rocks and the links between density and engineering properties. Compression of soils and rocks typically results in a decrease in volume and increase in density as fluids are expelled due to a reduction in the pore space. It should be noted that geologists commonly refer to the gravitational compression of sediments as compaction while the geotechnical engineering community refers to same phenomenon as consolidation. Herein both are referred to simply as compression, with the understanding that the term compression encompasses the plastic and elastic strain ranges as the elastic strain range for soils is so small it can be considered negligible.

Geological studies on and observations of compression have been performed since the seventeenth century when Niels Steenson observed “attitudes in sedimentary strata may be due to settling of the sediments.” In the 1920 and 1930’s significant advancements in the study of the compressibility of sediments came from the field of geology including a study on the initial deposition and loading of sediments and review of field rock porosities, which led to the correlation of increasing overburden pressure to decreasing porosity Hedberg (1926). Figure 2-7 presents Hedberg’s gradients of porosity by burial depth obtained through measurements of porosity on well cuttings and mapping them by depth. Expanding on Hedberg’s work Athy (1930) presented equations for density and porosity by burial depth, creating models to estimate the behavior. These models were developed through the measurement of

porosity on rock core collected from a continuous well bore. Athy's model for porosity as a function of burial is presented in Figure 2-8.

During the 1920's Karl Terzaghi was publishing his theories on the effective stress principle and one-dimensional consolidation of clastic sediments Terzaghi (1923), Terzaghi (1925). These works provided fundamental understanding on the load sharing that occurs within a porous saturated media between the grain networks and the permeant, as well as the relationship between time, compression of soil grain networks, and the expulsion of permeants. Karl Terzaghi's effective stress principal states that when stress is applied to a saturated porous media the stress is opposed by fluid filling the pores as well as the soil grains this is represented through $\sigma' = \sigma - u$ Equation 2-1.

$$\sigma' = \sigma - u \qquad \text{Equation 2-1}$$

Where:

σ'= Effective Stress (Force by Area)

σ= Total Stress (Force by Area)

u= Pore Pressure (Force by Area)

Terzaghi's effective stress principal links the stress state of the soil to the fluid pressure contained within the soil grain matrix. Karl Terzaghi's work with the compression of soils led to his development of the theory of one-dimensional consolidation, which made simplified assumptions of the compression of saturated soils is linked to the expulsion of pore fluids. Terzaghi's work shows the interrelated nature of permeability of soil with compressibility of the soil, which lead to a separation of behavior by soil type either fine-grained or coarse-grained. That is saturated sandier more permeable soils with a grain supported soil fabric will drain faster with less resultant deformation than saturated fine grained soils that derive their fabric from a clay matrix. The relatively impermeable fine-grained soils more

compressible and undergo long term consolidation settlements as the excess pore pressures from the applied load leaks off.

Terzaghi's theories of effective stress and one dimensional consolidation were applied to understand field observations of pore pressures in excess of hydrostatic conditions within wells drilled in the Gulf of Mexico. Zones of rock with fluid pressures up to 1.87 times hydrostatic conditions were observed in wells in the Gulf of Mexico as reported in Dickinson (1953). Dickinson linked the zones of overpressure to lithologic conditions where relatively permeable sands had been enveloped within impermeable shales (Clays and Silts) this is schematically shown in Figure 2-9, Dickinson (1953). The over pressured fluid within the sands was attributed to fluid being ejected from the continued gravitational compression of the overlying shales, and the lack of drainage within the sands. Identifying potential zones of overpressure pore fluids and understanding the effective earth stress becomes vitally important to the balancing of earth pressures by drilling mud during the drilling of wellbores. A study on the effects of fluid overpressure on earth deformations is presented in Hubbert and Rubey (1959), which indicates large earth deformations manifested as overthrust faults are possible due to zones of lowered effective stresses from over pressured pore fluids. The overpressure being a result of subsiding sediment basins as detailed within Dickinson (1953) and the driver of the overthrust fault is attributed to lateral stresses from plate tectonics. This work provides a link between the observed large earth deformations especially apparent in zones of orogeny and gravitational compression of sediments. Hubbert and Rubey (1959) reinforces the necessity to understand the effective stress state of the rocks during drilling for the design of casing strings and drilling mud density

The total weight of the soil, rock, and fluids vertically above a point in the ground is generally considered as the largest force acting at that point in the ground with few exceptions and is commonly referred to as the lithostatic stress or overburden pressure. Considering Equation 2-1 the effective stress

at that point is the weight of the soil, rock, and fluids minus the fluid pressure at that point. The resultant force is commonly known as the effective overburden stress. Bothe the total and effective overburden stress act in the vertical direction and are heavily influenced by the density of the overburden soils and the continuing compression of the overburden soils, significant research was performed on understanding variations of compressibility between different soils and rocks to evaluate the effects on material compressibility on the effective overburden stress. One significant study on variations of earth stresses is McCulloh (1967), which presents ranges of probable total overburden earth stress and hydrostatic pressures based on the densities of the mineral components of sediments and variations of water density. The estimated ranges are presented in Figure 2-10. Also discussed in McCulloh (1967) were estimates of probable ranges of porosity for sedimentary rocks based on core samples from a large data set encompassed variations in constituent minerals, in situ temperatures, and permeants see Figure 2-11.

With the broad understanding of the connection of soil burial stresses, pore pressures, and vertical earth stresses (total and effective) researchers began to work on generalized compression models for predicting porosity as a function of burial under hydrostatic conditions. The majority of the early models were limited to fits of experimental data from porosity measurements on well cores or cuttings during well drilling such as Hedberg (1926), Athy (1930), Hubbert and Rubey (1959), McCulloh (1967), Nakayama and Van Siclen (1981) and Baldwin and Butler (1985). Comparison of compression models based on porosity measurements from wells in varying geographic locations indicated that compression behaviors was a function of sediment composition, geologic setting, and pore space permeants. This is illustrated in Figure 2-12, a comparison of rock density by depth adopted from Rieke and Chilingar (1974). Experimental laboratory measurements on the compression of sediments lead to the development of new compression models Butterfield (1979). Variations in compressibility of soils between different geotechnical engineering classifications and by intrinsic vs. fabric derived behaviors is

evaluated in Burland (1990). A detailed study on the compressibility of granular soils is presented in Mesri and Vardhanabhuti (2009). Casey, Reece, and Germaine, 2019, present an evaluation of various soil compression models over a large range of effective stresses and conclude that the recommended model is dependent of the plasticity of the soil being compressed. The studies above show that soil compression is dependent on mineralogy, composition, depositional environment, fabric, and a multitude of other specific conditions to the geologic are of interest.

Laboratory compression testing has been performed on both collected core samples (intact natural fabric) and reconstituted specimens (synthetic fabrics). Research into the comparison of the compression behavior of intact specimens and synthetic specimens became a major topic for soil compression research due to the cost of sample collection as compared to sample generation. A detailed study on compression of deep-sea sediments Velde (1996), supported by observations from Wijeyesekera and De Freitas (1976), Taylor and Leonard (1990) and Bryant, et al. (1990), found that the top estimated 300m of soil sediments below the mudline would be subject to natural fabrics influence by the time of deposition (age of the sediment), depositional environment, and the creation of flocculate structures due to chemical bonding of clay particles from the available cations in seawater. Velde hypothesized that around a 300m depth, chemical bonds can be overcome by the gravitational compression of the sediments. Below the 300m limit is where gravity driven mechanical compression is anticipated to be the controlling mechanism for the density of the soil assuming K_0 conditions. Broichhausen, Littke and Hantschel (2005) present a theoretical depth limit of 2,000m where gravity driven mechanical compression is no longer the controlling factor for porosity. Beyond the 2,000m depth Broichhausen, Littke and Hantschel (2005) indicates that temperature dependent chemical compaction processes may be the controlling mechanism for porosity, based on comparison of modeled porosities to measured porosities in the North Sea. Betts (2014) compared laboratory compression tests of a reconstituted clay to in situ porosity measurements below an 1,800m depth and found a reasonable

agreement between the resedimented compression measurements and the in situ porosity measurements with the theoretical limits of Velde (1996) and Broichhausen, Littke and Hantschel (2005). Finnegan (2020) compared laboratory testing on intact and reconstituted marine clay specimens and found that variations in density can be attributed to variations in stress history as well as natural fabrics. Figure 2-13 provides a comparison of the compression behavior of reconstituted specimens and intact specimens to a 100 MPa stress adopted from Finnegan (2020). Figure 2-13 shows the intact specimen to be denser at lower effective stresses than the reconstituted specimens, but at high stresses (>40 MPa) the compression behavior of reconstituted and intact specimens converge. The initial density difference is attributed to the stress history difference of the previously buried intact specimen and reconstituted specimen. The convergence of behaviors at high stresses is attributed to the idea of a material dependent intrinsic compression behavior discussed within Rieke and Chilingar (1974), and Burland (1990). A rigorous study on intrinsic compression behavior in reconstituted specimens is presented within Shipton and Coop (2012), where the authors found that the convergence of a reconstituted soils compression behavior to an intrinsic compression behavior is largely dependent on the lithology and mineralogy of the soil. Where fine grained soils of a uniform lithology are more likely to converge than a more coarse-grained soil of varying mineralogy.

Work has been performed in evaluating the effects of clay mineralogy on the compression behavior of a soil. Some notable studies are Burland (1990), Mondol, Bjorlykke and Jahren (2008), and Casey (2014). Burland (1990) and Casey (2014) provide comparisons on the compression behavior of two databases consisting of compression testing on intact and reconstituted soils up to a 100 MPa maximum compression stress. Figure 2-14 provides a comparison of the compression curves up to a 100 MPa stress for the soils studied within Casey (2014). These studies are comparative to show the variation in soil compressibility with variations in mineralogy and lithology, and both provide a strong link between the liquid limit and compressibility. Mondol, Bjorlykke and Jahren (2008) created specimens of mixtures

of Smectite and Kaolinite clays to provide a direct study on the effects of the clay mineralogy on compression. Chong and Santamarina (2016) and Casey, Reece, and Germaine (2019) provide summaries of porosity models and recommendations for estimating the compression behavior of soils over various stress ranges and accounting for variations due to the mineralogy and soil behavior classification.

The evaluation of the effects clay content on compression behavior has been studied. Hedberg (1926) presents a comparison of the compression behaviors of various clays and sands, presented in Figure 2-15. Figure 2-15 shows under increasing stresses the sand has small decreases in porosity as compared to the clay soils. The observation that soils of lower clay contest are less compressible has been repeatedly observed in studies comparing the compression behavior of intact specimens of varying lithology. Notably D. N. Dewhurst, et al. (1998), which compared the compression behaviors of two intact specimens of the same geologic deposit with their clay content varied by about 27% by mass. Figure 2-16 presents the compression curves from D. N. Dewhurst, et al. (1998) of the two clay specimens with varying clay content and indicates that the two curves may converge at stresses above 30 MPa. Another notable study on the variation of compression behaviors of intact lithology is Yang & Aplin (2004) which directly link compression behavior of mudrocks to the clay content of the mudrock through field testing results.

Many other studies on the variation of compression behavior by lithology through compression testing of reconstituted specimens have been performed some notable studies are Marion, et al. (1992), Pandian, Nagaraj and Raju (1995), Monkul and Ozden (2007), N. Mondol, (2009), Cabalar and Hasan (2013), Simpson and Evans (2016), Chang, Meidani and Deng (2017), and Reece (2021). These studies employ various specimen preparation techniques of sand, silt, and clay mixture and subject the mixed specimens to one dimensional compression testing. These studies indicate that higher clay content soils

are expected to have larger void ratios at low effectives stress levels and be more compressible than lower clay content soils. Figure 2-17 provides an example of a group of compression curves of varying Kaolinite clay contents mixed with sand specimens adopted from Monkul and Ozden (2007). Figure 2-17 shows compression data of soils with clay contents between 4.5% and 42.7% by mass. The compression curves with clay contents less than 30% clay by mass do not show convergence through a 1 MPa stress. Figure 2-18 shows the one dimensional compression curves of a resedimented clay mixed with a manufactured silt specimens, ranging between 34% and 59% clay content by mass adopted from Reece (2021). Figure 2-18 shows a well ordered trend of decreasing void ratio with decreasing clay content at lower stress, and higher compressibility for the higher clay content materials. Figure 2-18 also illustrates a crossing of the compression curves due to the relatively lower compressibility of the 34% clay content specimen and 39% clay content specimen material to the 43% clay content specimen prior to an effective stress of around 2 MPa. This crossing of the compression curves is significant behavior for related specimens of varying lithology, as the crossing indicates the lower clay content materials may be supported by grain to grain contacts and not by the clay fabric.

Lateral Stress Ratio, K, K_0 and K_0 Compression

K is the stress matrix coefficient as discussed within Matthews and Kelly (1967), that relates effective vertical stress to the effective horizontal stress of a formation. K is commonly referred to in geology as the lateral stress ratio. K is defined as the ratio of the horizontal effective stress to the vertical effective stress as shown in Equation 2-2.

$$K = \frac{\sigma'_h}{\sigma'_v} \qquad \text{Equation 2-2}$$

Where:

K= Lateral Stress Ratio

σ= Total Stress (Force by Area)

u= Pore Pressure (Force by Area)

K is used during well drilling to determine a safe mud weight to circulate within the well to maintain the borehole stability. The mud weight required for stability must be larger than pore pressures to limit fluid inflow in the well, but less than the minimum principal stress to limit inducing fractures in the sediments. K is an empirically derived value as such it includes the pore water pressure conditions from the in situ measurements that the correlated values are derived from Matthews and Kelly (1967). Within the geotechnical community the idea of lateral earth stress is significant for the design of soil retaining structures and K_0 conditions are commonly referred to as "at rest" conditions. K_0 within the geotechnical community is the at rest coefficient of earth pressure, which is equivalent to the at rest lateral stress ratio.

Initial estimations of lateral earth pressures were developed in Coulomb (1776) who considered a rigid soil mass sliding along a shear plane, and improved upon by Rankine (1856) who assumed lateral deformations from either a horizontal extension failure of the soil (active conditions) or horizontal compression failure (passive conditions). The Rankine solutions were developed for granular materials but were adapted to cohesive and frictional materials in Bell (1915). Neither Coulomb nor Rankine quantified a K_0 condition. Within Terzaghi (1923) the first quantification of the K_0 condition was provided as function of the mobilized friction angle. It is important to note the distinction between the mobilized friction angle and the maximum friction angle. The mobilized friction angle is the slope of the stress patch during one dimensional compression (no radial deformation) and the mobilized friction angle represents the frictional resistance of the soil under one dimensional compression conditions. The mobilized friction angle is a smaller value than the maximum friction which represents the failure envelope. Several correlations for estimating the mobilized friction angle of a soil are discussed within Federico and Elia (2009). Figure 2-19 adopted from Federico and Elia (2009) illustrates the difference between the mobilized friction angle and the maximum friction. The maximum friction angle is

commonly referred to as the critical state friction angle as it typically corresponds with critical state conditions during shearing of a soil.

K_0 compression denotes a specific laboratory condition where the soil specimen is compressed in uniaxial strain (one-dimensional), through restricted radial deformation. This experimental program imposed the K_0 conditions through confinement of the specimen in a rigid walled testing apparatus or through incrementally increasing the triaxial fluid chamber pressure to maintain the no radial deformation condition. These experimental methods are discussed in more detail within Chapter 3.

K_0 conditions are a specific analog to deposited sediments that are laterally constrained, leading to zero lateral deformation. K_0 conditions imply that the intermediate (σ_2) and minor (σ_3) principal stresses are equal. Equation 2-2 defines K_0, but the resultant horizontal total stress can be calculated using Equation 2-3.

$$\sigma_h = K_0(\sigma_V - u) + u \qquad \text{Equation 2-3}$$

Where:

σ_h= Total Horizontal Stress ($\sigma_h = \sigma_2 = \sigma_3$ at K_0 condition) (Force by Area)

K_0= At Rest Lateral Stress Ratio

u= Pore Pressure (Force by Area)

The most used derivation for K_0 is from Jaky (1944) which is provided in Equation 2-4.

$$K_0 = 1 - sin\phi' \qquad \text{Equation 2-4}$$

Where:

K_0= At Rest Lateral Stress Ratio

ϕ'= Effective Friction Angle (Degrees)

Jaky derived his equation from an analysis of the stress field in a wedge prism of loose granular soil. Jaky's equation for K_0 agrees with field measurements in (Brooker and Ireland 1965), with a minor

modification to the equation to improve the statistical fit. Within Mayne and Kulhawy (1982), the Jaky equation was shown to be in good agreement with laboratory experiments on normally consolidated clays, and in fair agreement with laboratory experiments on granular materials. A derivation of K_0 is presented in Pantelidis (2019) based on Cauchy's first law of motion to deformable bodies with internal resistance and the sand heap analysis presented in Jaky (1944). Within Pantelidis (2019) a generalized equation for K_0 is presented that resolves to the active (horizontal extensional failure) and passive (horizontal compressional failure) solutions provided in Bell (1915) for cohesion and friction materials. Pantelidis (2019) also provides a means to calculate intermediate stress states between passive, at rest, and active conditions and indicates that the mobilized cohesion corresponds to the peak strength of the cohesive material under static conditions.

In the field of geology, the K_0 condition is not as significant as it is in engineering due to geological variations that effect principal stresses and may void K_0 conditions, such as the presence of seismic faults, tectonic stresses, and time. At depth tectonic stresses play a significant role in the principal stress orientations and the horizontal stresses may be less or greater than the vertical stress depending on the geological setting as shown in Anderson (1951). Geological conditions vary over time and in some areas, the earth stress state is not consistent with large-scale geologic structures because those structures evolved during previous tectonic regimes that have not been active for tens, or even hundreds, of millions of years Zoback (2007). For geologic formations where the maximum principal stress is in the vertical direction tectonic stress may be required to be superimposed on the K_0 stresses creating a difference between the intermediate and least principal stresses as discussed in Fjaer (2008), and Zoback (2007). An acceptable first order approximation for a geologic evaluation is to assume the maximum principal stress is the overburden weight acting in the vertical direction and the minimum principal stress is equal to the lateral stress estimated for K_0 conditions. These assumptions do not

account for active regional tectonic faulting which can be a significant contributor to horizontal earth stresses.

The determinations of K in appropriate geologic settings have been predominantly presented as empirical relationships as shown in Hubbert and Willis (1957), Matthews and Kelly (1967), Eaton (1969), Breckels and van Eekelen (1982), Zoback and Healy (1984), and Holbrook, Maggiori, et al., (1993). These empirical relationships are based on leak-off tests (LOT's) conducted during drilling operations and are site specific and indifferent to K_0 conditions. Each of the methods uses a different rationale to derive the K value. Hubbert and Willis (1957) indicated that K should be set to a constant of 0.33 which was later was found to consistently underpredicted the least principal stress by Eaton (1969). Matthews and Kelly (1967) back calculated the matrix stress coefficient K from fraction initiation pressures at known depths an fluid pressures. The (Eaton, 1969) method correlates the K value to a function of the Poisson Ratio (ν) of the formation sediments. Breckels and van Eekelen (1982) provide site specific correlations for the least principal stress directly (no K derivation) with a correction for variations in pore pressures that deviate from hydrostatic conditions. Zoback and Healy (1984) provides a derivation for K as a function of the frictional coefficient for the formation sediments under the assumption that the sediments are at frictional equilibrium. Holbrook, Maggiori, et al., 1993 presents a derivation of K based on the porosity of the formation sediments. Figure 2-20 provides a comparison of the least principal stress calculated by the methods above in a Gulf of Mexico well where overburden stress and pore pressures are known and where the maximum principal stress is overburden stress.

K_0 is found to vary by soil composition cohesive or cohesionless, fines content, and relative soil density. Variations in K_0 by soil type and stress history are presented within Mayne and Kulhawy (1982), where K_0 is shown to vary for cohesive or cohesionless soils, and soil stress history (overconsolidation ratio). Figure 2-21 provides a plot of K_0 by friction angle for various cohesive and non-cohesive soils from

Mayne and Kulhawy (1982). Also presented within Mayne and Kulhawy (1982) is confirmation that variation of K_0 by stress history can be related to the effective friction angle of the soil as originally proposed in Schmidt (1966). Casey, Germaine, et al.(2015) provides experimental measurements of K_0 for eight different resedimented fine-grained soils and provides a correlation for estimating K_0 as a function of the liquid limit. Casey, Germaine, et al. (2015) indicates that clay mineralogy is significant to K_0 behavior of fine-grained soils and that K_0 behavior can be estimated through correlations with a soil's liquid limit. The effect of fines content and relative density on K_0 of predominantly sandy soils is presented in Lee, Lee, and Park (2014). Figure 2-22 adopted from Lee, Lee, and Park (2014) shows that relatively small changes in fines content can cause appreciable differences in the measured K_0 value. The variation in K_0 by fines content is not as significant as the variation in K_0 by relative density of the soil. Li, et al. (2023) expand on the dependence of K_0 to the relative density of a soil, by showing the increase in K_0 with increases in relative density. Figure 2-23 presents Li, et al. (2023) experimental results of K_0 by relative density for sand specimens with a relative density range of 30% to 95%.

2.2. Permeability of Soils

The flow of fluids through soils is significant in both engineering and geology applications, subsurface fluid flow can have significant impacts on the design of earthen dams, support of excavation systems, permanent and temporary dewatering systems, contamination remediation projects and other civil engineering works. In offshore drilling, permeability can have significant impacts on flow of extractable hydrocarbons, and the generation of pore pressures, as well as determinations of the safe drilling window. Pore pressure being a significant factor in well design both as representing a lower bound for a safe mud weight to limit fluid inflow into the borehole and due to the contribution pore pressure has on the effective stress of the geologic formation.

Hydrogeology as a study can be traced back to 1856 Dijon France, in which an engineer named Henry Darcy published a report on his experimental results of water flow through sands devised to evaluate the water supply for the city of Dijon Darcy (1856). Henry Darcy's experiment was developed into an empirical law of groundwater flow that is referred to as Darcy's law and is presented as Equation 2-5.

$$Q = -KiA \qquad \text{Equation 2-5}$$

Where:

Q= Volumetric Flow (Volume by Time)

K= Hydraulic Conductivity (Length by Time)

i= Hydraulic Gradient

$A =$ Cross Sectional Area (Length Squared)

Where the hydraulic conductivity represents the effects of both the porous medium and the fluid permeant. King Hubbert presented a parameter discussed within K. M. Hubbert (1956), referred to as permeability to classify the porous medium alone. The relationship between permeability and hydraulic conductivity are presented in Equation 2-6.

$$K = \frac{k\rho g}{\mu} \qquad \text{Equation 2-6}$$

Where:

K= Hydraulic Conductivity (Length by Time)

k= Permeability (Length squared)

$\rho =$ Fluid Density of the Permeant (Mass by Volume)

$g =$ Acceleration due to Gravity (Length by Time squared)

$\mu =$ Dynamic Viscosity of the Permeant ((Mass by length) by Time)

The development of a fluid free conductance parameter was mostly due to the existence of gas, oil and water multiphase systems and the convenience of not determining the hydraulic conductivity of such complex conditions.

Permeability of clay and silt lithologies varies in orders of magnitude by porosity as illustrated in Figure 2-24 adopted from Neuzil (2019). Permeability has been found to be influenced by particle grain size, pore size distribution, grain shape, tortuosity, clay content and temperature P. C. Carman (1937), Kozeny (1927); Lapierre, Lerouil and Locat (1990), D. N. Dewhurst, et al. (1998); Spinelli, Giambalvo and Fisher (2004), Yang & Aplin, (2004) and Schneider (2011). Fluid flow through sediments and rocks is significantly anisotropic Adams (2014), Nordquist (2015), Mondol, Jahren, et al. (2010) and for convenience permeability discussed herein is generally limited to the typically smaller value of vertical permeability. Permeability has been measured from field testing or laboratory testing; this discussion will be focused on laboratory test measurements. Laboratory measurement of permeability is performed through several means all of which used a fixed specimen cross sectional area and a controlled permeant to reduce the Darcy flow equation to a function of the hydraulic gradient and permeability of the porous medium. Laboratory techniques to determine permeability include flow-through experiments Zhang, et al.(2002), pressure-pulse decay tests Yang and Aplin, (2007), Lecampion, Constantinescu and Malinsky (2006), and deformation based tests, such as incremental loading or constant rate of strain consolidation tests Wissa, et al. (1971), N. Mondol, K. Bjorlykke, et al. (2007), N. Mondol, (2009), B. Casey (2014), Reece (2021). The variation in testing methods is mostly due to the difficulty in measuring permeability of fine-grained soils. The permeability in fine grained soils can be so low that a significant amount of time is required to get a measurable amount of flow through the material. This long test duration of flow through methods can create artifacts in the measurements due to microbial growth, evaporation or other difficult to control conditions that can be avoided through deformation-based methods. Another issue that needs to be balanced is that large hydraulic gradients

that produce flows through fine grained soils in a timely manner may mechanically disturb the soil creating erroneous measurements.

The connection between soil composition and permeability has been established through several studies. Hazen (1930), Kozeny (1927), Carman (1937), Carman (1956), and Carrier III (2003) provide increasingly complex correlations for the hydraulic conductivity and particle size, with additional terms in some correlations for particle shape, particle size distribution characteristics, specific surface area, void ratio, and other physical properties. Figure 2-25 provides typical ranges of hydraulic conductivity and permeability for various geologic materials adopted from Freeze and Cherry (1979). Figure 2-25 indicates a thirteen order of magnitude difference between the most permeable gravel soils and the least permeable metamorphic and igneous rocks, illustrating how wide a range of permeability can occur in natural geologic materials.

For fine grained soils, mudrocks, and shales permeability, significant research has been performed within the past 30 years on variability with lithology as presented within Yin (1992), Yang & Aplin, (1998), Dewhurst, Aplin, & Sarda, (1999), Yang & Aplin, (2007), Shafiee (2008), Mondol, (2009), Yang & Aplin, (2010), Schneider (2011), and Zeng, et al. (2020). The research finds consensus with permeability correlating with porosity, and higher clay content materials having lower permeability at the same porosity. These findings are illustrated in Figure 2-26 which presents direct measurements of permeability by porosity for a range of lithologies as well as modeled permeability by porosity adopted from Yang & Aplin, (2010). Other significant studies on the permeability of fine-grained soils are B. Casey (2014), and Mondol, (2009), the former compares permeability measurements of resedimented soils from a wide range of geologic origins and the latter compares permeability measurements of synthetic silt and clay mixtures of controlled clay mass fractions. Both studies indicate a reliance of not just

permeability to soil particle size but also dominant clay mineralogy. Figure 2-27 presents ranges in permeability for mudrocks of various geologic origins as adapted from Casey (2014).

2.3. Dynamic Properties of Soils

The measurement of the dynamic mechanical properties of soils has been a longstanding subject of research in the field of geotechnical engineering and geology. Understanding the mechanical properties of soil under dynamic loads is important for the design and performance of structures in earthquake prone areas, and structures subjected to dynamic conditions such as supporting machinery. Both geotechnical engineering and geology have adapted the dynamic measurements of soil as an exploratory method for geologic site evaluations. Field measurements of dynamic soil properties are typically performed by measuring waves traveling through sediments. This is done through surficial survey methods Nazarian and Stokoe II (1984), Matthews, Hope and Clayton (1996), Lin, Lin and Chang (2004), downhole methods; s seismic Cone Penetration Testing Robertson, et al. (1986), suspension logging methods Summers and Broding (1952), Vogel (1952), or Pickett (1963), logging while drilling methods Varsamis, et al. (1999), and by controlled blasting methods Jana, et al.(2021). Laboratory measurements of dynamic soil properties are made by several notable test apparatuses, these methods are categorized by either large strain tests such as the cyclic direct shear testing, Casagrande and Rendon (1978), cyclic triaxial test Bishop and Henkel (1962), cyclic torsional ring shear Ishihara and Yasuda (1975), and small strain tests such as the resonant column device Casagrande and Rendon (1978) and bench top wave propagation by bender elements or piezoelectric crystals Shirley and Hampton (1978), Ayres and Theilen (1991), Marion, et al. (1992), M. Prasad (2002), M. Zimmer (2003), Mondol, Bjorlykke, et al. (2007), Marjanovic (2016), and Ranjpour (2020).

Measurements of the dynamic properties of soils were largely started by geologists working with lithified rocks. Birch and Bancroft (1938) resonated stone columns to measure the mechanical

properties of the stones under dynamic conditions. Advancements in wave propagation methods specifically the introduction of piezoelectric transducers by Hughes, Pondrom and Mims (1949), lead to research into variations of dynamic properties by variation in geologic origin, saturation, and temperature Hughes & Jones, (1950), Hughes & Cross, (1951), and Hughes & Kelly (1952). Wyllie, Gregory and Gardner (1956), used piezoelectric transducers to evaluate compressional wave propagation through a mixed system by measuring velocities of aluminum discs embedded in Lucite epoxy, evaluated the effect of discontinuities on compressional wave velocity by measuring the wave velocity through stacked glass plates of varying heights, and evaluated the effect of confining pressure and saturation on compressional wave velocity. Figure 2-28 provides a plot adapted from Wyllie, Gregory, and Gardner (1956), that illustrates compressional wave velocities increase with confining pressure through sandstones and have large variations with changes in saturation. Within Wyllie, Gregory, and Gardner (1956) the 100% saturated specimen was not allowed to drain during external load application and the results reflect the excess water pressure on the solids phase. Nur and Simmons (1969) showed that specimen fluid saturation had a large effect on the compressional wave velocity but negligible effect on shear wave velocity. Other research included the measurements of shear wave and compressional wave velocities for evaluation of the elastic parameters of rocks from various geologic sources with classification of the tested rock by mineralogy Woeber, Katz, and Ahrens (1963). Several studies published correlations for P and S wave velocities as a function of porosity, lithology, and permeability. A few notable correlations with a clay content term are Tosoya (1982) Equation 2-7 and Equation 2-8, Han, Nur, and Morgan (2011) Equation 2-9 and Equation 2-10, Eberhart-Phillips, Han and Zoback (1989) Equation 2-11 and Equation 2-12, and Klimentos (1991) Equation 2-13.

$$V_P = -2.4C - 8.6\phi + 5.8 \quad \text{Equation 2-7}$$

$$V_S = -2.1C - 6.3\phi + 3.7 \quad \text{Equation 2-8}$$

$$V_P = 5.59 - 6.93\phi - 2.18C \quad \text{Equation 2-9}$$

$$V_S = 3.52 - 4.91\phi - 1.89C \quad \text{Equation 2-10}$$

$$V_P = 5.77 - 6.94\phi - 1.73\sqrt{C} + 0.446(P_e - e^{-16.7P_e}) \quad \text{Equation 2-11}$$

$$V_S = 3.70 - 4.94\phi - 1.57\sqrt{C} + 0.361(P_e - e^{-16.7P_e}) \quad \text{Equation 2-12}$$

$$V_P = 5.66 - 6.11\phi - 3.53C + 0.0007K \quad \text{Equation 2-13}$$

Where:

V_P= P Wave Velocity (kilometers per second)

V_S= S Wave Velocity (kilometers per second)

$C =$ Volume Fraction of Clay

$\phi =$ Porosity Fraction

P_e= Effective Pressure (kbar)

K= Permeability (millidarcy)

A robust study on the dynamic properties of shale samples is presented within Deng, et al. (2021), where 82 samples of the Longmaxi Shale formation were classified by powder X-Ray diffraction for evaluation of their mineral composition and viewed through focused Ion Beam scanning electron microscopy for evaluation of their microtextural character. The samples were classified by total organic content, clay content, and crystalline quartz content. The formation was found to have two different depositional environments, a deepwater environment that had significant biogenic quartz formation that preserved the deposited clay structure from mechanical compression and a shallow water depositional environment that resulted in the supporting clay particles being subjected to significant

mechanical compression. Velocity experiments were performed at 30 MPa confining stress and the results show a significant variation in velocity by depositional environment. Figure 2-29 shows the velocity measurements from Deng, et al. (2021), and their link between depositional environment; shallow water depositional environment indicates a decrease in velocity with an increase in quartz content attributed to a less mechanically compressed specimen due to the presences of the quartz grains. The deep-water depositional environment does not indicate a trend with quartz content which is attributed to this depositional environment allowing biogenic quartz crystalline growth limiting compression of the clay content. For the deep-water depositional environment increases in quartz content were reported to lead to more defined pore spaces in Deng, et al. (2021). The effects of depositional environment on the mechanical properties of will be discussed for geological context for the interpretation of the studies experimental results.

Research on the dynamic properties of unlithified soils indicate velocities vary by lithology, effective stress, and shear stress Lawrence (1965). Domenico (1977) showed that wave velocities in soil were most dependent on effective stresses, but P wave velocities also varied by soil saturation as shown in Figure 2-28 and Figure 2-30. Domenico (1977) found that saturation had a negligible effect on S wave velocities. Murphy III (1982) found that the dynamic properties of sands are dependent on the grain contact area, grain contact area is dependent on the actual number of contacts per grain, and grain angularity influences the dynamic properties due to variations in the grain contact area and mean particle size. Murphy III (1982) also indicates that the grain contact area is logarithmically related to 1 minus the soil's porosity. Building on Murphy's work Prasad and Meissner (1992) performed a study on wave attenuation in dry and saturated sand specimens of varying grain size and angularity. Prasad and Meissner (1992) found that S wave velocity was largely unaffected by grain size and that P wave velocity decreased with decreasing mean grain size and increasing particle angularity as shown in Figure 2-31. Prasad and Meissner (1992) also looked at the evolution of the particle contact area in sands by

modeling their measurements with a contact radius model Duffy and Mindlin (1957), and with a friction model Winkler and Nur (1982). The contact radius model results indicate both large and small sand particles show increases in contact area with increases in stress to a limiting value after which the particles are effectively locked in and there is minor change in contact area. Larger particles have larger increases in contact areas with increasing stress as opposed to smaller particles. The friction model results show that wave attenuation is grain size dependent, with larger particles having higher attenuation rate that decreases rapidly with increasing pressure and smaller particles have lower attenuation rate with slight decreases in attenuation with increasing pressure. These results indicate that for larger grain particles strain from dynamic loads with strains more than 10^{-7}%, are potentially plastic and unrecoverable depending on the confining pressure and contact radius of the sands. Smaller sand particles are less sensitive to attenuation and behave generally more elastically. Figure 2-32 shows the Prasad and Meissner (1992) evolution of contact radius by pressure for four sand specimens of varying particle and with varying initial contact areas.

Zimmer (2003), and Zimmer, et al. (2007) investigated the effects of particle sorting and porosity by velocity experiments on dry and water saturated sand and glass bead specimens. Particle sorting was explored by comparing the velocity results of particle size-controlled specimens at similar stresses and porosities. Particle sorting was found to have a weak correlation with velocity; shear wave velocities show about a 10% increase and P wave velocities show about a 15% increase with increasing particle size. The sorting effects were most prominent below a stress of 1 MPa. Zimmer, et al. (2007) explored the porosity and stress effects on velocities on controlled sand and glass bead specimens by loading them hydrostatically with 1 to 9 unload and reload pressure cycles up to an ultimate pressure of 20 MPa. Velocity measurements were collected for both the loading and unloading portions of the tests. Zimmer, et al. (2007) show that velocity measurements in overconsolidated sands were higher than velocity measurements in normally consolidated sands at the same effective stress and that the increase

in velocity increased with preconsolidation pressure, these results are illustrated in Figure 2-33. This indicates that grain supported materials have locked in grain contacts based on the stress history of the material.

The effect of clay content on the dynamic properties of soils evolved from research on the in situ velocity measurements as discussed in Vogel (1952) and Pickett (1963) and was later combined with laboratory velocity measurements of lithified rocks as presented in Tosoya (1982), and Castagna, Batzle and Eastwood (1985). D.-H. Han (1986) directly evaluated the effects of clay content on dynamic properties of unconsolidated sands, through wave velocity measurements in specimens comprised of mixtures of sands and clays. The specimens consisted of Ottawa Sand and smectite clay with clay contents by mass between 0% and 40%. Wave velocity measurements were conducted during loading the specimens to 50 MPa and during unloading to about 20 MPa. The results indicated Ottawa Sand compression behavior is “elastic” relative to the smectite clay. At stresses above 30 MPa crushing of the sand grains was observed leading to increases in sand compressibility, reduction in particles sized and increased angularity of the grains. For the mixed specimen tests compressibility increased with increasing clay content. Under increasing stress, the clay was found to have stiffer behavior and during unloading of the specimens the overconsolidated clay velocity measurements were significantly higher than the normally consolidated velocity measurements at a same porosity. Beyond a clay content of 10% the velocity measurements increased as did the elastic moduli with increasing clay content. These trends are anticipated to reverse once the clay content is sufficient enough that the sand grains are suspended in a clay matrix, which was a condition not tested within D.-H. Han (1986). Figure 2-34 provides Han’s velocity measurements by burial depth for clay content specimens up to 30% clay.

Building on Han‘s work Yin (1992) created specimens of Ottawa Sand and Kaolinite Clay in controlled mass amounts of pure Ottawa Sand, 5%, 10%, 15%, 20%, 25%, 30%, 40%, 50%, 65%, 85% Kaolinite Clay,

and pure Kaolinite Clay. These specimens were subjected to compression between stresses of 2.5 MPa to 50 MPa, and P wave velocity measurements were conducted during loading of the specimens. An important concept for the packing of sand and clays introduced with Yin (1992) and Marion, et al. (1992), which is the critical clay-content, described as a percolation threshold for the binary mixture of clay particles and sand grains. "Below the critical clay-content, sand packing dominates the sample's character, and sand grains bear most confining stress; above the critical clay-content, clay packing dominates the sample's character, sand and clay share confining stress equally." Figure 2-35 presents a diagram of the spectrum of sand and clay mixture states, and the location of the critical clay-content as adapted from Marion, et al. (1992). Yin (1992) found the porosity of normally consolidated materials depends on the packing of the constituent grains, clay content and degree of cementation, and that the P wave velocity had a peak value around the critical clay-content which represents the most efficient particle packing and densest possible state for sand and clay mixtures. Figure 2-36 presents the porosity and P wave velocity measurements for Yin's mixtures at several confining stresses and illustrates the critical clay-content at those confining stresses, and that the peak P wave velocity occurs around the critical clay content. Yin also explored the effects of particle cementation through the addition of 10% epoxy cementation by volume in Yin (1992) to a sand specimen. The cementation resulted in an increase of P-wave and S-wave velocities from an uncemented state. Increases in added cementation volume beyond 10% in volume were found to have negligible increases in velocity.

Mondol, Bjorlykke, et al. (2007) performed an experimental study on the compression behavior and wave velocity measurements of synthetic Smectite and kaolinite mixtures to evaluate to dynamic properties of clays. The study mixed known amounts of powdered Kaolinite and Smectite clays to create both dry and brine saturated mixed clay specimens. The dry specimens were created using oven dried clay powders. The synthetic mixtures include the end member mixtures of 100% Smectite or Kaolinite and variations of the clay contents in 20% increments (20% Smectite and 80% Kaolinite, etc.). The

specimens were subjected to incremental loading up to 50 MPa effective stress and wave velocities measurements were collected during loading. The results indicate a monotonic porosity trend with stress and clay mineralogy, that for a given stress the porosity decreased from the 100% Smectite sample to the 100% Kaolinite sample. The brine saturated samples show an identical monotonic velocity trend with stress and clay mineralogy where the P and S wave velocities are largest in the 100% Kaolinite specimen and decrease with increasing Smectite clay content to 100% Smectite. These trends are attributed to density differences from compression and differences in clay particle interactions and trapped water double layer interactions. The influence of the double layer can be observed through comparison of the dry specimens' results which limit the double layer chemical interactions and are subject to particle-to-particle contacts. The results of the dry specimens do not show trends with stress level and clay mineralogy indicating that clay mineralogy is important for soil structure in saturated conditions. Figure 2-37 provides the velocity measurements by effective stress for both the brine saturated and dry test specimens from Mondol, Bjorlykke, et al. (2007).

Marjanovic (2016) developed a laboratory wave propagation technology specifically to measure clay soils stiffnesses between 1 MPa and 10 MPa within a triaxial cell. Marjanovic performed velocity measurements on intact clay, reconstituted sand, and resedimented clay specimens during the development of the new wave measurement technology. The measurements were evaluated for trends with soil plasticity, which was not found for velocity measurements, but a correlation was found for Vp/Vs ratio. Figure 2-38 provides the velocity measurements from Marjanovic (2016).

Building on the work of Marjanovic (2016), Ranjpour (2020) developed the tall constant rate of strain (TCRS) technology that was used in this testing program. The TCRS equipment allows for large specimen deformation during loading allowing for larger ultimate test stress levels. Within Ranjpour

(2020) velocity measurements for two resedimented clay materials were performed up to an approximate 25 MPa stress. Those results are provided in Figure 2-39.

2.4. Mechanical Strength Properties of Soils

The mechanical strength properties of soils have long been studied due to the importance of soil strength to many aspects of both geology and geotechnical engineering. This section will discuss soil strength in sands, clays, and mixtures of sands and clays. Due to the vast amount of research, discussion of soil strength herein, will generally be limited to a discussion of measurements made within the laboratory program including stress-strain behavior, shear strength, effective friction angle, and pore pressure generation during shearing.

When discussing strength of coarse grained soil (sands) the discussion of stress is based on macroscopic forces subjected to a specific soil area. Further definition of these forces Lambe and Whitman (1969) uses a reference plane through a sand section under an equilibrium condition considering each particle individually. Within the reference plane the stresses are carried by a sand skeleton, defined by resultant internal forces, both normal and shear, within each particle cut by the plane and summed over a specific area. The total forces, both normal and shear, are distributed over the area of the plane. The area of the plane selected should be large enough to not affect the magnitude of the stresses. Figure 2-40 illustrates an example plane through a sand mass and the forces subjected to the grains used to define soil stresses as adapted from Lambe and Whitman (1969). Macroscopic stresses (force by area) and not the microscopic contact stresses (forces between grains) are usually used to establish soil stress conditions due to the difficulty of measuring contact stresses between particles and due to external loading of a soil mass being an analog for most applied loads on soils.

Forces applied to a sand mass are resisted through interparticle frictional forces at grain contact points. Frictional contacts follow two basic laws of friction known as Amontons laws of Friction. The first

law being the shear resistance between two objects is proportional to the normal force between the objects. The second law being shear resistance between two objects is independent of the size of the objects. Equally important to frictional force is the contact area, and the understanding that contact areas between sand particles are small, and likely have already yielded plastically to state of equilibrium under high point stresses. That is portions of each particle likely locally yields at the contact point. Even the most highly polished surfaces are rough at the microscopic level and contacts between particles are limited to small areas due to particle roughness. Interparticle stresses at small contact areas are significantly larger than the macroscopic stresses the sand mass is subjected to leading the localized yielding.

The macroscopic behavior of sands resistance to stresses is commonly modeled using the Mohr-Coulomb failure criteria defined in Equation 2-14.

$$\tau_F = c + \sigma_F \tan \phi \qquad \text{Equation 2-14}$$

Where:

$\tau_F =$ Shear Stress at Failure (Force by Area)

$c =$ Cohesion Intercept (Force by Area)

$\phi =$ Friction Angle (Degrees)

The Mohr-Coulomb failure criteria is used for the convenience of representing the stress state of a sand mass by a Mohr's circle, and for the close relationship of the theoretical failure plain to the measured failure plane in sand specimens. The theoretical failure plane is found to be within 5 degrees of the measured failure plane in sands Lambe and Whitman (1969). Figure 2-41 provides a representation of a Mohr's circle for a sand specimen, the Mohr-Coulomb failure envelope, and the theoretical failure plane as adapted from Lambe and Whitman (1969). The cohesion intercept term is the apparent strength that is independent of the frictional resistance of the soil. This term is attributed to many different mechanisms including particle cementation, capillary pressures, shear induced pore

pressures, interparticle chemical interactions, interparticle electrostatic forces, etc. For dry uncemented sands the non-frictional forces are typically insignificant and thus cohesion is considered negligible. The friction angle is the angle between a linear fit of the tangent line to Mohr's circle at failure and the stress axis, within a shear stress by confining stress plot. The friction angle is a simplification applicable to a narrow stress range as the failure surface tends to be curved indicating a relationship of friction angle with stress level as will be discussed further herein.

Terzaghi's effective stress principle (Equation 2-1) holds true for strength evaluations of granular material but due to their relatively permeable nature, shear induced excess pore pressures are thought to drain rapid enough not to contribute to strength effects. That is granular materials in general are permeable enough to drain shear induced pore pressure such that the limiting strength state of a granular materials is the drained condition.

Strain behavior of sand is attributed to three fundamental mechanisms, elastic compression of the particles which is considered elastic and recoverable and the irrecoverable grain displacements from rigid body motions (sliding, rolling etc.) or by crushing of the grains Andersen (1991). The rigid body motions of these particles are governed by the location and magnitude of the interparticle contact forces. If the resulting deformations do not involve the crushing or fracturing of the individual particles, then the overall deformations experienced by the sand mass can, in principle, be described by force equilibrium equations for each particle Andersen (1991). Rigid body forces and particle crushing have been studied through experiments on idealized granular materials such as Horne (1965), Skinner (1969), Rowe, (1971), Oda and Konishi (1974), and Athanasiou-Grivas and Harr(1980), through experiments on sands such as Rowe, (1971), Yu (2017), Wu, et al.(2020), and by discrete element modeling Cundall, Drescher and Stack (1982), Robertson, Bolton and McDowell (1997), Cheng and Meidani (2013). These works provide a great deal of insight to the deformation behavior of sands under loads, a few key

observations are, forces are not transmitted through a particulate medium in a uniform way, but are concentrated in chains of particles extending between the boundaries Cundall, Drescher and Stack (1982). Particles not associated with these force chains carry little to no load. The normal contact points between grains tend to concentrate in the directions of the maximum principal stress axis during shear Oda and Konishi (1974).

The other major contributor to strains within sands is particle breakage through crushing of grains under loading. Particle crushing is attributed to force contacts that exceed the strength of the individual particle. K. Lee (1977) found that grain crushing was more predominant in sands that have been subjected to shear stresses than sands that have been isotopically consolidated. Hardin (1985) found that particle crushing was dependent on effective stress and effective stress path, initial void ratio, particle shape, and particle hardness, and that silt and clay size particles are not very susceptible to breakage.

The state parameter which relates the instantaneous void ratio and stress level to a reference state is a significant parameter for evaluating the strength of sands Been and Jefferies (1985). The reference state is represented by the Steady State compression line and it coincides with the void ratio by stress of a sand mass deforming under constant effective stress, void ratio, and velocity. These conditions theoretically represent a “flow” structure in sands that is unique and not influenced by the initial conditions. Figure 2-42 illustrates the steady state line and test specimens with both negative and positive state parameters from Been and Jefferies (1985) for Kogyuk 350/2 sand. Sands with a positive state parameter are in a looser state than the Steady State Line and will experience contractive behavior during shear until steady state conditions are reached. Sands with a negative state parameter are in a denser state than the Steady State Line and will experience dilative behavior during shearing until reaching steady state conditions. This density dependent behavior is unique to grain supported

materials and is one of the reasons geotechnical engineers separate soil behaviors into grain supported and clay supported.

Clay minerals are complex aluminum silicates that are defined by the elemental composition of their crystalline structure that is generally composed of two basic units' silica tetrahedron and alumina octahedron. These units combine to make a silica sheet (combination of the silica tetrahedral structures) and a gibbsite sheet (combination of the alumina octahedral structures). Clay particles are generally comprised of stacked silica and gibbsite sheets, with differentiations of mineralogy from variations in the gibbsite sheet due to isomorphous substitution. Where isomorphous substitution is the substitution for one element for another within the crystalline structure without a change in the crystalline structure. These stacks of sheets tend to create flat platy clay particles with positively charged faces and negatively charged edges. The positive charged faces of the particles attract cations and dipolar water molecules to several hundred angstroms away from the molecule face creating a trapped layer referred to as the diffuse double layer. The size of the double layer is dependent on the availability of water and the charge of the clay particles, which varies by clay mineralogy. Attractions of clay particles and resultant soil fabrics are largely attributed to double layer interaction through dipolar water bond attractions, cation attractions, and oxygen bonds Das (2010). Oven dried clay particles have been found to develop a shear strength through edge to face attractions, particle contacts, and electrostatic Van der Waals forces. These forces must also contribute to the overall behavior of saturated clay soils.

As the availability of absorbed water is important to the behavior of clays, clay soil strength is typically separated between undrained and drained behavior. Where Undrained behavior is representative of saturated clays under rapid loading conditions, and drained behavior is representative of slowly loaded free draining clays. Normally consolidated saturated clays experience contractive behavior during shearing that generates positive excess pore pressure, and as discussed in section 2.3

clays are relatively impermeable so unlike sands the excess pore pressures cannot drain fast enough to not significantly affect the effective stress state of the soil. Overconsolidated clays do not necessarily experience contractive behavior during shearing and may experience dilative behaviors and as such will not be discussed in full detail. Skempton (1961), and Lade and de Boer (1997) evaluated the suitability of the Terzaghi's effective stress principle to soils and found the theory to be applicable over the general ranges of stress for engineering. Within Lade and de Boer (1997) two variations of the Terzaghi's effective stress principle are proposed; one soils, Equation 2-15, and one for rocks and concrete, Equation 2-16.

$$\Delta\sigma' = \Delta\sigma - \left[1 - (1 - n)\frac{C_{gu}}{C_{sks}}\right]\Delta u \qquad \text{Equation 2-15}$$

$$\Delta\sigma' = \Delta\sigma - \left[1 - \frac{C_{gu}}{C_{sks}}\right]\Delta u \qquad \text{Equation 2-16}$$

Where:

$\Delta\sigma' =$ Change of Effective Stress (Force by Area)

$\Delta\sigma =$ Change of Total Stress (Force by Area)

$n =$ Porosity (Percent)

$C_{gu} =$ Compressibility of Soil Grains Due to Pore Pressure Change (Degrees)

$C_{sks} =$ Compressibility of Soil Skeleton Due to Total Confining Stress Change (Degrees)

$\Delta u =$ Change in Pore Pressure

Terzaghi's effective stress principle indicates that there are two different strength parameters for soil under the same conditions, the total stress parameters which includes internal pore pressures and effective stress parameters which only account for soil resistance. In general, the effective strength parameters are of more importance for the behavior of soils and are the focus of this study. Drained clay soil shear strength behavior is a direct analog to granular materials where the strength is typically characterized by the Mohr Coulomb failure envelope.

Skempton (1954) introduced two parameters A and B to quantify the effects of pore water pressure during shearing and developed equation 2-17.

$$\Delta u = B[\Delta\sigma_3 + A(\Delta\sigma_3 - \Delta\sigma_1)] \quad \text{Equation 2-17}$$

Where:

$\Delta u =$ Change in pore water pressure (Force by Area)

$\Delta\sigma_3 =$ Change in least principal stress (Force by Area)

$\Delta\sigma_1 =$ Change in max. principal stress (Force by Area)

$A =$ Skempton's A Parameter symbolizing change in pore water pressure under shearing.

$B =$ Skempton's B Parameter symbolizing degree of saturation in the specimen.

For the case where the specimen is completely saturated and therefore the B parameter is equal to unity then the A parameter is defined by Equation 2-18.

$$A = \frac{\Delta u - \Delta\sigma_3}{\Delta\sigma_1 - \Delta\sigma_3} \quad \text{Equation 2-18}$$

The B parameter is a function of the saturation of the specimen and is measured in the triaxial cell as the change in pore pressure corresponding with a change in the confining pressure of the specimen as shown in Equation 2-19.

$$B = \frac{\Delta u}{\Delta\sigma_3} \quad \text{Equation 2-19}$$

The A and B parameters are important for the understanding of the stress path during undrained shearing. The A parameter relates the change in pore pressure to changes in shear stress and allows for the development of undrained stress paths. The B parameter relates change in stress response to saturation to account for partial saturation of a specimen during shearing. In theory a fully saturated specimen will have an equivalent increase in pore pressures with an increase increment of confining stress indicating full adequate saturation. B values less than unity can lead to significant effects on

material behavior during testing. An unsaturated specimen can have reductions in hydraulic conductivity due to zones of unsaturated flow, and a differing undrained shear response as shear induced pore pressures are allowed to distribute into unsaturated pore spaces. Figure 2-43 illustrates the effects excess pore pressure have on the undrained stress path quantified by the A parameter with the B parameter at unity adapted from Lambe and Whitman (1969).

Clay behavior is commonly characterized by normalizing the shear stresses to consolidation stress which is referred to as the Normalized Soil Parameter (NSP) concept. NSP provides a framework in which behavioral trends can be compared for clay soils. NSP was developed to explain the observation that clay specimens with the same overconsolidation ratio and different consolidation stresses had similar interpreted engineering parameters when normalized to the consolidation stress Ladd and Foott, (1974). Figure 2-44 presents a plot of normalized shear stress by shear strain for three specimens of a Maine organic clay consolidated to three different effective stresses to illustrate the NSP framework. Burland (1990) presents a study on the NSP strength of various clays and found the peak strength to depend primarily on the structure (fabric) of the clays and in situ effective stress state.

The influence of clay content on the strength of soil and rocks has few studies over a large ranges of clay contents and stress. Studies performed on rocks historically have not quantified percentages of clay minerals by mass and studies on soils have typically been limited to around 40% clay as an upper limit to the clay content. One significant study on lithified rocks with a large range of clay contents is Jizba (1991) which performed unconfined compression testing on tight gas sandstones and shales. Figure **2-45** provides the compressive strength by clay volume fraction for all rock specimens in the testing program of Jizba (1991). Figure 2-45 shows trends of decreasing compressive strength with increasing clay content and increasing compressive strength with increasing confining pressure. Figure **2-46** shows the effect of clay content on the linear Mohr-Coulomb failure envelope for the shaley sandstones and shales

tested in Jizba (1991). Figure 2-46 shows that the friction angle of the linear Mohr-Coulomb failure envelope decreases with increasing clay content. Plumb, Herron and Olsen (1992) found the same trends in decreasing strength with increasing clay content of lithified rocks but furthered the work through petrographic analysis of the tested specimens. They evaluated grain contacts within the rocks and found that strength varied as a function of grain contacts, with increasing strength with an increasing average number of contacts per grain. The variations of unconfined compressive strength by average number of grain contacts is presented in Figure 2-47 as adapted from Plumb, Herron and Olsen (1992).

Clay content was found to have an effect of shearing behavior of soil in Georgiannou, Burland and Hight (1990) who conducted an experimental program of CK_0UC triaxial tests on mixtures of sands and clays up to 30% clay by mass. Figure 2-48 presents stress paths from Georgiannou, Burland and Hight (1990) that indicates specimens up to 20% clay content may have dilative behavior during shearing but for clay contents above 30% clay dilative behavior was not observed. Prakasha and Chandrasekaran (2005) performed CK_0DC triaxial tests on mixtures of sands and clays ranging from 10% to 100% clay content. They found that the same general trend as Jizba (1991) and Plumb, Herron and Olsen (1992) of decreasing shear strength with increasing clay content as illustrated in Figure 2-49. Simpson and Evans (2016) performed CIUC triaxial tests on clay and sand mixtures between 0% clay and 100% clay and found similar results, of dilative tendencies for specimens of 20% clay content or less and a decrease in shear strength with increasing clay content. Simpson and Evans (2016) also observed a general decrease in the maximum friction angle with increasing clay content. Figure 2-50 provides the stress paths for the CIUC tests from Simpson and Evans (2016) including bounds on the upper (100% sand) and lower (100% clay) critical state lines. Simpson and Evans (2016) inferred the trend of decreasing friction angle with increasing clay content as binary either high friction angle in the grain supported regime or low friction angle in clay supported regime as shown by Figure 2-51. This interpretation may be due to a data point

at 30% clay that shows an increase in critical state friction angle from the previous data points of 0%, 10% and 20% clay, respectively. Simpson and Evans (2016) used a dry tamping method of specimen preparation which may have led to an issue with the relative density and the state parameter of the generally granular 30% clay specimen leading to a higher-than-expected critical state friction angle. Shen, et al. (2021) subjected mixtures of Calcareous sands with low plasticity Calcareous silts to CIDC triaxial testing to evaluate the effects of low plasticity fines on the shear strength of the sands. Shen, et al. (2021) and Jizba (1991) both show a consistent monotonic decrease in friction angle with increase in clay content for 0% to 40% clay content in sand and clay mixture specimens and 20% to 63% clay in shaley sandstones and shale specimens, respectively. Simpson and Evans (2016) show the same trend aside for the one potential erroneous point. The variations of friction angle by clay content from Shen, et al. (2021) are illustrated in Figure 2-52.

2.5. Summary

The literature review indicates that the longstanding engineering practice of separating the behavior of grain supported and clay matrix supported soils is valid for general behavioral assumptions. But the actual behavior for the engineering properties of interest is a continuum between the end members of fully grain supported and fully clay supported soil. The critical clay content which corresponds to the densest state a mixture of clays and grains is the demarcation point for clay and grain behavior. The critical clay content is stress dependent and will trend towards higher clay contents under increasing stress. Engineering parameters that are sensitive to density such as the dynamic properties shows a behavioral inflection point around the critical clay content. Engineering parameters which are dependent on the soil fabric such as compressibility, permeability, and mechanical strength properties show monotonic behavior of by variations in clay content.

The review of the literature indicates that there is not comprehensive study on lithology controlled specimens that includes measures, of compressibility, permeability, dynamic mechanical properties, and strength mechanical properties over a wide range of lithologies or stresses. The studies have been focused on select engineering parameters of interest and are typically limited by either narrow ranges of studied lithologies or by low testing effective stresses. This work is intends to provide a more holistic view of the behavior of silt and clay mixtures by testing lithologies over a wide range of clay contents at high stress levels.

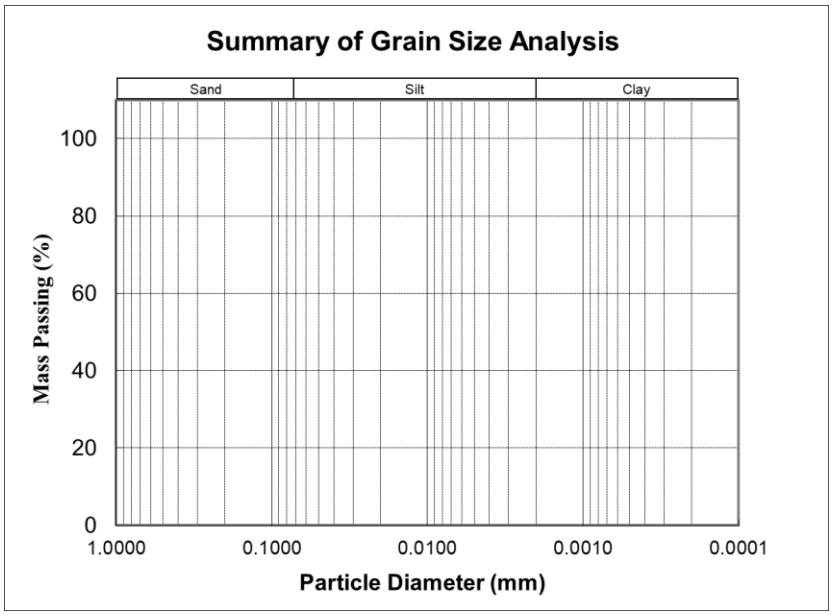


Figure 2-1: Classification of soils by particle size from sand to clay within the Unified Soil Classification System (USCS).

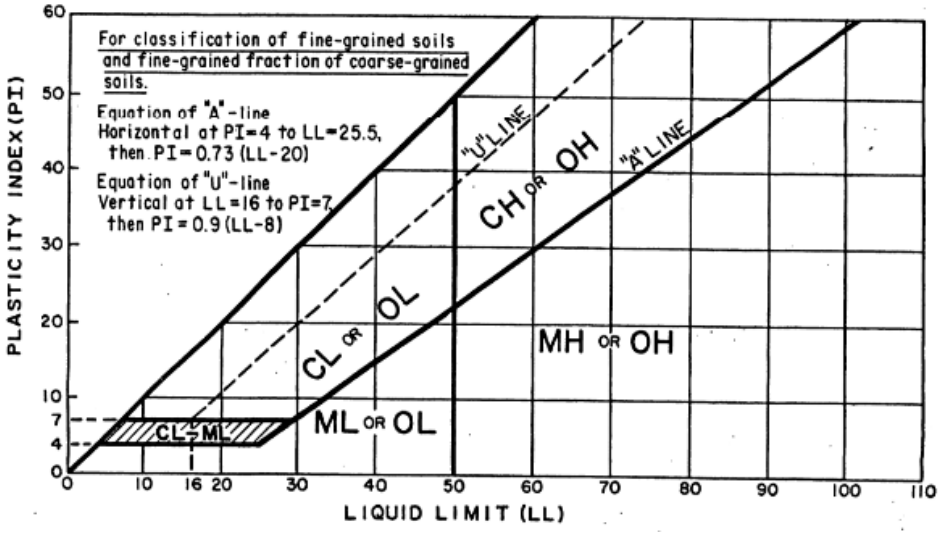


Figure 2-2: Classification of fine-grained soils and fine-grained soil fractions from the Atterberg Limits within the USCS adopted from ASTM D2487.

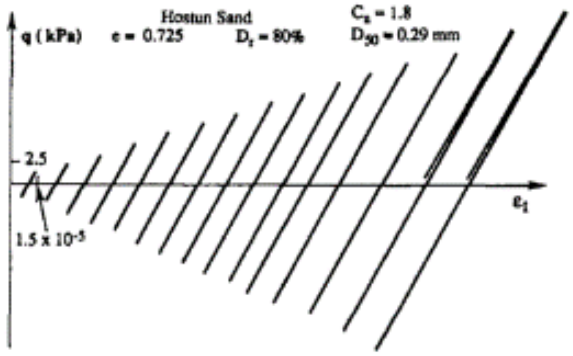


Figure 2-3: Stress-Strain relationship in cyclic loading at small strains in dry sand adopted from Hicher (1996). Each cycle is centered around the origin and a shifted representation is presented to distinguish individual cycles. The elastic recoverable strain limit is shown at a strain of $1.5X10^{-5}$.

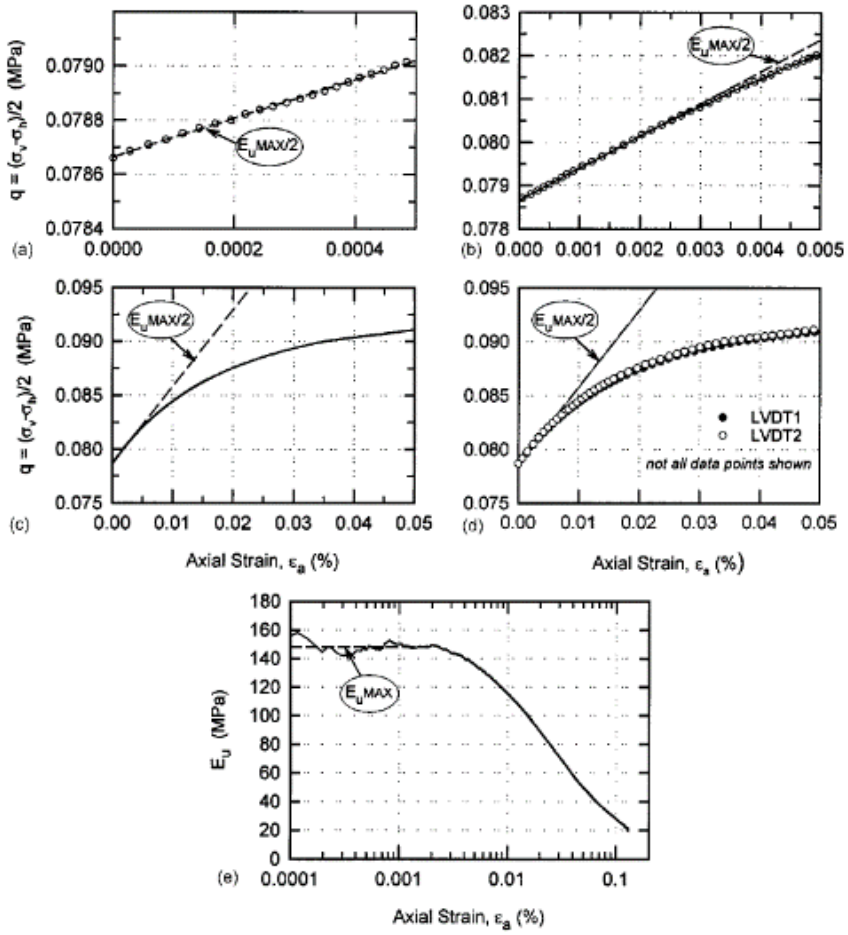


Figure 2-4: Pre-failure behavior of a normally consolidated, K_0 consolidated resedimented Boston blue clay consolidated to a vertical effective stress of about 03. MPa. Figure 2-2 a) -c) are stress–strain curves in 0–0.0005, 0–0.005, and 0.05% axial strain ranges; d) is a comparison of strains measured by two linear variable differential transducers in the 0–0.05% strain range; and e) is the stiffness degradation curve for the tested specimen.

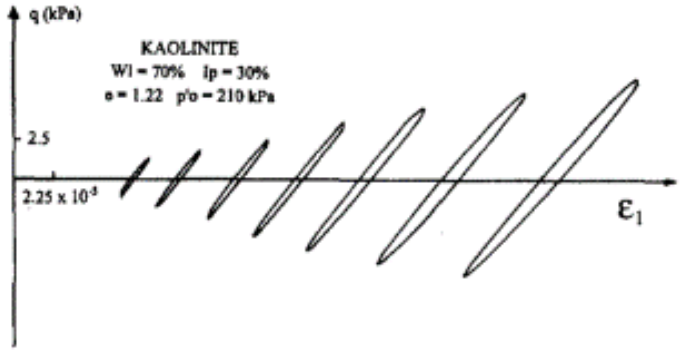


Figure 2-5: Stress-Strain relationship in cyclic loading at small strains in saturated clays adopted from Hicher (1996). Each cycle is centered around the origin and a shifted representation is presented to distinguish individual cycles. The hysteretic nature of the cyclic loads indicates the non-recoverable nature of the strains.

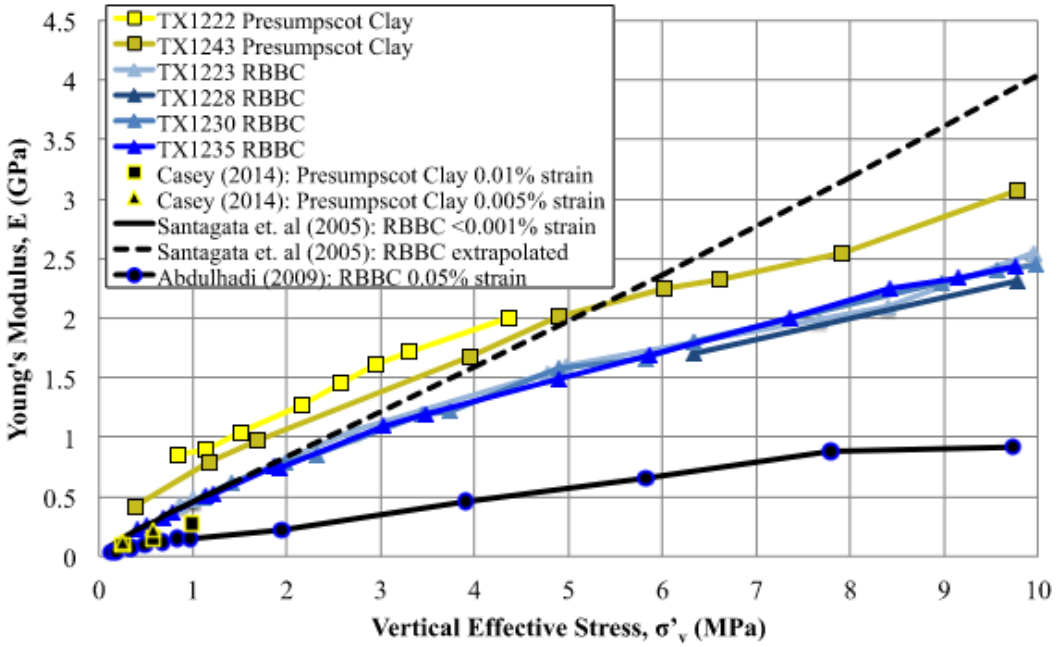


Figure 2-6: Published measurements of Young's modulus from specimen-mounted small-strain measurements Santagata (1998) and CK_0UC triaxial test results Abdulhadi (2009), Casey (2014) are compared to the velocity-derived Young's modulus Marjanovic (2016). Adopted from Marjanovic (2016).

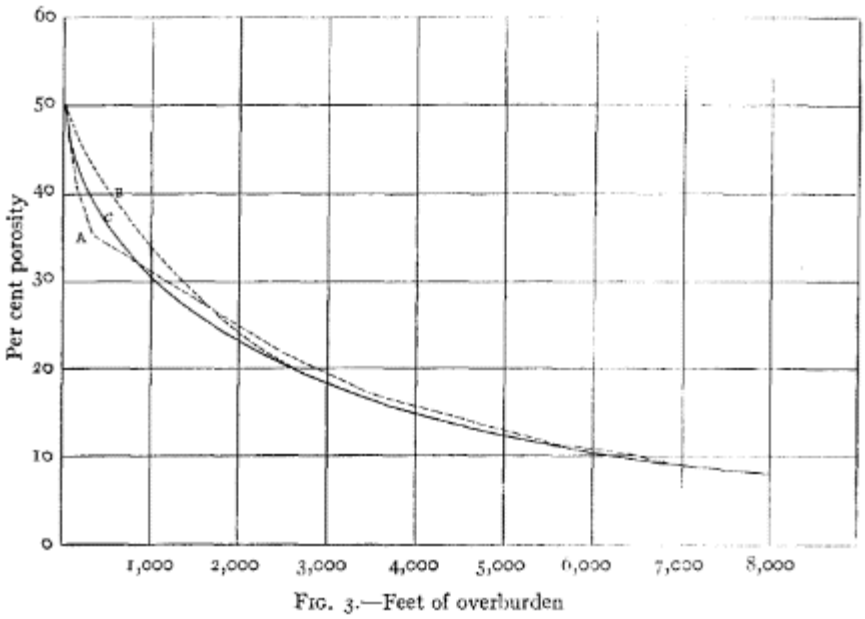


Figure 2-7: Porosity gradient by burial depth obtained by mapping the measured porosity of well cuttings by depth adopted from Hedberg (1926). Curve A represents the data from the porosity measurements. Curve B represents the theoretical porosity calculated based on 50% porosity as mud and 8% porosity at an 8,000 ft burial depth and an increase in density with burial depth. Curve C is an adjustment to curve A to remove irregularities within the measurements using considerations from curve B.

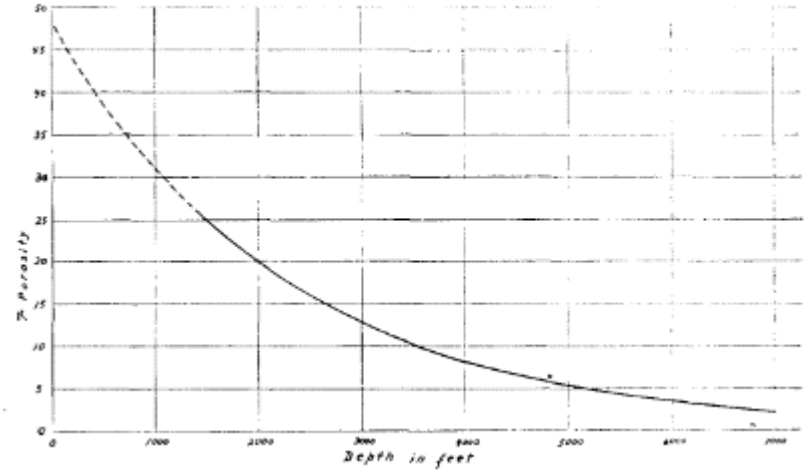


Figure 2-8: A logarithmic model for sediment porosity as a function of burial depth, using the equation $n = n_0(e^{-bx})$. Where n is the porosity, n_0 is the average surficial porosity, e is the natural logarithm, b is a constant and x is the depth of burial. Adopted from Athy (1930).

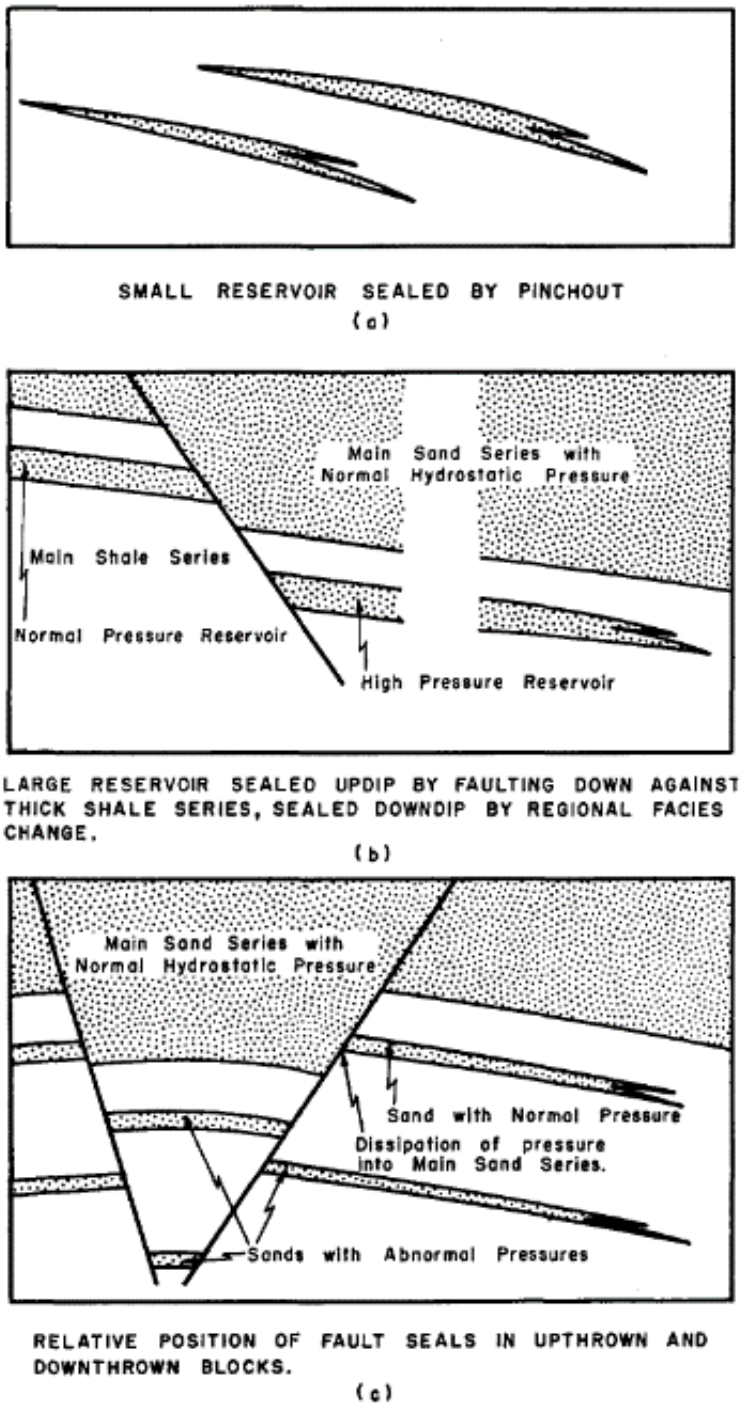


Figure 2-9: Geological mechanisms for pressurized zones in excess of hydrostatic pressures within the Gulf of Mexico adopted from Dickinson (1953). The shaded facies represent permeable sands while the unshaded facies represent impermeable shales.

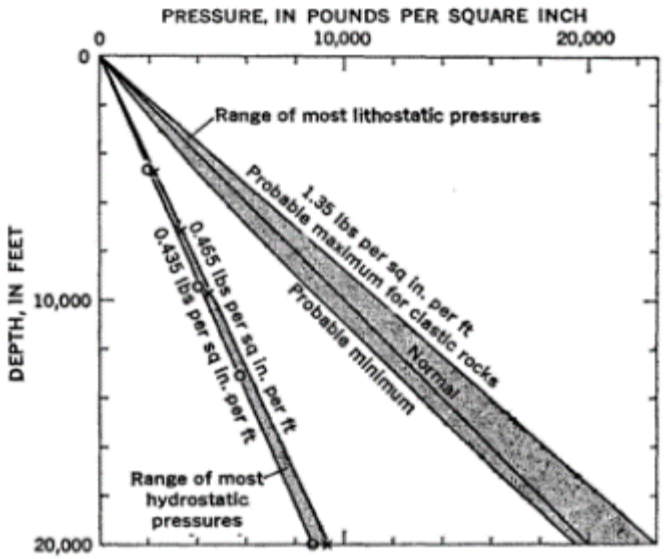


Figure 2-10: Ranges of probable earth stress for lithostatic pressures and hydrostatic pressures based on variations in mineral density and water density of distilled water to brine containing 100,000 ppm dissolved solids adapted from McCulloh (1967).

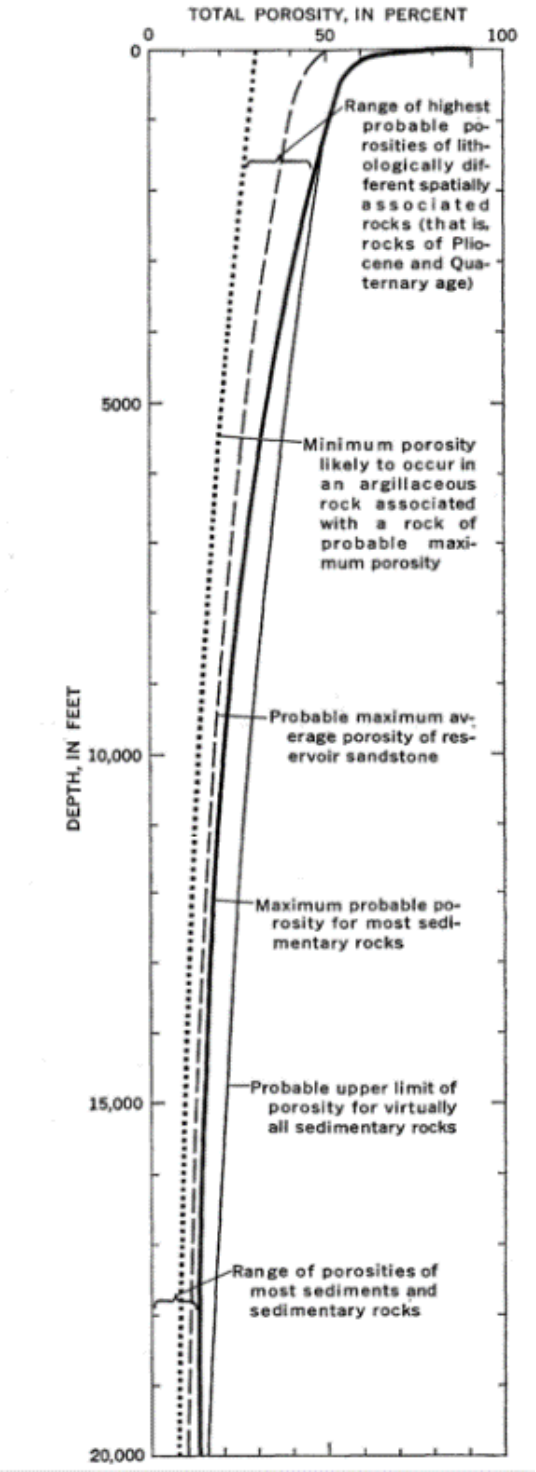


Figure 2-11: Total porosities of sedimentary rocks versus depth derived empirically from laboratory measurements of more than 4,000 samples of conventional cores from the Los Angeles and Ventura basins of California, other scattered localities in the United States, and the Po basin of Italy. Adopted from McCulloh (1967).

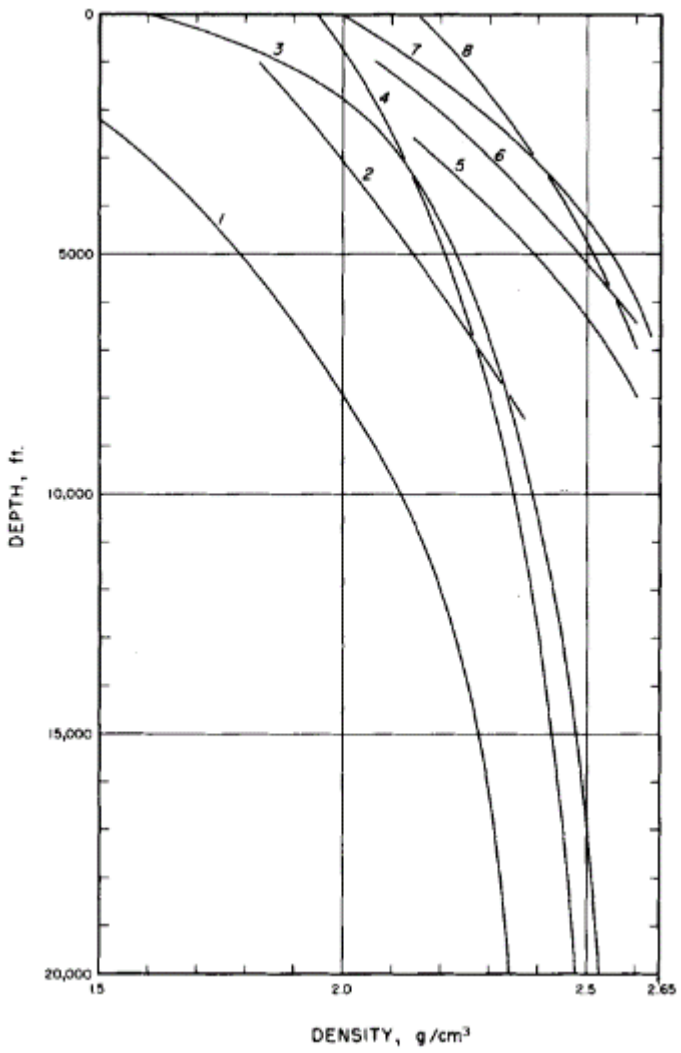


Figure 2-12: Variation of shale bulk densities with depth in sedimentary basins. 1 = methane-saturated clastic sedimentary rock (probable minimum density) McCulloh (1967); 2 = mudstone- Po Valley Basin, Italy Storer (1959); 3 = average Gulf Coast shale densities; values derived from geophysical data Dickinson (1953); 4 = average Gulf Coast shale densities derived from density logs and formation samples Eaton (1969); 5 = Motatan-1 - Maracaibo Basin, Venezuela Dallmus (1958); 6 = Gorgeteg No.1 - Hungary; calculated wet density values Skeels (1943); 7= Pennsylvanian and Permian dry shale density values, Oklahoma and Texas; Athy's adjusted curve Dallmus (1958); 8 = Las Ollas-1 - eastern Venezuela Dallmus (1958). Figure 2-10 is adopted from Rieke and Chilingar (1974).

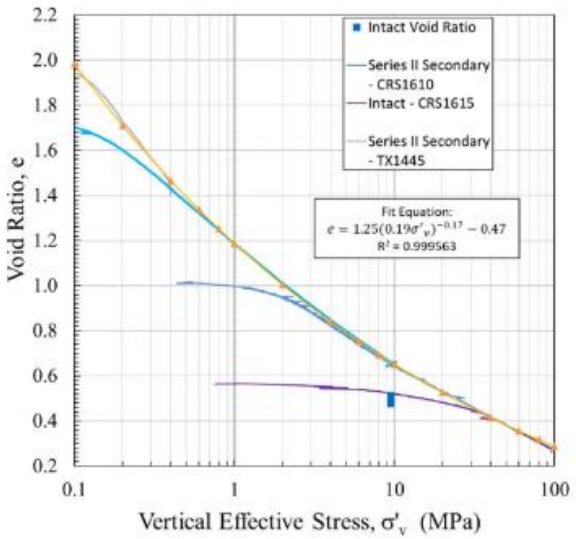


Figure 2-13: Comparison of the compression of reconstituted clay specimens (Series II) to intact clay specimens to a 100 MPa stress adopted from Finnegan (2020). The intact specimen is significantly denser at lower effective stresses than the reconstituted specimens, but at high effective stresses the compression behavior converges. The difference at low effective stresses is attributed to the stress history of the intact specimens which is not present in the reconstituted specimens. The convergence of the behavior at high stresses is attributed to the intrinsic compression discussed within Burland (1990).

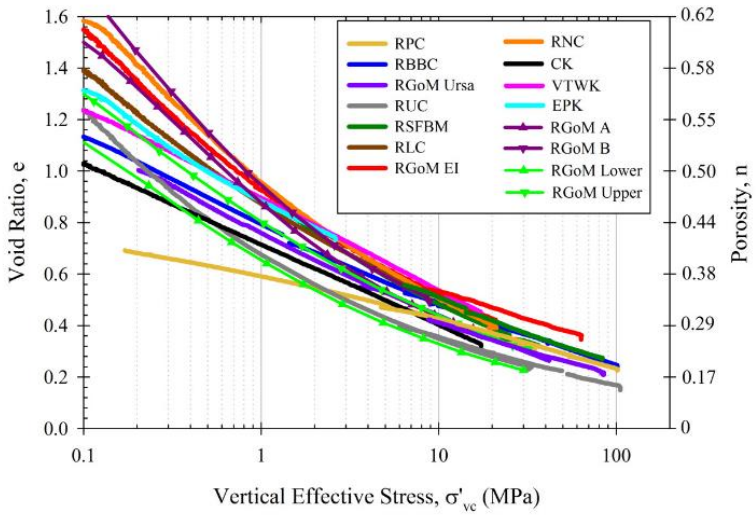


Figure 2-14: A comparison of the compression behavior of resedimented silts and clays up to a 100 MPa effective stress level adopted from Casey (2014).

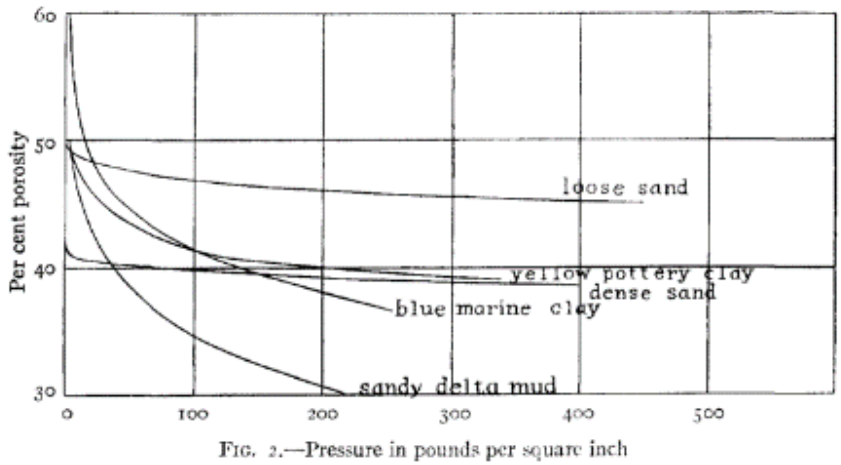


FIG. 2.—Pressure in pounds per square inch

Figure 2-15: Comparison of the compression of various sand and clays adopted from Hedberg (1926).

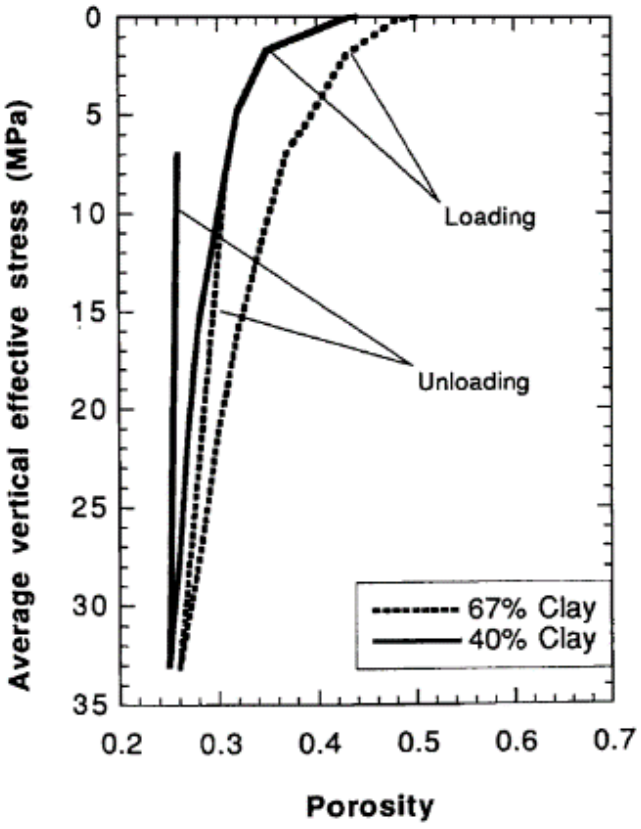


Figure 2-16: Compression curves of two London clay specimens with different clay fractions adopted from Dewhurst, et al. (1998).

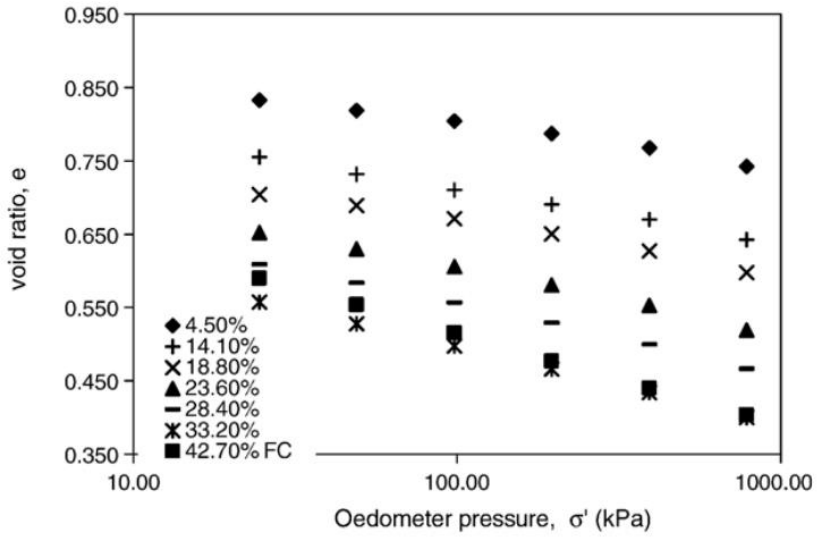


Figure 2-17: Compression curves of seven sand and Kaolinite clay mixtures from one dimension compression testing on the mixture adopted from Monkul and Ozden (2007). The FC percentage shown represent the added Kaolinite clay content by mass.

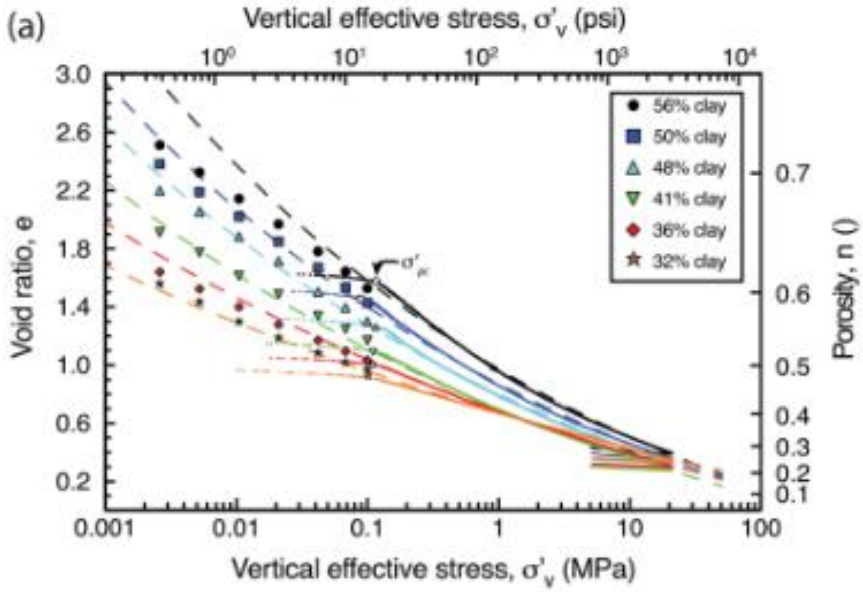


Figure 2-18: Compression curves of six amended resedimented clay and silt mixtures from uniaxial constant-rate-of-strain consolidation tests adopted from Reece (2021). All samples were consolidated to a maximum vertical effective stress of 20 MPa.

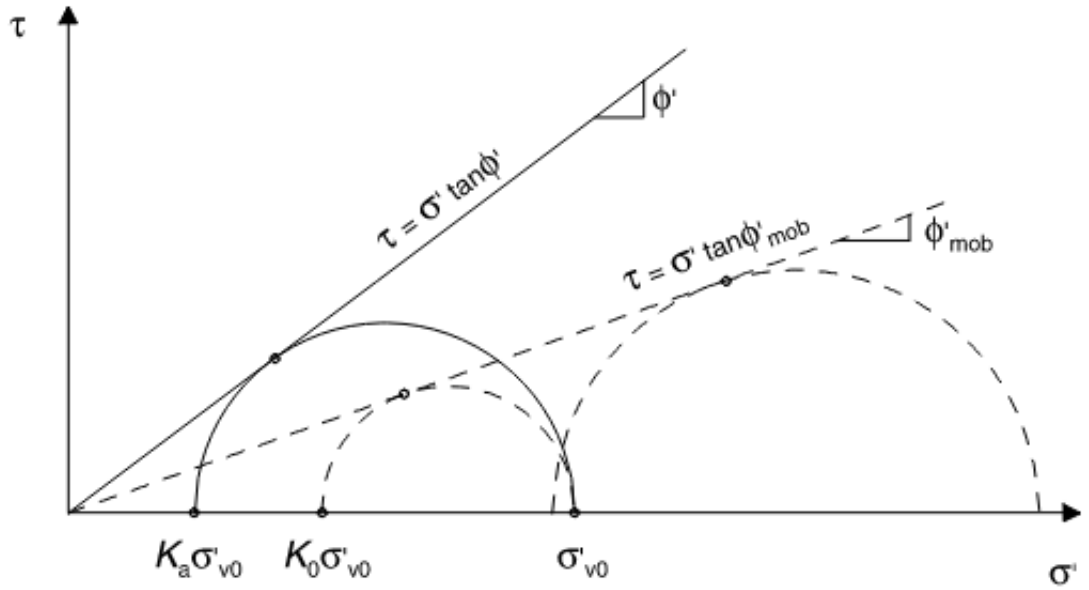


Figure 2-19: Mohr's circles at failure under one dimensional loading adopted from Federico and Elia (2009). The dashed circles and line represent the state of stress at maximum stress and the mobilized friction angle. The solid circle and line represent the state of stress at the friction failure envelope.

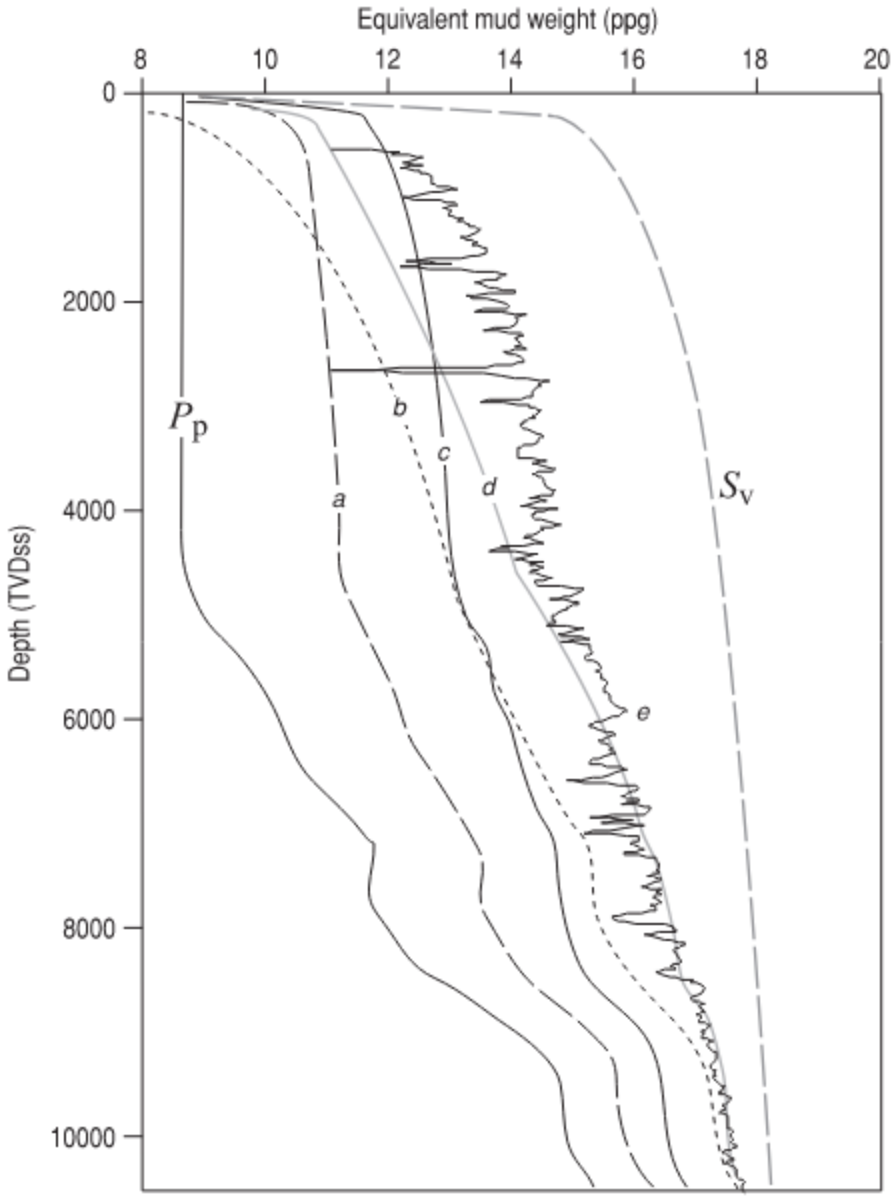


Figure 2-20: Different determinations of least principal stress from pore pressure (curve $P_{P)}$ and vertical stress data (curve S_V) for a well in the Gulf of Mexico. **Curve a** from Zoback and Healy (1984) method, **curve b** is Breckels and van Eekelen (1982), **curve c** is from Hubbert and Willis (1957) utilizing a modified empirical coefficient of 0.5, **curve d** is based on Holbrook, Maggiori et al. (1993), and **curve e** is from Eaton (1969), the figure is adopted from Zoback (2007).

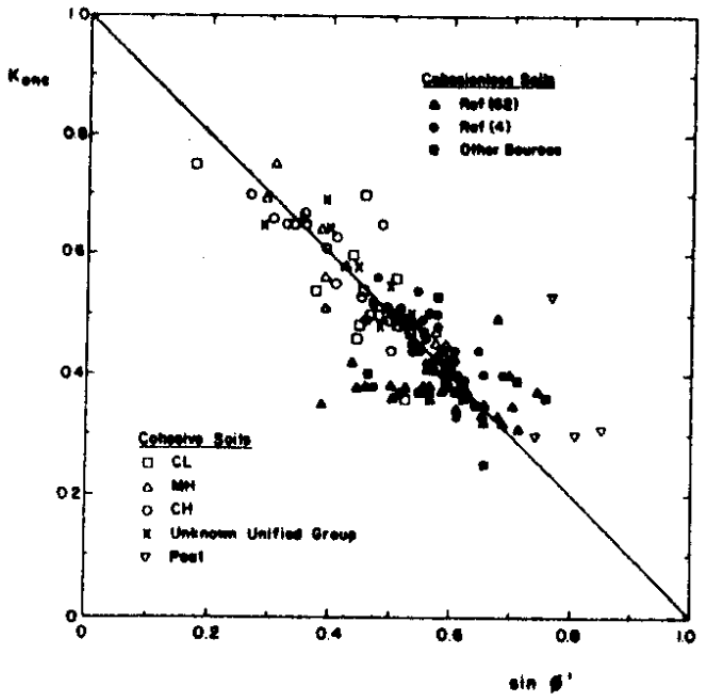


Figure 2-21: Observed relationship between the normally consolidated K_0 and sin of the effective friction angle for various soil types adopted from Mayne and Kulhawy (1982).

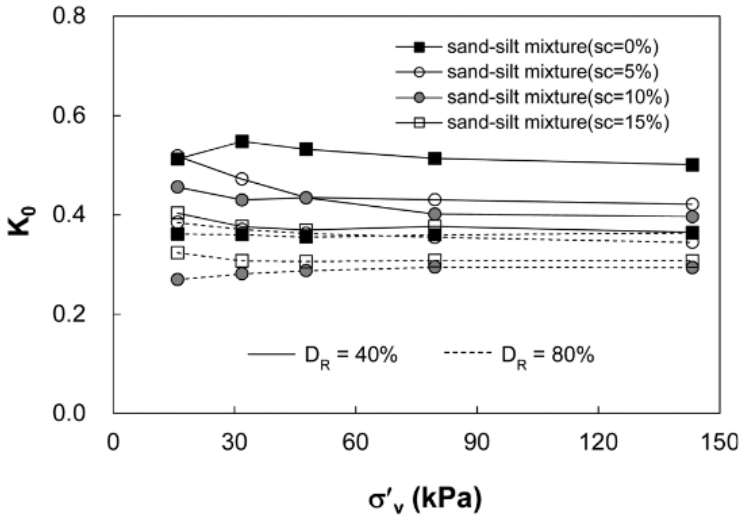


Figure 2-22: Variations of K_0 by fines content and relative density adopted from Lee, Lee and Park (2014).

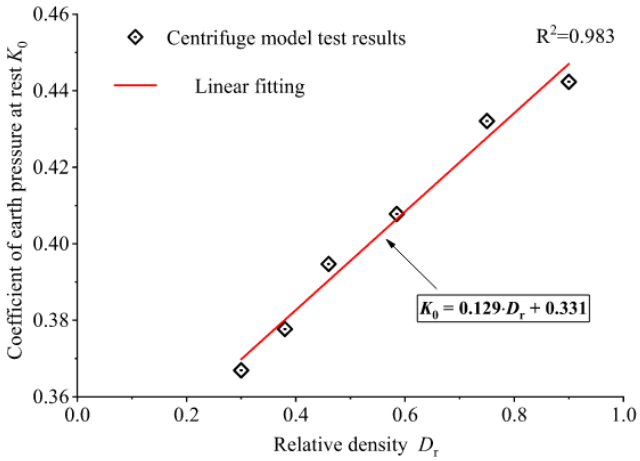


Figure 2-23: Measured relationship between K_0 and relative density of sand specimens adopted from Li, et al. (2023).

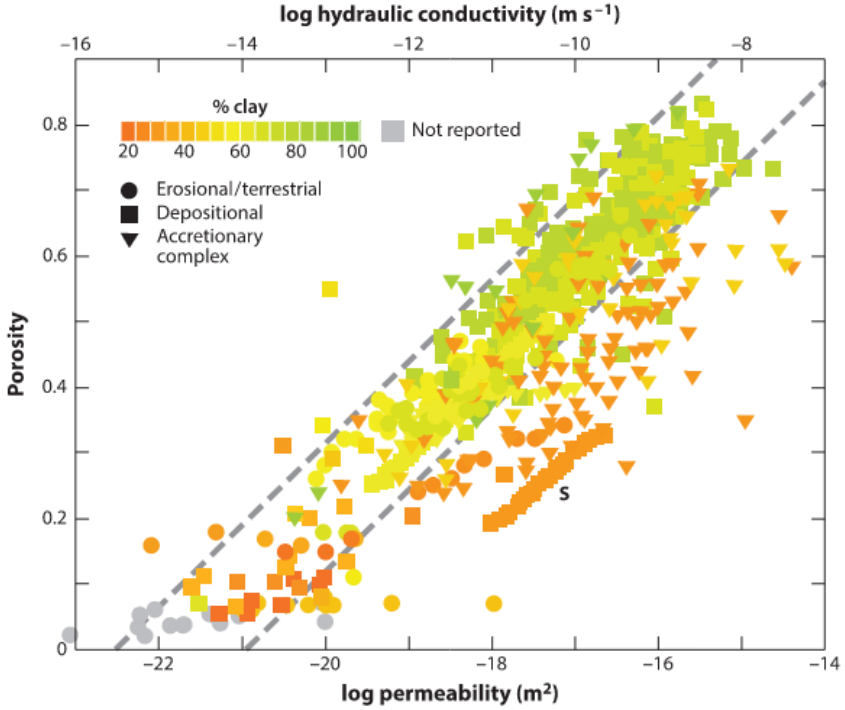


Figure 2-24: Permeability of clay and shale from laboratory tests plotted versus porosity and showing clay fraction and geologic setting adopted from Neuzil (2019). The hydraulic conductivity scale is for aqueous fluids at room temperature. Data from various studies as presented in Neuzil (2019). The dashed lines indicate minimum and maximum theoretical permeabilities from the log permeability linear porosity relationship presented within Bekins, Mcaffrey and Dreiss (1995).

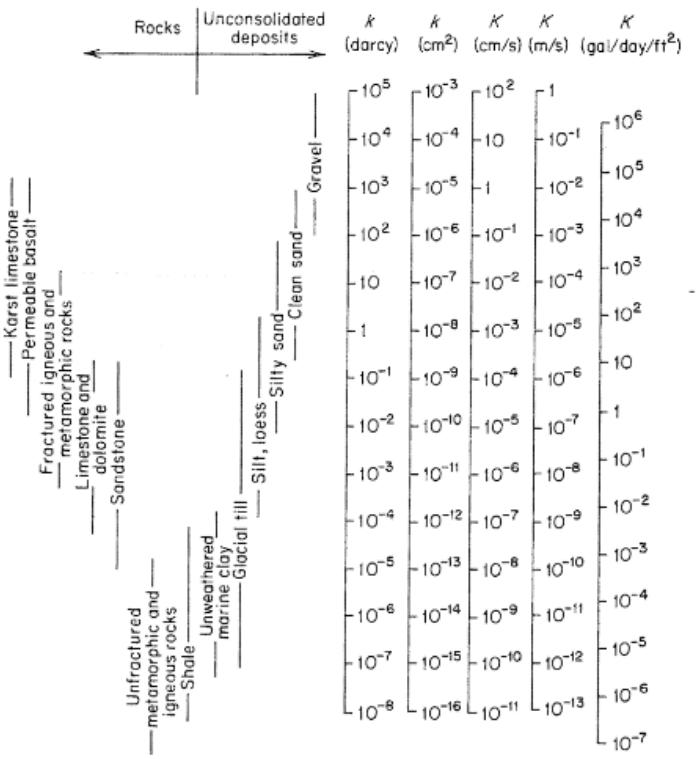


Figure 2-25: Ranges in hydraulic conductivity and permeability for various geologic materials adopted from Freeze and (Cherry 1979).

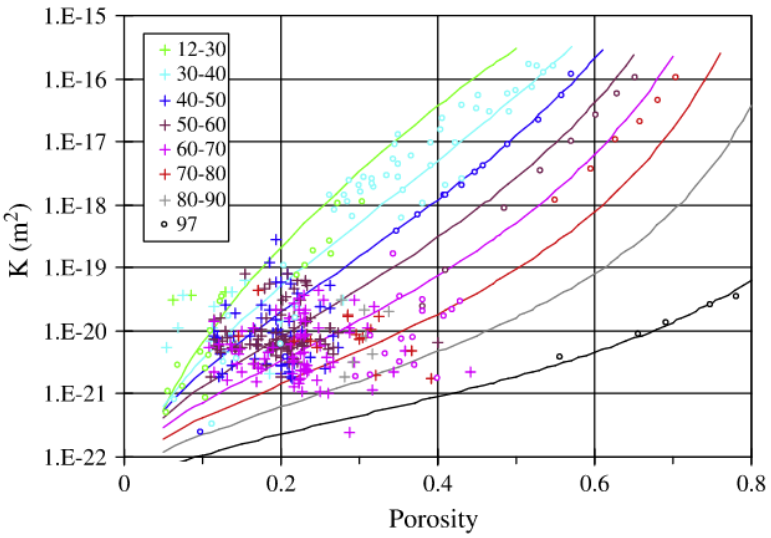


Figure 2-26: Permeability of clay and silt mixtures by porosity from a model (continuous lines) and direct measurements (data points) adopted from Yang & Aplin, (2010). The clay contents range to the corresponding colored model result and data points are presented in the key.

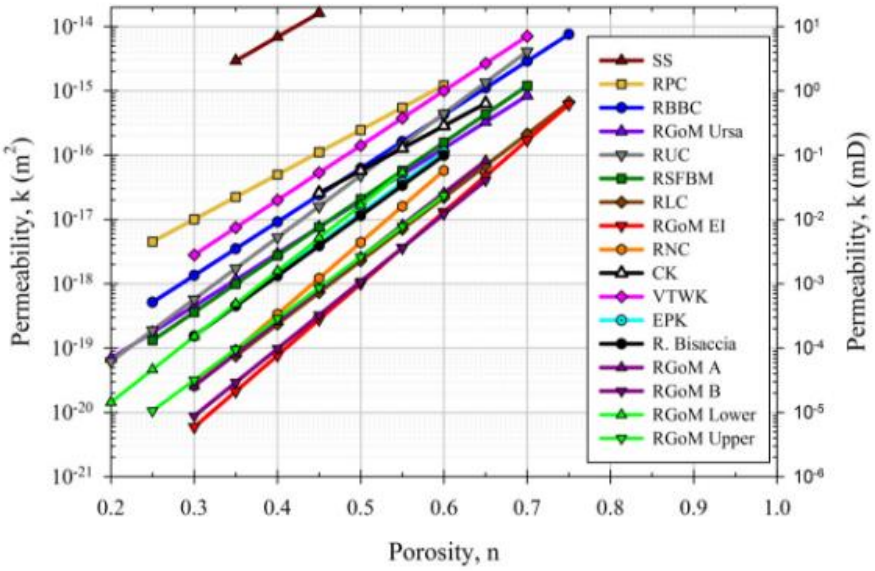


Figure 2-27: Ranges in permeability by hydraulic conductivity for resedimented mudrocks adapted from Casey (2014).

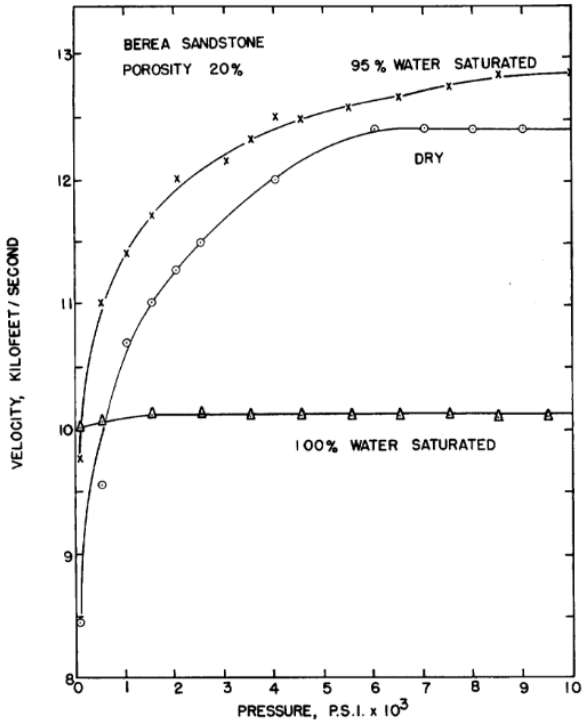


Figure 2-28: Effect of uniform confining pressure on the compressional velocity through a dry, saturated, and partially saturated Berea Sandstone specimens adapted from Wyllie, Gregory and Gardner (1956).

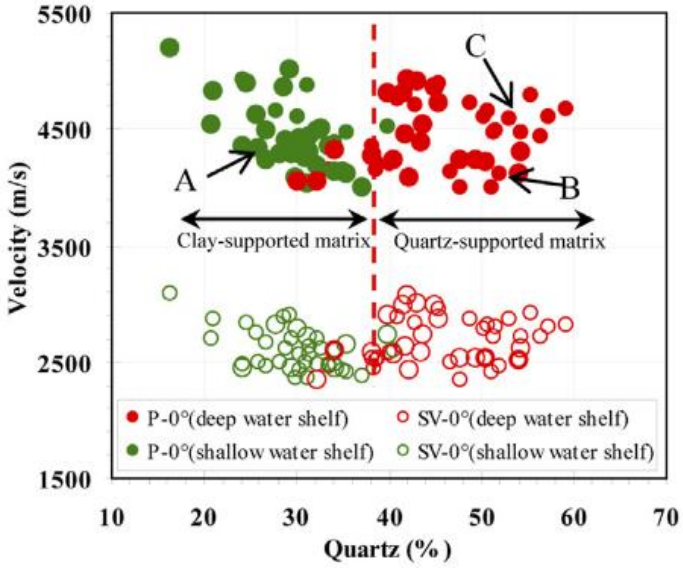


Figure 2-29: Wave velocities normal to the bedding plane by quartz content and depositional environment for the Longmaxi Shale Formation at 30 MPa confining stress adapted from Deng, et al. (2021). The green points are measurements on samples formed in a shallow water depositional environment and the red points are measurements on samples formed in a deep-water depositional environment. The green points show a trend in decreasing velocity with increasing quartz content while the red points have no discernable trends.

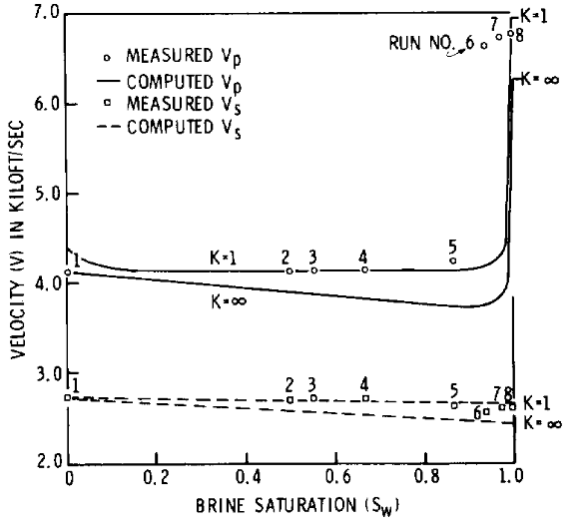


Figure 2-30: Wave velocities by brine saturation for Ottawa Sand specimens, where K is a parameter that estimates the interaction between the soil grains and pore fluid adapted from Domenico (1977). The plot indicates the significant effect saturation has on compressional wave velocities and the relatively negligible effect on shear wave velocities.

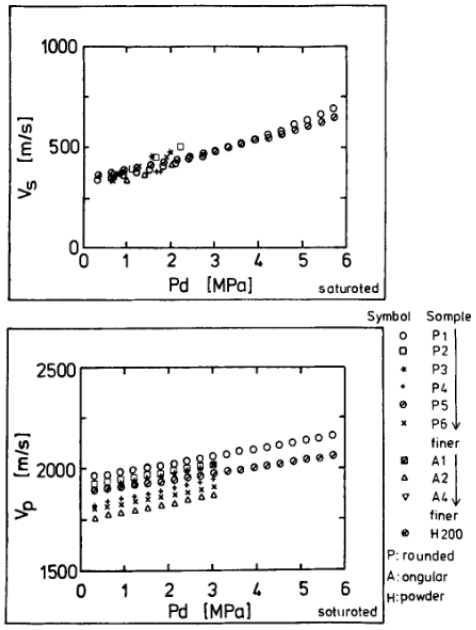


Figure 2-31: Variations in S wave velocity (top) and P wave velocity in saturated sands of varying particle size, and angularity adopted from Prasad and Meissner (1992). The S wave velocities are unaffected by grain size and angularity. The P wave velocities decrease with decreasing particle size and increasing particle angularity.

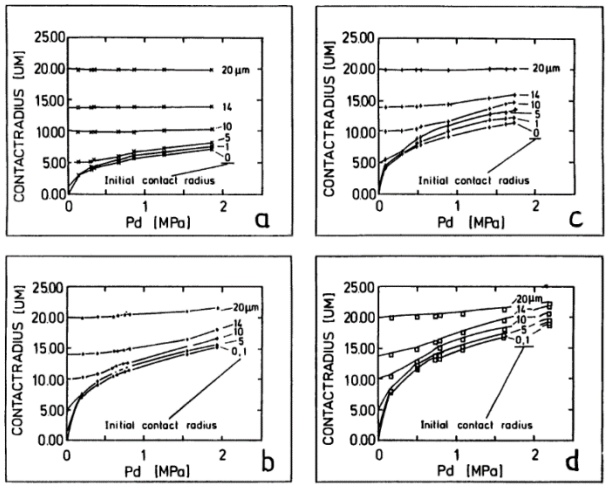


Figure 2-32: Change in contact radius by pressure Contact Radius Models of soils with different mean grain sizes adopted from Prasad and Meissner (1992). (a) R = 110 µm, (b) R = 150 µm, (c) R = 225 µm, (d) R = 275 µm. The number on each curve denotes the initial contact radius taken for the curve's calculation.

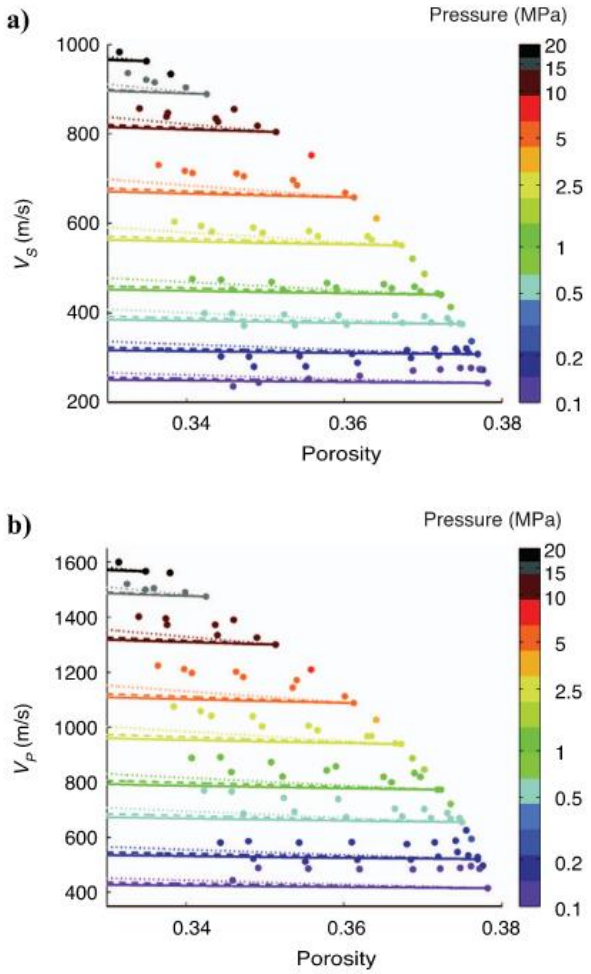


Figure 2-33: Variations in S wave velocity (top) and P wave velocity in a saturated sand specimen consisting of 65% by mass 0.295 mm to 0.35 mm quartz sand grains and 35% by mass 0.053 to 0.088 quartz sand grains as adapted from Zimmer, et al. (2007). The specimen was subjected to seven load unload pressure cycles up to a maximum stress of 20 MPa and velocity measurements were conducted during both the loading and unloading portions of the test. The color code represents the effective stresses, modeled measurements for the modified Reuss average model (solid), modified Hashin-Shtrikman average model (dotted), and Hardin and Blandford empirical model (dashed) are also shown as discussed within Zimmer, et al. (2007).

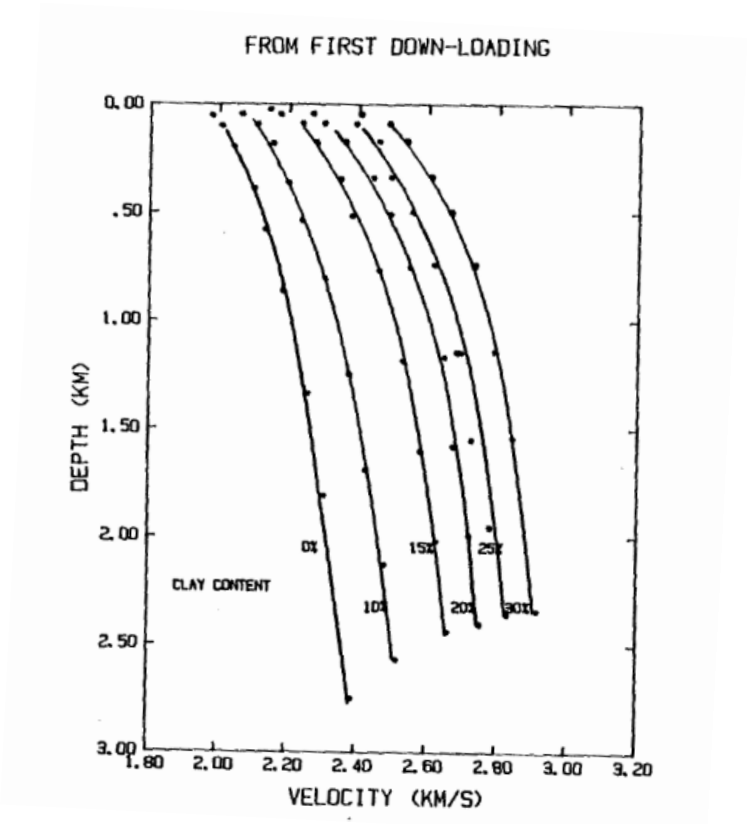


Figure 2-34: The effect of burial depth on p wave velocity in mixtures of Ottawa Sand and Smectite clay from D.-H. Han (1986).

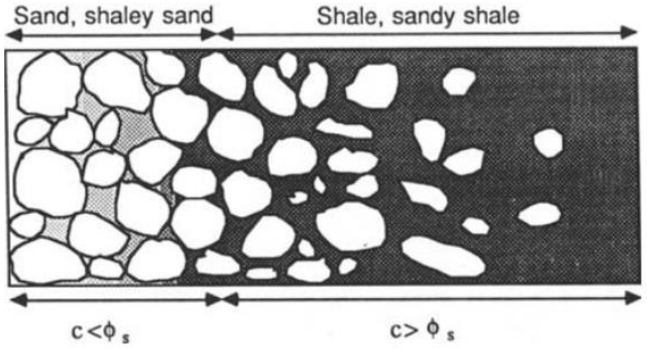


Figure 2-35: Diagrammatic spectrum of sand and clay mixtures and critical clay-content adapted from (Marion, Nur, Yin, & Han, 1992), c is the clay content by volume and ϕ_s is the porosity of the sand grains.

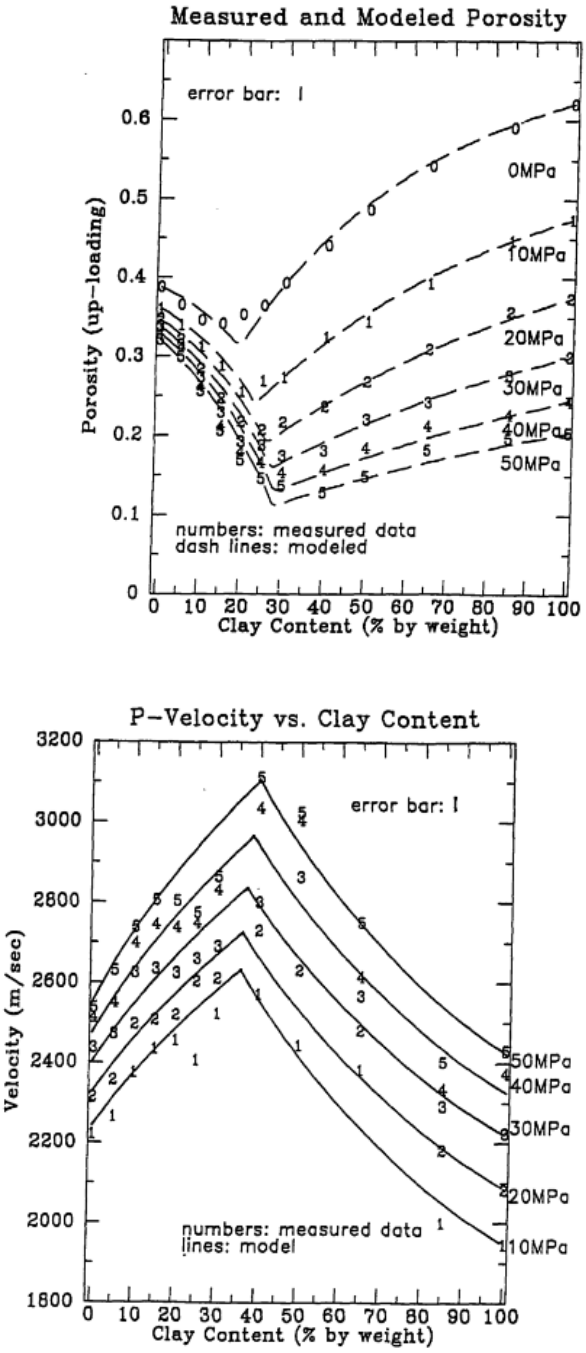


Figure 2-36: Left: Porosity by specimen clay content at the indicated confining stress level. Right: P Wave velocity by clay content at the indicated confining stress level. For both plots the numbers represent the measured data and the lines represent modeled fits to the data. Both plots are adapted from Yin (1992).

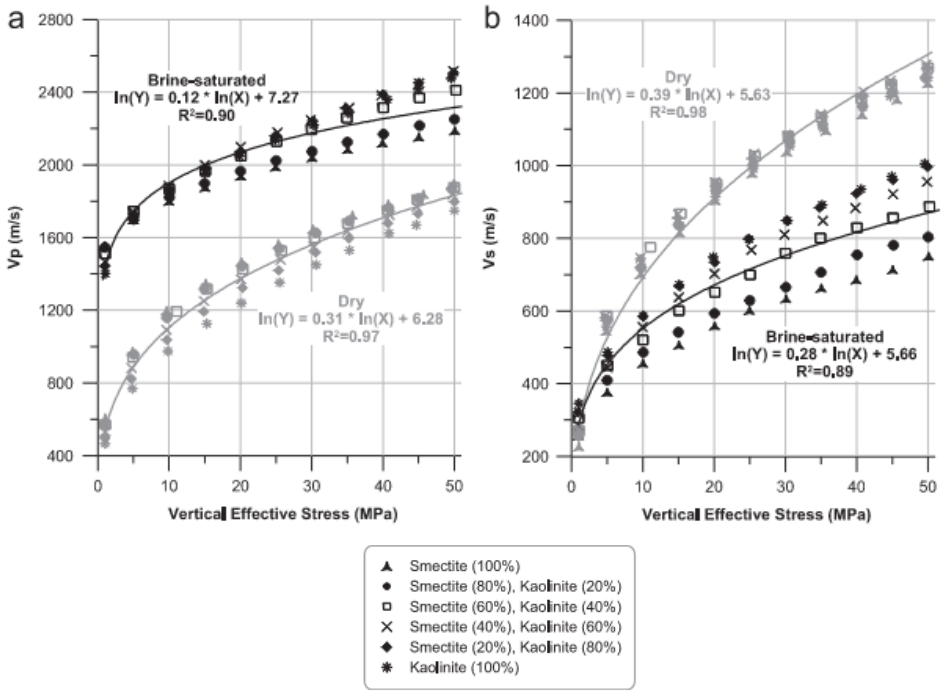


Figure 2-37: Velocity measurements by vertical effective stress for dry and brine saturated synthetic mixtures of Smectite and Kaolinite clay adapted from Mondol, Bjorlykke, et al. (2007). Left: P-wave velocities, Right: S-Wave velocities.

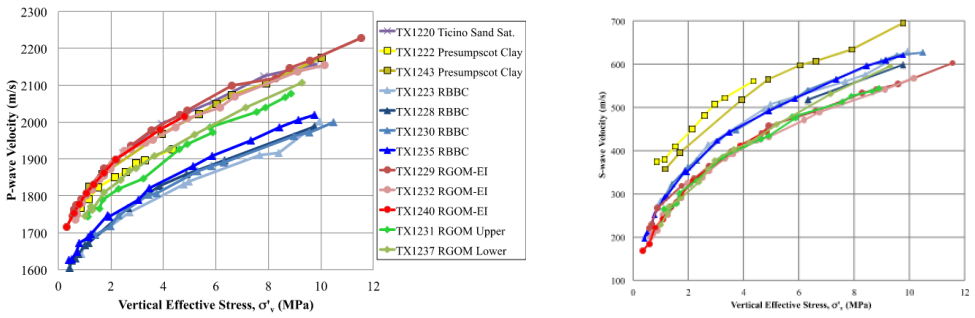


Figure 2-38: P-wave and S-wave velocity measurements by vertical effective stress for various intact, reconstituted and resedimented sand and clay specimens adapted from Marjanovic (2016). Left: P-wave velocities, Right: S-Wave velocities.

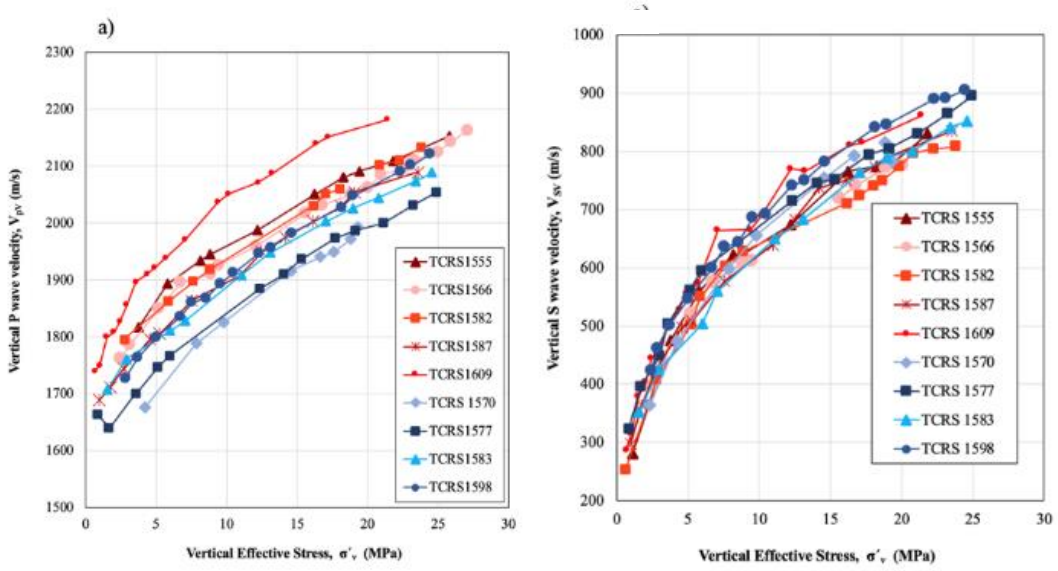


Figure 2-39: P-wave and S-wave velocity measurements by vertical effective stress for resedimented clay specimens adapted from Ranjpour (2020). Left: P-wave velocities, Right: S-Wave velocities.

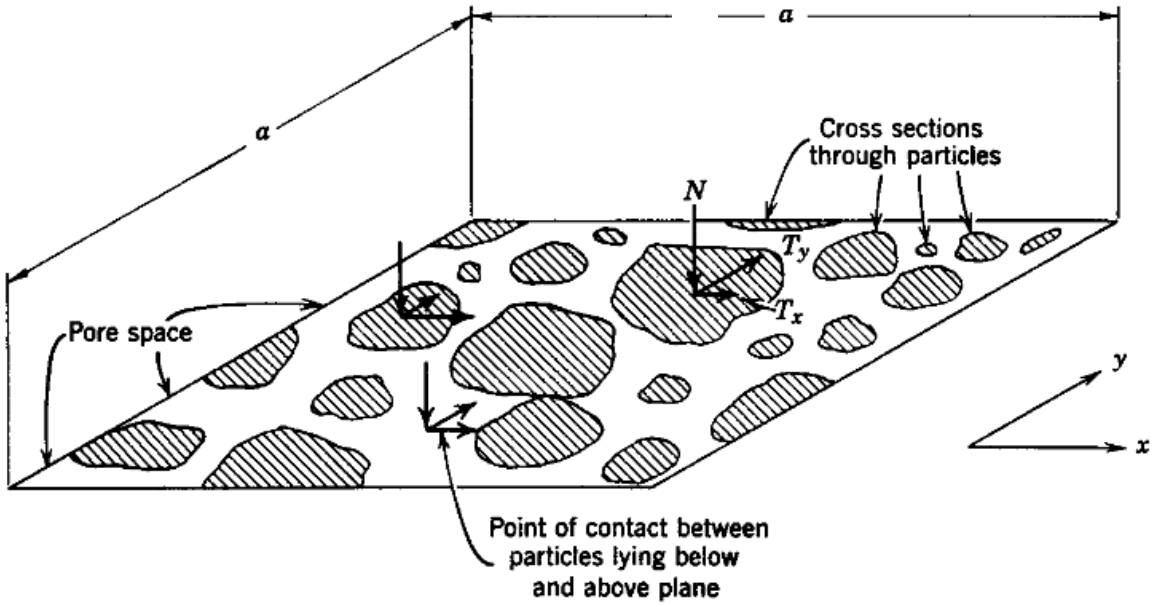


Figure 2-40: Defining stress in a particulate system as adapted from Lambe and Whitman (1969). The normal macroscopic stress is defined as force N dived by the area of the plane, and the macroscopic shear components acting on the plane are the shear forces T_x and T_y divided by the area of the plane.

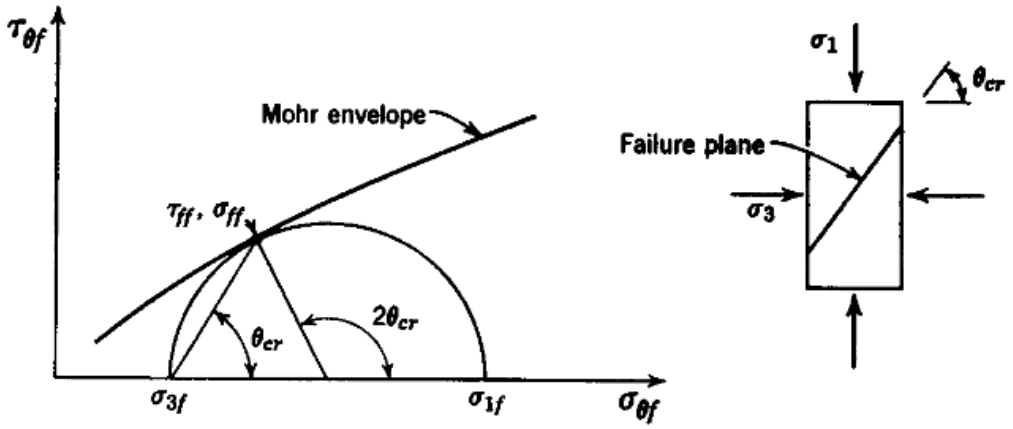


Figure 2-41: Stresses at failure, relationship of Mohr circle at failure, the Mohr-Coulomb failure criteria, and the theoretical failure plane as adapted from Lambe and Whitman (1969).

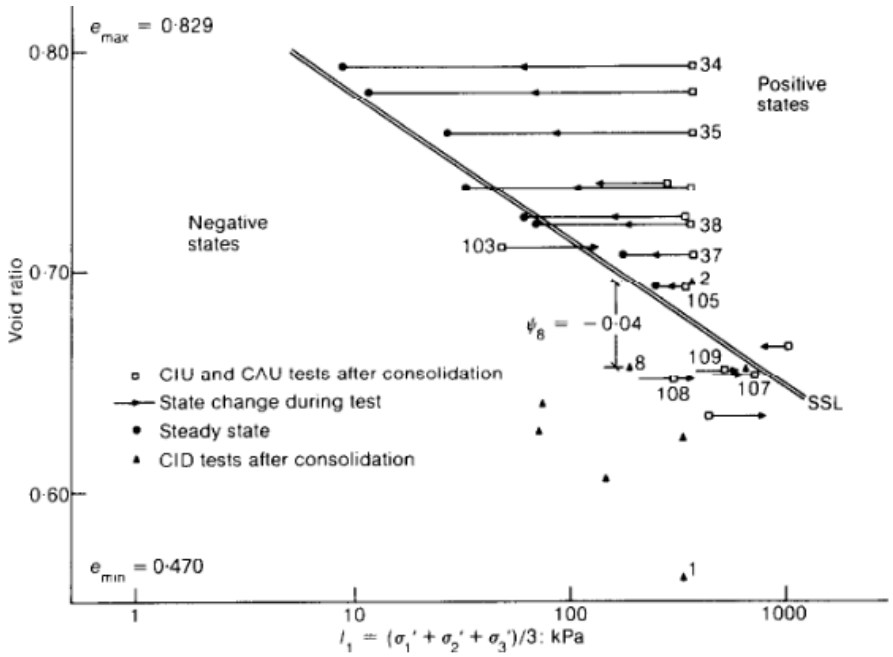


Figure 2-42: State parameter from tests performed on Kogyuk 350/2 sand from Been and Jefferies (1985). The positive state parameter indicate contractive behavior towards the Steady State Line and the negative state parameter indicates dilative behavior towards the steady state line during shearing.

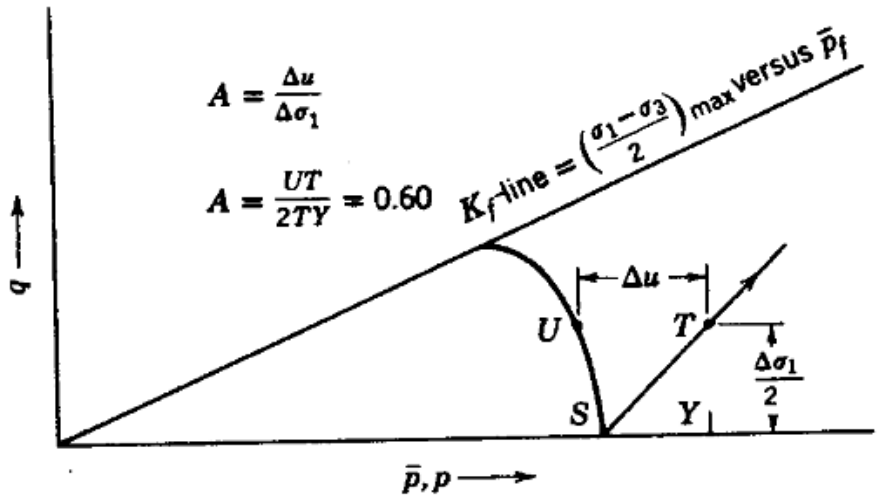


Figure 2-43: The effect of pore pressure on the undrained stress path as quantified by the A parameter adapted from Lambe and Whitman (1969).

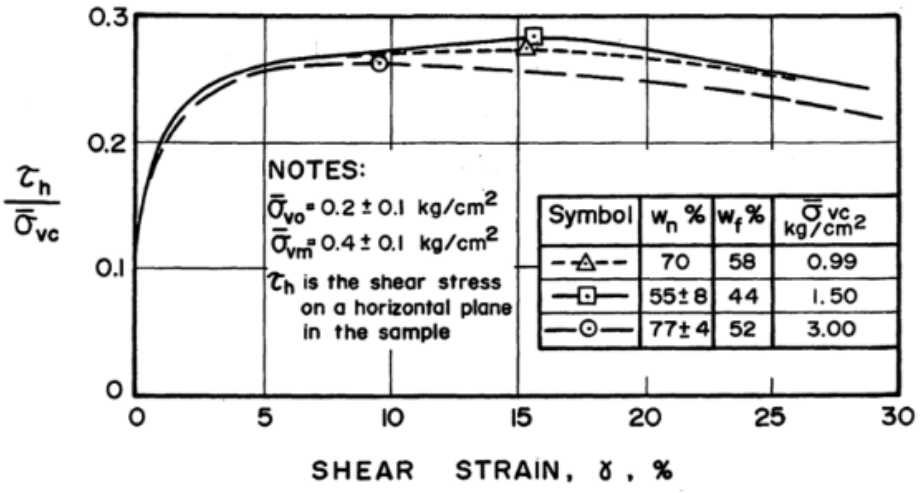


Figure 2-44: Normalized shear stress to effective consolidation stress by shear strain for three Maine organic clay specimens as an example of Normalized Soil Parameter concept adapted from Ladd and Foott (1974)

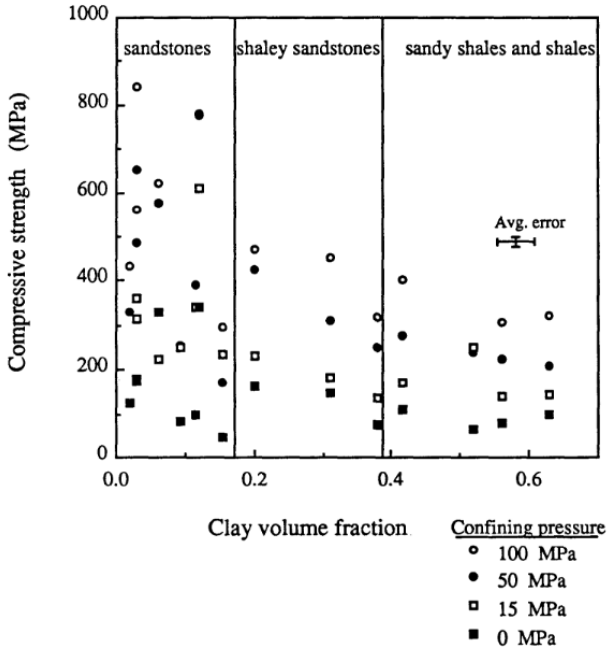


Figure 2-45: Compressive strength of mudrocks by clay content over varying confining pressures adapted from Jizba (1991)

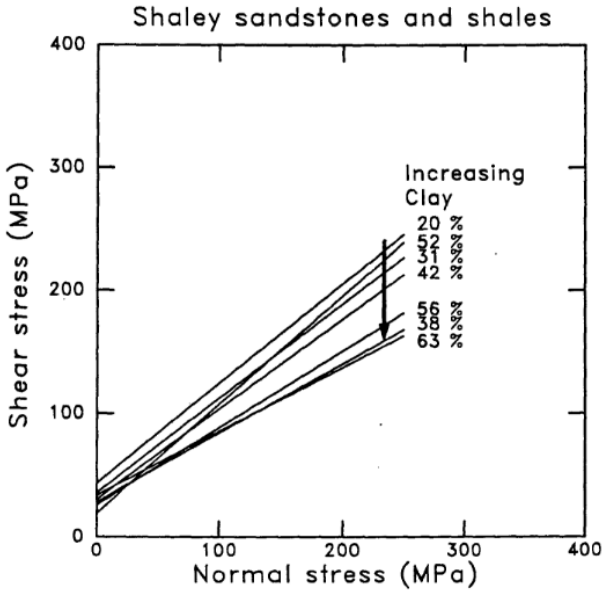


Figure 2-46: Clay content effects on the linear Mohr-Coulomb failure envelopes for shaley sandstones and shales adapted from Jizba (1991).

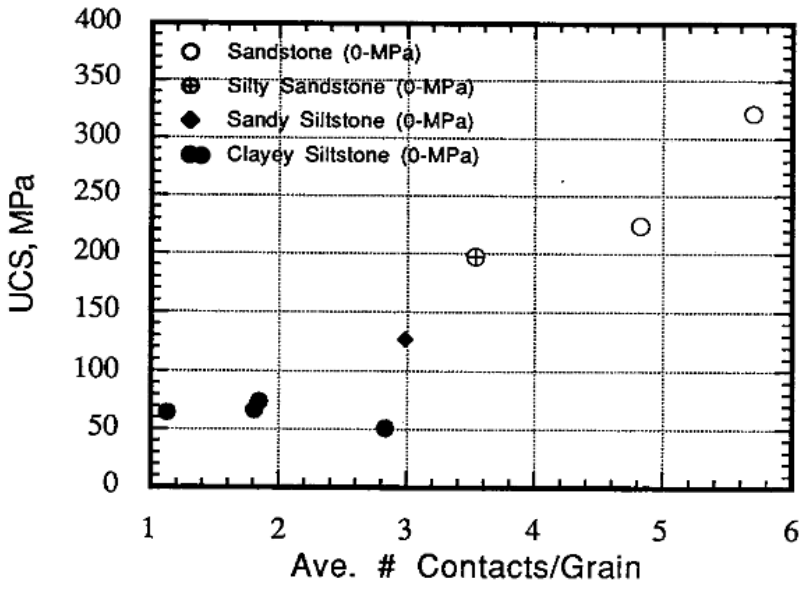


Figure 2-47: Unconfined Compressive Strength (UCS) for Travis Peak samples by grain contacts adapted from Plumb, Herron and Olsen (1992). The grain contacts were evaluated by petrographic analyses of thin sections from the tested lithofacies.

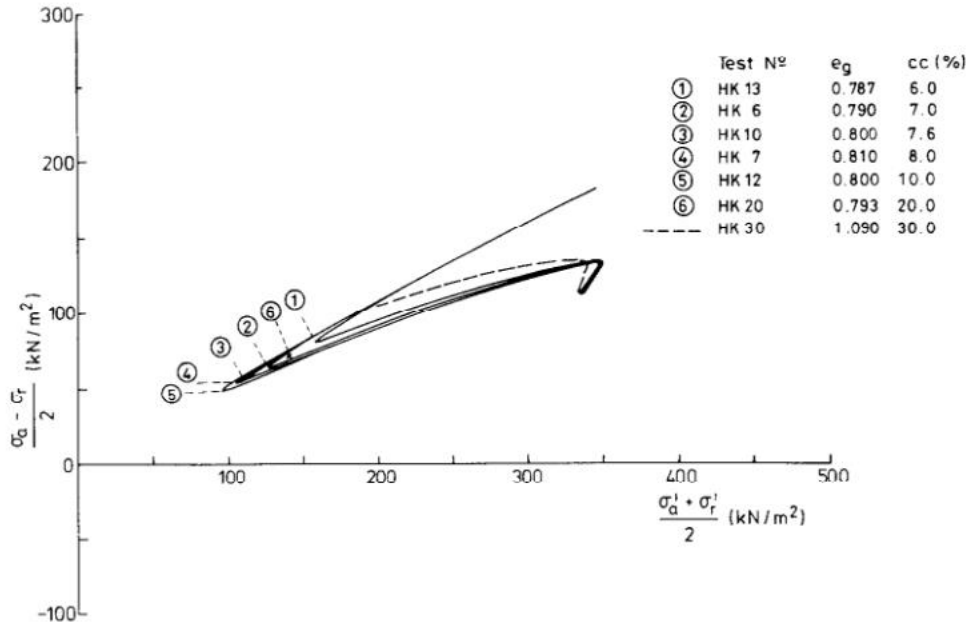


Figure 2-48: Clay content effects on stress paths and shear behavior of sand and clay mixtures adapted from Georgiannou, Burland and Hight (1990). CC is the clay content by mass and the specimens were subjected to CK_0UC triaxial testing.

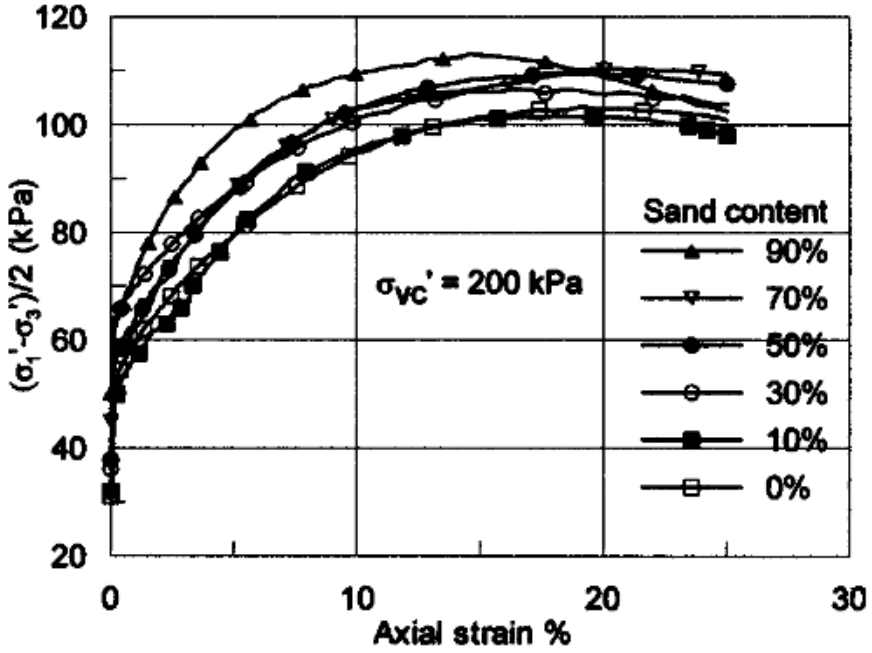


Figure 2-49: Stress strain plots for clay and sand mixtures consolidated to a 200 kPa effective stress and sheared in a CK_0DC triaxial test adapted from Prakasha and Chandrasekaran (2005).

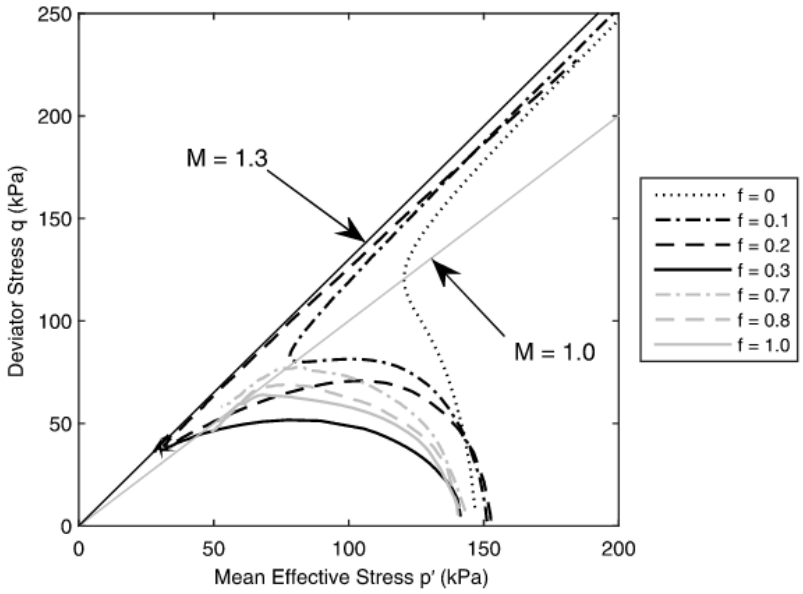


Figure 2-50: CIUC test stress paths on mixtures of Kaolinite clay and Ottawa Sand adapted from Simpson and Evans (2016). Where f is the clay content by mass and M is the slope of the critical state line.

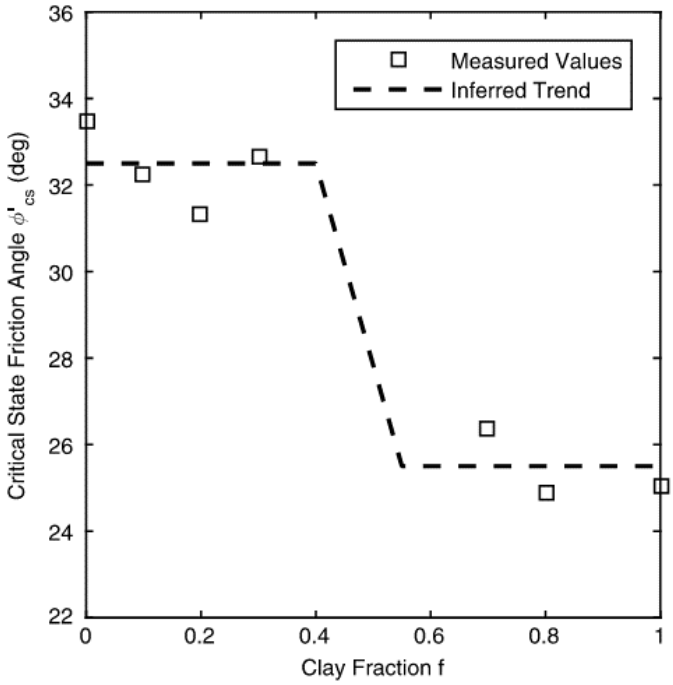


Figure 2-51: Critical state friction angle by clay fraction from Simpson and Evans (2016). The critical state friction angle at 30% clay may be higher than anticipated due to difficulties in maintaining a consistent specimen density with the dry tamped method employed.

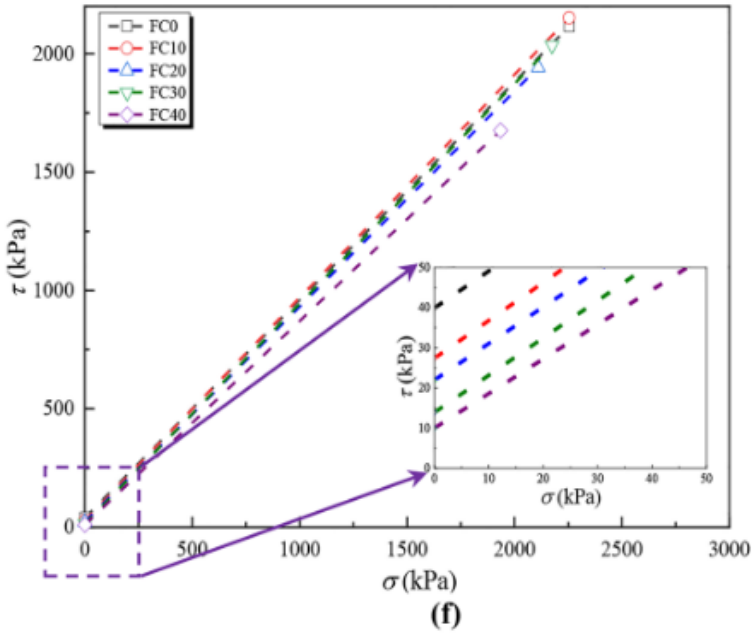


Figure 2-52: Interpreted Mohr-Coulomb failure envelopes for CIDC triaxial tests adapted from Shen, et al. (2021). FC indicates the clay content between 0% and 40% clay by mass.

CHAPTER 3. Experimental Testing Equipment and Procedures

3-1 Introduction

Determining silt-clay mixture behavior is reliant on accurate experimental measurements performed in the laboratory testing program. The testing program consisted of soil index tests, compression tests, and triaxial shear tests. Soil index tests provide general information on the soil used for the classification of the soil, by particle size and fines behavior. Compression testing is used to provide the unique relationship between effective stress and soil density (void ratio, porosity, etc.). Two different testing apparatuses were utilized for this study, a high stress Constant Rate of Strain (CRS) apparatus and a tall CRS Apparatus. The high stress CRS apparatus is rated to compress a specimen to an effective stress around 90 MPa, the tall CRS apparatus is equipped with piezoelectric elements to allow for the generation and capture of shear waves and pressure waves during compression. Two different triaxial shear testing apparatuses were utilized. A low stress acrylic cell that is rated for an ultimate internal fluid pressure of around 1.4 MPa and a medium stress steel cell that is rated for an ultimate internal fluid pressure of around 14 MPa. These devices were used to perform triaxial compression shear testing of specimens at maximum consolidation stress of 1 MPa and 10 MPa, respectively.

Section 3.2 details the means and methods used for test specimen creation. This section details the resedimentation procedure for the creation of specimens with 10% clay content by mass or greater, including the method used for calculating clay content during resedimentation. This section includes the undercompaction procedure creating specimens with 0% clay content.

Section 3.3 describes the Tufts Advanced Geo-Materials (TAG) Laboratories automated testing equipment, electronic instrumentation, computer control systems, and data acquisition system used during the laboratory program.

Section 3.4 details the laboratory testing methods used for the soil index property tests, high stress CRS, tall CRS, and triaxial shear tests.

3-2 Specimen Creation Methods

Resedimentation (Slurry Sedimentation) Process

The resedimentation process starts with a bulk Gulf of Mexico Eugene Island (GoM_EI) clay powder as shown in Figure 3-1. The GoM_EI powder is the result of a soil sample collected in the field, air dried, and ground so that 99% of the material passes a #100 sieve. The air-dried ground powder is blended until thoroughly homogenous. The blending process greatly reduces natural variability, increasing the reproducibility in the experimental results. For this study, a manufactured crushed quartz material was added to the clay powder in controlled mass amounts to adjust the silt content of the specimen. The crushed quartz material Min-U-Sil 40 (MUS), is manufactured by US Silica, has a manufacturer reported specific gravity of 2.65, and a reported average particle size of 40 microns. The clay content of a resedimented specimen was calculated using the following method. First the final volume of the specimen at the end of resedimentation was calculated from the typical test specific specimen dimensions and the void ratio corresponding to the maximum resedimentation stress from a compression curve. If no compression tests had been previously performed, the end of resedimentation void ratio was approximated from compression curves of similar materials. For the mixed GoM_EI and MUS specimens the mass of the clay and silt were calculated assuming a predetermined clay fraction of 0% to 60% in 10% increments. The silt content of each specimen was calculated using Equation 3-1 during resedimentation.

$$f_s = \frac{M_{cl} f_{sn} + M_s}{M_t} \qquad \text{Equation 3-1}$$

Where:

f_s = Silt fraction of test specimen (percent)

M_{cl} = Mass of clay powder (mass)

f_{sn} = Natural silt fraction of clay powder (percent)

M_s = Mass of added silt (mass)

M_t = Total mass of specimen calculated from the final volume (mass)

A natural silt fraction of 35% silt was used during the resedimentation process which is near the measured value of 37% in Casey (2014). The total mass of the specimen was determined from the predicted volume using a weighted average of the specific gravity of GoM_EI and MUS, Equation 3-2, and Equation 3-3.

$$G_{sm} = \frac{1}{\frac{f_{cl}}{G_{scl}} + \frac{(1 - f_{cl})}{G_{ss}}} \qquad \text{Equation 3-2}$$

Where:

G_{sm} = Specific gravity of the mixed silt and clay

f_{cl} = Fraction of added Gulf of Mexico Eugene Island Clay (includes natural silt) (percent)

G_{scl} = Specific Gravity of Gulf of Mexico Eugene Island Clay 2.775

G_{ss} = Specific Gravity of Min-U-Sil 40 Silt 2.65

Equation 3-3 was used to calculate the total mass required of the combined GoM_EI and MUS powder for a specimen.

$$M_t = \frac{\frac{V_F}{G_{sm}}}{(1+e_F)} * (1 + F_L) \qquad \text{Equation 3-3}$$

Where:

M_t = Total mass of specimen calculated from the final volume (mass)

G_{sm} = Specific gravity of the mixed silt and clay

V_F = Estimated final specimen volume (volume)

e_F = Estimated specimen void ratio at maximum resedimentation stress

F_L = Loss factor to account for lost material during the resedimentation process (percent)

A 35 g/L sea salt (from the San Francisco salt company) saline solution was used as the pore fluid during the resedimentation process for every test within the study. The powders and saline solution are mixed in the calculated mass amounts and thoroughly blended with a KitchenAid stand mixer until a resultant homogenous stable slurry is formed as shown in Figure 3-2 The slurry is considered stable when there is no free water on its surface after a 24 hour resting period. The mixed slurry is allowed to temper in a confined container for a minimum of 12 hours. During tempering, the clay minerals are hydrated with the saline solution. After tempering the clay slurry is evacuated using a vacuum pump and a pressure chamber as shown in Figure 3-3. The evacuation of the clay slurry assists with saturation of the specimen and removes potentially trapped air that would result in voids within the sample during resedimentation. The evacuated slurry is then tremied into a thick walled consolidometer shown in Figure 3-4 with a funnel and tube to place the slurry from the bottom upwards under a positive pressure head. This method of placement limits the potential for entrapping air within the specimen. Prior to the slurry being placed in the thick walled consolidometer cylinder, the interior of the cylinder is cleaned with silicon oil to reduce friction during the consolidation process. Porous stones and filter paper sandwich the slurry column to allow for drainage during consolidation. The porous stones are approximately the same diameter as the interior of the rigid walled cylinder to limit extrusion of the slurry around the porous stone during loading. The circumference of the stone is tapered to have a

smaller diameter away from the sediment. This prevents the stone from getting stuck in the tube. Nylon filter fabric is used to separate the porous stone from the slurry column to limit clay particles from migrating into the porous stones. The placement of low clay content, high silt content materials within the consolidometer is assisted via liquefaction using a shake table. The consolidometer and funnel setup are placed on the shake table and a vibration was applied until the material liquefied and flowed.

The soil slurry is incrementally loaded by applying a load to a plastic spacer at the top of the slurry column with a load increment ratio $\frac{\Delta\sigma_V}{\sigma_V} = 1$. Figure 3-5 shows the slurry underloading with a weight and hanger setup. The slurry is loaded to a prescribed maximum vertical stress then unloaded to an overconsolidation ratio (OCR) of 4. At an OCR=4, the effective stress state of the sample is close to hydrostatic as such the shear stresses induced during extrusion and trimming of the sample are minimal as confirmed by Santagata (1994). The load is typically applied using dead weights hung from a hanging centralizer to ensure that the point of loading is at the center of the slurry column. During consolidation, a single displacement transducer (LVDT) may be used to measure the vertical deformation. From the LVDT data the time to end of primary consolidation is determined using Casagrande's log time method Germaine & Germaine (2009). For RGoM_EI the time to the end of primary consolidation was typically 48 hours. The time to the end of primary consolidation was found to decrease with increases in silt content. Each load increment is held until the end of primary consolidation, and the maximum load increment is held until the end of 1 log cycle of secondary consolidation typically 48 hours. The unloading increment to an OCR of 4 at the end of resedimentation consolidation was typically held for a minimum of 48 hours.

The soil specimen is extruded from the consolidometer and prepared for the testing apparatus. The sample is extruded by using a piston to push the sample while carefully holding the consolidometer. A hydraulic jack can be used if the resistance does not allow for extrusion by hand. The sample is trimmed

using a trimming stand, a wire saw, and a razor. A photo of the triaxial test trimming setup is shown in Figure 3-6. For the CRS test, the sample is trimmed with a trimming stand, a cutting shoe that is integral to the CRS apparatus and a specialty tool to remove excess material from the cutting shoe. A photo of the typical CRS trimming setup is shown in Figure 3-7. During both trimming processes, the excess material is used to determine the water content of the material prior to testing.

Undercompaction Process

The undercompaction method for specimen preparation used for the 0% clay materials within the laboratory program, is adapted from Ladd (1978). The undercompaction method creates a specimen of uniform density by mechanically compacting the material in layers within a mold. The method recognizes and accounts for the incidental compaction of initial layers with the placement of additional layers by lowering the initial target densities to "undercompacted" values. The first step is to determine the water content of Min-U-Sil 40 at typical lab conditions, using a minimum of 2 determinations. The water content of MUS was found to be around 2% in typical lab conditions. If higher water contents are desired during testing the material can be moisture conditioned as needed. The next step is to determine the initial volume required for a test specimen. This is done by measuring the cross-sectional area of the CRS confining ring, or an external split mold for triaxial test specimens and selecting an initial specimen height that meets the limitations of the testing apparatus. If an external split mold is used, the area measurement should account for the thickness of the rubber membrane lining the mold. Once an initial height is selected and the volume is calculated, then the number of layers for specimen preparation is determined. The general guidance provided on determining the number of layers is that they should not exceed 1-inch thickness. Approximately ¼ inch thick layers were used to create the CRS specimens and approximately ½ inch thick layers were used to create the triaxial specimens. Next, the testing density is selected, and the total wet weight of the specimen is calculated using Equation 3-4.

$$W_T = \gamma_{dr} \times (1 + W_a) \times V_m \qquad \text{Equation 3-4}$$

Where:

W_T = Total wet weight of material required (mass)

γ_{dr} = Required dry unit weight of test specimen (mass per volume)

W_a = Average water content of prepared material

V_m = Final volume of compacted material (volume)

The moist weight of material for each layer is calculated using Equation 3-5.

$$W_L = {}^{W_T}/_{n_t} \qquad \text{Equation 3-5}$$

Where:

W_T = Total wet weight of material required (mass)

W_L = Weight of material required for each layer (mass)

n_t = Total number of layers

During the placement of the material, it was found to be more efficient to portion out the measured required masses into individual containers rather than measuring the mass as the layer is placed.

During placement of the material each layer is assigned a value of undercompaction. This is a value that is typically between 0% and 15%, where 0% corresponds to dense specimens and 15% for loose specimens. Methods on selecting the optimum undercompaction percentage are presented within Ladd (1978). The 0% specimens for this study were typically constructed in 5 layers, each with a 2% difference in undercompaction value from 8% decreasing to 0 at the topmost layer. The total height of each layer is calculated using Equation 3-6.

$$h_n = \frac{h_t}{n_t}\left[(n-1) + \left(1 + \frac{U_n}{100}\right)\right] \qquad \text{Equation 3-6}$$

Where:

h_n = Height of compacted material at the top of layer n (length)

h_t = Total Specimen height (length)

n_t = Total number of layers

n = Current considered layer number

U_n = Percent undercompaction for layer n (percent)

A tamping rod is used to apply the mechanical compaction effort. The rod is equipped with a variable brass collar and is paired with a brass base that seats on the external split mold, or CRS confining ring. The rod, and brass base used during this laboratory program are shown in Figure 3-8. The rod extends through the brass base during tamping. The rod collar is adjusted so that the length of the rod through the brass base is equal to the difference of the top of mold height and top of layer height. That is when tamping is complete at a layer, and the rod collar is flush to the top of the brass base the height of layer n is equal to the height layer n calculated using Equation 3-6. Once the collar is adjusted properly, the material is added to the mold, and a compactive effort is applied using the tamping rod guided by the brass base. Tamping should start in a circular pattern keeping to the periphery of the mold and working toward the center of the mold. A light tamping force is used to distribute and flatten the material uniformly within the mold. The tamping force gradually increases until the collar uniformly hits the top of the brass base. The last few layers may require hitting the tamping rod with a rubber mallet in order to compact the material into a dense state. Upon completion of densifying the layer, the compacted surface is scarified to a depth equal to about one tenth of the thickness of the layer. The above steps of collar adjustment through scarifying the tamped layer are repeated until the final layer. During the compaction of the last layer, the tamping rod should be used until the surface of the compacted material is about 0.4 mm (1/64 in.) higher than required. The top of the material is then leveled if required and the pore stones/top cap assemblies are placed for testing

and set using a rubber mallet until the determine initial height is reached. At this point, the mass of the test assembly can be measured, and the initial specimen mass can be calculated from subtraction of the previously measured setup assembly without the material. If using an external split mold for triaxial testing, once the top cap is assembled and the membrane is secured, a vacuum pressure can be applied through the drainage lines to the specimen to limit effects of disturbance during geometry measurements and test setup.

3-3 Laboratory Testing Equipment

Introduction

This section describes the computer controlled automated testing equipment used within the laboratory testing program. The Constant Rate of Strain (CRS) testing methods and equipment is based on previous technology that was developed at MIT Wissa, Christian, Davis, & Heiberg (1971). Additional modification to the CRS testing equipment allows for compression of soils to high stress (~90 MPa) from Fahy (2014), and for the collection of shear and pressure waves during compression by Ranjpour (2020). The triaxial testing methods and systems described herein are based on previous technology that was developed at MIT by Sheahan & Germaine (1992).

The adaption of electronic instrumentation on soil testing apparatuses improved the resolution of the measurements and opened the door for automation through computer control. Through computer control, testing rates and specimen stress can be controlled allowing for the minimization or generation of excess pore fluid pressures and the recreation of exact stress states within the earth. It is through computer control that the uniaxial strain conditions required for K_0 consolidation loading stress path is possible within a triaxial cell. The following sections describe the electronic instrumentation, and computer control utilized for the high stress CRS, tall CRS and triaxial shear testing within the study laboratory program.

Electronic Laboratory Instrumentation

Accurate and timely measurements of force, distance, and pressure are required to run triaxial and CRS tests on soil. Electronic instrumentation was used in order, to run tests semi-autonomously, to provide high measurement frequency, and to provide precision in measurements made. A Tufts Advanced Geomaterials computer automated testing equipment station typically has a computer controller, electronic instrumentation, and a localized multiplexer that is attached to a centralized data acquisition system (DAQ). Each station has a localized power supply to provide around 5.5 volts Direct Current (DC) to the station's electronic instrumentation. The exact input voltage is recorded with each measurement collection from the DAQ, allowing for the normalization of the electronic instrumentation reading voltages to the input voltage. This normalization is performed to reduce sensitivity of the electronic instrumentation measurement to changes in the input voltage. Due to normalization when electronic instrumentation is calibrated, the input voltage is also collected with each reading to normalize the calibration measurements, as such a typical calibration factor is then unit of measurement per volts per volts. The instrumentation can be separated into distinct categories of distance measurements (Linear Variable Displacement Transducers (LVDTs) and string pot potentiometers), Load and pressure measuring instrumentation (load cells, diaphragm type pressure transducers, and piezoelectric elements), and fluid volume and pressure control instrumentation (Pressure-Volume Actuators (PVAs)). The following sections describe the instrumentation used for each of the Tufts University testing devices used within this experimental program.

Displacement Transducers

Linear Variable Displacement Transducers (LVDT)

Trans-tek (series 240) LVDTs were the standard LVDT used to measure displacement during resedimentation, triaxial tests, and tall CRS tests. These transducers are energized with DC voltage and provide a DC output proportional to the displacement. These transducers have a linear working range of

2.5 cm with an additional 1.3 cm non-linear zone. The transducers have a precision of ± 0.5% over the linear working range. When possible, measurement by LVDTs were limited to the linear working range. LVDTs consist of two parts; a ferrous rod core, and cylindrical body that is a faraday cage enveloping two coils of wire. The ferrous core is inserted into the body and an input voltage is run through one of the wire coils. The resulting magnetic field is sensitive to the position of the ferrous core and the output voltage from the non-electrified coil is directly proportional to the location of the ferrous core. The ferrous core is typically spring loaded to ensure a smooth and consistent measurement.

String Pot Potentiometers

The high stress CRS testing apparatus utilizes two M150 ultra-miniature String Pot potentiometers to measure piston displacement. A string pot potentiometer consists of a cable spooled around a potentiometer shaft. An internal spring to the potentiometer shaft maintains cable tension. As the transducer's cable is extended along with the movable object, it causes the spool and sensor shafts to rotate. The rotating shaft creates an electrical signal proportional to the cable's linear extension or velocity. The devices are powered by DC voltage. These transducers have a 1.5 inch stroke range and a precision of ± 1% over the stroke range.

Load and Pressure Transducers

Load Cells

Load cells used within the laboratory varied by testing apparatus and ultimate testing loads. The range in load cell capacity was between 500 lbs. (2.2 kN) (Data Instruments (model JP-500) and 50,000 lbs. (222 kN) (Sentran PG3). The triaxial testing equipment had the load cells mounted internally within the triaxial chamber for a direct measurement of specimen load. The CRS device had an external load cell, and axial stress calculations were performed to include the mass of the CRS piston. The load cells

operated under the same basic principle, during loading the DC input and output voltages are monitored; changes of voltage are proportional to the elastic deformation of the steel section.

Pressure Transducers

Pressure transducers are used to measure the pore pressure and cell pressure during a triaxial test as well as the generated pore pressure during a CRS test. Data Instruments AB/HP diaphragm type pressure transducers with capacities ranging from 50 psi (0.34 MPa) to 6,000 PSI (40 MPa) were used in various test apparatuses. The pressure transducer consists of a steel diaphragm with four strain gauges, two of which are thermally matched. Similar to the load cell, during loading the input and output voltages are monitored; changes of voltage are proportional to the elastic deformation of the steel diaphragm.

Piezoelectric Elements

Piezoelectric elements were used to measure the compressional and shear wave speeds within soil specimens. Noliac NAC2015 extender elements were used to measure compressional signals. Noliac CSAP03 shear plates were used to measure shear signals. These transducers work through the principle of piezoelectricity. Where piezoelectricity is the electrical charge that accumulates on certain solid materials in response to applied mechanical stress. This stored voltage can be measured through high impedance measuring instruments. The compressional plate element NAC2015 is 10×10×2 mm, has a stiffness of 1273.0 N/µm, a capacitance of 760.0 nF, and provides a free stroke of 3.3 µm. The Noliac shear plate elements are characterized by providing a large stroke for a very compact design. The shear plate CSAP03 element measures 10×10×0.5 mm and provides a free stroke of 1.5 µm and a capacitance of 3.321 nF.

Pressure-Volume Actuators (PVA)

A computer-controlled pressure volume actuator is used to control fluid pressures during testing, for both triaxial and high stress CRS testing apparatuses. A typical Tufts PVA consists of a piston in a sealed tube; a computer controlled electric motor to actuate the piston, a fluid reservoir connected by a valve to the tube and a LVDT to measure to position of the piston. The PVA piston has a set area and as such displacement of the piston within the hollow tube is proportional to changes in fluid pressure. A pressure transducer and the electric motor allow for a computer-controlled feedback loop to control fluid pressures during a test. The PVA piston position is measured with either a Trans-tek (series 240) LVDT with 10 cm working range or a Celesco (SP1) linear position transducer (string pot) with a 30 cm working range.

Central Data Acquisition System (DAQ)

The TAG Laboratory is equipped with a central data acquisition system (DAQ). This allows for the cost-efficient and accurate collection of a large volume of electronic instrumentation measurements. The system is flexible and allows for changes in data collection timing and instrumentation. The system consists of four components, the first being the laboratory box which contains the power supply, junction box, voltmeter, and ground. Second, a laboratory wide multiplexer allows the DAQ system to switch between instrumentation channels. Third, the analog to digital converter; the TAG lab DAQ includes a Hewlett Packard HP3497A 5-1/2 digit integrating analog to digital (A/D) converter. The HP3497A A/D converter is capable of monitoring 1000 analog channels simultaneously. The HP3497A A/D converter is sensitive enough to resolve 1 microvolt signals and has auto range matching over four voltage scales (0.1, 1, 10 & 100 Volts). The fourth component is a computer to store the data and perform the administrative scheduling tasks for the A/D converter. The TAG lab A/D converter, once scheduled, runs independent of the instrumentation at the testing apparatus. It only reads the

instrumentation channel in accordance with the programmed testing schedule. Figure 3-9 shows a photograph of the TAG lab DAQ system.

Computer Control System

The initial automation of a triaxial control system was performed at MIT documented in Sheahan (1991). The addition of electronic instrumentation, a computer control program, and a localized A/D converter to a traditional triaxial cell, which allowed for increased quality control and increased testing flexibility, while minimizing a source of human error.

The computer control equipment used to run a Tufts University automated triaxial cell is one with a disk operating system (DOS) environment, an Analog Devices AD1170 A/D converter, a multiplexer and a digital motor encoder or a D/A converter. The analog devices A/D converter is a minimum 22 bit resolution device. The Tufts University CRS and Triaxial computer controllers, depend on programming written in quick basic (QB) within the DOS environment. A few of the tests reported herein were run on a Windows 98 computer in the DOSBox simulated DOS environment. As newer computers no longer support Industry Standard Architecture (ISA) ports, an ISA to Universal Serial Bus (USB) converter is sometimes required. An ISA to USB converter manufactured by ARS Technologies was used for those tests. The ARS converter works by inputting a series of hexadecimal bits within the computer memory to allocate the input/output channels as the ISA channels. Older model computers had to dedicate memory for ISA peripherals; modern computers no longer allocate dedicated memory as it is not necessary for USB peripherals. The ARS computer interface allows the user to provide dedicated input/output channels for an ISA peripheral on a modern computer.

The multiplexer for a typical triaxial test setup has eight separate channels. There are six dedicated channels for the LVDT, load cell, pore pressure transducer, cell pressure transducer, PVA, and input voltage. Two channels available for additional instrumentation. The multiplexer connects to the

computer controller and the voltages from each channel are converted to digital signals through the very high-resolution local A/D converter, as required for very precise control in the testing apparatus. This equipment and terminology are discussed in greater detail within Sheahan & Germaine (1992)

Computer control is provided through a feedback loop, the computer controller reads the instrumentation, the QB program then compares the measured values to the target values. The program determines corrective action (minimizing the difference between the measured value and target value) using either intermittent proportional or continuous proportional integral differentiation (PID) control to generate a digital signal. The computer controller sends this digital signal to a Strawberry Tree Inc. D/A converter with a 12 bit resolution and ∓ 5 volt range. The Strawberry tree circuit card converts the digital signal to an analog voltage for the Electro-craft variable voltage motors. Through these feedback loops, strain rate, specimen stresses, fluid pressures and volumetric changes can be controlled during a test.

An update to the control system has been made within Casey (2014), as the Electro-craft motors had become obsolete and were updated with Maxon brand electric motors. The Maxon brand motors are controlled by Escon 50/5 servo controllers. The Escon controllers take the analog signal from the Strawberry Tree card and drive the Maxon band motor at a rotation rate that is proportional to the control voltage. Power for the motors is provided by a 50-volt DC power supply. The Escon 50/5s servo controllers can run the relic Electro craft motors if the input voltage from the tachometer is split such that 1/3 of the generated voltage is used for feedback control. When required the voltage was split by wiring resistors into the motors wiring harness.

Automated High Stress Constant Rate of Strain Test Apparatus

The high stress CRS tests were performed with a modified CRS apparatus as detailed within Fahy (2014). The apparatus consists of a rigid cell made of either steel or plastic, a steel base with drainage

port, a steel top with linear piston bearing, rubber O-rings seals and bolts to connect the three parts. The high stress CRS apparatus is shown in Figure 3-10. A soil sample is trimmed into a fixed rigid steel ring and then sandwiched between layers of nylon fabric filter screens and silicon carbide porous stones. The steel piston of the high stress CRS testing apparatus has a larger area than a typical CRS apparatus piston to accommodate the higher stress. The fixed side boundary conditions of the steel trimming ring force one dimensional deformation. Prior to loading, the specimen is incrementally back pressured to ensure saturation, and the pore fluid pressure is controlled by a PVA. During the constant rate of strain test, the sample is initially loaded slowly, as the computer controller increases the load continuously up to a predetermined constant rate of strain. The strain rate is measured by a pair of external LVDTs. The excess pore pressure generated during loading at the bottom of the sample is measured by a 2,000 psi (13.7 MPa) diaphragm type pressure transducer. The controlled chamber fluid pressure where the top of the sample drains is measured by a 200 psi (1.4 MPa) diaphragm type pressure transducer. Modifications to the control program have been made to allow for the computer control of the specimen compression based on generated pore pressures. This allows for compression to high stress (90+ MPa) while maintaining control of the vertical effective stress. At high stress strain rate-controlled compression could theoretically generate pore pressures within the specimen up to 40 MPa Fahy (2014).

The high stress CRS apparatus is set in a temperature-controlled enclosure. The high stress CRS base is placed on the top of an Enerpac RCS-1002 low profile hydraulic piston with a 199,400 lbs. (887 kN) load capacity. The hydraulic piston is computer controlled by a PVA. The top of the high stress CRS piston is set flush against an integral moment break on the Sentran PG3 load cell. The load cell is mounted on a 3-inch-thick steel plate sized to be a non-yielding reaction beam for the hydraulic piston force during loading. The steel plate is held in place by 4, 1-½ inch threaded steel rods provide a flat even surface for reacting to the hydraulic jack.

Automated Tall Constant Rate of Strain Test Apparatus

The tall CRS tests were performed with a modified CRS apparatus as detailed within Marjonovic (2016) and Ranjpour (2020). The apparatus consists of a stainless-steel confining ring, ring porous stones, a brass top cap with piezoelectric elements, a brass bottom cap with piezoelectric elements, a thick latex membrane, O-ring seals, and a screw driven piston load frame with a 10,000 lbs. (44.5 kN) capacity. The tall CRS apparatus is shown in Figure 3-11. The load frame includes two vertical columns, and an adjustable crossbar connecting the two vertical columns for the reaction reference. A specimen is trimmed into the confining steel ring, and the top and bottom caps with attached porous stones are placed within the steel confining jacket flush to the specimen. The top cap and bottom cap have been modified to include a cylindrical protrusion within the center of the cap of 2.225 cm diameter extending 0.65 cm. Ring shaped porous stones with an external diameter of 3.54 cm and internal diameter of 2.225 cm, are set around the cylindrical protrusion and within the confining steel ring. The porous stones allow for the drainage of excess pore pressures at the top and bottom of the specimen through a drainage line plumbed through each brass cap. A thick latex membrane is placed over the steel confining ring and sealed to the top and bottom cap by a rubber O-ring seal. The membrane encased setup is placed on the load frame and adjusted for vertical level. The bottom cap is set in contact with the load frame piston, and top cap is set in contact with the load cell attached to the underside of load frame cross bar. Drainage line stubs are screwed into the brass end caps and rubber drainage lines are attached to the drainage stubs. The rubber lines are filled with a saline solution matching the resedimentation pore fluid batching salinity and the free ends of the rubber lines are submerged in a reservoir of the same saline solution. The mechanical load frame is started in order to compress the specimen on the slowest gear ratio. This ratio corresponds to a strain rate of around 0.09 to 0.12 %/hr. depending on initial specimen height. A slow rate was used to limit the generation of pore pressures during compression. The pore pressures are not monitored during the test, but due to the slow strain

rate and free drainage at specimen top and bottom, the assumption is made that excess pore pressures do not build up within the specimen. This assumption was evaluated by calculating the expected generated pore pressures from the applied strain rate using Equation 3-8 developed in Wissa, Christian, Davis, & Heiberg, (1971) discussed in more detail within Section 3-4. The calculated generated pore pressures were sufficiently small to dissipate during loading. The material is compressed until an ultimate stress of 30 MPa. In general, at each 1 MPa interval a measurement is made of the compressional wave velocity and a shear wave velocity.

Centered within each end cap protrusion is a sandwiched tandem of Noliac NAC2015 extender element and Noliac CSAP03 shear plate shear element, used to generate and receive compression and shear signals. The piezoelectric elements are constructed in sandwiches according to the procedures outlined within Marjonovic (2016). Where each sandwich consists of the piezoelectric element, brass shims, Dupont Kapton insulating plates and various epoxies. The piezoelectric elements are wired through the brass caps to allow for the connection of a signal generator and oscilloscope. A B&K Precision 3003 Function Generator is used to create 10 MHz waveforms with frequency accuracy of 0.02% and 0.1 Hz frequency resolution. The settings of the pulser are set to send a ±5 V square pulse with a frequency of 115 Hz, the repetition of these square waves is set at a low frequency, f = 0.11 kHz. The elements are energized using a step function to include infinite frequencies and allowing the waves to propagate at an optimal frequency. The generator is connected to the circuit box using a BNC connector with a 50 Ω terminal. The design of the circuit box is presented in more detail within Ranjpour (2020). The circuit box connects the signal generator to a 23 V DC power supply, the input signal to the oscilloscope through a series of resistors, and connects the input signal to the piezoelectric elements in the bottom cap through a metal-oxide-semiconductor field effect (MOSFET) transistor and an operational amplifier. The circuit box is entirely contained within a Faraday cage to limit electromagnetic interference during wave velocity measurement. The piezoelectric elements in the top

cap are directly connected to a Tektronix TBS1072B-EDU digital oscilloscope. The oscilloscope has two recording channels, allowing for the simultaneous collection of the input and output signals. The oscilloscope measurements sensitivity is based on the divisions of axis in the integral readout screen. The oscilloscope has variable measurement sensitivities between 1 mV/div signals at a 2 ns/div time up to 10 V/div at a 100 s/div. The oscilloscope includes a universal serial bus (USB) 2.0 port for removable flash memory drives to collect and save each wave recording.

Automated Stress Path Triaxial Cell

The triaxial tests reported herein were carried out in low and medium capacity pressure triaxial cells, designed for internal ultimate fluid pressure of 1.5 MPa and 20 MPa respectively. A diagram of a typical automated triaxial test setup is shown in Figure 3-12 and a photograph of a typical low stress and medium stress Tufts University triaxial apparatus are shown in Figure 3-13 and Figure 3-14. The development of the automated triaxial apparatus is documented in significant detail within Sheahan & Germaine (1992). The triaxial testing apparatus consists of an acrylic or steel cell, internal posts (low stress cell only), base and top pedestals, base and top drainage lines, internal load cell, a movable top piston, and all necessary rubber O-ring seals to maintain pressure within the cell. The soil specimen is separated from the chamber fluid using two thin impermeable rubber membranes (low stress cell) or one thin impermeable rubber membrane and one thick impermeable rubber membrane (medium stress cell). The thin rubber membranes typically consisted of unlubricated Trojan brand latex condoms. The thick rubber membranes consisted of Humboldt brand latex membranes. The membranes are sealed against the base and top pedestals by rubber O-rings. The top cap is connected by a threaded rod connection to a compact shear beam load cell within the triaxial cell. The internal load cell eliminates the effect of piston friction on the loading measurement. The electronics for the load cell are wired through the base of the triaxial cell. The load cell is connected to the base of a piston centered in the

triaxial cell, aligned by an O-ring seal and linear bearing within the top of the triaxial cell. The Piston movement is monitored by an externally mounted LVDT.

The triaxial cell is filled with Dow-corning "200 fluid," 20 centistokes silicone oil. This silicone oil has a low viscosity under a wide range of temperatures which makes it ideal for triaxial testing. The oil is also transparent and does not degrade the rubber O-ring seals or membranes. The oil is also non-conductive which allows for the use internal electronics such as the internal load cell without the need of a sealed connection.

Both triaxial cell apparatuses, low and medium, stress are located within temperature-controlled enclosures. The low stress triaxial cell is set in a ½ ton Wykeham Ferrance screw driven load frame with adjustable gear ratios. The screw driven load frame consists of a base with a gear driven piston, two vertical columns, and an adjustable crossbar connecting the two vertical columns. The medium stress triaxial cell is set in a 9 ton (89 kN) hydraulic piston load frame. The hydraulic load frame also includes two vertical columns, and an adjustable crossbar connecting the two vertical columns. The triaxial cell base is placed on the top of the load frame piston, and an adjustable crossbar is set so that it restricts the vertical movement of the triaxial piston with a spherical moment break between the top of the piston and load frame crossbar. The load frame is powered by either a computer-controlled DC-servo electric motor attached to the load frame gears, or through a hydraulic oil filled PVA. The cell fluid and pore fluid pressures are controlled using PVAs. Both the cell fluid and pore fluid pressures are monitored by diaphragm type pressure transducers. To assist in system compliance through limiting necessary piping, the fluid pressure transducers are located on the base of the triaxial cell.

3-4 Laboratory Testing Methods

Introduction

The laboratory testing methods utilized within this research are common practice within the geotechnical community and can be parsed into four distinct groups. First, there are the index property tests. These tests are used to classify the material and its constituents. The second distinct category of tests is compression tests. Compression tests measure the compression behavior of the soil and provide the link between effective stress and density (void ratio, porosity). The third distinct group is permeability testing. Permeability of the material is measured during high stress CRS testing, calculated from the difference of measured excess pore pressures bottom of the specimen during compression and a controlled pore pressure gradient at the top of the specimen. Two direct measurement tests were performed through modifying the high stress CRS test equipment to perform permeability measurements through constant head or constant flow testing. The final category of tests is triaxial shear tests. K_0 consolidated undrained compression shear triaxial testing was performed to measure the compressive shear strength of each mixture and to determine the lateral stress ratio and effective friction angle. The following sections provide the test methods followed to perform the study measurements.

Index Property Tests

Index properties are measurable values that help classify a soil. The classification of soils by geotechnical engineers is typically performed through a measurement of the constituent particles sizes, behavior at various water contents, and organic material content. For this study the index property tests are limited to the determination of the specific gravity and Atterberg Limits for each soil mixture. The calculated constituent specimen mass fractions used in the Resedimentation of test specimens are from measurements performed for other laboratory test programs Casey (2014).

An important note on terminology within this research; clay generally refers to a particle that is less than 0.002 mm Germaine & Germaine, (2009) in size and not clay classified by mineralogy unless indicated otherwise.

Atterberg Limits

The Atterberg limits are determined for fine grained soils (>50% smaller than 0.075 mm). The limits are conceptual boundaries between various states of material behavior involving changes in water content. The liquid limit test determines the water content that separates the material behavior of a soil from a solid to a viscous liquid. Two different methods were used to measure the liquid limit, the Casagrande Cup method, and the Fall Cone Method. In lower clay content mixtures, the fall cone method was used solely, as the material was unable to be tested via the Casagrande cup.

The Casagrande cup method is fully described in ASTM D4318 and was used for test mixtures of higher clay content. In general, the soil is placed in a testing apparatus known as a Casagrande cup and a vertical groove is cut into the soil. The test is performed by measuring how many ½ inch height drops (blows) of the cup are required to close ½ in. of the vertical groove. This test is performed for a minimum of five readings, with blows between 10 and 50. At each determination of blows for a unique water content, the test is performed until the measured blows is consistently repeated with three determinations. The water content of the soil is measured through oven drying of a minimum of 10 grams of soil after each blow determination. For best practice, the soil is tempered with water and slowly allowed to dry to control the water content. A plot of the water content by blows is created. The liquid limit of a soil is the water content that corresponds to 25 blows on a linear best fit line through the recorded data Germaine & Germaine (2009). Figure 3-15 shows a photograph of the Casagrande cup used for the liquid limit test.

The fall cone test method was used to determine the liquid limit of all test mixtures, as the test method allows for easier testing of significantly stiffer materials. The procedures used for the fall cone method are detailed within Campbell & Blackford (1984) and Wood (1981) and follow the British Standard BS 1377. The fall cone test is performed with a stainless-steel cone of a standardized weight and tip angle. The cone is positioned so that its tip just touches a constrained soil sample of sufficient depth. The soil sample is required to have a depth greater than the height of the cone. The cone is released 5 seconds, so that it may penetrate the soil. After 5 seconds the penetration depth is recorded, and the water content is measured through oven drying of a minimum of 10 grams of soil from the penetrated sample. A plot of the water content by penetration is created. The liquid limit of a soil is the water content that corresponds to 20 mm penetration on a linear best fit line through the recorded data. This criterion corresponds to the British Standard BS 1377 which require an 80 gram cone with a 30 degree angle. Figure 3-16 shows a photograph of the fall cone apparatus used for the liquid limit test.

The plastic limit is the water content that separates a semi-solid material behavior from the plastic material behavior. The test is fully described in ASTM D4318. In general, the soil is rolled into a thread on a glass plate to a 1/8 in. diameter. When the thread crumbles at exactly a 1/8 in. diameter the soil is at the plastic limit. The plastic limit for a soil is determined as the average water content for a minimum of three threads that crumble at 1/8 in. diameter Germaine & Germaine (2009).

The difference between the liquid limit and plastic limit is the plasticity index. A plot of liquid limit by plasticity index is used to classify the behavior of fine-grained materials within the Unified Soil Classification System (USCS).

Specific Gravity

The specific gravity of a soil is the ratio of its density to a standard density, which is typically pure water at 20 degrees Celsius in the geotechnical community. Several testing procedures and phase relationship calculations are reliant on accurate specific gravity measurements of the soil. The procedure is fully described in ASTM D854. In general, a sample of soil is submerged in distilled water inside a flask of known volume. The mass of the flask and submerged soil is measured several times under controlled temperature conditions. The flask is also measured containing only distilled water. From these two sets of measurements, a relationship of the displaced water and the mass of the solids can be made to determine the specific gravity of the soil. The temperature is closely monitored and used to correct for variations in water density.

Constant Rate of Strain (CRS) Compression Tests

The Constant Rate of Strain test (CRS) methodology was developed in 1969 by Smith and Wahls Smith & Wahls *1969). Wissa improved the equipment developed by Smith and Wahls by adding the ability to back pressure saturate a specimen prior to the compression Wissa, Christian, Davis, & Heiberg (1971). As outlined in the test equipment section two different modified CRS apparatuses were used with similar testing procedures within the laboratory testing program.

High Stress Constant Rate of Strain Procedures

High stress CRS tests begin with the thorough cleaning of the equipment, checking saturation of the drainage lines and pressure transducers, and refilling the reservoir of saline solution if required. The saline solution used to control the CRS chamber pressure is kept at the same salinity as the pore fluid during specimen resedimentation. After initial cleaning and preparations, the next step is the application of a light film of Dow Corning high vacuum grease to the specimen confining ring and all rubber O-ring seals of the CRS apparatus. Then the specimen cutting ring is mounted on a specimen

trimming stand and lowered gently in contact with the top of an untrimmed specimen cut from a Resedimentation consolidometer tube. The untrimmed specimen from the resedimentation consolidometer has a slightly larger diameter than the specimen cutting ring. The specimen is trimmed by lightly removing the excess material restricting the cutting edge using a tapered dental tool, while advancing the cutting ring. The weight of the cutting ring and trimming stand will drive the cutting ring down as the excess material is removed creating a very tight seal between the soil specimen and ring sidewalls. The top and bottom of the specimen is trimmed with a razor and the cutting ring is used as a guide. After trimming is complete the initial height of the specimen is measured within the cutting ring. Nylon filter fabric is set against the top and bottom of the specimen and porous stones are set against the filter fabric. The initial mass of the specimen, cutting ring, porous stones, and filter fabric is measured prior to installing the cutting ring into the CRS apparatus. The cutting ring is then set into the CRS test chamber, and the chamber is assembled and bolted together. The base of the CRS assembly is placed on the top of the Enerpac hydraulic piston, and the top of the CRS piston is set flush in direct contact with the moment break of the stations external load cell on the underside of the 3-inch thick steel plate. Once aligned and in contact with the load cell and hydraulic piston, the drainage lines are connected, and the specimen is back pressure saturated for a minimum of 24 hours. After back pressure saturation, the specimen is loaded at a constant rate of strain. The strain rate is determined by a string pot potentiometer mounted to the piston to monitor the deformation within the specimen and a computer controller using a PID feedback loop. The bottom drain line is closed off from the PVA during loading to allow the generation of excess pore pressures on the bottom of the specimen. The measured excess pore pressure is used to compute the effective stress within the specimen as well as the hydraulic conductivity of the specimen for a given stress level. The hydraulic conductivity of a soil specimen during a constant rate of strain test is calculated by the computer controller from the following equations.

$$\sigma'_{a,n} = \left(\sigma_{a,n} - \frac{2}{3}u_{m,n}\right) \qquad \text{Equation 3-7}$$

Where:

$\sigma'_{a,n}$ = Axial effective stress at time n. (force by area)

$\sigma_{a,n}$ = Total axial stress at time n. (force by area)

$u_{m,n}$ = Base pressure at time n. (force by area)

$$k_n = \frac{1}{2}\frac{\varepsilon_n^{\circ} H_n H_0 \gamma_w}{u_{m,n}} \qquad \text{Equation 3-8}$$

Where:

k_n = Hydraulic Conductivity at time n (length by time)

ε_n° = Strain Rate at time n (percent by time)

H_0 = Initial Drainage Height in the sample (length)

H_n = Drainage Height in the sample at time n (length)

γ_w = Unit weight of water (mass by volume)

$u_{m,n}$ = Base pressure at time n.

The drainage height at time n is calculated through Equation 3-2.

$$H_n = H_0 - \Delta H_n \qquad \text{Equation 3-9}$$

Where:

H_n = Height at point n (length)

H_0 = Initial specimen height (length)

ΔH_n = Change in specimen height (length)

The change in height of the specimen is calculated by Equation 3-4 which incorporates corrections due to apparatus compressibility and uplift forces.

$$\Delta H_n = \delta_n - \delta_{af,n} - \delta_{ap,n} \qquad \text{Equation 3-10}$$

Where:

δ_n = Axial Deformation (length)

$\delta_{af,n}$ = Apparatus compressibility correction due to loading (length)

$\delta_{ap,n}$ = Apparatus compressibility correction due to cell uplift forces (length)

The total axial stress at any time step during the test is calculated by Equation 3-11.

$$\sigma_{a,n} = \frac{f_{a,n}}{A} \qquad \text{Equation 3-11}$$

Where:

$f_{a,n}$ = The net force (force)

A = Specimen area (area)

A data reduction program converts the recorded instrumentation readings to the measured strain, cell pressure, pore pressure, void ratio, hydraulic conductivity, and effective and total stresses using Equation 3-7 to Equation 3-11. During data reduction two string pot potentiometers are averaged to calculate the deformation of the specimen. Taking the average of two measurements helps with issue of eccentricity during loading.

Tall Constant Rate of Strain Procedures

Similar to the high stress CRS tests, the tall CRS tests begin with the thorough cleaning of the equipment, checking saturation of the drainage lines, and refilling the reservoir of saline solution if required. The saline solution used to maintain specimen saturation is the same salinity as the pore fluid during specimen resedimentation. After initial cleaning and preparations, the next step is the application of a light film of Dow Corning high vacuum grease to the specimen confining ring and rubber O-ring seals. An acrylic rod is used to push the specimen slightly proud of the end of the consolidometer for trimming of the end with a wire saw and razor blade. Once the end is trimmed, the specimen is

again pushed using an acrylic rod within the consolidometer until approximately 1 cm of material is no longer constrained. The consolidometer tube, and confining ring are then set in a foot actuated pneumatic piston, which allows for the clay specimen to be jacked into the confining ring after careful alignment of the consolidometer and confining ring. During the installation of the clay specimen within the confining ring a minimum 0.5 cm gap between the consolidometer and confining ring is maintained to allow for the extrusion of excess material. The extruded material is collected to measure the initial specimen water content. Once the specimen is installed within the confining ring to the desired height, the bottom of the specimen is trimmed flush to the steel confining ring with a wire saw and razor blade. Once trimmed, the specimen is centered within the confining ring by pushing the specimen with the brass top caps outfitted with the porous stone rings. Care is taken to align the end caps so that the piezoelectric elements are in alignment for optimal signal transmission. A layer of nylon filter paper separates the porous stones from the specimens, the nylon filters are also in a ring shape and do not cover the piezoelectric elements in the center of each end cap. A rubber membrane is installed over the steel confining ring and end caps enveloping the confining ring. Rubber O-ring seals hold the rubber membrane to the brass end caps and maintain a watertight connection during the test. The membrane is installed to limit losing pore fluids into the laboratory by diffusion or evaporation during testing. After installation of the membrane drainage line stubs are screwed into the end caps.

Once assembled the membrane covered testing assembly can be installed within the load frame. The bottom cap is set flush to the top of the screw jack piston and the top cap is set flush to the load cell set on the bottom of the load frame cross bar. Verticality of the membrane covered assembly is verified through confirmatory measurements of the distance between the top of load frame piston to the top of the brass top cap at three locations 120 degrees apart around the membrane covered assembly. Once verticality is confirmed a slight initial load is applied to the specimen to maintain verticality during the attachment of the drainage lines. Rubber tubing filled with a saline solution

matching the salinity used for pore fluid during resedimentation is attached to the drainage stubs to maintain the specimen's saturation during testing. The free ends of the rubber tubes are within a beaker containing the same saline solution to act as a reservoir.

Once the assembly is set in the load frame and sufficiently plumbed, the specimen is loaded at a constant rate equal to the slowest gear ratio of the load frame. Computer control is not used for this test as the load frame operates independently of the computer. The CRS control program is used as a real time readout of the axial stress and axial strain during loading. A Panamalar Kamtron internet accessible camera was used to monitor the computer controller during testing to confirm current axial stresses while the equipment is running. In general, at each 1 MPa interval during the test, the load frame was stopped, and compressional and shear wave velocity measurements were performed. The velocity measurements were performed to an ultimate stress of 30 MPa at which time each test was concluded.

For the tall CRS tests the initial specimen mass was calculated as the difference between the mass of the confining ring measured prior to the start of testing and the mass of the trimmed specimen and confining ring measured prior to the installation of the end caps. The specimen's area was calculated from the internal diameter of the confining ring. The initial specimen heigh is calculated as the difference between the total height of the confining ring and the distance from the top of the confining ring to the top of the specimen after final trimming. During testing the axial stress of the specimens is calculated using Equation 3-5 and the height of the specimen is calculated using Equation 3-4. Due to the very slow strain rate and free drainage at the top and bottom of the specimen the total axial stress calculated using Equation 3-5 is assumed to equal the effective axial stress.

Constant Head Permeability Testing

The high stress CRS test apparatus was modified to allow for constant head permeability testing using the apparatus. The test was performed for the 0% clay specimen as a verification on the permeabilities measured during high stress CRS testing. The apparatus modifications were to disconnect the base pore pressure transducer used to measure generated excess pore pressures and replace it with a drainage line vented to the atmosphere. The modifications allow saline water to flow through the specimen from the PVA reservoir through the modified drain line. During testing the phreatic surface within the PVA reservoir was assumed to be at a constant height above the lab floor and the outlet of the drain line is set to different heights above the lab floor. The hydraulic gradient was calculated as the difference between the reservoir height and the drain out flow height from the lab floor divided by the average specimen height during the flow Changing the height of the drain outlet changed the gravitational fluid gradient within the specimen and the driving fluid pressure. The specimen height was determined from the average axial strain during the stress increment. The outlet drained into a beaker of known mass, and a stopwatch was used to measure the time of flow. In general, a minimum of 10 g of water was collected during each flow before the mass was measured. The hydraulic conductivity was calculated using Equation 3-12.

$$q = KiA \qquad \text{Equation 3-12}$$

Where:

K = Hydraulic conductivity (length by time)

q = Volume of flow per unit time (volume by time)

i = Hydraulic gradient

A = Cross sectional area of specimen (area)

During the test, the time of flow was directly measured, and the volume of water was calculated from the mass of water collected. The specimen cross sectional area was known and constant during

the test and the gradient was determined through the elevation head difference of the reservoir and drain outlet. A vertical stress was applied to the specimen through the hydraulic piston and measured using the load cell. A string pot potentiometer was used to measure axial deformation during loading. As both the PVA and drain line were open to atmospheric pressure the total stress applied was assumed to be the effective stress within the specimen. The hydraulic conductivity was measured at 13 vertical stresses ranging from 0.2 MPa to 90 MPa. Three gradients were tested at each stress level and three determinations were performed for each gradient to determine if there were equipment biases due to hydraulic gradient. The measured hydraulic conductivity was converted to permeability through Equation 3-13.

$$k = \frac{K\mu}{\rho g} \qquad \text{Equation 3-13}$$

Where:

k = Permeability (area)

K = Hydraulic conductivity (length by time)

μ = Dynamic Viscosity of permeant (mas by length time)

ρ = Density of Permeant (mass by volume)

g = Gravitational Constant (mass by time squared)

Constant Head Permeability Testing with Backpressure

Further modification of the high stress CRS test apparatus allowed for constant head permeability testing using a backpressure at the outlet end. The test was performed for the 10% clay specimen as a verification on the permeabilities measured during high stress CRS testing. The initial low permeability required higher hydraulic gradients during testing to complete a measurement within 24 hours. Which would not be possible with a hydraulic gradient due to different elevation heads and gravitational driving force. The apparatus modifications were to plumb a pneumatic pressure chamber to the base of the CRS apparatus that was also plumbed to the base pore pressure transducer. The

pneumatic pressure chamber was attached to a compressed air supply line with an inline pressure gauge to control the back pressure. The modifications allowed for a constant driving water pressure from the PVA and a constant back pressure for control of the hydraulic gradient. The high stress CRS load frame is used to control the axial stress of the specimen during testing. A PVA is used to control the volume of water flowed through the specimen. The PVA maintains the driving water pressure on the inlet side and the change in position over time was measured by the PVA's string pot potentiometer. The linear change in position multiplied the cross-sectional area of the PVA piston is equal to the volume of water through the specimen over the time of flow less any equipment losses. Equipment losses were measured by running the test equipment without a specimen at several flow rates and axial stress levels. Figure 3-17 provides three interpretations of the equipment head losses due to variations of flow rate at three stress levels, <1 MPa, 1 MPa to 10 MPa and >10 MPa.

The volume of water flowed over time can be used to calculate the hydraulic conductivity using Equation 3-12 and converted to permeability using Equation 3-13. The hydraulic conductivity was measured at 11 vertical stresses ranging from 0.5 MPa to 90 MPa. Three gradients were tested at each stress level and three determinations were performed for each gradient to determine if there were equipment biases due to hydraulic gradient.

Triaxial Consolidation/Shear Test Methods

Triaxial tests were performed with a Tufts University automated triaxial cell rated for either low internal fluid pressures (~1.4 MPa) or medium internal fluid pressures (~20 MPa). ASTM D4767 was the standard procedure typically followed for triaxial testing, with variations to accommodate the different testing apparatuses. A triaxial specimen was trimmed from the soil extruded out of a resedimentation consolidometer. Each specimen consisted of a cylinder with nominal dimensions of 8 cm tall and 3.5 cm in diameter. The specimen was sandwiched between pairs of nylon fabric, pre-saturated porous stones,

and the pedestals of a triaxial cell. The low stress specimen was then fully enveloped in two thin rubber membranes (Durex brand unlubricated condoms), the medium stress specimen was fully enveloped in one thin rubber membrane and one thick rubber membrane (Humboldt brand Latex rubber membrane). The membranes are sealed against the top and bottom pedestals with three rubber O-ring seals. The internal drain line is connected to the top pedestal. The medium stress cell incorporates a floating top pedestal design as such the drain line is attached while the top cap is centered within a jig. The centering of the specimen and drainage line attachment is performed while the specimen is under vacuum pressure from an external vacuum pump attached to the triaxial cells drainage lines. The jig is machined to match the alignment of the triaxial cells piston so that specimens aligned within the jig have a higher chance of being properly aligned and seated to the triaxial cell's piston.

Once the specimen is sealed, the triaxial cell is assembled, and the cell is filled with silicon oil. The cell oil is initially pressurized to a level that is equal to one fourth of the maximum axial stress during specimen resedimentation. This pressure up step puts the specimen in an isostatic stress state and generates a slight positive pore pressure which provides a record of the sampling effective stress. After a minimum of 12 hours of pressure up the specimen is back pressure saturated at a constant effective stress. Back pressure saturation is achieved by slowly incrementing the cell pressure and the pore pressure in small steps to increase the pore pressure while leaving the samples effective stress generally constant. Back pressure saturation: both drives water into the specimen and any trapped air bubbles into the pore fluid. For low stress tests the minimum back pressure used during testing was 2.0 ksc, in the medium stress test a minimum back pressure of 4.0 ksc is used. The specimen saturation is of critical importance as soil stresses are dependent on an Effective Stress Principle, which states that the total stress on the specimen is the sum of the effective stress on the soil skeleton and the pore pressure within the specimen. If the specimen is not fully saturated than the effective stress cannot be accurately calculated. The specimen is back pressure saturated for a minimum of 48 hours or until the Skempton B

value is larger than 0.96. The Skempton B value is an experimental parameter defined as the change in pore pressure due to an incremental change in total octahedral stress that provides a way to approximate specimen saturation. It is described in great detail within Skempton (1954). The B value is measured at the end of the back pressure saturation step.

After initial pressure up and back pressure saturation the specimen was consolidated to a predetermined stress state. Consolidation of a specimen allows for control of the stress state within a triaxial cell prior to shearing. A resedimented specimen is typically over consolidated at the end of the resedimentation process due to the unloading of the specimen prior to extrusion. The consolidation phase forces the stress within the sample past the maximum stress applied during resedimentation and back to the virgin compression line where it can be sheared to determine normally consolidated behavior. This testing program consists of K_0 consolidated tests. K_0 consolidation is performed similarly through compressing the specimen axially at a set strain rate and using computer control to adjust the cell fluid pressure in order to maintain a constant specimen cross sectional area. The height and volume of the specimen is reduced during K_0 consolidation. This is thought to be a realistic analog to the stress state within most naturally deposited soils. For very stiff specimens (20% clay content or less) stress path consolidation was used as K_0 consolidation is not feasible. Stress path consolidation uses a computer controller to consolidate the specimen to a predetermined stress state along a linear stress path at a predetermined strain rate. The end stress state and the desired axial strain rate are entered into the computer controller, the computer controller will then consolidate the specimen by calculating a stress path from the current stress state to the desired ending state. The ultimate stress state at the end of consolidation, was held for a minimum of 48 hours to allow for one log cycle of secondary compression.

After the consolidation phase, the specimens are sheared in undrained compression. First a pre-shearing leak check of the drainage lines is performed. The leak check consists of closing the drainage lines and monitoring the specimen pore pressure for significant changes indicating internal leaking of fluids. The leak check typically lasted for 5 minutes to allow the pore pressures to equilibrate. After a successful leak check the specimen is then sheared. In the undrained compression shearing mode the specimen undergoes axial deformation at a controlled strain rate (typically 0.5%/hour) and the cell fluid is controlled to maintain a constant pressure. The specimen pore pressures are directly measured so that effective stresses can be easily calculated. From the undrained compression shear test measurements, the materials internal failure friction angle and shear strength can be calculated.

Triaxial tests require several calculations during the test and during data post processing to ensure accurate results. Measurements must be made to determine the specimen's initial height, diameter, and mass. These measurements are used to determine the initial density of the specimen and are the basis for measured changes in volume. The height of the specimen post consolidation is calculated using Equation 3-9.

The cross-sectional area of the specimen, at the end of consolidation is calculated by Equation 3-14. This equation assumes that the specimen is a right cylinder.

$$A_c = A_0 \frac{(1-\varepsilon_{vol})}{(1-\varepsilon_a)} \qquad \text{Equation 3-14}$$

Where:

A_c = End of consolidation cylindrical volume (area)

A_0 = Initial cylindrical volume (area)

ε_{vol} = Volumetric strain at end of consolidation phase

ε_a = Axial strain at end of consolidation phase

The cross-sectional area for specimens during shear in compression is calculated using a parabolic area correction. Equation 3-15 provides the parabolic area correction as detailed within Germaine & Ladd (1988).

$$A_{parabolic} = A_c \left(-0.25 + \frac{\sqrt{25 - 20\varepsilon_a - 5\varepsilon_a^2}}{4(1-\varepsilon_a)} \right)^2 \qquad \text{Equation 3-15}$$

Where:

A_c = Specimen cylindrical cross sectional area at the end of consolidation (area)

ε_a = Axial strain

During the test the principal stress difference needs to be corrected for the effect of the rubber membrane. This correction is provided in Equation 3-16.

$$\Delta(\sigma_1 - \sigma_3)_m = (4E_m t_m \varepsilon_a)/D_c \qquad \text{Equation 3-16}$$

Where:

$\Delta(\sigma_1 - \sigma_3)_m$= Membrane correction to be subtracted from the principal stress difference (stress)

E_m = Young's modulus of membrane material

t_m = Thickness of membrane (length)

ε_a = Axial strain

D_c = Diameter of specimen at the end of consolidation (length)

Lastly the corrected principal stress difference can be calculated with equation 3-17.

$$(\sigma_1 - \sigma_3)_c = \frac{P}{A} - (\sigma_1 - \sigma_3)_m \qquad \text{Equation 3-17}$$

Where:

$(\sigma_1 - \sigma_3)_c$= Corrected principal stress difference

P = Applied Force (force)

A = Corrected specimen area (area)

$\Delta(\sigma_1 - \sigma_3)_m$= Membrane correction to be subtracted from the principal stress difference



Figure 3-1: Left: bulk Gulf of Mexico Eugene Island Powder. Right: Min-U-Sil 40 in bowl and 35 g/L sea salt solution in beaker



Figure 3-2: Using a stand mixer to blend the GoM_EI and MUS powders with a saline

solution to create a stable slurry for use in resedimentation

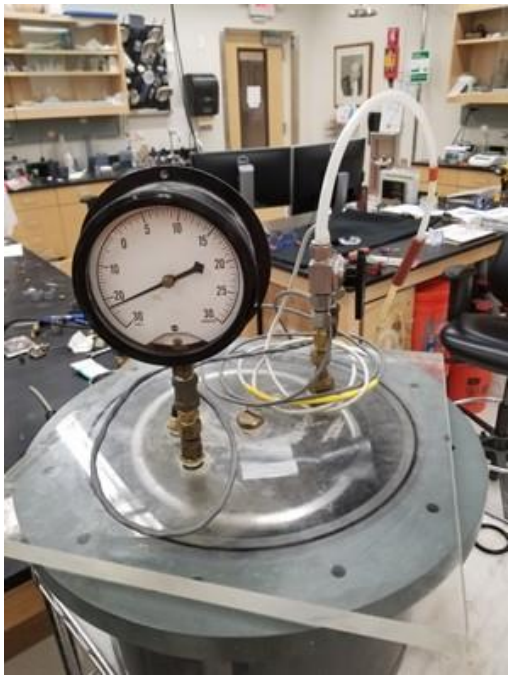


Figure 3-3: Evacuating the tempered slurry within a vacuum chamber prior to placement in a consolidometer



Figure 3-4: Placement of evacuated slurry in a consolidometer by a tremie tube and funnel



Figure 3-5: Typical consolidometer and weight hanger setup used during resedimentation

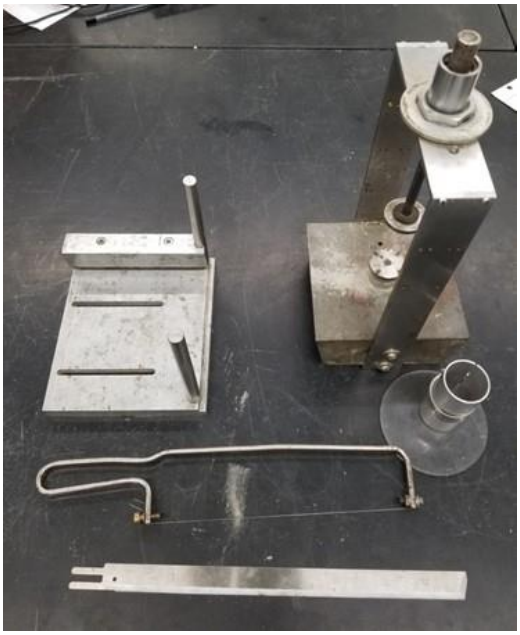


Figure 3-6: Triaxial specimen trimming equipment. Bottom: wire saw and straight razor. Right: guide for trimming diameter and aluminum confine jacket for trimming ends. Left: jug for trimming perpendicular ends.

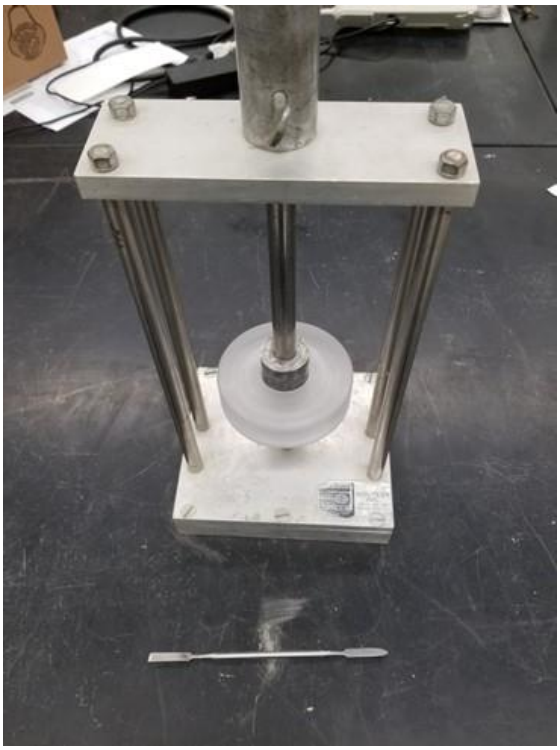


Figure 3-7: Constant Rate of Strain trimming equipment. Top: vertical trimming stand sized for the CRS confining ring. Bottom: dental tool to remove excess material



Figure 3-8: Brass base assembly and acrylic rod with adjustable brass collar used for undercompaction method to make 0% clay content specimens



Figure 3-9: Tufts electronic data acquisitions system. Top: personal computer to access system. Below: HP3497A A/D converter above multiplexer



Figure 3-10: Tufts high stress CRS testing apparatus

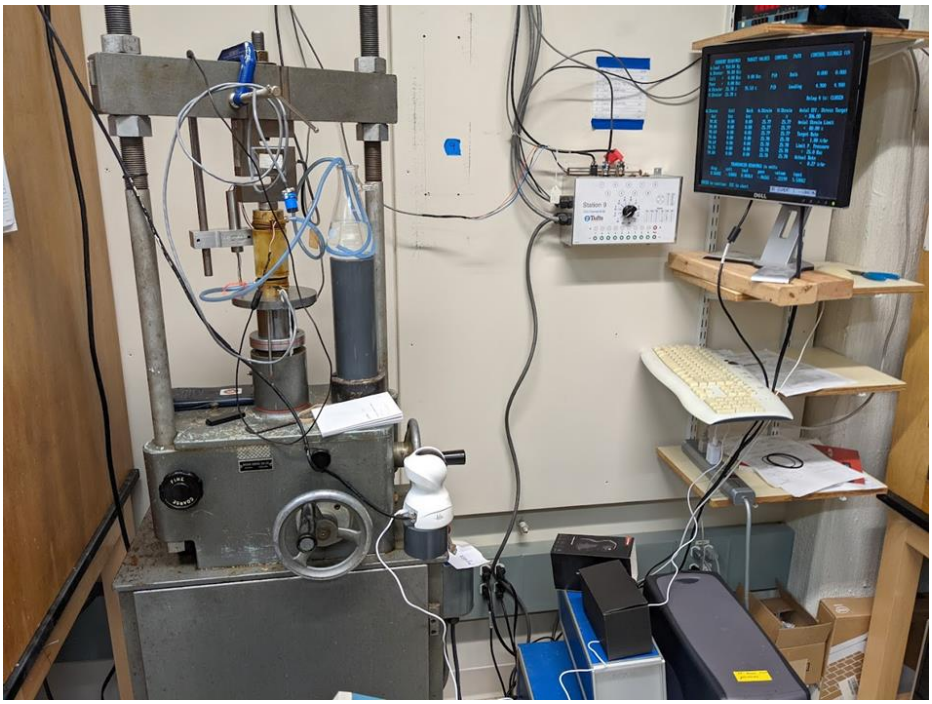
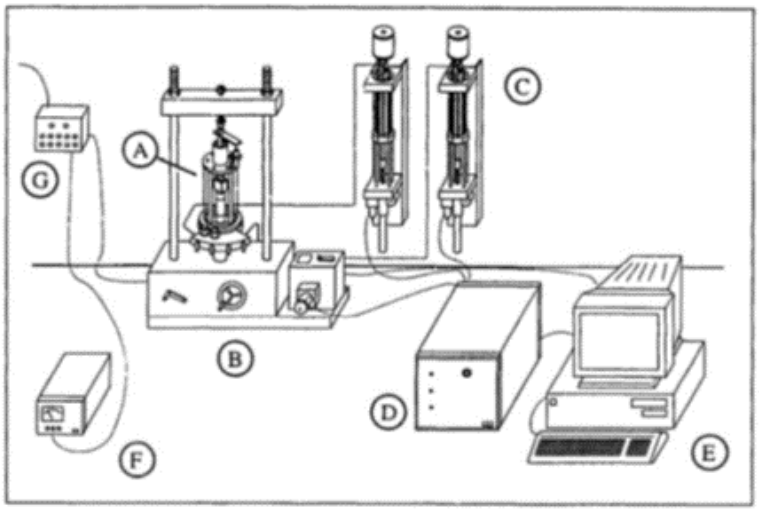


Figure 3-11: Tufts tall CRS testing apparatus and test setup



A - Triaxial Cell
B - Load Frame
C - Pressure/Volume Controllers
D - Motor Control Box
E - Personal Computer
F - DC Power Supply
G - Data Acquisition Channels

Figure 3-12: Schematic Diagram of Components for a Typical Tufts Automated Triaxial Test Apparatus adapted from Santagata (1998)



Figure 3-13: Tufts low stress triaxial testing apparatus, rated for an internal fluid pressure of 1 MPa



Figure 3-14: Tufts medium stress triaxial testing apparatus, rated for an internal fluid pressure of 10 MPa



Figure 3-15: Casagrande cup used for determinations of the liquid limit



Figure 3-16: Fall cone apparatus used for determinations of the liquid limit

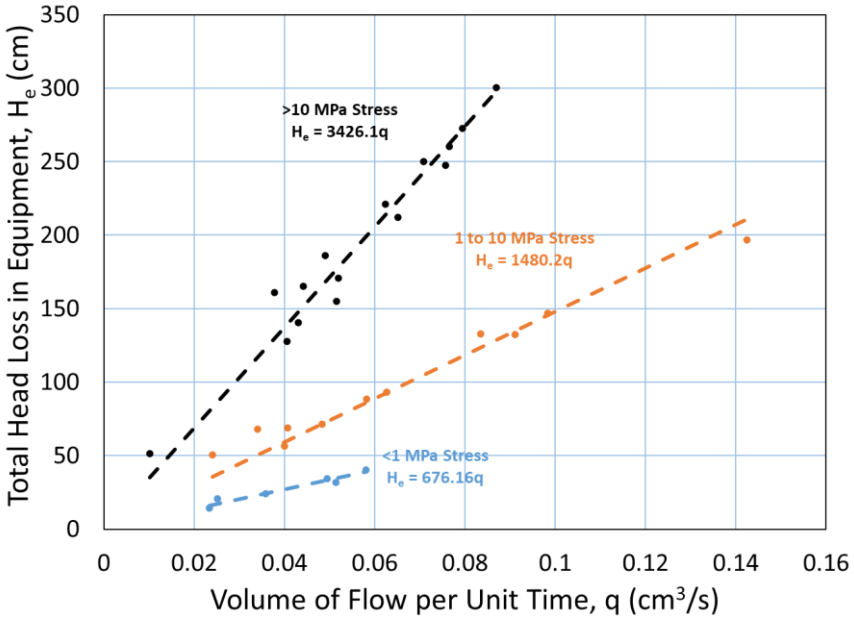


Figure 3-17: Head loss due to the high stress CRS equipment modified for permeability testing with a back pressure at three axial stress ranges, <1 MPa stress (blue line), 1 to 10 MPa stress orange line, and >10 MPa stress black line.

CHAPTER 4. Characterization of the Study Materials

4-1 Introduction

This chapter presents and discusses the origin and classification of the studied silt and clay mixtures. Section 4.2 presents the geologic origin of the parent materials for the mixtures Gulf of Mexico Eugene Island and Min-U-Sil 40. Section 4.3 presents the results of index testing performed on the mixtures. Timed sedimentation tests, Atterberg limits, and specific gravity measurements were performed to classify the soil mixtures within the Unified Soil Classification System. Section 4.4 discusses images of the mixtures, from various sources taken to verify specimen uniformity and visual observations.

4-2 Geologic Origin of Parent Materials

Gulf of Mexico Eugene Island (GoM_EI)

The study parent clay is from the Eugene Island (EI) Block 330 oilfield, located on the outer continental shelf of offshore Louisiana, about 270 km southwest of New Orleans as shown in Figure 4-1. A full geologic description is provided in Betts (2014). The core material used for the bulk sample were collected from wells A-12 and A-20ST within the same geologic unit, which was described as “silty shale with minor sand beds” Losh, Eglinton, & Wood, (1994). Hart, Flemings, & Deshpande, (1995) described the pore pressure and overburden stress for well A-12 and A-20ST. The upper 1500 m are hydrostatically pressured, followed by a moderately overpressured transition zone of 500 m, and then severe overpressures, equaling up to 95% of the total overburden pressure occurring below 2000 m. The cores used for the study clay parent material were taken within the severely overpressured zone. Figure 4-2 provides a cross section of the interpreted geologic conditions for wells A-12 and A-20ST adapted from Alexander & Flemings, (1995). The cores were processed for resedimentation prior to testing as described within Chapter 3.

Min-U-Sil 40

The study parent silt is Min-U-Sil 40 manufactured and distributed by US Silica. Min-U-Sil 40 is created through crushing of larger Quartz particles which leads to smaller angular particles. The crushed particles are screened and mixed to create materials of predetermined particle distributions. Min-U-Sil 40 has reported particle sizes between 5 µm and 40 µm measured by SediGraph sedimentation methods. Figure 4-3 presents reported material properties of Min-U-Sil 40 from the manufacture US Silica adapted from US Silica (2017). Min-U-Sil 40 is reported to consist of >99% quartz mineral. This material is mixed directly with the processed GoM_EI powder during specimen creation.

4-3 Index Testing and Soil Classification

Particle Size Distributions

Timed sedimentation tests to measure the grain size distributions of Gulf of Mexico Eugene Island and Min-U-Sil 40 were performed in other studies. Figure 4-4 provides a comparison of the grain size distributions for Gulf of Mexico Eugene Island in Casey (2014) and Min-U-Sil 40 from Schneider (2011). Figure 4-5 provides the results of four timed sedimentation tests performed on Min-U-Sil 40 as a part of this laboratory testing program. 90% to 95% of Min-U-Sil 40 is within the Silt sized particle range of 0.002 mm to 0.075 mm. The remaining 5% to 10% of particles are within the clay sized particle range of <0.002 mm. 37% of the Gulf of Mexico Eugene Island particles are within the Silt sized particle range of 0.002 mm to 0.075 mm with the remaining 63% of the particles within the clay sized particle range of <0.002 mm. Both materials have particle size distributions that classify them as fine-grained soils through the Unified Soil Classification System as greater than 50% of the mass of the particles are finer than the #200 sieve (0.075 mm).

Specific Gravity

The specific gravity of the study soil mixtures solids was measured using a water pycnometer. The measurements are summarized in Table 4-1 and provided in a plot against specimen clay content by mass in Figure 4-6. The specific gravities used for phase relation calculations in the testing program is calculated using the equation for mixed soils (Equation 3-2) as detailed within chapter 3 section 3.2. Specific gravities used for the calculations are the reported GoM_EI value of 2.775 from Casey (2014) and the MUS value of 2.65 from US Silica (2017). Measurement of specific gravity was made to verify the calculated values. The specific gravity of GoM_EI was found to be 2.802 an increase from the 2.775 reported within Casey (2014). The 2.775 value is used for calculating the masses required during specimen creation for consistency. As, the specific gravity of GoM_EI was measured around the end of the testing program.

Atterberg Limits

Atterberg limits provide a basic measure of the critical water contents for a fine-grained soil's behavior. From the tests one gets the liquid limit, and plastic limit. The plastic limit being the minimum water content at which the soil will experience plastic deformation. The liquid limit indicates the minimum water content at which the soil will behave like a liquid. Testing was performed on the different soil mixture within the testing program except for Min-U-Sil 40. Min-U-Sil 40 was found to be non-plastic at all water contents and is omitted from the test results. Determinations of the liquid limit was done through both the Casagrande cup and fall cone methods as detailed within Chapter 3. Table 4-1 provides the tabulated determinations of the Atterberg limits, and Figure 4-7 provides a plot of the results.

Classification of the Study Soils

The Unified Soil Classification System (USCS) is a common method of soil classification that separates soils into two major categories, coarse grained or fine grained. The separation is made with the #200 sieve (0.075 mm) particle size. Materials with >50% passing though the #200 sieve are fine grained and inversely materials with <50% passing through the #200 sieve are coarse grained. All of the mixtures are assumed to be fine grained as the parent materials both exceed >50% passing the #200 sieve. The USCS then categories fine grained material based on the results of the Atterberg limits testing. The 0% clay material (Min-U-Sil 40) was found to be not plastic at all water contents and would be classified as a Low Plasticity Silt (ML). The 10%, 20% and 30%, mixtures plotted above the A-line in Figure 4-7, exceeded a plasticity index of 7, and had liquid limits <50% and therefore are classified as low plasticity clays (CL). The 30% clay material could have been classified as a high plasticity clay (CH) as the Casagrande cup determination of the liquid limit marginally exceeded the 50% criterion. The 40%, 50% and 60%, mixtures plotted above the A-line in Figure 4-7, and with liquid limits >50% and therefore are classified as high plasticity clays (CH).

4-4 Imaging of Study Soil Mixtures

Imaging of Triaxial Test Specimens

Triaxial test specimens sheared at a 1 MPa consolidation stress were used to create thin sections. The triaxial specimens were oven dried post shearing, packaged, and shipped to Spectrum Petrographics of Vancouver Washington for thin section preparation. Thin sections were prepared by embedding specimens under vacuum with a low viscosity clear resin, trimming a cross section of the full height of the specimen, grinding the cross section to a 30 µm thickness, and mounting the cross section on a glass slide.

The triaxial thin sections were viewed using a Leica DMS100 petrographic digital microscope. Figure 4-8 to Figure 4-14 show a cross polarized image from the top and bottom of each specimen between 10% clay and 63% clay (RGoM_EI). Through comparison of the top and bottom thin section images it was visually confirmed that the soil mixing and resedimentation process used in the laboratory program created uniform specimens.

Changes in specimen composition are observed through comparison of Figure 4-8 to Figure **4-14**, which consist images of thin sections from specimens that were consolidated to 1 MPa and sheared in a triaxial cell and oven dried prior to thin section creation. The highest silt content mixtures (10% clay, and 20% clay) are shown in Figure 4-8 and Figure 4-9, the mixtures have a light grey to dark grey coloration, when viewed through two cross polarized lenses. The 30% clay and 40% clay mixtures in Figure 4-10 and Figure 4-11 show the intermediary mixtures as the clay particles are filling the voids of the silt particles. The 30% and 40% clay specimens have a tan to light brown coloration when viewed through cross polarized lenses. The 50%, 60% and RGoM_EI specimens shown in Figure 4-12, Figure **4-13**, and Figure 4-14 indicate the clay particles have filled the silt void space and are the dominant factor in the mixture's fabric. The 50%, 60% and RGoM_EI specimens have a brown to dark brown coloration.

Figure 4-15 through Figure 4-21 are Scanning Electron Microscope (SEM) images a 1,000 times magnification of CRS specimens consolidated to 90 MPa prior to imaging. The figures show images of specimens with incrementally increasing clay contents, from 10% clay in Figure 4-15 to RGoM_EI (63% clay) in Figure 4-21. The darker grey shapes with well-defined edges are the quartz silt grains of the Min-U-Sil or natural clasts in the GoM_EI powder. The dull gray materials with ill-defined edges are the compressed clay particles. The SEM images show the evolution of the fabric of the materials with changes in clay content. The low clay materials (10% and less) have a high density of silt grain contacts

with large frequently empty void space between the contacts. The images of the transitional materials of 30% to 40% clay contents show frequent grain contacts of silt particles as well as a compressed clay matrix between the silt grains. The images of the high clay content materials of 50% clay to RGoM_EI show infrequent silt grain contacts with the grains floating in a compressed clay matrix. Extraordinarily little void space is observed in the images above a clay content of 20% clay.

Table 4-1: Summary of Atterberg Limits and Specific Gravity Testing

Specimen Clay Content	10%	20%	30%	40%	50%	60%	RGoM_EI (63%)
Liquid Limit,[1] W_L (%)	32.3	41.4	50.2	62.7	70.8	83.5	85.8[4]
Liquid Limit,[2] W_L (%)	32.4	39.0	46.5	55.3	64.0	75.3	80.8
Plastic Limit W_p (%)	17.6	15.5	17.0	14.9	16.4	19.8	22.9[4]
Plasticity Index[3], I_P (%)	14.8	23.5	29.5	40.4	47.6	55.5	57.9
Calculated[4] Specific Gravity, G_{SC}	2.669	2.689	2.708	2.726	2.746	2.765	2.775[5]
Measured Specific Gravity, G_S	2.680	2.688	2.718	2.741	2.770	2.791	2.802

Notes:

1. Liquid limit as determined with the Casagrande cup method.
2. Liquid limit as determined with the fall cone method.
3. Plasticity index calculated as $I_P = W_l - W_P$ using W_L from the fall cone method.
4. Calculated using Equation 3-2.
5. Reported within (Casey B. , 2014).

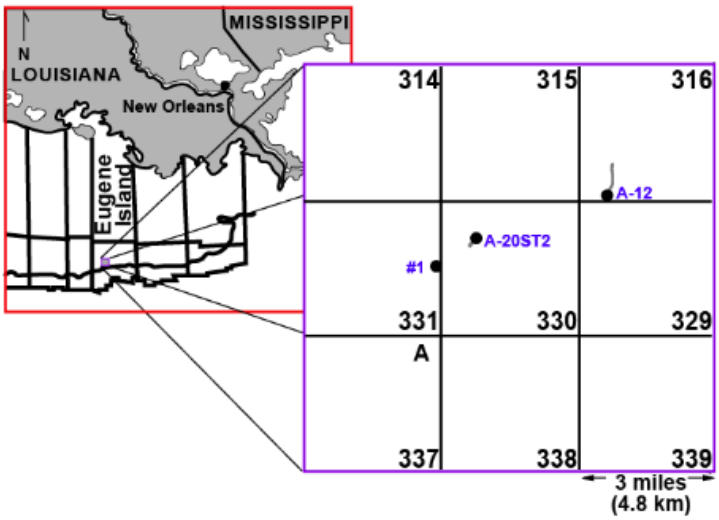


Figure 4-1: Index map showing Eugene Island Block 330 oilfield, consisting of block 330 and the surrounding blocks, and the locations of wells used in this study. Adapted from Betts (2014)

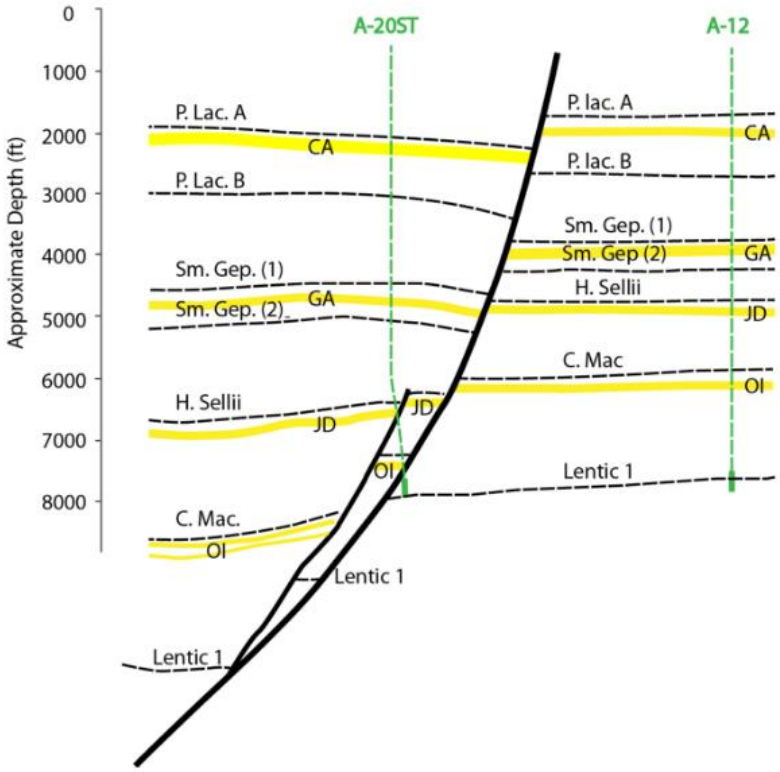


Figure 4-2: Generalized geologic cross section of the Eugene Island 330 block minibasin. Sediments from well A-12 and A-20ST were used in the resedimentation experiments. The cored interval is represented by a solid green line. Adapted from (Alexander & Flemings, 1995)

MEASURED PROPERTIES	TYPICAL PARTICLE SIZE ANALYSIS (Particle size distribution analyzed using SediGraph method)			
	MIN-U-SIL® 5	MIN-U-SIL® 10	MIN-U-SIL® 30	MIN-U-SIL® 40
-40 µm (%)	100	100	99	98
-30 µm (%)	100	100	98	95
-10 µm (%)	99	96	59	50
-5 µm (%)	97	74	34	28
+325 Mesh (%)	0.0	0.0	0.1	0.4
D 10 (µm)	0.3	0.9	1.7	2.0
D 50 (µm)	1.6	4.0	8.5	10
D 90 (µm)	3.5	7.5	20	25
Green Reflectance (%)	94	93	90	89
Yellow Index (%)	3.2	3.5	4.1	4.3
pH (5% suspension)	6.6	6.5	6.5	6.5
Tapped Bulk Density (lb/ft³)*	45	57	69	78
Loose Bulk Density (lb/ft³)*	25	29	39	45

*Not routinely measured as part of quality testing

TYPICAL GENERAL PROPERTIES			
Hardness (Mohs)	7	SiO_2 (Silicon Dioxide)	> 99%
Mineral	Quartz	Specific Gravity	2.65

September 2017

Figure 4-3: Reported properties of Min-U-Sil 40 by the manufacturer US Silica adapted from (US Silica, 2017). The red box indicates grain sized distribution for Min-U-Sil 40 measured with the SediGraph method

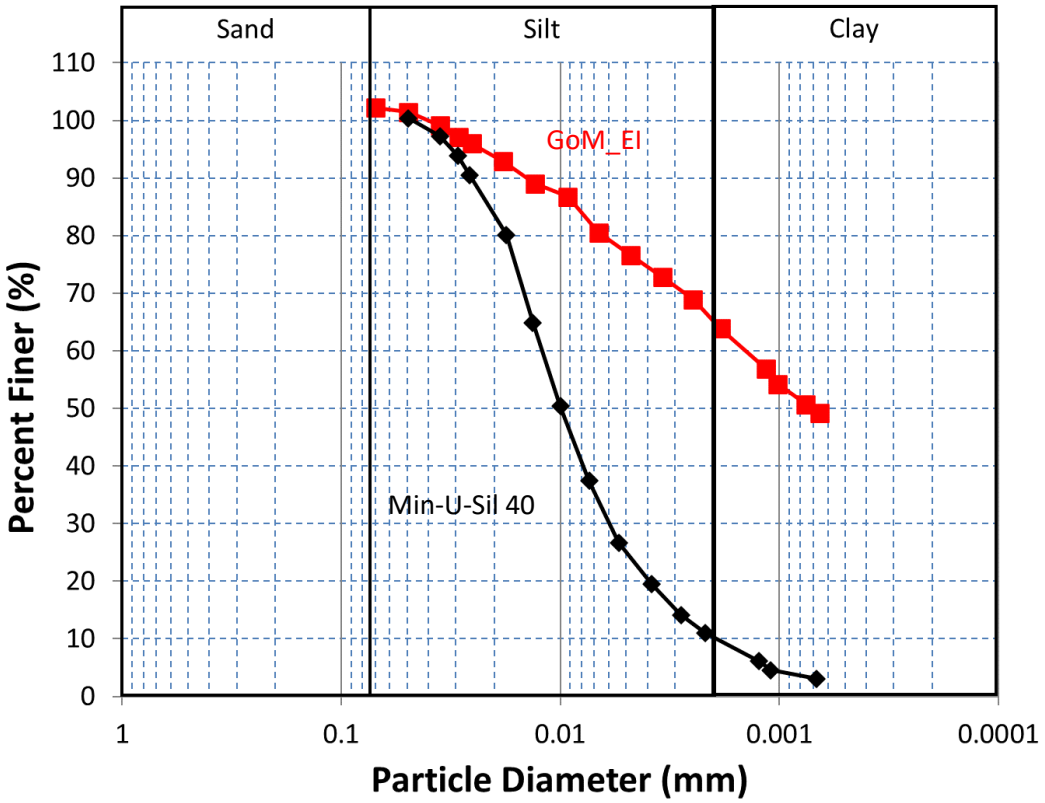


Figure 4-4: Comparison of particle size distribution of Gulf of Mexico Eugene Island (red line and points) to Min-U-Sil 40 (black line and points), measured through timed sedimentation testing. GoM_EI measurements adapted from (Casey B. , 2014), and MUS measurements adapted from (Schneider, 2011)

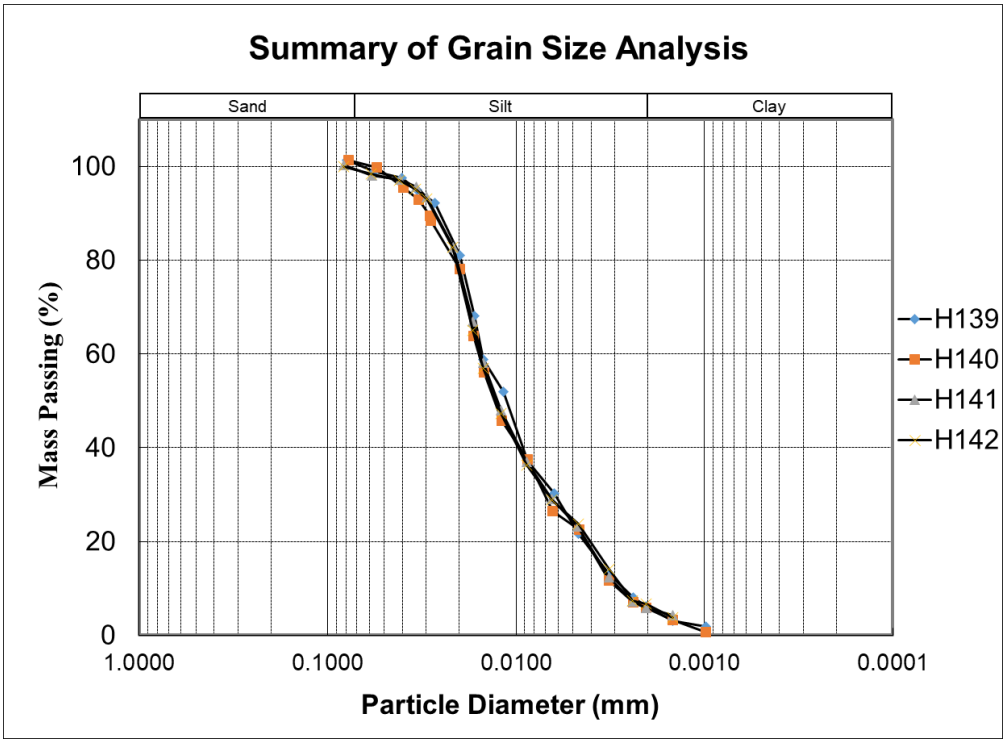


Figure 4-5: Grain size distribution testing results from four timed sedimentation hydrometer tests on Min-U-Sil 40. The TAG lab hydrometer testing number is provided in the key to the plot.

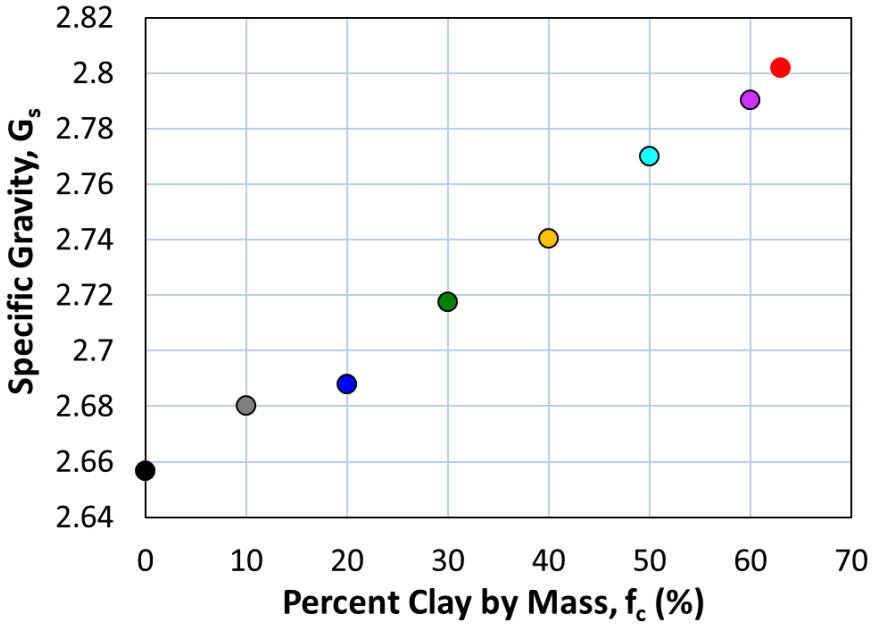


Figure 4-6: Determinations of the specific gravity of each 10% clay content increment of the silt and clay mixtures.

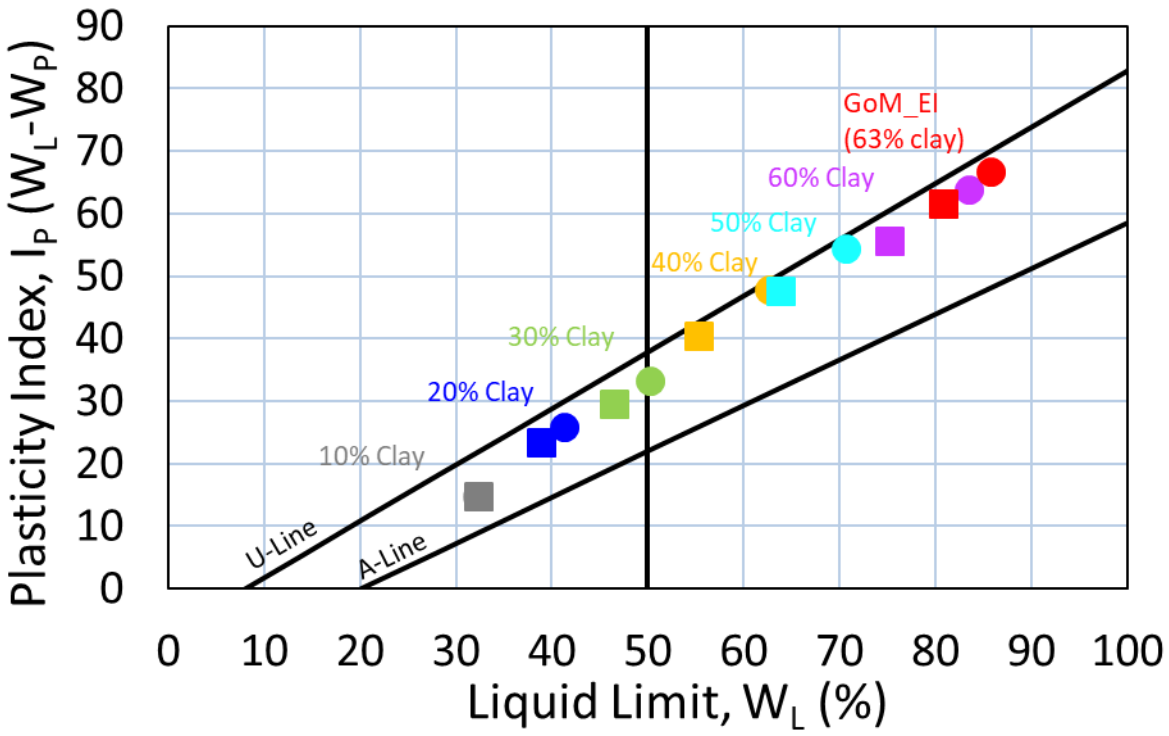


Figure 4-7: Plot of plasticity index by liquid limit indicating the results of the Atterberg Limit tests performed on the mixtures of GoM_EI and MUS. The fall cone method determinations are represented by square points and the Casagrande cup method is represented by the circular points.

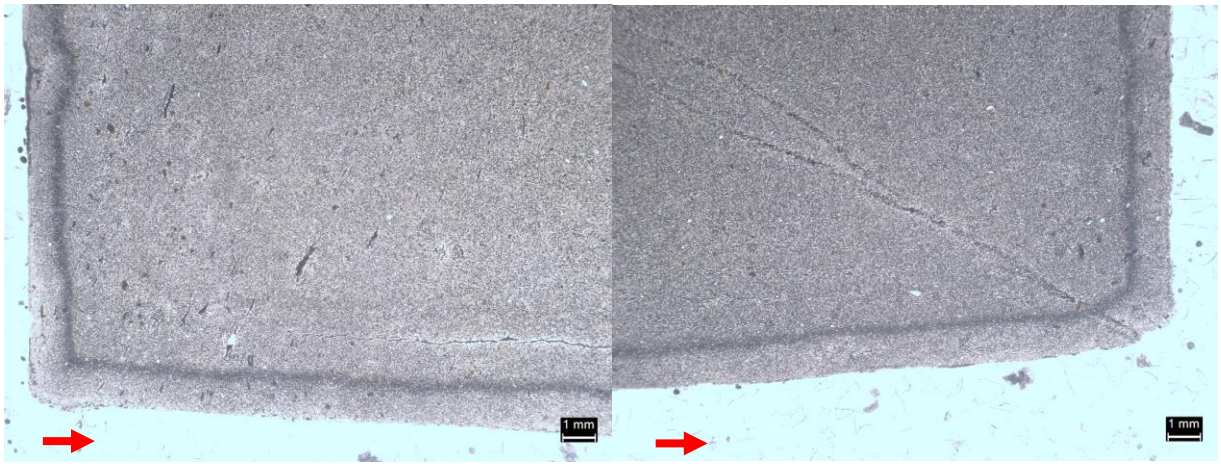


Figure 4-8: Cross polarized images of the top and bottom of TX1388 a 10% clay low stress (1 MPa) triaxial specimen thin section. The red arrow denotes the direction of the top of the specimen.

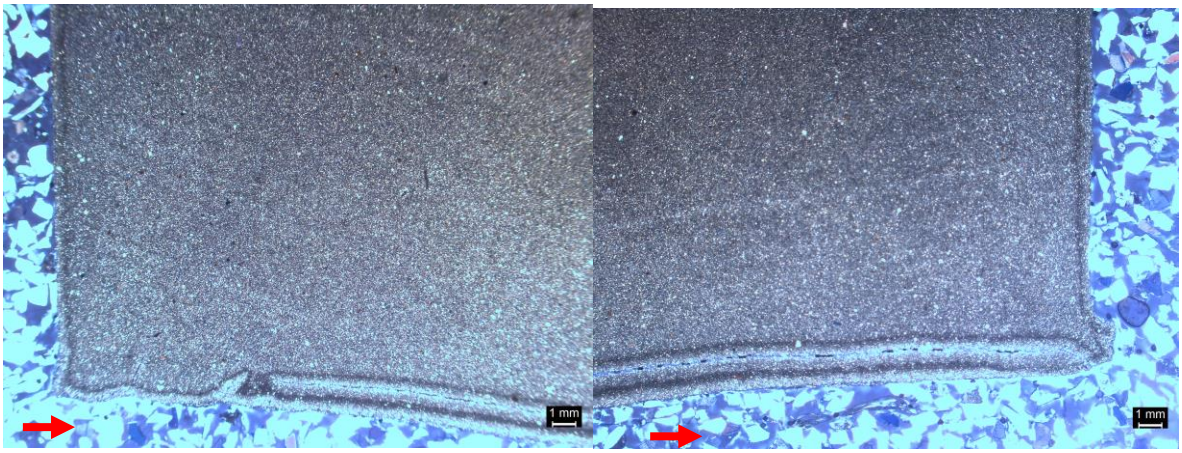


Figure 4-9: Cross polarized images of the top and bottom of TX1353 a 20% clay low stress (1 MPa) triaxial specimen thin section. The red arrow denotes the direction of the top of the specimen.

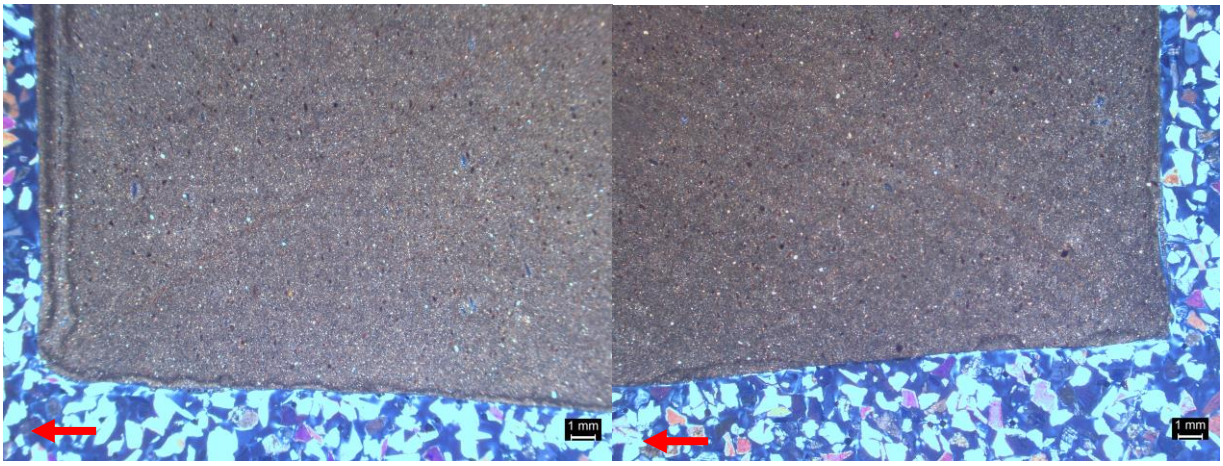


Figure 4-10: Cross polarized images of the top and bottom of TX1390 a 30% clay low stress (1 MPa) triaxial specimen thin section. The red arrow denotes the direction of the top of the specimen.

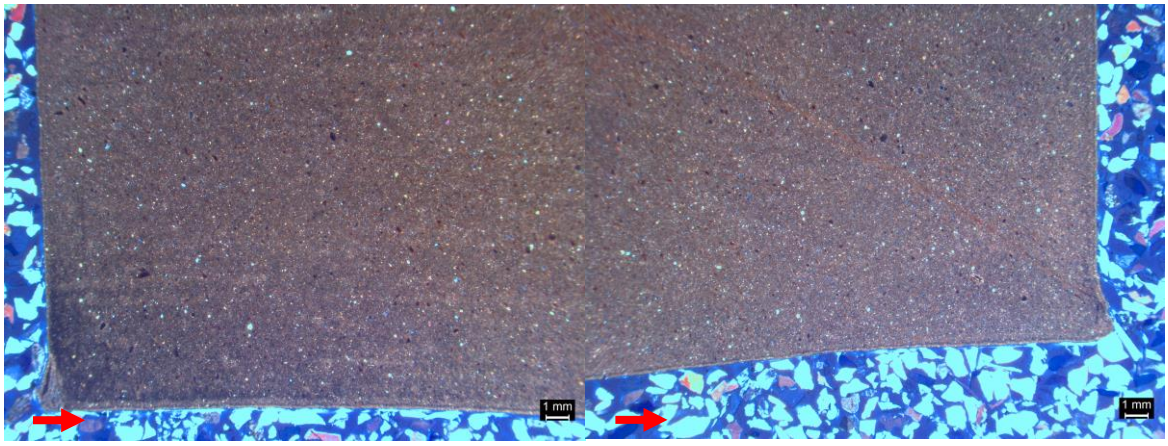


Figure 4-11: Cross polarized images of the top and bottom of TX1355 a 40% clay low stress (1 MPa) triaxial specimen thin section. The red arrow denotes the direction of the top of the specimen.

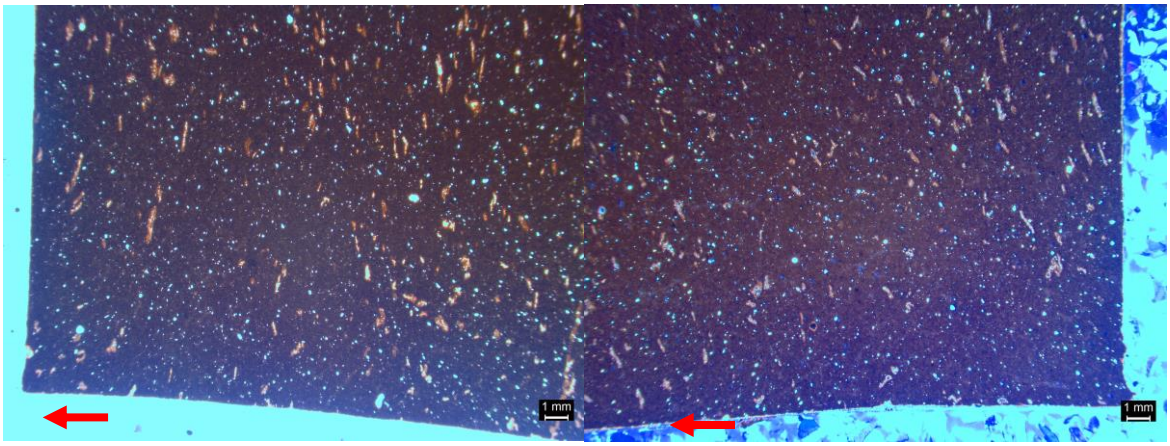


Figure 4-12: Cross polarized images of the top and bottom of TX1385 a 50% clay low stress (1 MPa) triaxial specimen thin section. The red arrow denotes the direction of the top of the specimen.

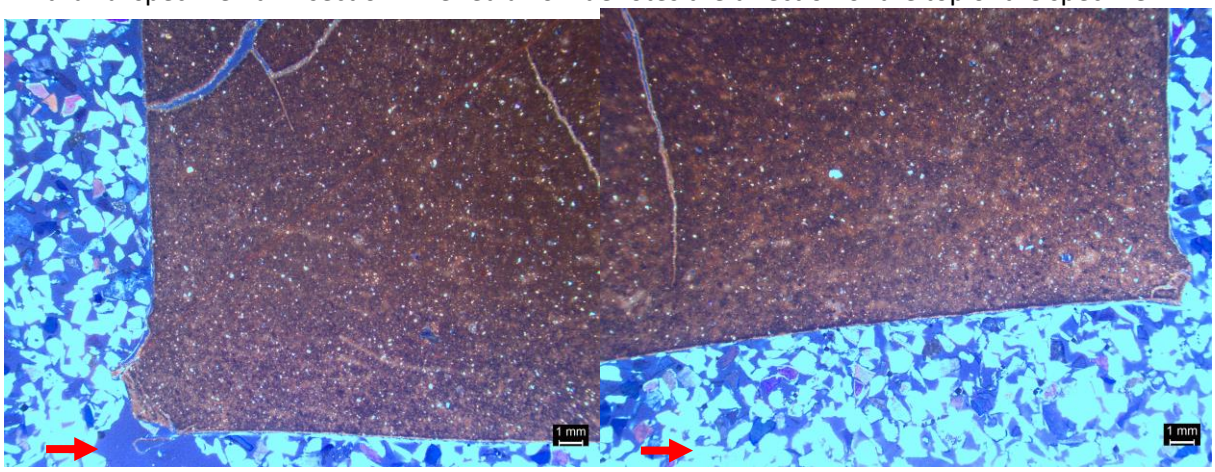


Figure 4-13: Cross polarized images of the top and bottom of TX1350 a 60% clay low stress (1 MPa) triaxial specimen thin section. The red arrow denotes the direction of the top of the specimen.

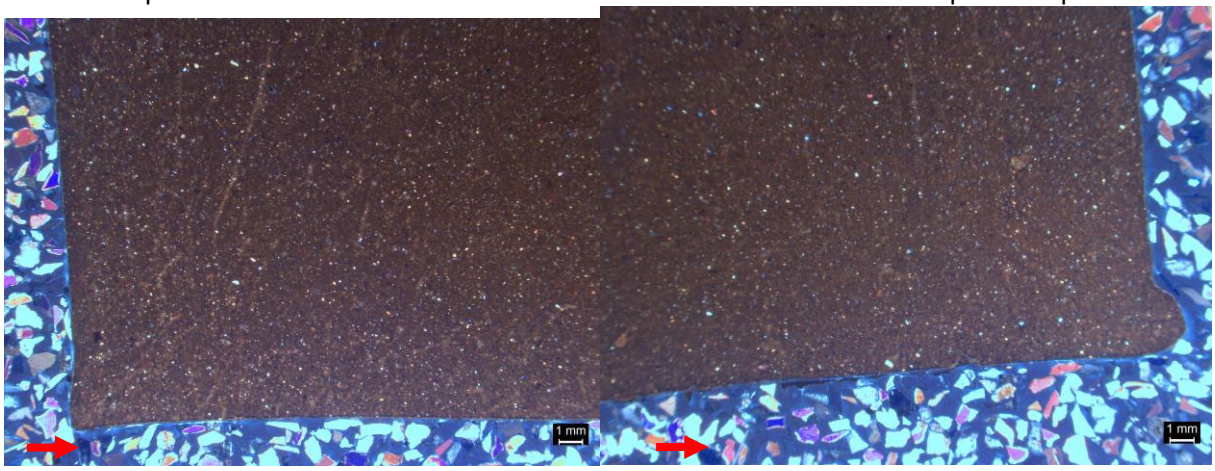


Figure 4-14: Cross polarized images of the top and bottom of TX1363 a RGoM_EI low stress (1 MPa) triaxial specimen thin section. The red arrow denotes the direction of the top of the specimen.

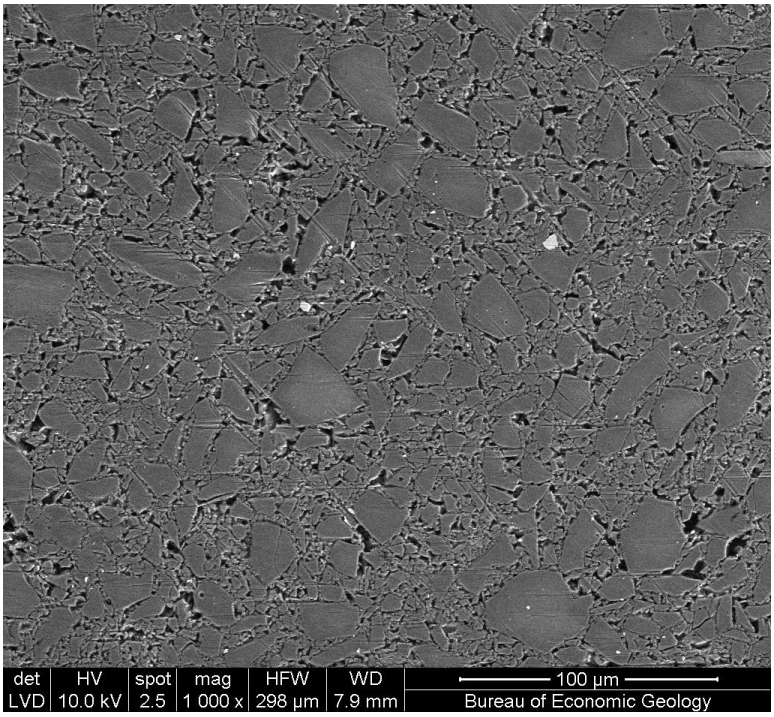


Figure 4-15: SEM image at 1000x magnification of CRS1622 a 10% clay specimen consolidated to a 90 MPa effective stress.

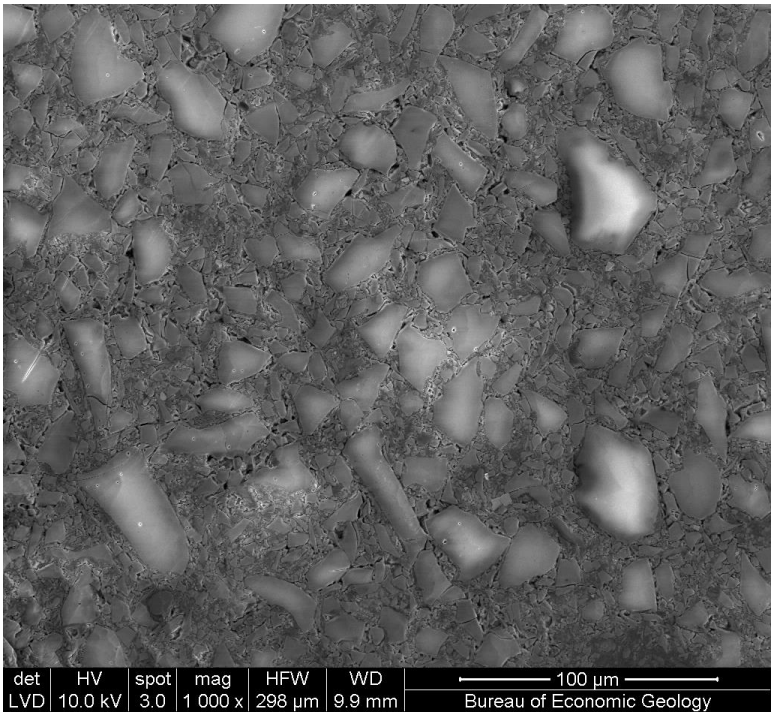


Figure 4-16: SEM image at 1000x magnification of CRS1619 a 20% clay specimen consolidated to a 90 MPa effective stress.

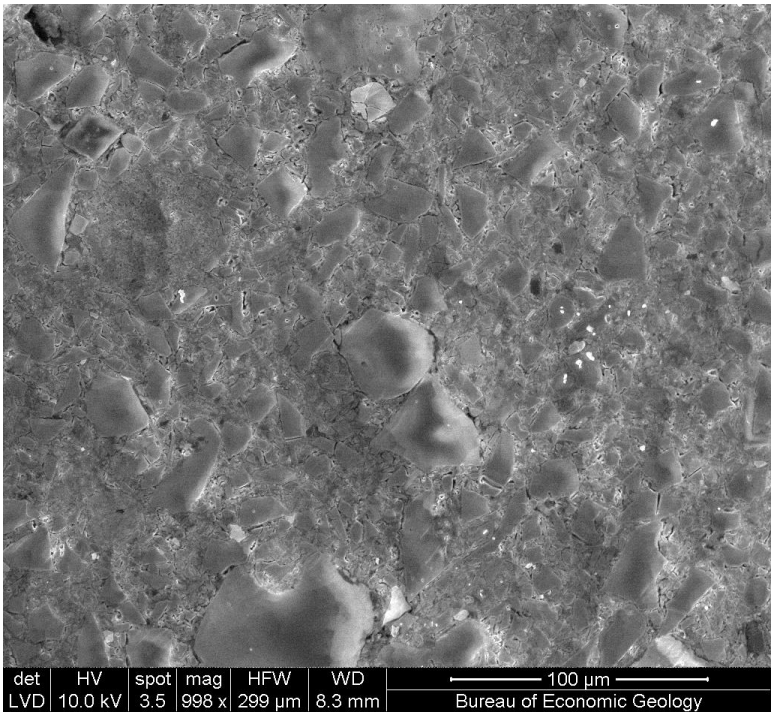


Figure 4-17: SEM image at 998x magnification of CRS1616 a 30% clay specimen consolidated to a 90 MPa effective stress.

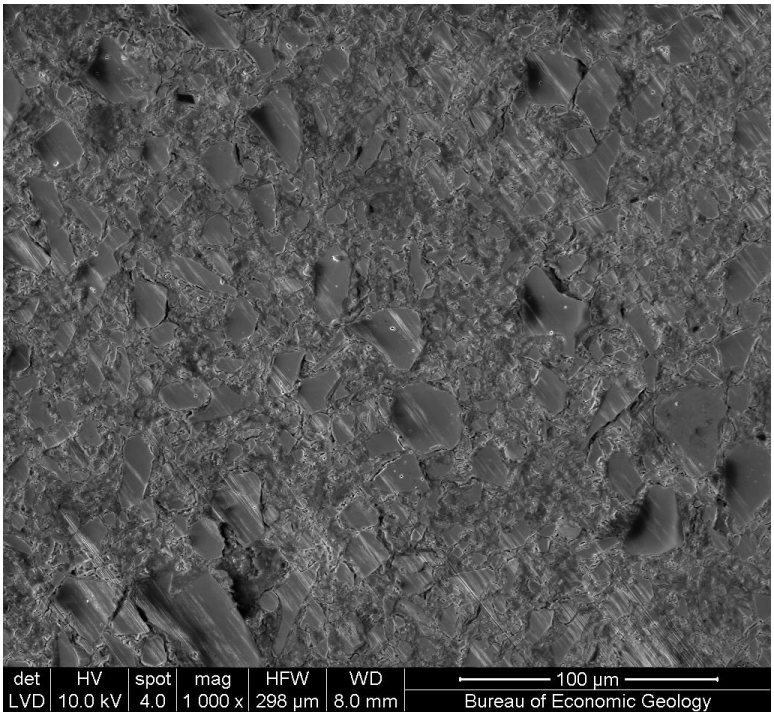


Figure 4-18: SEM image at 1000x magnification of CRS1617 a 40% clay specimen consolidated to a 90 MPa effective stress.

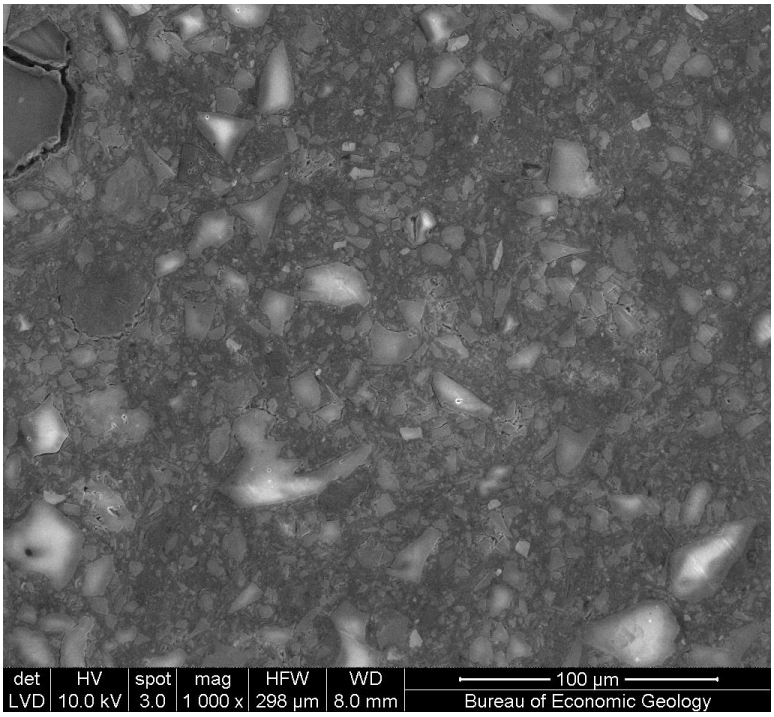


Figure 4-19: SEM image at 1000x magnification of CRS1582 a 50% clay specimen consolidated to a 90 MPa effective stress.

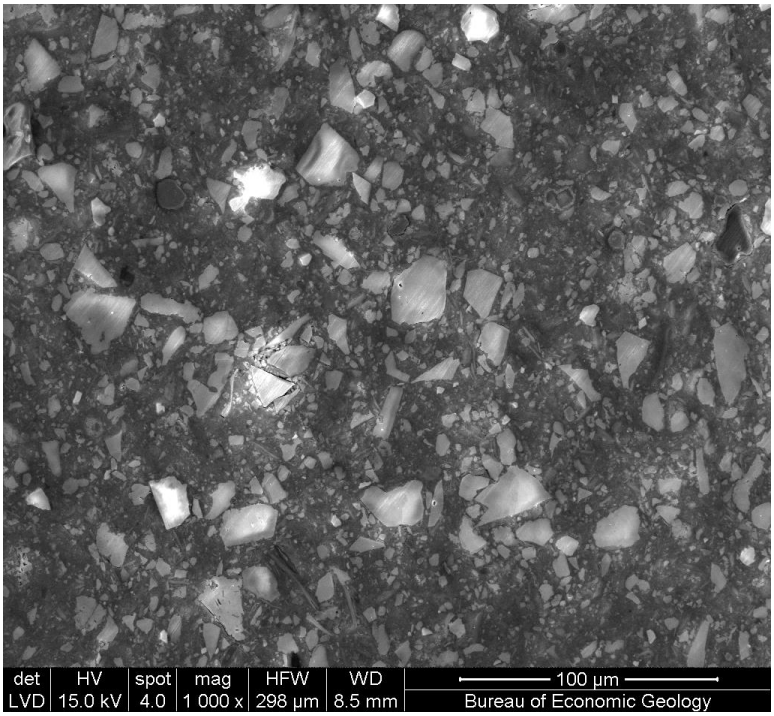


Figure 4-20: SEM image at 1000x magnification of CRS1550 a 60% clay specimen consolidated to a 90 MPa effective stress.

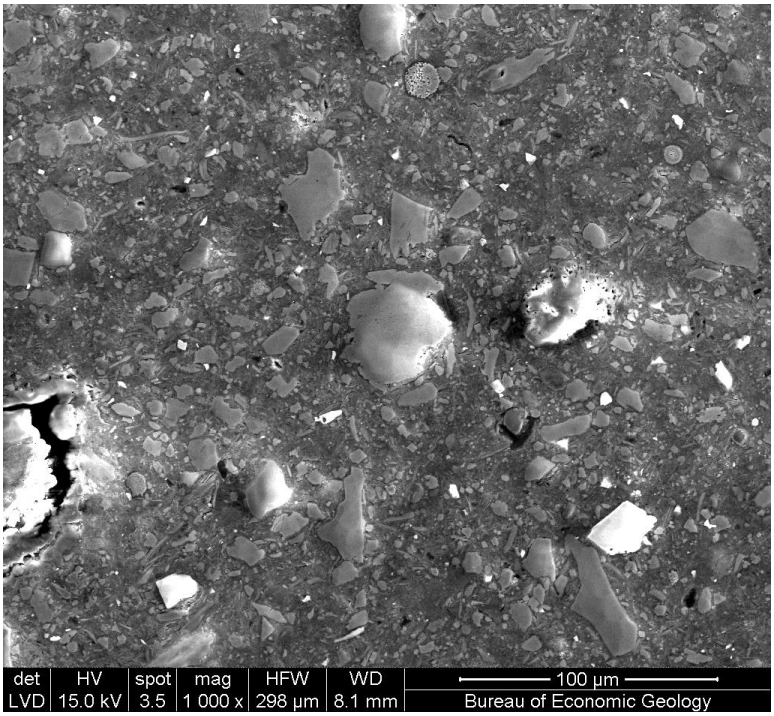


Figure 4-21: SEM image at 1000x magnification of CRS1584 a RGoM_EI specimen consolidated to a 90 MPa effective stress.

CHAPTER 5. Compression And Permeability Test Results

5.1. Introduction

This chapter presents and discusses the compression behavior of the silt and clay mixtures. Compression behavior is measured within the high stress CRS testing apparatus, within the tall CRS testing apparatus, and during the K_0 consolidation phase of a triaxial test. Within the CRS testing apparatuses, the lateral deformation of the specimen is restricted by a confining steel jacket making the compression behavior uniaxial. A uniaxial compression is also maintained within the triaxial cell during consolidation through computer control of the confining fluid pressure within the cell. Section 5.2 presents the uniaxial compression behavior of the soils and describes how this behavior changes as a function of clay content. Included in section 5.2 is a discussion on the packing of silt and clay particles due to mechanical compression. Section 5.3 discusses test apparatus specific corrections to the uniaxial compression results. A correction to the tall CRS device is presented due to sidewall friction between the tall specimen and confining steel ring. A correction to the triaxial test consolidation phase due to the development of excess pore pressures from a "too fast" axial strain rate is presented. Section 5.4 discusses permeability, uniaxial grain compressibility, and coefficient of consolidation for the studied soils.

Table 5-1 provides a summary of test conditions for all high stress CRS tests performed for this laboratory program including, resedimentation sample number, clay content, initial specimen phase relations, saturation back pressure, seating axial strain, compression strain rate, and excess pore pressure at maximum stress. Table 5-2 provides a summary of test conditions for all tall CRS tests performed during the course of the research including, resedimentation sample number, clay content, initial specimen phase relations, seating axial strain, and compression strain rate. Table 5-3 provides a summary of consolidation results for all triaxial tests performed during the research including,

resedimentation sample number, clay content, initial specimen phase relations, maximum effective stress conditions during consolidation, and pre-shear effective stresses. The phase relations for establishing the initial test specimen density for all three testing apparatuses accounts for the salinity of the pore fluid used during specimen creation.

5.2. Compression of the Silt and Clay Mixtures

Introduction

Compression for this study is defined as the axial loading of the test specimen leading to a reduction of volume within the specimen. Three different testing apparatuses were used to measure the effects of compression on the silt-clay mixtures. All three-testing apparatus constrained the lateral deformation of the specimen making these K_0 consolidation tests (uniaxial deformation). The compression behavior of the soils was measured to explore the unique relationship between the effective stress level and the density of the soil. As many soil engineering parameters are density dependent and, they are also stress dependent.

Experimental Results

High Stress CRS Compression Behavior

Figure 5-1 through Figure 5-8 provide plots of the lower bound, average, and upper bound compression curves for the study mixtures as void ratio(e), and porosity (n), by log effective axial stress, $\sigma'_{a,}$ measured through the high stress CRS apparatus. Each figure presents the results of one clay content from 0% clay (Figure 5-1) to RGoM_EI (Figure 5-8). Individual tests are down sampled to a few characteristic effective stress points and averaged, to create the average behavior line. The upper and lower bounds represent the range in void ratio at each stress level between tests performed on the same clay content specimens. Reloading to the resedimented maximum stress and secondary compression that occurs at the end of compression has been removed from the curves. Figure 5-9

presents the average compression lines from high stress CRS testing on a singular plot for comparison of compression behavior between different clay mixtures.

The largest range in void ratios during compression were observed in the 0% clay mixtures and the RGoM_EI mixtures, all clay contents generally were within a 0.1 void ratio range at all stress levels. The void ratio differences in the 0% clay mixture are attributed to initial density variations as a result of the under-compaction method used for specimen preparation. Even with best laboratory methods utilized, the silt specimens were not prepared to the exact same initial density leading to a scatter in the initial void ratio. As the compressibility of the materials is very similar an offset in initial void ratio is generally maintained over all effective stress levels.

The variations in void ratio within the RGoM_EI specimens are attributed to errors in measurement for specimen initial phase relations, extrusion during piston seating, and the small specimen size used for the high stress CRS test. The RGoM_EI specimens were generally from different resedimentation batches, while the other high stress CRS tests of other mixtures were generally performed on specimens from the same resedimentation batch. Due to the small initial mass of the high stress CRS test specimen, small variations in density can led to large differences in void ratio. As the compressibility of the materials is very similar an offset in initial void ratio is generally maintained over all effective stress levels.

Tall CRS Compression Behavior

Figure 5-10 through Figure 5-16 provide plots of the lower bound, average, and upper bound compression curves as void ratio(e), and porosity (n), by log effective axial stress σ'_a, measured using the tall CRS test apparatus. Each figure presents the results of one clay content mixture from 10% clay (Figure 5-10) to RGoM_EI (Figure 5-16). Individual tests are down sampled to a few characteristic axial effective stress points and averaged to generate the average behavior line. The upper and lower bounds

represent the range in void ratio at each stress level between the tests performed on the same clay content specimens. Reloading to the resedimented maximum stress and secondary compression that occurs at the end of compression has been removed from the curves. Figure 5-17 presents the average compression lines from tall CRS testing on a singular plot for comparison of compression behavior between different clay mixtures.

Due to the larger specimen size of the tall CRS as compared to the high stress CRS variations in initial densities or errors in initial measurements have significantly less of an impact on the initial void ratio. As such the tall CRS compression curves shown in Figure 5-10 to Figure 5-16 have a much closer range in void ratios as compared to the high stress CRS compression curves.

Triaxial Consolidation Compression Behavior

Figure 5-18 through Figure 5-25 provide plots of the lower bound, average, and upper bound compression curves as void ratio(e), and porosity (n), by log effective vertical stress, σ'_a, from the consolidation phase of the triaxial tests. Each figure presents the results of one clay content mixture from 0% clay (Figure 5-18) to RGoM_EI (Figure 5-25). Individual tests are down sampled to a few characteristic axial effective stress points and averaged to generate the average behavior line. The upper and lower bounds represent the range in void ratio at each stress level between the tests performed on the same clay content specimens. Reloading to the resedimented maximum stress and secondary compression that occurs at the end of compression has been removed from the curves. Figure 5-26 presents the average compression lines from the consolidation phase of the triaxial tests on a singular plot for comparison of compression behavior between different clay mixtures.

Figure 5-26 presents the consolidation phases from both the low stress and medium stress triaxial shear tests. The compression curves of the low stress tests end at the targeted pre-shear σ'_a stresses of 1 MPa 10 MPa for the low and medium stress cells respectively. Which is why the

compression curves are broken into two segments. The compression measurements indicate that there are differences in measurements between the low stress and medium stress triaxial cells. The compression behavior from the 1 MPa tests should have a smooth transition to the initial porosities of the 10 MPa tests. Figure 5-26 shows the curves are not in agreement. The differences are attributed to variations in the stress history from specimen creation between the 1 MPa and 10 MPa stress levels and differences in the system compliance of the two testing apparatus effecting the measurements. The 0% clay specimens have a specimen creation density issue. The 0% clay specimens are not created in a stress history controlled method like resedimentation and are instead mechanically compacted using the undercompaction method. It is difficult to create dense specimens for the 10 MPa tests using the undercompaction method.

Compressibility of the Silt Clay Mixtures

Trends in compression by clay content are apparent through comparison of the compression curves between the different silt and clay mixtures. Clay content mixtures greater than 50% clay, exhibit the highest void ratios at low confining stresses (<1 MPA). Higher clay content materials have larger changes in void ratio with changes in stress at low confining stress (<1 MPA), and become stiffer when compressed, leading to smaller changes in void ratio with changes in effective stress at higher effective stress levels (>10 MPa). The stiffening behavior at higher effective stresses of the high clay content material results in concave upwards compression curve in an e-Log(σ'_a) plot.

Silt dominant mixtures of less than 20% clay, exhibit lower void ratios at low confining stresses (<1 MPA) than the clay rich materials. Have a much stiffer initial compression trend at low effective stress (<1 MPA) and have an increase in compressibility at higher effective stresses (>10 MPa). This behavior results in a concave downwards compression curve in an e-Log(σ'_a) plot.

The transition silt and clay mixtures of 20% clay to 50% clay exhibited lower void ratios at low confining stresses (<1 MPA) than the clay rich mixtures and depending on the testing apparatus lower void ratios at low stress than the silt rich mixtures. The transition materials have compression curves that are generally linear in an e-Log(σ'_a) plot. The compression behavior of the mixtures is illustrated best through the average compression summary figures for each test apparatus Figure 5-9, and Figure **5-17**.

To compare the stress dependent compression behavior of the soils, Figure 5-27 and Figure 5-28 shows the Coefficient of Compressibility (a_v) of the silt clay mixtures calculated from the average compression curves of the high stress and tall CRS apparatuses. Where a_v is the change in void ratio over the change in effective axial stress between the plotted stress and a 1 MPa reference stress. The a_v values shown Figure 5-27 and Figure 5-28 reinforce the observed trend of clay content effecting the compressibility of the material. The av values are well ordered, with a_v monotonically decreasing with decreasing clay content for a given stress. The high stress CRS and tall CRS apparatuses show good agreement in av values. The a_v values for the mixtures trend towards convergence with increasing stress. Around a 20 MPa all the specimens have a CR within the range of 0.008 and 0.026. At a 90 MPa stress the range of a_v values is between 0.003 and 0.006. Figure 5-27 illustrates this behavior as the High Stress CRS tests are the only compression tests to exceed the 30 MPa axial stress level.

Compressibility of the Silt Clay Mixtures and Material Packing

The compression behavior of the silt and clay mixtures is related to the interparticle packing of the silt and clay particles and the overall compressibility of the resultant soil fabric. Theoretically a 100% clay material composed of flat platy particles would have the largest possible initial void ratio. This theoretical clay material would also have the largest initial compressibility. These behaviors are possible, because of the physio-chemical forces associated with the clay particles, which can support a

stable soil fabric at very low densities. This initial fabric is subject to natural variations during the clay deposition process.

While a theoretical 100% percent silt material would have an initial density that is entirely a result of particle packing due to gravity, and other depositional factors. This is due to the silt's fabric deriving its structure from direct particle contact. The silt grains being too large to have significant effect of physio chemical forces, and therefore are dependent on direct crystalline grain contacts, therefore the silt soil fabric is entirely a result of the depositional processes.

A mixture of the two theoretical soils will exist as one of two dominant soil fabrics depending on the constitutive contents of the clay and silt particles, and the effective stress of the mixture. Either the crystalline grains are supporting the material by force chains through direct contacts, or the clay particles support the material grains in a clay matrix. For the clay matrix supported fabric the silt grains may or may not be in direct contact with each other, but loads are distributed over the clay grains. The transition point between the grain supported and clay supported fabrics is known as the critical clay fraction for the mixtures. At the critical clay fraction the crystalline grains of a mixture are in contact, but the pore space between the grains is filled with clay to the point that any additional clay would move the grains out of contact. Figure 5-29 adapted from Marion, Nur, Yin, & Han, (1992), illustrates the range in soil fabrics in which silt and clay mixtures can exhibit at a singular effective stress including the critical clay fraction. The critical clay fraction being the transition point between the grain supported and clay supported fabrics. The critical clay content is dependent on a multitude of factors, some of which being the crystalline grain sizes, the activity of the clay mineralogy, the compressibility of both the clay and crystalline grain particles, and the effective stress of the mixture.

The change in soil fabric with changes in clay content at an effective stress state is apparent through examination of the compression curves of the silt and clay mixtures. Figure 5-30 plots the

average void ratio of each test mixture in the high stress CRS test at a 1 MPa stress level. An interpretation reference line is included in Figure 5-30 as a general representation of the trend of changes in density due to changes in specimen clay content. The trend being a general decrease in void ratio/porosity starting from 0% clay with increasing in clay content to the critical clay fraction and then an increase in void ratio/porosity at clay contents exceeding the critical clay fraction. A red X indicates the interpreted critical clay fraction for the 1 MPa stress of the tested mixtures in Figure 5-30. The increase in density from 0% clay to the critical clay fraction is attributed to the filling of the grain porosity with clay particles creating a denser soil fabric. At clay contents greater than the critical clay fraction the decrease in density is attributed to clay particles dominating the soil fabric. The clay particles can create stable fabrics with higher void ratios lowering the overall bulk density of the mixture.

The effects of changes in effective stress level and changes in the soil fabric of mixtures is illustrated in Figure 5-31. Where the void ratio/porosity of the average high stress CRS test of each mixture is plotted at 9 effective stress levels 1 MPa, 2 MPa, 5 MPa, 10 MPa,15 MPa, 20 MPa, 30 MPa, 40 MPa, and 50 MPa. The silt rich materials at clay contents less than the critical clay content (<30% clay) indicate very consistent compression behavior. Where the change in void ratio is relatively linearly proportional to the change in effective stress. The clay rich materials indicate a stiffening with large changes in void ratio with changes in effective stress at low effective stresses and smaller changes in void ratio with changes in effective stress at higher stresses. Figure 5-31 also shows the trend observed at 1 MPa of decreasing void ratio/porosity from a 0% clay content to a critical clay content and then increasing void ratio/porosity as the clay content increase beyond the critical content at a given stress level continues to be true at higher stress levels. The interpreted critical clay content represented by the red x on each interpretation line at each stress level in Figure 5-31 shows a stress dependent behavior. Where the critical clay content increases to higher clay contents with increases in effective

stress level and decreases in void ratio. The increase in the critical clay content with increasing stress is attributed to the high compressibility of the clay particles compared to the silt grain particles. At low clay contents (20% clay or less) the soil structure is supported by grain to grain contacts of the silt particles and increases in clay content decrease pore space by filling them with clay. When low clay content materials are compressed the grain to grain contacts supports theses loads. At intermediary mixtures between 20% clay and 50% clay depending on stress level, the grains may or may not be in contact and compressible clay particles are contributing to the soil fabric. As theses intermediary mixtures are compressed the grains can compress the clay particles until either grain are in contact or the clay particles stiffen sufficiently to support the load. This mechanism results in more clay particles being forced into grain pore spaced at higher stress shifting the critical clay content to higher clay content values. Due to the stiffening nature of clays under compression there is a functional upper clay content limit for the critical clay content. At high clay contents (>50% clay) the silt grains are separated in the clay matrix. As these materials are compressed the clay matrix supports the load and uniformly stiffens maintaining separation of the silt grains. That is the silt grains do not contribute to the behavior of the high clay content soils and act as rigid inclusion where that loads are distributed through into the surrounding clay matrix. Understanding the effects of stress and clay content on the packing of the silt and grain particles is important for an understanding of the soils mechanical behavior as is discussed further in the interpretation of the test results Chapter 8.

5.3. Compression Curve Corrections

Introduction

This section presents corrections to the compression behavior of the tall CRS tests and the consolidation phase of the triaxial tests. These corrections are due to testing apparatus specific conditions and are beyond the standard recommended corrections for each test based on the ASTM

guidance standards. These corrections were applied to every test from the indicated apparatus in addition to any standard corrections as applicable.

Tall Constant Rate of Strain Sidewall Friction Correction

Most compression test specimens have a height to diameter ratio in the 0.17 to 0.40 range to limit the effect of sidewall friction on the compression behavior of the material. The tall CRS test is performed on specimens with a height to diameter ratio in the 1 to 2 range, where the sidewall friction is not negligible and needs to be accounted for. This correction was performed by accounting for the friction between the confining steel jacket and specimen during compression. The correction for the sidewall friction is presented in Equation 5-1 and is based on the work of Lovisa & Sivakugan (2015) and Ranjpour (2020).

$$\sigma_P = qe^{-4Ktan\delta(\frac{z}{D})} \qquad \text{Equation 5-1}$$

Where:

σ_P = Is the corrected average axial stress (stress)

q = Applied stress, load cell measurement divided by specimen area (stress)

K = Lateral Stress Ratio (unitless)

δ = Interface friction angle between specimen and sidewall (Degrees)

z = Depth from top of specimen calculated from the initial specimen height and the axial strain incurred to the stress level where the correction is applied (length)

D = Specimen diameter constant (length)

Equation 5-1 assumes that the frictional force due to self-weight of the specimen is negligible as such that term is omitted from the correction. This is a realistic assumption for a specimen at the dimensions required for tall CRS tests. The correction also assumes a linear distribution of the friction forces from the midpoint of the specimen to the top and bottom for simplification, as the friction is likely to be a parabolic distribution. The interface friction angle is taken to be one half of the critical state friction angle consistent with Han, Ganju, Salgado, & Prezzi (2018) for the interface friction angle on a polished

metal surface. As the confining steel ring for the test was made of stainless steel and is smooth. As the lateral stress ratio and the critical state friction angle are dependent on stress as well as dependent on specimen clay content stress dependent liquid limit correlations were used to estimate both parameters to estimate the friction correction. The lateral stress ratio (K_0) was estimated using Equation 5-2 to Equation 5-4 which correlates the lateral stress ratio at a value of 10 MPa to soil plasticity with a stress dependence from Casey (2014).

$$K_0 = K_{010}\left(0.1\sigma'_{a(MPa)}\right)^J \qquad \text{Equation 5-2}$$

$$K_{010} = 0.0056W_{L(\%)} + 0.33 \qquad \text{Equation 5-3}$$

$$J = 0.257Log_{10}\left(W_{L(\%)}\right) - 0.398 \qquad \text{Equation 5-4}$$

Where:

K_0 = Lateral stress ratio at rest (unitless)

$\sigma'_{a(MPa)}$ = Effective axial stress (MPa) correlation specific unit

K_{010} = Lateral Stress Ratio at 10 MPa (unitless)

J = Fitting parameter (unitless)

$W_{L(\%)}$ = Liquid Limit (percent)

The critical state friction angle was estimated from a similar correlation of with the material liquid limit and stress dependence from Casey (2014). Equation 5-5 to Equation 5-7 were used to estimate the critical state friction angle for the friction correction.

$$\phi_{CS} = A\left(0.001\sigma'_{a(MPa)}\right)^{B} \quad \text{Equation 5-5}$$

$$A = -75Log_{10}\left(W_{L(\%)}\right) + 148 \quad \text{Equation 5-6}$$

$$B = -0.39Log_{10}\left(W_{L(\%)}\right) + 0.59 \quad \text{Equation 5-7}$$

Where:

K_{0NC} = Normally consolidated lateral stress ratio at rest (unitless)

$\sigma'_{a(MPa)}$ = Effective axial stress (MPa) correlation specific unit

K_{010} = Lateral Stress Ratio at 10 MPa (unitless)

J = Fitting parameter (unitless)

$W_{L(\%)}$ = Liquid Limit (percent)

An estimate lateral stress ratio and critical state friction angle was calculated at each measurement in the tall CRS test. These estimated parameters were used within Equation 5-1 to estimate the corrected axial stress at the midpoint of the specimen for the tall CRS measurement, where the maximum correction is anticipated to be required. The difference in the corrected stress at the midpoint of the specimen and the uncorrected stress was then distributed linearly over the top and bottom halves of the specimens as the total specimen correction. Figure 5-32 shows the difference in axial effective stress between the applied stress and the stress corrected for friction at the midpoint of the specimen for CRS1652, a 10% clay test. Figure 5-33 shows the difference in axial effective stress between the applied stress and the distributed stress corrected for friction for CRS1652. Figure 5-34 shows the difference in the corrected for sidewall friction compression curve and the uncorrected compression curve for test CRS1652 in an e-log(σ'_a) plot. The sidewall friction correction was applied to all tall CRS tests.

The friction correction was found to be directly proportional to the height of the specimen. As such the effects were normalized to initial specimen height and presented as % error in effective stress by cm height of specimen. The effect of friction was greatest in the specimens with lower clay contents (≤30%

clay) due to their higher initial critical state friction angles. These specimens had average errors in effective stress of 4.1% per cm of height. The higher clay content materials (>30% clay) had average errors in effective stress of 3.5% per cm of height. For all specimens, the error associated with friction forces decreased with increases in effective axial stress. This is due primarily to the change in height of the specimen decreasing therefore the area of which the force is applied continually decreases. The stress dependance of the lateral stress ratio and critical state friction angle general offset each other as the lateral stress ratio increased with increasing stress and the critical state friction angle decreased with increasing stress.

Excess Pore Pressure Correction Due to Fast Axial Strain Rate in Triaxial Tests

During the consolidation phase of a triaxial shear test the specimen is compressed through a computer-controlled axial strain rate. The rate is user selected and intended to be low enough to allow for the drainage of excess pore pressures due to the contraction of the soil during consolidation. For this testing program, the axial strain rate during triaxial consolidation was varied between 0.07-0.11 %/hour. High clay content mixtures have very low permeabilities and as such may not have been fully drained during the consolidation phase of the triaxial test. Results from the consolidation phase of the triaxial test were evaluated for a correction due to the potential error of a “too fast” strain rate. The correction is based on work presented by Wissa et al. Wissa, Christian, Davis, & Heiberg (1971), where a calculation for excess pore pressure during constant rate of strain compression is presented. The boundary conditions during triaxial k_0 consolidation are similar to a CRS test. As the triaxial computer controller maintains a constant axial strain rate during the consolidation phase, a constant cross section area is assumed during K_0. Equation 5-8 is used to calculate the theoretical excess pore pressure at the midpoint of the specimen due to the consolidation strain rate.

$$u_h = \frac{\dot{\epsilon}(H_0 H_n)\gamma_w}{2k}$$ Equation 5-8

Where:

u_h = Excess pore pressure at the midpoint of the specimen (stress)

$\dot{\epsilon}$ = Average strain rate during consolidation

H_0 = Half the starting specimen height (length)

H_n = Half the specimen height at evaluation point n (length)

γ_w = Specific weight of the pore water (force by volume)

k = Hydraulic conductivity (length by time)

The vertical distribution of pore pressures within the specimen is assumed to be parabolic from the center to the ends and symmetric about the centerline of the specimen. The soil is assumed to be a linear type for simplification of the calculation for average axial effective stress within the specimen. The average axial effective stress is calculated as the total measured axial stress less two thirds of the predicted excess pore pressure at the center of the specimen. Figure 5-35 shows a comparison of the measured compression curve, and the compression curve corrected for excess pore pressures for triaxial test TX1484 a RGoM_EI specimen consolidated to 10 MPa. The correction relies on the hydraulic conductivity of the soil which is calculated from the permeability of the soil using Equation 5-9.

$$k = \frac{Kg\gamma_w}{\mu}$$ Equation 5-9

Where:

k = Hydraulic conductivity of the soil (length by time)

K = Permeability of the soil (area)

g = Acceleration due to gravity 9.81 (length by time squared)

γ_w = Specific weight of water (force by volume)

μ = Dynamic Viscosity of Water (stress with time)

The permeability of the soil is dependent on effective stress, and the clay content, as such the permeability for the excess pore pressure correction used a predictive model of permeability by porosity

based on the laboratory measurements and explained further in CHAPTER 8. Each clay content has a unique permeability model to predict permeability as a function of porosity.

The excess pore pressure correction was small for the specimens with a clay content of 40% or less. These specimens had a range in error of effective stresses between 0% and 5.19% with an average error of 1.14%. The higher clay content specimens, >50% clay had a range in error of effective stress between 6.37% and 25% with an average error of 13.64%. The large range in error is attributed to variations in the applied strain rate between tests. Each specimen was held at the maximum consolidation stress at the end of consolidation for a minimum of 24 hours. During this time excess pore pressures were allowed to dissipate, and the errors in effective stress reported is the final error at the end of the hold stress Period.

5.4. Permeability of the Silt and Clay Mixtures

Introduction

The effects of clay content on the permeability of soils have been studied extensively and some notable works are Mondol, Bjorlykke, & Jahren (2008), Yang & Aplin (2010), Casey (2014), and Reece (2021) all of which indicate the sensitivity of the permeability of fine grained soil to the clay content of the soil through various laboratory measurements and field observations. The permeability of fine-grained soils is found to be affected, by pore size distribution, particle shape, mean particle diameter, particle orientation, clay content, clay mineralogy, and the double layer interactions of clay particles. Permeability is a function of the soil properties with no considerations to the permeating fluid.

Experimental Results

Figure 5-36 presents the average measured permeability by porosity for each of the study soil mixtures. Permeability was measured as discussed within Chapter 3 either through a constant head test (0% Clay), constant flow test (10% Clay), or through high stress CRS testing. 0% and 10% clay content materials were found to have a too high of a permeability for reliable measurements of permeability due to excess pore pressure during CRS testing. Figure 5-36 shows the trends of decreasing permeability with increasing specimen clay content and decreasing permeability with decreasing porosity. The 0% clay material the lowest studied clay content has the highest permeability over the full stress range. The 0% clay specimens were not created using the resedimented specimen preparation technique, leading to a significant amount of variability in the initial density for these tests, creating variability in the measured permeability. This variability should be considered when looking at trends in the data. Figure 5-36 indicates that relatively small changes in clay content create significant changes in permeability for clay contents less than 50% clay. For clay contents equal to 50% or greater, increases in clay content correspond with small decreases in permeability at a given porosity. This behavior indicates a minimum permeability corresponding with a theoretically 100% clay material at a given stress state. The decrease in the sensitivity of soil permeability to increases in clay content beyond 50% clay was also observed by Yang & Aplin (2010).

Figure 5-37 presents the average measured permeability of each test mixture by axial effective stress. Figure 5-37 presents general trends of decreasing permeability with increasing clay content, as well as decreasing permeability with increasing axial effective stress. This plot provides a good representation of the differences between permeabilities in soils of different clay contents at the same burial depth (axial effective stress). Figure 5-37 also provides log-log linear regressions for each tested mixture for use in further discussion of general trends.

5.5. Coefficient of Consolidation and Uniaxial Grain Compressibility, M_v

Introduction

The coefficient of consolidation c_v is used to quantify the time dependent dissipation of pore water pressures more than hydrostatic conditions generated during uniaxial loading of soil, from complete overpressure due to instantaneous load to dissipation. The coefficient of consolidation is related to the permeability of soil as well as the uniaxial compressibility of the soil through equation 5-10 as shown within Terzaghi (1925) and others.

$$c_v = \frac{K}{\mu M_v} \qquad \text{Equation 5-10}$$

Where:

c_v = Coefficient of Consolidation (m^2/s)

K = Permeability of the soil (m^2)

μ = Dynamic Viscosity of Water (kg/m^2 s, Pa s)

M_v = Uniaxial Compressibility of Soil (1/Pa)

Uniaxial compressibility (commonly referred to as the coefficient of volume change) is calculated as the change in strain over the change in effective stress under uniaxial compression conditions.

Experimental Results

The changes in c_v of the tested silt clay mixtures from the high stress CRS tests are shown in Figure 5-38, which plots c_v by axial effective stress on a log-log plot that includes solid lines indicating a log-log linear regression of the data. There are some notable trends in c_v by soil clay content. 0% and 10% clay specimens indicate that c_v increases with increasing axial effective stress. The 20% clay to 63% clay content specimens indicate c_v is static or very slightly decreasing over a 90 MPa stress range. Each clay content has a very different initial c_v which is ordered by clay content where the higher clay content specimens have a lower initial c_v.

The changes in M_v of the tested silt clay mixtures are shown in Figure 5-39 the solid lines indicate a log-log linear regression of the data. Clay content mixtures greater than 40% clay have significant scatter due to the nature of the measurement. In general, the soil mixtures indicate a 1 order of magnitude range in the uniaxial grain compressibility at a 1 MPa axial effective stress, with higher clay content materials having a higher M_v than lower clay content materials. All mixtures indicate that the compressibility decreases with increasing effective stress. For any given effective stress level, M_v of the mixtures has a parabolic shape when plotted against clay content, like the trend in density shown in Figure 5-31. The range in M_v values between different clay contents decreases with increasing effective stress level. At a 25 MPa effective stress, the values of M_v for all the mixtures is within 50% of the highest value. By a 55 MPa effective stress variations in M_v are negligible (<2% of the highest value). Beyond a 55 MPa effective stress the higher clay content materials have a lower M_v indicating that the clay matrix acts stiffer than the silt grains at very high effective stresses.

Discussion

The dependence of permeability, coefficient of consolidation, and uniaxial grain compressibility on the clay content provides insight to the behavior of soils. The uniaxial grain compressibility for all studied soils is within a very narrow range that further narrows with increasing axial effective stress. With the compressibility of the mixture being similar then the variations in the coefficient of consolidation are attributed to variations of permeability. For materials with a clay content of 20% or greater the changes in M_v and k are consistent leading to a near constant C_v. For the 0% and 10% materials the uniaxial grain compressibility changes at a rate that is greater than the change in permeability leading to an overall increase in C_v. These trends are presented in Figure 5-40 in which the trend lines for M_v, k, and C_v are presented by axial effective stress. Figure 5-40 indicates that k is dependent on the initial clay content of the specimen and therefor C_v is dependent on the initial clay content as well.

Table 5-1: Summary of High Stress CRS Tests

Spec. Location		Index Tests			Specimen Data		Test Conditions				Remarks
Test #	Depth (ft)	T_v	ω_c	ω_p	ω_n	e_i	u_b			$\Delta u/\sigma_v$	
Boring		SD	SD	ω_n	I_p	S_i(%)	σ'_s	ε_i	$d\varepsilon/dt$	@ σ'_{vm}	
Sample	Markers	# obs	# obs	%2µ	γ_t	G_s	(ksc)	(%)	(%/hr)	(%)	
CRS1550					37.25	0.965	3.92			11.0295	60% Clay - Bad Initial Measurements
					0.49	109.5		-0.96	0.15	932.1	40% Silt
RS579					1.954	2.77				1.18%	By Mass
CRS1554					52.45	1.589	3.77			0.47	65% Clay - Bad Initial Measurements
					0.61	94.4		2.90	0.11	110.48	35% Silt
RS594					1.662	2.78				0.42%	By Mass
CRS1562					41.06	0.734	4.08			0.73	30% Clay - Bad Initial Measurements
					0.42	155.403		0.25	0.09	680.46	70% Silt
RS581					2.2	2.71				0.11%	By Mass
CRS1565					34.70	0.741	3.89			12.98	50% Clay Issues - Bad Initial Measurements
					0.43	131.747		-0.02	0.21	1241.45	50% Silt
RS615					2.1	2.75				1.05%	By Mass
CRS1567					20.67	0.556	3.96			8.66	30% Clay - Bad Initial Measurements
					0.36	102.571		-0.01	0.48	973.20	70% Silt
RS614					2.1	2.71				0.89%	By Mass
CRS1571					33.06	0.877	3.99			-0.15	0% Clay
					0.47	100.000	N/A	1.01	0.90	977.05	100% Silt
Undercomp.					1.9	2.65				-0.02%	By Mass
CRS1572					31.31	0.929	3.91			15.43	60% Clay
					0.48	95.302		0.25	0.14	999.52	40% Silt
RS626					1.9	2.77				1.54%	By Mass
CRS1581					50.21	1.429	4.05			14.98	65% Clay
					0.59	100.433		0.47	0.19	891.33	35% Silt
RS623					1.7	2.78				1.68%	By Mass
CRS1584					24.86	0.659	3.96			0.14	0% Clay
					0.40	100.000	N/A	1.41	1.66	972.75	100% Silt
Undercomp.					2.0	2.65				0.01%	By Mass
CRS1585					27.24	0.818	4.10			15.29	40% Clay
					0.45	92.775		1.16	0.42	969.96	60% Silt
RS626					1.9	2.73				1.58%	By Mass
CRS1586					42.15	1.201	4.03			15.41	50% Clay
					0.55	98.987	3.73	1.81	0.33	996.99	50% Silt
RS615					1.8	2.75				1.55%	By Mass
CRS1591					22.60	0.753	4.19			0.19	10% Clay
					0.43	81.721		1.14	0.69	973.23	90% Silt
RS638					1.9	2.67				0.02%	By Mass
CRS1592					31.50	0.950	4.07			16.32	60% Clay
					0.49	93.813		1.62	0.18	987.69	40% Silt
RS606					1.9	2.77				1.65%	By Mass
CRS1593					30.98	0.896	3.93			9.67	40% Clay
					0.47	96.382		1.50	0.35	968.35	60% Silt
RS626					1.9	2.73				1.00%	By Mass
CRS1594					42.79	1.368	4.17			17.37	65% Clay
					0.58	89.181	1.09	0.83	0.20	985.80	35% Silt
RS623					1.7	2.78				1.76%	By Mass
CRS1600					44.51	1.368	3.56			9.72	50% Clay
					0.58	91.817	0.91	1.73	0.32	996.91	50% Silt
RS615					1.7	2.75				0.98%	By Mass
CRS1608					23.36	0.702	3.95			1.88	20% Clay
					0.41	91.328	2.38	0.73	0.49	976.06	80% Silt
RS658					2.0	2.69				0.19%	By Mass
CRS1611					40.03	1.254	3.78			3.61	50% Clay
					0.56	89.983	0.91	2.92	0.15	963.57	50% Silt
RS616					1.7	2.75				0.38%	By Mass
CRS1616					26.79	0.788	3.93			0.63	30% Clay
					0.44	93.962	3.56	0.79	0.40	985.21	70% Silt
RS666					1.9	2.71				0.06%	By Mass
CRS1617					29.95	0.905	4.06			4.67	40% Clay
					0.48	92.232		0.26	0.32	101.37	60% Silt
RS633					1.9	2.73				4.61%	By Mass
CRS1618					50.26	1.517	3.75			14.89	65% Clay DAQ Issue did not record to
					0.60	94.700	2.28	-0.03	0.15	693.05	35% Silt Max Stress
RS624					1.7	2.78				2.15%	By Mass
CRS1619					26.11	0.803	4.09			1.09	20% Clay
					0.45	89.291	2.92	2.50	0.50	973.13	80% Silt
RS658					1.9	2.69				0.11%	By Mass
CRS1620					18.17	0.713	4.05			-0.29	0% Clay
					0.42	68.760	N/A	1.18	0.61	968.35	100% Silt
Undercomp.					1.8	2.65				-0.03%	By Mass
CRS1621					28.59	0.860	3.87			5.74	30% Clay
					0.46	92.020	4.13	0.12	0.34	971.25	70% Silt
RS666					1.9	2.71				0.59%	By Mass
CRS1622					24.49	0.722	3.93			0.03	10% Clay
RS624					0.42	92.332	3.86	1.91	0.64	974.90	90% Silt
					1.9	2.67				0.00%	By Mass
CRS1630					27.63	0.803	3.83			1.83	20% Clay
					0.45	94.519	2.75	0.98	0.44	911.93	80% Silt
RS658					1.9	2.69				0.20%	By Mass
CRS1640					27.55	0.836	3.96			15.68	60% Clay
					0.46	91.777	3.77	2.36	0.26	975.28	40% Silt
RS634					1.9	2.73				1.61%	By Mass
CRS1682					26.66	0.771	4.46			0.04	10% Clay
					0.44	94.202	1.41	4.11	0.30	949.41	90% Silt
RS718					1.9	2.67				0.00%	By Mass

a) Markers - Location within tube b) Stresses in kg/cm^2 c) 1 kg/cm^2 = 2048 psf d) Water Contents in %

ω_n Water content prior to testing.
I_p Plasticity Index
γ_t Total mass density
e_i Initial void ratio
S_i Initial saturation
G_s Specific gravity of solids
u_b Back pressure saturation pressure for B value
$\sigma's$ Maximum effective stress from consolidometer
ε_i Initial axial strain
$d\varepsilon/dt$ Axial strain rate
$\Delta u/\sigma_v$ Normalized pore pressure
@ σ'_{vm} Normalized pore pressure at maximum stress
(%) Pore pressure percentage of maximum stress

Table 5-2: Summary of Tall CRS Tests

Spec. Location		Index Tests			Specimen Data		Test Conditions				Remarks
Test #	Depth (ft)	T_v	ω_c	ω_p	ω_n	e_i	u_b			$\Delta u/\sigma_v$	
Boring		SD	SD	ω_l	I_p	S_i(%)	σ'_s	ε_i	$d\varepsilon/dt$	@ σ'_{vm}	
Sample	Markers	# obs	# obs	%2μ	γ_t	G_s	(ksc)	(%)	(%/hr)	(%)	
CRS1629					39.86	1.136	N/A				65% Clay
					0.53	99.9			0.158	N/A	35% Silt
RS688					1.840	2.78					By Mass
CRS1632					29.89	0.859	N/A				30% Clay
					0.46	96.3			0.061	N/A	70% Silt
RS666					1.908	2.71					By Mass
CRS1633					32.78	0.934	N/A				50% Clay
					0.48	98.620			0.065	N/A	50% Silt
RS617					1.9	2.75					By Mass
CRS1638					31.19	0.856	N/A				40% Clay
					0.46	101.629			0.051	N/A	60% Silt
RS689					1.9	2.73					By Mass
CRS1646					39.53	1.119	N/A				60% Clay
					0.53	100.236			0.072	N/A	40% Silt
RS691					1.8	2.77					By Mass
CRS1652					26.50	0.707	N/A				10% Clay
					0.41	102.096			0.020	N/A	90% Silt
RS663					2.0	2.67					By Mass
CRS1663					24.63	0.738	N/A				20% Clay
					0.42	91.526			0.055	N/A	80% Silt
RS694					1.9	2.69					By Mass
CRS1668					4.54	0.939	N/A				0% Clay
					0.48	12.969			0.049	N/A	100% Silt
Undercomp.					1.4	2.65					By Mass
CRS1672					39.69	1.133	N/A				65% Clay
					0.53	99.790			0.060	N/A	35% Silt
RS717					1.8	2.78					By Mass
CRS1678					28.21	0.797	N/A				20% Clay
					0.44	97.187			0.097	N/A	80% Silt
RS694					1.9	2.69					By Mass
CRS1679					38.16	1.113	N/A				60% Clay
					0.53	97.204			0.086	N/A	40% Silt
RS689					1.8	2.77					By Mass
CRS1688					30.90	0.853	N/A				40% Clay
					0.46	100.989			0.15	N/A	60% Silt
RS689					1.9	2.73					By Mass
CRS1693					33.19	0.927	N/A				50% Clay
					0.48	100.666			0.08	N/A	50% Silt
RS724					1.9	2.75					By Mass
CRS1698					28.23	0.794	N/A				30% Clay
					0.44	98.359			0.07	N/A	70% Silt
RS719					2.0	2.71					By Mass
CRS1700					26.56	0.739	N/A				10% Clay
					0.42	97.997			0.11	N/A	90% Silt
RS718					2.0	2.67					By Mass

a) Markers - Location within tube b) Stresses in kg/cm^2 c) 1 kg/cm^2 = 2048 psf d) Water Contents in %

- ω_n Water content prior to testing.
- I_p Plasticity Index
- γ_t Total mass density
- e_i Initial void ratio
- S_i Initial saturation
- G_s Specific gravity of solids
- u_b Back pressure saturation pressure for B value
- $\sigma's$ Maximum effective stress from consolidometer
- ε_i Initial axial strain
- $d\varepsilon/dt$ Axial strain rate
- $\Delta u/\sigma_v$ Normalized pore pressure
- @ σ'_{vm} Normalized pore pressure at maximum stress
- (%) Pore pressure percentage of maximum stress

Table 5-3: Summary of Consolidation Phase of Triaxial Tests

Spec. Location		Index Tests			Specimen Data		Conditions			Consolidation Results						Remarks
										General		@ Max Stress		@ Preshear		
Test #	Depth	$\bar{T}_v$	ω_n	ω_p	ω_n	e_i	σ'_i	u_b	B	σ'_p	CR	ε_a	σ'_{vm}	ε_a	σ'_{vc}	
Boring		SD	SD	ω_l	I_p	S_i				ε_{vol}		K_c		ε_{vol}	OCR	
Sample	Markers	# obs	# obs	%2µ	γ_t	G_s	ε_a	ε_a	ε_{vol}	ε_a/hr	RR	C_α	t_s	K_c	t_s	
TX1347	NA				25.83	0.73	1.72	2.15	0.93	8.00		6.28	9.92	6.98	9.90	32% Clay
						97.59						6.34	0.53	7.05	1.00	68% Silt
RS481	NA				1.98	2.71	0.05	-0.57	-0.59	0.30			0.00	0.54	46.67	By Mass
TX1348	NA				29.14	0.83	1.80	3.99	0.91	8.00		4.18	9.94	4.55	9.88	50% Clay
						98.48						5.46	0.71	5.72	0.99	50% Silt
RS482	NA				1.95	2.75	-0.21	-2.25	-2.25	0.30			0.00	0.70	30.33	By Mass
TX1350	NA				31.65	0.94	2.00	4.00	0.89	8.00		3.77	9.79	6.09	9.85	60% Clay
						94.99						3.77	0.73	6.80	1.01	40% Silt
RS486	NA				1.89	2.77	-0.10	-0.09	-0.96	0.30			0.00	0.72	46.17	By Mass
TX1353	NA					0.66	1.89	2.33	-	8.00		4.69	9.93	5.18	9.99	20% Clay
						99.16						4.60	0.46	5.09	1.01	80% Silt
RS484	NA				2.02	2.69	-0.09	-0.10	-0.04	0.30			0.00	0.45	55.29	By Mass
TX1355	NA					0.76	1.97	4.00	0.90	8.00		3.19	9.98	4.44	9.95	40% Clay
						94.68						3.21	0.63	4.94	1.00	60% Silt
RS490	NA				1.97	2.73	0.01	0.03	-0.38	0.30			0.00	0.61	39.75	By Mass
TX1358	NA					0.70	2.04	1.97	0.84	8.00		1.92	9.98	1.91	10.02	10% Clay
						102.17						1.78	0.50	1.87	1.00	90% Silt
RS491	NA				2.00	2.67	-0.09	-0.09	0.57	0.30			0.00	0.50	27.58	By Mass
TX1359	NA					0.93	1.10	1.89	0.92	5.00		11.25	9.74	12.22	9.77	50% Clay
						98.27						10.77	0.61	11.44	1.00	50% Silt
RS495	NA				1.90	2.75	0.14	0.14	-1.05	0.15			0.00	0.61	39.58	By Mass
TX1360	NA					0.70	0.60	2.00	0.56	NA		1.50	8.02	1.79	7.69	0% Clay
						100.00						4.14	0.98	8.47	0.96	100% Silt
UND	NA				1.97	2.65	-0.10	-0.10	-1.45	0.15			0.00	0.99	58.80	By Mass
TX1362	NA					1.10		2.01	0.44	NA		6.18	9.56	6.49	9.56	0% Clay
						100.00						12.72	0.66	4.65	1.00	100% Silt
UND	NA				1.78	2.65		2.95	-5.76	0.30			0.00	0.66	22.00	By Mass
TX1363	NA						1.24	2.99	0.94	5.00		10.99	10.03	11.93	9.94	65% Clay
						99.30						11.27	0.68	12.30	0.99	35% Silt
RS496	NA				1.86	2.78	-0.08	-0.06	-2.03	0.15			0.00	0.68	56.60	By Mass
TX1364	NA					0.82	0.65	2.00	0.44	NA		1.19	9.56	1.28	9.58	0% Clay
						100.00						0.35	0.55	0.43	1.00	100% Silt
UND	NA				1.90	2.65	-0.07	-0.15	-2.02	0.30			0.00	0.55	44.47	By Mass
TX1367	NA					0.73	1.24	2.99	0.92	5.00		6.68	9.94	7.25	9.98	30% Clay
						99.37						6.68	0.50	7.01	1.00	70% Silt
RS562	NA				1.98	2.71	0.01	0.06	-0.22	0.15			0.00	0.50	90.83	By Mass
TX1368	NA					0.88		1.99	0.64			1.81	10.25	2.06	9.88	0% Clay
						100.00						0.67	0.51	0.23	1.04	100% Silt
UND	NA				1.88	2.65		-0.01	-7.30	0.30			0.00	0.50	42.00	By Mass
TX1369	NA					0.89	0.51	2.01				2.36	10.05	2.55	10.06	0% Clay
						100.00						0.69	0.51	0.42	1.00	100% Silt
UND	NA				1.87	2.65	0.04	0.07	-1.43	0.30			0.00	0.51	33.00	By Mass
TX1373	NA					0.86	0.50	2.47				2.86	10.13	3.13	10.18	0% Clay
						100.00						1.17	0.43	2.07	1.00	100% Silt
UND	NA				1.88	2.65	0.02	0.11	-0.67	0.30			0.00	0.42	18.00	By Mass
TX1380	NA					0.75	1.24	1.99	0.98	5.00		7.94	9.82	8.50	9.79	20% Clay
						102.74						7.90	0.47	8.77	1.00	80% Silt
RS574	NA				1.97	2.69	-0.01	-0.01	0.54	0.15			0.00	0.46	66.30	By Mass
TX1381	NA					1.05	1.25	1.87	0.96	5.00		10.56	10.88	11.85	10.92	65% Clay
						99.44						10.65	0.69	12.50	1.00	35% Silt
RS568	NA				1.86	2.78	-0.04	-0.03	-0.55	0.15			0.00	0.68	72.84	By Mass
TX1383	NA					0.88	1.04	1.91	0.89	5.00		7.15	10.01	8.35	9.91	50% Clay
						96.98						7.11	0.64	8.18	0.99	50% Silt
RS537	NA				1.91	2.75	-0.03	-0.02	-1.89	0.15			0.00	0.59	33.37	By Mass
TX1385	NA					1.06	1.43	1.80	0.94	5.00		14.66	9.95	15.29	9.97	60% Clay
						99.04						14.92	0.65	14.93	1.00	40% Silt
RS579	NA				1.85	2.77	-0.03	-0.03	-0.10	0.15			0.00	0.65	39.12	By Mass
TX1386	NA					0.82	1.31	2.08	0.87	5.00		10.36	10.01	10.95	10.04	40% Clay
						96.28						10.16	0.77	10.57	1.00	60% Silt
RS580	NA				1.94	2.73	0.00	0.07	-1.37	0.15			0.00	0.78	51.92	By Mass
TX1388	NA					0.75	1.12	2.04	0.91	5.00		4.31	10.10	4.54	10.24	10% Clay
						91.73						4.10	0.48	4.20	1.01	90% Silt
RS583	NA				1.92	2.67	-0.02	-0.01	-1.14	0.15			0.00	0.49	38.00	By Mass

ω_n	Water content prior to testing.	ε_{vol}	Volumetric strain
I_p	Plasticity Index	σ'_p	Maximum effective stress from consolidometer
γ_t	Total mass density	ε_a/hr	Consolidation strain rate
e_i	Initial void ratio	CR	Compression ratio
S_i	Initial saturation	RR	Recompression ratio
G_s	Specific gravity of solids	C_α	Coefficient of secondary compression
σ'_i	Initial specimen setup effective stress no drainage	σ'_{vm}	Maximum effective during consolidation
ε_a	Axial strain	K_c	Lateral stress ratio
u_b	Back pressure saturation pressure for B value	t_s	Duration of time at indicated stress
B	Skempton's B value		

Spec. Location		Index Tests			Specimen Data		Conditions			Consolidation Results						Remarks
										General		@ Max Stress		@ Preshear		
Test #	Depth	T_v	ω_n	ω_p	ω_n	e_i	σ'_i	u_b	B	σ'_p	CR	ε_a	σ'_{vm}	ε_a	σ'_{vc}	
Boring		SD	SD	ω_l	I_p	S_i						ε_{vol}	K_c	ε_{vol}	OCR	
Sample	Markers	# obs	# obs	%2μ	γ_t	G_s	ε_a	ε_a	ε_{vol}	ε_a/hr	RR	C_α	t_s	K_c	t_s	
TX1390	NA					0.83	1.08	1.93	0.97	5.00		10.32	10.11	10.66	10.14	30% Clay
						99.62						10.33	0.50	10.51	1.00	70% Silt
RS581	NA				1.98	2.71	-0.05	-0.04	-0.27	0.15			0.00	0.50	53.49	By Mass
TX1401	NA					1.12	0.99	2.07	0.89			13.62	10.03	15.02	10.13	65% Clay
						100.40						13.52	0.65	15.92	1.00	35% Silt
RS594	NA				1.85	2.78	0.00	0.01	-1.53	0.15			0.00	0.64	45.69	By Mass
TX1403	NA					0.48	0.50					3.92	10.41	3.95	10.41	0% Clay
						100.00						0.36	0.50	0.37	1.00	100% Sand
UC	NA				1.79	2.65	0.07			0.30			0.00	0.44	16.40	By Mass
TX1407	NA					1.02	1.00	1.87	0.94			12.33	10.13	12.69	10.13	60% Clay
						101.61						12.89	0.65	13.10	1.00	40% Silt
RS599	NA				1.89	2.77	-0.04	-0.02	-0.67	0.15			0.00	0.65	28.20	By Mass
TX1410	NA					0.75	0.75	2.04	0.96			7.42	10.08	8.60	10.31	20% Clay
						102.44						7.88	0.48	8.51	1.02	80% Silt
RS597	NA				1.98	2.69	-0.06	-0.21	-0.21	0.15			0.00	0.42	68.70	By Mass
TX1411	NA					0.86	0.90	2.42	0.96			11.76	10.17	12.33	10.09	40% Clay
						96.11						11.65	0.57	11.97	0.99	60% Silt
RS598	NA				1.92	2.73	-0.02	-0.01	-0.55	0.15			0.00	0.57	19.50	By Mass
TX1413	NA					0.72	1.89	3.02	0.90			3.03	9.85	3.39	9.85	10% Clay
						99.17						3.43	0.49	3.81	1.00	90% Silt
	NA				1.97	2.67	-0.01	-0.05	-0.08	0.15			0.00	0.47	50.00	By Mass
TX1415	NA					0.88	0.75	2.16	0.94			12.42	10.11	13.00	10.11	40% Clay
						99.47						12.20	0.68	13.87	1.00	60% Silt
RS606	NA				1.92	2.73	-0.02	0.00	-1.35	0.15			0.00	0.68	25.00	By Mass
TX1420	NA					0.81	1.00	1.88	0.92			10.62	10.14	10.98	10.16	30% Clay
						97.88						10.39	0.55	10.65	1.00	70% Silt
RS614	NA				1.94	2.71	0.01	0.02	-0.20	0.15			0.00	0.55	25.00	By Mass
TX1431	NA					0.60	10.49	4.00	0.71			3.05	102.00	3.34	102.21	10% Clay
						98.75						3.00	0.48	2.69	1.00	90% Silt
RS627	NA				2.04	2.67	0.03	-3.56	-3.57	0.15			0.00	0.48	30.50	By Mass
TX1433	NA					0.61	13.21	3.73				4.49	99.65	6.24	98.78	60% Clay
						98.89						3.83	0.83	5.42	0.99	40% Silt
RS625	NA				2.09	2.77	0.45	0.37	-7.71	0.15			0.00	0.83	46.60	By Mass
TX1435	NA					0.52	9.00	4.10	0.57			6.09	99.11	6.51	99.38	30% Clay
						96.77						6.14	0.61	6.24	1.00	70% Silt
RS619	NA				2.11	2.71	0.63	-2.70	-2.70	0.15			0.00	0.61	29.00	By Mass
TX1436	NA					0.58	9.80	4.00	0.50			6.75	98.94	7.25	99.24	20% Clay
						97.21						6.29	0.52	6.61	1.00	80% Silt
RS632	NA				2.06	2.69	0.02	0.51	-4.50	0.15			0.00	0.52	26.00	By Mass
TX1437	NA					0.54	8.10	3.89	0.55			7.69	99.16	8.51	99.16	40% Clay
						96.31						7.19	0.69	8.31	1.00	60% Silt
RS633	NA				2.11	2.73	0.22	0.34	-2.43	0.15			0.00	0.69	27.00	By Mass
TX1438	NA					0.89	5.10	6.04	N/A			4.01	98.45	4.40	98.80	0% Clay
						100.00						-2.74	0.50	-5.75	1.00	100% Silt
NA	NA				1.87	2.65	0.02	0.02	####	0.15			0.00	0.50	22.00	By Mass
TX1439	NA					0.96	5.00	3.85	N/A			7.67	99.00	8.04	99.54	0% Clay
						100.00						7.74	0.50	8.05	1.01	100% Silt
NA	NA				1.84	2.65	3.26	3.26	####	0.15			0.00	0.49	12.00	By Mass
TX1442	NA					0.62	10.41	3.90	0.47			9.80	99.30	10.97	99.63	50% Clay
						97.61						9.35	0.76	11.40	1.00	50% Silt
RS640	NA				2.08	2.75	0.01	-0.04	-0.88	0.15			0.00	0.76	36.00	By Mass
TX1443	NA					0.69	7.40	4.85	0.89			6.17	100.76	6.64	100.77	10% Clay
						97.31						7.70	0.50	8.43	1.00	90% Silt
RS638	NA				1.98	2.67	0.12	0.25	0.56	0.15			0.00	0.49	25.30	By Mass
TX1444	NA					0.62		4.00	0.85			10.16	99.37	10.63	99.30	20% Clay
						98.32						7.58	0.50	8.12	1.00	80% Silt
RS645	NA				2.04	2.69		0.24	-0.32	0.15			0.00	0.49	20.25	By Mass
TX1446	NA					0.74	9.74	11.45	0.86			13.24	99.39	14.77	99.35	60% Clay
						98.08						12.89	0.79	17.15	1.00	40% Silt
RS646	NA				2.01	2.77	0.57	0.47	-2.91	0.15			0.00	0.77	36.00	By Mass
TX1447	NA					0.57	6.92	12.27	0.63			10.06	99.04	10.66	99.81	30% Clay
						99.17						9.83	0.56	10.42	1.01	70% Silt
RS652	NA				2.09	2.71	0.34	0.59	-0.68	0.15			0.00	0.56	44.00	By Mass

ω_n	Water content prior to testing.	ε_{vol}	Volumetric strain
I_p	Plasticity Index	σ'_p	Maximum effective stress from consolidometer
γ_t	Total mass density	ε_a/hr	Consolidation strain rate
e_i	Initial void ratio	CR	Compression ratio
S_i	Initial saturation	RR	Recompression ratio
G_s	Specific gravity of solids	C_α	Coefficient of secondary compression
σ'_i	Initial specimen setup effective stress no drainage	σ'_{vm}	Maximum effective during consolidation
ε_a	Axial strain	K_c	Lateral stress ratio
u_b	Back pressure saturation pressure for B value	t_s	Duration of time at indicated stress
B	Skempton's B value		

Spec. Location		Index Tests			Specimen Data		Conditions			Consolidation Results						Remarks
										General		@ Max Stress		@ Preshear		
Test #	Depth	T_v	ω_n	ω_p	ω_n	e_i	σ'_i	u_b	B	σ'_p	CR	ε_a	σ'_{vm}	ε_a	σ'_{vc}	
Boring		SD	SD	ω_l	I_p	S_i				ε_{vol}		ε_{vol}	K_c	ε_{vol}	OCR	
Sample	Markers	# obs	# obs	%2μ	γ_t	G_s	ε_a	ε_a	ε_{vol}	ε_a/hr	RR	C_α	t_s	K_c	t_s	
TX1452	NA					0.54	13.69	4.00	0.44			3.83	98.24	6.02	99.10	65% Clay
						103.87						3.36	0.86	6.48	1.01	35% Silt
RS649	NA				2.09	2.65	0.28	0.12	-3.44	0.15			0.00	0.85	45.00	By Mass
TX1456	NA					0.58		4.34	0.89			10.20	96.53	11.09	96.93	40% Clay
						99.15						9.96	0.65	11.08	1.00	60% Silt
RS655	NA				2.10	2.73		0.46	-1.30	0.15			0.00	0.64	49.78	By Mass
TX1458	NA					0.61	8.72	3.93				9.59	98.16	10.85	98.61	50% Clay
						100.90						9.30	0.74	11.29	1.00	50% Silt
RS656	NA				2.10	2.75	-0.07	0.01		0.15			0.00	0.73	35.00	By Mass
TX1459	NA					0.74	8.46	6.49	0.98			8.25	99.31	8.81	98.31	10% Clay
						100.68						8.02	0.44	8.44	0.99	90% Silt
RS662	NA				1.97	2.67	0.02	0.35	-0.21	0.15			0.00	0.44	38.00	By Mass
TX1463	NA					0.59	9.21	5.96	0.95			7.25	99.78	7.88	100.20	20% Clay
						97.33						7.54	0.50	8.19	1.00	80% Silt
RS672	NA				2.06	2.69	0.19	0.18	-0.15	0.15			0.00	0.49	41.25	By Mass
TX1464	NA					0.56	10.31	4.25	0.86			8.61	99.27	9.18	99.59	30% Clay
						96.42						8.44	0.53	9.14	1.00	70% Silt
RS673	NA				2.08	2.71	0.28	0.25	-0.83	0.15			0.00	0.53	31.25	By Mass
TX1468	NA					1.19		4.00				13.32	99.54	13.63	99.91	0% Clay
						100.00						7.92	0.50	8.13	1.00	100% Silt
NA	NA				1.75	2.65		0.89	-4.25	0.15			0.00	0.50	4.50	By Mass
TX1473	NA					0.68	11.65	4.00	0.58			8.38	99.86	9.84	99.86	65% Clay
						97.86						8.34	0.80	10.42	1.00	35% Silt
RS678	NA				2.06	2.78	0.11	0.00	-1.25	0.15			0.00	0.80	32.00	By Mass
TX1475	NA					0.63	9.23	4.14	0.55			11.54	99.24	12.75	99.33	50% Clay
						99.53						11.39	0.74	13.54	1.00	50% Silt
RS680	NA				2.07	2.75	0.35	0.37	-1.00	0.15			0.00	0.73	44.50	By Mass
TX1478	NA					0.57		4.14	0.85			10.27	100.31	10.93	100.63	40% Clay
						98.67						10.27	0.62	11.26	1.00	60% Silt
RS681	NA				2.10	2.73		0.30	-0.16	0.15			0.00	0.62	22.00	By Mass
TX1480	NA					0.64		4.07	0.71			7.34	100.28	8.63	100.09	60% Clay
						98.78						7.07	0.83	9.09	1.00	40% Silt
RS684	NA				2.08	2.77		0.16	-1.19	0.11			0.00	0.83	22.33	By Mass
TX1481	NA					0.66	9.14	4.15	0.76			10.36	100.20	11.32	100.18	60% Clay
						99.22						10.01	0.80	11.51	1.00	40% Silt
RS683	NA				2.06	2.77	0.20	0.31	-0.52	0.11			0.00	0.80	20.00	By Mass
TX1484	NA					0.75	8.89	4.19	0.81			13.61	99.98	14.78	100.10	65% Clay
						98.30						13.16	0.80	15.15	1.00	35% Silt
RS687	NA				2.01	2.78	0.31	0.23	-0.34	0.11			0.00	0.80	33.70	By Mass
TX1486	NA					0.67	12.28	4.22	0.68			9.89	99.63	10.88	99.45	65% Clay
						101.02						9.56	0.80	11.11	1.00	35% Silt
RS688	NA				2.08	2.78	0.27	0.29	-0.64	0.11			0.00	0.79	24.50	By Mass
TX1490	NA					0.93	1.29	2.48	0.85			9.66	10.25	11.11	10.32	50% Clay
						100.48						9.49	0.65	11.06	1.01	50% Silt
RS690	NA				1.92	2.75	-0.05	-0.07	-1.14	0.15			0.00	0.64	47.22	By Mass
TX1491	NA					0.74	0.90	3.01				5.77	10.07	6.49	9.99	30% Clay
						99.84						5.60	0.54	6.21	0.99	70% Silt
RS693	NA				1.99	2.71	0.00	-0.03	-3.58	0.15			0.00	0.51	33.20	By Mass
TX1492	NA					0.78	0.84	2.08	0.88			5.93	10.00	6.40	10.02	20% Clay
						100.89						7.39	0.51	7.81	1.00	80% Silt
RS694	NA				1.96	2.69	0.01	-0.04	-0.56	0.15			0.00	0.51	28.20	By Mass
TX1495	NA					0.55	10.32	3.99	0.79			7.80	101.21	8.22	100.24	30% Clay
						94.93						7.91	0.53	8.46	0.99	70% Silt
RS692	NA				2.09	2.71	0.41	0.56	-0.51	0.15				0.54	38.92	By Mass
TX1499	NA					0.54	13.38	4.11	0.69	0.15		8.02	100.26	8.86	100.70	40% Clay
						97.62						7.82	0.64	9.19	1.00	60% Silt
RS703	NA				2.11	2.73	0.53	0.59	-0.72					0.63	68.75	By Mass
TX1501	NA					0.65	11.32	4.03	0.67	0.11		10.10	99.87	11.11	100.15	60% Clay
						100.13						9.93	0.78	11.31	1.00	40% Silt
RS712	NA				2.08	2.77	0.17	0.13	-0.97					0.77	22.60	By Mass
TX1504	NA					1.16	3.23	1.77	0.83	0.11		14.31	9.33	16.02	9.34	60% Clay
						99.26						14.27	0.70	15.72	1.00	40% Silt
RS713	NA				1.82	2.77	0.15	0.00	-0.17				0.00	0.66	31.60	By Mass

a) Marker location in tube
b) Stresses in kg/cm^2
c) 1 kg/cm^2 = 2048 psf
d) Depth in Feet
e) Time in hours
f) Water content, limits, saturation, strain, and B value in %
g) density in gm/cm^3

ω_n	Water content prior to testing.	ε_{vol}	Volumetric strain
I_p	Plasticity Index	σ'_p	Maximum effective stress from consolidometer
γ_t	Total mass density	ε_a/hr	Consolidation strain rate
e_i	Initial void ratio	CR	Compression ratio
S_i	Initial saturation	RR	Recompression ratio
G_s	Specific gravity of solids	C_α	Coefficient of secondary compression
σ'_i	Initial specimen setup effective stress no drainage	σ'_{vm}	Maximum effective during consolidation
ε_a	Axial strain	K_c	Lateral stress ratio
u_b	Back pressure saturation pressure for B value	t_s	Duration of time at indicated stress
B	Skempton's B value		

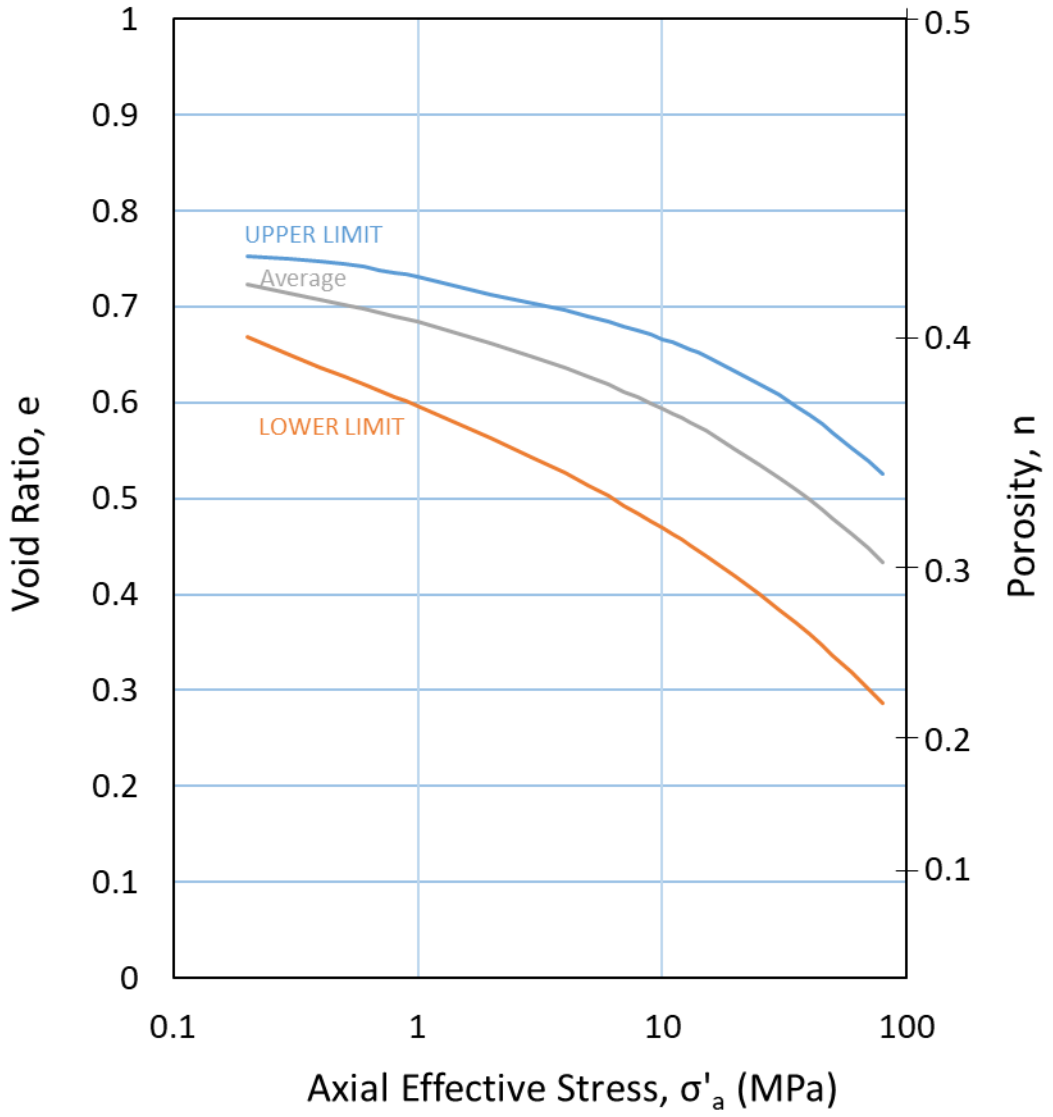


Figure 5-1: Upper limit, lower limit, and average compression curves for 0% clay specimens. Limits and average from high stress CRS tests CRS1571, CRS1584, and CRS1620.

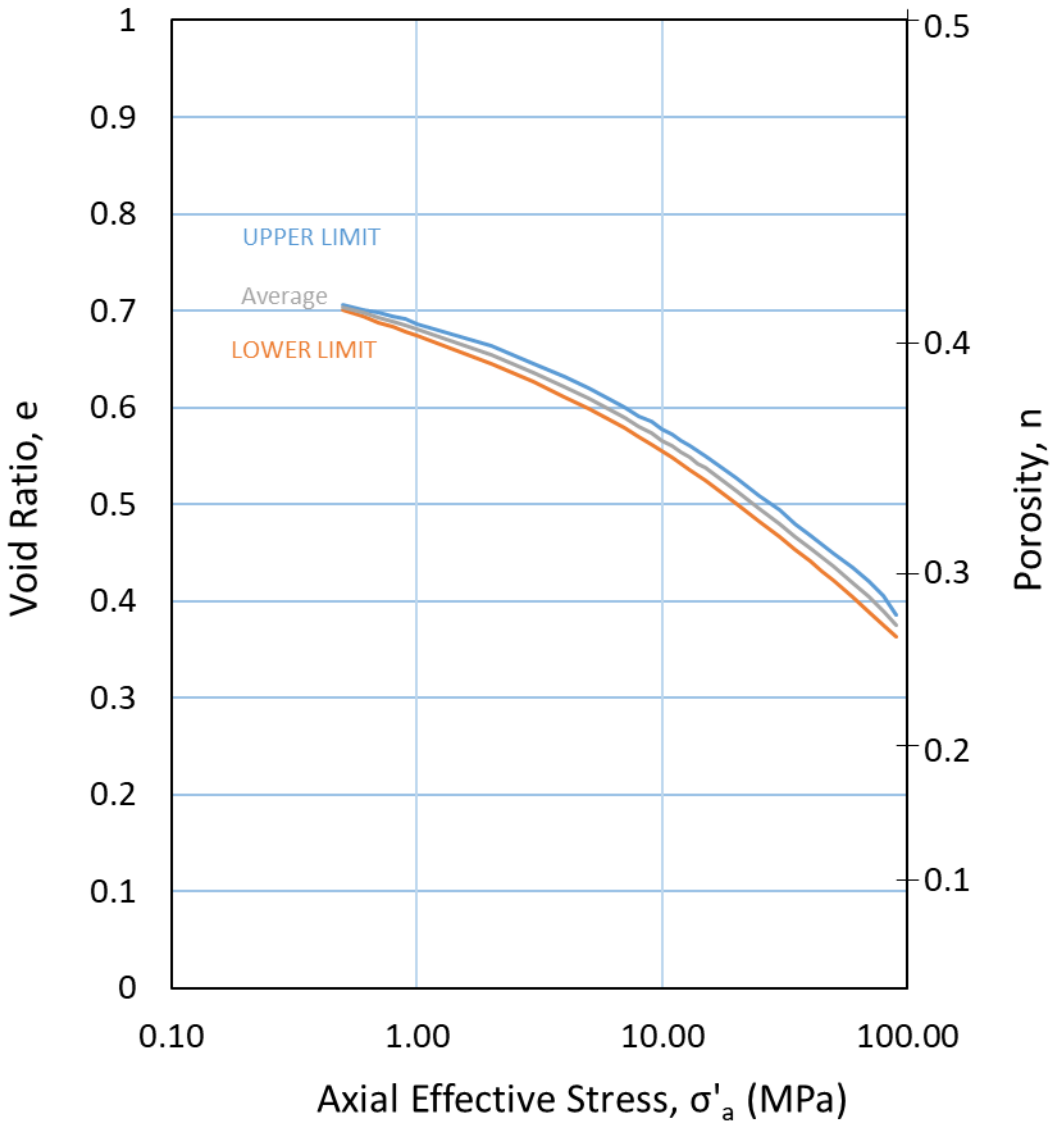


Figure 5-2: Upper limit, lower limit, and average compression curves for 10% clay specimens. Limits and average from high stress CRS tests CRS1591, and CRS1682.

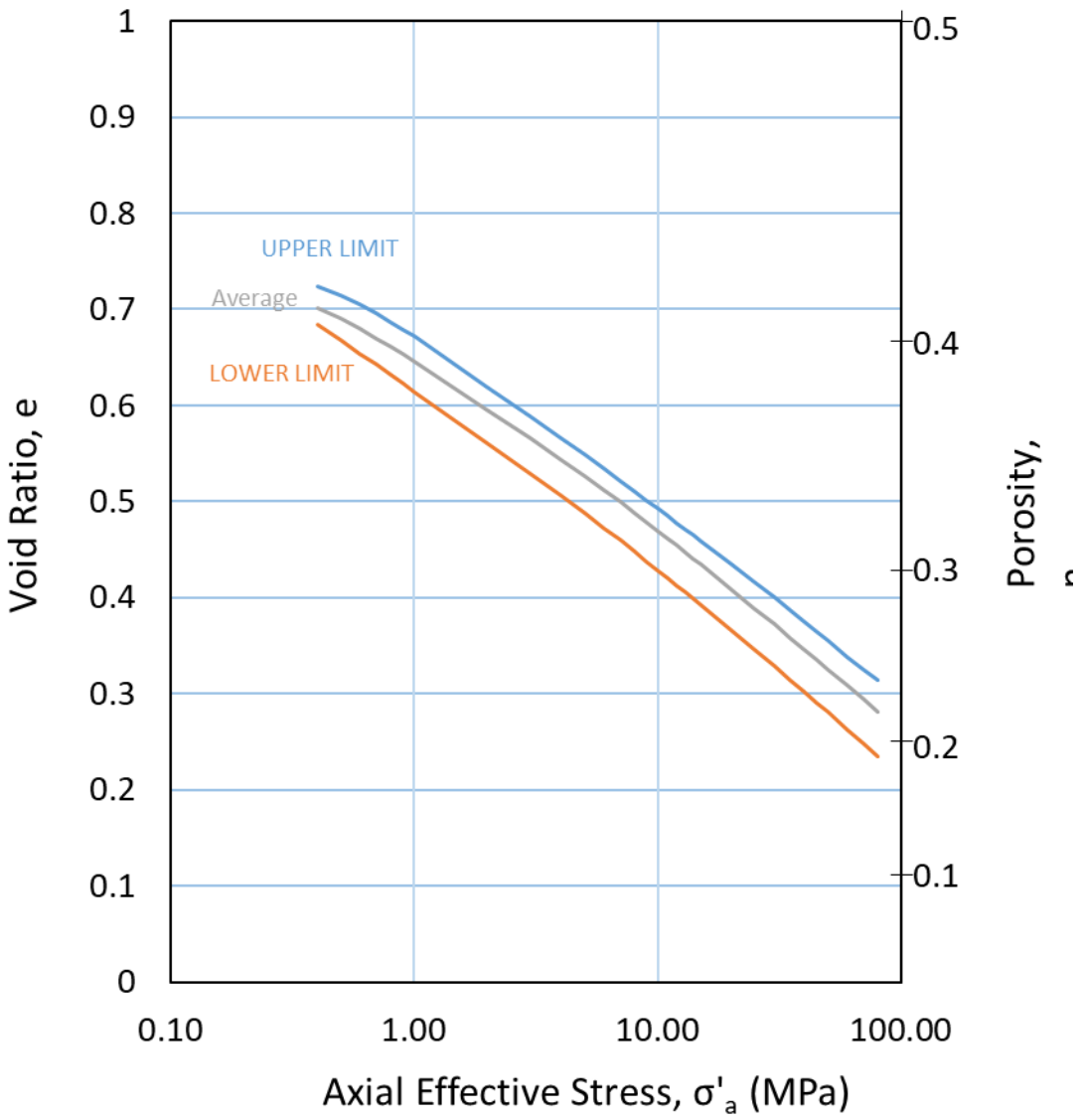


Figure 5-3: Upper limit, lower limit, and average compression curves for 20% clay specimens. Limits and average from high stress CRS tests CRS1608, CRS1619, and CRS1630.

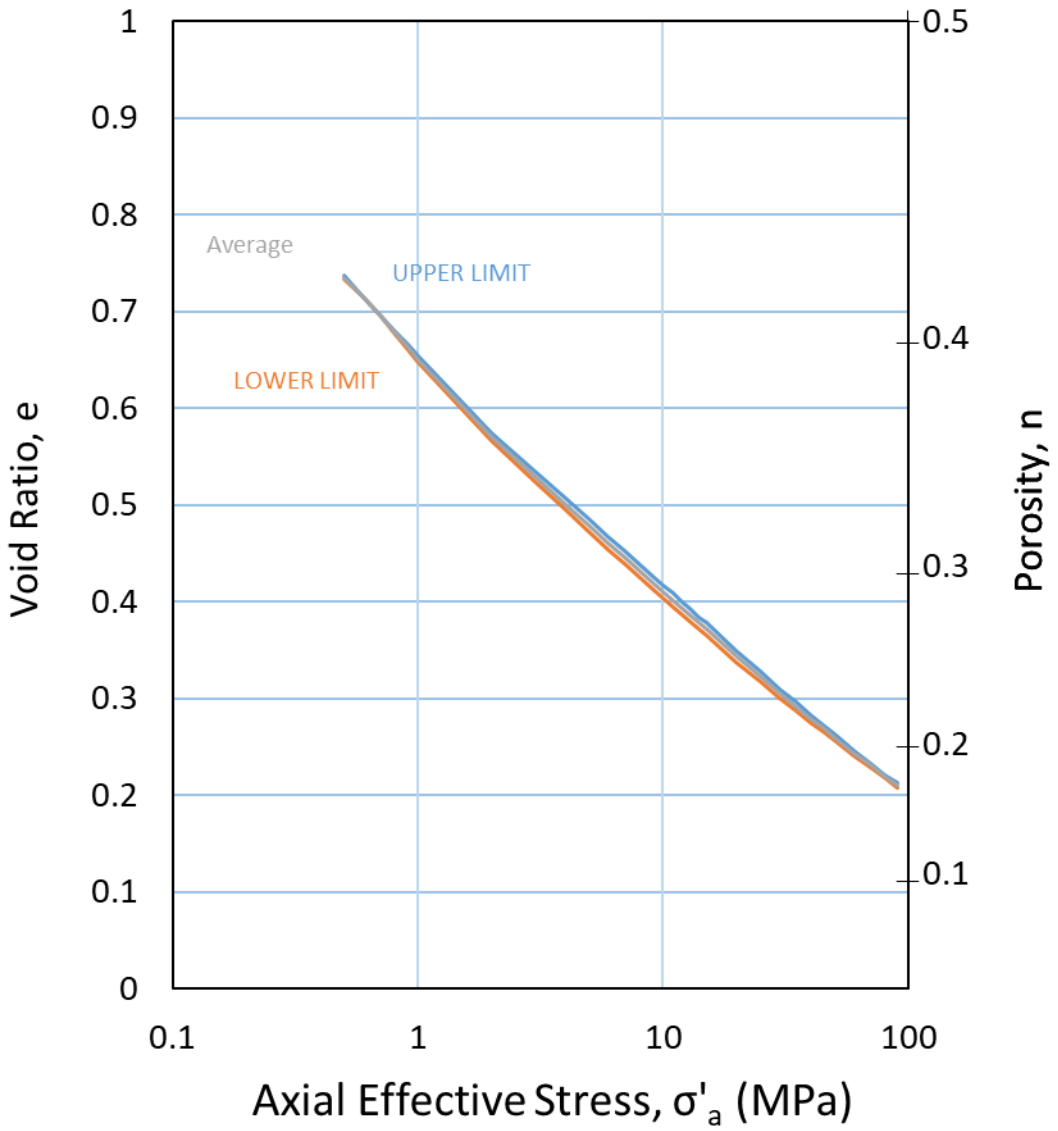


Figure 5-4: Upper limit, lower limit, and average compression curves for 30% clay specimens. Limits and average from high stress CRS tests CRS1616, and CRS1621.

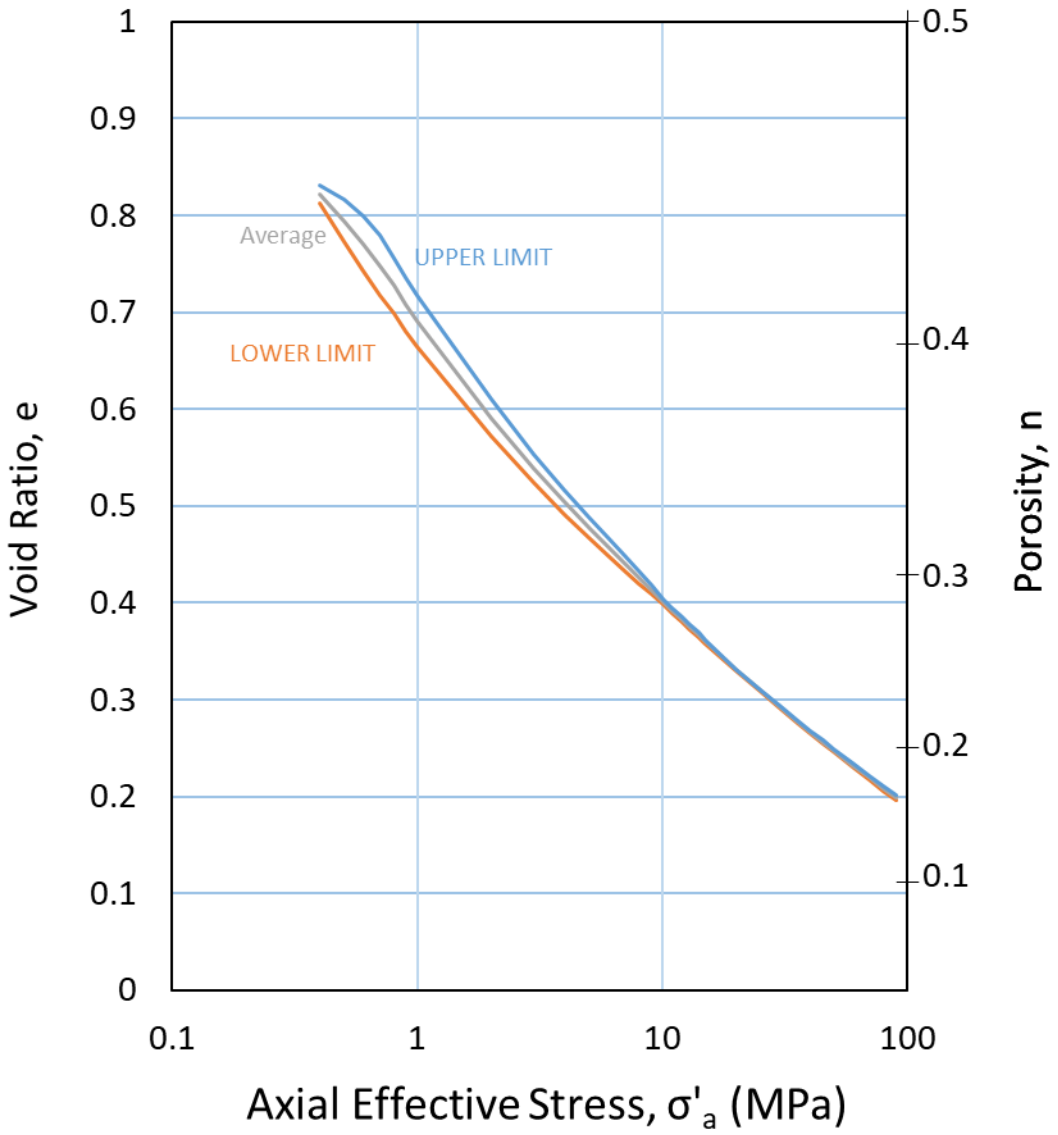


Figure 5-5: Upper limit, lower limit, and average compression curves for 40% clay specimens. Limits and average from high stress CRS tests CRS1585, and CRS1593.

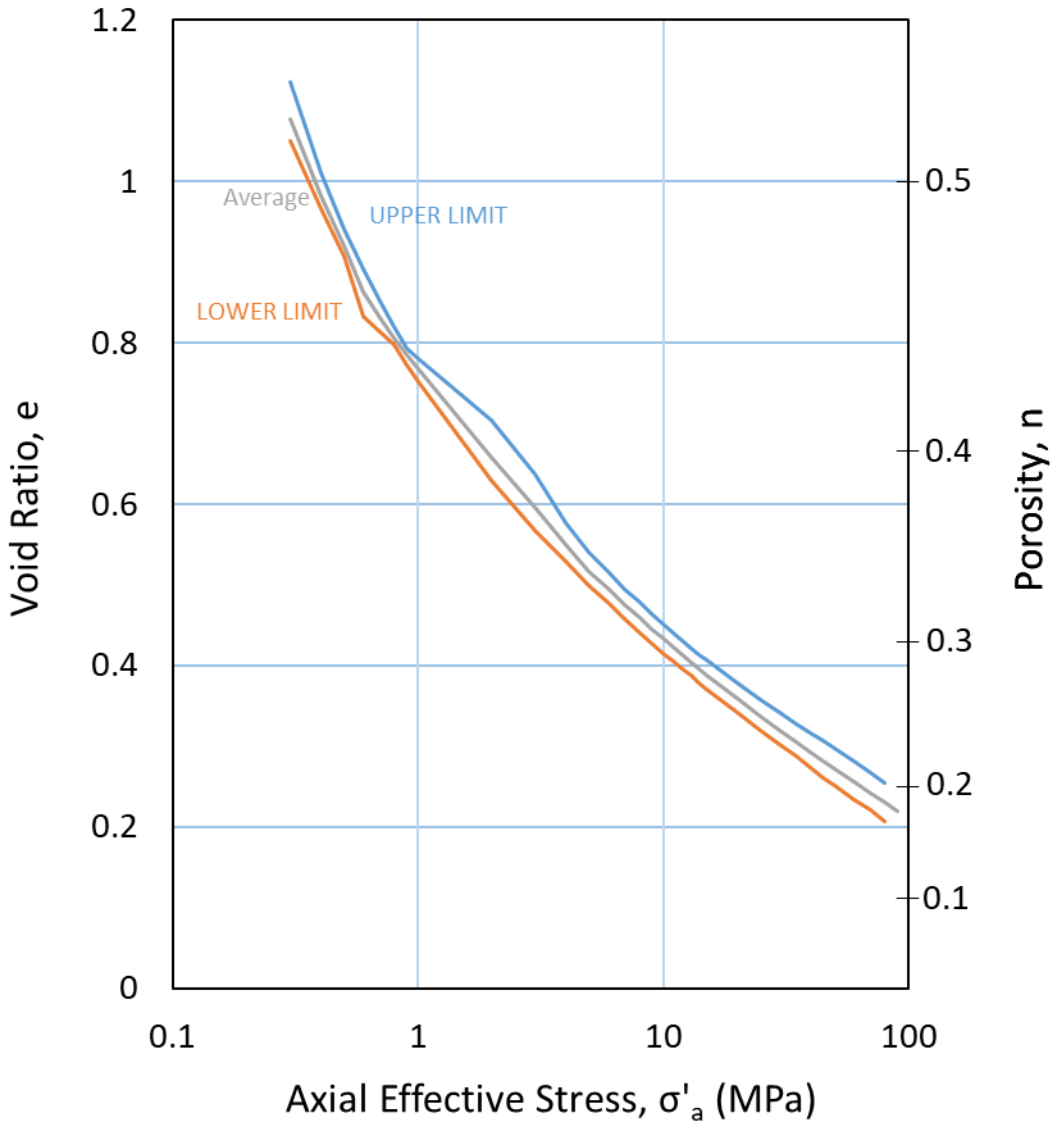


Figure 5-6: Upper limit, lower limit, and average compression curves for 50% clay specimens. Limits and average from high stress CRS tests CRS1585, and CRS1593.

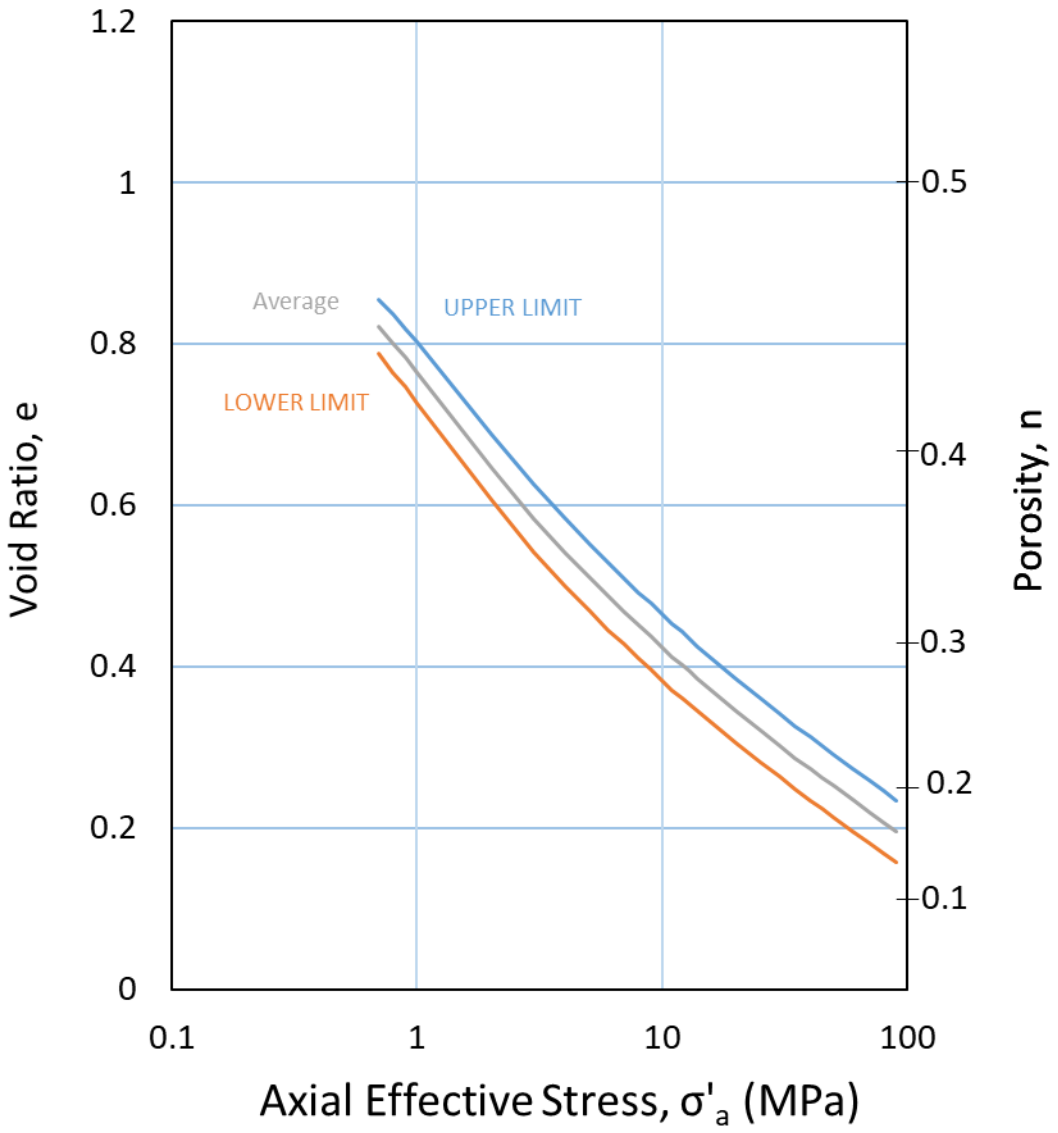


Figure 5-7: Upper limit, lower limit, and average compression curves for 60% clay specimens. Limits and average from high stress CRS tests CRS1572, and CRS1592.

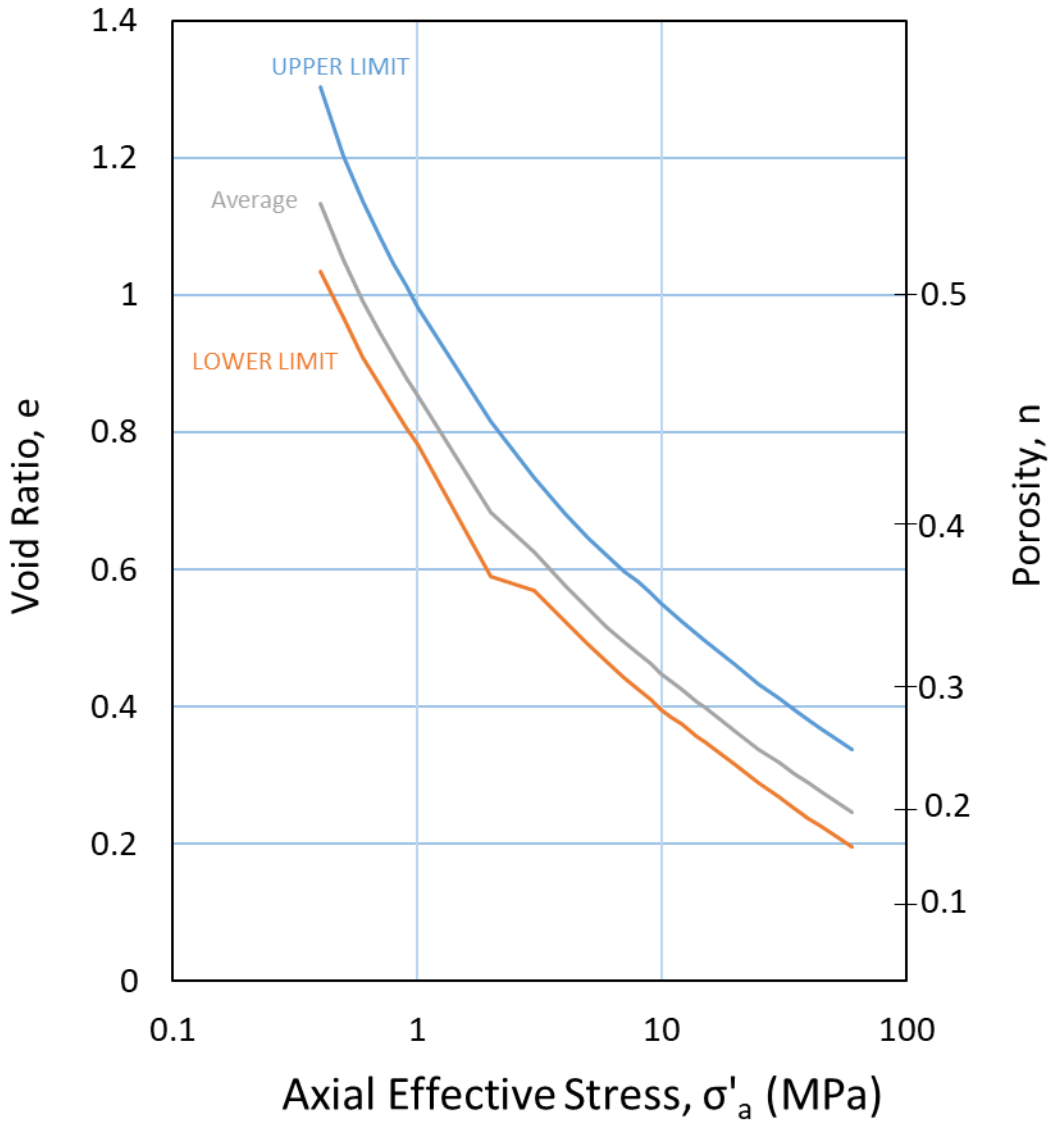


Figure 5-8: Upper limit, lower limit, and average compression curves for RGoM_EI specimens. Limits and average from high stress CRS tests CRS1581, CRS1594, and CRS1618.

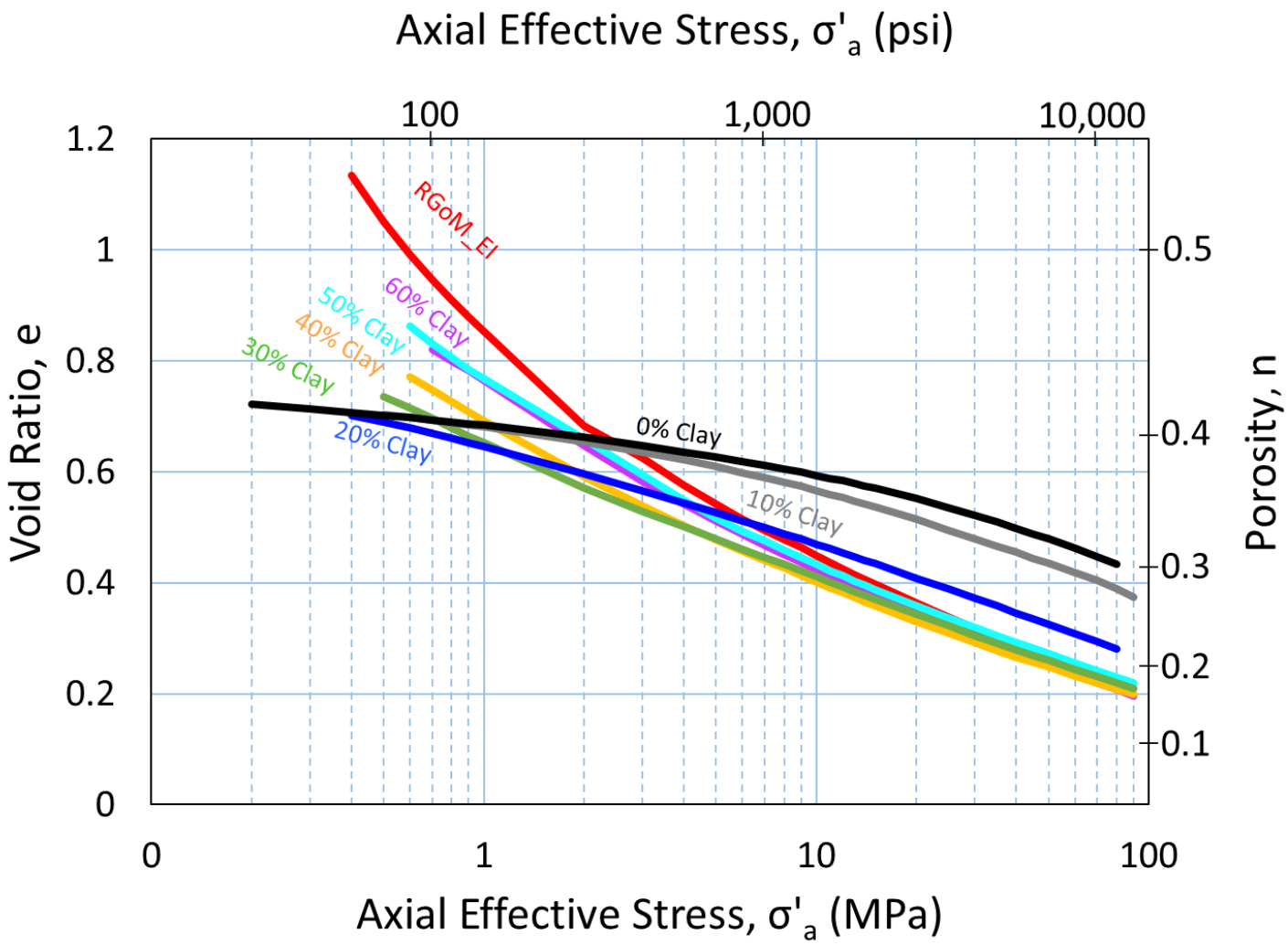


Figure 5-9: Average compression curves from high stress CRS measurements. The bounds for compression behavior of the different silt and clay mixtures are presented in Figure 5.1 through Figure 5.8.

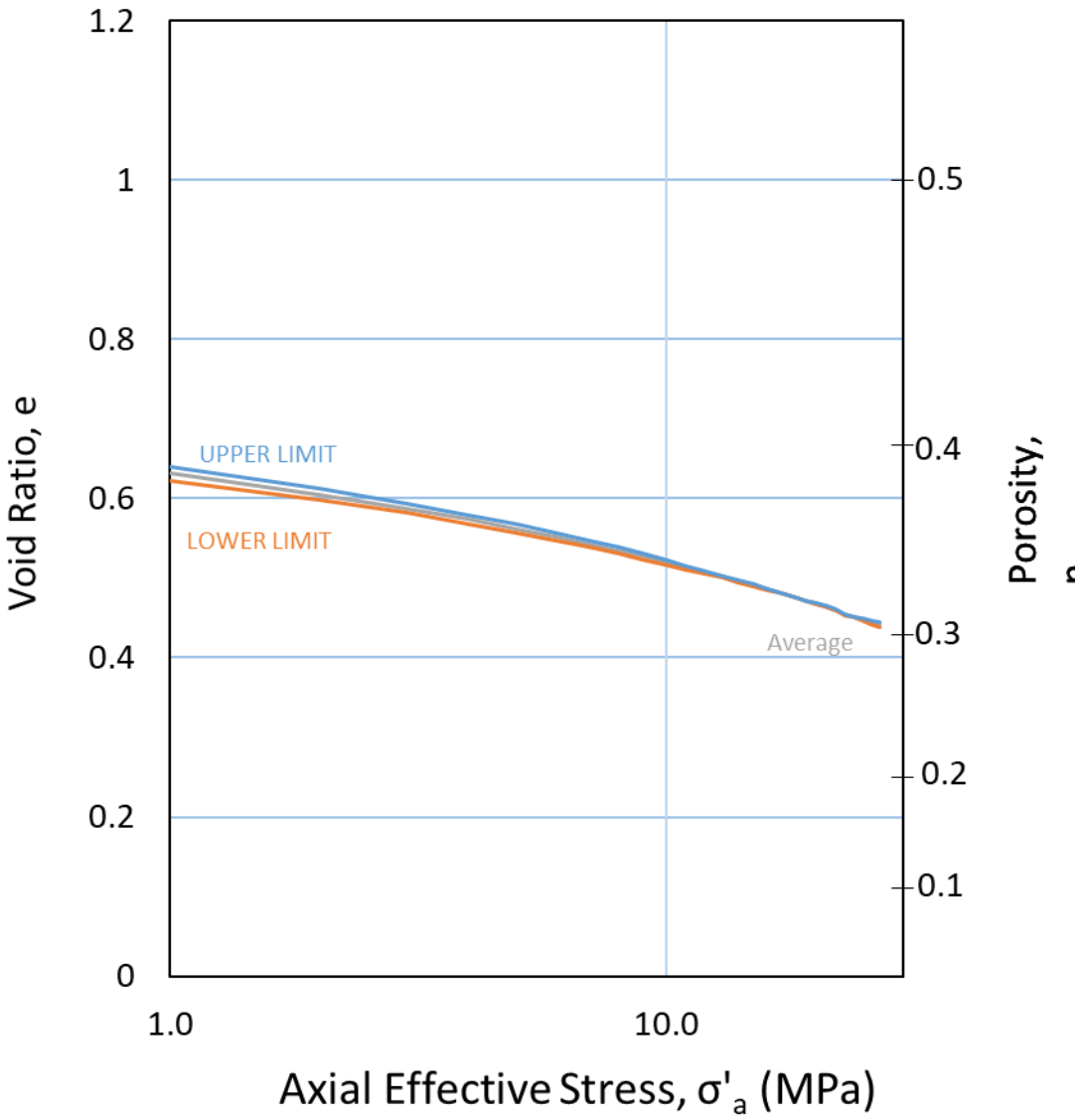


Figure 5-10: Upper limit, lower limit, and average compression curves for 10% clay specimens. Limits and average from Tall CRS tests CRS1652, and CRS1700.

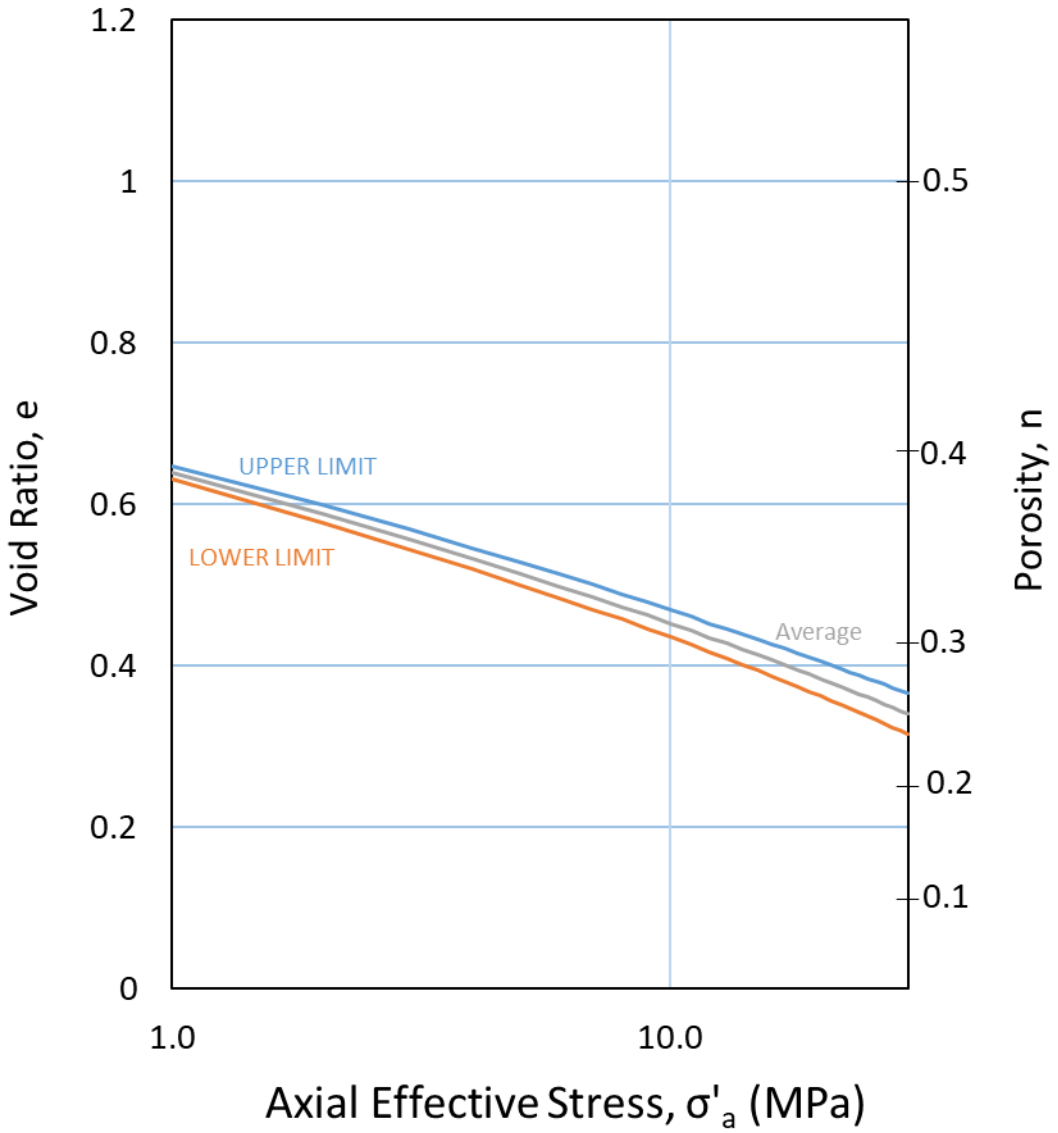


Figure 5-11: Upper limit, lower limit, and average compression curves for 20% clay specimens. Limits and average from Tall CRS tests CRS1663, and CRS1678.

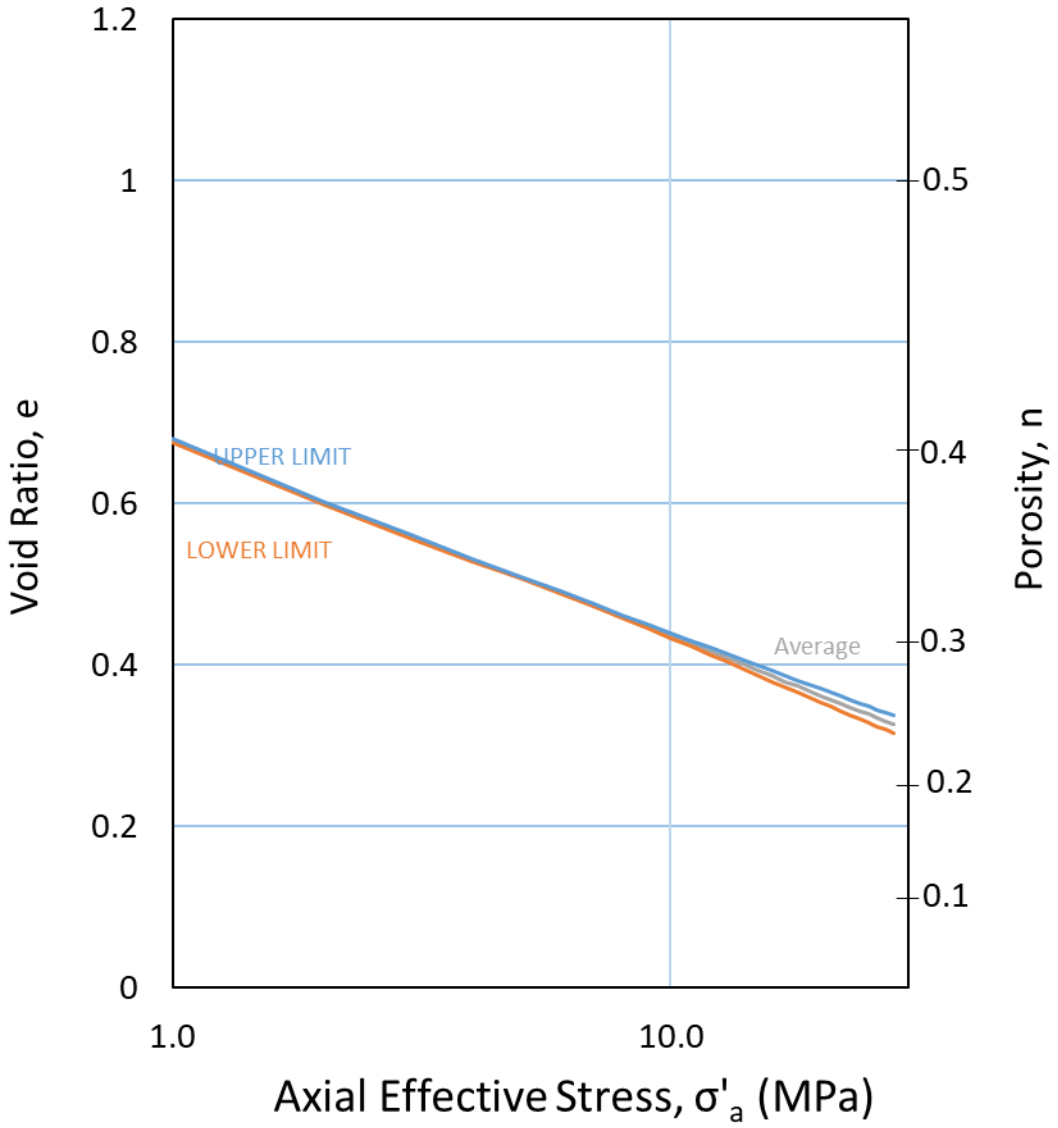


Figure 5-12: Upper limit, lower limit, and average compression curves for 30% clay specimens. Limits and average from Tall CRS tests CRS1632, and CRS1698.

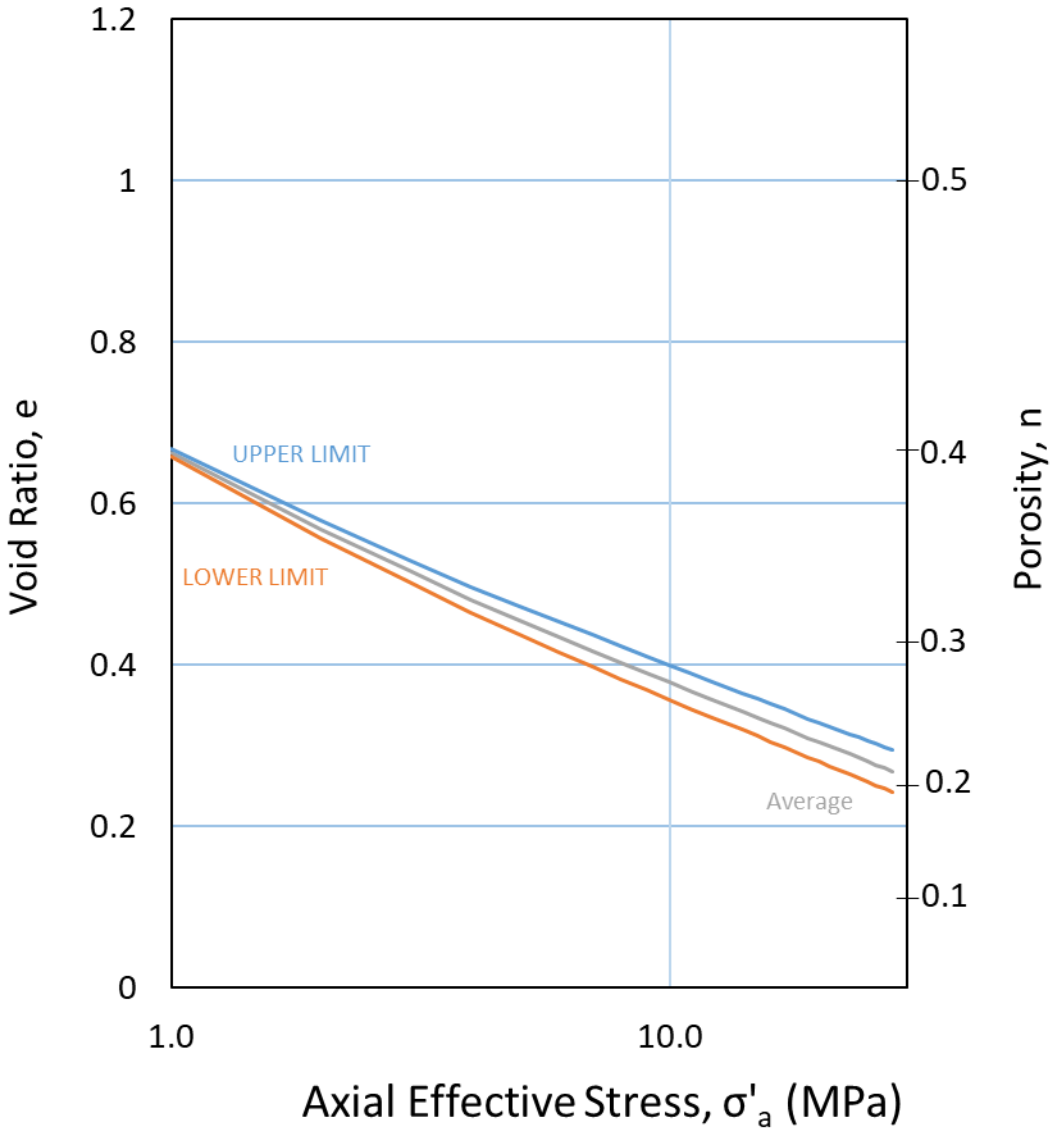


Figure 5-13: Upper limit, lower limit, and average compression curves for 40% clay specimens. Limits and average from Tall CRS tests CRS1638, and CRS1688.

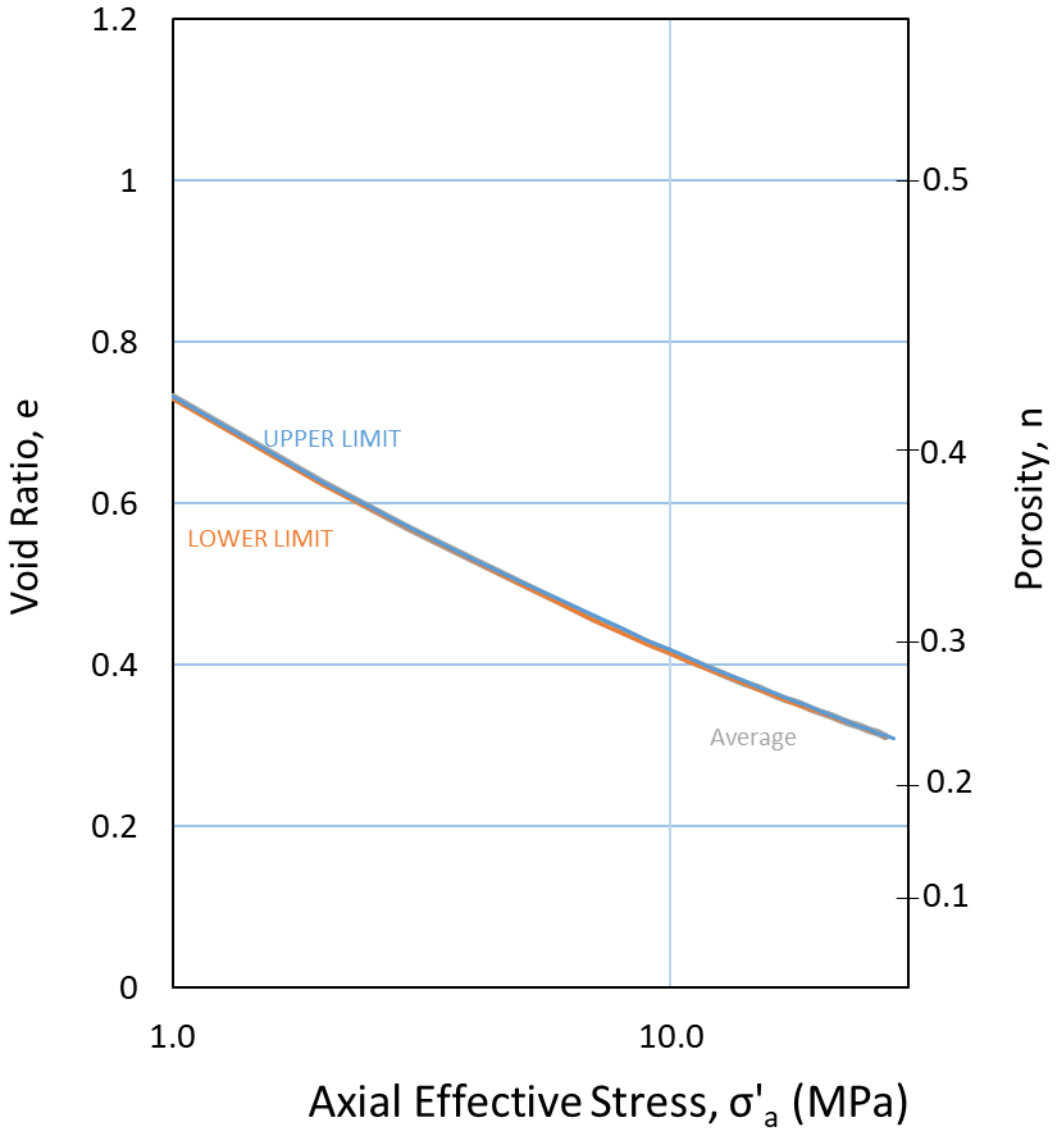


Figure 5-14: Upper limit, lower limit, and average compression curves for 50% clay specimens. Limits and average from Tall CRS tests CRS1633, and CRS1693.

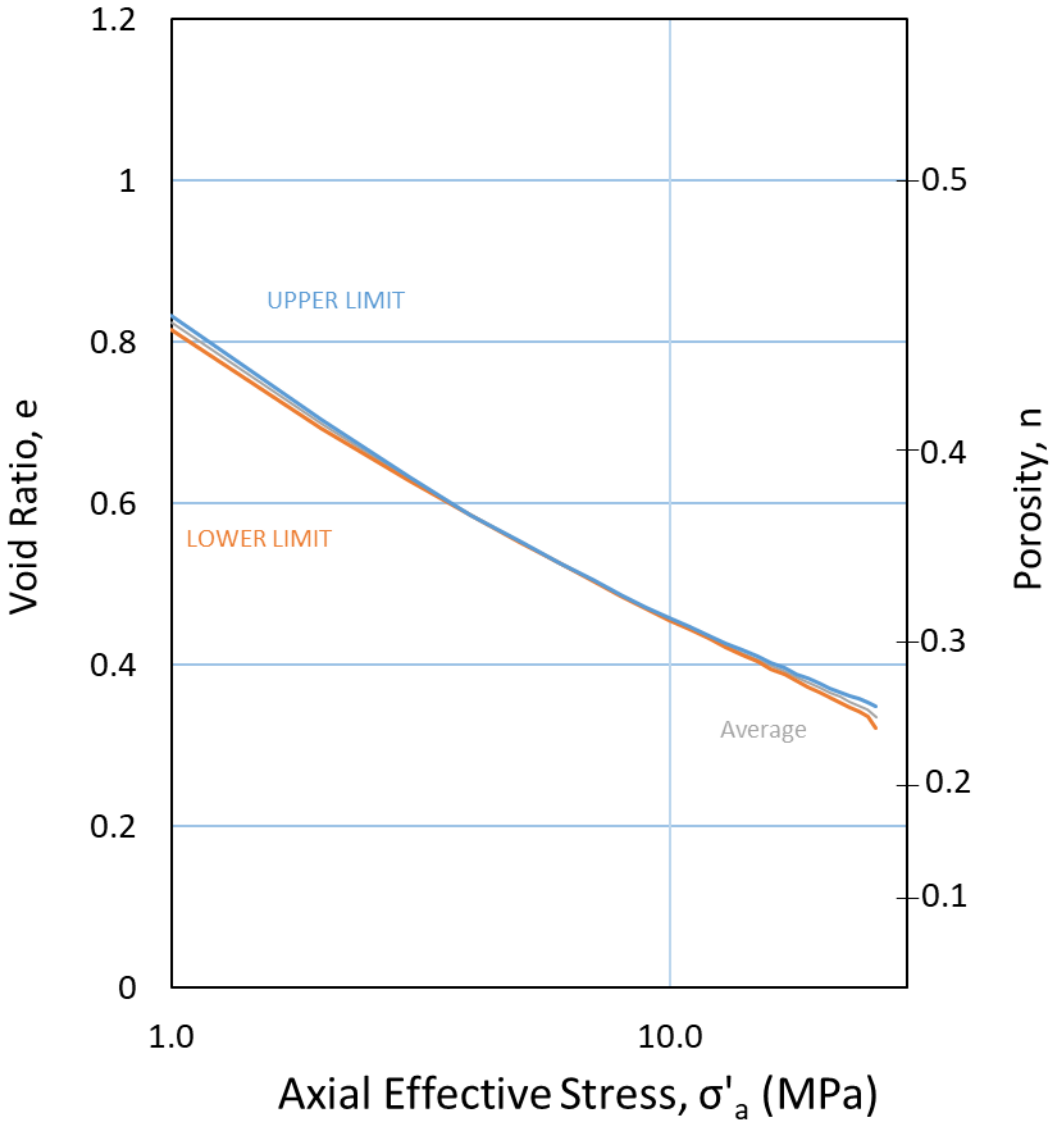


Figure 5-15: Upper limit, lower limit, and average compression curves for 60% clay specimens. Limits and average from Tall CRS tests CRS1646, and CRS1679.

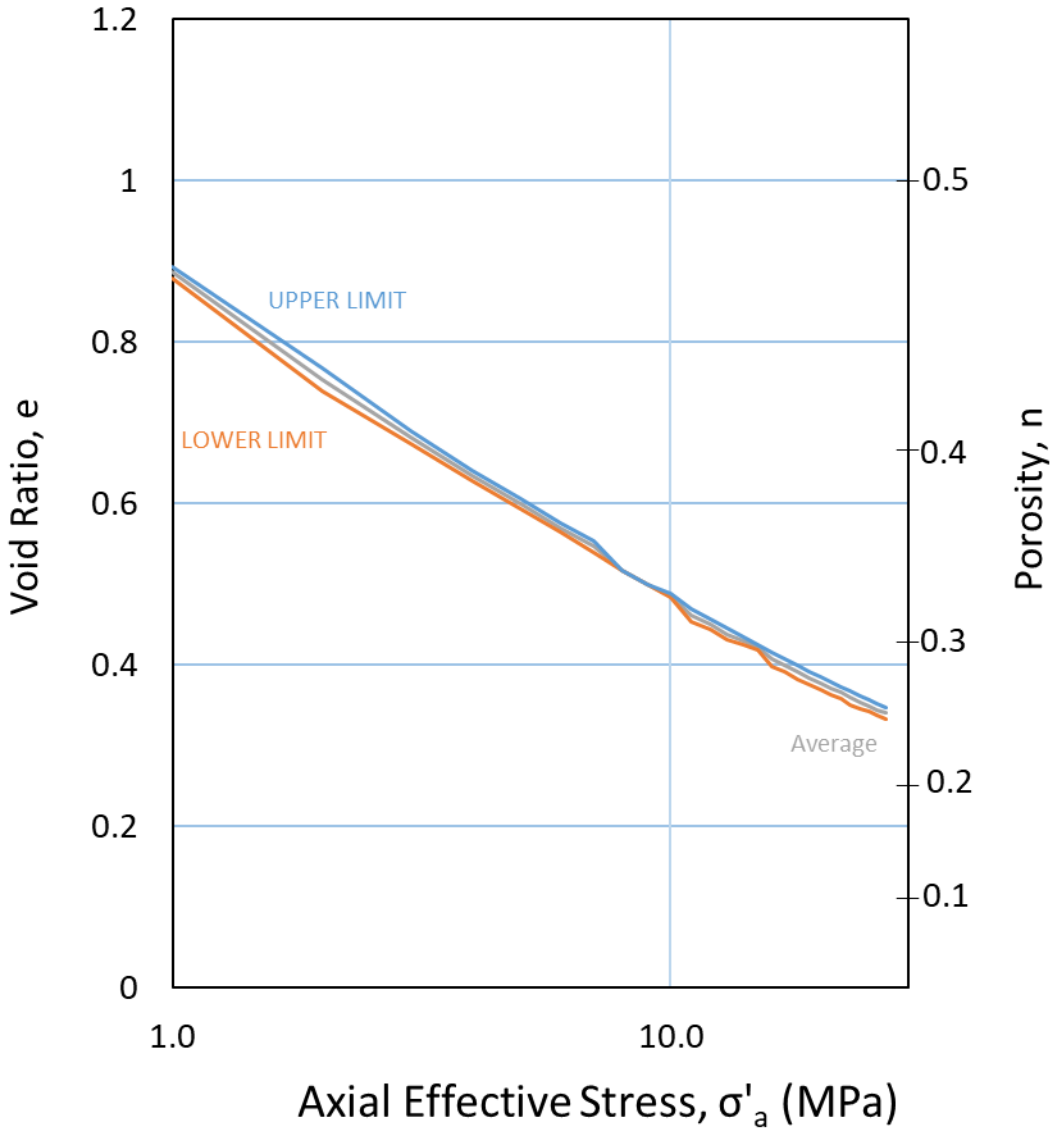


Figure 5-16: Upper limit, lower limit, and average compression curves for RGoM_EI clay specimens. Limits and average from Tall CRS tests CRS1629, and CRS1672.

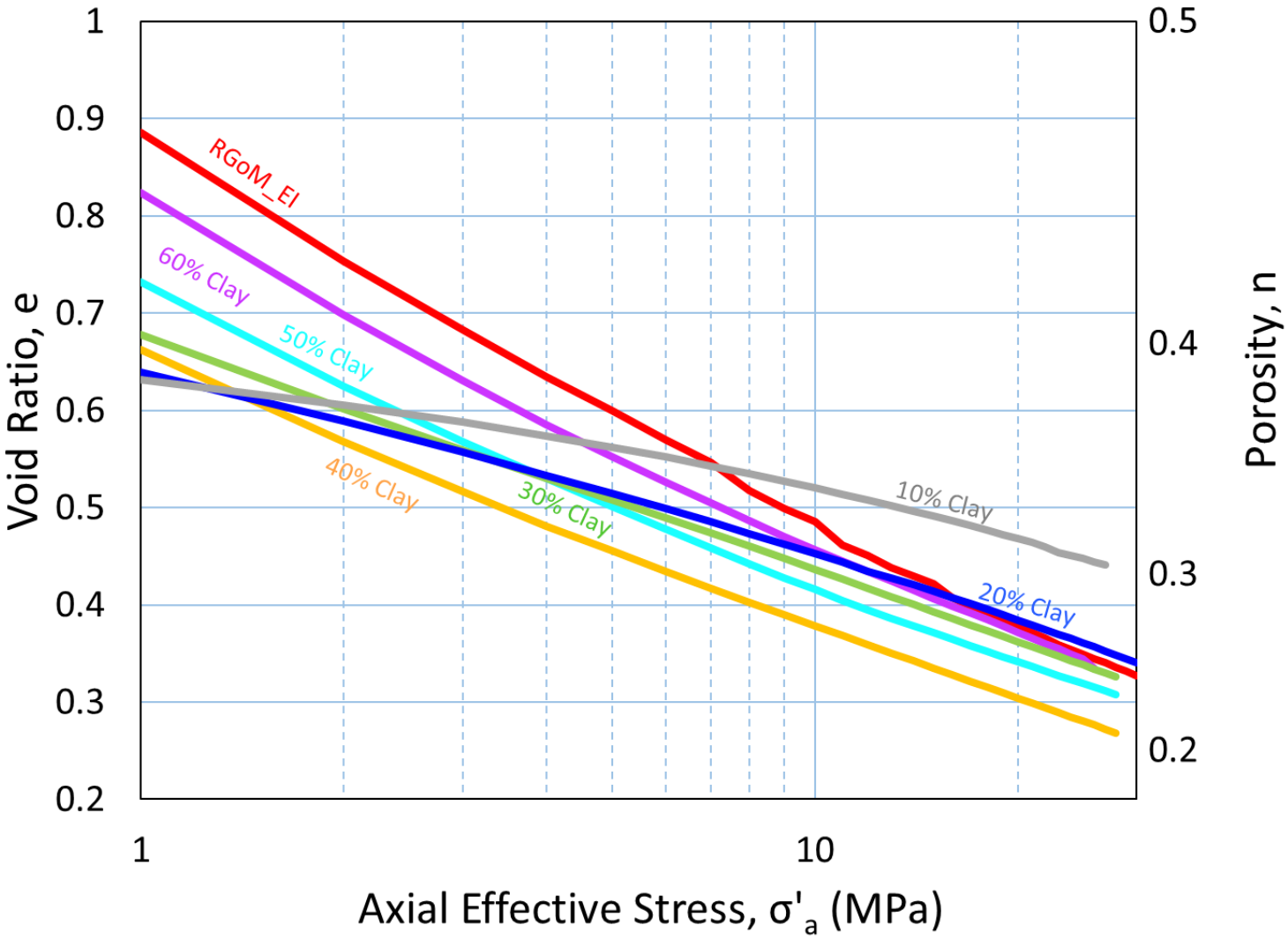


Figure 5-17: Average compression curves from tall CRS measurements. The bounds for compression behavior of the different silt and clay mixtures are presented in Figure 4.10 through Figure 4.16.

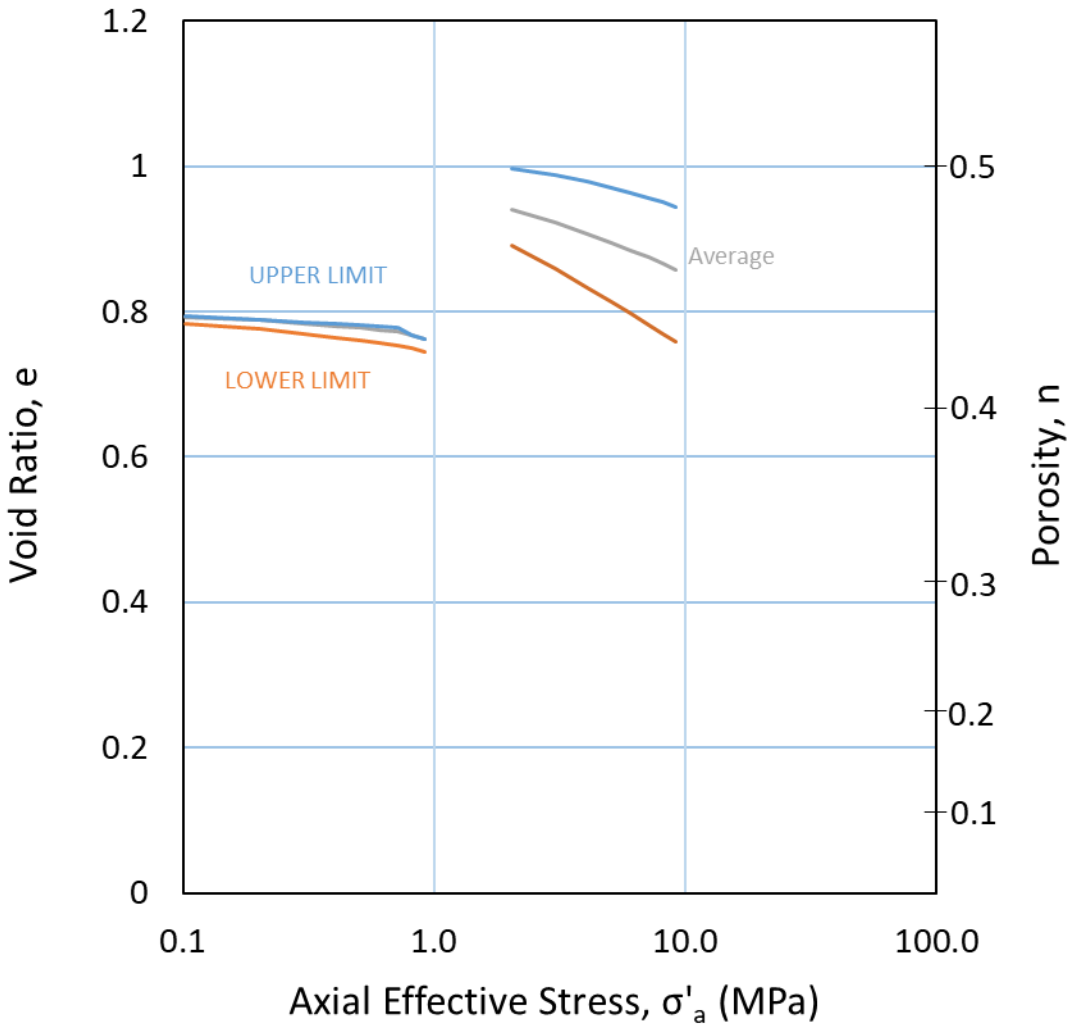


Figure 5-18: Upper limit, lower limit, and average compression curves for 0% clay specimens. Limits and averages from 1 MPa and 10 MPa triaxial test consolidation phases.

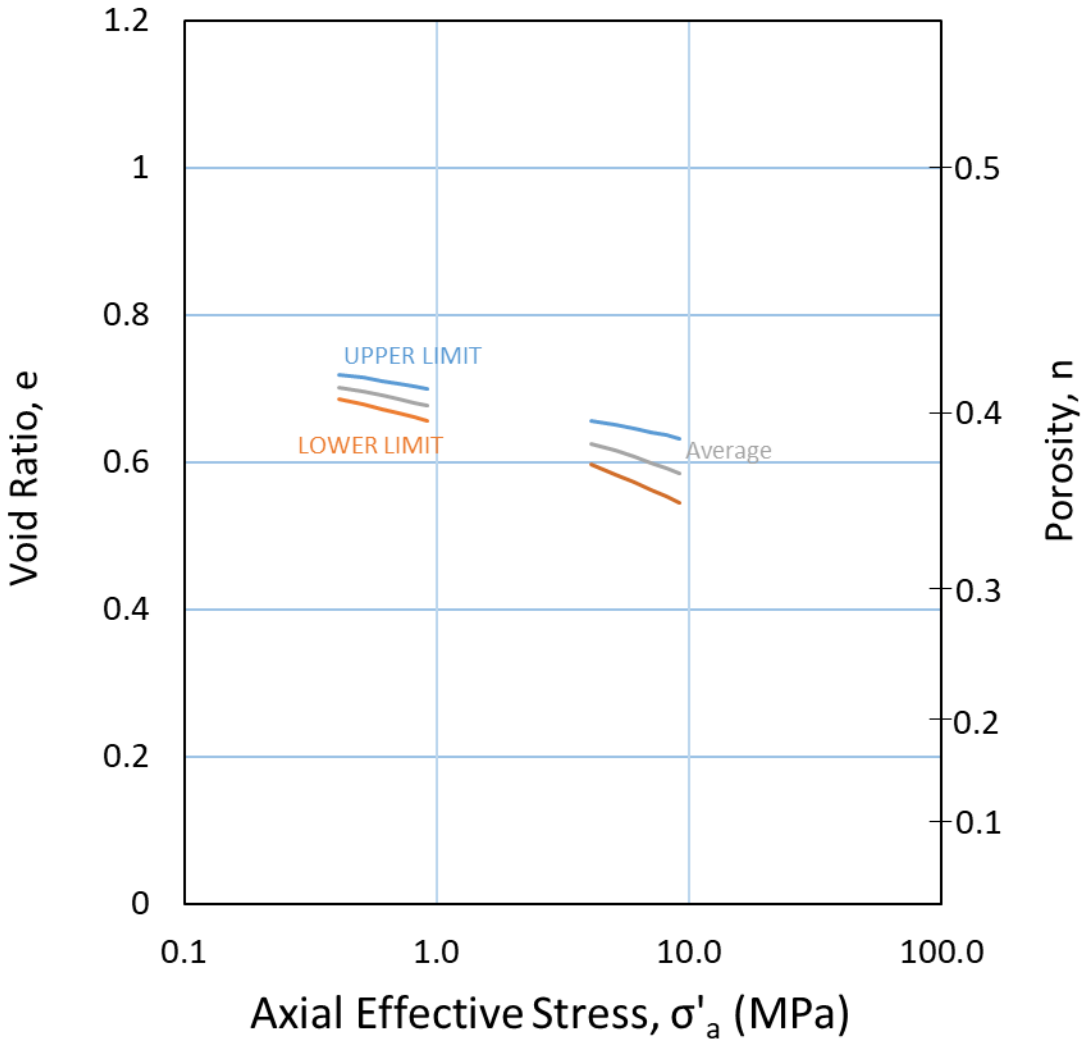


Figure 5-19: Upper limit, lower limit, and average compression curves for 10% clay specimens. Limits and averages from 1 MPa and 10 MPa triaxial test consolidation phases.

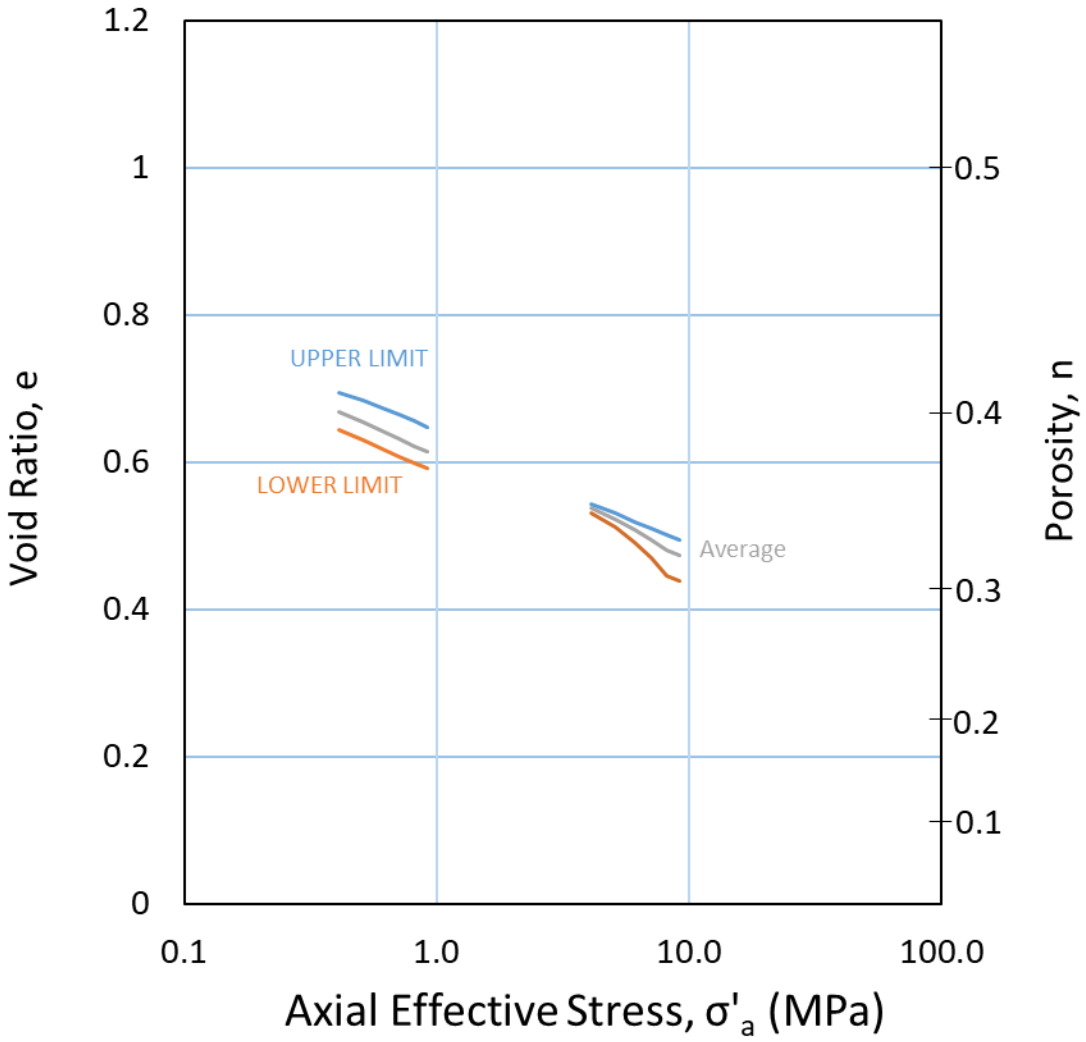


Figure 5-20: Upper limit, lower limit, and average compression curves for 20% clay specimens. Limits and averages from 1 MPa and 10 MPa triaxial test consolidation phases.

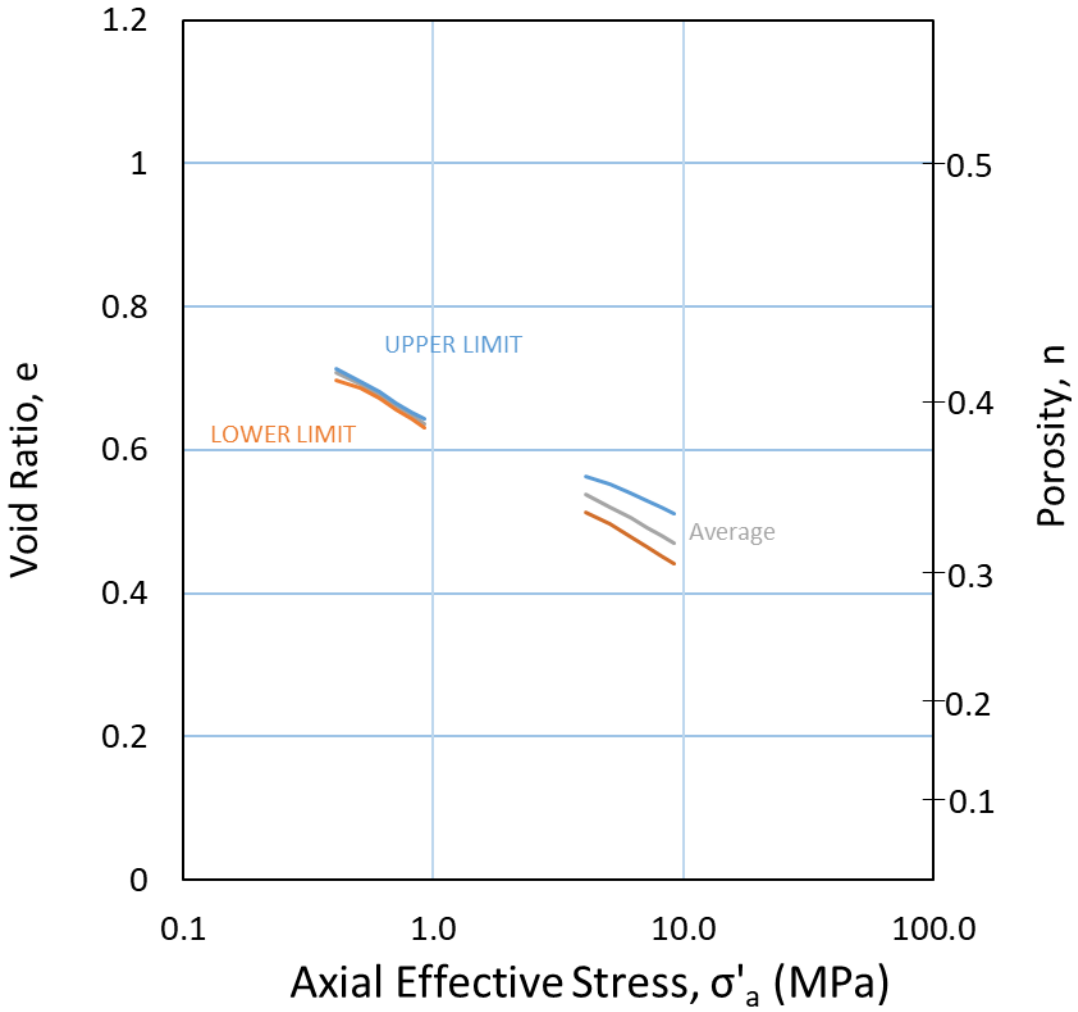


Figure 5-21: Upper limit, lower limit, and average compression curves for 30% clay specimens. Limits and averages from 1 MPa and 10 MPa triaxial test consolidation phases.

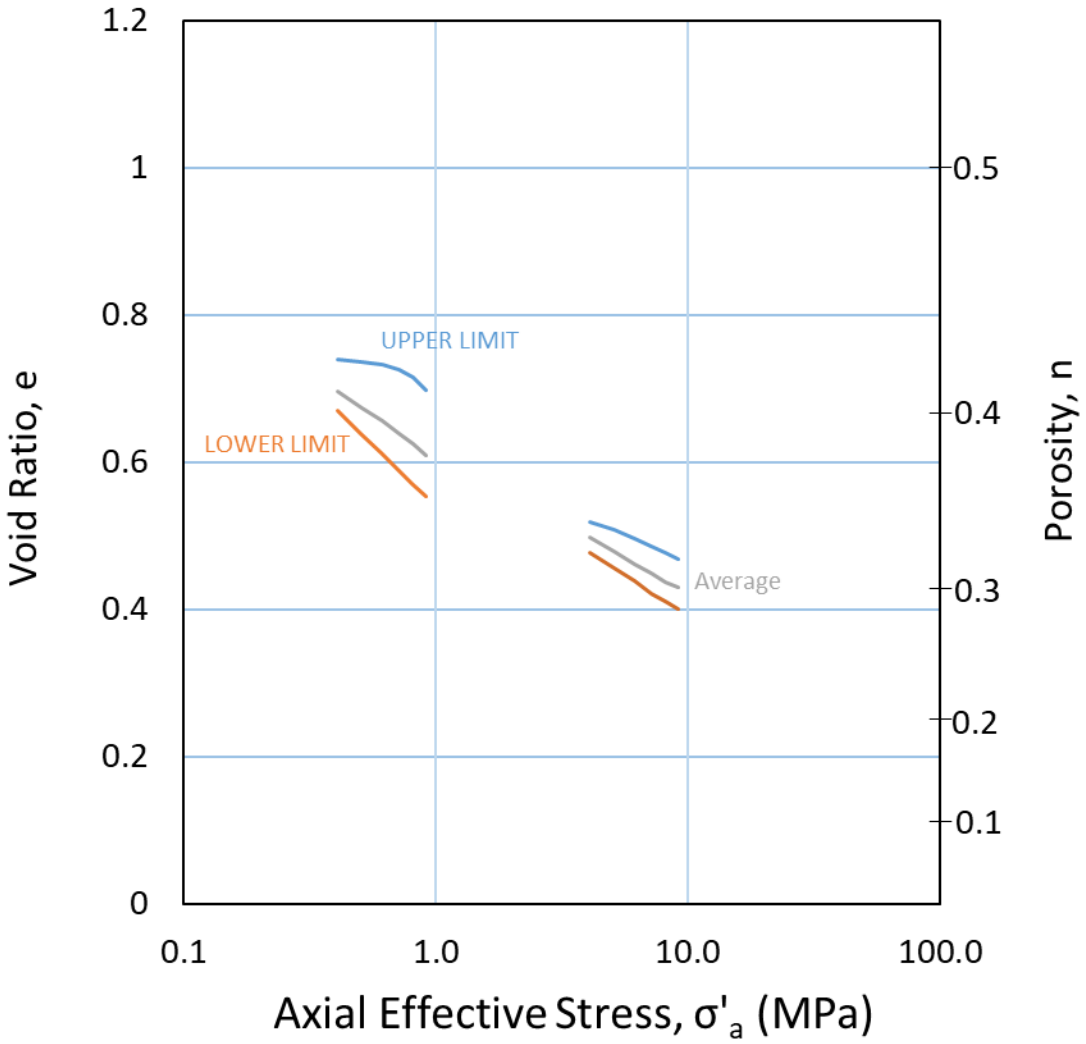


Figure 5-22: Upper limit, lower limit, and average compression curves for 40% clay specimens. Limits and averages from 1 MPa and 10 MPa triaxial test consolidation phases.

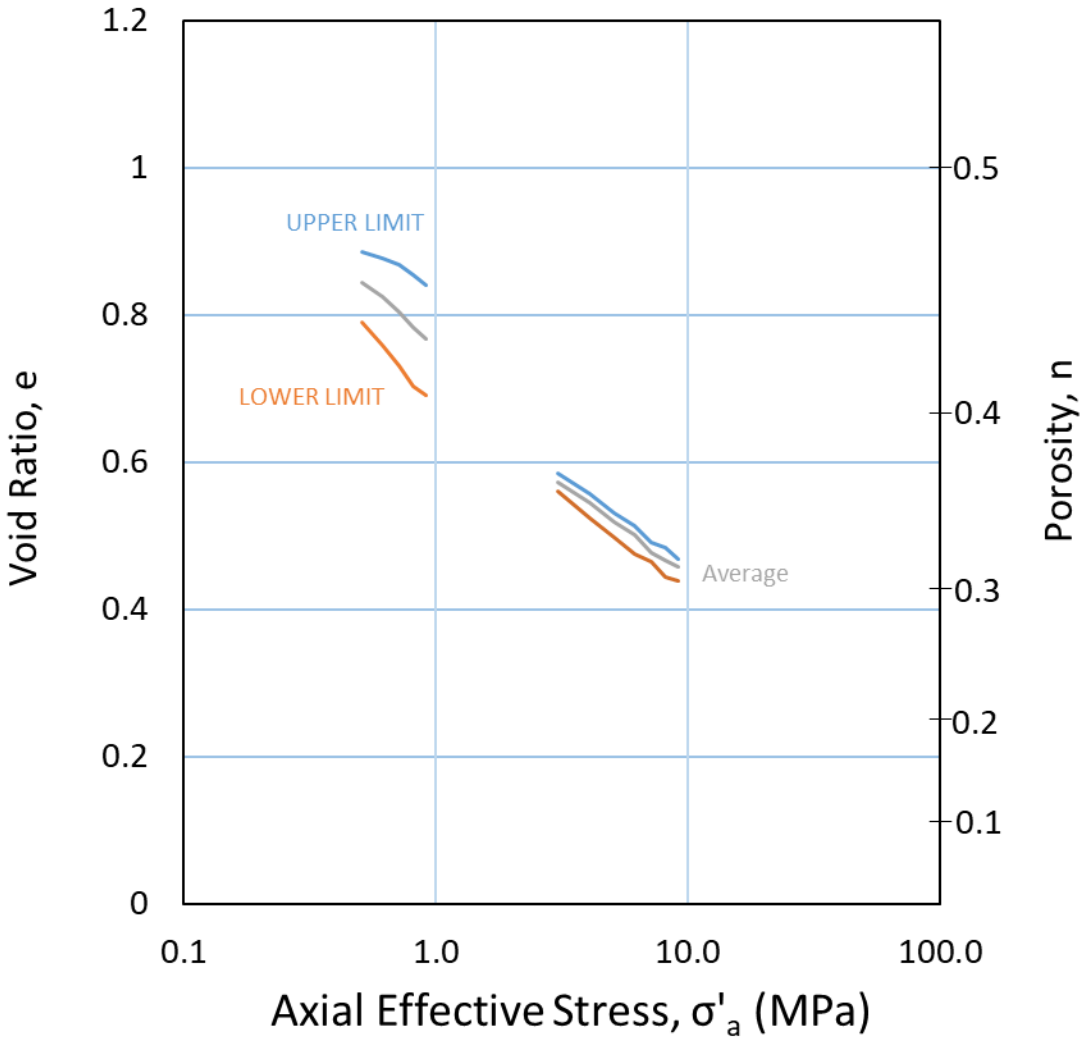


Figure 5-23: Upper limit, lower limit, and average compression curves for 50% clay specimens. Limits and averages from 1 MPa and 10 MPa triaxial test consolidation phases.

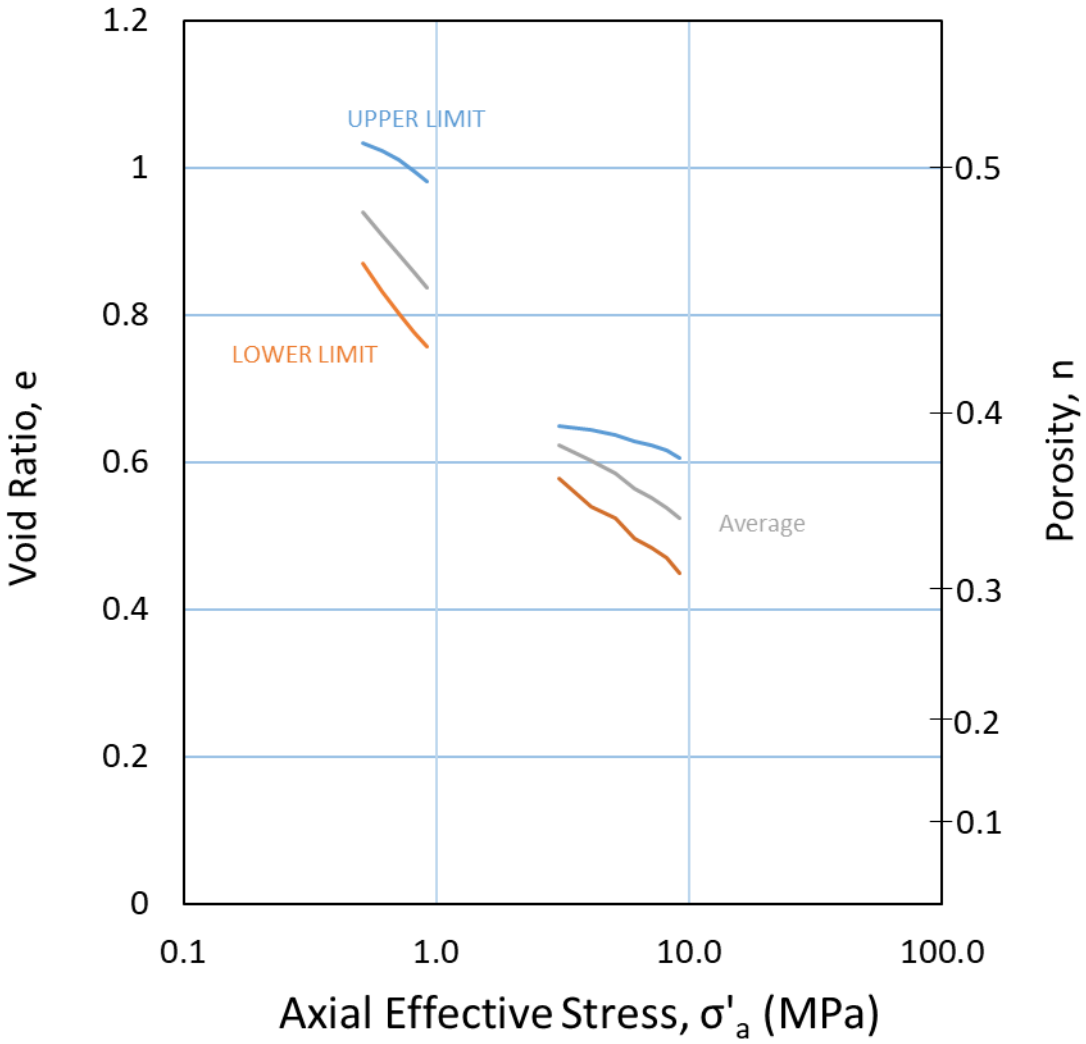


Figure 5-24: Upper limit, lower limit, and average compression curves for 60% clay specimens. Limits and averages from 1 MPa and 10 MPa triaxial test consolidation phases.

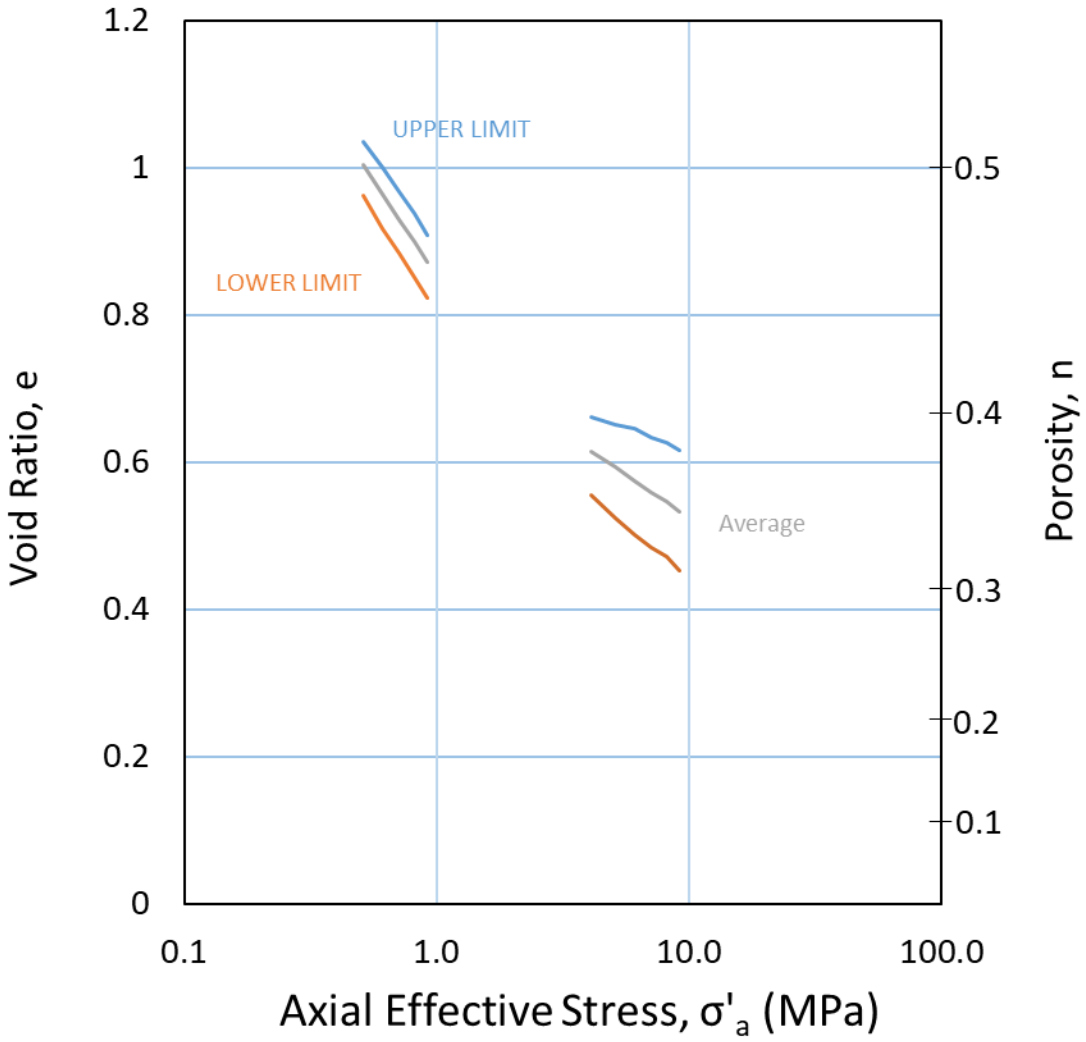


Figure 5-25: Upper limit, lower limit, and average compression curves for RGoM_EI specimens. Limits and averages from 1 MPa and 10 MPa triaxial test consolidation phases.

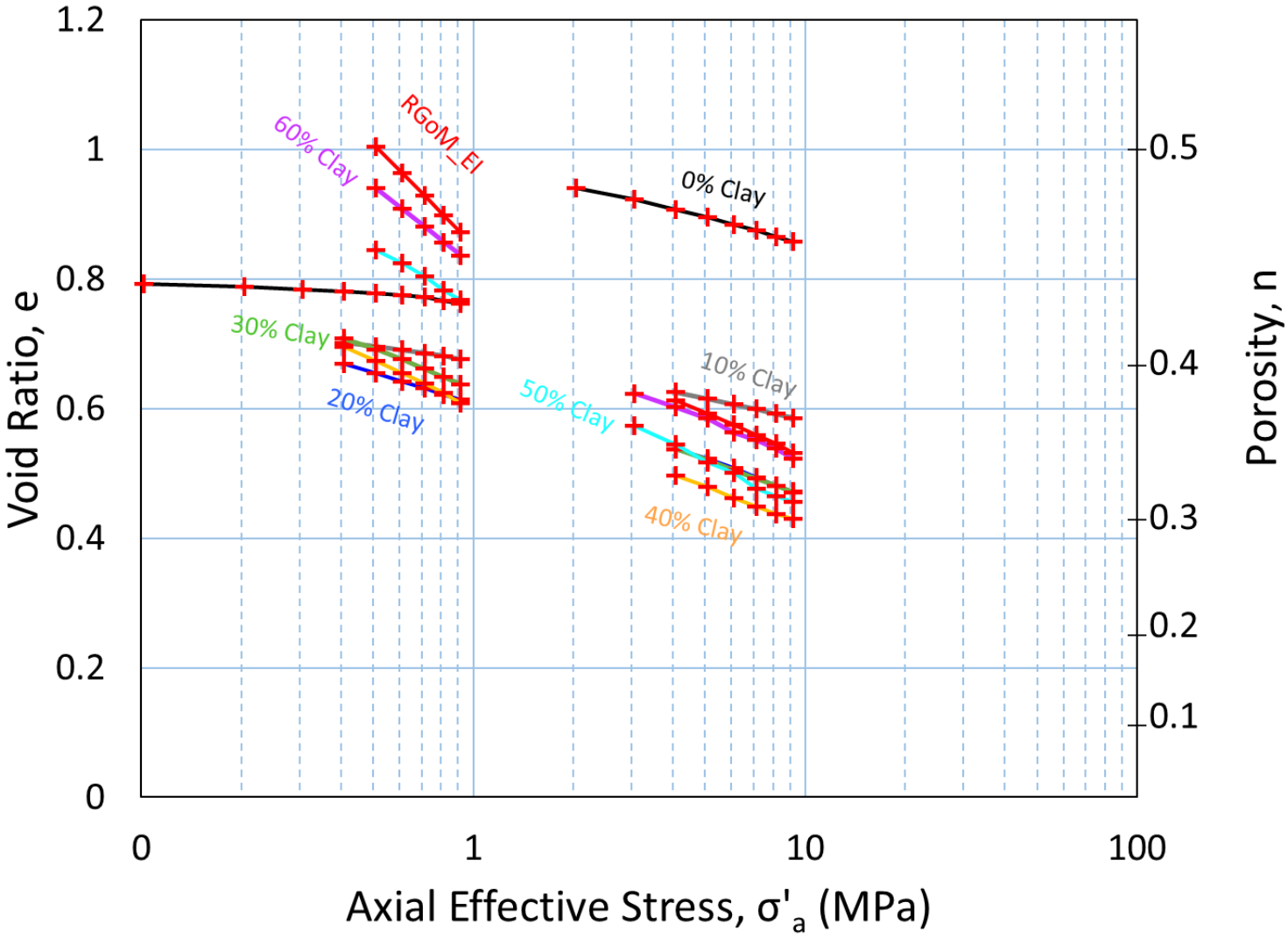


Figure 5-26: Upper limit, lower limit, and average compression curves for RGoM_EI specimens. Limits and averages from 1 MPa and 10 MPa triaxial test consolidation phases.

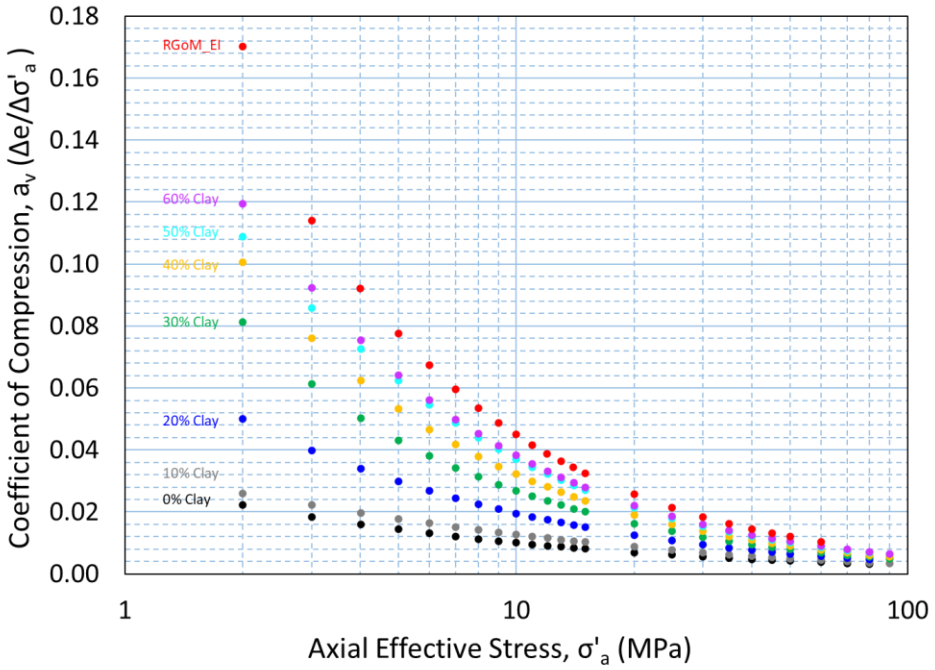


Figure 5-27: Coefficient of Compression (a_v) determined from the indicated axial effective stress from a 1 MPa reference stress in the high stress CRS apparatus.

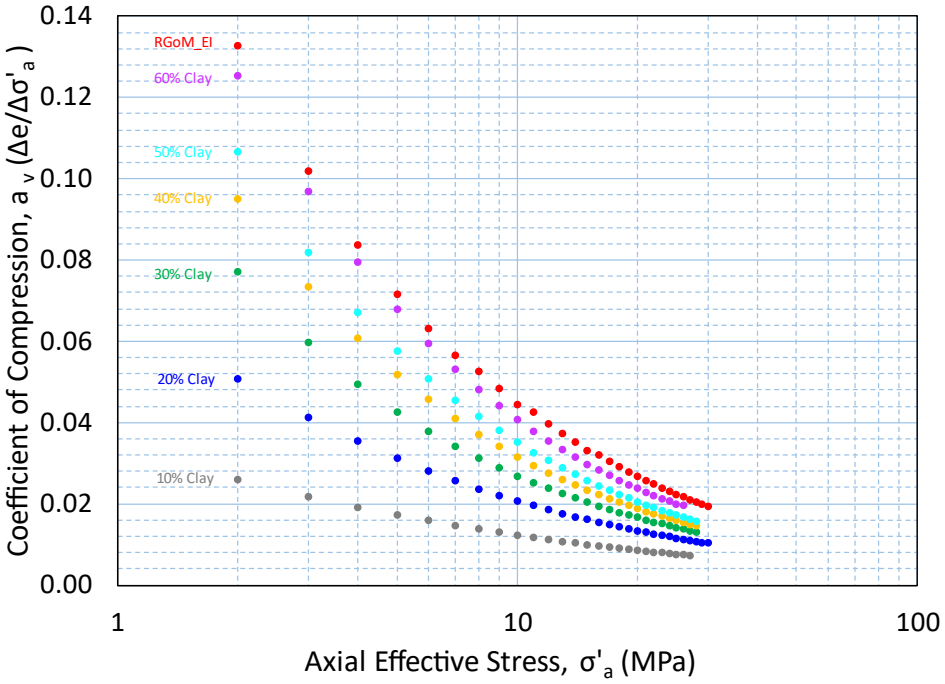


Figure 5-28: Coefficient of Compression (a_v) determined from the indicated axial effective stress from a 1 MPa reference stress in the tall CRS apparatus.

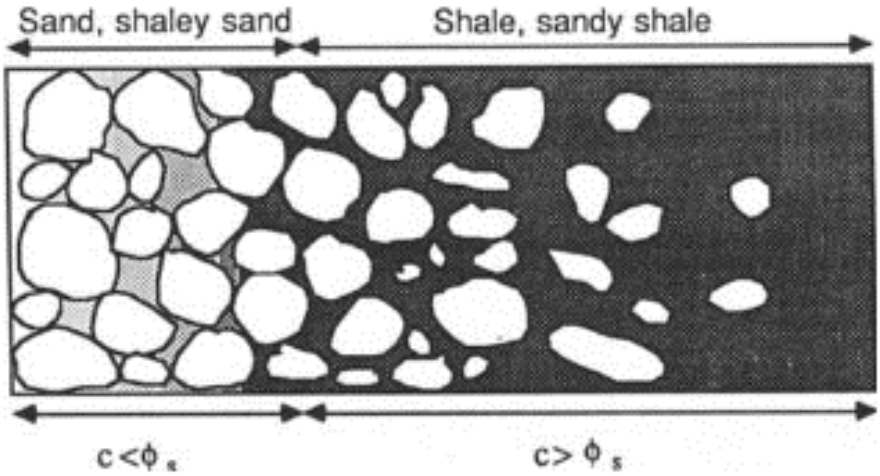


Figure 5-29: Soil fabrics due to crystalline grain (silts and sands) and clay (shale) packing adapted from (Marion, Nur, Yin, & Han, 1992). ϕ_S represents the critical clay content at which the sand porosity is completely filled with clay particles and is the transition point between grain supported and clay supported soil fabrics.

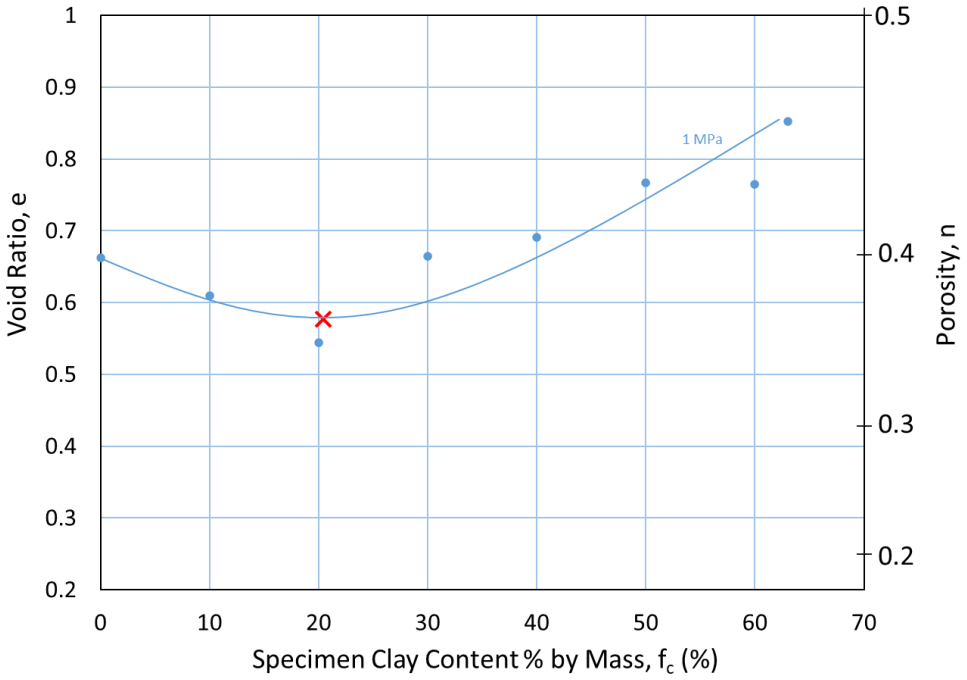


Figure 5-30: Average void ratio/porosity from the high stress CRS tests of each studied mixture at a 1 MPa Vertical Stress. The red X indicates the interpreted critical clay fraction.

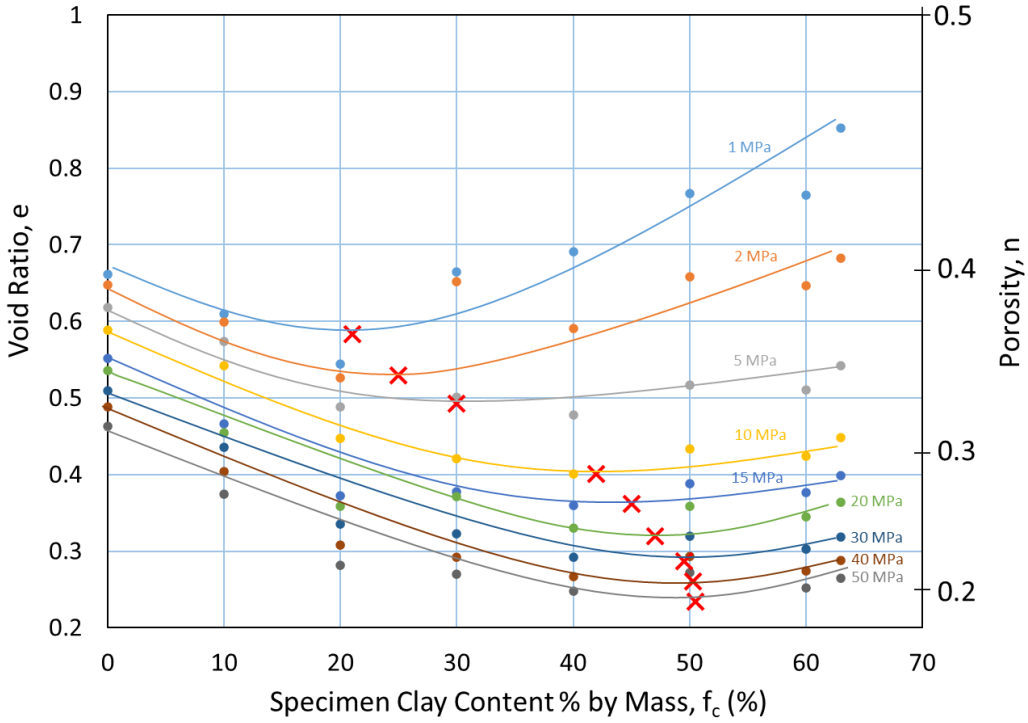


Figure 5-31: Average void ratio/porosity from the high stress CRS tests of each studied mixture at a 1 MPa, 2 MPa, 5 MPa ,10 MPa, 15 MPa, 20 MPa, 30 MPa, 40 MPa, and 50 MPa Vertical Stress. The red X indicates the interpreted critical clay fraction.

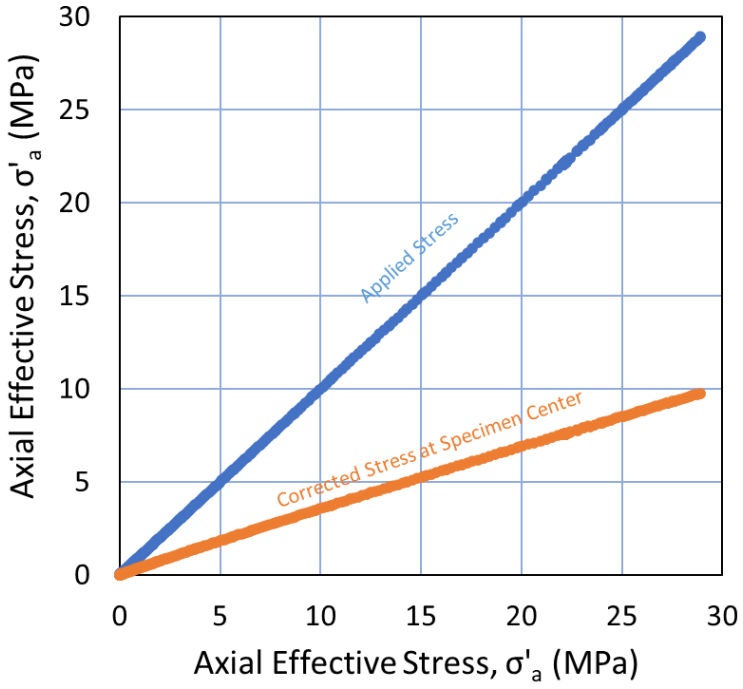


Figure 5-32: Comparison of the applied axial effective stress against the axial effective stress at the midpoint of the specimen corrected for sidewall friction forces in tall CRS test CRS1652 a 90% silt material.

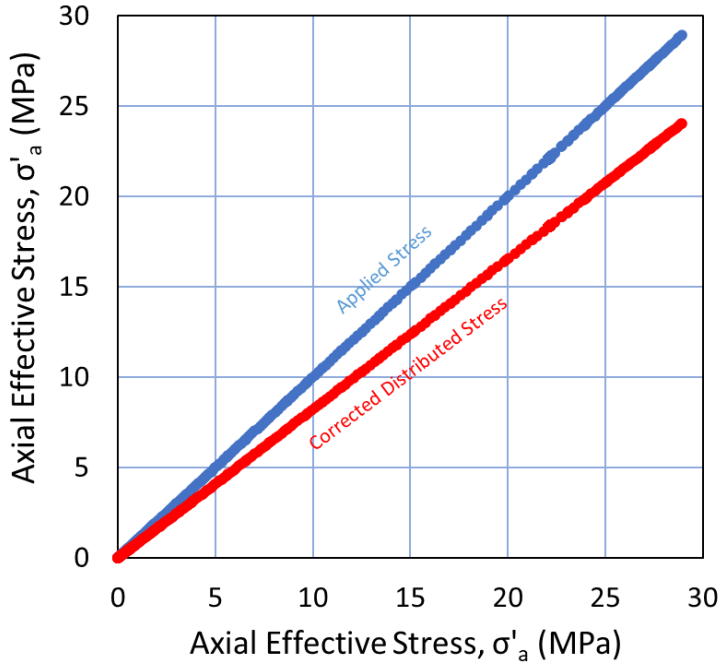


Figure 5-33: Comparison of the applied axial effective stress against the distributed axial effective stress corrected for sidewall friction forces in tall CRS test CRS1652 a 90% silt material.

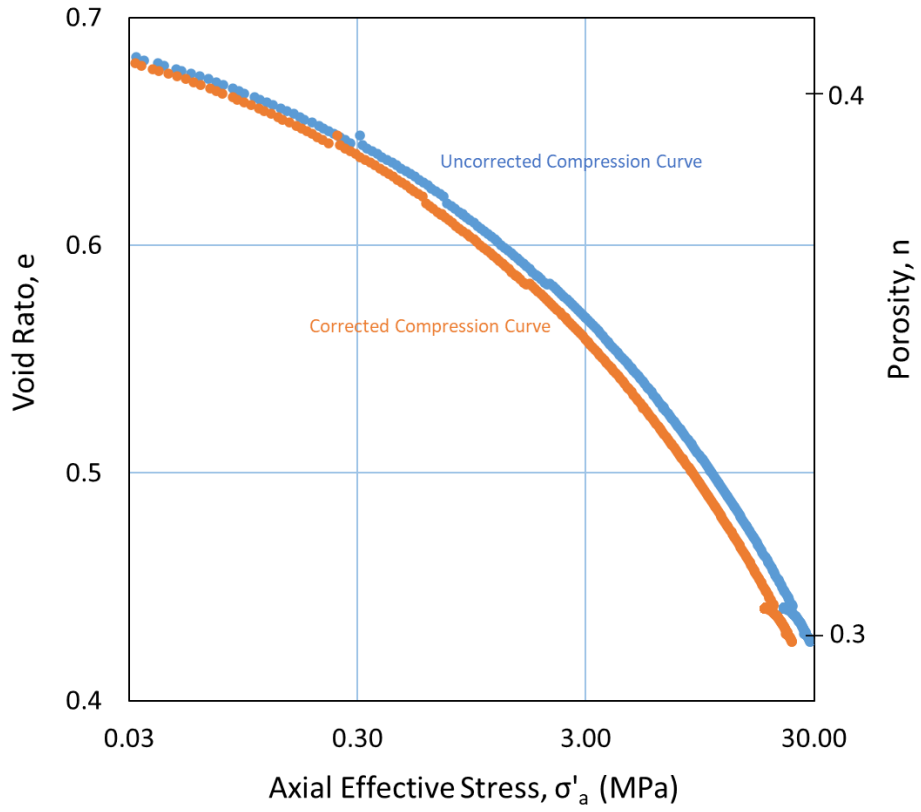


Figure 5-34: Comparison of the uncorrected compression curve against the compression curve corrected for sidewall friction forces in tall CRS test CRS1652 a 90% silt material.

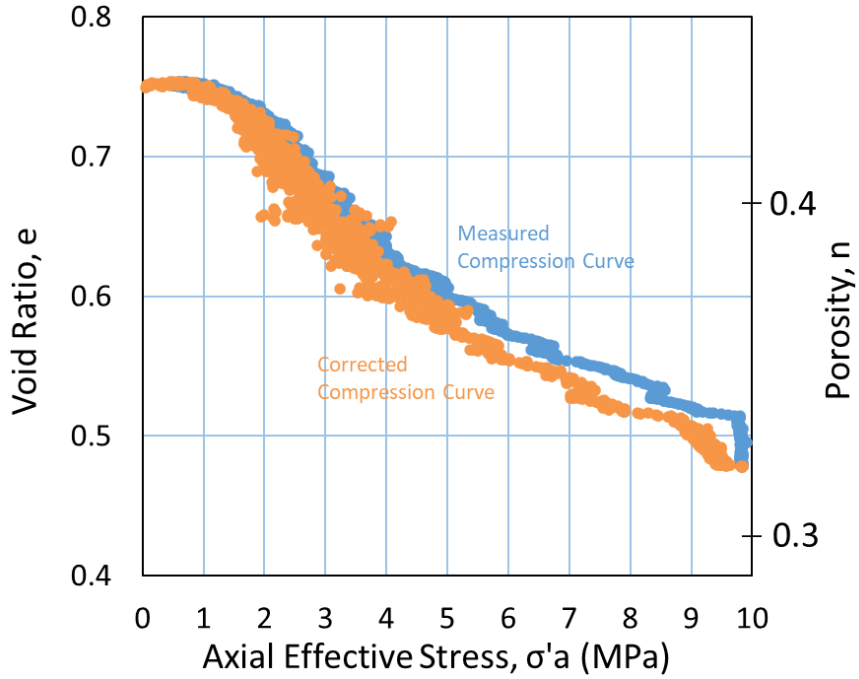


Figure 5-35: Comparison of the measured effective stress compression curve and the effective stress compression curve corrected for excess pore pressures during consolidation of specimen TX1484, a RGoM_EI specimen.

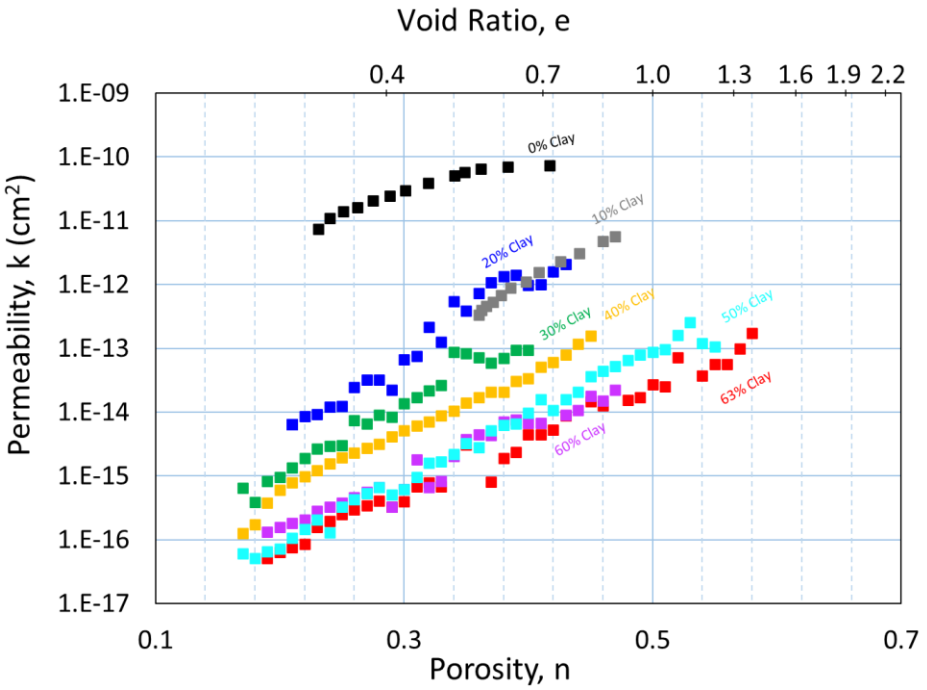


Figure 5-36: Average permeability presented by porosity for each test clay content as measured through constant head testing or constant rate of strain tests.

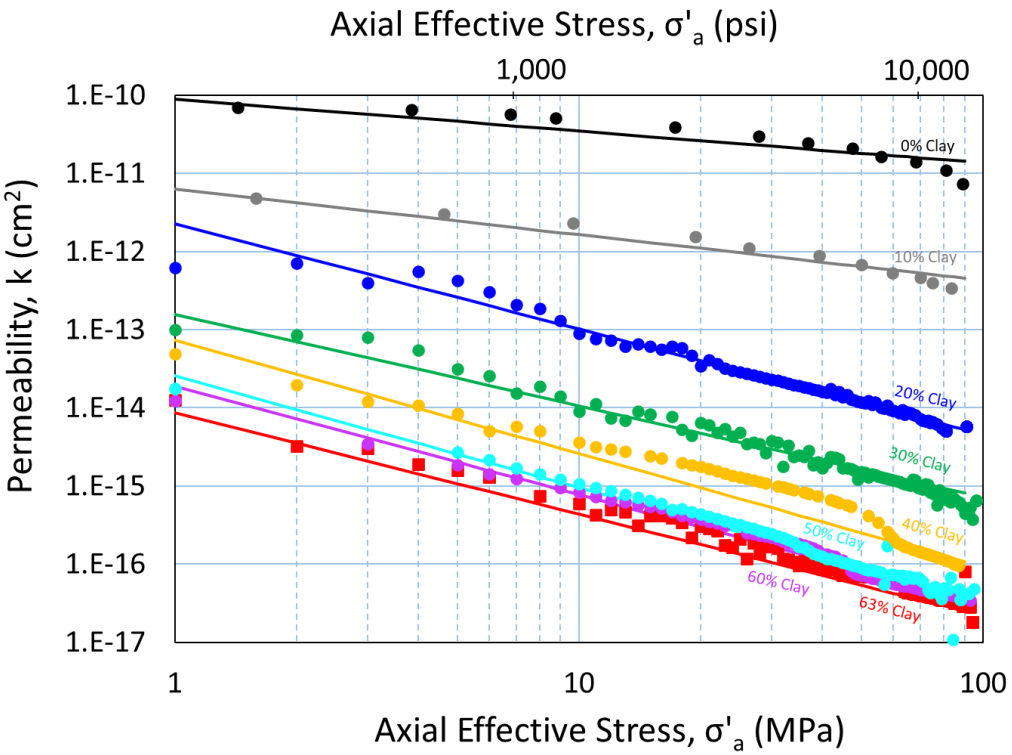


Figure 5-37: Average permeability (k) presented by axial effective stress level for each test clay content as measured through constant head testing or CRS tests. Solid lines indicate a log-log linear regression.

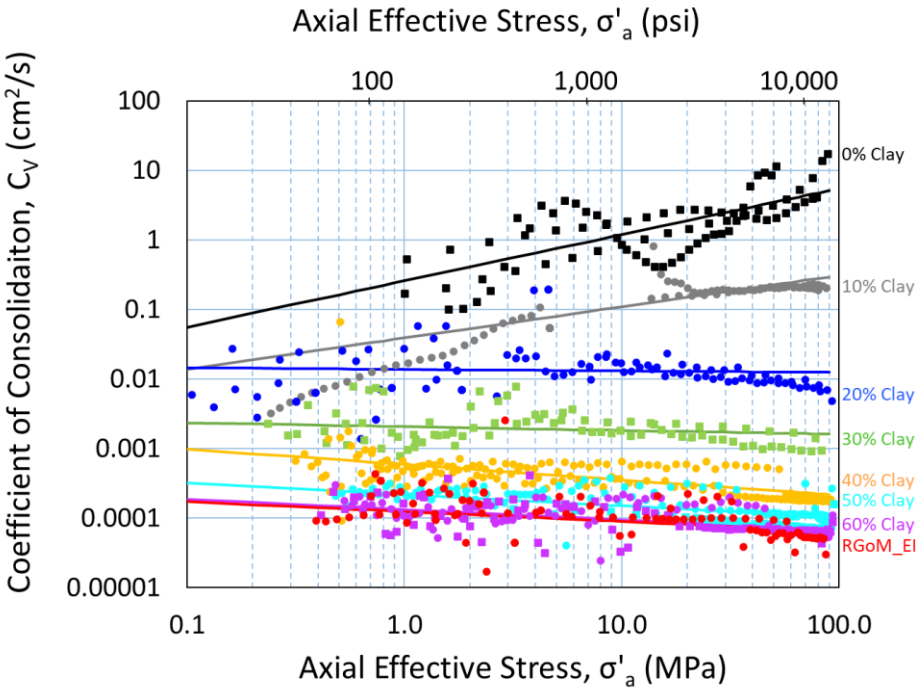


Figure 5-38: Average coefficient of consolidation (C_v) presented by axial effective stress level for each test clay content as measured through high stress CRS tests. Solid lines indicate a log-log linear regression.

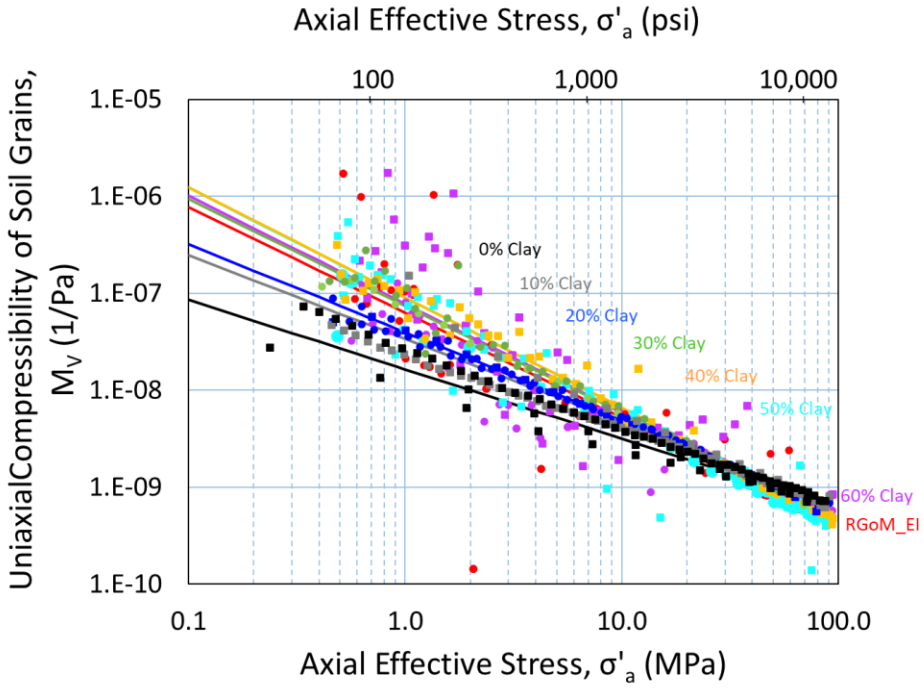


Figure 5-39: Average uniaxial compressibility of soil grains (M_v) presented by axial effective stress level for each test clay content as measured through high stress CRS tests. Solid lines indicate a log-log linear regression.

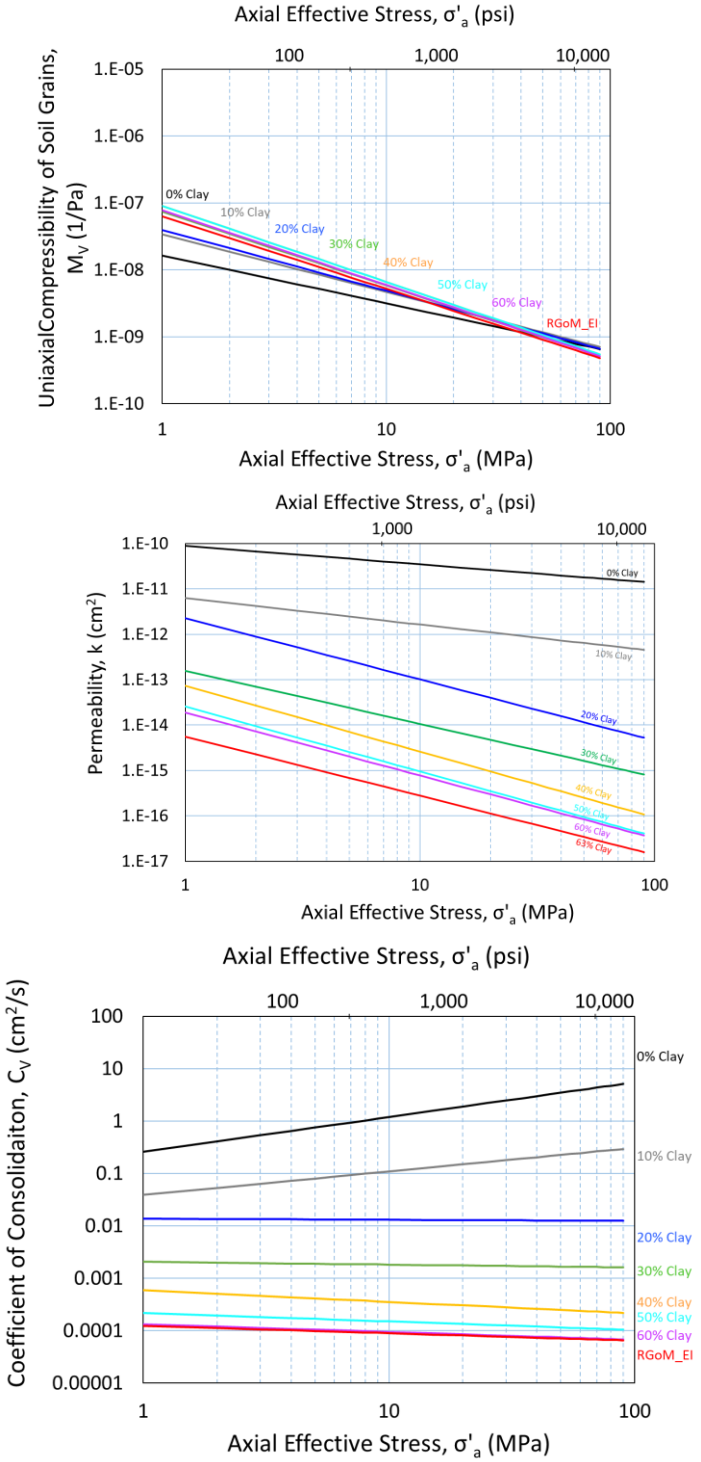


Figure 5-40: Top log-log linear regression of uniaxial grain compressibility by effective axial stress for each studied soil clay content. Middle log-log linear regression of permeability by effective axial stress for each studied soil clay content. Bottom log-log linear regression of coefficient of consolidation by effective axial stress for each studied soil clay content from the high stress CRS tests.

CHAPTER 6. Vertical Velocity Measurements of Silt-Clay Mixtures

6-1 Introduction

This chapter presents and discusses the vertical velocity measurements made during tall constant rate of strain (TCRS) test on the silt and clay mixed specimens. As presented within Chapter 3, the TCRS apparatus is outfitted with piezometric crystals within the bottom and top caps, in contact with the specimen to transmit and receive a shear (S) and pressure (P) wave. During TCRS tests shear and pressure wave measurements were conducted at approximately 1 MPa intervals up to an ultimate effective axial stress of 30 MPa. Section 6.2 presents the processing and methodology used to interpret the arrival time of the received waveforms for use in velocity calculations. Section 6.2 includes discussion on the selection of a digital filter used in the signal processing, as well a discussion on the correction for delay inherent to the wave measurement system. Section 6.3 presents the velocity measurements of the tested silt and clay mixtures. Section 6.4 presents the dynamic material properties calculated from the measured wave velocities and soil densities. Section 6.5 presents a discussion on the experimental results and observed trends. Section 6.5 includes model fits for the experimental data for use in predicting P or S wave velocity by clay content and effective stress and a comparison to similar models from similar previous studies.

6-2 Waveform Processing and Velocity Calculation

Both P and S waves in the TCRS experiments are triggered by sending a square input signal through the generating piezoelectric actuator. The output signal is then captured by the piezoelectric receiver as voltage changes over time and recorded by an oscilloscope. The oscilloscope used for this study averages every 128 waveform readings to smooth the received signal. The sampling frequency and voltage amplitude sensitivity of the collected wave were controlled through settings on the oscilloscope. Sampling frequency and voltage sensitivity were varied as required to collect the clearest wave possible.

The input box wave and received wave are collected simultaneously for use in determining the trigger time. Each wavelet saved includes measurements prior to the 0-time trigger point, to provide clarity on false triggers. The process of collecting a wave during the TCRS testing was manual in nature. The mechanical load frame driving compression of the specimen was turned off to limit electrical noise present in the collected signals while the frame was running. Both the P and S waves were collected within a 5-minute period of shutting off the load frame to limit secondary consolidation effects during velocity measurement. The signals were transferred from the oscilloscope to a USB disk drive and transferred to a personal computer. Equation 6-1 is used to calculate the wave velocity from the arrival time of the P or S wave.

$$V_{S/P} = \frac{L_t}{T_a - T_{off}} \qquad \text{Equation 6-1}$$

Where:

$V_{S/P}$ = S or P wave velocity (length by time)

L_t = Specimen height at time t (length)

T_a = Selected arrival time (time)

T_{off} = Inherent system delay offset time see discussion at end of Section 6.2 (time)

The specimen height during compression was calculated from the measured axial strain using equation 6-2.

$$L_t = L_0\left(1 - \frac{\epsilon_{at}}{100}\right) \qquad \text{Equation 6-2}$$

Where:

L_t = Specimen height at time t (length)

L_0 = Initial specimen height at start of test (length)

ϵ_{at} = Measured axial strain at time t (strain)

Both the P and S wave signals were processed through a MATLAB function code of the authors creation and plotted in Microsoft Excel for the selection of the arrival time. The MATLAB function code for the S-wave processing is provided as Appendix A. The code uses file indexing characteristics from the oscilloscope and the authors data storage structure to locate each input and output oscilloscope file in the selected directory. The selected directory file path is an input variable for the function. The MATLAB function saves the input and output waveforms to an array indexed by the subfile name which was named to be the effective stress level during measurement. The code averages each output wavelet using an n-point moving average, where n is an input variable for the function. Typical moving averages are between 5 and 11 points. The pre-trigger data is removed and if required the wavelet samples are reduced to 2048 data points for a more efficient Fast Fourier Transformation (FFT) within MATLAB. A frequency vector is calculated for each wavelet using the sampling time data. An FFT is performed to provide an understanding of the frequency information of the signal, the code plots the amplitude by the frequency vector and saves the frequency corresponding to the largest amplitude to an array. The largest spectral amplitude and corresponding frequency were used to track the change in dominant frequency by stress. The S-wave signals are filtered using a Hamming window high pass filter. The cutoff frequency is an input variable for the function code, but a cutoff frequency of 7,000 Hertz was used to process all of the S-wave data presented herein. The group delay effects due to filtering are calculated and removed from the filtered signal. The code outputs a table that has two header rows, and three columns for each measured stress level. The first header row provides the stress level

measured and the second header row provides the dominant frequency from the FFT. The three output columns are the wave time data, the unaltered input wave, and the filtered signal wave respectively. This table is copied into an excel template that internally references the table for use in selection of the S-wave arrival time.

The P wave signals were similarly processed through a MATLAB function code of the authors creation and plotted in Microsoft Excel for the selection of the arrival time. The MATLAB function code for the P-wave processing is provided as Appendix B. The code uses file indexing characteristics from the oscilloscope and the authors database structure to locate each input and output oscilloscope file in the input directory and save them to an array indexed by effective stress level during measurement. The input file directory is an input variable of the MATLAB function. The code averages each wavelet using an n-point moving average, where n is an input variable for the function. Typical moving averages are between 3 and 9 points. The pre-trigger data is removed and if required the wavelet samples are reduced to 2048 data points for a more efficient Fast Fourier Transformation (FFT). The frequency vector is calculated for each wavelet using the sampling time data. The FFT is performed to provide an understanding of the frequency information of the signal. The function plots the amplitude by frequency vector and saves the frequency corresponding to the largest spectral amplitude to an array. The code outputs a table that has two header rows, and three columns for each measured stress level. The first header row provides the stress level measured and the second header row provides the dominant frequency from the FFT analysis. The three columns are the wave time data, the unaltered input wave, and the averaged signal wave respectively. This table is copied into a template excel file that references the table for selection of the P-wave arrival time.

Selection of the arrival time for the P-waves was automated to the extent possible using the Aikake Information Criterion (AIC) Aikake (1974), as modified within Maeda (1985) to directly compute the AIC

values from the time series without the use of autoregressive model coefficients. This is done using Equation 6.3.

$$AIC(k) = k\ log(var\{x(1,k)\}) + (N-k-1)\log(var\{x(k+1,n)\}) \quad \text{Equation 6-3}$$

Where:

k = sliding sample time (time)

N= end time of the total time series (time)

$var\{x(1,k)\}$ = Variance of the time series before the sliding sample time

$var\{x(k+1,n)\}$= Variance of the time series after the sliding sample time

The modified AIC method assumes that the windows before and after the arrival time are two separate time series and that the largest difference in variance between the two-time series occurs at the wave arrival time. The AIC value is calculated at each time k, and the global minimum of the AIC series is selected as the wave arrival time. A median filter was applied to the P-wave signals to smooth the data prior to the automated wave arrival time selection per the recommendations within Zhou, Chen, Rui, & Wang (2019). The median filter selects the median value of a moving interval of size n, n is typically 7 data points for this study. Figure 6-1 presents an example of the automated P-wave arrival time selection for the 25 MPa stress level of test CRS1672 a RGoM_EI test. Figure 6-2 presents the AIC values by time for the 25 MPa stress level of test CRS1672, the global minimum of the AIC values in Figure 6-2 corresponds to the selected P-wave arrival time.

Selection of the arrival time for S-waves was a mostly manual process after processing of the waves through MATLAB. Selection of the S-wave arrival is complicated by both the P and S waves traveling through the specimen coincidently during S wave measurements, as the P wave can obscure the arrival time of the S wave. The S wave arrival time was determined as the intersection of the first major trough and the zero-crossing frequency. The shear waves measured in the TCRS setup consistently had a

leading trough (negative displacement) as the first arrival feature. The oscilloscope has a variable offset voltage for the zero-crossing value, this was accounted for by considering the zero-crossing voltage as the average voltage over the period after the initial voltage noise induced from the start of the square wave input and prior to the arrival time of the P wave. Figure 6-3 presents a typical manually selected S wave arrival time for the 25 MPa stress level of test CRS1672 a RGoM_EI test. Figure 6-3 indicates the average zero value and the selected arrival time. The S wave arrival times were typical determined at

the end of a test, and the arrival times were determined in order from the highest stress to the lowest stress. The higher stress levels tended to have a more distinct wavelet and less interference from the P waves which allowed for an easier arrival selection. The selection times for the higher stress were used to determine a trend in velocity and stress that was then used to inform the selection of lower stress level arrival times. This stacking method worked well for establishing a repeatable and consistent method for determining the S wave arrival time.

Uncertainty in the Velocity Measurements

The measurement and calculation of the wave velocities presented have an associated degree of uncertainty due to the effects of digital signal processing, and physical limitations of the testing equipment. The following section attempts to quantify the uncertainty associated with different aspects of the tall CRS test setup.

The S wave velocity experiments were filtered through a digital filter in the time domain. Digital filters are known to affect the time data of a wave form. Five different digital filters were compared to evaluate the effects of each filter on the selected arrival time and calculated velocities. The five filters compared consisted of a high pass filter, a low pass filter, a finite impulse response (FIR) low pass filter, and two FIR band pass filters. The filters were compared at two stress levels 5 MPa and 25 MPa to evaluate specimen stress effects. The filters were compared for each silt clay mixture to evaluate

lithology effects. A MATLAB code was created that applied the compared filters to the selected waveforms. The filter frequency limits were varied to evaluate their effects as described within this section. To easily automate the process of comparison the peak of the shear wavelet and not the arrival time was selected in MATLAB and used to calculate a velocity using equation 6-1. Where the time to the peak value was substituted for the arrival time. The processed velocities were then compared to a standard peak velocity without any processing to evaluate the relative change in velocity due to the selected filter or filter frequency limits.

Filter 1 is a high pass filter, which requires a cutoff frequency input. The filter removes any signal data at the cutoff frequency or lower frequencies. To determine the effects of the cut off frequency the cutoff frequency was incremented by 1 kHz from 0 to 50 kHz.

Filter 2 is a low pass filter, which requires a cutoff frequency as an input. The filter removes any signal data at the cutoff frequency or higher frequencies. To determine the effects of the cut off frequency the cutoff frequency was incremented by 1 kHz from 50 to 0 kHz.

Filter 3 is a FIR low pass filter, which requires a cutoff frequency as an input. The filter removes any signal data at the cutoff frequency or higher frequencies. To determine the effects of the cut off frequency the cutoff frequency was incremented by 2 kHz from 100 to 2 kHz.

Filter 4 is a FIR band pass filter, which requires a low cutoff frequency and a high cutoff frequency as inputs. The filter removes any signal data at the lower cutoff frequency or below and at the or higher cutoff frequency or above. To determine the effects of the cut off frequencies the low cutoff frequency was maintained at 7 kHz and the high cutoff frequency was incremented by 2 kHz from 108 to 10 kHz.

Filter 5 is also a FIR band pass filter like filter 4. To determine the effects of the cut off frequencies the high cutoff frequency was maintained at 75 kHz and the low cutoff frequency was incremented by 1 kHz from 0 to 50 kHz.

Figure 6-4 illustrates the typical results of the filter comparison by showing the relative velocity differences calculated by the digital filters for the 5 MPa stress level of the 60% clay mixture test CRS1688. The relative difference in velocity ranges between -0.3% and 6.4% depending on the digital filter and cutoff frequency combination selected. The results presented in Figure 6-4 were representative of the findings at other stress levels and clay contents. Based on the result of the comparison, a high pass filter with a cutoff frequency of 7 kHz, and a moving average window around 11 data points was used to process all of the shear wave velocity results presented within this study. Figure **6-5** presents a comparison of a 5 MPa shear wave measured within a 60% clay specimen (CRS1688), with and without processing through the MATLAB code.

There is an inherent delay in the system between signal actuation and collection by the oscilloscope. The delay is due to travel time through the wires and through the epoxy coated piezoceramic elements. This delay is quantified and subtracted from the selected arrival time to determine the wave speed through the specimen. The delay was quantified by making wave measurements using the experimental setup on dummy specimens of varying height. The dummy specimens were made of polyvinyl chloride. The arrival times were plotted against the dummy height, and the data were fit linearly. The Y intercept of the linear fit was taken as the inherent delay in the system. Figure 6-6 presents the determination of the P wave delay and Figure 6-7 presents the determination of the S-wave delay.

6-3 Velocity Measurements

Table 6-1 to Table 6-14 provide summaries of the test conditions at the time of the wave velocity measurement for each TCRS test. The calculated specimen height, axial effective stress, P/S wave

velocities, void ratio, porosity, and density are all provided. The tables are ordered by the specimen's axial effective stress during testing including any unload/reloading cycles that may have occurred as a part of the test.

Figure 6-8 to Figure 6-21 presents the measured P and S wave velocities by axial effective stress for each clay mixture as individual plots. These plots include the axial stress correction accounting for friction between the specimen and confining steel ring discussed in Chapter 5. Figure 6-22 and Figure **6-23** present the measured P and S wave velocities by axial effective stress for each clay mixture on the same plot for ease of comparison between the different clay contents. The error between velocity measurements for the same mixtures is on average over the 30 MPa stress range between 0.7% to 6.1% for the S wave velocities and 1.0% to 3.9% for the P wave velocities.

6-4 Dynamic Elastic Parameters

Elastic moduli of the clay-silt mixtures are calculated from the density and wave velocity measurements to provide an understanding of the dynamic behavior of the material. The elastic moduli were calculated under the assumption of isotropic elastic behavior. The shear modulus (G) is calculated by Equation 6-4.

$$G = \rho V_S^2 \qquad \text{Equation 6-4}$$

Where:

G = Shear Modulus, (Stress by strain)

ρ = Soil Bulk Density, (Mass by volume)

V_S = Shear wave velocity, (length by time)

The constrained modulus (M) is calculated through Equation 6-5.

$$M = \rho V_P^2 \qquad \text{Equation 6-5}$$

Where:

M = Constrained modulus, (Stress by strain)

ρ = Soil bulk density, (Mass by volume)

V_S = Shear wave velocity, (length by time)

The remaining elastic parameters bulk modulus (K), Young's modulus (E), Lame's first parameter (λ), and Poisson's ratio (ν) are calculated from Equation 6-6 to Equation 6-9.

$$K = M - \frac{4G}{3} \qquad \text{Equation 6-6}$$

$$E = \frac{G(3M-4G)}{M-G} \qquad \text{Equation 6-7}$$

$$\lambda = M - 2G \qquad \text{Equation 6-8}$$

$$\nu = \frac{\lambda}{M+\lambda} \qquad \text{Equation 6-9}$$

Where:

K = Bulk Modulus, (Stress by strain)

M = Constrained modulus, (Stress by strain)

G = Shear Modulus, (Stress by strain)

E = Young's Modulus, (Stress by strain)

λ = Lame's Parameter, (Stress by strain)

ν = Poisson's Ratio

Figure 6-24 through Figure 6-29 provide the calculated elastic parameters, shear modulus. Constrained modulus, bulk modulus, Young's modulus, Lame's first parameter, and Poisson's ratio by effective axial stress for each of the studied silt and clay mixtures. Figure 6-30 through Figure 6-35 provide the calculated elastic parameters, shear modulus. Constrained modulus, bulk modulus, Young's modulus, Lame's first parameter, and Poisson's ratio by the bulk soil density for each of the studied silt and clay mixtures.

6-5 Discussion

The velocity experiments on resedimented mudrocks reinforce previous observations by Bowers (1995), Choo & Burns (2015), Marion, Nur, Yin, & Han (1992), Marjanovic (2016), Ranjpour (2020), Vernik (1993), Zimmer, Prasad, & Mavko (2002) and others on the relationships between effective stress and soil lithology with the transmission of waves.

The effects of effective stress are evident on both P and S waves through changes in arrival time with changes in effective stress. Higher effective stress levels have wave arrival times occurring quicker than lower effective stress levels, thus indicating the relationship of P wave velocity and S wave velocity increasing with increasing effective stress. This was observed to be true for all tested mixtures and can be seen in the velocity measurement summaries presented in Figure 6-22 and Figure 6-23. The macrolevel effects of lithology on the velocity measurements are best illustrated in Figure 6-36 and Figure 6-37 which present the average P wave and S Wave velocities by specimen clay content as measured in the TCRS tests at select stress levels. Both P wave and S wave velocities show a trend that was presented in Marion, Nur, Yin, & Han (1992), where the maximum velocity does not correspond to an end member of the mixtures (10% Clay or RGoM_EI) but to mixtures around 30% to 50% clay by mass. Within Marion, Nur, Yin, & Han (1992), this behavior is attributed to fabric controls. They hypothesized that velocity increased with increasing clay content in low clay content soils the added clay

particles stiffen the pore space increasing the velocity and that velocity decreased in higher clay content materials with increasing clay content as the void space increased with increasing clay content.

A summary of P wave and S wave velocities by soil effective stress state for all the tested silt and clay mixtures is provided in Figure 6-22 and Figure 6-23 respectively. Figure 6-22 indicates that the P wave velocities follow the general trend that velocity increases with increasing soil effective stress. The rate of increase of velocity with effective stress is shown to be nonlinear and is initially faster at lower stress states and slows at higher stress states. The lowest velocities measured were above the 1,500 m/s average P wave velocity of water indicating that the soil is contributing to the wave speed. Figure **6-23** indicates that the S wave velocities follow the same general trend of increasing velocity with increasing soil effective stress. The rate of increase of velocity with effective stress is shown to be nonlinear and is initially faster at lower stress states and slows at higher stress states. Figure 6-36 shows that the P wave velocity for the mixtures at a 1 MPa stress level vary by 85 m/s, with the highest average velocity of 1,754 m/s occurring at 40% clay and the lowest average velocity of 1,669 occurring at the RGoM_EI specimen (63% clay). At a 5 MPa stress level the range in velocity measurements has increased to 220 m/s, with the highest average velocity of 2,019 m/s occurring at 40% clay and the lowest average velocity of 1,799 occurring at the 10% clay specimen. The range of velocities continues to increase with increasing stress at a 25 MPa stress level the range in velocity measurements is 440 m/s, with the highest average velocity of 2,482 m/s occurring at 40% clay and the lowest average velocity of 2,042 m/s occurring at the 10% clay specimen.

Figure 6-37 shows an identical trend for the S wave velocities. At a 1 MPa stress level the velocities vary by 73 m/s, with the highest average velocity of 282 m/s occurring at 40% clay and the lowest average velocity of 209 occurring at the 10% clay specimen. At a 5 MPa stress level the range in velocity measurements has increased to 172 m/s, with the highest average velocity of 564 m/s occurring at 40%

clay and the lowest average velocity of 392 m/s occurring at the 10% clay specimen. The range of velocities continues to increase with increasing stress at a 25 MPa stress level the range in velocity measurements is 276 m/s, with the highest average velocity of 939 m/s occurring at 40% clay and the lowest average velocity of 663 m/s occurring at the 10% clay specimen.

Through comparison of the characteristics of the recorded wavelets the effects of lithology and stress were explored at a microlevel. Figure 6-38 and Figure 6-39 presents recorded P wave wavelets at a 5 MPa and 25 MPa stress level within a RGoM_EI, and 10% clay material TCRS test respectively. The effect of lithology is observed within these wavelets as changes to the shape of the recorded wavelet. The P wave comparison shows that the wavelet changes shape with stress and lithology. The RGoM_EI wavelet in Figure 6-38 shows a flattening of the first peak with increasing stress level. This is not observed with changes in stress of the 10% clay material in Figure 6-39 which maintains a distinct initial peak. The P wave wavelets in both Figure 6-38 and Figure 6-39 indicate a similar frequency for both stress levels and lithologies

Figure 6-40 and Figure 6-41 present recorded S wave wavelets at a 5 MPa and 25 MPa stress level within a RGoM_EI and 10% clay material respectively. The RGoM_EI wavelet at the 5 MPa level indicates a much lower frequency and smaller amplitude than the S wave at the 25 MPa level. The difference in amplitude may be attributed to the coupling of the piezoelectric transducer to the soil at lower effective stress, where the coupling improves with compression of the specimen. The change in wave frequency is attributed to the change in rigidity from a lower rigidity at lower effective stress to a higher rigidity at higher effective stress. The change in frequency is observed within the 10% clay mixture as presented within Figure 6-41. The change in S wave frequency is not as drastic for the 10% mixture as it is for the RGoM_EI mixture and this is attributed to the lithology dependent compression behavior of the two mixtures. Chapter 5 presented the compression behavior of the tested mixtures,

and RGoM_EI was shown to be much more compressible than the 10% clay mixture through a 30 MPA stress level. RGoM_EI would be expected to have a larger change in rigidity between 5 MPa and 25 MPa, therefore a larger shift in S wave frequency would be expected in RGoM_EI rather than the 10% clay specimen at those stress levels.

Dynamic Elastic Moduli of the Silt Clay Mixtures

Figure 6-24 to Figure 6-29 provides the velocity-derived elastic moduli of the tested soils assuming isotropic behavior, between a 0 and 30 MPa stress. Elastic moduli calculated from wave velocities are referred to as dynamic moduli. The elastic moduli follow the trends of the wave velocities of increasing value with increasing effective stress attributed to the increasing rigidity of the soil. The 40% clay or 50% clay mixtures were observed to have the largest moduli values at any stress level.

Poisson's ratio is the only elastic constant that decreases with increasing effective stress as shown in Figure 6-29. Poisson's ratio starts between 0.487 and 0.5 for all mixtures around a 1 MPa stress level and decreases to a range between 0.402 and 0.438 around a 25 MPa stress level. The high values of Poisson's ratio around a 1 MPa stress level are consistent with the expected Poisson ratio for a suspension of particles in fluid, or extremely soft, water-saturated sediments under essentially zero effective stress, such as pelagic ooze Mavko, Mukerji, & Dvorkin (2020).

Figure 6-30 to Figure 6-35 provide plots of the elastic moduli by the bulk density of the soil, where the bulk density is calculated through the porosity and specific gravity of the soil and includes the saline pore fluid. These figures present a clear trend that the elastic moduli increase with increasing soil density. These figures also show that the lower clay content materials behave stiffer at lower soil densities i.e., have larger moduli values than higher clay content materials at the same density. Due to the compression behavior of the low clay content materials as compared to higher clay content material (smaller changes in porosity with changes in stress), the low clay content materials have a smaller range

of elastic moduli values over the 30 MPa stress range. This is attributed to the smaller range in soil densities due to the lower clay content materials being less compressible. For example, Figure 6-30 provides the shear modulus of the mixtures, the 10% clay mixture average shear modulus was found to range between 0.09 GPa and 1.07 GPa over an average density range of 2,033 kg/m^3 to 2,175 kg/m^3. The shear modulus of the 30% clay mixtures was found to range between average values of 0.14 GPa and 1.91 GPa over an average density range of 2,116 kg/m^3 to 2,302 kg/m^3. The shear modulus of the 40% clay mixtures was found to range between average values of 0.20 GPa and 2.34 GPa over an average density range of 2,064 kg/m^3 to 2,236 kg/m^3. The shear modulus of the RGoM_EI mixtures was found to range between average values of 0.12 GPa and 1.77 GPa over an average density range of 1,964 kg/m^3 to 2,354 kg/m^3.

Modeling of Soil Wave Velocity by Lithology and Effective Stress

Both the P and S wave velocities were fit using a power equation for the relationship between velocity and effective stress, popularized by Bowers (1995) as presented in Equation 6-10.

$$V = C + A{\sigma'}_a^{\,B} \qquad \text{Equation 6-10}$$

Where:

V = Velocity (length by time)

A = Material specific constant (m/s/MPa or ft/s/psi depending on measurement units)

B = Unitless material specific constant

C = Material specific constant for P wave speed of pore fluid (1,524 m/s for this study)

$\sigma a'$ = Axial Effective stress (stress)

The measurements of velocity by stress were fit with a power equation to get the A and B parameters. The C parameter was taken to be 1,524 m/s which corresponds the P wave velocity of 35 g/l saline solution. The C parameter was subtracted from the experimental data prior to being fit with the power equation. When Equation 6-10 is used for estimating shear wave velocities the material specific constant is zero (C=0) as fluids do not transmit shear waves. The A, B, and C parameters and the

coefficient of determination (R^2) value for the P wave fits are presented in Table 6-15. Plots of the A and B parameters for the P wave measurement models are provided by specimen clay content by mass in Figure 6-43 and Figure 6-44. The A, and B parameters and coefficient of determination (R^2) value for the S wave fits are presented in Table 6-16. Plots of the A and B parameters for the S wave measurement models are provided by specimen clay content by mass in Figure 6-45 and Figure 6-46.

Comparison of Modeled Velocities

This section provides a comparison between the author's fitted velocity measurements for RGoM_EI to similar data interpretations measured in the vertical direction in RGoM_EI specimens. Fits of P wave measurements are from Marjanovic (2016) and Ranjpour (2020). Fits of S Wave measurements are from Ranjpour (2020). Figure 6-47 provides a plot of the modeled P wave velocity curves, as well as the fitting parameters for the models. Figure 6-47 indicates a range in the predicted P wave velocities around 146 m/s at 1 MPA and increasing with increasing effective stress to be around 360 m/s at 30 MPa. The fit presented in Marjanovic (2016) based on average values from individual tests represents an upper bound of P wave velocities for this comparison. The lower bound is represented by the TCRS measurements from Ranjpour (2020). The variations between researchers are attributed to difference in experimental means and methods, difference in compensations of the compression curve for frictional effects and excess pore pressures, and variances in inherent errors due to specimen volume measurements. An average P wave velocity model is presented on Figure 6-47 for reference.

Figure 6-48 provides a plot of the modeled S wave velocity curves, as well as the fitting parameters for the models from this study and Ranjpour (2020). Figure 6-48 indicates a range in the predicted S wave velocities around 64 m/s at 1 MPA and increasing with increasing effective stress to be around 90 m/s at 30 MPa. The fit presented in Ranjpour (2020) based on triaxial test measurements represents an upper bound of S wave velocities for this comparison. The lower bound is represented by test CRS1629

from this study. The variations between the different S wave velocity measurements are much smaller than what was observed for the P wave velocities. This is attributed to S waves being generally insensitive to specimen pore fluid pressures. The variations between researchers are attributed to difference in experimental means and methods, difference in compensations of the compression curve for frictional effects and excess pore pressures, and variances in inherent errors due to specimen volume measurements. An average S wave velocity model is presented on Figure 6-48 for reference.

Table 6-1: Summary of test conditions during velocity measurements for CRS1652.

CRS1652 (10% Clay)						
Specimen Height	Axial Effective	Calculated Velocity		void ratio	porosity	Density
		P	S			
(m)	(MPa)	(m/s)	(m/s)		(%)	(g/cm^3)
0.0519	0.70	1667	231	0.614	0.380	2.047
0.0510	1.48	1704	292	0.587	0.370	2.064
0.0504	2.43	1751	335	0.568	0.362	2.076
0.0501	3.07	1759	354	0.557	0.358	2.084
0.0497	3.88	1777	383	0.546	0.353	2.092
0.0494	4.61	1803	407	0.537	0.349	2.098
0.0491	5.39	1825	433	0.529	0.346	2.104
0.0489	6.36	1834	453	0.519	0.342	2.110
0.0486	7.13	1854	465	0.513	0.339	2.115
0.0484	7.96	1860	479	0.506	0.336	2.120
0.0483	8.64	1874	491	0.501	0.334	2.124
0.0481	9.43	1888	504	0.495	0.331	2.128
0.0479	10.30	1903	524	0.490	0.329	2.132
0.0477	11.07	1906	532	0.485	0.327	2.135
0.0476	11.78	1908	543	0.481	0.325	2.139
0.0475	12.51	1927	551	0.477	0.323	2.142
0.0473	13.41	1927	564	0.472	0.321	2.145
0.0472	14.08	1939	573	0.468	0.319	2.148
0.0470	15.68	1954	593	0.461	0.315	2.154
0.0468	16.46	1969	604	0.457	0.314	2.157
0.0467	17.61	1982	618	0.452	0.311	2.161
0.0466	18.41	1997	625	0.448	0.309	2.164
0.0465	19.13	2002	633	0.445	0.308	2.166
0.0463	18.33	2000	642	0.441	0.306	2.170
0.0463	18.30	2004	643	0.441	0.306	2.170
0.0463	19.92	2019	652	0.439	0.305	2.171
0.0462	20.79	2019	656	0.437	0.304	2.173
0.0461	21.39	2027	660	0.435	0.303	2.174
0.0460	22.96	2043	677	0.430	0.301	2.179
0.0458	24.03	2053	683	0.426	0.299	2.182

Table 6-2: Summary of test conditions during velocity measurements for CRS1700.

CRS 1700 (10% Clay)						
Specimen Height	Axial Effective	Calculated Velocity		void ratio	porosity	Density
		P	S			
(m)	(MPa)	(m/s)	(m/s)		(%)	(g/cm^3)
0.0301	0.82	1732	188	0.657	0.397	2.020
0.0295	1.79	1772	302	0.627	0.385	2.038
0.0291	2.78	1778	346	0.607	0.378	2.051
0.0289	3.82	1797	385	0.591	0.371	2.061
0.0287	4.56	1820	401	0.581	0.367	2.068
0.0285	5.26	1834	423	0.573	0.364	2.073
0.0283	6.30	1852	445	0.562	0.360	2.081
0.0282	7.00	1864	462	0.555	0.357	2.085
0.0281	7.88	1879	478	0.547	0.354	2.091
0.0279	9.01	1896	499	0.538	0.350	2.097
0.0277	9.97	1913	516	0.529	0.346	2.104
0.0276	10.66	1923	527	0.524	0.344	2.107
0.0275	11.59	1942	543	0.517	0.341	2.112
0.0274	12.68	1953	558	0.511	0.338	2.116
0.0273	13.49	1966	569	0.506	0.336	2.120
0.0271	15.53	1991	596	0.494	0.331	2.129
0.0270	16.26	1997	606	0.490	0.329	2.132
0.0269	17.29	2008	616	0.485	0.326	2.136
0.0269	18.03	2017	623	0.481	0.325	2.139
0.0268	18.84	2021	631	0.477	0.323	2.142
0.0267	19.48	2035	639	0.474	0.321	2.144
0.0267	20.18	2043	647	0.471	0.320	2.146
0.0266	21.12	2056	659	0.466	0.318	2.150
0.0265	22.33	2065	670	0.461	0.316	2.154
0.0264	23.61	2083	682	0.456	0.313	2.158
0.0264	22.63	2083	685	0.455	0.313	2.158
0.0264	23.77	2090	688	0.453	0.312	2.160
0.0263	24.24	2091	691	0.452	0.311	2.161
0.0263	25.09	2094	697	0.449	0.310	2.163
0.0262	25.96	2106	706	0.446	0.308	2.165
0.0262	27.05	2121	722	0.442	0.307	2.169

Table 6-3: Summary of test conditions during velocity measurements for CRS1663.

CRS1663 (20% Clay)						
Specimen Height	Axial Effective Stress	Calculated Velocity		void ratio	porosity	Density
		P	S			
(m)	(MPa)	(m/s)	(m/s)		(%)	(g/cm^3)
0.0509	0.86	1721	273	0.615	0.381	2.050
0.0494	1.68	1766	334	0.569	0.363	2.081
0.0487	2.36	1794	374	0.545	0.353	2.097
0.0480	3.18	1825	406	0.523	0.343	2.113
0.0474	4.08	1854	441	0.503	0.335	2.127
0.0469	4.93	1879	465	0.488	0.328	2.138
0.0465	5.76	1902	491	0.476	0.322	2.148
0.0462	6.55	1921	513	0.465	0.317	2.156
0.0458	7.62	1943	541	0.452	0.311	2.166
0.0455	8.34	1959	556	0.445	0.308	2.172
0.0453	9.17	1980	579	0.436	0.304	2.179
0.0450	10.10	1995	591	0.428	0.300	2.185
0.0450	9.32	1991	595	0.427	0.299	2.186
0.0449	10.07	1998	596	0.426	0.299	2.187
0.0448	10.85	2001	605	0.422	0.297	2.190
0.0446	11.70	2022	620	0.415	0.293	2.196
0.0444	12.65	2036	640	0.408	0.290	2.202
0.0442	13.42	2043	655	0.403	0.287	2.206
0.0440	14.29	2058	670	0.397	0.284	2.211
0.0439	15.10	2070	682	0.392	0.282	2.215
0.0437	15.98	2085	693	0.387	0.279	2.220
0.0435	17.07	2100	707	0.380	0.276	2.225
0.0434	17.70	2108	715	0.377	0.274	2.228
0.0433	18.52	2124	723	0.373	0.272	2.232
0.0431	19.32	2130	733	0.369	0.270	2.235
0.0430	20.20	2143	744	0.365	0.267	2.239
0.0429	21.16	2151	754	0.360	0.265	2.243
0.0428	22.04	2169	764	0.356	0.263	2.247
0.0426	22.94	2173	775	0.353	0.261	2.250
0.0425	23.72	2195	783	0.349	0.259	2.253
0.0424	24.45	2199	793	0.347	0.257	2.256
0.0423	25.43	2209	805	0.343	0.255	2.259

Table 6-4: Summary of test conditions during velocity measurements for CRS1678.

CRS1678 (20% Clay)						
Specimen Height	Axial Effective Stress	Calculated Velocity		void ratio	porosity	Density
		P	S			
(m)	(MPa)	(m/s)	(m/s)		(%)	(g/cm^3)
0.0250	1.77	1764	335	0.604	0.377	2.058
0.0244	2.68	1818	378	0.569	0.363	2.081
0.0241	3.60	1863	417	0.545	0.353	2.097
0.0238	4.45	1902	446	0.526	0.345	2.110
0.0235	5.40	1917	478	0.509	0.337	2.122
0.0233	6.26	1928	502	0.496	0.331	2.133
0.0231	7.26	1942	527	0.482	0.325	2.143
0.0229	8.17	1970	547	0.470	0.320	2.152
0.0227	9.06	1991	568	0.460	0.315	2.160
0.0226	10.09	2026	591	0.449	0.310	2.168
0.0224	10.90	2048	606	0.441	0.306	2.174
0.0223	11.87	2066	625	0.432	0.302	2.182
0.0222	12.88	2076	642	0.424	0.298	2.189
0.0220	13.97	2091	662	0.415	0.293	2.196
0.0219	14.86	2121	675	0.408	0.290	2.201
0.0218	15.75	2137	686	0.402	0.287	2.207
0.0218	16.36	2138	695	0.398	0.285	2.210
0.0217	17.14	2160	706	0.393	0.282	2.215
0.0216	18.11	2159	717	0.386	0.279	2.220
0.0215	19.10	2181	730	0.380	0.276	2.225
0.0214	20.24	2201	743	0.374	0.272	2.231
0.0213	21.37	2209	755	0.367	0.269	2.237
0.0211	23.42	2234	781	0.357	0.263	2.246
0.0211	23.94	2249	787	0.354	0.262	2.249
0.0210	24.74	2261	796	0.350	0.259	2.252
0.0210	25.67	2264	807	0.346	0.257	2.256
0.0209	26.59	2276	815	0.342	0.255	2.260
0.0208	27.60	2288	825	0.337	0.252	2.264

Table 6-5: Summary of test conditions during velocity measurements for CRS1632.

CRS1632 (30% Clay)						
Specimen Height	Axial Effective Stress	Calculated Velocity		void ratio	porosity	Density
		P	S			
(m)	(MPa)	(m/s)	(m/s)		(%)	(g/cm^3)
0.0569	0.64	1658	226	0.735	0.424	1.998
0.0538	1.46	1715	324	0.639	0.390	2.055
0.0522	2.21	1779	382	0.593	0.372	2.085
0.0513	2.97	1831	415	0.563	0.360	2.105
0.0505	3.86	1871	455	0.539	0.350	2.122
0.0499	4.53	1899	473	0.522	0.343	2.134
0.0494	5.33	1928	519	0.505	0.336	2.146
0.0489	6.15	1953	538	0.491	0.330	2.157
0.0485	6.96	1976	552	0.478	0.323	2.167
0.0480	7.89	1993	586	0.464	0.317	2.178
0.0477	8.66	2029	606	0.453	0.312	2.186
0.0474	9.40	2044	619	0.444	0.307	2.194
0.0470	10.33	2078	652	0.433	0.302	2.203
0.0467	11.10	2092	665	0.424	0.298	2.210
0.0464	11.88	2114	686	0.416	0.294	2.217
0.0462	12.75	2133	700	0.408	0.290	2.224
0.0460	13.39	2149	713	0.403	0.287	2.228
0.0458	14.29	2169	729	0.395	0.283	2.235
0.0456	15.06	2186	742	0.390	0.280	2.240
0.0454	15.88	2206	754	0.384	0.277	2.245
0.0452	16.58	2215	766	0.379	0.275	2.249
0.0449	17.68	2232	780	0.370	0.270	2.257
0.0448	18.42	2243	790	0.366	0.268	2.261
0.0447	19.18	2259	803	0.362	0.266	2.265
0.0445	19.84	2266	818	0.358	0.263	2.268
0.0444	20.75	2290	832	0.352	0.261	2.273
0.0442	21.56	2288	840	0.348	0.258	2.277
0.0441	22.32	2300	856	0.344	0.256	2.281
0.0440	23.01	2313	865	0.341	0.254	2.284
0.0438	24.12	2329	883	0.336	0.251	2.289

Table 6-6: Summary of test conditions during velocity measurements for CRS1698.

CRS1698 (30% Clay)						
Specimen Height	Axial Effective Stress	Calculated Velocity		void ratio	porosity	Density
		P	S			
(m)	(MPa)	(m/s)	(m/s)		(%)	(g/cm^3)
0.0469	0.91	1751	296	0.634	0.388	2.057
0.0450	1.74	1802	373	0.569	0.363	2.100
0.0440	2.51	1862	421	0.533	0.347	2.125
0.0432	3.35	1910	485	0.504	0.335	2.146
0.0424	4.48	1957	517	0.476	0.322	2.168
0.0421	4.97	1981	542	0.466	0.318	2.175
0.0416	5.97	2019	570	0.448	0.309	2.190
0.0413	6.66	2039	601	0.437	0.304	2.199
0.0409	7.66	2073	627	0.423	0.298	2.210
0.0405	8.76	2093	649	0.411	0.291	2.221
0.0403	9.34	2115	669	0.405	0.288	2.226
0.0401	10.14	2134	685	0.397	0.284	2.233
0.0399	10.95	2148	702	0.389	0.280	2.239
0.0397	11.84	2176	724	0.382	0.276	2.246
0.0395	12.74	2189	740	0.375	0.273	2.252
0.0393	13.64	2215	759	0.368	0.269	2.258
0.0391	14.65	2234	783	0.361	0.265	2.264
0.0389	15.66	2249	798	0.355	0.262	2.270
0.0387	16.71	2276	816	0.348	0.258	2.276
0.0386	17.46	2290	829	0.344	0.256	2.280
0.0385	18.07	2290	840	0.341	0.254	2.283
0.0384	18.79	2316	845	0.337	0.252	2.287
0.0383	19.66	2334	863	0.333	0.250	2.291
0.0381	20.57	2332	874	0.328	0.247	2.295
0.0380	21.51	2345	888	0.324	0.245	2.299
0.0378	23.10	2374	911	0.317	0.241	2.306
0.0377	24.15	2390	926	0.313	0.238	2.310
0.0376	24.74	2404	928	0.311	0.237	2.312
0.0375	26.03	2426	939	0.306	0.234	2.317

Table 6-7: Summary of test conditions during velocity measurements for CRS1638.

CRS1638 (40% Clay)						
Specimen Height	Axial Effective Stress	Calculated Velocity		void ratio	porosity	Density
		P	S			
(m)	(MPa)	(m/s)	(m/s)		(%)	(g/cm^3)
0.0553	0.69	1728	254	0.688	0.408	2.038
0.0521	1.51	1845	330	0.591	0.371	2.100
0.0503	2.36	1908	396	0.536	0.349	2.139
0.0493	3.10	1940	488	0.505	0.336	2.161
0.0485	3.92	1987	549	0.479	0.324	2.181
0.0478	4.76	2034	579	0.460	0.315	2.197
0.0473	5.51	2053	614	0.444	0.308	2.209
0.0469	6.34	2092	633	0.430	0.301	2.221
0.0464	7.16	2118	669	0.417	0.294	2.232
0.0461	8.04	2139	686	0.406	0.289	2.242
0.0457	8.84	2168	709	0.396	0.284	2.250
0.0455	9.64	2191	731	0.388	0.279	2.257
0.0452	10.60	2210	748	0.378	0.274	2.266
0.0449	11.34	2235	765	0.370	0.270	2.273
0.0447	12.21	2247	778	0.363	0.266	2.280
0.0444	13.12	2269	793	0.356	0.262	2.287
0.0442	14.00	2284	812	0.349	0.259	2.293
0.0441	14.71	2300	826	0.344	0.256	2.297
0.0439	15.51	2317	843	0.339	0.253	2.303
0.0437	16.13	2325	855	0.335	0.251	2.307
0.0436	16.87	2347	875	0.330	0.248	2.311
0.0435	17.72	2355	903	0.326	0.246	2.315
0.0433	18.59	2373	908	0.320	0.243	2.320
0.0431	19.56	2389	921	0.316	0.240	2.324
0.0429	20.52	2405	930	0.311	0.237	2.330
0.0428	21.45	2421	942	0.307	0.235	2.333
0.0427	22.14	2440	950	0.304	0.233	2.337
0.0426	23.00	2439	961	0.299	0.230	2.341
0.0425	23.72	2459	986	0.296	0.229	2.344
0.0424	24.64	2463	992	0.293	0.226	2.348

Table 6-8: Summary of test conditions during velocity measurements for CRS1688.

CRS1688 (40% Clay)						
Specimen Height	Axial Effective Stress	Calculated Velocity		void ratio	porosity	Density
		P	S			
(m)	(MPa)	(m/s)	(m/s)		(%)	(g/cm^3)
0.0220	1.00	1781	311	0.644	0.392	2.065
0.0208	1.85	1868	401	0.554	0.357	2.125
0.0201	2.86	1926	473	0.496	0.332	2.167
0.0194	4.16	2025	543	0.449	0.310	2.205
0.0191	4.95	2051	578	0.428	0.300	2.222
0.0190	5.44	2088	595	0.417	0.294	2.231
0.0187	6.77	2136	638	0.392	0.281	2.253
0.0184	8.08	2201	675	0.372	0.271	2.271
0.0183	8.70	2208	693	0.363	0.266	2.279
0.0181	9.53	2229	715	0.353	0.261	2.288
0.0180	10.54	2244	735	0.342	0.255	2.299
0.0179	11.48	2280	756	0.333	0.250	2.308
0.0178	12.23	2297	771	0.326	0.246	2.315
0.0177	13.21	2312	790	0.317	0.241	2.323
0.0175	14.22	2335	809	0.309	0.236	2.331
0.0174	15.49	2388	829	0.300	0.231	2.340
0.0174	16.02	2394	836	0.296	0.228	2.344
0.0173	16.80	2397	849	0.291	0.225	2.350
0.0172	17.86	2418	865	0.284	0.221	2.357
0.0171	19.31	2457	884	0.276	0.216	2.365
0.0170	19.90	2451	893	0.272	0.214	2.369
0.0170	21.16	2481	907	0.266	0.210	2.376
0.0169	21.84	2511	914	0.262	0.208	2.380
0.0168	23.90	2544	937	0.252	0.201	2.391
0.0167	25.52	2544	955	0.245	0.197	2.399
0.0166	26.23	2569	962	0.241	0.194	2.402
0.0166	27.26	2567	971	0.237	0.192	2.407
0.0165	27.64	2588	975	0.235	0.190	2.409
0.0165	28.35	2614	984	0.232	0.189	2.413

Table 6-9: Summary of test conditions during velocity measurements for CRS1633.

CRS1633 (50% Clay)						
Specimen Height	Axial Effective Stress	Calculated Velocity		void ratio	porosity	Density
		P	S			
(m)	(MPa)	(m/s)	(m/s)		(%)	(g/cm^3)
0.0542	0.73	1656	263	0.756	0.431	2.015
0.0505	1.62	1754	369	0.635	0.388	2.089
0.0486	2.49	1821	439	0.575	0.365	2.130
0.0476	3.18	1862	464	0.543	0.352	2.153
0.0467	4.00	1892	525	0.514	0.339	2.174
0.0458	5.08	1937	561	0.485	0.326	2.197
0.0453	5.75	1987	595	0.468	0.319	2.210
0.0449	6.47	2013	609	0.454	0.312	2.222
0.0444	7.40	2042	645	0.438	0.305	2.235
0.0440	8.36	2074	669	0.426	0.299	2.245
0.0437	9.05	2070	688	0.415	0.293	2.255
0.0434	9.91	2114	707	0.406	0.289	2.262
0.0431	10.81	2139	721	0.395	0.283	2.272
0.0428	11.67	2139	736	0.387	0.279	2.279
0.0426	12.39	2163	748	0.380	0.276	2.285
0.0424	13.08	2181	760	0.375	0.273	2.291
0.0423	13.84	2178	772	0.370	0.270	2.295
0.0421	14.54	2210	785	0.364	0.267	2.300
0.0418	15.81	2238	801	0.356	0.262	2.308
0.0416	16.84	2250	837	0.348	0.258	2.316
0.0414	17.91	2271	855	0.342	0.255	2.322
0.0413	18.79	2290	873	0.337	0.252	2.327
0.0412	19.42	2292	881	0.333	0.250	2.330
0.0411	20.06	2302	888	0.330	0.248	2.333
0.0409	20.98	2317	885	0.325	0.246	2.338
0.0408	21.90	2336	898	0.322	0.244	2.341
0.0407	22.76	2345	906	0.318	0.241	2.345
0.0405	23.57	2352	944	0.314	0.239	2.350
0.0404	24.37	2360	946	0.310	0.237	2.353
0.0403	25.38	2375	950	0.306	0.234	2.357

Table 6-10: Summary of test conditions during velocity measurements for CRS1693.

CRS1693 (50% Clay)						
Specimen Height	Axial Effective Stress	Calculated Velocity		void ratio	porosity	Density
		P	S			
(m)	(MPa)	(m/s)	(m/s)		(%)	(g/cm^3)
0.0402	0.87	1750	253	0.726	0.421	2.032
0.0373	1.95	1839	415	0.605	0.377	2.108
0.0363	2.71	1901	478	0.561	0.359	2.138
0.0355	3.56	1949	515	0.526	0.345	2.164
0.0347	4.66	2004	562	0.491	0.329	2.191
0.0342	5.46	2035	599	0.469	0.319	2.209
0.0337	6.34	2078	643	0.450	0.310	2.224
0.0334	7.20	2111	675	0.435	0.303	2.237
0.0330	8.31	2147	697	0.419	0.295	2.251
0.0327	9.38	2175	734	0.405	0.288	2.262
0.0325	10.20	2193	753	0.396	0.284	2.270
0.0323	11.16	2217	810	0.387	0.279	2.279
0.0321	11.99	2242	812	0.379	0.275	2.286
0.0319	12.92	2258	812	0.371	0.271	2.293
0.0318	13.62	2271	821	0.366	0.268	2.298
0.0316	14.49	2297	830	0.360	0.264	2.304
0.0315	15.35	2314	845	0.354	0.261	2.310
0.0313	16.41	2333	857	0.347	0.258	2.316
0.0312	17.48	2354	870	0.341	0.254	2.322
0.0311	18.52	2366	881	0.335	0.251	2.327
0.0310	19.29	2389	891	0.332	0.249	2.330
0.0309	20.06	2397	901	0.328	0.247	2.334
0.0308	20.71	2414	909	0.325	0.245	2.337
0.0308	21.41	2428	919	0.322	0.244	2.340
0.0307	22.20	2429	929	0.319	0.242	2.344
0.0306	23.22	2448	944	0.314	0.239	2.348
0.0305	24.21	2464	956	0.310	0.237	2.352
0.0303	26.55	2497	982	0.302	0.232	2.361
0.0302	27.45	2511	991	0.299	0.230	2.364

Table 6-11: Summary of test conditions during velocity measurements for CRS1646.

CRS1646 (60% Clay)						
Specimen Height	Axial Effective Stress	Calculated Velocity		void ratio	porosity	Density
		P	S			
(m)	(MPa)	(m/s)	(m/s)		(%)	(g/cm^3)
0.0545	0.78	1690	247	0.835	0.455	1.984
0.0507	1.63	1787	350	0.706	0.414	2.057
0.0487	2.49	1846	413	0.639	0.390	2.099
0.0475	3.28	1887	458	0.598	0.374	2.126
0.0465	4.13	1930	508	0.565	0.361	2.149
0.0457	5.03	1963	534	0.537	0.349	2.170
0.0450	5.92	1998	591	0.515	0.340	2.187
0.0444	6.84	2030	602	0.495	0.331	2.202
0.0440	7.68	2053	638	0.480	0.324	2.214
0.0435	8.64	2078	657	0.465	0.317	2.227
0.0432	9.46	2107	675	0.454	0.312	2.236
0.0429	10.23	2120	693	0.444	0.308	2.244
0.0426	11.22	2143	711	0.434	0.302	2.253
0.0424	12.01	2159	725	0.426	0.299	2.259
0.0421	12.89	2185	735	0.418	0.295	2.267
0.0419	13.83	2200	748	0.410	0.291	2.274
0.0417	14.65	2210	761	0.403	0.287	2.280
0.0415	15.53	2231	778	0.397	0.284	2.285
0.0413	16.41	2243	791	0.390	0.281	2.291
0.0411	17.26	2255	818	0.385	0.278	2.296
0.0409	18.26	2270	831	0.379	0.275	2.302
0.0408	19.19	2284	866	0.373	0.272	2.307
0.0407	19.91	2298	867	0.369	0.270	2.311
0.0406	20.61	2302	869	0.365	0.268	2.314
0.0404	21.40	2317	873	0.361	0.265	2.318
0.0403	22.49	2329	885	0.356	0.262	2.323
0.0400	24.33	2361	956	0.348	0.258	2.331
0.0399	25.12	2361	958	0.345	0.256	2.334
0.0398	26.18	2381	955	0.340	0.254	2.339

Table 6-12: Summary of test conditions during velocity measurements for CRS1679.

CRS1679 (60% Clay)						
Specimen Height	Axial Effective Stress	Calculated Velocity		void ratio	porosity	Density
		P	S			
(m)	(MPa)	(m/s)	(m/s)		(%)	(g/cm^3)
0.0387	0.70	1652	242	0.879	0.468	1.960
0.0376	0.91	1677	263	0.826	0.452	1.987
0.0351	1.82	1758	348	0.703	0.413	2.057
0.0335	2.78	1825	412	0.627	0.385	2.106
0.0325	3.78	1876	467	0.578	0.366	2.139
0.0319	4.64	1913	504	0.548	0.354	2.161
0.0314	5.42	1939	534	0.526	0.345	2.178
0.0310	6.34	1972	566	0.504	0.335	2.195
0.0305	7.45	2007	594	0.482	0.325	2.212
0.0301	8.60	2043	626	0.463	0.316	2.227
0.0298	9.84	2073	648	0.446	0.309	2.241
0.0296	10.78	2100	678	0.434	0.303	2.251
0.0295	11.21	2110	691	0.429	0.300	2.256
0.0292	12.53	2133	719	0.415	0.294	2.268
0.0291	12.88	2140	725	0.412	0.292	2.271
0.0289	14.04	2171	740	0.401	0.286	2.281
0.0287	15.11	2193	754	0.391	0.281	2.289
0.0285	16.30	2214	769	0.381	0.276	2.299
0.0283	17.17	2225	784	0.375	0.273	2.304
0.0282	18.01	2236	797	0.369	0.270	2.310
0.0280	19.13	2258	809	0.361	0.265	2.318
0.0279	20.12	2271	818	0.353	0.261	2.325
0.0278	21.00	2293	827	0.348	0.258	2.330
0.0277	21.93	2306	838	0.343	0.255	2.335
0.0276	22.78	2305	848	0.338	0.252	2.340
0.0274	24.61	2343	868	0.327	0.247	2.350
0.0273	25.52	2355	879	0.323	0.244	2.355
0.0272	22.98	2361	898	0.322	0.243	2.356
0.0272	25.10	2356	896	0.319	0.242	2.359
0.0271	26.54	2374	898	0.315	0.240	2.363
0.0270	27.52	2389	903	0.312	0.238	2.366
0.0270	28.42	2387	909	0.309	0.236	2.370

Table 6-13: Summary of test conditions during velocity measurements for CRS1629.

CRS1629 (RGoM_EI Clay)						
		Calculated Velocity				
Specimen Height	Axial Effective Stress	P	S	void ratio	porosity	Density
(m)	(MPa)	(m/s)	(m/s)		(%)	(g/cm^3)
0.0618	0.70	1675		0.936	0.483	1.940
0.0567	1.65	1704	290	0.776	0.437	2.023
0.0547	2.35	1736	344	0.713	0.416	2.059
0.0528	3.27	1774	397	0.654	0.395	2.096
0.0515	4.23	1908	433	0.612	0.380	2.124
0.0507	4.97	1896	478	0.588	0.370	2.141
0.0499	5.88	1895	482	0.563	0.360	2.158
0.0494	6.61	1909	522	0.547	0.353	2.170
0.0487	7.61	1936	544	0.527	0.345	2.185
0.0482	8.52	1968	577	0.511	0.338	2.198
0.0475	9.34	2003	604	0.487	0.328	2.216
0.0461	11.18	1994	605	0.443	0.307	2.253
0.0456	12.95	2009	665	0.428	0.300	2.266
0.0456	12.94	2019	667	0.428	0.300	2.266
0.0454	12.96	2024	665	0.424	0.298	2.269
0.0451	13.48	2047	671	0.411	0.291	2.280
0.0446	14.93	2077	704	0.396	0.284	2.294
0.0442	15.98	2101	721	0.386	0.278	2.304
0.0441	16.85	2100	723	0.380	0.275	2.309
0.0438	18.03	2135	747	0.371	0.270	2.318
0.0436	18.79	2149	750	0.367	0.268	2.321
0.0435	19.54	2159	758	0.362	0.266	2.326
0.0433	20.36	2171	765	0.356	0.262	2.332
0.0430	21.66	2176	783	0.348	0.258	2.339
0.0429	22.51	2197	796	0.345	0.256	2.343
0.0428	23.41	2217	814	0.340	0.254	2.347
0.0427	24.19	2224	821	0.336	0.252	2.351
0.0425	25.09	2223	829	0.332	0.250	2.355
0.0425	25.79	2228	833	0.330	0.248	2.357
0.0423	27.01	2227	830	0.324	0.245	2.363
0.0421	27.90	2259	844	0.320	0.243	2.367
0.0421	27.63	2266	845	0.319	0.242	2.368

Table 6-14: Summary of test conditions during velocity measurements for CRS1672.

CRS1672 (RGoM_EI Clay)						
		Calculated Velocity				
Specimen Height	Axial Effective Stress	P	S	void ratio	porosity	Density
(m)	(MPa)	(m/s)	(m/s)		(%)	(g/cm^3)
0.0435	0.87	1663	243	0.883	0.469	1.964
0.0399	1.92	1757	356	0.727	0.421	2.049
0.0387	2.71	1801	390	0.673	0.402	2.083
0.0376	3.62	1838	439	0.628	0.386	2.112
0.0367	4.73	1882	482	0.587	0.370	2.141
0.0361	5.49	1926	513	0.562	0.360	2.158
0.0355	6.53	1944	547	0.535	0.349	2.178
0.0351	7.26	1965	568	0.518	0.341	2.191
0.0346	8.39	2009	594	0.496	0.332	2.208
0.0343	9.15	2020	616	0.484	0.326	2.218
0.0339	10.18	2065	642	0.468	0.319	2.231
0.0336	11.17	2068	661	0.454	0.312	2.242
0.0334	12.08	2102	685	0.443	0.307	2.252
0.0331	13.11	2114	698	0.432	0.302	2.262
0.0329	13.97	2136	714	0.422	0.297	2.270
0.0327	14.80	2151	733	0.416	0.294	2.276
0.0325	15.82	2164	751	0.405	0.288	2.285
0.0323	16.80	2168	758	0.399	0.285	2.291
0.0321	17.74	2208	807	0.390	0.281	2.299
0.0320	18.68	2201	813	0.384	0.277	2.305
0.0318	19.73	2226	813	0.377	0.274	2.311
0.0317	20.62	2231	822	0.372	0.271	2.316
0.0316	21.41	2246	825	0.367	0.269	2.320
0.0315	22.38	2259	839	0.361	0.265	2.326
0.0313	23.22	2266	841	0.356	0.263	2.331
0.0312	24.24	2287	851	0.351	0.260	2.336
0.0311	25.24	2302	862	0.346	0.257	2.341
0.0309	27.33	2327	878	0.336	0.251	2.351
0.0308	28.22	2329	886	0.333	0.250	2.353

Table 6-15: Summary of P wave power equation fits for TCRS tests.

Test Number	CRS1652	CRS1700	CRE1663	CRS1678	CRS1632	CRS1698	CRS1638	CRS1688	CRS1633	CRS1693	CRS1646	CRS1679	CRS1629	CRS1672
Clay Content	10%	10%	20%	20%	30%	30%	40%	40%	50%	50%	60%	60%	63% (RGoM_EI)	63% (RGoM_EI)
A (m/s/MPa)	157	188	197	193	172	232	262	268	183	247	210	172	163	167
B	0.37	0.33	0.38	0.41	0.49	0.42	0.40	0.42	0.49	0.42	0.44	0.50	0.45	0.48
C (m/s)	1,524	1,524	1,524	1,524	1,524	1,524	1,524	1,524	1,524	1,524	1,524	1,524	1,524	1,524
A (ft/s/psi)	80	118	98	81	48	95	115	108	52	98	77	48	56	50
B	0.37	0.33	0.38	0.41	0.49	0.42	0.40	0.42	0.49	0.42	0.44	0.50	0.45	0.48
C (ft/s)	5,000	5,000	5,000	5,000	5,000	5,000	5,000	5,000	5,000	5,000	5,000	5,000	5,000	5,000
R^2	0.995	0.980	0.998	0.997	0.997	0.999	0.998	0.997	0.992	0.998	0.996	0.995	0.984	0.994

Table 6-16: Summary of S wave power equation fits for TCRS tests.

Test Number	CRS1652	CRS1700	CRE1663	CRS1678	CRS1632	CRS1698	CRS1638	CRS1688	CRS1633	CRS1693	CRS1646	CRS1679	CRS1629	CRS1672
Clay Content	10%	10%	20%	20%	30%	30%	40%	40%	50%	50%	60%	60%	63% (RGoM_EI)	63% (RGoM_EI)
A (m/s/MPa)	254	232	282	273	277	310	306	332	314	320	293	285	256	273
B	0.31	0.35	0.32	0.33	0.36	0.34	0.37	0.33	0.35	0.35	0.36	0.36	0.36	0.37
A (ft/s/psi)	178	137	186	171	149	184	156	210	183	179	157	159	135	146
B	0.31	0.35	0.32	0.33	0.36	0.34	0.37	0.33	0.35	0.35	0.36	0.36	0.36	0.37
R^2	0.998	0.996	0.999	0.999	0.999	0.999	0.991	0.996	0.996	0.981	0.994	0.995	0.994	0.994

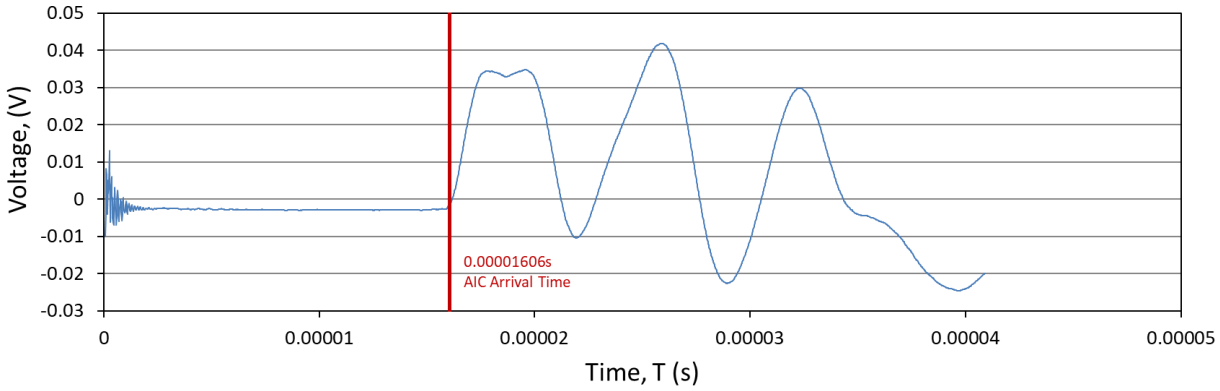


Figure 6-1: AIC selected P-wave arrival time for 25 MPa stress level of test CRS1672 a RGoM_EI specimen. The red line indicates the arrival time select by the automated method.

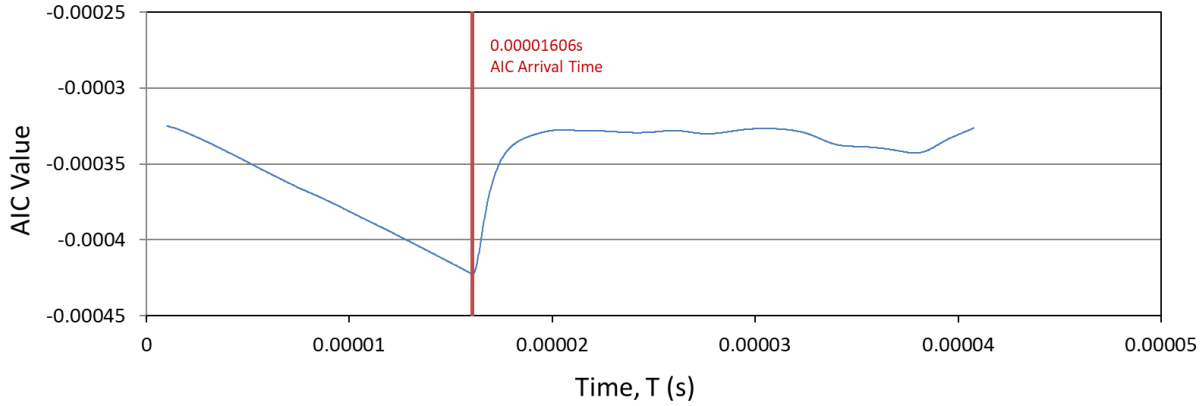


Figure 6-2: AIC series for P-wave arrival time selection for 25 MPa stress level of test CRS1672 a RGoM_EI specimen. The red line indicates the global minimum of the AIC series that corresponds to the automated selected arrival time.

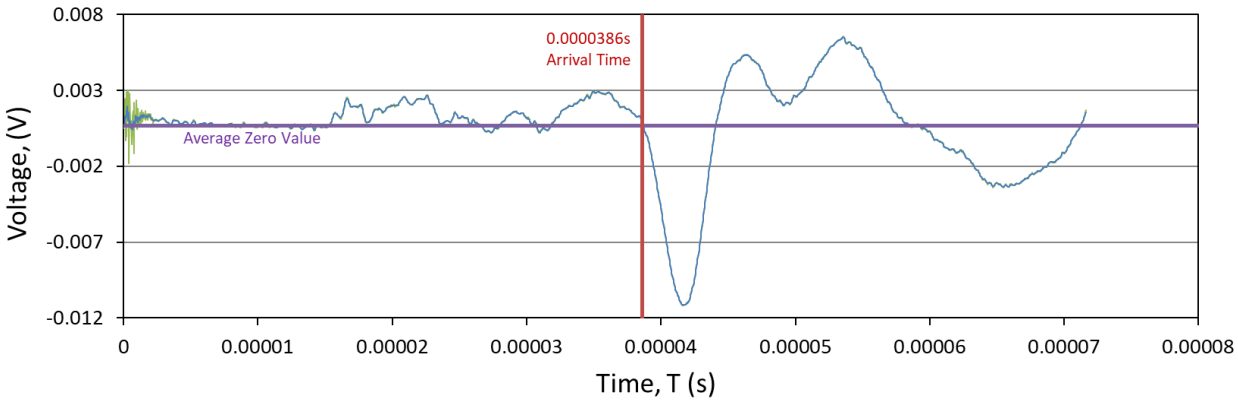


Figure 6-3: Comparison of S-waves collected at a 5 MPa effective stress level and a 25 MPa effective stress level during TCRS test CRS 1672 performed on a RGoM_EI test specimen.

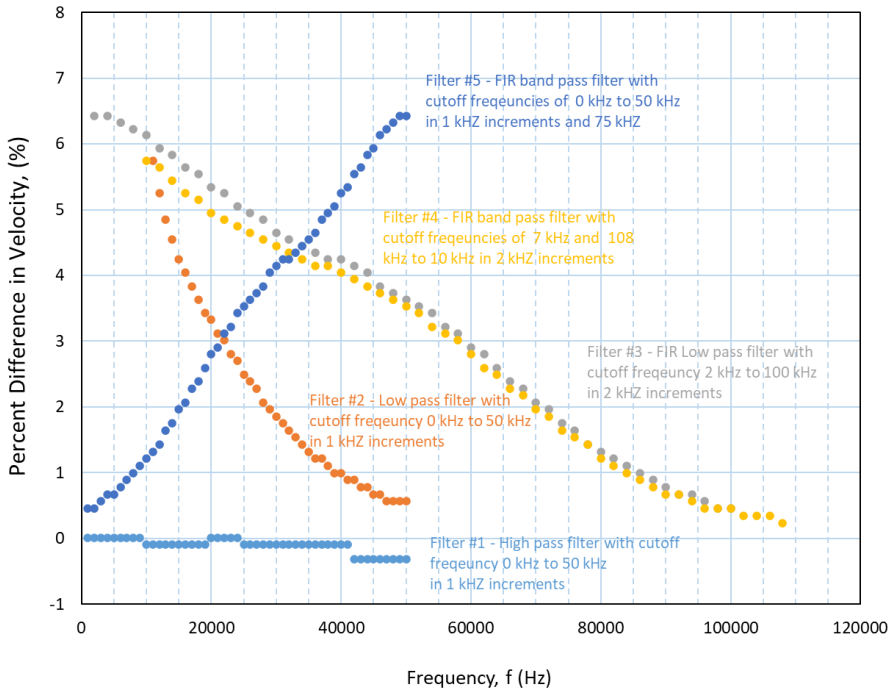


Figure 6-4: Example comparison of relative percent difference in wave velocity for S wave measured at 5 MPa in CRS1688 a 60% clay specimen. The frequency represents the cutoff frequency input for each filter, the cutoff frequency was incremented as discussed in Section 6.2. The presented difference in velocity is the percent difference between the calculated velocity with the associated cutoff frequency and filter combination relative to the calculated velocity without filtering.

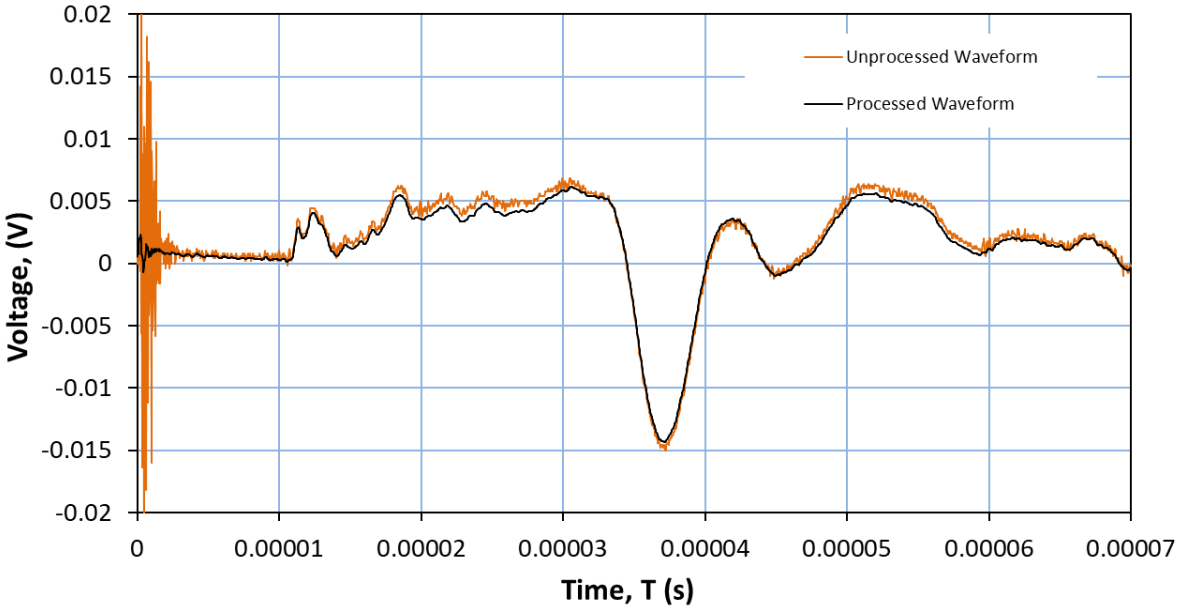


Figure 6-5: Comparison of processed and unprocessed S-waves collected at a 5 MPa stress level of CRS1688 a 60% clay specimen. The processed S wave has been subjected to a moving average interval of 11 points and a 7 kHz high pass filter.

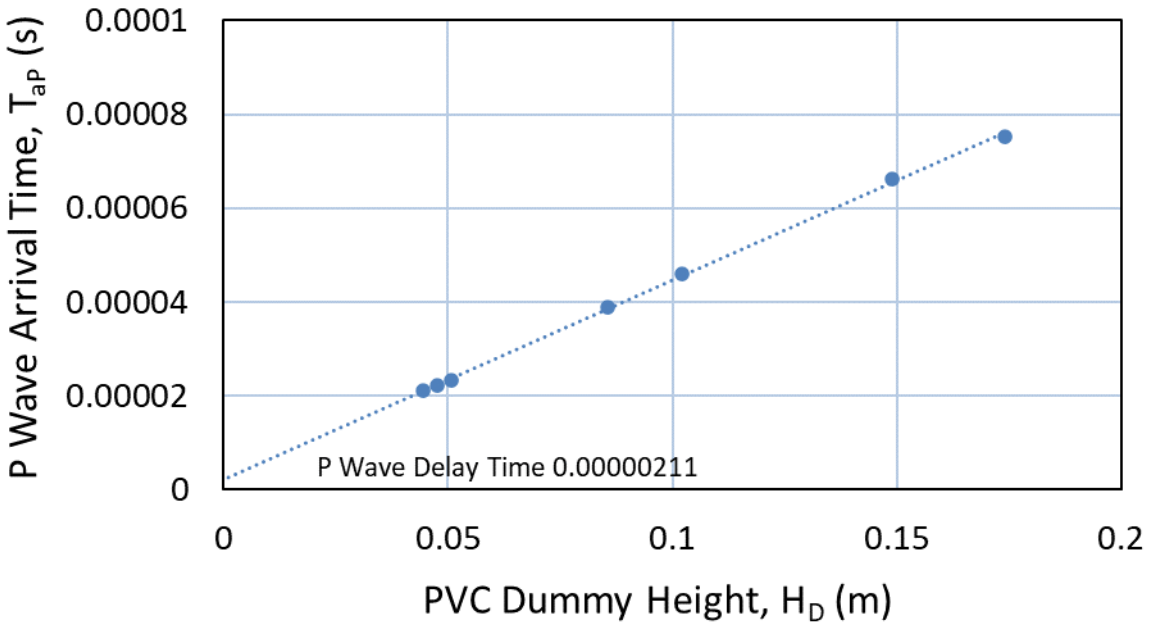


Figure 6-6: Determination of inherent delay in the system when measuring P Waves. The delay was selected as the Y intercept of a linear fit through the dummy measurements and determined to be 0.00000211 seconds.

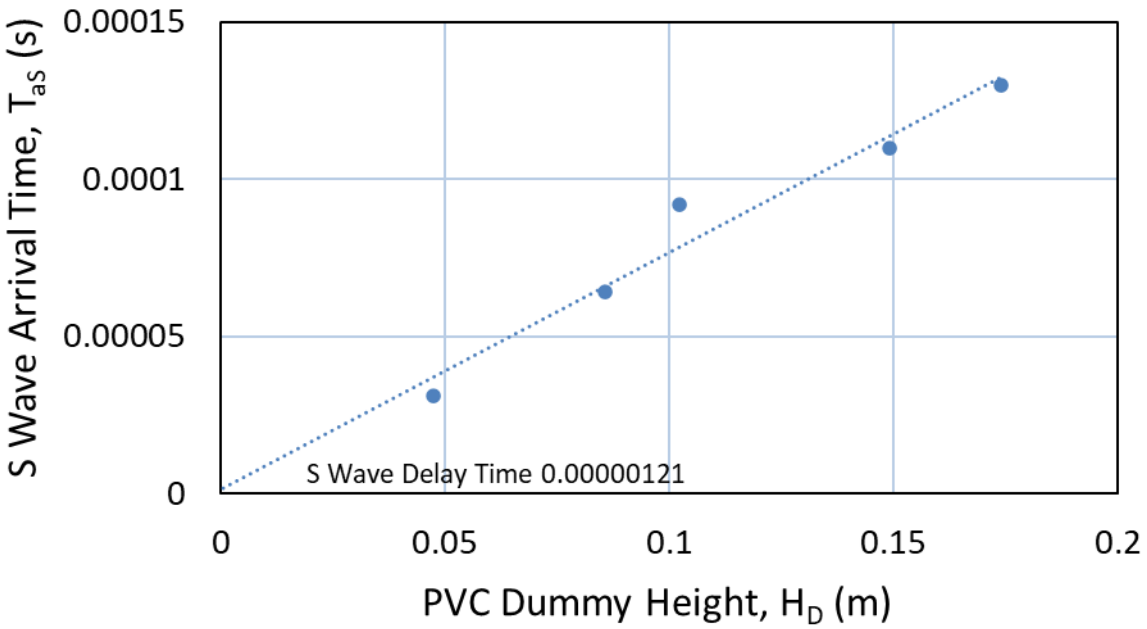


Figure 6-7: Determination of inherent delay in the system when measuring S Waves. The delay was selected as the Y intercept of a linear fit through the dummy measurements and determined to be 0.00000121 seconds.

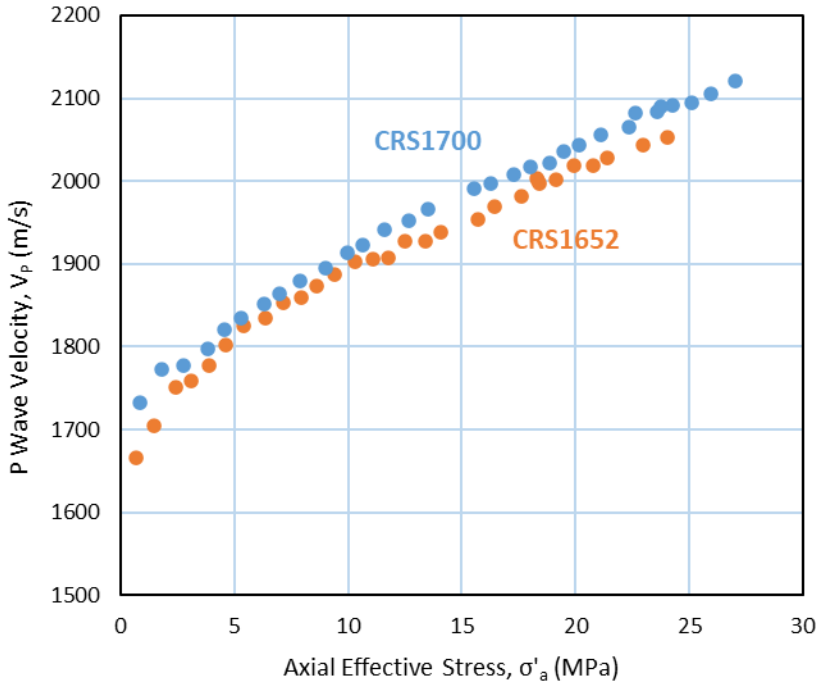


Figure 6-8: Measured P wave velocity by axial effective stress for 10% clay specimens.

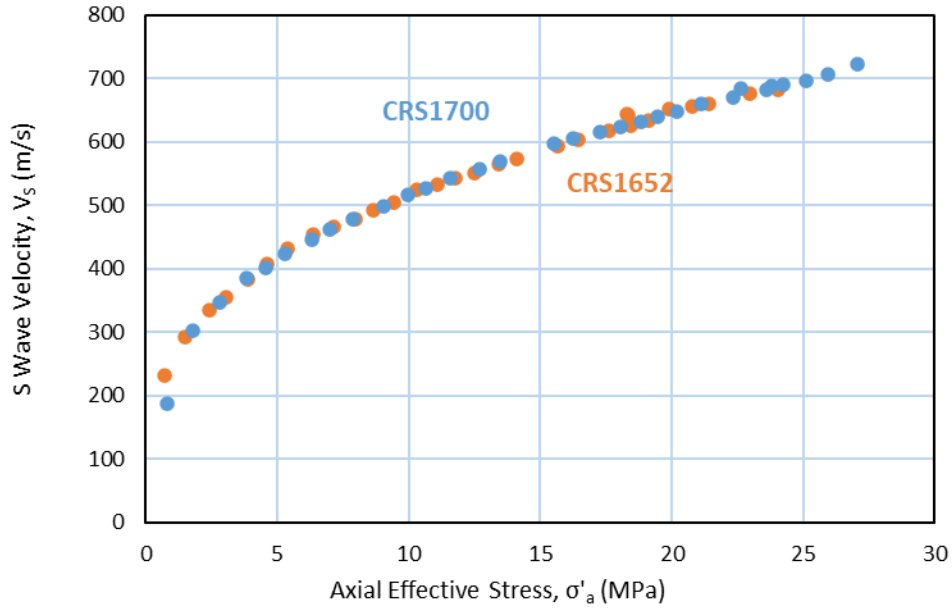


Figure 6-9: Measured S wave velocity by axial effective stress for 10% clay specimens.

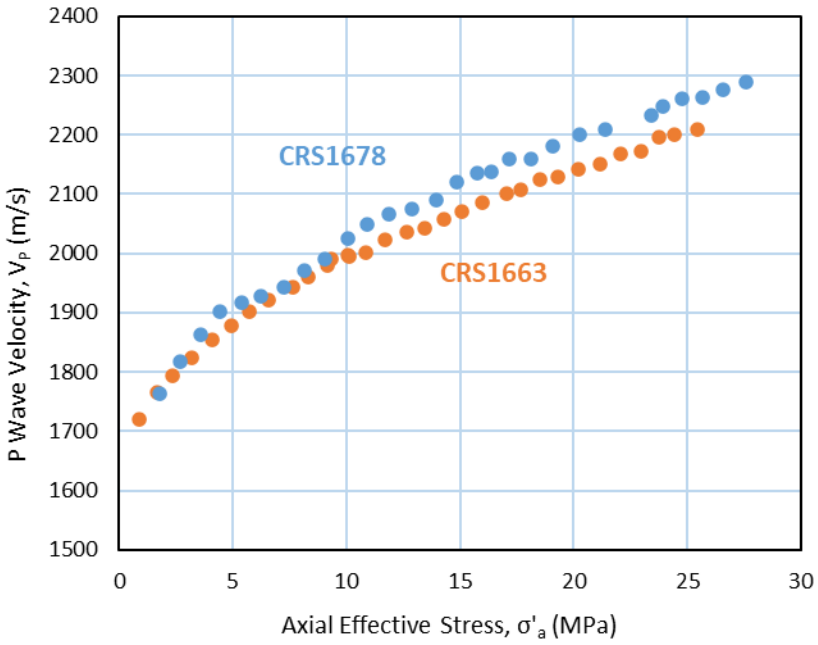


Figure 6-10: Measured P wave velocity by axial effective stress for 20% clay specimens.

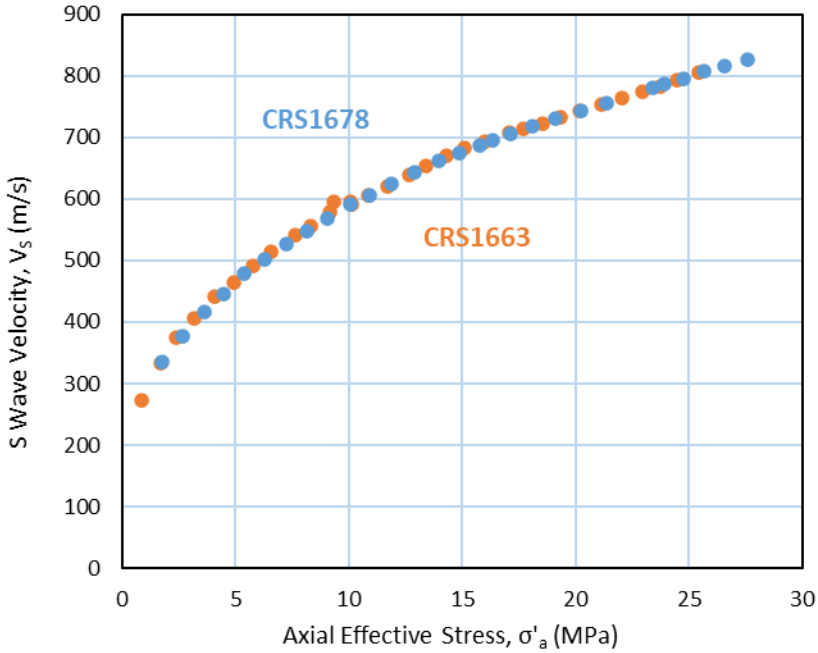


Figure 6-11: Measured S wave velocity by axial effective stress for 20% clay specimens.

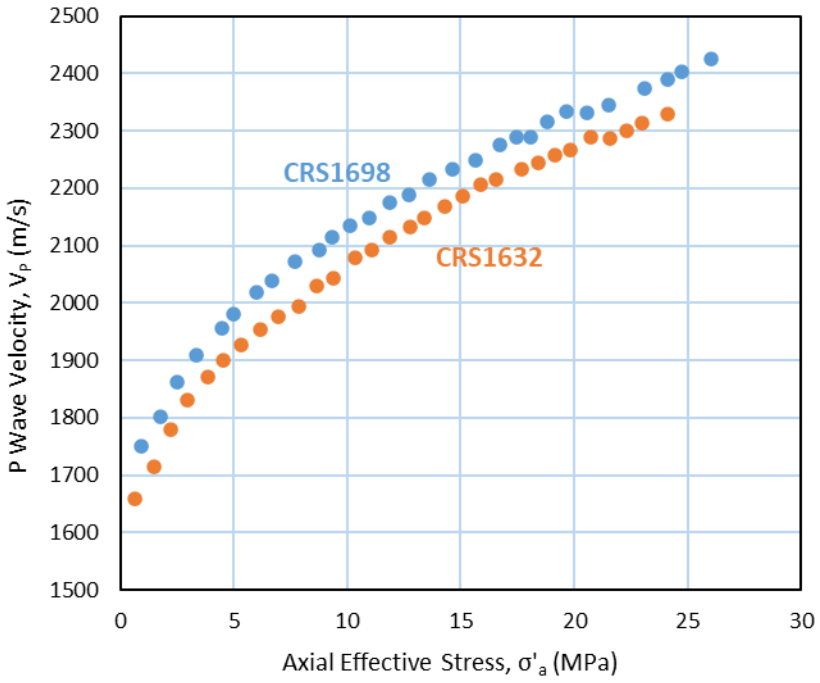


Figure 6-12: Measured P wave velocity by axial effective stress for 30% clay specimens.

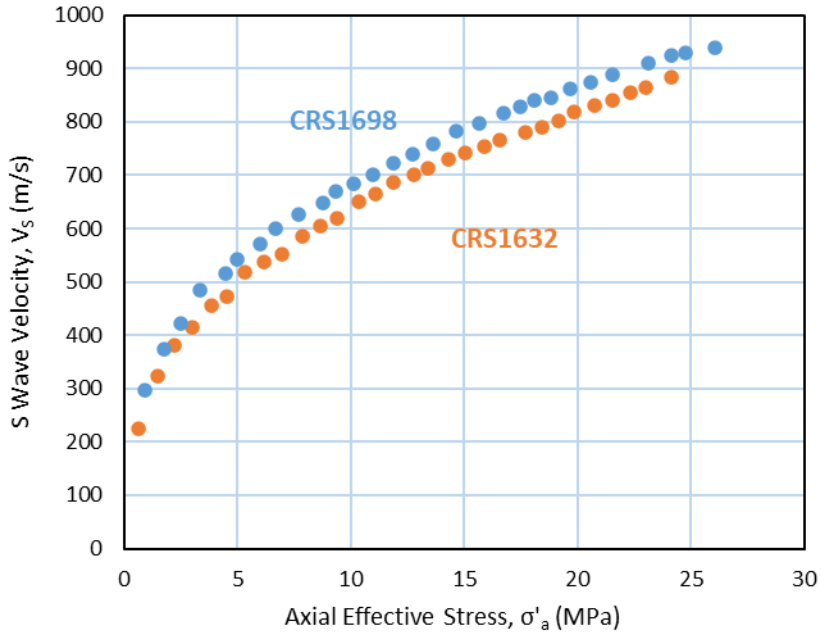


Figure 6-13: Measured P wave velocity by axial effective stress for 30% clay specimens.

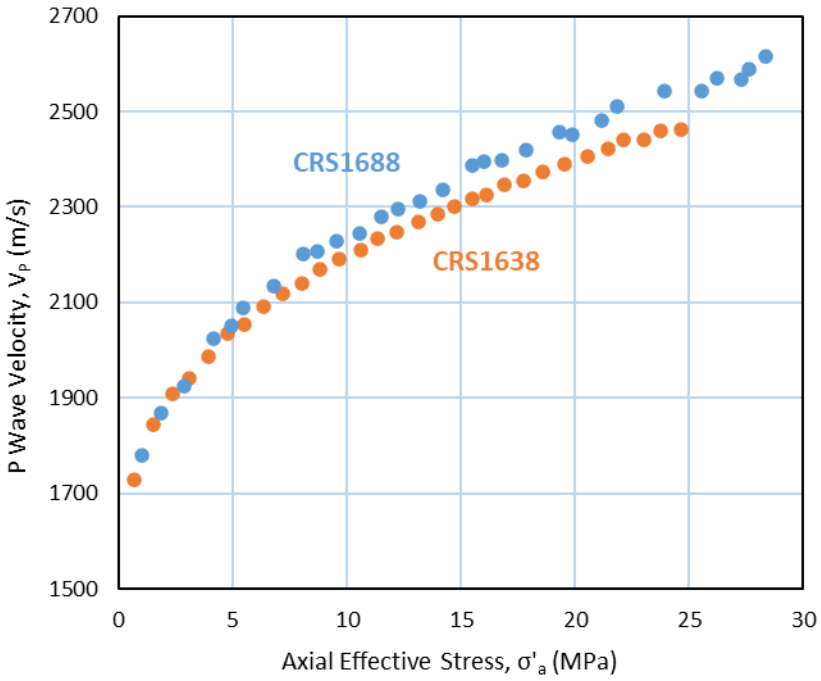


Figure 6-14: Measured P wave velocity by axial effective stress for 40% clay specimens.

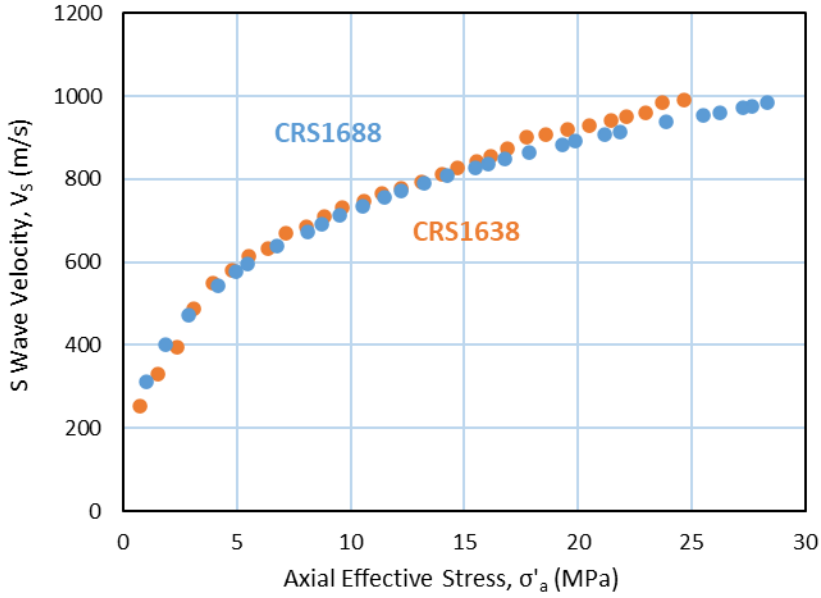


Figure 6-15: Measured P wave velocity by axial effective stress for 40% clay specimens.

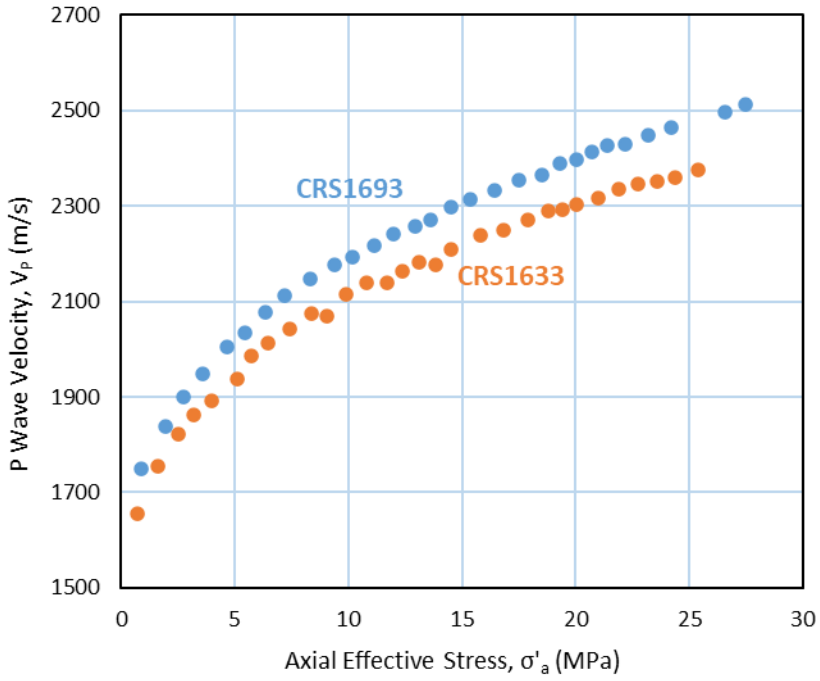


Figure 6-16: Measured P wave velocity by axial effective stress for 50% clay specimens.

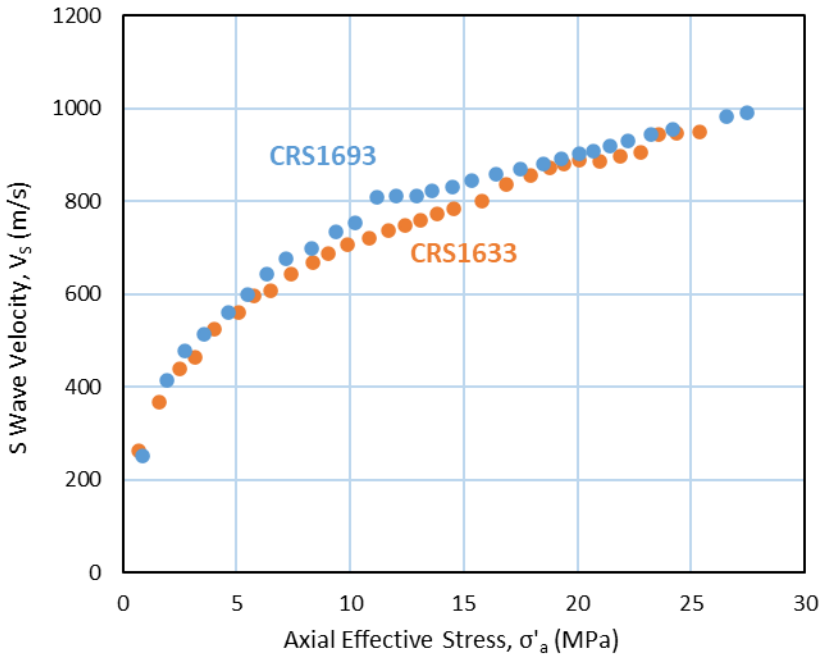


Figure 6-17: Measured P wave velocity by axial effective stress for 50% clay specimens.

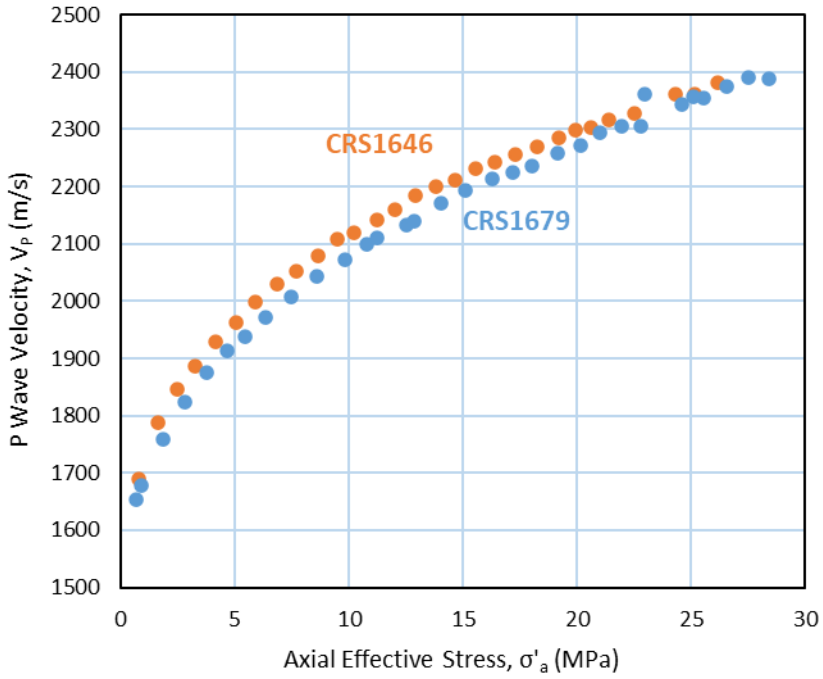


Figure 6-18: Measured P wave velocity by axial effective stress for 60% clay specimens.

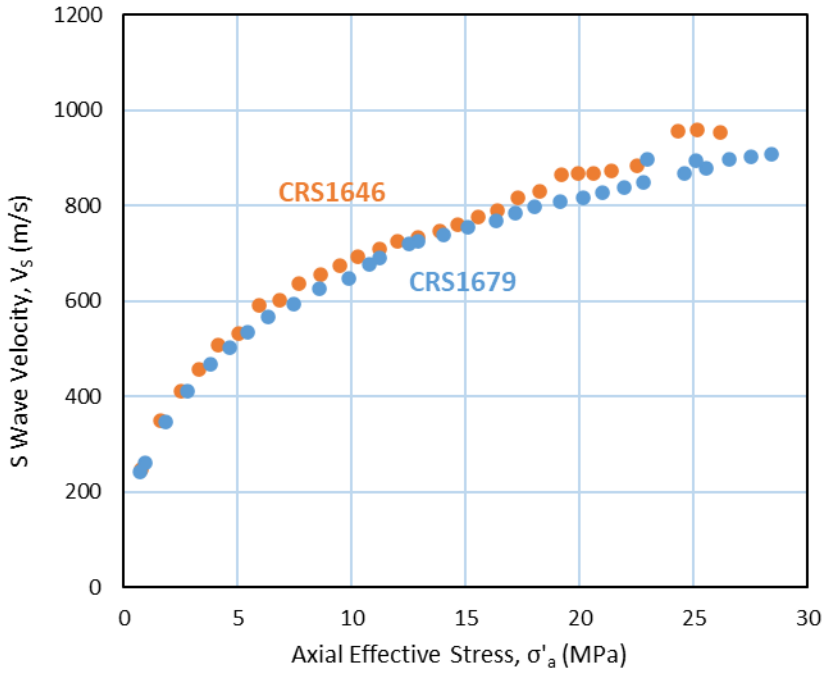


Figure 6-19: Measured P wave velocity by axial effective stress for 60% clay specimens.

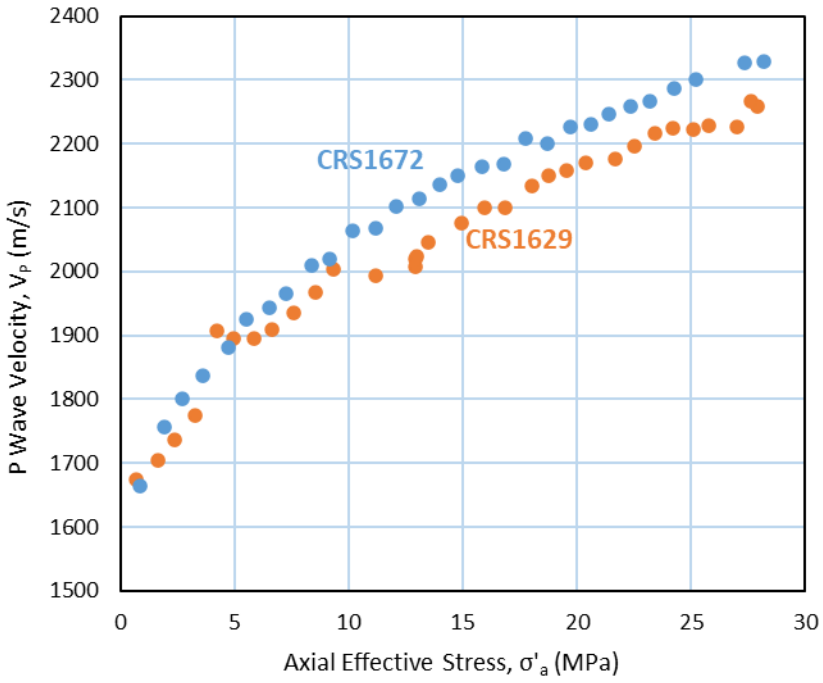


Figure 6-20: Measured P wave velocity by axial effective stress for RGoM_EI specimens.

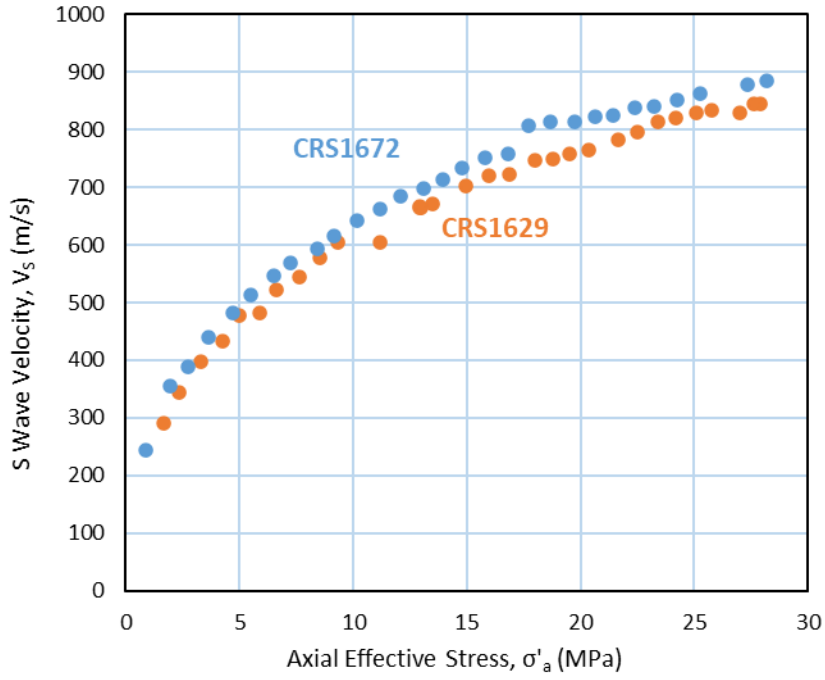


Figure 6-21: Measured P wave velocity by axial effective stress RGoM_EI specimens.

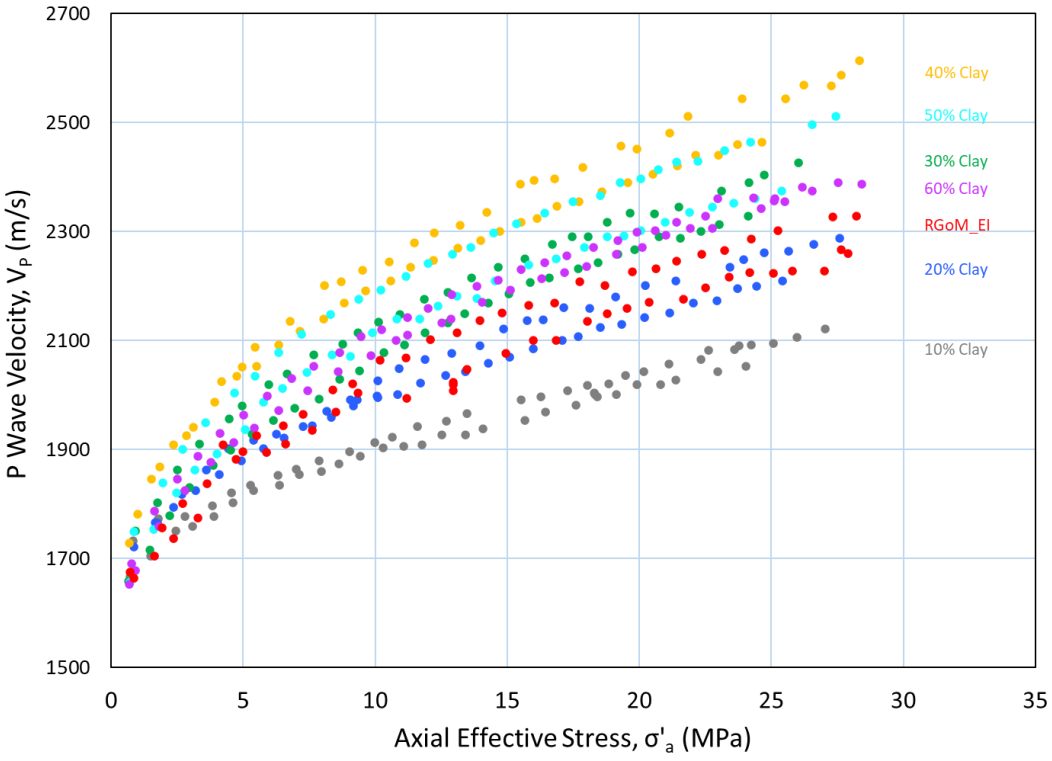


Figure 6-22: Measured P wave velocity by axial effective stress for all studied silt-clay mixtures.

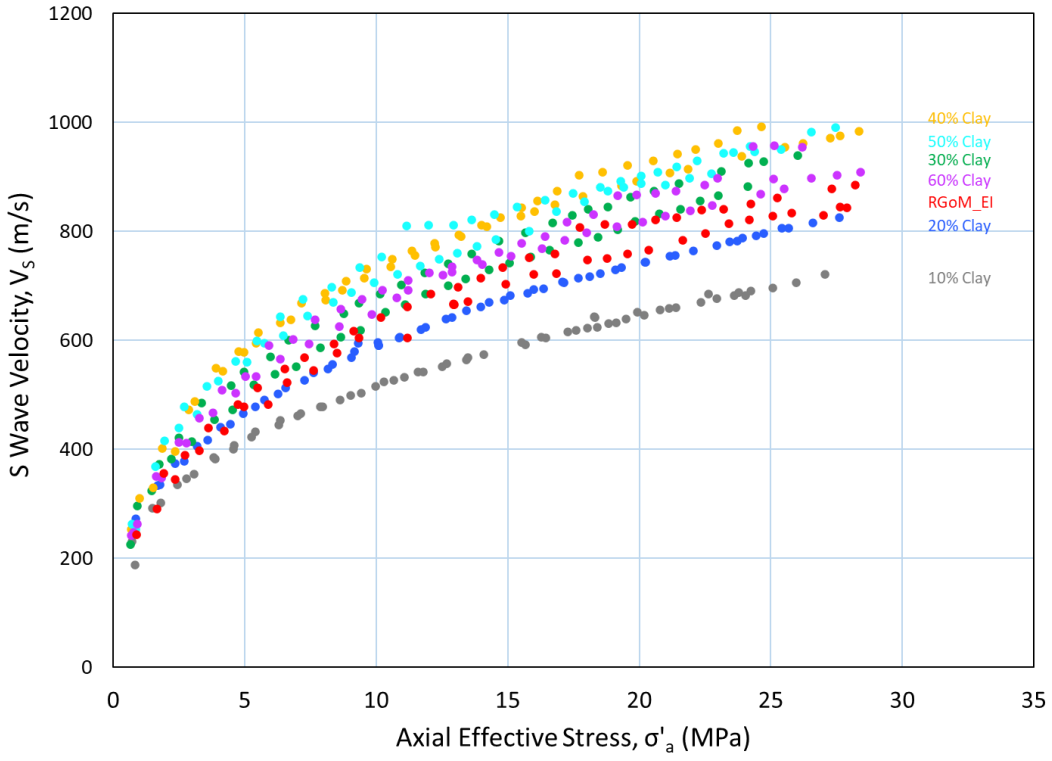


Figure 6-23: Measured S wave velocity by axial effective stress for all studied silt-clay mixtures

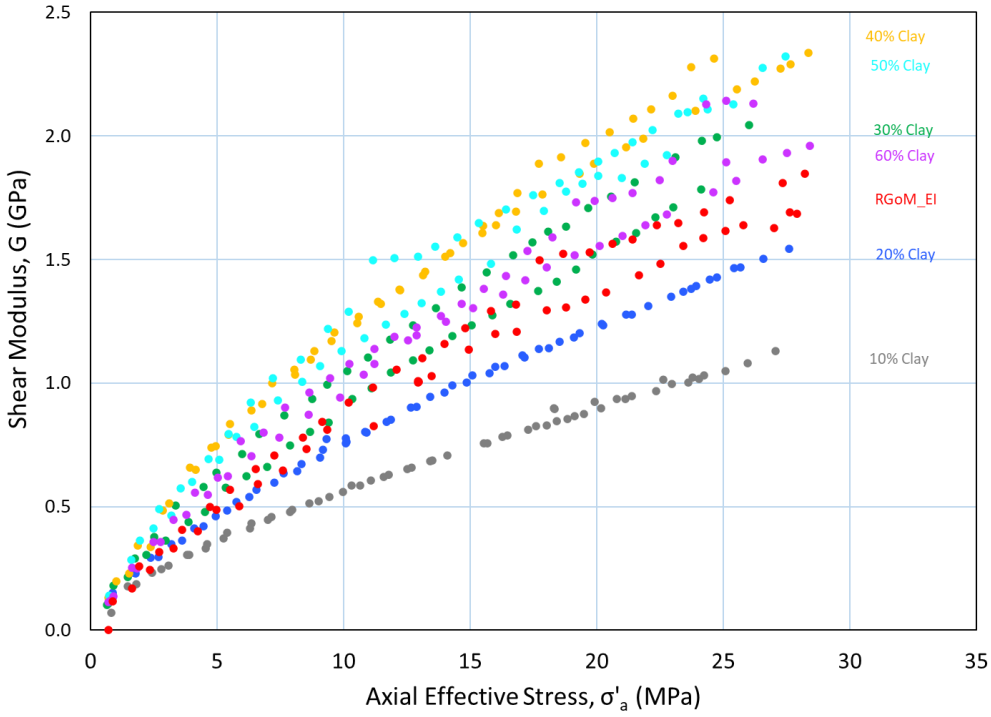


Figure 6-24: Calculated shear modulus (G) by axial effective stress for all studied silt-clay mixtures.

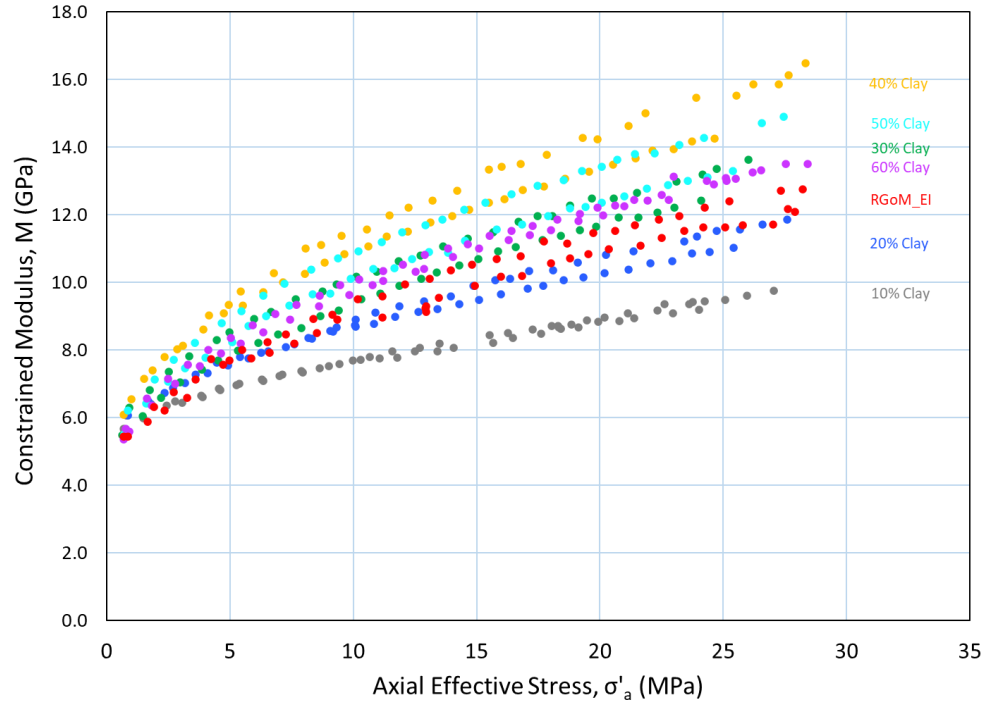


Figure 6-25: Calculated constrained modulus (M) by axial effective stress for all studied silt-clay mixtures.

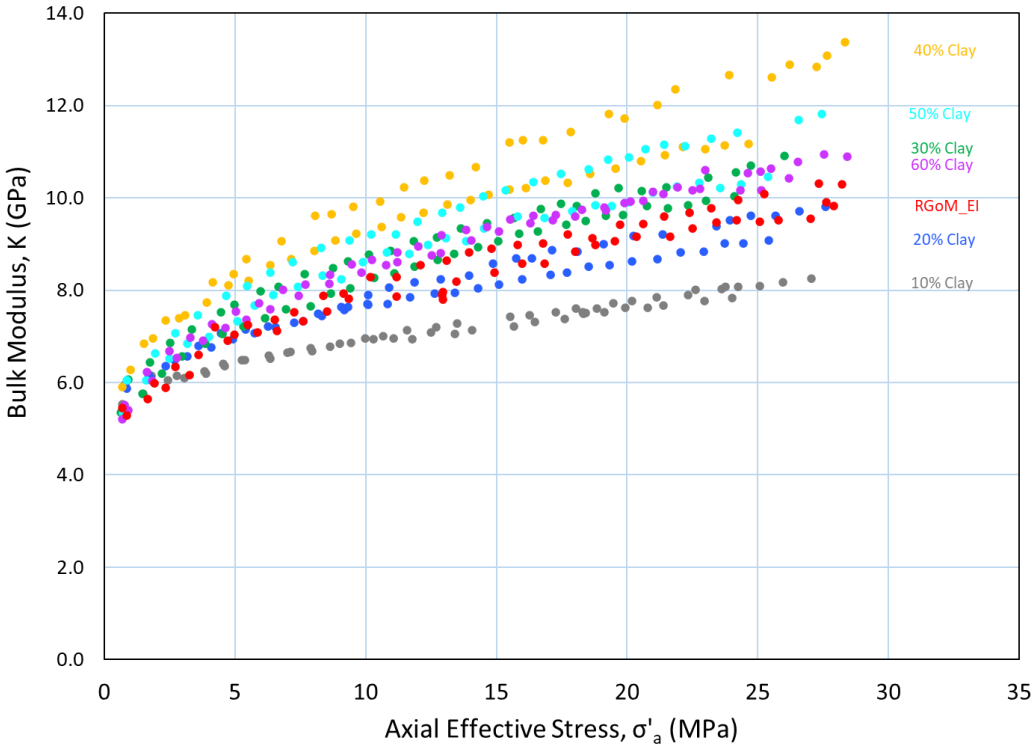


Figure 6-26: Calculated bulk modulus (K) by axial effective stress for all studied silt-clay mixtures.

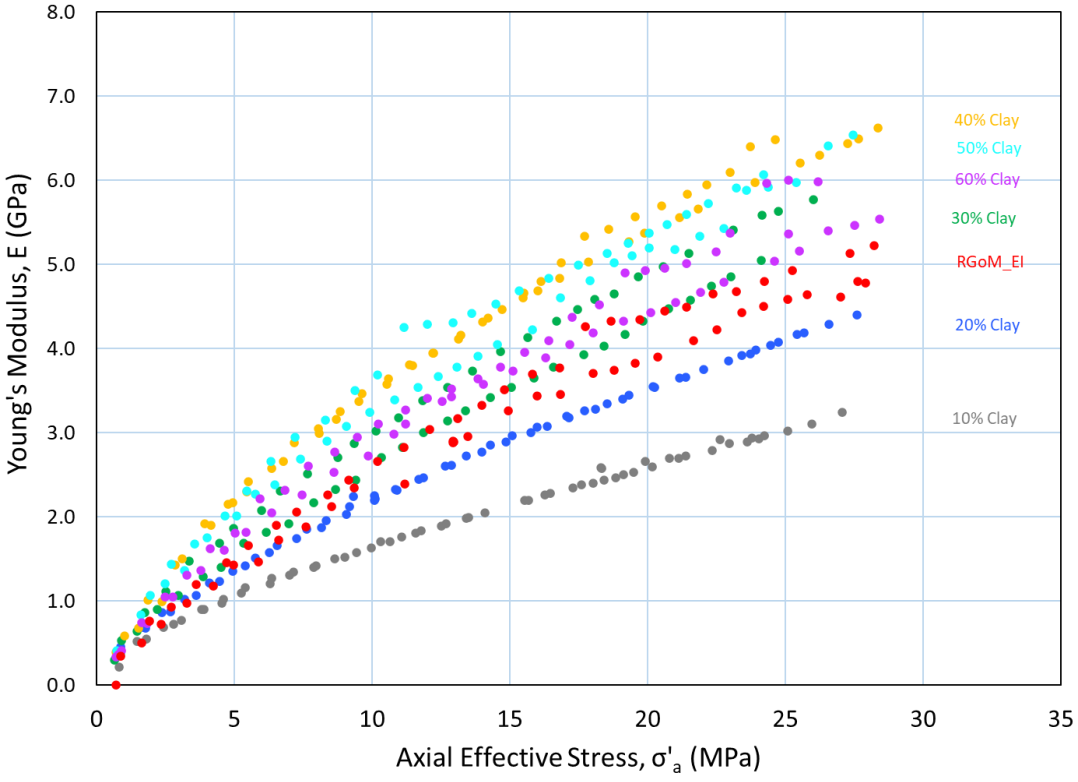


Figure 6-27: Calculated Young's modulus (E) by axial effective stress for all studied silt-clay mixtures.

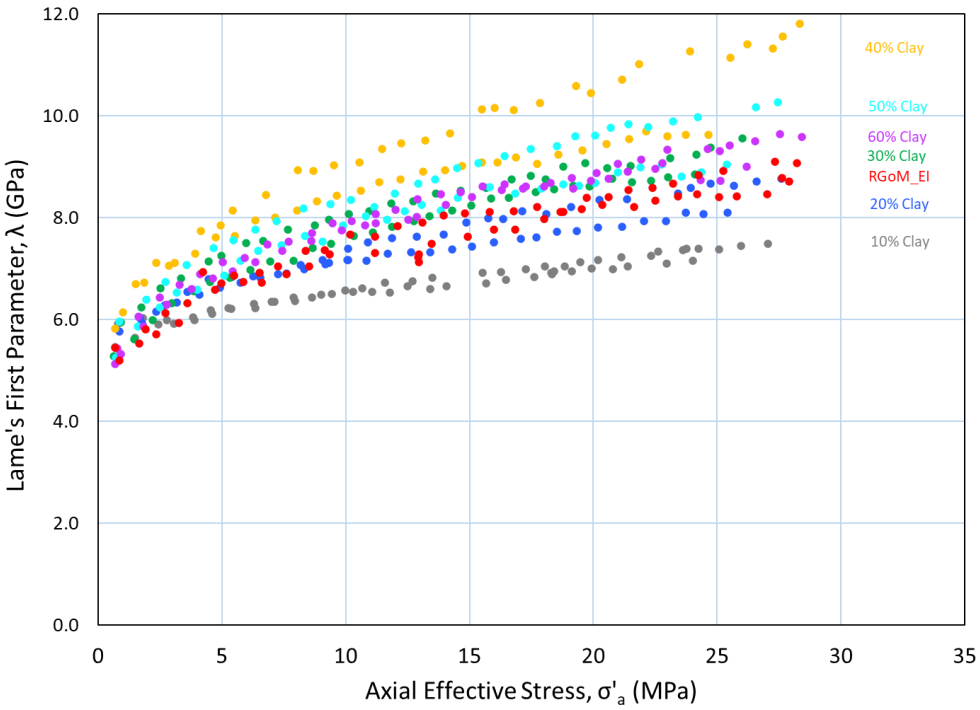


Figure 6-28: Calculated Lame's first parameter (λ) by axial effective stress for all studied silt-clay mixtures.

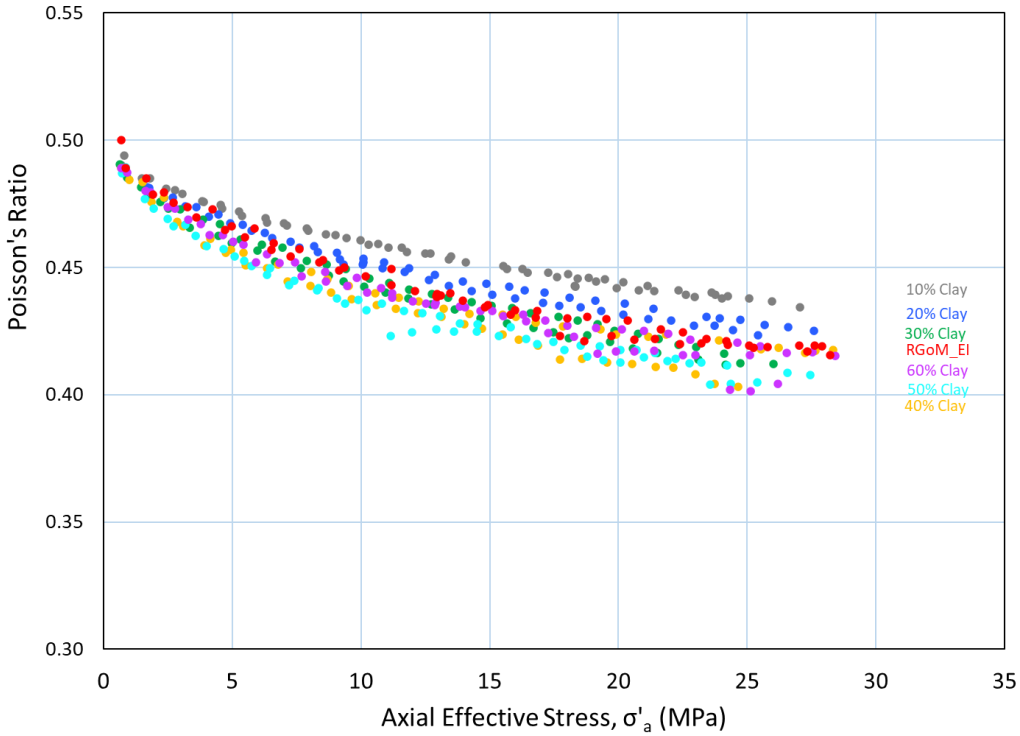


Figure 6-29: Calculated Poisson ratio (v) by axial effective stress for all studied silt-clay mixtures.

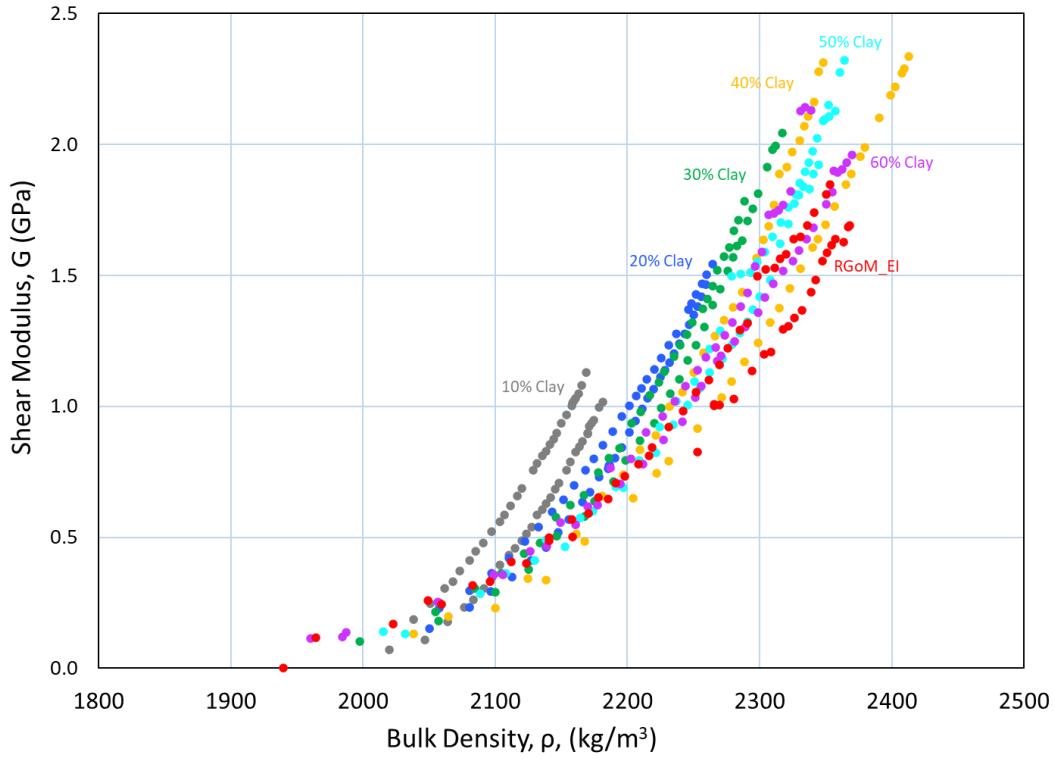


Figure 6-30: Calculated shear modulus (G) by bulk soil density for all studied silt-clay mixtures.

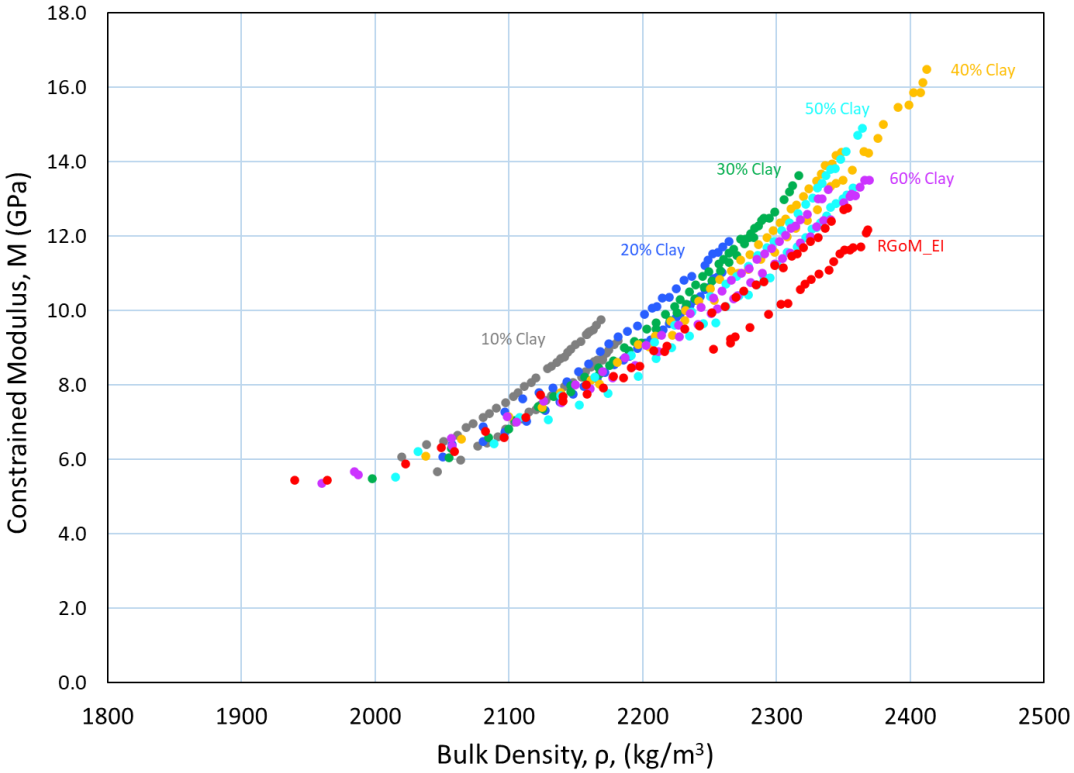


Figure 6-31: Calculated constrained modulus (M) by bulk soil density for all studied silt-clay mixtures.

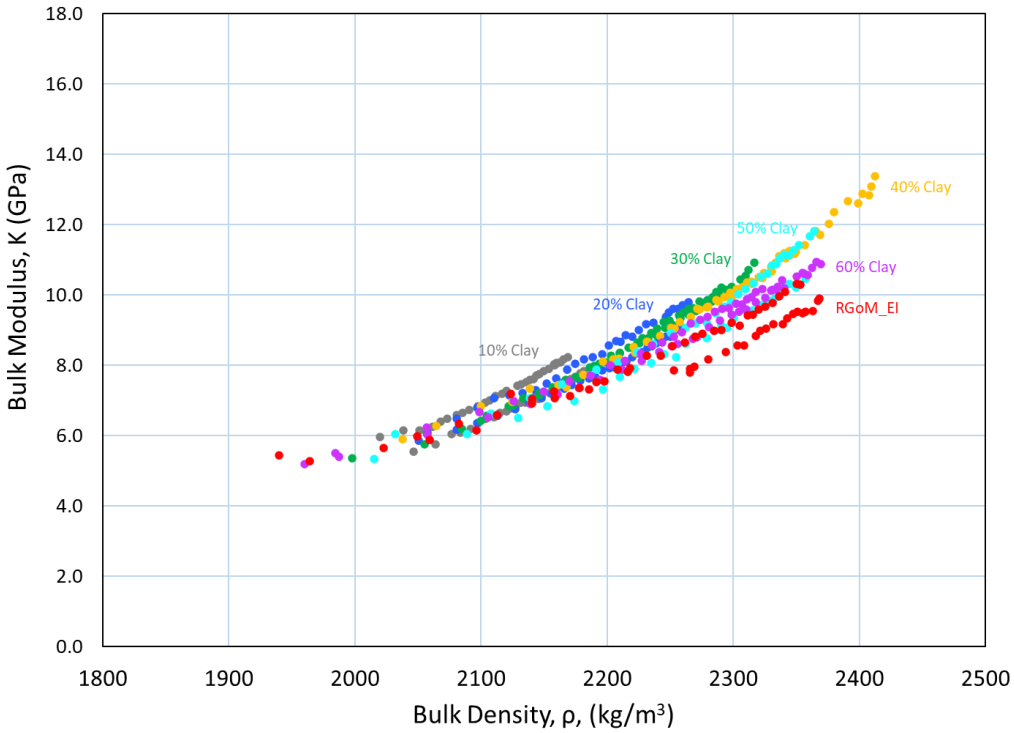


Figure 6-32: Calculated bulk modulus (K) by bulk soil density for all studied silt-clay mixtures.

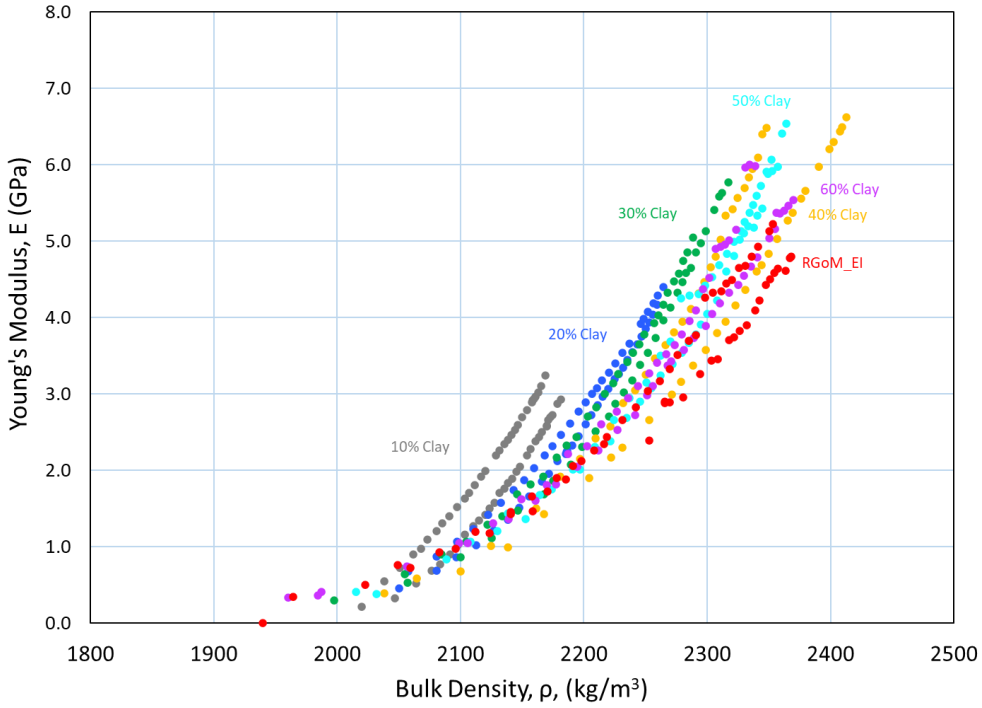


Figure 6-33: Calculated Young's modulus (E) by bulk soil density for all studied silt-clay mixtures.

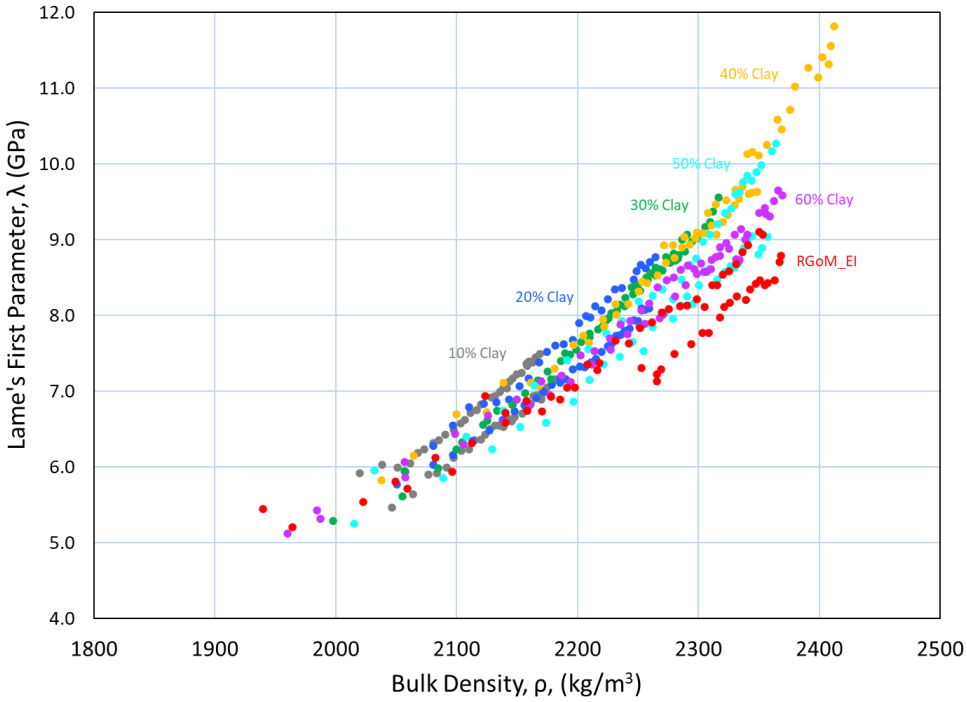


Figure 6-34: Calculated Lame's first parameter λ) by bulk soil density for all studied silt-clay mixtures.

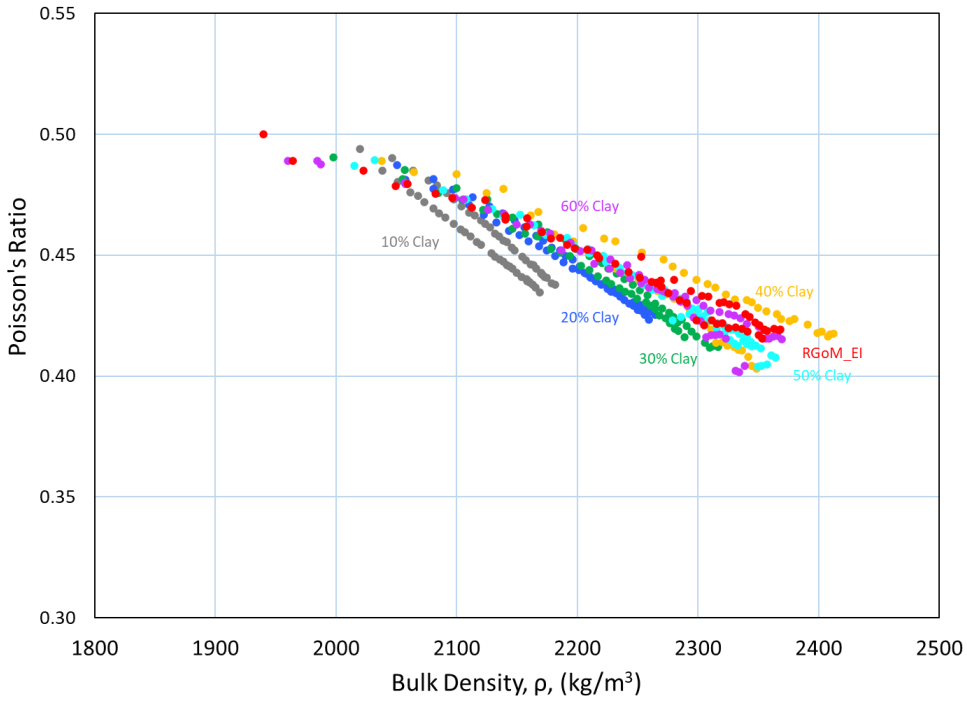


Figure 6-35: Calculated Poisson's ratio (ν) by bulk soil density for all studied silt-clay mixtures.

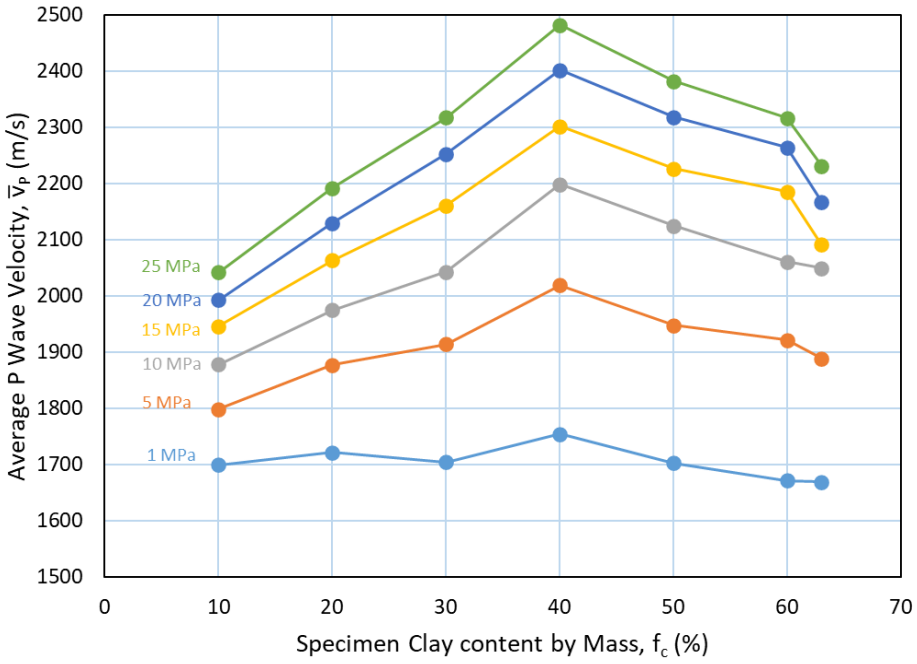


Figure 6-36: Average measured P wave velocity in Tall CRS tests by clay content (% clay of specimen mass) at 6 effective stress levels ,1 MPa, 5 MPa, 10 MPa, 15 MPa, 20 MPa, and 25 MPa as indicated in the plot.

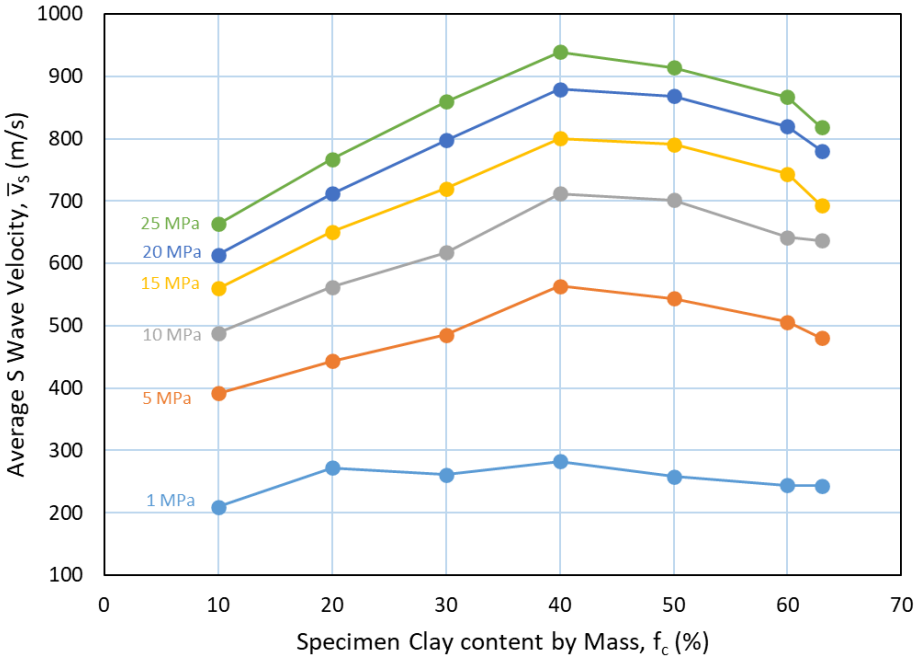


Figure 6-37: Average measured S wave velocity in Tall CRS tests by clay content (% clay of specimen mass) at 6 effective stress levels ,1 MPa, 5 MPa, 10 MPa, 15 MPa, 20 MPa, and 25 MPa as indicated in the plot.

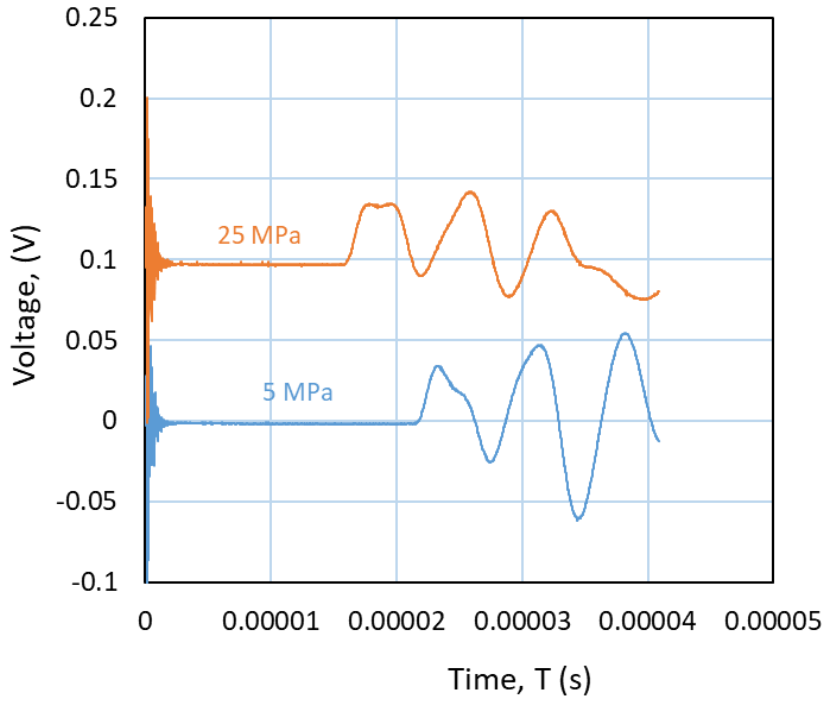


Figure 6-38: Comparison of P-waves collected at a 5 MPa effective stress level and a 25 MPa effective stress level during TCRS test CRS 1672 performed on a RGoM_EI test specimen.

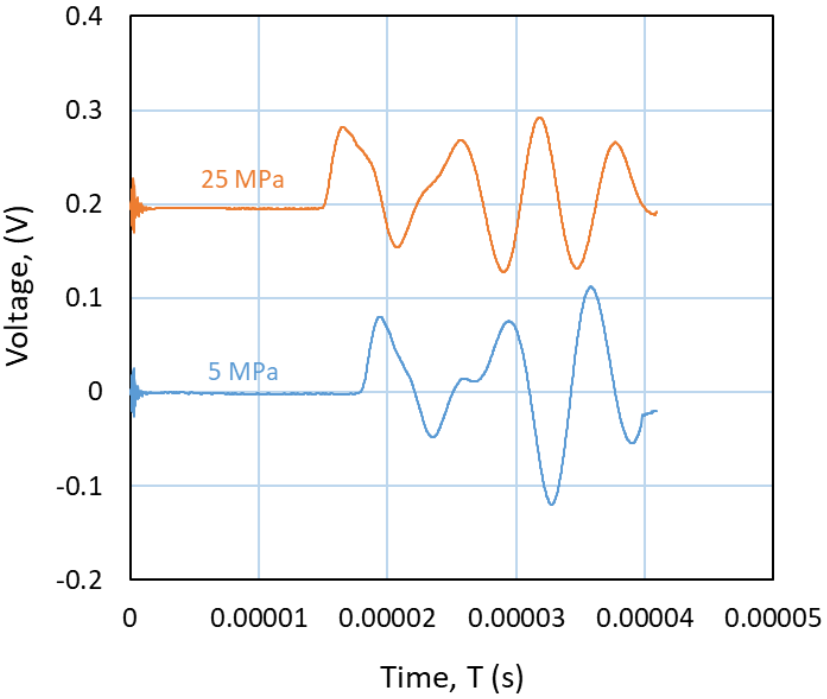


Figure 6-39: Comparison of P-waves collected at a 5 MPa effective stress level and a 25 MPa effective stress level during TCRS test CRS 1700 performed on a 10% clay test specimen.

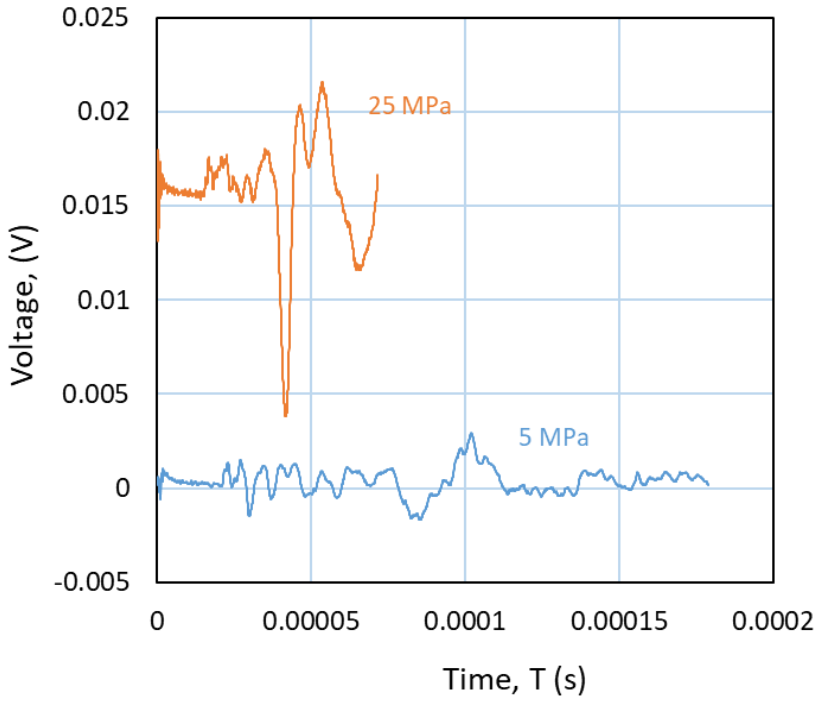


Figure 6-40: Comparison of S-waves collected at a 5 MPa effective stress level and a 25 MPa effective stress level during TCRS test CRS 1672 performed on a RGoM_EI test specimen.

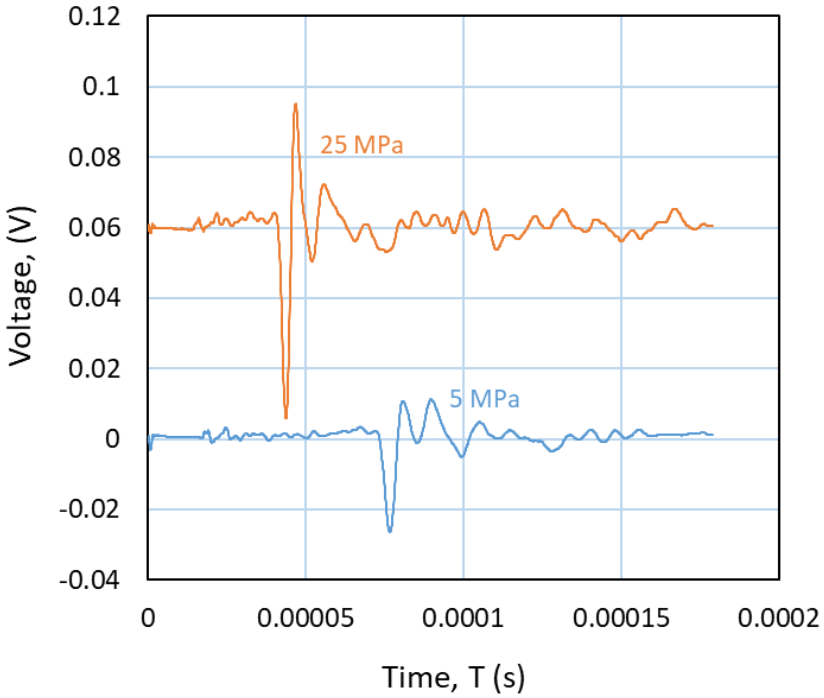


Figure 6-41: Comparison of S-waves collected at a 5 MPa effective stress level and a 25 MPa effective stress level during TCRS test CRS 1700 performed on a 10% clay test specimen.

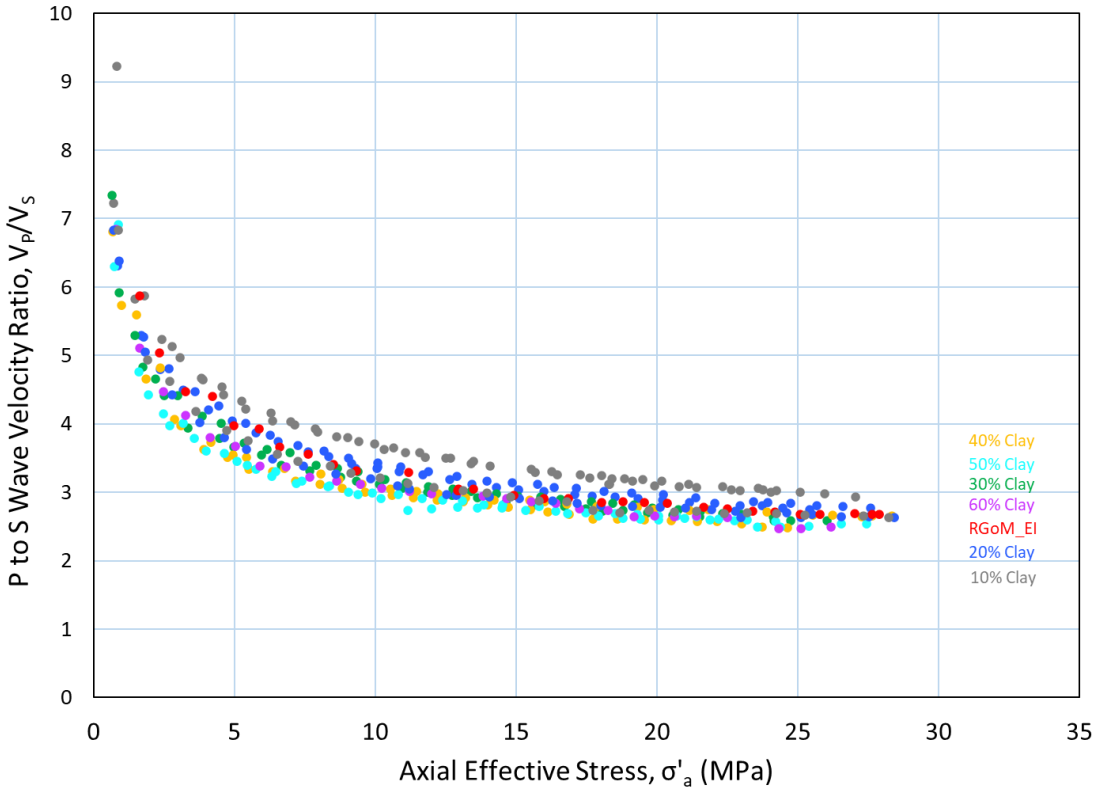


Figure 6-42: Ratio of the P wave velocity to the S wave velocity at each velocity measurement stress from 1 to 30 MPa, for the tested silt and clay mixtures.

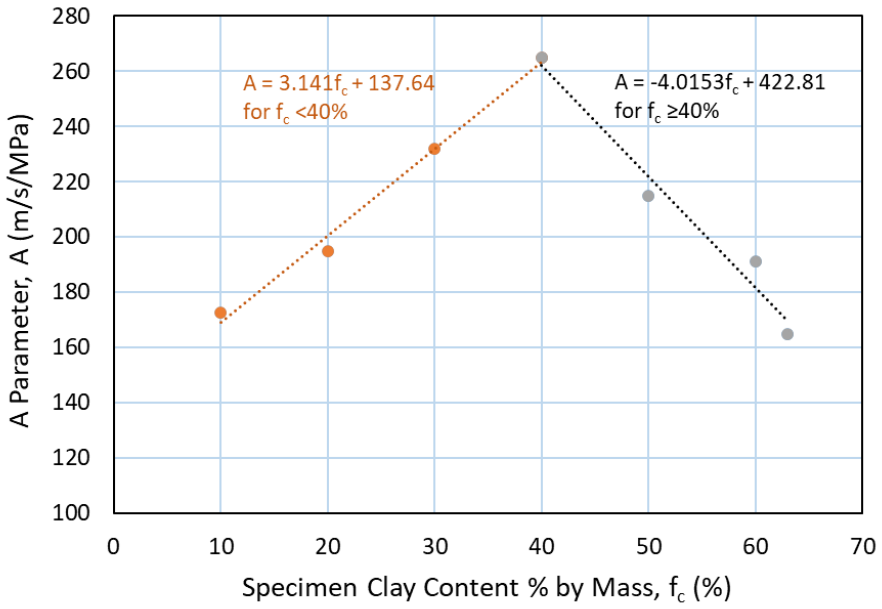


Figure 6-43: P wave velocity power equation A parameter by specimen clay content. A parameter from power equation fits for P wave measurements from individual TCRS tests were averaged over clay contents and plotted by clay content. The 30% clay specimens A parameter were not average instead CRS1698s value was used for a better fit. The data was fit linearly in segments to capture observed trends. The linear fit equations shown can be used to provide the A parameter for P waves as a function of clay content.

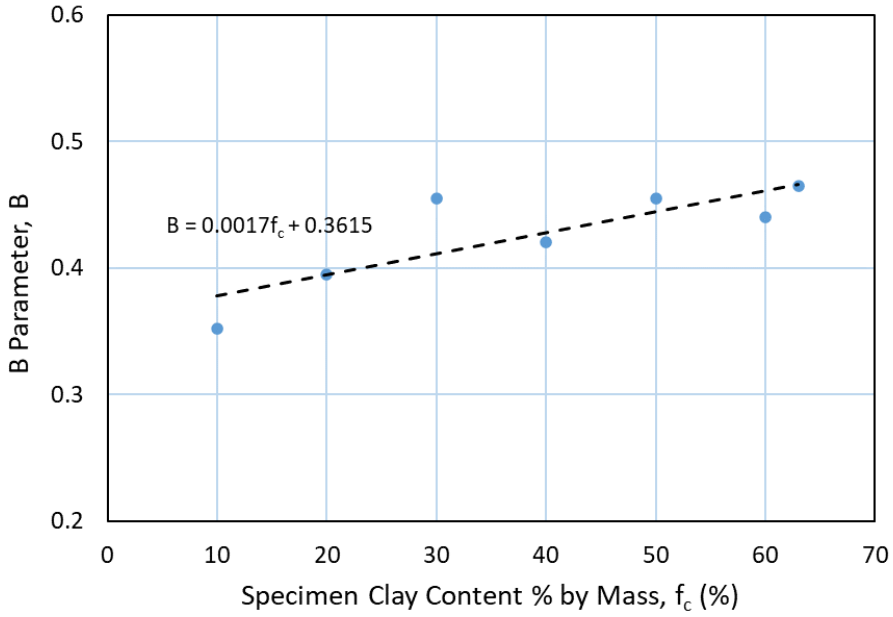


Figure 6-44: P wave velocity power equation B parameter by specimen clay content. B parameter from power equation fits for individual TCRS tests were averaged over clay content and plotted by clay content. The data was fit linearly to capture observed trends. The linear fit equations shown can be used to provide the B parameter for P waves as a function of clay content.

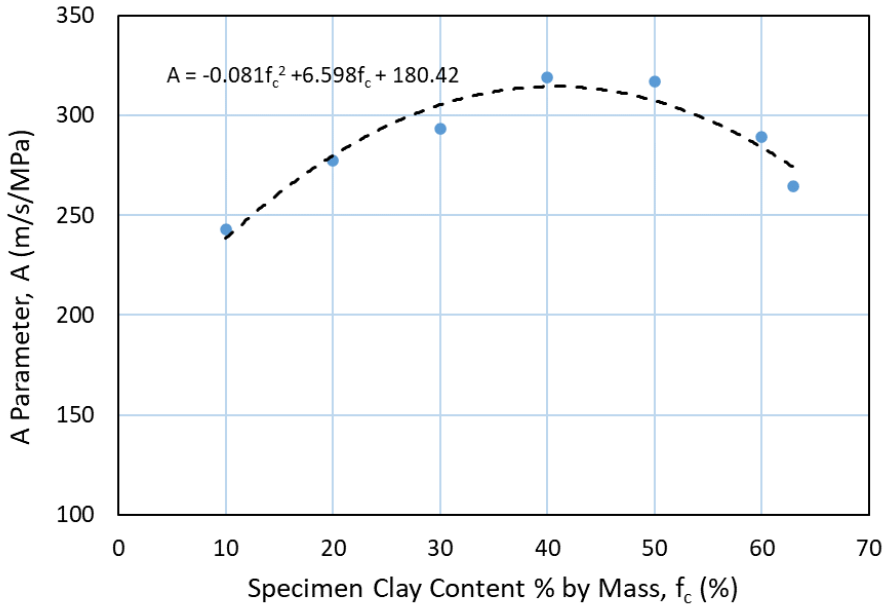


Figure 6-45: S wave velocity power equation A parameter by specimen clay content. A parameter from power equation fits for S wave measurements from individual TCRS tests were averaged over clay contents and plotted by clay content. The data was fit with a second order polynomial to capture observed trends. The linear fit equations shown can be used to provide the A parameter for S waves as a function of clay content.

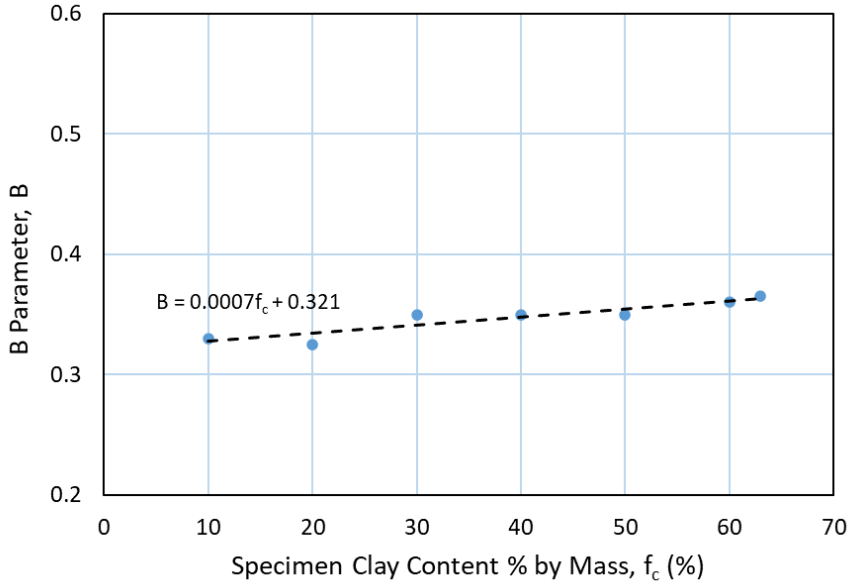


Figure 6-46: S wave velocity power equation B parameter by specimen clay content. B parameter from power equation fits for individual TCRS tests were averaged over clay content and plotted by clay content. The data was fit linearly to capture observed trends. The linear fit equations shown can be used to provide the B parameter for S waves as a function of clay content.

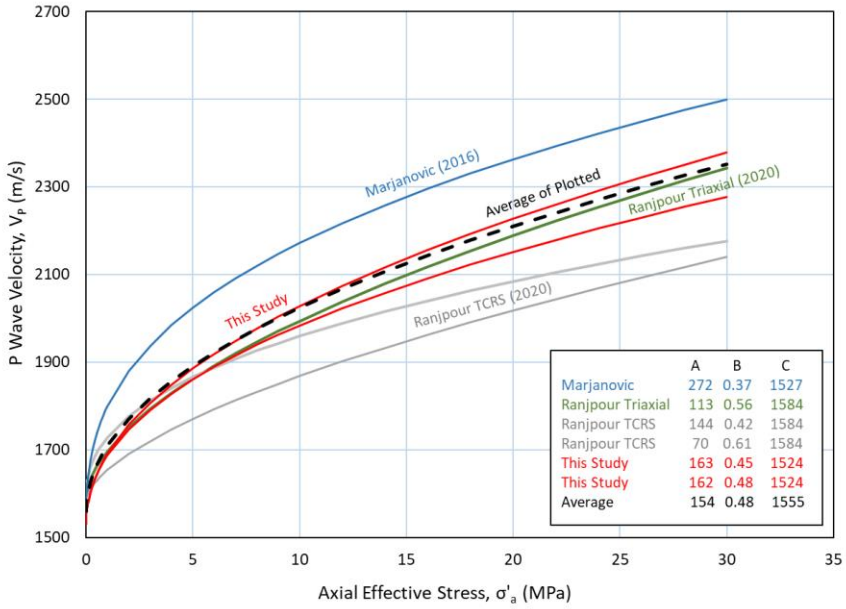


Figure 6-47: P wave velocity power models, fit using Equation 6-10 to laboratory measurements published within Marjanovic 2016, Ranjpour 2020, and this study. The fitting parameters are provided within the legend on the plot.

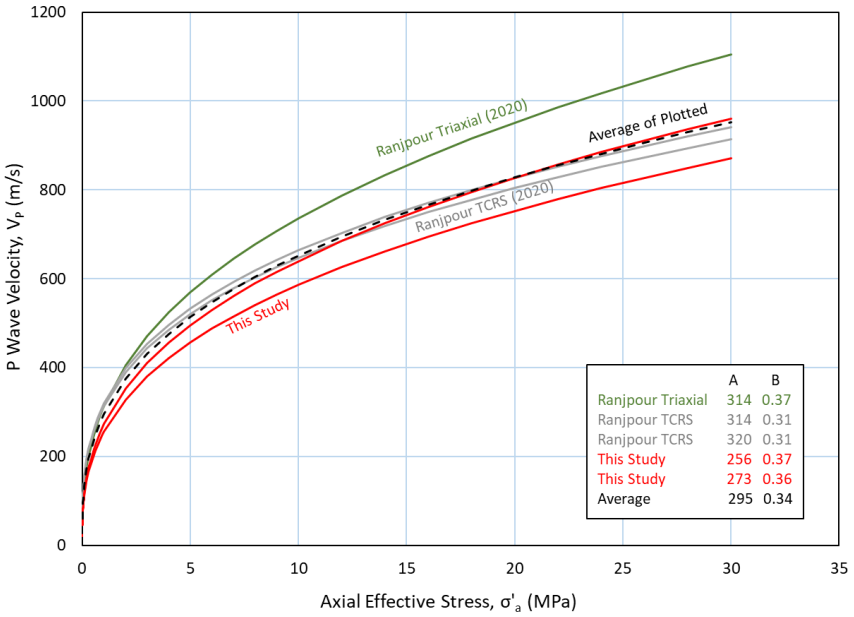


Figure 6-48: S wave velocity power models, fit using Equation 6-10 to laboratory measurements published within Ranjpour 2020, and this study. The fitting parameters are provided within the legend on the plot.

CHAPTER 7. Undrained Shear Results

7-1 Introduction

This chapter presents the results obtained during the undrained shearing phase of triaxial tests performed on the silt and clay mixtures. K_0 Consolidated undrained triaxial compression shear tests were carried out at two effective stress levels 1 MPa and 10 MPa on normally consolidated test specimens (Over Consolidation Ratio, OCR=1). Section 7.2 presents the undrained shear behavior of clay and silt mixtures, including shear stress-strain response, strength properties, and shear induced pore pressure generation. The results are generally presented normalized to the maximum consolidation stress for easy comparison of behavior between the two tested stress levels.

Section 7.3 summarizes and compares the shear measurements of different silt and clay mixtures and discusses trends observed in the undrained shear measurements. Trends with varying specimen clay content and trends varying specimen effective stress are discussed.

The undrained shear section of the experimental program includes fifty-four (54) triaxial tests carried out using the low and medium pressure triaxial systems. Several more triaxial shear tests were performed that had equipment or procedural issues which invalidated the data. The most common cause of issues is an internal leak within the medium pressure cell drainage lines. Table 7-1 provides a summary of the shear results from all triaxial tests performed for this study including pre-shear effective stresses, stress conditions at peak shear strength, and stress conditions at the measured maximum friction angle. The 0% clay, 10% clay, and 20% clay materials were not K_0 consolidated but instead were anisotropically consolidated along a computer-controlled stress path with a predetermined K value. This modification to the test program was done as the lower clay content materials were too stiff for the computer controlled K_0 consolidation feedback loop to properly function. The different consolidation

stress path is anticipated to effect the strain measurements but not strength measurements (undrained strength, and effective friction angle) during undrained shearing.

7-2 Undrained Strength Properties and Shear Behavior

This section presents results from the undrained shear phase where the specimens were sheared in compression by applying an axial strain rate of 0.5% per hour. When possible, the shearing phase is maintained through >10% axial strain, to measure conditions at large deformations and potentially at critical state line. The determination of the maximum effective friction angle is made with considerations to whether failure shear planes occurred during the shearing phase of each test. Shearing planes interfere with accurate measurements of maximum effective friction angle. In general, the primary failure type across all tested mixtures were bulging failures, where the center of the specimen radially expanded during compression. Each of the following sections describes the behavior of the different silt and RGoM_EI clay mixtures during the undrained shearing phase. Table 7-1 provides a summary of the test conditions and engineering parameters measured during undrained shearing for the triaxial shear tests. The shear behaviors observed are discussed based on pore pressure changes and shearing stress paths measured during the triaxial shearing phase.

Undrained Strength Properties 0% Clay Mixtures

Figure 7-1 presents the shear stress normalized to the effective maximum axial consolidation stress by axial strain for the 0% clay specimens. Where shear stress is defined by Equation 7-1.

$$q = \frac{\sigma_1 - \sigma_3}{2} \qquad \text{Equation 7-1}$$

$Where$:

q = Shear stress (force by area)

σ_1 = Major principal stress (force by area)

σ_3 = Minor principal stress (force by area)

The principal stresses σ_1 and σ_3 vary by the mode of shearing, but for triaxial compression testing σ_1 is interpreted as the axial stress and σ_3 is interpreted as the radial stress. Five triaxial tests; TX1362, TX1364, TX1368, TX1369, and TX1373 were sheared at an effective consolidation stress of 1 MPa (black points) and three tests; TX1438, TX1439, and TX1468 were sheared at a 10 MPa effective consolidation stress (blue points). Figure 7-1 indicates the point at which each test reached maximum shear stress by a red X symbol and the point at which each test reached maximum effective friction angle with a green ж symbol. The coloring scheme in Figure 7-1 used to differentiate 1 MPa tests and 10 MPa tests, as well as maximum shear stress and maximum effective friction angle is maintained throughout this chapter to present the test results of the different clay content specimens consistently. The 1 MPa tests have a large range of initial normalized shear stress values between 0.14 and 0.28, which is attributed to issues with the computer controller maintaining K_0 conditions during consolidation of the stiff soil as well variations in initial specimen density due to the under compaction method of specimen creation. The 1 MPa test measurements have a range of normalized maximum shear stress between 0.33 to 0.58 with an average of 0.46. The range in effective friction angle at the maximum shear stress is between 28.4 to 39.3 degrees with an average of 34.5 degrees. The strain to maximum shear stress ranges between 0.8% to 3.3% with an average value of 1.9%. The maximum effective friction angle ranges between 35.5 degrees to 46.4 degrees with an average value of 39.8 degrees. The strain to the maximum friction angle ranges between 4.1% to 14.1% with an average value of 8.0%. The 1 MPa tests stress strain curves indicate significant strain softening after maximum shear stress.

The 10 MPa test measurements have a range of normalized maximum shear stress between 0.32 and 0.43 with an average of 0.36. The range in effective friction angle at the maximum shear stress is between 28.5 to 36.6 degrees with an average of 32.2 degrees. The strain to maximum shear stress ranges between 2.3% to 8.6% with an average value of 4.7%. The maximum effective friction angle ranges between 32.0 degrees to 39.6 degrees with an average value of 34.0 degrees. The strain to the

maximum friction angle ranges between 6.6% to 9.2% with an average value of 8.1%. The 10 MPa stress strain curves indicate very consistent continued deformation rates after reaching the maximum shear stress.

Figure 7-2 provides an example stress path of the consolidation and shear phase from the triaxial tests. Figure 7-2 is used to illustrate the engineering parameters measured during the triaxial undrained shearing phase. The stress path indicates the shear stress by average effective stress normalized to the maximum axial consolidation stress corresponding to the top of the Mohr's circle at each measurement during shearing. Where average effective stress is defined by Equation 7-2.

$$p' = \frac{\sigma'_1 + \sigma'_3}{2} \qquad \text{Equation 7-2}$$

$Where$:

p' = Average effective stress (force by area)

σ'_1 = Major effective principal stress (force by area)

σ'_3 = Minor effective principal stress (force by area)

The stress paths from the 0% clay content specimens undrained compression shear tests at effective consolidation stresses of 1 MPa and 10 MPa are shown on Figure 7-3. The relationship between an effective friction angle (ϕ') in the Mohr-Coulomb failure criterion (σ-τ space) is related to p'-q stress space by Equation 7-3.

$$Sin(\phi') = Tan(\alpha') \qquad \text{Equation 7-3}$$

$Where$:

ϕ' = Effective friction angle Mohr-Coulomb failure criterion (Degrees)

α' = Effective friction angle p-q space (Degrees)

Stress paths provide a convenient way to describe the behavior of the specimens during undrained shearing and the specimen stress state in relation to the failure envelope. When initially loaded the

specimens initially show increases in both normalized shear stress and normalized average effective stress, for a brief period, then the stress path shifts depending on the behavior of the specimen. For specimens that have contractive behavior due to generating positive pore pressures the stress path curves to a lower average effective stress and generally increases in shear stress until reaching the shear strength of the material. For specimens that have dilative behaviors due to generating negative pore pressures, the stress paths curve to a higher average effective stresses and higher shear stresses until reaching the shear strength of the material. The 1 MPa stress paths on Figure 7-3 show variability in the shape of the undrained stress path. One test indicates contractive behavior for the entirety of the shear phase through a stress path that curves continually to a lower average effective stress. The other stress paths tend to show initial dilative behavior as the stress path moves to a higher average effective stress and shear stress until maximum shear stress, after which the specimens begin to fail, and the stress path turns to decrease in both shear and average effective stress. The abrupt change post maximum shear stress corresponds to strain softening behavior post maximum shear stress shown in Figure 7-1. The variability of the 1 MPa stress paths is attributed to different specimen densities due to the under-compaction specimen creation method for the 0% clay specimens. The 10 MPa stress tests (blue points) generally showed slight dilative behavior during the initial shearing phase, followed by contractive behavior through the end of the shearing phase.

In general, the 0% clay content tests, indicate initial dilative behavior followed by prolonged contractive behavior during undrained shearing. This is best illustrated through shear induced pore pressures as shown in Figure 7-4. Where the shear induced pore pressures are calculated as the change in pore pressure from the start of the shearing phase minus the change in total octahedral stress. Dilative behavior is shown as a negative shear induced pore pressure on Figure 7-4 and all 0% specimens indicate negative pore pressures at the start of shearing. By about 1% of axial strain the 0% specimens begin to display contractive behaviors which is indicated as positive generated pore pressures on Figure

7-4. The dilative behaviors are indicated in the stress path on Figure 7-3, through an initial increase in both average and shear stress. The longer the dilative behavior occurs within the specimen the larger the increase in stress. The contractive behavior manifests as a decrease in average effective stress, while shear stress usually continues to increase towards the maximum shear stress. After reaching maximum shear stress, both shear and average effective stress will decrease in specimens that exhibit contractive behavior. The behavior of the material (dilative or contractive) during shearing has a significant effect on the measured engineering parameters, longer initial dilative behaviors corresponded with larger maximum shear stresses and larger friction angles at maximum shear stress. Dilative behaviors were observed in the lower clay content specimens and higher clay content specimens indicated predominantly contractive behavior.

The 0% clay specimens have significant scatter in the measured strength properties. Difficulty in creating repeatable densities for test specimens contributes to the scatter. The initial bulk density of the 0% clay specimens for the 1 MPa test ranged between 1.781 g/cm^3 to 1.902 g/cm^3 and the initial densities for the 10 MPa tests ranged between 1.750 g/cm^3 to 1.869 g/cm^3. The results presented in this chapter will show that scatter in the data is linked to soil fabric with grain supported soil having more scatter in the strength measurements. The scatter in the data will be shown to decreases with increasing clay content and effective stress.

Undrained Strength Properties 10% Clay Mixtures

Figure 7-5 presents the shear stress normalized to the effective maximum axial consolidation stress by axial strain for the 10% clay specimens. Three triaxial tests; TX1358, TX1388, and TX1413, were sheared at 1 MPa effective consolidation stress and three tests; TX1431, TX1443, and TX1459, were sheared at a 10 MPa effective consolidation stress. The 1 MPa test measurements have a range of normalized maximum shear stress between 0.35 to 0.70 with an average of 0.52. The range in effective friction

angle at the maximum shear stress is between 34.2 to 35.5 degrees with an average of 35.0 degrees. The strain to maximum shear stress ranges between 11.8% to 16.2% with an average value of 14.6%. The maximum effective friction angle ranges between 35.5 degrees to 36.9 degrees with an average value of 36.0 degrees. The strain to the maximum friction angle ranges between 7.6% to 9.8% with an average value of 8.7%. The 1 MPa tests stress strain curves indicate significant strain hardening indicative of dilative behavior.

The 10 MPa test measurements have a range of normalized maximum shear stress between 0.33 to 0.67 with an average of 0.46. The range in effective friction angle at the maximum shear stress is between 28.2 to 36.0 degrees with an average of 33.3 degrees. The strain to maximum shear stress ranges between 0.8% to 11.4% with an average value of 7.7%. The maximum effective friction angle ranges between 35.7 degrees to 37.1 degrees with an average value of 36.3 degrees. The strain to the maximum friction angle ranges between 8.6% to 11.4% with an average value of 10.3%. Test TX1431 shows significant strain hardening indicative of dilative behavior and the other two 10 MPa tests TX1443 and TX1459 show consistent deformation behavior at the maximum shear stress.

Figure 7-6 provides normalized stress paths and Figure 7-7 provides the normalized shear induced pore pressures for the shear phase of the 10% clay specimens. When initially loaded all the test stress paths follow a 45-degree angle increasing in both normalized shear stress and normalized average effective stress. Two tests, one consolidated to 1 MPa (TX1358) and one consolidated to 10 MPa (TX1431), show significant dilative behavior over the duration of the shear phase and continued to increase in both shear and average effective stress until reaching the maximum shear stress. The other two 1 MPa tests (TX1388 and TX1413) indicate dilative behavior as the specimen reached the friction failure envelope resulting in a turn to higher shear stresses at lower average effective stress along the presumed failure envelope. The remaining 10 MPa tests (TX1443 and TX1459) indicate contractive behavior until the

specimen reached the friction failure envelope typical of fine-grained soils. Figure 7-7 indicates the dilative behaviors as negative generated pore pressures during the shearing phase. Test TX1358 showed significant dilative behavior throughout the shearing phase had a contractive period indicated by positive pore pressure generation in Figure 7-7 that manifested as a shift in the stress path to a lower average effective stress in Figure 7-6. The Test TX1431 indicated significant dilative behavior throughout the shear phase does not indicate any contractive behavior as positive pore pressures on Figure 7-7. The other 1 MPa tests (TX1388 and TX1413) indicate dilatative behavior as the stress path approached the failure envelope by about 4% axial strain. The remaining 10 MPa tests (TX1443 and TX1459), indicate a small initial dilative behavior followed by contractive behavior through the end of the shear phase typical of normally consolidated fine-grained soils.

The 10% clay specimens like to 0% clay specimens had significant scatter in the measured strength properties. The 10% specimens were created using the resedimentation specimen creation method with a controlled stress history. The initial bulk density of the 10% clay specimens for the 1 MPa tests ranged between 1.922 g/cm^3 to 1.995 g/cm^3 and the initial densities for the 10 MPa tests ranged between 1.966 g/cm^3 to 2.044 g/cm^3. Variations in initial density had a significant effect on the material behavior of the 10% clay content specimens. The added clay content was not significant enough to effect he material behavior.

Undrained Strength Properties 20% Clay Mixtures

Figure 7-8 presents the shear stress normalized to the effective axial consolidation stress by axial strain for the 20% clay specimens. Three triaxial tests; TX1353, TX1380, and TX1410, were sheared at 1 MPa effective consolidation stress and three tests; TX1444, TX1463, and TX1492, were sheared at a 10 MPa effective consolidation stress. The 1 MPa test measurements have a range of normalized maximum shear stress between 0.33 to 0.37 with an average of 0.35. The range in effective friction angle at the

maximum shear stress is between 25.9 to 28.5 degrees with an average of 27.2 degrees. The strain to maximum shear stress ranges between 0.04% to 0.3% with an average value of 0.2%. The maximum effective friction angle ranges between 33.0 degrees to 36.7 degrees with an average value of 34.9 degrees. The strain to the maximum friction angle ranges between 7.4% to 9.2% with an average value of 8.4%. The 1 MP tests stress strain curves indicate strain softening of the soil after maximum shear stress.

The 10 MPa test measurements have a range of normalized maximum shear stress between 0.31 to 0.32 with an average of 0.32. The range in effective friction angle at the maximum shear stress is between 25.2 to 27.6 degrees with an average of 26.4 degrees. The strain to maximum shear stress ranges between 0.3% to 1.0% with an average value of 0.7%. The maximum effective friction angle ranges between 31.3 degrees to 35.9 degrees with an average value of 33.9 degrees. The strain to the maximum friction angle ranges between 5.6% to 9.3% with an average value of 7.7%. The 10 MPa tests stress strain curves indicate strain softening of the soil after maximum shear stress similar to the 1 MPa tests.

Figure 7-9 provides normalized stress paths and Figure 7-10 provides the normalized shear induced pore pressures for the shear phase of the 20% clay specimens sheared at effective consolidation stresses of 1 MPa and 10 MPa. When initially loaded all of the test stress paths follow a 45-degree angle increasing in both normalized shear stress and normalized average effective stress. The tests then curve to a larger normalized shear stress and smaller normalized average effective stress indicating contractive behavior of the soil. After reaching the maximum shear stress, the stress paths decrease in both shear stress and average effective stress with continued shearing. A few of the tests indicated rapid decreases in both shear stress and average effective stress after reaching maximum friction angle, which is interpreted as the material completely failing and following the friction failure envelope. Figure 7-10 indicates that

every 20% clay specimen exhibited dilative behavior at strains generally less than 0.2% followed by prolonged contractive behavior through the end of shearing. This behavior is well-documented to be typical of normally consolidated fine-grained soils.

The 20% clay specimens have less scatter in the measured strength properties and the scatter in the measurements is smaller for the 10 MPa tests. The 20% specimens were created using resedimentation. The initial bulk density of the 20% clay specimens for the 1 MPa tests ranged between 1.974 g/cm^3 to 2.019 g/cm^3 and the initial densities for the 10 MPa tests ranged between 1.962 g/cm^3 to 2.055 g/cm^3. The ranges in initial bulk density of the 20% clay specimens were very similar to that of the 10% clay specimens. The reduction in scatter for the 20% clay specimens compared to the 10% clay specimens, is interpreted as the clay content being significantly high enough to influence the material behavior.

Undrained Strength Properties 30% Clay Mixtures

Figure 7-11 presents the shear stress normalized to the effective maximum axial consolidation stress by axial strain for the 30% clay specimens. Five triaxial tests; TX1347, TX1367, TX1390, TX1420 and TX1491, were sheared at 1 MPa effective consolidation stress and three tests; TX1447, TX1464, and TX1495, were sheared at a 10 MPa effective consolidation stress. The 1 MPa test measurements have a range of normalized maximum shear stress between 0.29 to 0.33 with an average of 0.31. The range in effective friction angle at the maximum shear stress is between 22.4 to 25.7 degrees with an average of 24.5 degrees. The strain to maximum shear stress ranges between 0.3% to 0.6% with an average value of 0.4%. The maximum effective friction angle ranges between 29.4 degrees to 32.1 degrees with an average value of 31.4 degrees. The strain to the maximum friction angle ranges between 8.0% to 8.8% with an average value of 8.4%. The 1 MPa tests stress strain curves indicate strain softening of the soil after maximum shear stress.

The 10 MPa test measurements have a range of normalized maximum shear stress between 0.30 to 0.31 with an average of 0.30. The range in effective friction angle at the maximum shear stress is between 24.6 to 26.9 degrees with an average of 25.4 degrees. The strain to maximum shear stress ranges between 0.6% to 11.1%. The 11.1% strain to maximum shear stress in TX1447 was anomalous compared to the other two 10 MPa test which both had 0.6% strain to maximum shear stress. The average strain to maximum shear stress for the 30% clay 10 MPa tests is 0.6% which excludes to 11.1% measurement. The maximum effective friction angle ranges between 26.9 degrees to 32.6 degrees with an average value of 29.9 degrees. The strain to the maximum friction angle ranges between 9.9% to 13.1% with an average value of 11.3%. The 10 MPa tests stress strain curves indicate strain softening of the soil after maximum shear stress similar to the 1 MPa tests.

Figure 7-12 provides normalized stress paths and Figure 7-13 provides the normalized shear induced pore pressures during the shear phase for the 30% clay specimens sheared at effective consolidation stresses of 1 MPa and 10 MPa. The tests all show an initial increase in average effective stress and then curve to a larger normalized shear stress and smaller normalized average effective stress indicating contractive behavior of the soil. After reaching the maximum shear stress both the shear stress and average effective stress decrease with continued shearing. Figure 7-13 indicates that every 30% clay specimen had prolonged contractive behavior through the end of shearing, typical of fine-grained soils. Figure 7-13 shows that the shear induced pore pressures for the 10 MPa tests were different but that had limited effect on the stress paths shown in Figure 7-12. Test TX1447 in Figure 7-13 generated one half to on third of the shear induced pore pressure of test TX1495. Test TX1447 developed a shear plan and reached the maximum effective friction angle at a higher average effective stress than the other 10 MPa tests (green ж around an average effective stress of 0.7 in Figure 7-12).

Undrained Strength Properties 40% Clay Mixtures

Figure 7-14 presents the shear stress normalized to the effective maximum axial consolidation stress by axial strain for the 40% clay specimens. Three triaxial tests; TX1355, TX1411, and TX1415, were sheared at 1 MPa effective consolidation stress and three tests; TX1456, TX1478, and TX1499, were sheared at a 10 MPa effective consolidation stress. The 1 MPa test measurements have a range of normalized maximum shear stress between 0.25 to 0.28 with an average of 0.26. The range in effective friction angle at the maximum shear stress is between 20.6 to 22.4 degrees with an average of 21.3 degrees. The strain to maximum shear stress ranges between 0.4% to 1.3% with an average value of 0.8%. The maximum effective friction angle ranges between 25.7 degrees to 28.1 degrees with an average value of 26.7 degrees. The strain to the maximum friction angle ranges between 8.5% to 9.7% with an average value of 9.1%. The 1 MPa tests stress strain curves indicate strain softening of the soil after reaching the maximum shear stress.

measurements have a range of normalized maximum shear stress between 0.26 to 0.27 with an average of 0.26. The range in effective friction angle at the maximum shear stress is between 21.5 to 22.5 degrees with an average of 21.9 degrees. The strain to maximum shear stress ranges between 1.2% to 1.5% with an average value of 1.3%. The maximum effective friction angle ranges between 23.4 degrees to 26.4 degrees with an average value of 25.4 degrees. The strain to the maximum friction angle ranges between 8.5% to 11.9% with an average value of 10.3%. The 10 MPa tests stress strain curves indicate strain softening of the soil after maximum shear stress similar to the 1 MPa tests.

Figure 7-15 provides normalized stress paths and Figure 7-16 provides the normalized shear induced pore pressures for the shear phase for the 40% clay specimens sheared at effective consolidation stresses of 1 MPa and 10 MPa. When initially loaded all the 40% clay content stress paths increase in both average effective stress and shear stress for a period and then tests curve to larger normalized

shear stresses and smaller normalized average effective stress indicating contractive behavior of the soil. After reaching the maximum shear stress, both the shear stress and average effective stress decrease with continued shearing. Figure 7-16 indicates that the pore pressure generated during the shear phase were similar for all of the 40% clay content tests. Two of the 10 MPa tests TX1478 and TX1499 had near identical curves and the third 10 MPa test TX1456 generated less pore pressures overall due to the development of a failure plane during shearing.

Undrained Strength Properties 50% Clay Mixtures

Figure 7-17 presents the shear stress normalized to the effective maximum axial consolidation stress by axial strain for the 50% clay specimens. Four triaxial tests; TX1348, TX1359, TX1383 and TX1490, were sheared at 1 MPa effective consolidation stress and three tests; TX1442, TX1458, and TX1475, were sheared at a 10 MPa effective consolidation stress. The 1 MPa test measurements have a range of normalized maximum shear stress between 0.25 to 0.26 with an average of 0.25. The range in effective friction angle at the maximum shear stress is between 19.2 to 22.0 degrees with an average of 20.5 degrees. The strain to maximum shear stress ranges between 0.3% to 2.4% with an average value of 1.3%. The maximum effective friction angle ranges between 24.7 degrees to 25.0 degrees with an average value of 24.8 degrees. The strain to the maximum friction angle ranges between 8.9% to 11.2% with an average value of 9.8%. The 1 MPa tests stress strain curves indicate strain softening of the soil after reaching the maximum shear stress.

The 10 MPa test measurements have a range of normalized maximum shear stress between 0.21 to 0.22 with an average of 0.22. The range in effective friction angle at the maximum shear stress is between 15.5 to 18.6 degrees with an average of 17.5 degrees. The strain to maximum shear stress ranges between 2.2% to 4.3% with an average value of 3.0%. The maximum effective friction angle ranges between 15.5 degrees to 24.1 degrees with an average value of 19.8 degrees. The strain to the

maximum friction angle ranges between 4.0% to 11.9% with an average value of 8.9%. The 10 MPa tests stress strain curves indicate strain softening of the soil after maximum shear stress similar to the 1 MPa tests.

Figure 7-18 provides normalized stress paths and Figure 7-19 provides the normalized shear induced pore pressures of the shear phase for the 50% clay specimens sheared at effective consolidation stresses of 1 MPa and 10 MPa. When initially loaded all the test stress paths tend to increase in both normalized shear stress and normalized average effective stress. The tests then curve to a larger normalized shear stress and smaller normalized average effective stress indicating contractive behavior of the soil. After reaching the maximum shear stress, both the shear stress and average effective stress decrease with continued shearing. Figure 7-19 indicates that every 50% clay specimen exhibited contractive behavior through the end of shearing, typical of normally consolidated fine-grained soils. The four 1 MPa tests had very similar behavior. Test TX1442 developed a shear plane during shearing and generated less pore pressures than the other two 10 MPa tests. Test TX1475 had a strain rate computer control issue around 4-5% strain during shearing. A faster strain rate was applied due to the issue resulting in larger pore pressures.

Undrained Strength Properties 60% Clay Mixtures

Figure 7-20 presents the shear stress normalized to the effective maximum axial consolidation stress by axial strain for the 60% clay specimens. Three triaxial tests; TX1350, TX1385, and TX1407, were sheared at 1 MPa effective consolidation stress and four tests; TX1446, TX1480, TX1481, and TX1501, were sheared at a 10 MPa effective consolidation stress. The 1 MPa test measurements have a range of normalized maximum shear stress between 0.23 to 0.29 with an average of 0.25. The range in effective friction angle at the maximum shear stress is between 18.1 to 20.2 degrees with an average of 19.3 degrees. The strain to maximum shear stress ranges between 0.6% to 3.4% with an average value of

1.6%. The maximum effective friction angle ranges between 21.4 degrees to 24.7 degrees with an average value of 22.6 degrees. The strain to the maximum friction angle ranges between 7.5% to 9.3% with an average value of 8.5%. The 1 MPa tests stress strain curves indicate strain softening of the soil after reaching the maximum shear stress.

The 10 MPa test measurements have a range of normalized maximum shear stress between 0.15 to 0.18 with an average of 0.16. The range in effective friction angle at the maximum shear stress is between 13.3 to 15.3 degrees with an average of 14.5 degrees. The strain to maximum shear stress ranges between 3.5% to 3.8% with an average value of 3.6%. The maximum effective friction angle ranges between 14.3 degrees to 17.3 degrees with an average value of 16.2 degrees. The strain to the maximum friction angle ranges between 8.1% to 12.7% with an average value of 10.7%. The 10 MPa tests stress strain curves indicate slight strain softening of the soil after maximum shear stress.

Figure 7-21 provides normalized stress paths and Figure 7-22 provides the normalized shear induced pore pressures for the shear phase of the 60% clay specimens sheared at effective consolidation stresses of 1 MPa and 10 MPa. When initially loaded all the test stress paths tend to increase in both normalized shear stress and normalized average effective stress. The tests then curve to a larger normalized shear stress and smaller normalized average effective stress indicating contractive behavior of the soil. After reaching the maximum shear stress, both the shear stress and average effective stress decrease with continued shearing. Figure 7-21 indicates that every 60% clay specimen exhibited contractive behavior through the end of shearing, typical of normally consolidated fine-grained soils. The three 1 MPa tests had very similar behavior. Test TX1446 generated less pore pressure than the other 10 MPa tests. There was no visible evidence of a failure plain on the specimen at the end of shearing. The reason why the specimen behaved differently during shearing is unknown.

Undrained Strength Properties RGoM_EI

Figure 7-23 presents the shear stress normalized to the effective maximum axial consolidation stress by axial strain for the RGoM_EI clay specimens. Three triaxial tests; TX1363, TX1381, and TX1401, were sheared at 1 MPa effective consolidation stress and three tests; TX1473, TX1484, and TX1486, were sheared at a 10 MPa effective consolidation stress. The 1 MPa test measurements have a range of normalized maximum shear stress between 0.24 to 0.26 with an average of 0.25. The range in effective friction angle at the maximum shear stress is between 17.4 to 20.3 degrees with an average of 18.8 degrees. The strain to maximum shear stress ranges between 0.5% to 2.3% with an average value of 1.7%. The maximum effective friction angle ranges between 20.1 degrees to 22.6 degrees with an average value of 21.0 degrees. The strain to the maximum friction angle ranges between 5.7% to 8.2% with an average value of 7.4%. The 1 MPa tests stress strain curves indicate strain softening of the soil after reaching the maximum shear stress.

The 10 MPa test measurements have a range of normalized maximum shear stress between 0.15 to 0.16 with an average of 0.16. The range in effective friction angle at the maximum shear stress is between 14.3 to 15.9 degrees with an average of 14.8 degrees. The strain to maximum shear stress ranges between 3.9% to 5.0% with an average value of 4.3%. The maximum effective friction angle ranges between 16.0 degrees to 16.8 degrees with an average value of 16.6 degrees. The strain to the maximum friction angle ranges between 9.7% to 10.9% with an average value of 10.4%. The 10 MPa tests stress strain curves indicate slight strain softening of the soil after maximum shear stress.

Figure 7-24 provides normalized stress paths and Figure 7-25 provides the normalized shear induced pore pressures for the shear phase of the RGoM_EI clay specimens sheared at effective consolidation stresses of 1 MPa and 10 MPa. When initially loaded all the test stress paths tend to increase in both normalized shear stress and normalized average effective stress. The tests then curve to a larger

normalized shear stress and smaller normalized average effective stress indicating contractive behavior of the soil. After reaching the maximum shear stress, both the shear stress and average effective stress decrease with continued shearing. Figure 7-25 indicates that every RGoM_EI clay specimen exhibited contractive behavior through the end of shearing, typical of normally consolidated fine-grained soils.

7-3 Trends in Strength Parameters

Introduction

This section provides a discussion on trends in mechanical strength parameters by specimen clay content. The strength parameters of greatest interest from the triaxial tests is the maximum undrained shear strength (q_{Max}), maximum effective friction angle (ϕ'_{Max}) and the strains at which these parameters occur (ε_{ms}, ε_{mf} respectively). The maximum shear strength is the largest measured shear strength and is a combination of the effects of consolidation stress, friction angle, and shear induced pore pressures. The maximum effective friction angle is the largest friction angle measured and is a function of the frictional resistance in the soil. As shown in the normalized shear stress by strain plots discussed in Section 7.2 the two parameters rarely coincide at the same strain during the shear phase. Maximum shear strength tends to occur at lower strains and the maximum friction angle tends to occur at higher strains.

Maximum Shear Strength of the Silt and Clay Mixtures

Figure 7-26 provides the average maximum shear stress normalized to the maximum consolidation stress by specimen clay content by mass for the 1 MPa (blue points) and 10 MPa (red points) tests. Except for the 0% clay content specimens the normalized maximum shear stress was found to decrease with increasing clay content and to decrease with increasing stress. The largest measured shear stress was the 10% clay content mixtures for both the 1 MPa stress and the 10 MPa stress levels. The 10% clay content mixture had an average maximum normalized shear stress of 0.52 at 1 MPa and 0.46 at 10 MPa.

The lowest measured normalized shear stress for the 1 MPa tests was at the 50% clay to RGoM_EI mixtures, all having a measured value of 0.25. The lowest measured maximum shear stress for the 10 MPa tests was at the 60% clay and RGoM_EI mixtures with a measured value of 0.16. The 0% clay, 60% clay and RGoM_EI mixtures had the largest change in maximum normalized shear stress with stress level with a difference of 0.09 between 1 and 10 MPa. The 0% clay difference is attributed to scatter in the data as shown by the large ranges in measurements for 0% clay in Figure 7-26. The 60% clay and RGoM_EI difference is attributed to the sensitivity of clay supported materials to changes in consolidation stresses. The 30% clay content and 40% clay content materials show little stress sensitivity in maximum normalized shear strength between a the 1 MPa and 10 MPa tests. The reason for this limited sensitivity thought to be related to the materials being at a transitional fabric between grain supported and clay supported. The reasoning being that the materials have sufficient clay to normalize the mechanical behavior and limit scatter in the data, but also sufficient grains to limit large stress sensitivities associated with clay supported materials.

Figure 7-27 provides the average and range of triaxial specimen densities prior to testing for the different silt and clay mixtures. The densities are parabolic with increasing density with increasing clay content until the most efficient particle packing is achieved (largest density) after which decreasing density with increasing specimen clay content is observed. Within Figure 7-27 the 1 MPa tests show a maximum initial specimen density at 20% clay. The 10 MPa tests show a maximum initial specimen density at 40% clay. This would indicate that for the 1 MPa tests, materials with 20% or less clay would be grain supported and for the 10 MPa tests materials with 40% clay or less would be grain supported. Inversely the materials with clay contents larger than 20% for 1 MPa tests and 40% for 10 MPa tests would be clay supported. The importance of particle packing to the behavior of the materials was detailed in Chapters 5. Where it was shown that at a given stress level during compression the density of the materials organizes similarly with variations in clay content and that the point of the most efficient

packing increases in clay content with increasing effective stress as shown in Figure 7-27. The packing behavior was shown in Chapter 6 to be significant in the dynamic mechanical properties of soils. As the largest measured wave velocities corresponded with 40% clay content tests the mixture with the highest densities. The maximum normalized shear stress presented in Figure 7-26 appears to be indifferent to particle packing as it monotonically decreases with increasing clay content. If density was a controlling factor in strength, one would anticipate the strength results to reflect the parabolic curves of specimen density by clay content shown in Figure 7-27. Strength appears to be more related to the mass of grains within the material than the overall density of the material.

The lower shear strength in the 0% clay specimens is attributed to the lower densities of these test specimens. The 0% specimens were not created using resedimentation methods due to material not holding suction and collapsing during specimen trimming. Instead, these specimens were created through the undercompaction technique. The triaxial specimens created by the resedimentation technique (10% clay content and greater) were all created to a similar effective stress when extruded from the consolidometer, which is predetermined based on the planned maximum consolidation stress during triaxial testing. As such, the 1 MPa tests specimens are extruded at a lower effective stress than the 10 MPa test specimens. The undercompaction specimen creation method does not have control over the stress history of the specimen like the resedimentation method does and relies on mechanical tamping efforts of controlled soil masses in controlled volumes. Figure 7-27 indicates that the change in average specimen density between the 10% clay and 0% clay specimens is significantly larger than the change in specimen density between the 20% clay and 10% clay materials. The low density of the 0% materials is thought to be the cause for the lower maximum shear stress, and if the initial specimen densities for the 0% material was around the density of the 10% material, then the 0% materials would be expected to have a higher maximum shear stress than the 10% material.

Friction Angle of the Silt and Clay Mixtures

The effective friction angle of the material is a significant strength parameter, and two determinations of the friction angle were studied. The effective friction angle corresponding with the maximum shear stress is presented in Figure 7-28 by specimen clay content. Figure 7-28 indicates a trend of decreasing average effective friction angle at maximum shear stress with increasing clay content. The largest values were measured in the 0% and 10% clay content materials at a 1 MPa stress level, as 34.5 degrees and 35 degrees respectively. The lowest values at 1 MPa stress level is at the 60% clay content and RGoM_EI specimens, at 19.3 degrees and 18.8 degrees respectively. For the 10 MPa stress level the lowest value is also at the 60% clay content and RGoM_EI tests, at 14.5 degrees and 14.8 degrees respectively. The effective friction angle at the maximum shear stress generally decreases with increasing effective stress. The 0% Clay content to 30% clay content specimens indicate a 1 to 2 degree difference between 1 MPa and 10 MPa. The 30% clay and 40% clay content materials showed a negligible difference between 1 MPa and 10 MPa. The 50% clay content to RGoM_EI materials showed a decrease in average effective friction angle at the maximum shear stress between 3 and 5 degrees, between the 1 MPa and 10 MPa stress range.

The effective maximum friction angle during the shearing phase is presented by specimen clay content in Figure 7-29. Figure 7-29 indicates a consistent trend of decreasing maximum effective friction angle with increasing clay content. The largest values is measured at the 0% clay content material at a 1 MPa stress and at the 10% clay content material at a 10 MPa stress at 39.8 degrees and 36.3 degrees respectively. The lowest values for the 1 MPa stress level is at RGoM_EI clay at 21 degrees. For the 10 MPa stress level the lowest value is at the 60% clay content and RGoM_EI clay tests, at 16.2 degrees and 16.6 degrees respectively. The maximum effective friction angle generally decreases with increasing effective stress. Between clay contents of 20% and RGoM_EI the change in maximum friction angle with increasing stress is between 1 and 6 degrees over the 1 to 10 MPa stress range. With the change in

maximum effective friction angle generally increasing with increasing clay content. The change in maximum effective friction angle with stress at the 0% clay content tests is around 6 degrees but that is attributed to initial density differences between the 0% clay specimens. The 10% clay content tests showed a negligible stress dependence of the maximum effective friction angle.

Axial Strain During Shearing

The axial strain corresponding with the specimen's maximum shear strength is an indicator of the ductile behavior of the material. The larger the strain to maximum shear stress, the more ductile the material behaves. Figure 7-30 provides the axial strain at maximum shear stress by specimen clay content at both effective stress levels. The 0% clay, 10% clay, and 20% clay materials are not shown in Figure 7-30 as they were not K_0 consolidated but instead were anisotropically consolidated along a computer-controlled stress path with a predetermined K value. This modification to the test program was done as the lower clay content materials were too stiff for the computer controlled K_0 consolidation feedback loop to properly function. Figure 7-30 shows a trend that the axial strain to maximum shear stress increases with increasing clay content and increases with increasing effective stress. This indicates that higher clay content materials have a more ductile behavior and that for the same material a more consolidated material is more ductile. This trend is in agreement with results shown in Donaghe & Townsend, (1975) which illustrated that the K value during consolidation has a significant impact on the strain to maximum shear stress for a material and the larger the K value the higher the strain to maximum shear stress. Figure 7-30 also shows that the higher clay content materials are more sensitive to changes in stress. That is the difference between the strains to maximum shear stress between the 1 MPa and 10 MPa test results increases with increasing clay content.

"The steady state of deformation for any mass of particles is that state in which the mass is continuously deforming at constant volume, constant normal effective stress, constant shear stress and

constant velocity" Poulos (1981). Within the triaxial testing apparatus, there are difficulties in evaluating the critical state conditions due to potential uncontrolled localization, such as the development of shear planes that effect determining the state of stresses. Due to these difficulties critical state behavior was not explored in depth in this study. Instead, maximum friction angle is considered as a first order approximation of the critical state. This was adopted as the maximum friction angle tended to occur at sufficiently high strains, with small changes in shear induced pore pressures approximating a constant volume during shearing. Figure 7-31 provides the average axial strain corresponding to the measured maximum friction angle during undrained shear at two stress levels 1 MPa and 10 MPa. Figure 7-31 shows that the strain to the maximum friction angle is relatively indifferent to lithology but is sensitive to stress. The average strain to maximum friction angle for the 1 MPa tests is between 7.4% and 9.8 %. The average strain to maximum friction angle for the 10 MPa tests is between 7.3% and 11.3%.

Table 7-1: Summary of Triaxial Test Shear Phase Results

Specimen Location		Specimen Data		Conditions			At Max Shear			At Max Obliquity			E_u/σ'_{vc} @		Remarks
													ε_a =	$\Delta q/\Delta q_m$	
Test #	Depth	ω_n	e_i		e_c	σ'_{vc}	ε_a	$\Delta u_e/\sigma'_{vc}$	q/p'	ε_a	$\Delta u_e/\sigma'_{vc}$	q/p'	0.001%	0.3	
Boring		I_p	S_i					$\Delta u_s/\sigma'_{vc}$	ϕ'		$\Delta u_s/\sigma'_{vc}$	ϕ'	0.01%		
Sample	Markers	γ_t	G_s	ε_a/hr	K_c	OCR	q_f/σ'_{vc}	p'_f/σ'_{vc}	A	q_f/σ'_{vc}	p'_f/σ'_{vc}	A	0.1%	0.5	
TX1347	NA	25.830	0.73		0.64	9.92	0.55	0.121	0.43	8.80	0.290	0.53	554.39		32% Clay
			97.59					0.070	25.67		0.266	31.81	324.31		68% Silt
RS481	NA	1.984	2.71	0.3	0.54	1.00	0.33	0.751	0.79	0.29	0.542	3.94	117.08		By Mass
TX1348	NA	29.140	0.83		0.71	9.85	2.44	0.281	0.38	8.94	0.371	0.42	23.09		50% Clay
			98.48					0.216	22.03		0.316	24.77	113.65		50% Silt
RS482	NA	1.954	2.75	0.36	0.70	1.00	0.25	0.668	1.45	0.24	0.563	2.26	101.88		By Mass
TX1350	NA	31.650	0.94		0.80	9.85	3.44	0.267	0.34	9.26	0.339	0.37	366.78		60% Clay
			94.99					0.211	19.71		0.290	21.43	108.04		40% Silt
RS486	NA	1.892	2.77	0.507	0.72	0.96	0.23	0.684	1.59	0.22	0.601	2.31	86.51		By Mass
TX1353	NA		0.66		0.62	9.99	0.29	0.051	0.45	8.68	0.229	0.57			20% Clay
			99.16					0.011	27.05		0.212	34.91	35.39		80% Silt
RS484	NA	2.019	2.69	0.3	0.45	1.00	0.34	0.738	0.43	0.30	0.525	4.67	74.40		By Mass
TX1355	NA		0.76		0.69	9.97	0.66	0.165	0.38	8.91	0.335	0.47	379.66		40% Clay
			94.68					0.112	22.43		0.303	28.05	244.32		60% Silt
RS490	NA	1.965	2.73	0.385	0.61	1.00	0.28	0.723	1.05	0.25	0.522	3.50	112.87		By Mass
TX1358	NA		0.70		0.73	10.43	15.81	-0.005	0.58	7.57	0.108	0.60	444.02		10% Clay
			102.17					-0.303	35.52		-0.117	36.91	283.17		90% Silt
RS491	NA	1.995	2.67	0.5	0.48	1.00	0.70	1.206	-0.01	0.59	0.983	0.16	127.61		By Mass
TX1359	NA		0.93		0.72	9.77	1.00	0.124	0.35	11.20	0.296	0.42	115.74		50% Clay
			98.27					0.085	20.38		0.276	25.04	229.11		50% Silt
RS495	NA	1.904	2.75	0.5	0.61	1.00	0.26	0.740	1.05	0.23	0.539	5.05	87.17		By Mass
TX1362	NA		1.03		0.91	9.90	1.61	0.299	0.46	14.10	0.656	0.72			0% Clay
			100.00					0.196	28.36		0.631	46.45	9.72		100% Silt
UND	NA	1.781	2.65	0.5	0.64	1.00	0.33	0.727	0.97	0.18	0.248	8.78	82.34		By Mass
TX1363	NA				0.81	9.94	2.33	0.177	0.32	8.22	0.259	0.35	170.78		65% Clay
			99.30					0.130	18.81		0.220	20.51	206.30		35% Silt
RS496	NA	1.858	2.78	0.5	0.68	1.00	0.24	0.731	1.26	0.22	0.637	2.25	101.45		By Mass
TX1364	NA		0.76		0.82	9.58	2.04	0.270	0.63	4.11	0.291	0.64	180.14		0% Clay
			100.00					0.007	39.29		0.052	39.54	310.03		100% Silt
UND	NA	1.902	2.65	0.5	0.53	1.00	0.58	0.923	0.34	0.55	0.868	0.41	187.40		By Mass
TX1367	NA		0.73		0.61	9.98	0.27	0.067	0.43	8.31	0.263	0.53	314.09		30% Clay
			99.37					0.021	25.17		0.254	32.06	339.19		70% Silt
RS562	NA	1.980	2.71	0.5	0.50	1.00	0.32	0.752	0.49	0.27	0.501	9.21	113.88		By Mass
TX1368	NA		0.88		0.87	9.88	3.34	0.208	0.58	5.15	0.229	0.58	185.09		0% Clay
			100.00					0.034	35.24		0.075	35.53	204.01		100% Silt
UND	NA	1.876	2.65	0.5	0.50	1.04	0.48	0.828	0.40	0.45	0.779	0.50	132.92		By Mass
TX1369	NA		0.89		0.87	10.06	1.57	0.195	0.56	5.21	0.296	0.58	200.24		0% Clay
			100.00					0.029	33.93		0.201	35.53	239.99		100% Silt
UND	NA	1.868	2.65	0.5	0.50	1.00	0.46	0.833	0.39	0.36	0.626	1.05	141.54		By Mass
TX1373	NA		0.86		0.75	10.18	0.81	0.143	0.59	11.49	0.363	0.70	164.17		0% Clay
			100.00					0.047	35.51		0.426	41.93	211.80		100% Silt
UND	NA	1.884	2.65	0.5	0.42	1.00	0.42	0.730	0.49	0.18	0.269	-1.80	117.51		By Mass
TX1380	NA		0.75		0.61	9.79	0.26	0.065	0.61	7.35	0.253	0.61	8729.56		20% Clay
			102.74					0.021	28.53		0.239	36.71	491.16		80% Silt
RS574	NA	1.974	2.69	0.5	0.46	1.00	0.37	0.779	0.49	0.33	0.545	6.04	90.43		By Mass
TX1381	NA		1.05		0.83	10.92	2.29	0.193	0.61	8.23	0.287	0.61			65% Clay
			99.44					0.136	20.33		0.239	22.55	107.52		35% Silt
RS568	NA	1.860	2.78	0.5	0.68	1.00	0.26	0.762	1.12	0.25	0.653	2.00	118.58		By Mass
TX1383	NA		0.88		0.73	9.91	0.33	0.080	0.61	9.25	0.287	0.61	65.91		50% Clay
			96.98					0.051	19.16		0.276	24.65	227.79		50% Silt
RS537	NA	1.913	2.75	0.5	0.59	0.99	0.26	0.780	0.91	0.23	0.545	9.20	74.21		By Mass
TX1385	NA		1.06		0.75	9.97	0.62	0.107	0.61	8.60	0.283	0.61			60% Clay
			99.04					0.059	20.22		0.251	24.70	93.42		40% Silt
RS579	NA	1.849	2.77	0.5	0.65	1.00	0.29	0.827	0.75	0.26	0.627	3.01	97.49		By Mass

ω_n	Water content prior to testing.	OCR	Overconsolidaiton ratio
I_p	Plasticity Index	ε_a	Axial strain
γ_t	Total mass density	q_f/σ'_{vc}	Normalized shear stress
e_i	Initial void ratio	$\Delta u_e/\sigma'_{vc}$	Normalized excess pore pressure
S_i	Initial saturation	$\Delta u_s/\sigma'_{vc}$	Normalized shear induced pore pressure
G_s	Specific gravity of solids	p'_f/σ'_{vc}	Normalized mean effective stress
ε_a/hr	Shearing strain rate	ϕ'	Effective friction angle
e_c	Void ratio at end of consolidation	A	Skempton's A parameter
K_c	Lateral stress ratio at end of consolidation	E_u/σ'_{vc}	Estimated normalized Youngs Modulus at 0.001%, 0.01% and 0.1% Strain
σ'_{vc}	Vertical effective stress at end of consolidation		

Table 7-1: Summary of Triaxial Test Shear Phase Results Cont.

Specimen Location		Specimen Data		Conditions			At Max Shear			At Max Obliquity			E_u/σ'_{vc} @		Remarks
													ε_a =	$\Delta q/\Delta q_m$	
Test #	Depth	ω_n	e_i		e_c	σ'_{vc}	ε_a	$\Delta u_e/\sigma'_{vc}$	q/p'	ε_a	$\Delta u_e/\sigma'_{vc}$	q/p'	0.001%	0.3	
Boring		I_p	S_i					$\Delta u_s/\sigma'_{vc}$	ϕ'		$\Delta u_s/\sigma'_{vc}$	ϕ'	0.01%		
Sample	Markers	γ_t	G_s	ε_a/hr	K_c	OCR	q_i/σ'_{vc}	p'_i/σ'_{vc}	A	q_i/σ'_{vc}	p'_i/σ'_{vc}	A	0.1%	0.5	
TX1388	NA		0.75		0.67	10.24	16.12	0.093	0.61	8.63	0.183	0.61	7909.58		10% Clay
			91.73					-0.073	34.17		0.074	35.47	570.48		90% Silt
RS583	NA	1.922	2.67	0.5	0.49	1.01	0.51	0.910	0.19	0.43	0.736	0.56	107.46		By Mass
TX1390	NA		0.83		0.63	10.14	0.29	0.071	0.61	8.37	0.280	0.61			30% Clay
			99.62					0.027	24.78		0.276	31.76			70% Silt
RS581	NA	1.977	2.71	0.5	0.50	1.00	0.32	0.757	0.53	0.26	0.487	24.75			By Mass
TX1401	NA		1.12		0.76	10.13	0.54	0.084	0.30	5.69	0.212	0.61	495.52		65% Clay
			100.40					0.048	17.38		0.184	20.09	331.59		35% Silt
RS594	NA	1.850	2.78	0.5	0.64	1.00	0.24	0.794	0.77	0.22	0.654	2.52	85.52		By Mass
TX1407	NA		1.02		0.74	10.13	0.78	0.117	0.31	7.52	0.265	0.37	479.99		60% Clay
			101.61					0.076	18.05		0.235	21.57	200.30		40% Silt
RS599	NA	1.891	2.77	0.5	0.65	1.00	0.24	0.767	0.96	0.22	0.603	2.95	87.90		By Mass
TX1410	NA		0.75		0.59	10.31	0.04	0.013	0.44	9.15	0.199	0.55	1222.76		20% Clay
			102.44					-0.011	25.93		0.206	33.05	297.10		80% Silt
RS597	NA	1.984	2.69	0.5	0.42	1.02	0.33	0.754	0.18	0.29	0.524	-9.82	59.03		By Mass
TX1411	NA		0.86		0.63	10.09	0.37	0.082	0.36	8.54	0.278	0.44			40% Clay
			96.11					0.048	20.91		0.270	26.32	46.69		60% Silt
RS598	NA	1.916	2.73	0.5	0.57	0.99	0.27	0.751	0.81	0.23	0.516	11.64	84.55		By Mass
TX1413	NA		0.72		0.64	9.85	11.78	0.225	0.58	9.83	0.236	0.58	3448.87		10% Clay
			99.17					0.170	35.46		0.189	35.55	432.00		90% Silt
	NA	1.973	2.67	0.5	0.47	1.00	0.35	0.596	1.37	0.33	0.574	1.68	112.25		By Mass
TX1415	NA		0.88		0.61	10.11	1.29	0.215	0.35	9.73	0.378	0.43			40% Clay
			99.47					0.154	20.60		0.332	25.74	48.34		60% Silt
RS606	NA	1.924	2.73	0.5	0.68	1.00	0.25	0.712	1.19	0.23	0.527	2.74	96.00		By Mass
TX1420	NA		0.81		0.61	10.16	0.32	0.086	0.38	8.02	0.301	0.49			30% Clay
			97.88					0.045	22.37		0.288	29.43	190.49		70% Silt
RS614	NA	1.942	2.71	0.5	0.55	1.00	0.29	0.752	0.70	0.24	0.494	8.21	94.70		By Mass
TX1431	NA		0.60		0.55	102.21	11.35	0.009	0.58	11.35	0.009	0.58	3610.96		10% Clay
			98.75					-0.261	35.70		-0.261	35.70	6189.56		90% Silt
RS627	NA	2.044	2.67	0.5	0.48	1.00	0.67	1.147	0.01	0.67	1.147	0.01	86.09		By Mass
TX1438	NA		0.89		0.88	98.80	3.03	0.207	0.52	6.59	0.225	0.53	17.55		0% Clay
			100.00					0.146	31.38		0.166	32.15	194.88		100% Silt
NA	NA	1.869	2.65	0.5	0.50	1.00	0.32	0.623	1.08	0.32	0.602	1.22	82.35		By Mass
TX1439	NA		0.96		0.81	99.54	8.62	0.190	0.60	8.62	0.190	0.60			0% Clay
			100.00					0.079	36.61		0.079	36.61			100% Silt
NA	NA	1.838	2.65	0.5	0.49	1.01	0.45	0.750	0.57	0.45	0.750	0.57	106.60		By Mass
TX1442	NA		0.62		0.43	99.63	4.30	0.145	0.27	3.96	0.149	0.27			50% Clay
			97.61					0.085	15.52		0.088	15.53	27.59		50% Silt
RS640	NA	2.076	2.75	0.5	0.76	1.00	0.22	0.815	0.76	0.22	0.813	0.78	105.08		By Mass
TX1443	NA		0.69		0.54	100.77	0.76	0.125	0.47	8.61	0.283	0.60			10% Clay
			97.31					0.073	28.23		0.237	37.12			90% Silt
RS638	NA	1.980	2.67	0.5	0.49	1.00	0.33	0.702	0.80	0.32	0.535	2.05	90.52		By Mass
TX1444	NA		0.62		0.48	99.30	1.03	0.132	0.46	5.56	0.231	0.52			20% Clay
			98.32					0.092	27.61		0.212	31.31	316.79		80% Silt
RS645	NA	2.043	2.69	0.5	0.49	1.00	0.31	0.677	1.09	0.28	0.547	3.77	79.31		By Mass
TX1446	NA		0.74		0.44	99.35	3.51	0.164	0.23	8.14	0.238	0.25			60% Clay
			98.08					0.109	13.26		0.188	14.27	110.61		40% Silt
RS646	NA	2.013	2.77	0.5	0.77	1.00	0.18	0.801	1.05	0.18	0.721	1.67	69.54		By Mass
TX1447	NA		0.57		0.40	99.81	11.01	0.170	0.44	11.01	0.170	0.44	10.85		30% Clay
			99.17					0.107	26.86		0.107	26.86	563.15		70% Silt
RS652	NA	2.088	2.71	0.5	0.56	1.01	0.31	0.702	0.87	0.31	0.702	0.87	107.92		By Mass
TX1456	NA		0.58		0.40	96.93	1.23	0.182	0.37	11.86	0.280	0.40	291.16		40% Clay
			99.15					0.126	21.45		0.244	23.36	888.53		60% Silt
RS655	NA	2.095	2.73	0.5	0.64	1.00	0.26	0.725	1.07	0.24	0.597	2.46	115.69		By Mass

ω_n	Water content prior to testing.	OCR	Overconsolidaiton ratio
I_p	Plasticity Index	ε_a	Axial strain
γ_t	Total mass density	q_i/σ'_{vc}	Normalized shear stress
e_i	Initial void ratio	$\Delta u_e/\sigma'_{vc}$	Normalized excess pore pressure
S_i	Initial saturation	$\Delta u_s/\sigma'_{vc}$	Normalized shear induced pore pressure
G_s	Specific gravity of solids	p'_i/σ'_{vc}	Normalized mean effective stress
ε_a/hr	Shearing strain rate	ϕ'	Effective friction angle
e_c	Void ratio at end of consolidation	A	Skempton's A parameter
K_c	Lateral stress ratio at end of consolidation	E_u/σ'_{vc}	Estimated normalized Youngs Modulus at 0.001%, 0.01% and 0.1% Strain
σ'_{vc}	Vertical effective stress at end of consolidation		

Table 7-1: Summary of Triaxial Test Shear Phase Results Cont.

Specimen Location		Specimen Data		Conditions			At Max Shear			At Max Obliquity			E_{u}/σ'_{vc} @		Remarks
													ε_a =	$\Delta q/\Delta q_m$	
Test #	Depth	ω_n	e_i		e_c	σ'_{vc}	ε_a	$\Delta u_e/\sigma'_{vc}$	q/p'	ε_a	$\Delta u_e/\sigma'_{vc}$	q/p'	0.001%	0.3	
Boring		I_p	S_i					$\Delta u_s/\sigma'_{vc}$	ϕ'		$\Delta u_s/\sigma'_{vc}$	ϕ'	0.01%		
Sample	Markers	γ_t	G_s	ε_a/hr	K_c	OCR	q_f/σ'_{vc}	p'_f/σ'_{vc}	A	q_f/σ'_{vc}	p'_f/σ'_{vc}	A	0.1%	0.5	
TX1458	NA		0.61		0.42	98.61	2.45	0.264	0.31	10.84	0.358	0.34	143.01		50% Clay
			100.90					0.214	18.29		0.316	19.96	486.86		50% Silt
RS656	NA	2.096	2.75	0.5	0.73	1.00	0.21	0.680	1.68	0.20	0.572	2.91	79.81		By Mass
TX1459	NA		0.74		0.59	98.31	11.04	0.171	0.59	11.04	0.171	0.59			10% Clay
			100.68					0.104	35.99		0.104	35.99	396.46		90% Silt
RS662	NA	1.966	2.67	0.5	0.44	0.99	0.38	0.649	0.84	0.38	0.649	0.84	98.79		By Mass
TX1463	NA		0.59		0.46	100.20	0.29	0.067	0.43	8.14	0.282	0.57			20% Clay
			97.33					0.027	25.24		0.262	34.61	287.20		80% Silt
RS672	NA	2.055	2.69	0.5	0.49	1.00	0.32	0.744	0.55	0.28	0.498	4.95	78.41		By Mass
TX1464	NA		0.56		0.42	99.59	0.62	0.115	0.42	9.90	0.253	0.50			30% Clay
			96.42					0.073	24.58		0.220	30.16	318.65		70% Silt
RS673	NA	2.083	2.71	0.5	0.53	1.00	0.30	0.714	0.92	0.28	0.562	2.67	143.06		By Mass
TX1468	NA		1.19		1.02	99.91	2.32	0.136	0.48	9.17	0.234	0.55			0% Clay
			100.00					0.082	28.53		0.183	33.38	235.02		100% Silt
NA	NA	1.750	2.65	0.5	0.50	1.00	0.33	0.695	0.84	0.33	0.591	1.56	61.02		By Mass
TX1473	NA		0.68		0.49	99.86	3.91	0.306	0.24	10.59	0.397	0.27			65% Clay
			97.86					0.266	14.28		0.362	16.00	164.39		35% Silt
RS678	NA	2.056	2.78	0.5	0.80	1.00	0.16	0.639	2.58	0.14	0.538	3.94	62.99		By Mass
TX1475	NA		0.63		0.40	99.33	2.20	0.251	0.32	11.90	0.474	0.41			50% Clay
			99.53					0.189	18.55		0.440	24.05	580.77		50% Silt
RS680	NA	2.073	2.75	0.5	0.73	1.00	0.22	0.707	1.37	0.18	0.441	5.12	98.97		By Mass
TX1478	NA		0.57		0.38	100.63	1.49	0.192	0.38	10.44	0.335	0.44	2351.03		40% Clay
			98.67					0.142	22.45		0.310	26.36	572.90		60% Silt
RS681	NA	2.102	2.73	0.5	0.62	1.00	0.26	0.688	1.32	0.23	0.507	4.80	102.46		By Mass
TX1480	NA		0.64		0.48	100.09	3.62	0.370	0.25	12.65	0.467	0.28	5039.50		60% Clay
			98.78					0.319	14.41		0.427	16.50	359.53		40% Silt
RS684	NA	2.079	2.77	0.5	0.83	1.00	0.15	0.592	2.94	0.14	0.480	4.59	54.65		By Mass
TX1481	NA		0.66		0.46	100.18	3.77	0.329	0.26	11.30	0.426	0.29	958.95		60% Clay
			99.22					0.291	14.88		0.391	16.87	329.22		40% Silt
RS683	NA	2.065	2.77	0.5	0.80	1.00	0.16	0.618	2.88	0.15	0.514	4.43	52.99		By Mass
TX1484	NA		0.75		0.48	100.10	5.05	0.342	0.26	9.67	0.402	0.28			65% Clay
			98.30					0.297	15.92		0.361	16.83	502.75		35% Silt
RS687	NA	2.014	2.78	0.5	0.80	1.00	0.16	0.615	2.52	0.15	0.546	3.46	66.70		By Mass
TX1486	NA		0.67		0.47	99.45	3.94	0.301	0.24	10.90	0.397	0.27			65% Clay
			101.02					0.271	14.29		0.367	16.26	367.31		35% Silt
RS688	NA	2.076	2.78	0.5	0.79	1.00	0.15	0.623	2.94	0.14	0.525	4.37	59.86		By Mass
TX1490	NA		0.93		0.70	10.32	1.14	0.158	0.35	6.31	0.246	0.39	142.68		50% Clay
			100.48					0.107	20.38		0.202	22.68	328.75		50% Silt
RS690	NA	1.916	2.75	0.5	0.64	1.00	0.26	0.745	1.04	0.25	0.646	1.88	112.27		By Mass
TX1491	NA		0.74		0.62	9.99	0.33	0.087	0.42	8.73	0.277	0.53	102.89		30% Clay
			99.84					0.039	24.57		0.251	31.91	143.24		70% Silt
RS693	NA	1.988	2.71	0.5	0.51	0.99	0.31	0.746	0.61	0.28	0.523	3.74	120.13		By Mass
TX1492	NA		0.78		0.63	10.02	0.36	0.108	0.44	9.32	0.310	0.59	314.28		20% Clay
			100.89					0.064	26.28		0.293	35.87	270.46		80% Silt
RS694	NA	1.962	2.69	0.5	0.51	1.00	0.32	0.712	0.82	0.28	0.470	6.10	112.37		By Mass
TX1495	NA		0.55		0.41	100.42	0.61	0.118	0.42	13.09	0.327	0.54	8960.75		30% Clay
			94.93					0.077	24.69		0.314	32.56	768.98		70% Silt
RS692	NA	2.091	2.71	0.5	0.54	0.99	0.30	0.713	0.92	0.25	0.459	11.30	101.78		By Mass
TX1499	NA		0.54		0.40	100.70	1.20	0.181	0.37	8.46	0.332	0.44	10.07		40% Clay
			97.62					0.126	21.79		0.298	26.32	873.60		60% Silt
RS703	NA	2.114	2.73	0.5	0.63	1.00	0.27	0.718	1.08	0.24	0.537	3.00	118.50		By Mass
TX1501	NA		0.65		0.46	100.15	3.60	0.296	0.26	10.82	0.392	0.30	217.19		60% Clay
			100.13					0.257	15.26		0.358	17.27	321.12		40% Silt
RS712	NA	2.076	2.77	0.5	0.77	1.00	0.17	0.636	2.64	0.16	0.531	4.23	61.72		By Mass

ω_n	Water content prior to testing.	OCR	Overconsolidaiton ratio
I_p	Plasticity Index	ε_a	Axial strain
γ_t	Total mass density	q_f/σ'_{vc}	Normalized shear stress
e_i	Initial void ratio	$\Delta u_e/\sigma'_{vc}$	Normalized excess pore pressure
S_i	Initial saturation	$\Delta u_s/\sigma'_{vc}$	Normalized shear induced pore pressure
G_s	Specific gravity of solids	p'_f/σ'_{vc}	Normalized mean effective stress
ε_a/hr	Shearing strain rate	ϕ'	Effective friction angle
e_c	Void ratio at end of consolidation	A	Skempton's A parameter
K_c	Lateral stress ratio at end of consolidation	E_u/σ'_{vc}	Estimated normalized Youngs Modulus at 0.001%, 0.01% and 0.1% Strain
σ'_{vc}	Vertical effective stress at end of consolidation		

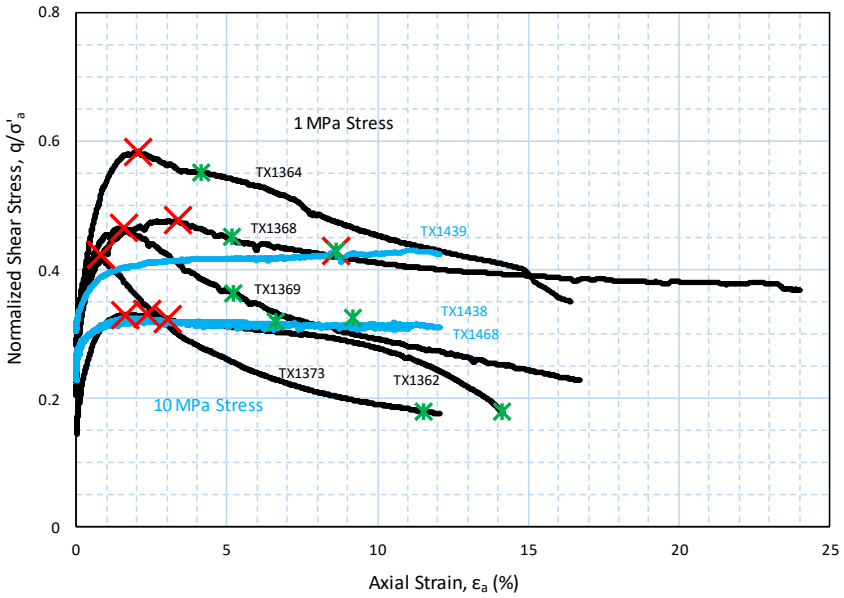


Figure 7-1: Normalized shear stress by axial strain from undrained shear phase of triaxial tests performed on 0% clay content specimens, at two consolidation stress levels 1 MPa and 10 MPa. The red crosses indicate maximum shear stress and the green crosses indicate maximum effective friction angle.

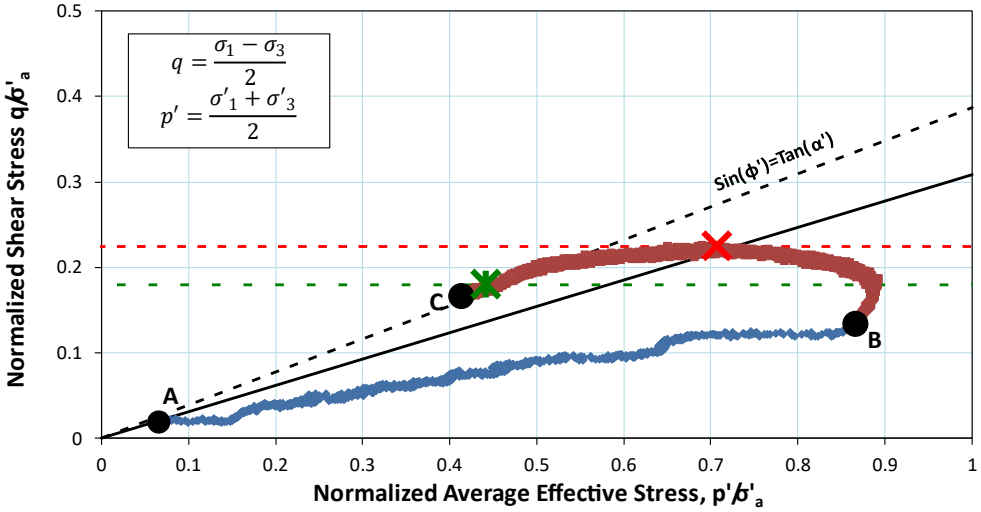


Figure 7-2: Example K_0 consolidated undrained compression triaxial test stress path from test TX1475 a 50% clay specimen. K_0 consolidation performed between points A and B (blue points), where the measured K_0 value is σ'_1/σ'_3 at point B. Undrained compression shearing stress path is presented as points B to C (red points). The maximum shear stress is labeled q_{Max}, and the corresponding effective friction angle (α') is represented as the solid line through the origin and q_{Max}. The maximum measured effective friction angle is indicated by the ϕ'_{Max} and the corresponding effective friction angle (α') is represented as the dashed line through the origin and ϕ'_{Max}. The p-q space friction angle (α') is related to the Mohr-Coulomb friction angle (ϕ') by $Sin(\phi') = Tan(\alpha')$.

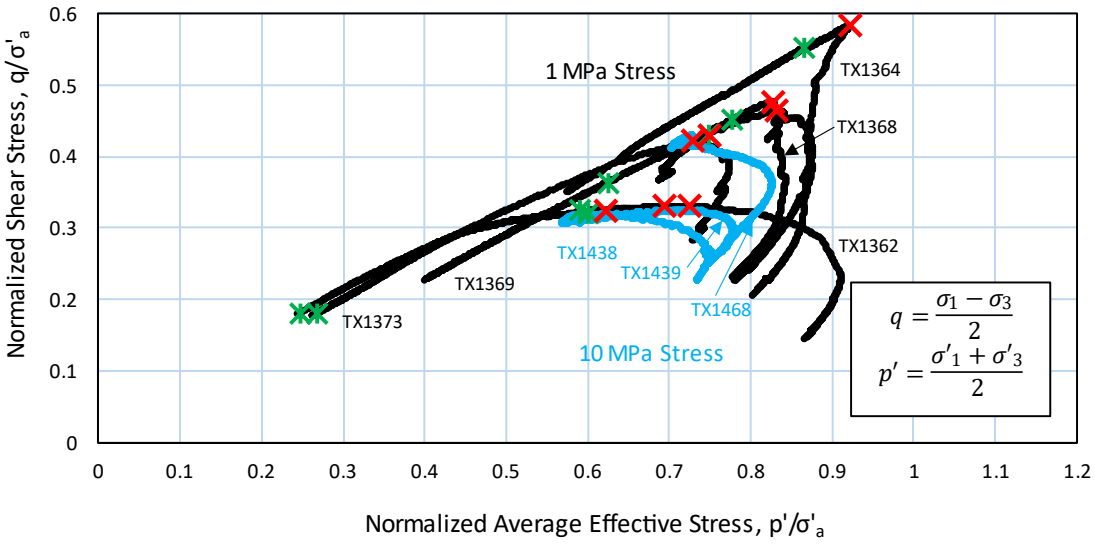


Figure 7-3: Normalized shear stress (q) by normalized average effective stress (p') from undrained shear phase of triaxial tests performed on 0% clay content specimens, at two consolidation stress levels 1 MPa and 10 MPa. The red crosses indicate maximum shear stress and the green crosses indicate maximum effective friction angle.

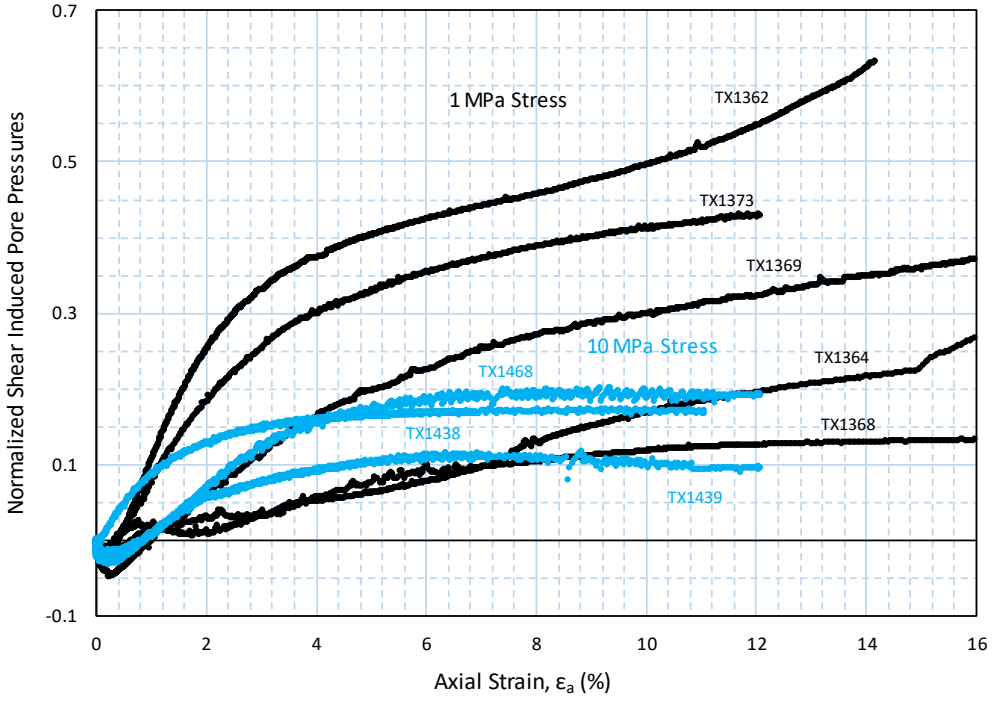


Figure 7-4: Normalized shear induced pore pressures from undrained shear phase of triaxial tests performed on 0% clay content specimens, at two consolidation stress levels 1 MPa and 10 MPa.

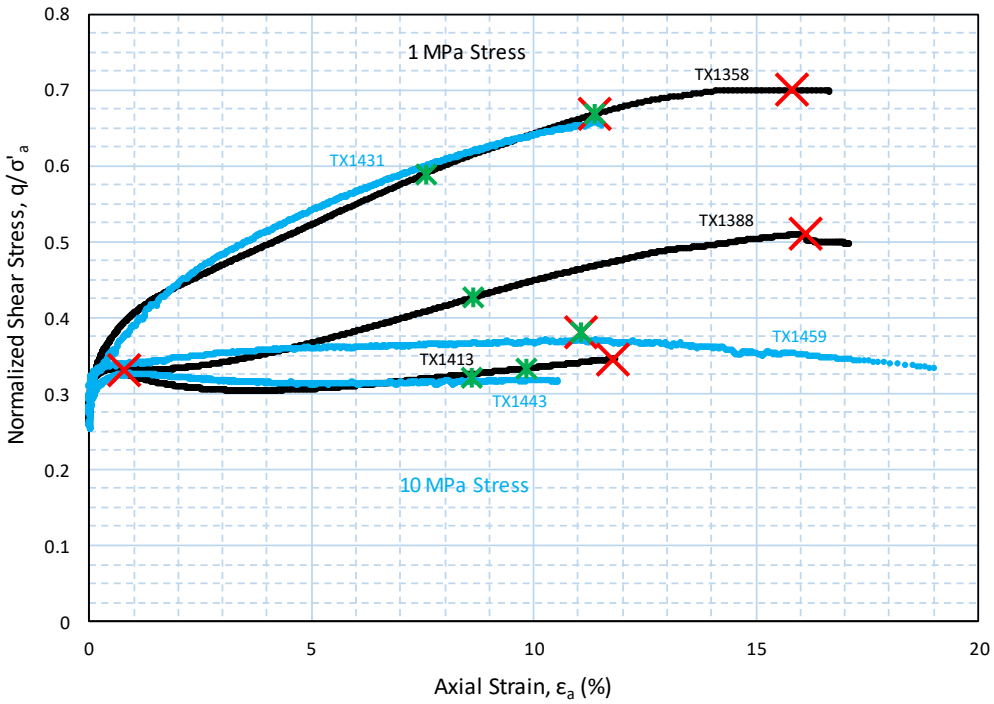


Figure 7-5: Normalized shear stress by axial strain from undrained shear phase of triaxial tests performed on 10% clay content specimens, at two consolidation stress levels 1 MPa and 10 MPa. The red crosses indicate maximum shear stress and the green crosses indicate maximum effective friction angle.

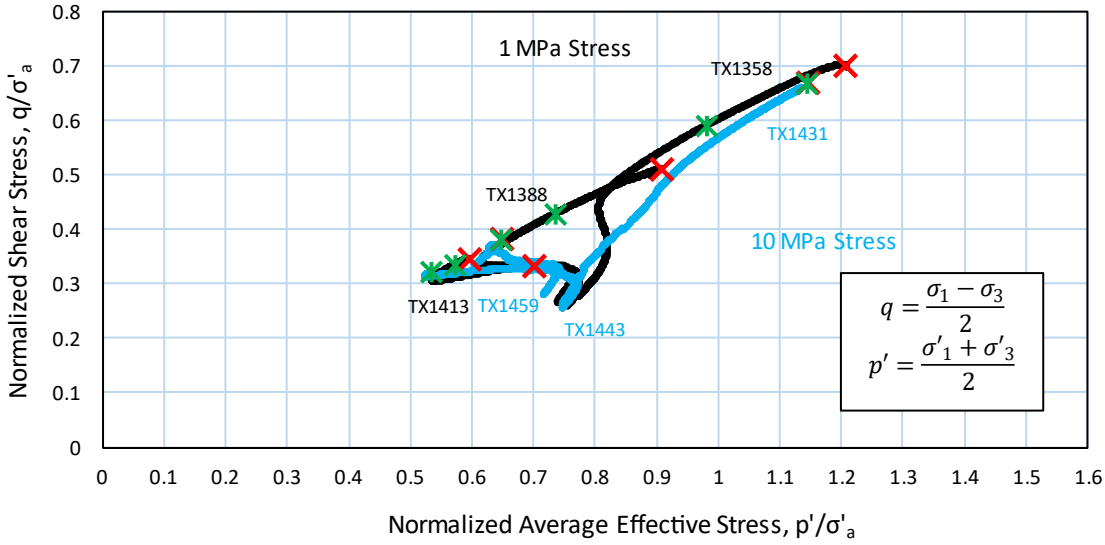


Figure 7-6: Normalized shear stress (q) by normalized average effective stress (p') from undrained shear phase of triaxial tests performed on 10% clay content specimens, at two consolidation stress levels 1 MPa and 10 MPa. The red crosses indicate maximum shear stress and the green crosses indicate maximum effective friction angle.

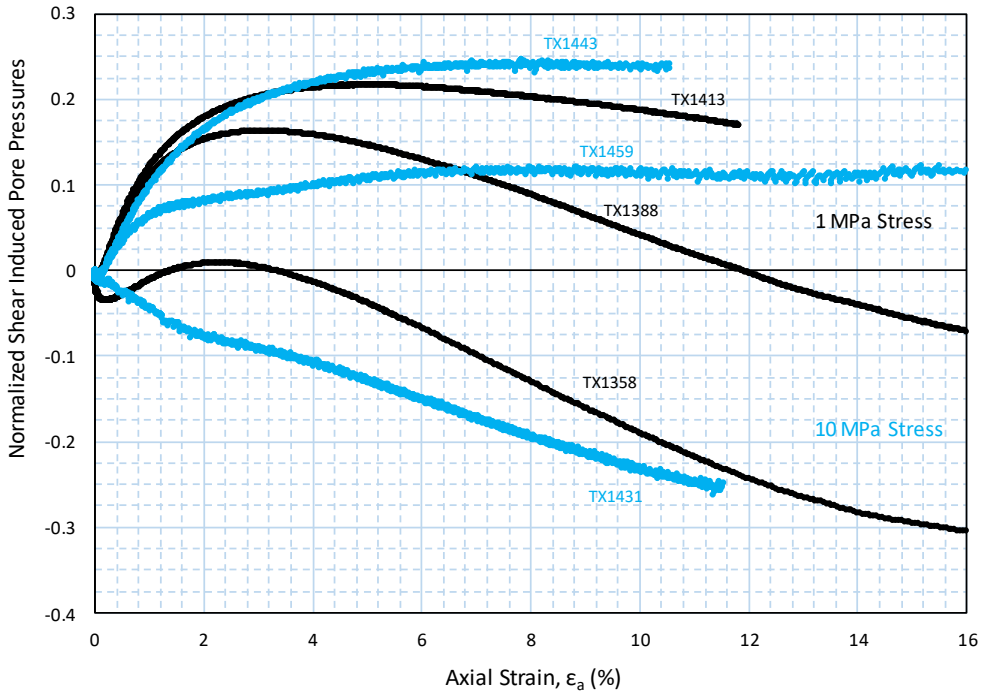


Figure 7-7: Normalized shear induced pore pressures from undrained shear phase of triaxial tests performed on 10% clay content specimens, at two consolidation stress levels 1 MPa and 10 MPa.

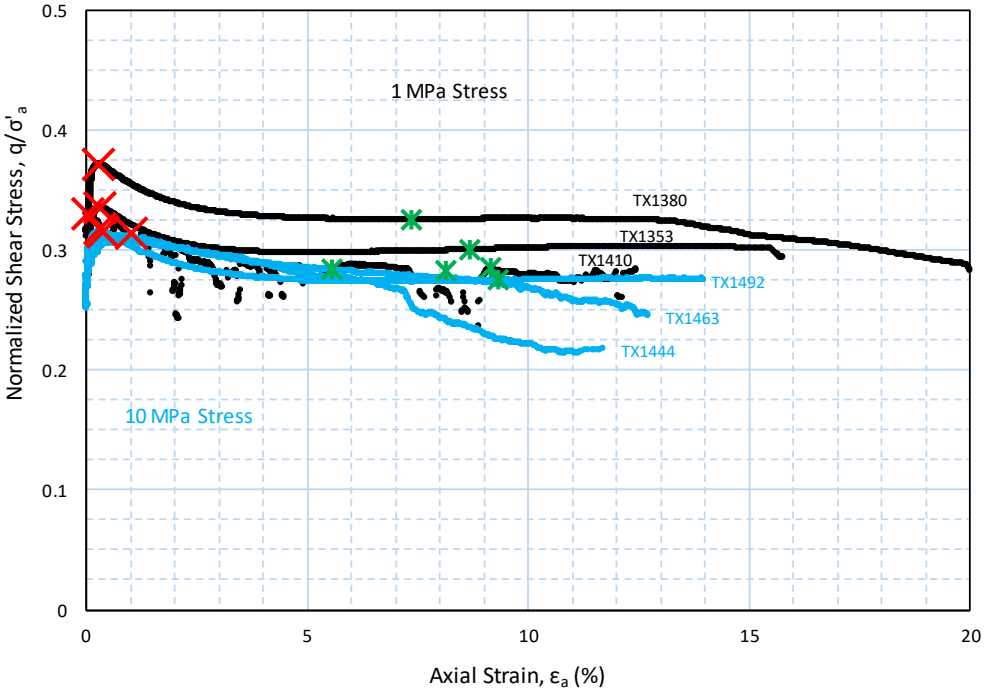


Figure 7-8: Normalized shear stress by axial strain from undrained shear phase of triaxial tests performed on 20% clay content specimens, at two consolidation stress levels 1 MPa and 10 MPa. The red crosses indicate maximum shear stress and the green crosses indicate maximum effective friction angle.

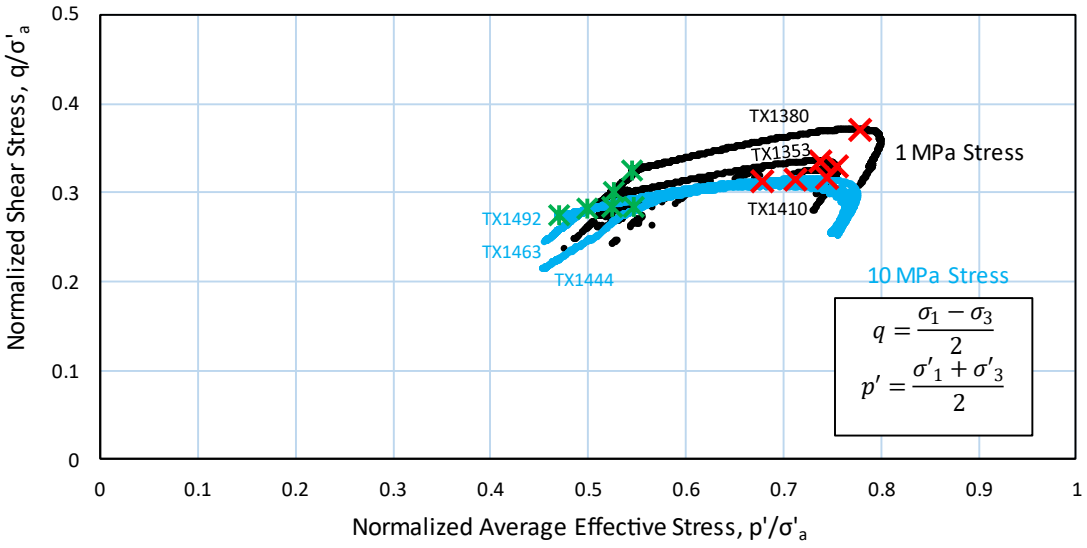


Figure 7-9: Normalized shear stress (q) by normalized average effective stress (p') from undrained shear phase of triaxial tests performed on 20% clay content specimens, at two consolidation stress levels 1 MPa and 10 MPa. The red crosses indicate maximum shear stress and the green crosses indicate maximum effective friction angle.

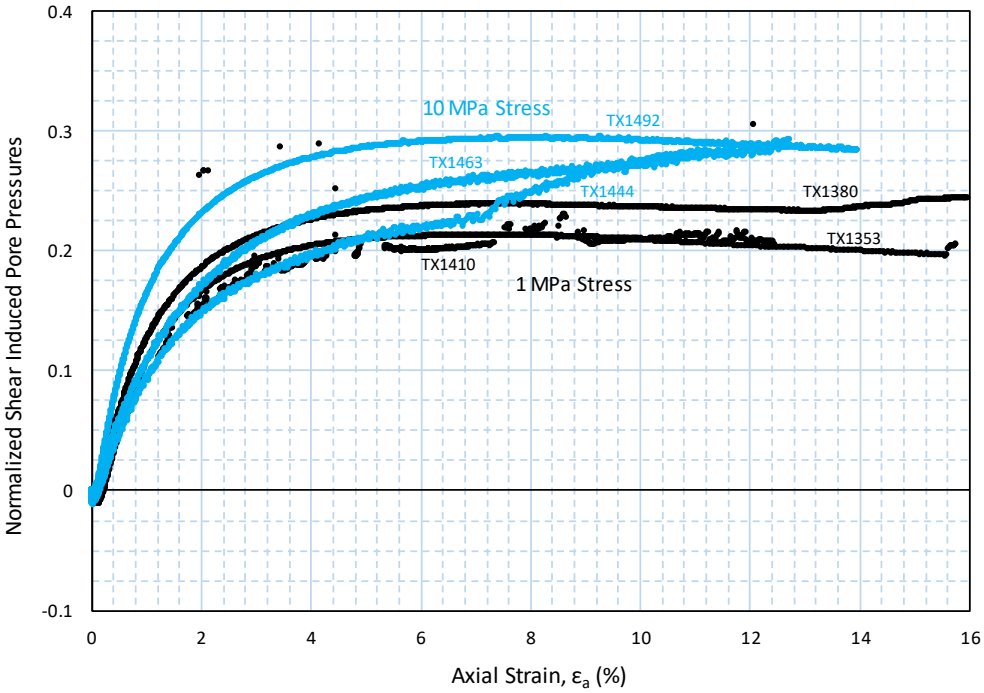


Figure 7-10: Normalized shear induced pore pressures from undrained shear phase of triaxial tests performed on 20% clay content specimens, at two consolidation stress levels 1 MPa and 10 MPa.

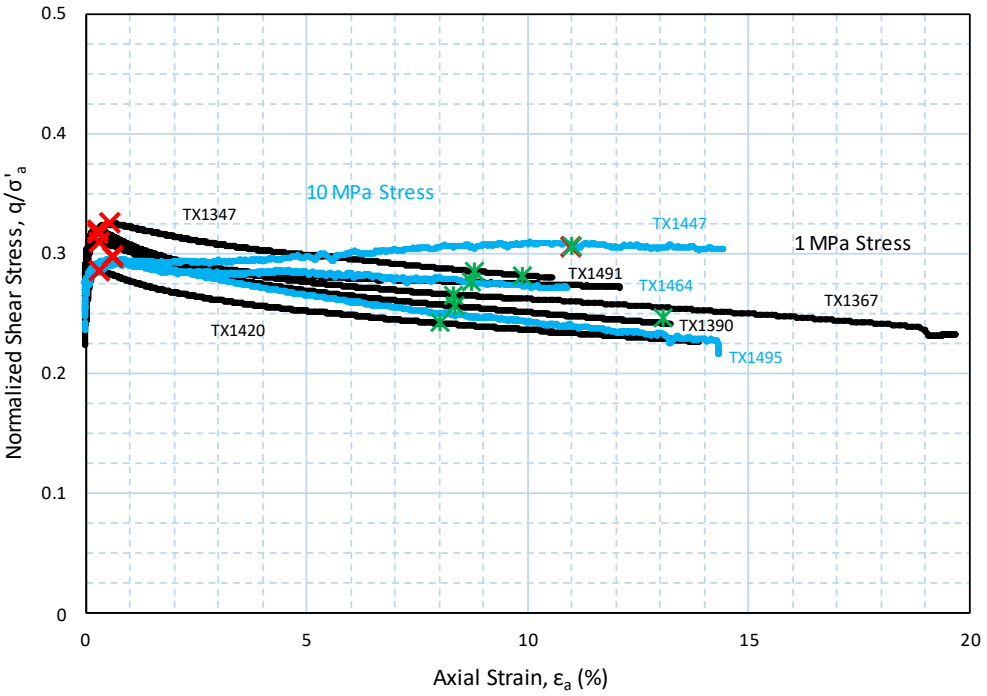


Figure 7-11: Normalized shear stress by axial strain from undrained shear phase of triaxial tests performed on 30% clay content specimens, at two consolidation stress levels 1 MPa and 10 MPa. The red crosses indicate maximum shear stress and the green crosses indicate maximum effective friction angle.

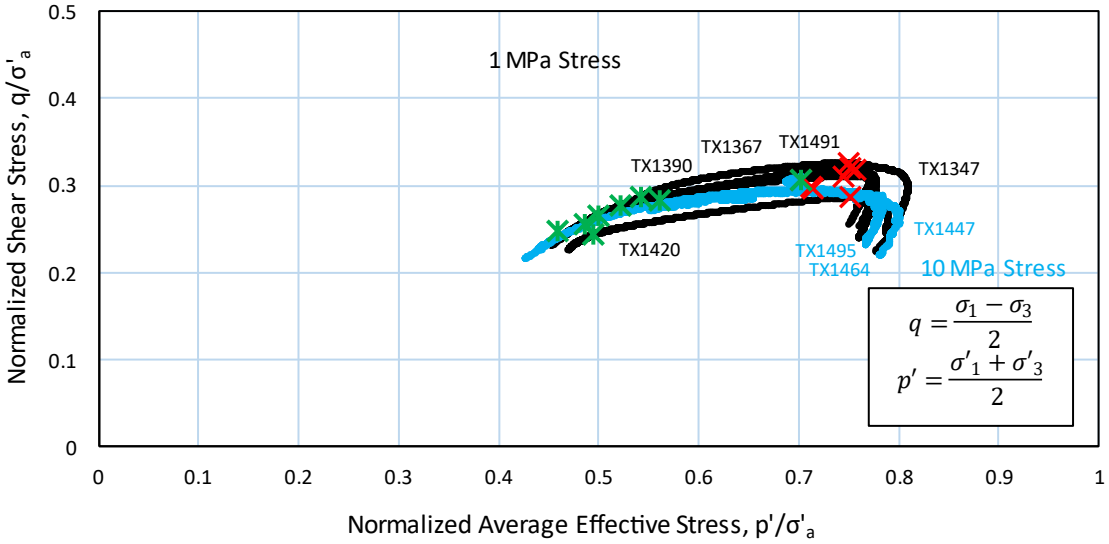


Figure 7-12: Normalized shear stress (q) by normalized average effective stress (p') from undrained shear phase of triaxial tests performed on 30% clay content specimens, at two consolidation stress levels 1 MPa and 10 MPa. The red crosses indicate maximum shear stress and the green crosses indicate maximum effective friction angle.

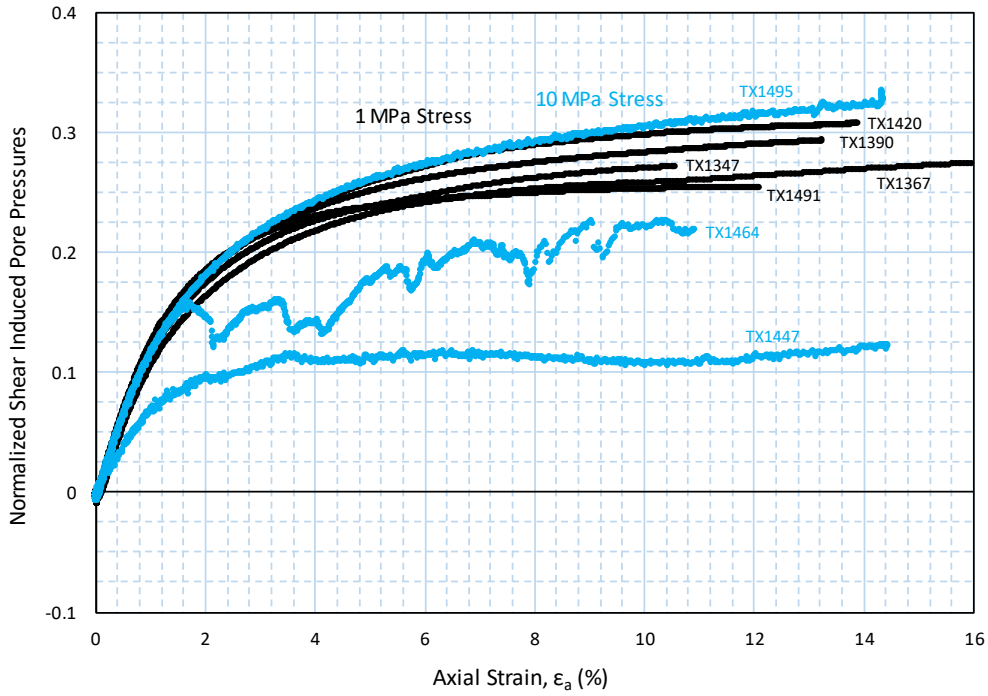


Figure 7-13: Normalized shear induced pore pressures from undrained shear phase of triaxial tests performed on 30% clay content specimens, at two consolidation stress levels 1 MPa and 10 MPa.

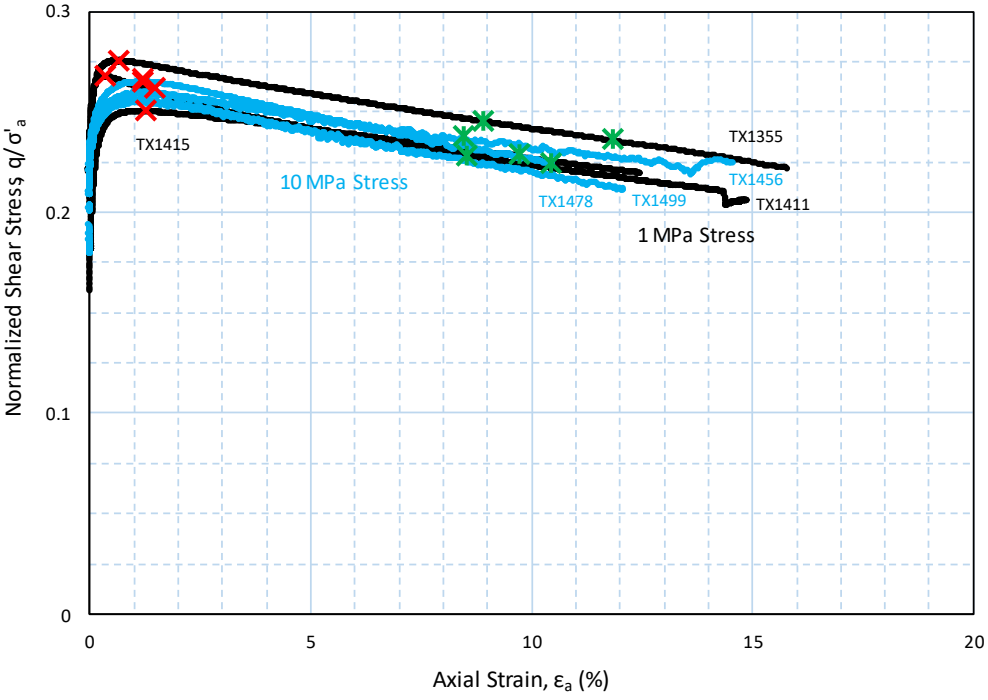


Figure 7-14: Normalized shear stress by axial strain from undrained shear phase of triaxial tests performed on 40% clay content specimens, at two consolidation stress levels 1 MPa and 10 MPa. The red crosses indicate maximum shear stress and the green crosses indicate maximum effective friction angle.

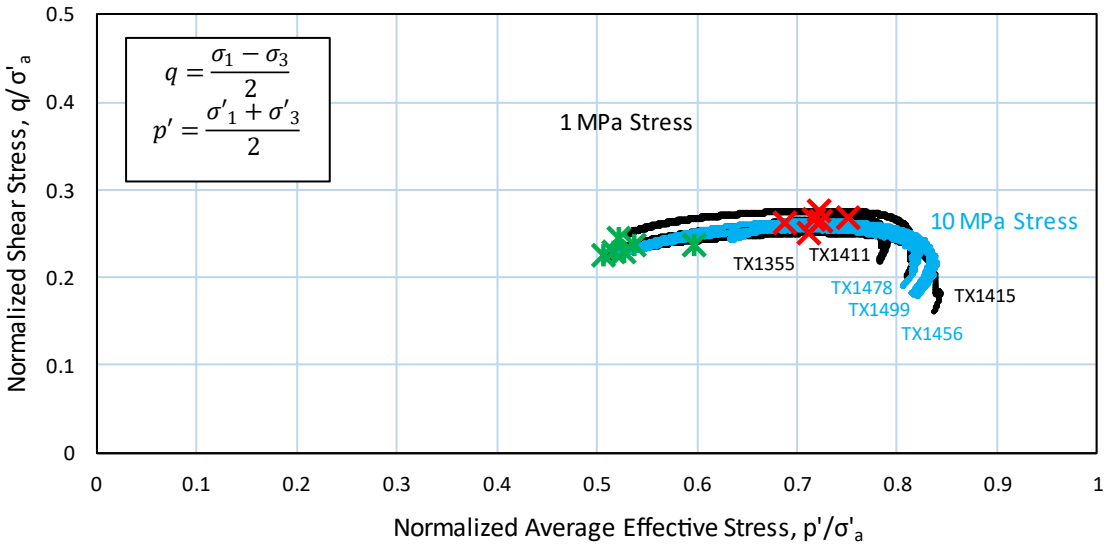


Figure 7-15: Normalized shear stress (q) by normalized effective average effective stress (p') from undrained shear phase of triaxial tests performed on 40% clay content specimens, at two consolidation stress levels 1 MPa and 10 MPa. The red crosses indicate maximum shear stress and the green crosses indicate maximum effective friction angle.

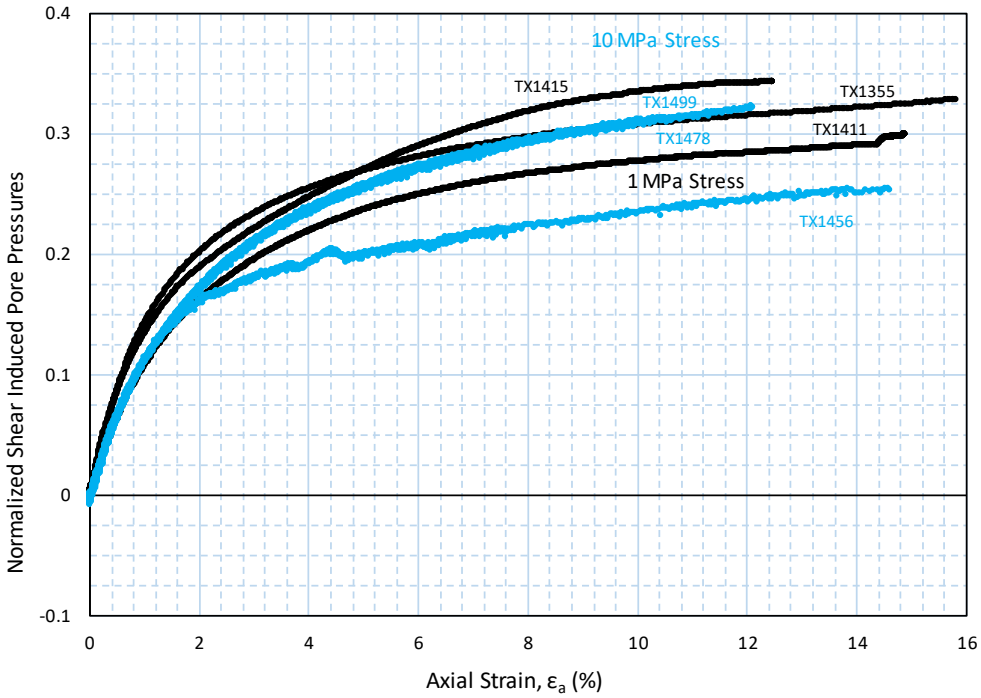


Figure 7-16: Normalized shear induced pore pressures from undrained shear phase of triaxial tests performed on 40% clay content specimens, at two consolidation stress levels 1 MPa and 10 MPa.

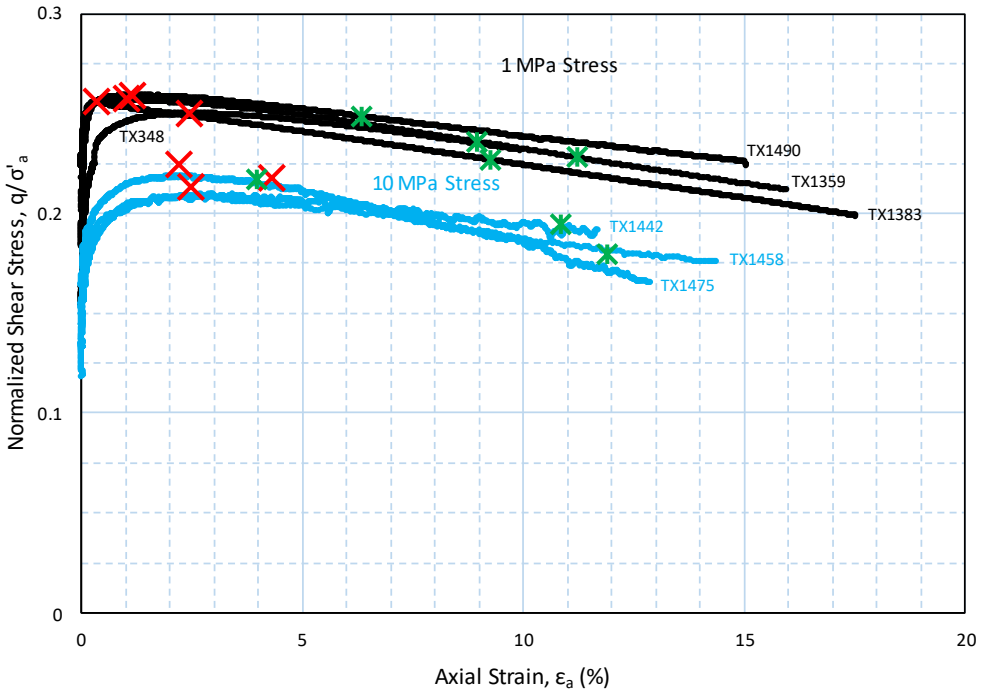


Figure 7-17: Normalized shear stress by axial strain from undrained shear phase of triaxial tests performed on 50% clay content specimens, at two consolidation stress levels 1 MPa and 10 MPa. The red crosses indicate maximum shear stress and the green crosses indicate maximum effective friction angle.

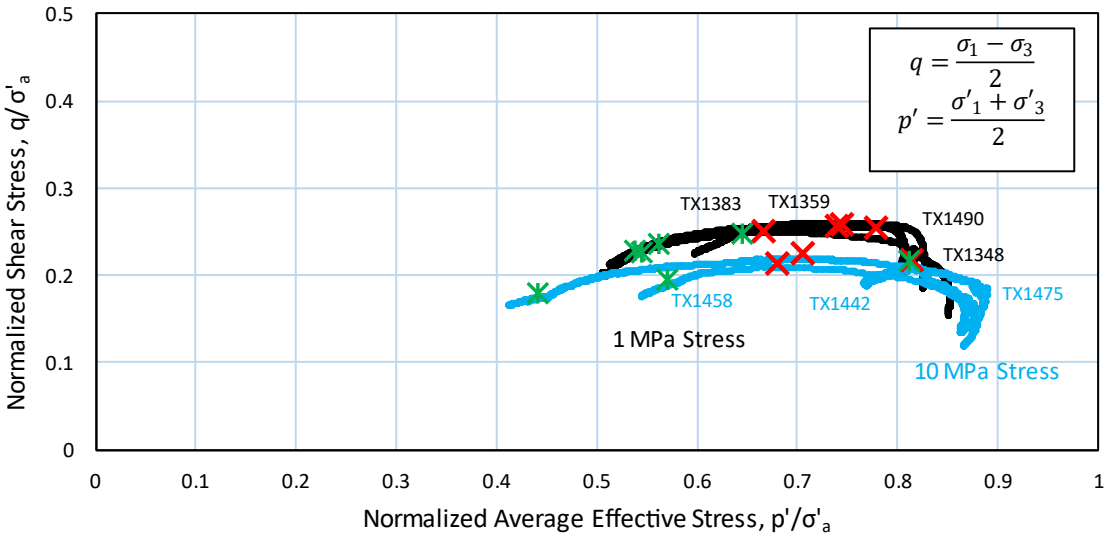


Figure 7-18: Normalized shear stress (q) by normalized average effective stress (p') from undrained shear phase of triaxial tests performed on 50% clay content specimens, at two consolidation stress levels 1 MPa and 10 MPa. The red crosses indicate maximum shear stress and the green crosses indicate maximum effective friction angle.

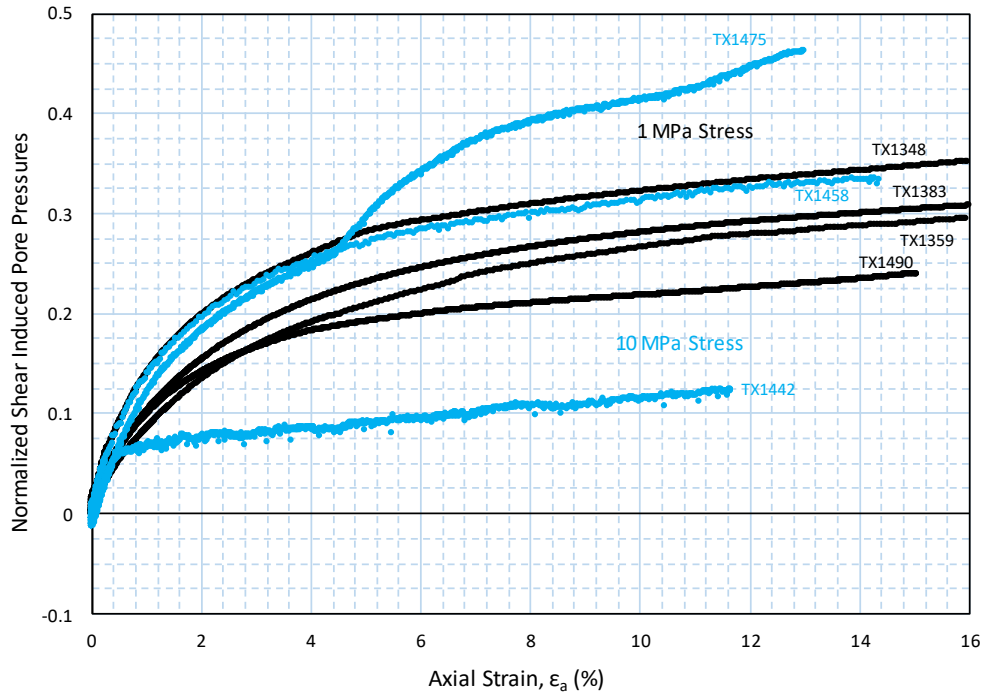


Figure 7-19: Normalized shear induced pore pressures from undrained shear phase of triaxial tests performed on 50% clay content specimens, at two consolidation stress levels 1 MPa and 10 MPa.

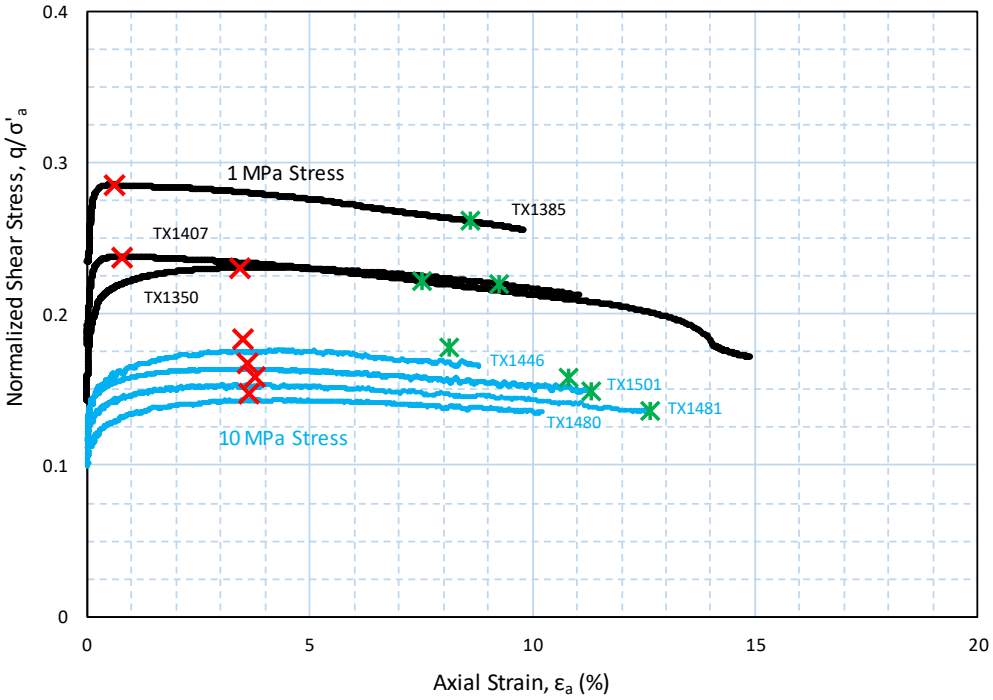


Figure 7-20: Normalized shear stress by axial strain from undrained shear phase of triaxial tests performed on 60% clay content specimens, at two consolidation stress levels 1 MPa and 10 MPa. The red crosses indicate maximum shear stress and the green crosses indicate maximum effective friction angle.

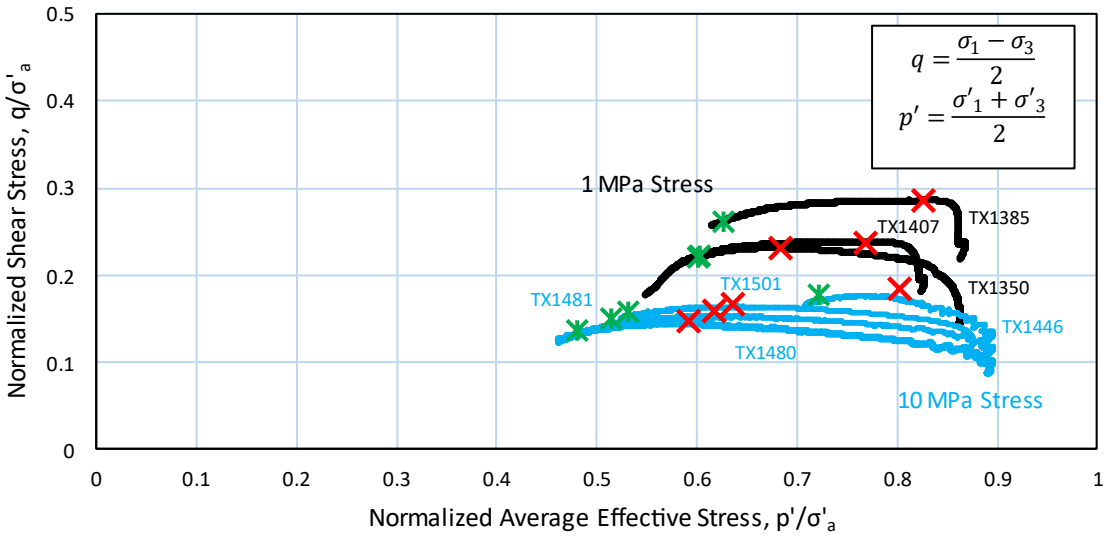


Figure 7-21: Normalized shear stress (q) by normalized average effective stress (p') from undrained shear phase of triaxial tests performed on 60% clay content specimens, at two consolidation stress levels 1 MPa and 10 MPa. The red crosses indicate maximum shear stress and the green crosses indicate maximum effective friction angle.

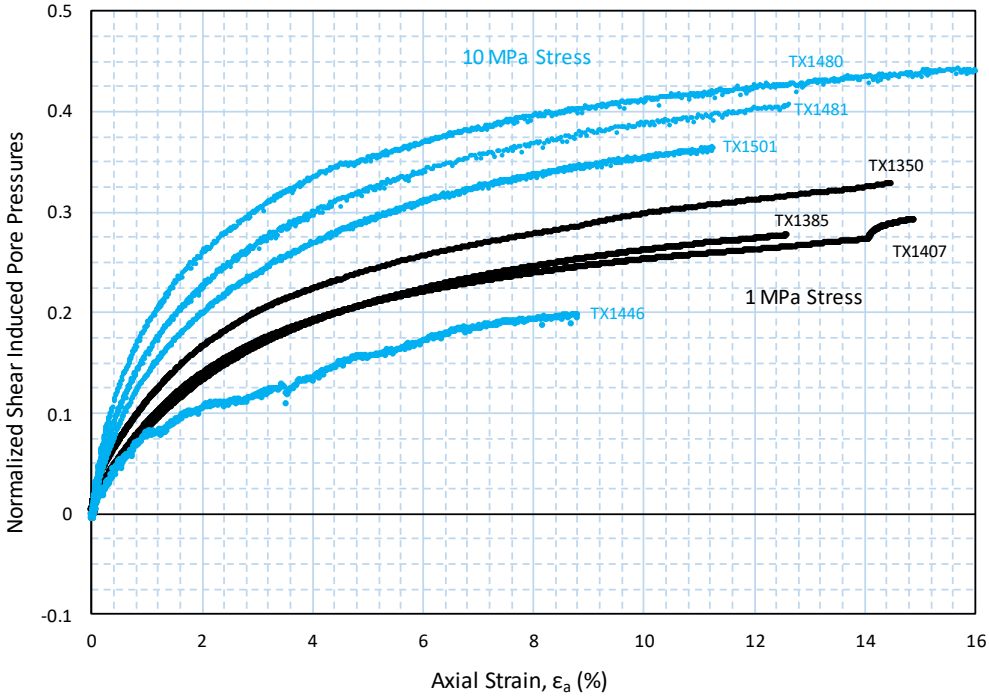


Figure 7-22: Normalized shear induced pore pressures from undrained shear phase of triaxial tests performed on 60% clay content specimens, at two consolidation stress levels 1 MPa and 10 MPa.

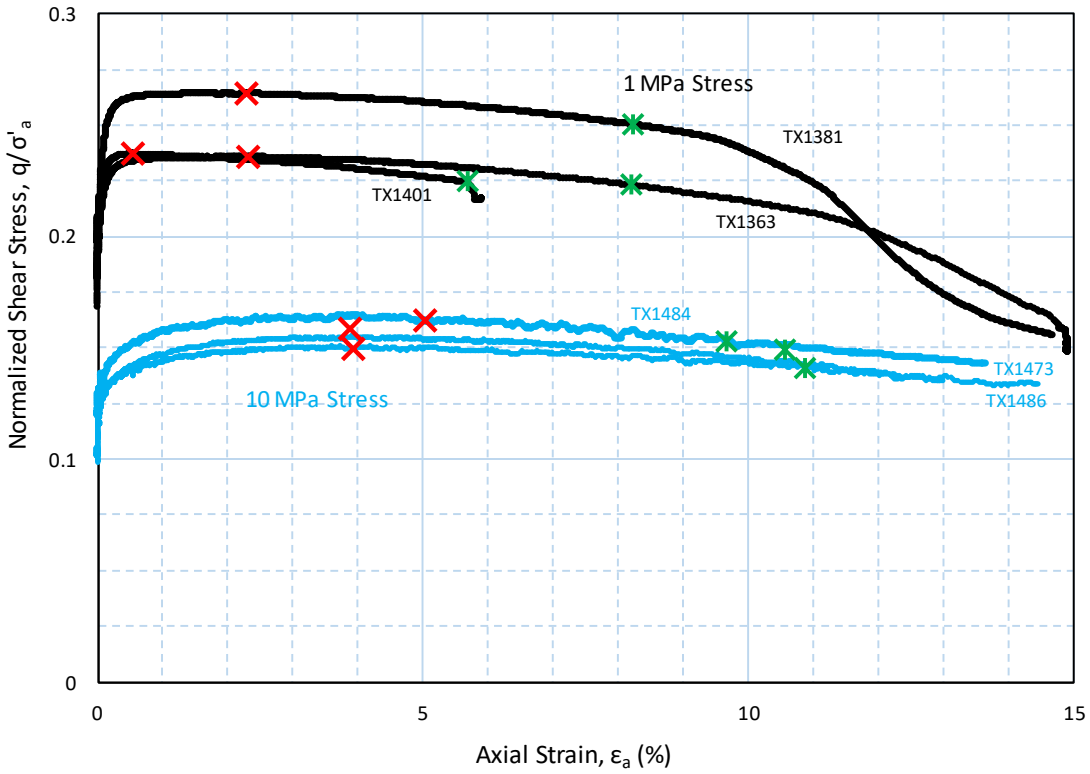


Figure 7-23: Normalized shear stress by axial strain from undrained shear phase of triaxial tests performed on RGoM_EI specimens, at two consolidation stress levels 1 MPa and 10 MPa. The red crosses indicate maximum shear stress and the green crosses indicate maximum effective friction angle.

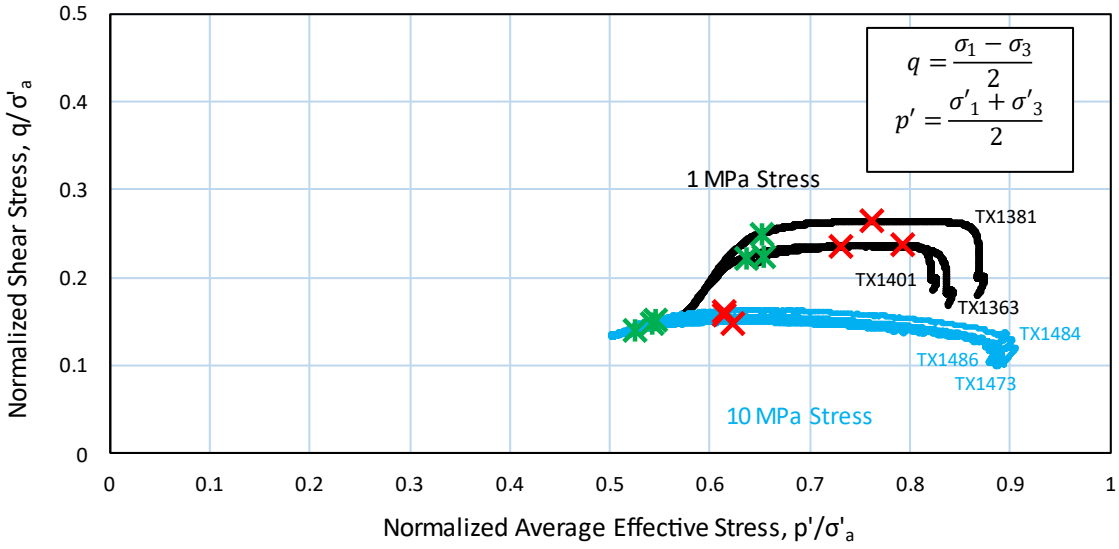


Figure 7-24: Normalized shear stress (q) by normalized average effective stress (p') from undrained shear phase of triaxial tests performed on RGoM_EI specimens, at two consolidation stress levels 1 MPa and 10 MPa. The red crosses indicate maximum shear stress and the green crosses indicate maximum effective friction angle.

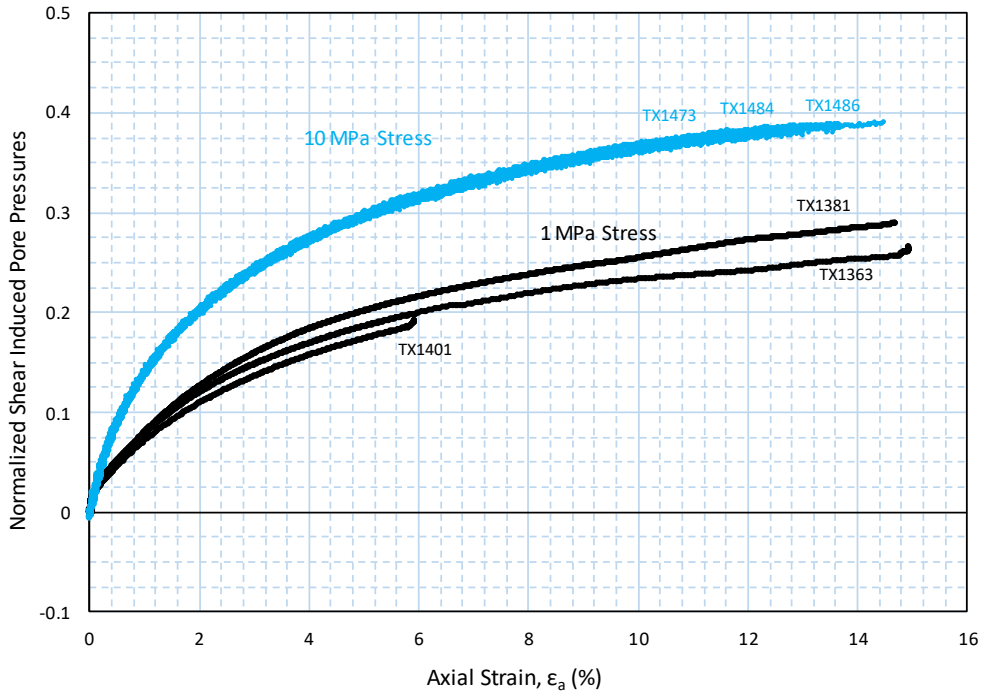


Figure 7-25: Normalized shear induced pore pressures from undrained shear phase of triaxial tests performed on RGoM_EI specimens, at two consolidation stress levels 1 MPa and 10 MPa.

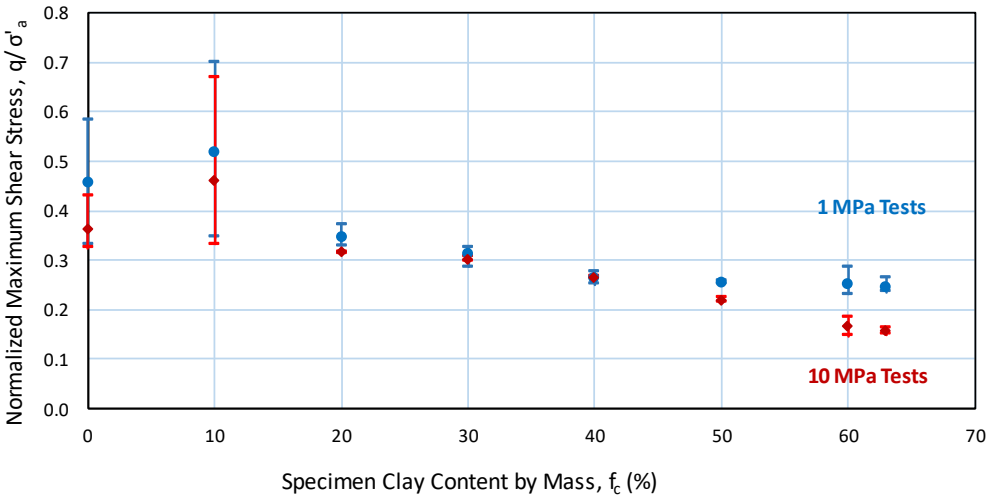


Figure 7-26: Average maximum normalized shear stress by specimen clay content from undrained shear phase of triaxial tests at two consolidation stress levels 1 MPa and 10 MPa. The range in measured values are shown in the error bars, blue for 1 MPa and red for 10 MPa tests.

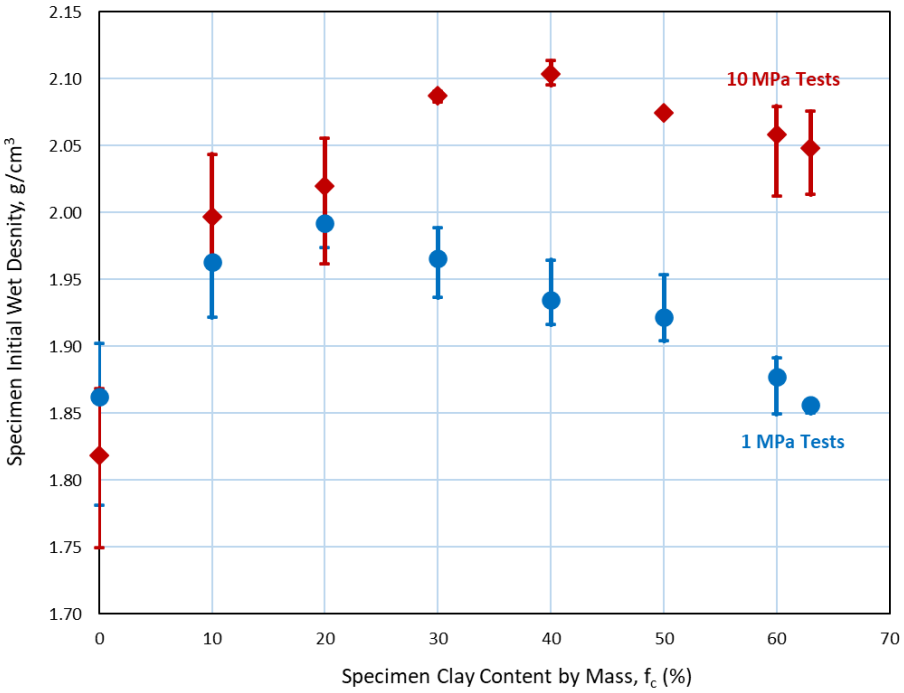


Figure 7-27: Average and range of triaxial specimen initial wet density prior to triaxial testing by specimen clay content by mass. The lines provide the range of specimen densities, the blue circles are the average specimen density for the 1 MPa tests and the red diamonds are the average specimen density for the 10 MPa tests.

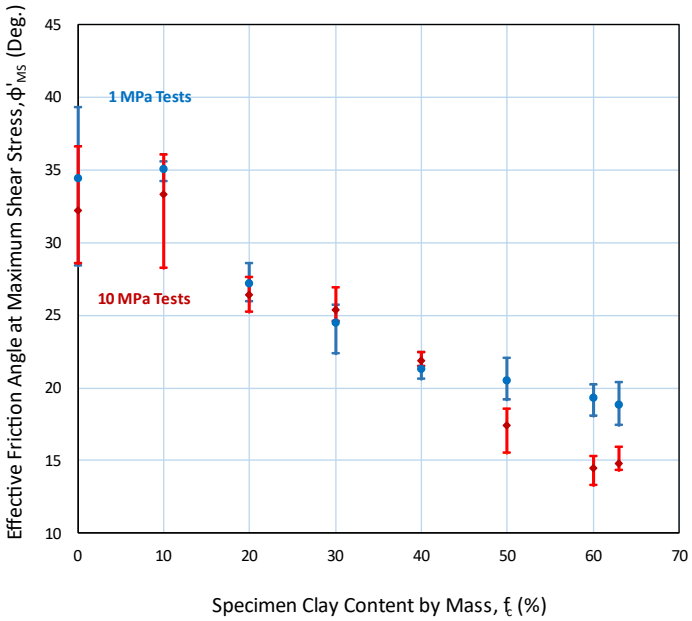


Figure 7-28: Average effective friction angle by specimen clay content measured at the maximum shear stress at two stress levels 1 MPa and 10 MPa. The range in measured values are shown in the error bars, blue for 1 MPa and red for 10 MPa tests.

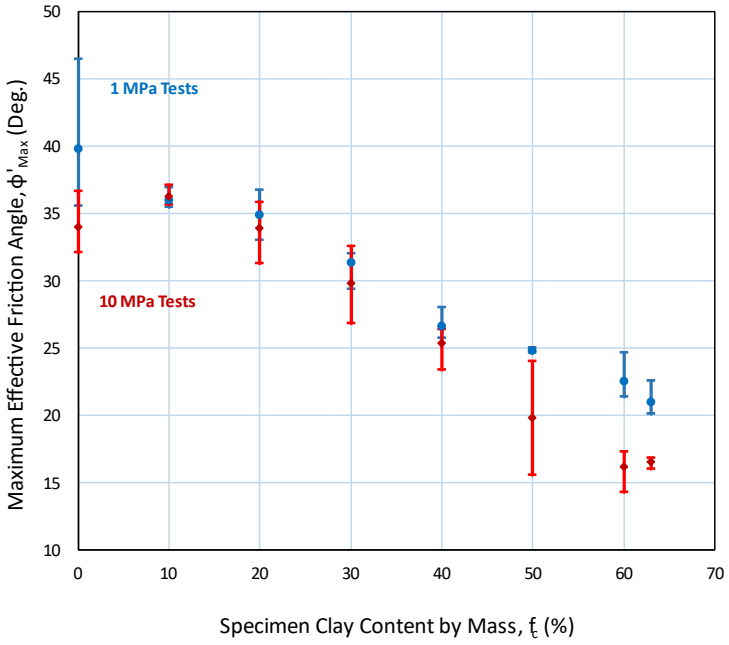


Figure 7-29: Average maximum effective friction angle by specimen clay content measured during the undrained triaxial shear phase at two stress levels 1 MPa and 10 MPa. The range in measured values are shown in the error bars, blue for 1 MPa and red for 10 MPa tests.

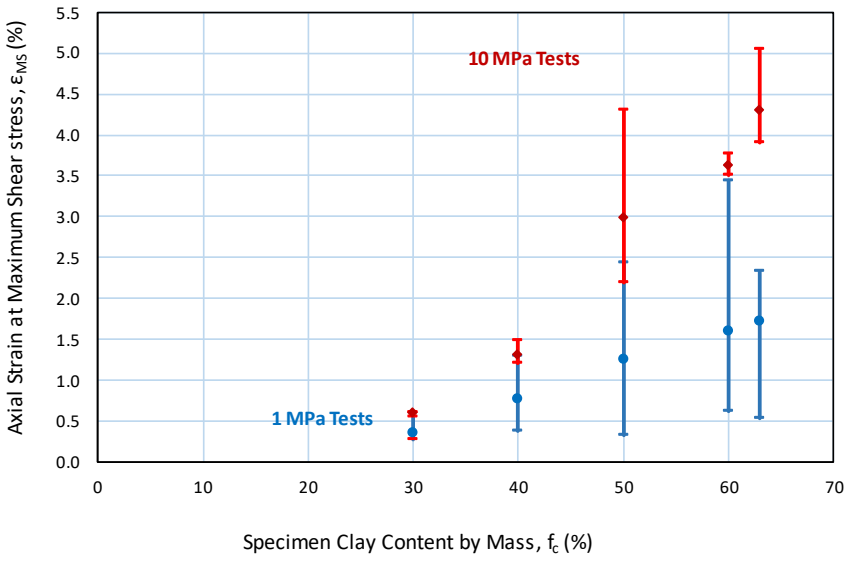


Figure 7-30: Average axial strain at maximum shear stress measure by specimen clay content from undrained shear phase of triaxial tests at two consolidation stress levels 1 MPa and 10 MPa. The 0% clay, 10% clay and 20% clay materials were not K_0 consolidated and instead were anisotropically consolidated along a predetermined computer controlled stress path with K value assumed to be K_0. These materials are not shown due to the difference in consolidation. The range in measured values are shown in the error bars, blue for 1 MPa and red for 10 MPa tests.

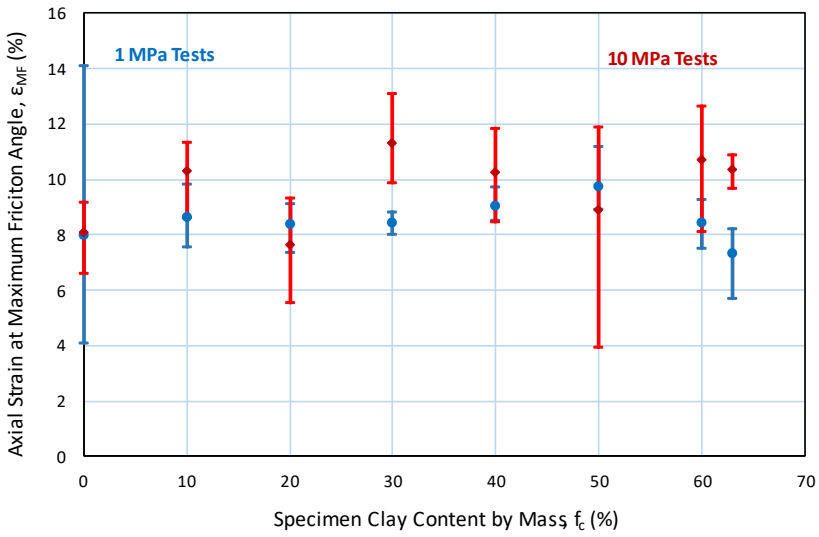


Figure 7-31: Average axial strain corresponding with the maximum measured friction angle by specimen clay content from undrained shear phase of triaxial tests at two consolidation stress levels 1 MPa and 10 MPa. The range in measured values are shown in the error bars, blue for 1 MPa and red for 10 MPa tests.

CHAPTER 8. Evaluation of Clay Dependency on Engineering Parameters and Soil Behavior

8-1 Introduction

This chapter presents an interpretation of the dependence of the measured soil engineering parameters on clay content. Relationships between mechanical properties and clay content are explored to evaluate grain supported vs. clay supported soil behaviors. Section 8.2 presents a discussion on the packing of fine grains and coarse grains. Four theoretical soil fabric casers within the binomial mixture theory, and the conceptual limits separating the different fabrics are discussed. The compression data presented in Chapter 5 is used to evaluate binomial mixture theory and the fabrics of the tested silt and clay mixtures. Section 8.3 examines the effect of clay on compression behavior over large stresses. Section 8.4 presents the effects of clay content on the lateral stress ratio. Section 8.5 discusses the effects of clay content on permeability. Section 8.6 presents the effects of clay content on wave velocity measurements, and isotropic elastic parameters derived from wave velocities. Section 8.7 discussed the influence of clay content on the mechanical strength parameters.

8-2 Influence of Clay Particles on Soil Structure

Understanding whether the soil derives its mechanical response from grain contacts or by a supporting clay matrix is important to understanding the behavior of a soil. Figure 8-1 presents the average compression curves from the high stress CRS testing presented in CHAPTER 5. Figure 8-2 presents the void ratio measurements by clay content at discrete stress levels between 1 MPa and 50 MPa from the high stress CRS testing presented in Figure 8-1. Determining whether the soils are clay supported, or grain supported is not readily identifiable from the compression state (void ratio/porosity – effective stress). As there is a non-unique void ratio for the mixtures at a given stress level as discussed within Chapter 5 and illustrated by Figure 5-31 and Figure 5-32 (included as Figure 8-2). As the mixtures are

compressed the variation in compressibility results in a parabolic shape for void ratio by clay content for a single stress level. The higher clay content soils compress more, flatting the parabolic shape and shifting the minimum void ratio (densest packing) to higher clay contents. The minimum void ratio interpreted from the experimental results as a function of stress level is provided on Figure 8-2.

To categorize the behavior of mixed materials, binary mixture theory is applied to the tested mixtures. Where binary mixture theory is explores the packing density of a mixture composed of two different particle sizes (or types). Binary mixture theory is applied to determine the conceptual limits between grain supported and clay supported behaviors and to evaluate the effect of high plasticity fines. Binary mixture theory has widely been applied to mixtures of sand and non-plastic fines and little research has been performed on mixtures with plastic fines. Thevanayagam, Shenthan, Mohan, & Liang (2002) presents a flow chart included as Figure 8-3 that illustrates four cases for soil fabrics.

Case i: The fine particles are fully confined within the void space of the coarse grains. The coarse grain contacts control the behavior of the soil. For Case I the fines content (f_c) is less than the minimum threshold fines content for the fines to contribute to behavior of the soil ($f_{c\ min}$).

Case ii: The fine particles are confined and partially in contact with the coarse grains. This is a transitional case where both the coarse grains and fines contribute to the soil behavior. Case ii is defined as the fines content exceeding $f_{c\ min}$ but being less than the critical clay content (threshold fines content f_{cth}).

Case iii: The fine particles are confined within the void space of the coarse grains but have begun separating the coarse grains. This is a transitional case where both the coarse grains and fines contribute to the soil behavior. Case iii is defined as the fines content exceeding f_{cth} but being less than the maximum fines content where the grains contribute to the soil behavior ($f_{c\ max}$).

Case iv: The fine particles have fully dispersed the coarse grains, and the soil is supported by the fine grains. This case is defined as the fines content exceeding $f_{c\,max}$.

Alternative void ratio parameters are used to evaluate soils to determine the different cases of soil support fabric. The void space between grain particles (intergranular void ratio) and the void space within a clay matrix (clay void ratio) are commonly used. The formulas for the intergranular and clay void ratios are presented in Equations 8-1 and 8-2.

$$e_s = \frac{V_V + V_f}{V_s} \qquad \text{Equation 8-1}$$

$$e_f = \frac{V_V}{V_f} \qquad \text{Equation 8-2}$$

Where:

e_s = Intergranular Void Ratio

e_f = Clay (fines) Void Ratio

V_V = Volume of Voids (volume)

V_f = Volume of Fines (Clay) (volume)

V_s = Volume of Grains (volume)

At low fines contents the value of e_f remains very high and the influence of fine grains is limited as the fines are isolated within the void of the coarser grains. As the fines content is increased to a threshold value (f_{cth}) the fine grains are expected to become the supporting fabric. The threshold value (f_{cth}) occurs when the fines void ratio is below the maximum void ratio of the silt grains and corresponds to the densest state of packing where the fines fully fill the coarse grain voids without separating the voids. Zuo & Baudet (2014) provide a thorough investigation in various means to determine f_{cth}, experimentally as shown in Figure 8-2, by an analytical means such as the binary packing theory presented in Lade, Liggio Jr., & Yamamuro (1998), or by a semi-analytical method presented in Rahman, Lo, & Gnanendran (2009). A basic definition of f_{cth} is presented in Equation 8-3 from Thevanayagam, Shenthan, Mohan, &

Liang (2002), and indicates that when the fines void ratio is less than the maximum possible void ratio for the sand, the fine grains are packed dense enough to control behavior. This method requires experimental testing to determine the maximum void ratio of the coarse grains.

$$f_{Cth} = \frac{100e}{e_{\max HF}} \qquad \text{Equation 8-3}$$

Where:

f_{Cth} = Threshold Fines Content (Critical Clay Content) (percent)

e = Void Ratio

$e_{\max HF}$ = Maximum Void Ratio for Coarse Grains

Lade, Liggio Jr., & Yamamuro (1998) presents a method for determining f_{Cth} assuming a binary packing model where the fine and coarse fractions are spherical particles, the fines are non-plastic and the minimum void ratio is independent of particles size. For this method Equation 8-4 presents the minimum possible void ratio for fines trapped within the voids of the coarse grains, and Equation 8-5 presents the minimum possible void ratio for the grains floating in the fine's matrix. When the specific gravity of the coarse and fines fraction is approximately equivalent then Equation 8-4 and Equation 8-5 can be simplified to Equation 8-6 and Equation 8-7 respectively. Figure 8-4 provides an example determination of F_{Cth} using the Lade, Liggio Jr., & Yamamuro (1998) equations for the high stress CRS tests at a 1 MPA stress level.

$$e_{mins} = \frac{(1+e_{min}^{s})}{(1+\frac{f_C G_{ss}}{(1-f_C)G_{sf}})} - 1$$ Equation 8-4

$$e_{minf} = \frac{(1+e_{min}^{f})}{(1+\frac{(1-f_C)G_{sf}}{f_C G_{sf}})}$$ Equation 8-5

$$e_{mins} = e_{min}^{s} - f_C(1 + e_{min}^{s})$$ Equation 8-6

$$e_{minf} = f_C e_{min}^{f}$$ Equation 8-7

Where:

e_{mins} = Theoretical Minimum Void ratio for Coarse Grained Supported Mixtures

e_{minf} = Theoretical Minimum Void ratio for Fine Grained Supported Mixtures

e_{min}^{s} = Minimum Void Ratio for Coarse Grained Material

e_{min}^{f} = Minimum Void Ratio for Fine Grained Material

f_C = Fines Content (percent)

G_{ss} = Specific Gravity of Coarse Grains

G_{ss} = Specific Gravity of Fine Grains

Equation 8-8 provides an alternative formulation for f_{cth} based on back analyses on nine sets of data presented in Rahman, Lo, & Gnanendran (2009) and evaluated within Hang, Wu, Cheng, Li, & Chen (2024).

$$f_{Cth} = A\left(\frac{1}{1+e^{\alpha-\beta\chi}} + \frac{1}{\chi}\right)$$ Equation 8-8

Where:

f_{Cth} = Threshold Fines Content (percent)

A = Asymptotic value of 0.4 independent of α and β

α and β = Curve fitting parameters α=0.5 and β=0.13 from Rahman et al 2009

χ = Particle parameter ratio of $\frac{D_{10}}{d_{50}}$

D_{10} = Diameter of coarse grain particles at 10% passing (length)

d_{50} = Diameter of fine grain particles at 50% passing (length)

Figure 8-4 provides an example determination of fC_{th} using the Rahman, Lo, & Gnanendran (2009) equation, fC_{th} evaluated experimentally by the Lade, Liggio Jr., & Yamamuro (1998), and by the Rahman, Lo, & Gnanendran (2009). The different methods are within a range of 20.4% to 31.5% fines for the 1 MPa stress level. Figure 8-5 and Figure 8-6 provide similar plots at a 10 MPa and 50 MPa stress level. The semi-analytical method from Rahman, Lo, & Gnanendran (2009) are not included on Figure 8-5 and Figure 8-6 as the method provides a single static value based on particle diameters and does not include stress dependence. Figure 8-2 and Figure 8-4 to Figure 8-6 show that the packing of the tested materials and the interpreted f_{Cth} is dependent on stress. The estimated f_{Cth} from the experimental measurements indicate a 30.1% shift in void ratio from an f_{Cth} of 20.4% at 1 MPa stress level to an f_{Cth} of 50.5% at 50 MPa. The Lade et al 1998 binary mixture method also indicates f_{Cth} is sensitive to stress with an approximate 5% shift from f_{Cth} of 22% at 1MPa to f_{Cth} of 25.5% and 50 MPa. The difference in determinations is attributed to the Lade et al 1998 determination being a geometrical solution that does not account for plasticity of the fine grained fraction.

RGoM_EI is a clay of high plasticity, and the plastic behavior has a clear effect on the binary mixture stress sensitivity due to the compressibility of the clay particles. Figure 8-7 provides an example plot of the binary mixtures for a non-plastic fine mixed with sand at one stress level. In Figure 8-7within the

Case i (1-1 on Figure 8-7) and Case iv (2-2 on Figure 8-7) zones the mixture void ratios fall on the theoretical minimum line for the coarse grain or fine grain soils. With increasing fines content beyond $f_{C\,min}$ the void ratios start to deviate from the theoretical minimum line for the coarse grains. Where $f_{C\,min}$ represents the start of the transition zone from case i to ii, where fines start contributing to the compression behavior of the soils. Case ii is still a predominantly grain structured soil and grain contacts control the behavior. As the fines content increases to greater than f_{Cth} the soil structure shifts from case ii to iii, where the soil is now a fine grained supported soil with the coarse grain contributing to the behavior. $f_{C\,max}$ represents the point separating case iii from iv where the coarse grains stop contributing to the behavior of the soil. Equations 8-9 and 8-10 present analytical formulations for $f_{C\text{-}min}$ and $f_{C\,max}$ based on correlations with data sets presented in Hang, Wu, Cheng, Li, & Chen (2024).

$$FC_{in-min} = 20(C_u^S) + 4.5 \qquad \text{Equation 8-9}$$

$$FC_{in-max} = -15arctan\left[12\log\left(d_{50}^S\sqrt{C_u^S C_u^f} + 0.5\right)\right] + 72 \qquad \text{Equation 8-10}$$

Where:

FC_{in-min} = Minimum Fines Content Where Fines Effect the Material Behavior (percent)

FC_{in-max} = Minimum Fines Content Where Coarse Grains Effect the Material Behavior (percent)

C_u^S = Coefficient of Uniformity for the Coarse grains

C_u^f = Coefficient of Uniformity for the Fines

d_{50}^S = Diameter of coarse grain particle size corresponding to 50% passing on a distribution curve (length)

Based on a calculated C_u^S of 0.62 for the Min-U-Sil silt the $f_{C\,min}$ values is 16.8%. There is difficulty in determining C_u^f due to the timing required for the 10% passing particle size to settle in a hydrometer grain size analysis. Due to the uncertainty in C_u^f, the sensitivity of $f_{C\,max}$ to C_u^f as estimated by Equation 8-10, was explored and presented in Figure 8-8. $f_{C\,max}$ varies between 49.9% and 95.4%,

decreasing with and increasing C_u^f. Thevanayagam, Shenthan, Mohan, & Liang (2002) provide an alternative formulation for $f_{C\ max}$ provided in Equation 8-11.

$$FC_{in-max} = 100\left[1 - \frac{\pi(1+e)}{6s^3}\right] \qquad \text{Equation 8-11}$$

Where:

FC_{in-max} = Minimum Fines Content Where Coarse Grains Effect the Material Behavior (%)

e = Void Ratio

s = $1 + \frac{10}{R_d}$

R_d = Grain Size Disparity Ratio Coarse Grain Size by Fine Grain Size

Figure 8-9 and Figure 8-10 provide the determinations of $f_{C\ min}$ (Equation 8-9) f_{Cth} (Lade et al 1998 method) and $f_{C\ max}$ (Equation 8-10 and Equation 8-11) for a 1 MPa stress level and a 50 MPA stress level. At low clay contents the binary mixture theories provide a reasonable framework for the material behavior. The $f_{C\ min}$ by C_u^s provides a reasonable threshold for separating Case i and Case three behavior, even with the inclusion of the plastic fines due to the separation being a characterization of the available void space for the coarse unit. $f_{C\ min}$ is anticipated to decrease with increasing stress level due to the loss of intergranular pore pace from particle rearrangement of breakage with increasing stress.

For evaluating the transition from grain supported to clay supported material the Lade et al 1998 method for evaluating f_{Cth} assumes a round particle and does not account for the separation of clay particles by the diffuse double layer. This method does not provide an adequate estimate of the stress effects of f_{Cth} for a mixture with plastic fines. The experimental results from the high stress CRS tests indicate that the f_{Cth} value is significantly more stress dependent for the RGoM_EI mixtures, which is not captured in current binary mixture theories. The f_{Cth} parameter serves as a reasonable limit between grain supported and clay supported behavior for mixtures of grains and high plasticity fines. But

additional research is required on determining the fines content associated with f_{Cth} for high plasticity fines.

Equations 8-10 and 8-11 for evaluating $f_{c\ max}$ the threshold between Case iii and Case iv is based on the particle size and distribution of the coarse grains and the particle distribution of the fine grains. Due to difficulties with measuring the particle size distribution of high plasticity clays such as RGoM_EI Equation 8-10 includes significant uncertainty. A particle size based equation for $f_{C\ max}$ for high plasticity clays will not capture the separation of clay particles due to the diffuse double layer.

Binary mixture theory provides an acceptable framework for characterizing a mixed coarse grain and high plasticity fine grained soil within the coarse grain domain ($f_C<f_{Cth}$). This is attributed to the binary mixture theory being derived from packing of shapes in contact and the grains in grain supported materials are in contact. Additional research is required to determine an effective method to establish f_{Cth} asides from experimental testing and the $f_{C\ max}$ threshold for mixtures with high plasticity clays. As the binary mixture is based on particle size and leads to significant uncertainty in the limits.

8-3 Influence of Clay Particles on Soil Compression

One-dimensional compression data for the clay/sand mixtures obtained from high stress CRS testing are shown in Figure 8-1 as void ratio by axial effective stress in e-logσ'_v space. The shapes of the curves are indicative of the soil structure. The high silt content (grain supported) mixtures have a concave down curve and the high clay content materials (clay supported) have a concave up curve. There is a clear trend in increasing soil compressibility with increasing clay content. The higher compressibility of the clay rich mixtures is correlated with a clay supported soil fabric with the silt grains suspended in the clay matrix. The silt rich mixtures derive their support from particle to particle contacts through force chains in the silt grain skeleton. Figure 8-1 shows the compression curves of 30% clay or greater trend towards the same value at very high stresses. This is in line with the limiting compression curve theory for sands

and clays presented within Pestana-Nascimento (1994), and the observation for compression over large stress ranges from Casey (2014).

Figure 8-11 shows the compression ratio (CR) by clay content over three different stress ranges, a low stress range 0.5 to 1 MPA, medium stress range 1 to 50 MPa, and high stress range 50 to 90 MPa. Where CR is the slope of the compression curve between the two stress levels and is a measure of the soil compressibility. CR is the change in strain by the log change of effective stress and is often provided as a percentage. Both the low and medium stress levels show the trend of increasing compressibility with increasing clay content. The low stress CR values show a much larger range of CR between 4.2% to 27.1%, while the medium stress has CR between 6.8% to 15.7%. The high stress values show a change in the trend with a decrease in compressibility with an increase in clay content. The high stress CR values are in a narrower range of 9.1% to 13.3%. These trends are interpreted as clay supported materials being very compressible and grain supported materials being relatively incompressible at low stress. With increasing stress, the clay supported materials stiffen and become less compressible while the grain supported materials become significantly more compressible. At very high stresses the grain supported materials are more compressible than the clay supported materials. The clay supported materials at high stress are in a narrow range of CR values (9.1% to 11.5%) indicating the clay matrix is deforming while the grains act as rigid inclusions. An example on the ramifications for the soil compression sensitivity to clay content is provided in Chapter 9.

8-4 Influence of Clay Particles on K_0 Compression

The higher clay content triaxial specimens are K_0 consolidated to continuously measure the K_O value of each test specimen during the consolidation phase of a triaxial test. Where K_0 represents one dimensional consolidation, that is consolidation with no change in cross sectional area. The triaxial computer controller maintains a constant axial rate of strain and equal volumetric strain by adjusting

cell pressures theoretically limiting radial strains. During the initial pressure-up and back-pressure saturation phases of a test, the over consolidated specimen is subjected to almost isotropic stress conditions. The value of K_O is therefore generally close to unity at the beginning of consolidation phase. The value of K_0 typically decreases back to a normally consolidated state. Figure 8-12 provides example K_0 consolidation measurements for the RGoM_EI triaxial tests. The K_0 value at the end of consolidation prior to the 24 hours hold stress period is taken as the K_0 value corresponding to the end of consolidation stress. The computer controlled K_0 consolidation path requires excess pore pressure generation to maintain equal axial and volumetric strains. For the very stiff grain supported specimens (20% clay or less) the smaller changes in volume during consolidation do not allow for meaningful computer controlled corrections. These specimens were consolidated along a stress path with a K value of 0.5.

Figure 8-13 presents the average measured K_0 value by specimen clay content at both 1 MPa and 10 MPa stresses. The average K_0 value for the 1 MPa test ranges between 0.53 at 30% clay to 0.67 at RGoM_EI and the 10 MPa test values range between 0.56 at 30% clay to 0.81 at RGoM_EI. Both the 1 MPa and 10 MPa stress levels indicate a clear trend of increasing K_0 with increasing clay content. The higher clay content materials show a higher sensitivity to stress changes. The 30% clay material show an approximately 7% increase in K_0 from 1 MPa to 10 MPa while the 50% clay, 60% clay, and RGoM_EI materials showed increases of approximately 42%, 53% and 55% respectively.

The lateral stress ratio at rest has been tied to the frictional resistance of the material through the maximum failure friction angle in many studies Terzaghi (1923), Jaky (1944), Brooker & Ireland (1965), Rowe (1962), Rowe (1971), Simpson (1992), Federico & Elia (2009), Casey (2014), Federico (2021), and others. Figure 8-14 presents the measured K_0 values by maximum friction angles for the triaxial tests.

Figure 8-14 also provides correlation lines between the maximum friction angle and K_0 from Jaky (1944) Equation 8-12 and Federico (2021) Equation 8-13.

$$K_0 = 1 - Sin(\varphi') \qquad \text{Equation 8-12}$$

$$K_0 = \frac{1-0.618Sin(\varphi')}{1+0.618Sin(\varphi')} = tan^2\left(45 - 0.618\frac{\varphi'}{2}\right) \qquad \text{Equation 8-13}$$

Where:

K_0 = Lateral Stress Ratio at Rest

φ' = Effective Friction Angle (Degrees)

The 0.618 factor included in Equation 8-13 represents the mobilized friction angle at the K_0 condition. K_0 represents a stress state between isotropic stress and shear failure. Figure 8-15 provides a Mohr's circle diagram from Federico (2021) that illustrates the intermediate state of K_0 and the tangent line that represents the mobilized friction angle. Figure 8-16 provides an example calculation for the mobilized friction angle from the end of consolidation stress in the consolidation phase of a triaxial test. Where the mobilized friction angle is the angle through the origin to the end of consolidation stress in MIT p'-q effective stress space (α' mob.) converted to a Mohr Coulomb σ'-τ' effective friction angle (ϕ' mob.). The 0.618 slope from Federico (2021) correlating the mobilized friction angle to maximum friction angle overestimates the relationship measured in the silt and clay mixtures. A best fit slope of 0.513 was found by comparing the measured mobilized friction angles to the failure friction angles presented in Figure 8-17. The 0.618 value may still represent a lower limit for K_0 as shown in Figure 8-14.

Within Chapter 5 there is a discussion on correction made to the effective stress computed during consolidation to account for excess pore pressure generated during consolidation, induced by a faster rate of consolidation. The excess pore pressures influence the measured K_0 value by increasing K_0. As K_0 has been found to be related to the frictional resistance of the soil Equation 8-13 is used to evaluate clay content effects based on the measured friction angles during triaxial shearing. Friction angle is used to

evaluate K_0 as the shearing phase is not anticipated to have been affected by excess pore pressure generation during consolidation. Figure 8-18 provides the measured K_0 values and the predicted K_0 values using Equation 8-13 by specimen clay content. The predicted values are calculated from the average maximum friction angle from each clay content and stress level. The predicted values show very similar trends of increasing K_0 with increasing clay content and stress level observed in the measurements. The stress sensitivity of the predicted K_0 values is lower increases in K_0 ranging from no change to 15% between 10% clay and RGoM_EI. The predicted values can be extended to the lower clay contents due to being dependent on the measured friction angle during shearing. As discussed in Chapter 7 the friction angle of the 0% clay material is dependent on the initial density of the specimens and low initial densities for the 10 MPa tests contributed to lower friction angles during shearing. The ramification on the variability of K_0 to clay content will be presented with the discussion on strength parameters in Chapter 9.

8-5 Influence of Clay Particles on Permeability

Permeability has been found to be influenced by particle grain size, pore size distribution, grain shape, tortuosity, clay content, clay plasticity, and temperature P. C. Carman (1937), Kozeny (1927); Lapierre, Lerouil and Locat (1990), D. N. Dewhurst, et al. (1998); Spinelli, Giambalvo and Fisher (2004), Yang & Aplin (2004), Schneider (2021) and others. Permeability of the silt and clay mixtures for this study is calculated from excess pore pressure generated during the high stress CRS consolidation testing, using standard linear theory (ASTM D4186) as discussed in Chapter 3. The permeability of the 0% and 10% clay materials is measured through direct flow testing, due to their limited generation of excess pore pressures during high stress CRS testing for these materials. Figure 8-19 presents the average measured permeability by porosity for the silt clay mixtures. The test results show that permeability decreases with increasing clay content, permeability decreases with decreasing porosity, and the magnitude in the change of permeability with change in stress is more significant in the higher clay content materials than

the lower clay content materials. The 0% clay content indicates a one order of magnitude change of permeability over the 100 MPa stress range and the change increases with clay content up to approximately four orders of magnitude change for RGoM_EI specimens.

Figure 8-20 provides permeability by clay content at four porosities (04, 0.35, 0.3, and 0.25) from the high stress CRS tests. Figure 8-20 highlights a trend of decreasing permeability with increasing clay content. Figure 8-20 also shows that once a material is clay supported (sufficiently high clay content) the decrease in permeability with increasing clay content is negligible. For example, at a porosity of 0.4 the 0% clay content is approximately 16,700 times more permeable than RGoM_EI. The 10% clay material is approximately 350 times more permeable, 20% clay material is approximately 220 times more permeable, and the 30% clay is approximately 20 times more permeable than RGoM_EI. The higher clay content materials of 40% clay, 50% clay, and 60% clay are 1.5 to 7.6 times more permeable than RGoM_EI. Being within an order of magnitude is negligible when the measured permeability of RGoM_EI is around $4E^{-15}$ m^2.

The stress and clay dependence of permeability can be shown by comparing the measurements between mixtures at a porosity of 0.25 in Figure 8-20. The permeability of the 0% clay content is approximately 55,000 times more permeable than RGoM_EI. The 20% clay material is approximately 50 times more permeable, and the 30% clay is approximately 12 times more permeable than RGoM_EI. The higher clay content materials of 40% clay, 50% clay, and 60% clay are 1.3 to 7.6 times more permeable than RGoM_EI.

The permeability of the high clay content materials (40% clay to RGoM_EI) is within an order of magnitude at the four compared porosity levels in Figure 8-20. This is interpreted as permeability being limited by soil fabric. The clay content of these materials is above the estimated F_{Cth} value, making them either case iii or iv supported materials as discussed in Section 8.2. The highly plastic fines have a large

impact on the compression behavior of these materials which then contributes to the trends in permeability. As shown in Figure 8-11 the compression ratio of these materials is similar over the 10 to 50 MPa stress range and even closer at the higher stress range 50 to 90 MPa. Which supports that the three materials are being supported by a clay matrix that deforms in an analogous manner and has the same permeability trends.

Two observations of significance in the permeability measurements are that the change in permeability with increasing clay content is most significant from 0% clay to 10% clay. An approximate 1 to 2 order of magnitude difference between the 0% clay and 10% clay materials is observed over the tested porosity range. The difference in permeability between 10% variations in clay content for the other mixtures (20% compared to 30% clay, 50% compared to 60% clay, etc.) is within an order of magnitude. The difference in permeability between 0% and 10% clay is attributed to the plastic clay particles fouling the void space of the silt grains. The second observation is that the permeability measurements are ordered very well in a permeability effective stress space as shown in Figure 8-21. Both observations and their impacts to permeability models are explored in more detail within Chapter 9.

8-6 Influence of Clay Particles on Dynamic Elastic Properties

The velocity measurements from the TCRS tests were compared to V_P-V_S correlations to evaluate if the measurements were within a reasonable range. Figure 8-22 presents the shear wave velocity by pressure wave velocity with three established V_P-V_S correlations from Castagna, Batzle, & Eastwood (1985), Han D.-H. (1986), and Brocher (2005). The correlations in Castagna, Batzle, & Eastwood (1985) and Han (1986) were developed from measurements in shales and mudrocks while the correlation from Brocher (2005) were developed from in situ testing of a wider range of lithology. The Han correlation overpredicts V_S over the entire range of values. The Castagna et al. “mudrock” line fits the data well, and the Brocher Line fits the data well around a 1,900 m/s V_P value and converges to the Castagna et al.

"mudrock" correlation around a V_P of 2,400 m/s. The Brocher correlation overpredicts the V_S values at low V_P values which is attributed to the correlation being derived from many different lithological sources including sands and gravels that are anticipated to have higher V_S values than the silt-clay mixtures. The Castagna et al. "mudrock" line is shown within Brocher (2005) to deviate from typical velocity measurements around a 4,500 m/s V_P, but is valid for the range of the TCRS experiments. Figure **8-22** in conjunction with the discussion on the comparison to other studies presented in Chapter 6, indicates that the measured velocities from the TCRS experiments are within a reasonable range for mudrocks.

Figure 8-23 presents a plot of specimen density by clay fraction at 6 stress level from the TCRS tests. Wave velocity through a soil is a complex process and is dependent on several factors including the pore space, the permeant, soil mineralogical composition among many other factors. For the wave measurements from the TCRS experiments, the permeant and soil composition are generally the same between the clay mixtures as such the variations of wave velocity are generally attributed to variations in the pore space between the mixtures. Figure 8-23 shows that at the 1 MPa stress level the density of 10% clay to 50% clay is very similar and the density decrease as for the 60% and RGoM_EI specimens. For higher stress a trend of increasing density with increasing clay content is observed in the low clay content materials. At a maximum value (thought to be f_{Cth} as discussed in Section 8.2) where maximum packing efficiency is achieved after which the density begins to decrease with increasing clay content. The interpreted change in the maximum density from the TCRS experiments shows an increase with increasing clay content between a 1 MPa and 5 MPa stress on Figure 8-23. Between a 5 MPa and 25 MPa stress the maximum density is constant at a 40% clay content, which is different than the observations from the high stress CRS testing. The reason for the deviation is unknown and warrants further study.

The velocity measurements provided in Figure 8-24 as S wave velocity and P Wave velocity by specimen clay content show a very similar trend. The velocities at low stresses are within a narrow band, 209 to 282 m/s for S wave velocities and 1,669 to 1,754 m/s for P wave velocities. At increasing stress levels, the wave velocities of the lower clay content materials show increasing velocity with increasing clay content to the critical clay content. At clay contents beyond the critical clay content the wave velocities start decreasing. This trend creates a non-unique velocity-clay content-stress relationship for the tested silt and clay mixtures that prohibits determining the clay content of the mixtures from velocity and effective stress without any additional inputs. This trend is reflected in the calculated elastic parameters as they are calculated from the measured shear wave velocities and interpreted densities.

To further evaluate the effects of clay content on the velocity and elastic parameters of the mixtures the Hashin-Shtrikman upper and lower bounds for bulk modulus and shear modulus were calculated. The Hashin-Shtrikman bounds are presented as a reference for the behavior of the tested mixtures and are not meant to be a predictor of the elastic parameters. The bounds were developed for isotropic, linear elastic materials, and soil does not behave elastically except for at very small strains. A two phase system was considered for the calculation of the bounds, where one phase consisted of solid soil particles and the other phase was the pore fluid within the void space assuming 100% fluid saturation. The bulk modulus of the pore fluid was assumed to be 2.3 GPa consistent with saltwater solutions. The elastic moduli for solid soil particles are estimated as the weighted average modulus from the constituent minerals in each mixture based on X-Ray Powder Diffraction testing results. Table 8-1 presents the mineralogy of the GoM_EI powder and Table 8-2presents the calculated elastic parameters used for the calculation of the Hashin-Shtrikman bounds. To estimate the moduli of the mixtures, the added Min-U-Sil fraction was added to the quartz mineral fraction and all other minerals in the GoM_EI powder were decreased proportionally. Figure 8-25 presents the Hashin-Shtrikman upper bound, average, and lower bound for the bulk modulus, and Figure 8-26 presents Hashin-Shtrikman upper

bound for the shear modulus. Only the upper bound of the shear modulus is provided as the water is considered in the two phase system, which is unable to support shear stresses (G=0). In Figure 8-25 the bounds for bulk modulus are ordered by clay content with RGoM_EI having the highest values, and the 10% clay material having the lowest values. This is due to the bulk modulus of GoM_EI being the largest and decreasing with added Min-U-Sil. An inverse trend is observed in Figure 8-26 as the estimated shear modulus increases with increasing quartz content (Min-U-Sil).

Equations 8-14 and 8-15 were used to calculate the Hashin-Shtrikman bounds.

$$K^{HS\pm} = K_1 + \frac{f_2}{\frac{1}{(K_2 - K_1)} + \frac{f_1}{(K_1 + \frac{4}{3}G_1)}} \qquad \text{Equation 8-14}$$

$$G^{HS\pm} = G_1 + \frac{f_2}{\frac{1}{(G_2 - G_1)} + \frac{2f_1(K_1 + 2G_1)}{5G_1(K_1 + \frac{4}{3}G_1)}} \qquad \text{Equation 8-15}$$

Where:

K = Bulk Modulus (Force/Area)

G = Shear Modulus (Force/Area)

f = Volume fraction of each phase (taken as porosity).

The upper bounds are calculated by using the stiffer phase in the subscript 1 locations and the lower bounds are calculated with the softer phase in the subscript 1 location in Equations 8-14 and 8-15. Where the upper bounds represent the bulk modulus and shear modulus of the solid phase and the lower bound represents the moduli of the liquid phase.

Figure 8-27 to Figure 8-33 present the elastic parameters calculated from the wave velocities measured in the TCRS tests against the Hashin-Shtrikman bounds. The calculated parameters for all mixtures fall within the bounds as anticipated. Figure 8-27 to Figure 8-33 indicate that the bulk modulus for all of the mixtures at the initial porosities (typically 0.4 or greater) is near the bulk modulus of saltwater and the bulk modulus increases with decreasing porosity. None of the mixtures have a bulk modulus

measurement that exceeds the Hashin-Shtrikman average value over the 30 MPa stress range. The largest changes in moduli are observed at the 40% and 50% clay mixtures. The 40% and 50% clay mixtures had the lowest porosity from a 5 MPa stress level and greater and therefore are closer the solid mineral upper boundary than the other mixtures.

Figure 8-34 and Figure 8-35 show the calculated bulk modulus and shear from the TCRS experiments. Figure 8-34 and Figure 8-35 are excerpted from CHAPTER 6 which provides plots of the isotropic elastic parameters by clay content and effective stress. A parabolic distribution of the elastic parameter by clay content for a given stress level similar the trends shown for density and velocity in Figure 8-23 and Figure 8-24 can be observed.

8-7 Influence of Clay Particles on Strength Properties

The data presented in Chapter 7 from the triaxial compression shear tests performed at 1 MPa and 10 MPa consolidation stresses provide the basis of evaluating the strength behavior of the silt and clay mixtures in terms of clay supported or grain supported behavior. Chapter 7 presents trends in strength behavior with clay content and stress and are shown both to have significant effects on soil behavior. Increases in clay content leads to increased ductility of the material and lower strengths; both at undrained strength and effective friction angle. The lower clay content materials are subject to the sand state parameter conditions and dilative behavior is observed in the 10% clay mixture during shearing. The lower clay content materials tend to be stronger and more brittle but have larger scatter in the undrained shear strength and friction angle due to the dependence of shear strength of grain contact density. The changes in behavior with changes in clay content are shown to monotonic for strength properties.

Figure 8-36 presents the axial strain to the maximum shear stress measured during shearing for the K_0 consolidated mixtures of 30% clay to RGoM_EI. Figure 8-36 shows a systematic trend of increasing axial

strain to maximum shear stress increases with increasing clay content. The 1 MPa test of the 30% clay specimen has the lowest average strain to maximum shear stress around 0.5%. The RGoM_EI specimen has an average strain to failure around 1.7%. Figure 8-36 also indicates the stress dependence of the material behavior. All of the mixtures show an increase in the strain to maximum shear stress with increasing stress. The high clay content materials are more sensitive to consolidation stress level. The strain to maximum shear stress roughly doubled for the 50% clay to RGoM_EI materials between 1 and 10 MPa.

Figure 8-37 presents the average shear stress normalized to the consolidation stress by specimen clay content for both the 1 MPa and 10 MPa stress levels. Figure 8-37 shows a clear trend of decreasing strength with increasing clay content. The average normalized shear strength at a 1 MPa stress for the 0% to 30% clay contents are in range of 0.56 to 0.31. The 40% to RGoM_EI specimens have average strengths between 0.26 to 0.24. Figure 8-37 also shows the stress dependance of strength as the maximum average normalized shear stress decreases from 1 to 10 MPa. At the 10 MPa stress the 0% to 30% clay contents are in the range of 0.46 to 0.32, and the 40% to RGoM_EI specimens have average strengths between 0.26 to 0.16.

Figure 8-38 shows these same trends but as the average effective friction angle. The 0% to 30% clay contents at a 1 MPa stress have a range in average effective friction angle of 40 to 31 degrees. The 40% to RGoM_EI specimens have average effective friction angles between 26 to 21 degrees at a 1 MPa stress. At the 10 MPa stress the 0% to 30% clay contents are in range of 36 to 29 degrees, and the 40% to RGoM_EI specimens have average strengths between 23 to 15 degrees.

The influence of clay content on the strength of clastic rocks is presented within Plumb (1994). Within Plumb (1994) the influence of clay content is explored through the V_{grain} concept. Where V_{grain} is the volume fraction of crystalline grains. V_{grain} can be calculated by equation 8-16.

$$V_{grain} = 1 - (n + V_{clay})$$ Equation 8-16

Where:

V_{grain} = Volume fraction of crystalline grains (percent)

n = Porosity (percent)

V_{clay} = Volume fraction of clay particles (percent)

Plumb (1994) organized the studied rocks by the volume fraction of clay particles (V_{clay}). Grain supported materials had V_{clay} < 15%, transitional materials 15% > V_{clay} < 35%, and clay supported materials V_{clay} >35%. For the study mixtures, 0% to 20% clay contents by mass are classified as grain supported materials and the remainder of the mixtures 30% clay to RGoM_EI are classified as transitional materials using V_{clay}, due to the natural silt content of RGoM_EI and the porosity of the specimens at 1 and 10 MPa. Table 8-3 provides a summary of the volumes used to determine V_{grain} in the 1 MPa stress triaxial tests as well as the normalized shear stress and maximum friction angle. Table 8-4 provides the same information for the 10 MPa tests. Plumb (1994) found that the friction angle of the studied rocks decreased with decreasing V_{grain} when the stress level of the rock was controlled. Plumb (1994) also found that the friction angle of the rocks decreased with increasing confining stress. Figure 8-39 presents both trends for the studied mixtures. Both the 1 MPa and 10 MPa stress levels are well ordered with decreasing friction angle with decreasing V_{grain}. Figure 8-39 also the shows the overall decrease in friction angle with increasing confining stress. V_{grain} is an easy parameter to calculate in well classified rocks that provides a good framework for understanding strength behaviors in silt and clay mixtures at known stresses.

8-8 Conclusion and Significant Findings

Through an experimental laboratory program this study provides a systematic measurement of the compressibility to stresses larger than 90 MPa, permeability over a 90 MPa stress range, elastic properties over a 30 MPa stress range, and mechanical strength behaviors at 1 MPa and 10 MPa stress

of the silt and clay mixtures. The intent of this study is to evaluate whether the properties can be attributed to clay supported or grain supported materials. Binary mixture theory was evaluated for applicability to the studied soils. The significant findings of this study are as follows.

- The critical clay content or threshold fines content (f_{Cth}) provides a reasonable limit between the grain supported behavior and clay supported behavior for mixtures of silts and high plasticity clays.
- Engineering parameters are shown to be clay dependent with systematic changes with changes in clay content. Density dependent parameters (such as isotropic elastic parameters) show that a reversal in trends with clay content, as clay content crosses a critical threshold value.
- Binary mixture theory has limited application to mixtures of grains and high plasticity fines. The theory has been developed for materials of low plasticity and does not account for high plasticity fines. The limits for determining the separation of case i to case ii are valid as they are primarily based on the pore space of the solid grains. Additional research is required to account for high plasticity fines in binary mixtures.
- This study validates that soil compressibility increases with increasing clay content and that soil compressibility is stress dependent with grain supported soils tending to become more compressible at higher stresses and clay supported soil stiffening and becoming less compressible.
- The compression curves of the 30% clay content and greater specimens trended towards an intrinsic compression line at high stresses.
- The lateral stress ratio at rest (K_0) is shown to increase with increasing clay content and increase with increasing stress level.

- K_0 estimated by the mobilized friction angle through the equation proposed by Federico (2021) is found to provide a reasonable lower bound for K_0 over the tested clay contents and stress levels.
- Permeability is shown to monotonically decrease with increasing clay content.
- The difference in permeability between 50% clay and RGoM_EI is negligible and the differences between them decrease with increasing stress indicating that a limiting clay fabric for permeability.
- The change in permeability by increasing stress is most significant in high clay content materials and least significant in low clay content materials.
- Over the stress range of the measurements both the shear wave velocities and specimen densities are found to be parabolic when plotted by clay content at one stress state. With the values increasing towards the critical porosity with increasing clay content and decreasing away from the critical porosity with increasing clay content. These trends are also shown in the calculated elastic parameters.
- Clay content has a significant impact on the strength of soil with both the undrained shear strength and effective friction angle monotonically decreasing with increasing clay content. Both the undrained shear strength and effective friction angle are shown to be sensitive to confining stress with the higher clay contents indicating larger stress sensitivities.
- The V_{grain} parameter is shown to order the effective friction angles at one stress level, where the highest friction angles are measured correspond the highest V_{grain} parameters and decrease with decreasing V_{grain} (increasing clay or porosity).

Table 8-1: Percentage of Minerals in GoM_EI powder based on X-Ray Powder Diffraction

	Quartz	Plagiclase	K-Feldspar	Calcite	Dolomite	Siderite	Pyrite	Halite	Muscovite	Illite-Smectite	Kaolinite	Chlorite	Barite	Anatase
Mineralogy of GoM_EI (%)	27.8	5.3	4.0	1.2	0.8	1.0	0.7	0.2	1.9	44.4	9.1	0.4	3.2	0.2

Table 8-2: Estimated Elastic Parameters for the Clay Mixtures Based on a Weighted Average of the Elastic Parameters of the Constituent Minerals[1]

	Bulk Modulus K (GPa)	**Shear Modulus G (GPa)**	**Constrained Modulus M (GPa)**
GoM_EI	44.5	28.1	82.0
60% Clay	44.0	28.8	82.5
50% Clay	43.4	30.4	83.9
40% Clay	42.7	31.9	85.2
30% Clay	42.0	33.4	86.6
20% Clay	41.4	34.9	88.0
10% Clay	40.6	36.5	89.3

[1] The elastic parameters of the minerals are from Katahara, (1996), Prasad, Kopycinska, Rabe, & Arnold (2002), and Wang, Wang, & Cates (2001).

Table 8-3: Volumes used to Determine V_{grain} and Strength Parameters from 1 MPa tests.

Test No.	Clay by Mass	Total Volume	Volume of fines	Percentage of Fines by Volume, V_{clay}	Pre-Shear Porosity	Percentage of Grains by Volume, V_{grain}	Normalized Shear Strength	Maximum Friction Angle
	%	cc	cc	%	%	%	q/σ'_a	Φ'_{max}
TX1360	0%	69.8	0.0	0%	35.7%	64.3%	1.08	41.4
TX1362	0%	82.1	0.0	0%	45.1%	54.9%	0.33	46.4
TX1364	0%	80.0	0.0	0%	44.5%	55.5%	0.58	40.6
TX1368	0%	77.9	0.0	0%	46.4%	53.6%	0.48	36.4
TX1369	0%	78.2	0.0	0%	46.6%	53.4%	0.46	35.5
TX1373	0%	79.4	0.0	0%	42.9%	57.1%	0.42	41.9
TX1358	10%	70.6	4.0	6%	39.8%	54.6%	0.68	37.3
TX1388	10%	75.6	4.1	5%	40.1%	54.4%	0.51	35.5
TX1413	10%	76.0	4.1	5%	39.1%	55.4%	0.35	35.6
TX1353	20%	75.5	8.8	12%	36.2%	52.2%	0.34	34.9
TX1380	20%	75.0	8.2	11%	37.4%	51.6%	0.37	36.6
TX1410	20%	78.8	8.7	11%	37.1%	51.8%	0.33	33.0
TX1492	20%	78.0	8.7	11%	38.5%	50.3%	0.32	35.9
TX1367	30%	79.0	13.3	17%	38.0%	45.2%	0.32	32.1
TX1390	30%	77.7	12.4	16%	38.7%	45.3%	0.32	31.8
TX1347	32%	80.0	14.4	18%	39.0%	43.0%	0.31	31.0
TX1420	30%	76.4	13.5	18%	37.8%	44.5%	0.29	29.4
TX1491	30%	82.1	13.5	16%	38.3%	45.2%	0.31	31.9
TX1355	40%	77.8	17.4	22%	39.8%	37.9%	0.28	27.9
TX1411	40%	80.2	16.9	21%	38.6%	40.3%	0.27	26.3
TX1415	40%	75.0	16.9	23%	38.2%	39.2%	0.25	25.7
TX1348	50%	78.4	21.2	27%	41.6%	31.3%	0.25	24.6
TX1359	50%	74.5	19.1	26%	41.1%	33.3%	0.26	25.0
TX1383	50%	79.3	20.7	26%	42.1%	31.8%	0.26	24.6
TX1490	50%	79.9	20.7	26%	41.2%	32.9%	0.26	22.7
TX1350	60%	79.2	24.4	31%	44.3%	24.9%	0.23	21.4
TX1385	60%	77.7	22.3	29%	42.9%	28.3%	0.29	24.7
TX1407	60%	79.4	23.5	30%	42.3%	28.0%	0.24	21.6
TX1504	60%	80.0	23.5	29%	44.6%	26.0%	0.22	19.9
TX1363	63%	74.7	22.6	30%	44.7%	25.0%	0.24	20.5
TX1381	63%	78.2	23.8	30%	44.3%	25.2%	0.26	22.5
TX1401	63%	78.0	23.2	30%	46.8%	23.4%	0.24	20.1

Table 8-4: Volumes used to Determine V_{grain} and Strength Parameters from 10 MPa tests.

Test No.	Clay by Mass	Total Volume	Volume of fines	Percentage of Fines by Volume, V_{clay}	Pre-Shear Porosity	Percentage of Grains by Volume, V_{grain}	Normalized Shear Strength	Maximum Friction Angle
	%	cc	cc	%	%	%	q/σ'_a	Φ'_{max}
TX1438	0%	79.2	0.0	0%	50.1%	49.9%	0.36	33.9
TX1439	0%	79.8	0.0	0%	44.6%	55.4%	0.40	34.5
TX1468	0%	77.7	0.0	0%	50.4%	49.6%	0.33	33.4
TX1431	10%	76.7	4.0	5%	35.5%	59.3%	0.67	35.7
TX1443	10%	76.2	4.0	5%	35.2%	59.6%	0.33	37.1
TX1459	10%	79.1	4.0	5%	37.0%	57.9%	0.38	36.0
TX1436	20%	76.2	8.8	12%	32.0%	56.4%	0.40	30.1
TX1444	20%	75.6	8.8	12%	32.4%	55.9%	0.31	31.3
TX1463	20%	82.0	8.8	11%	31.3%	57.9%	0.32	34.6
TX1435	30%	71.0	13.3	19%	29.7%	51.6%	0.37	29.6
TX1447	30%	76.4	13.3	17%	28.8%	53.9%	0.32	26.9
TX1464	30%	80.5	13.3	16%	29.4%	54.1%	0.30	30.2
TX1495	30%	79.6	13.3	17%	29.1%	54.2%	0.30	32.6
TX1437	40%	76.7	17.4	23%	28.9%	48.4%	0.26	17.4
TX1456	40%	73.6	17.4	24%	28.5%	47.9%	0.26	23.4
TX1478	40%	82.3	17.4	21%	27.8%	51.1%	0.26	26.4
TX1499	40%	80.0	17.4	22%	28.5%	49.8%	0.27	26.3
TX1442	50%	77.9	21.2	27%	29.9%	42.9%	0.22	15.5
TX1458	50%	80.2	21.2	26%	29.5%	44.1%	0.21	20.0
TX1475	50%	80.8	21.2	26%	28.8%	45.0%	0.22	24.0
TX1433	60%	77.3	24.4	32%	34.4%	34.1%	0.18	14.3
TX1480	60%	83.1	24.4	29%	32.5%	38.2%	0.15	16.5
TX1481	60%	82.1	24.4	30%	31.7%	38.6%	0.16	16.9
TX1501	60%	76.6	24.4	32%	31.3%	36.8%	0.17	17.3
TX1452	63%	79.0	22.6	29%	33.3%	38.1%	0.15	9.7
TX1473	63%	81.1	23.8	29%	33.1%	37.6%	0.16	16.0
TX1484	63%	78.4	23.2	30%	32.3%	38.0%	0.17	16.8
TX1486	63%	79.8	23.5	29%	32.1%	38.5%	0.16	16.3

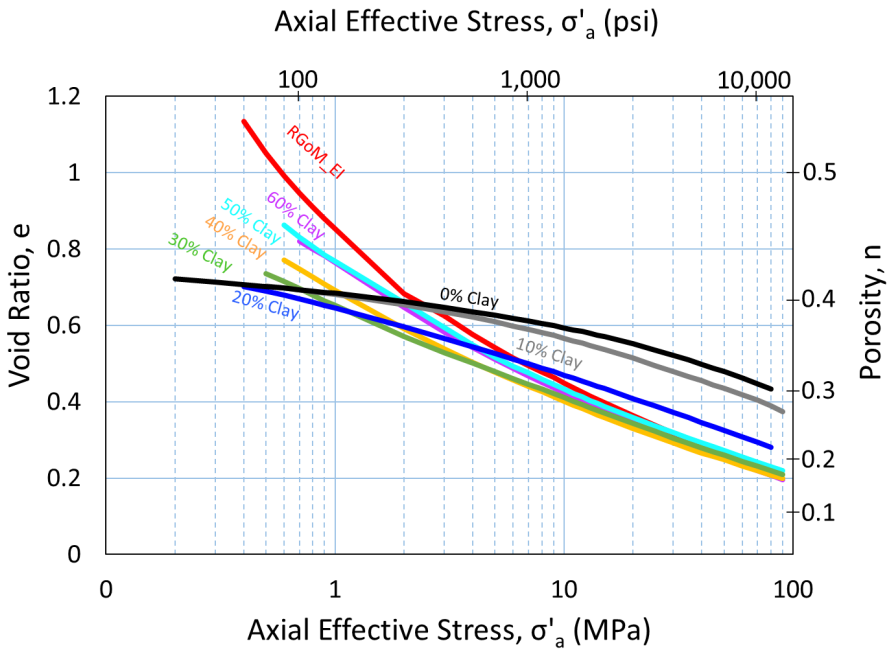


Figure 8-1: High stress CRS compression curves used to evaluate clay content effects on soil compressibility (Figure 5-9 reproduced).

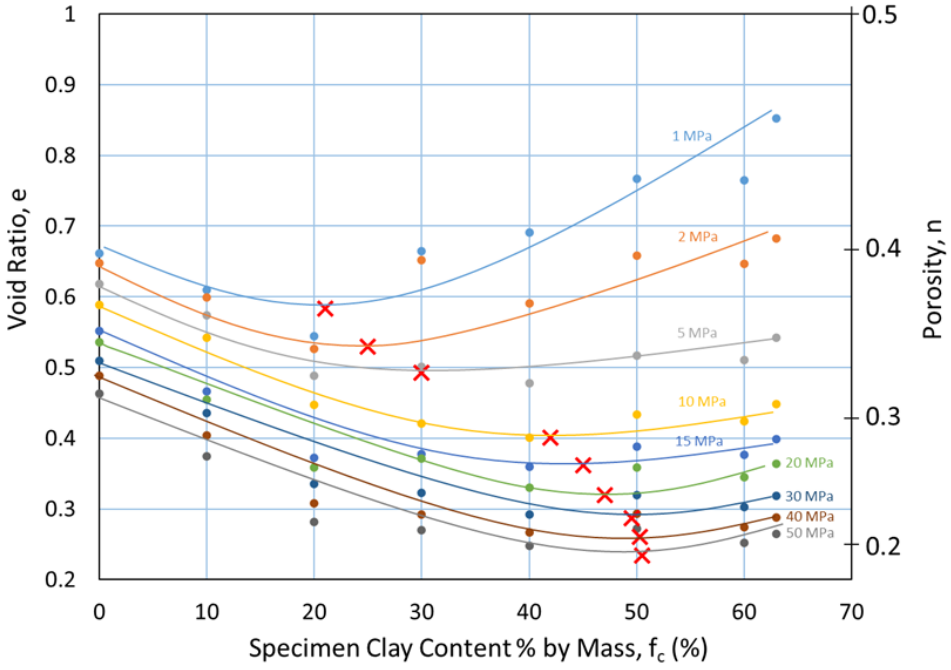
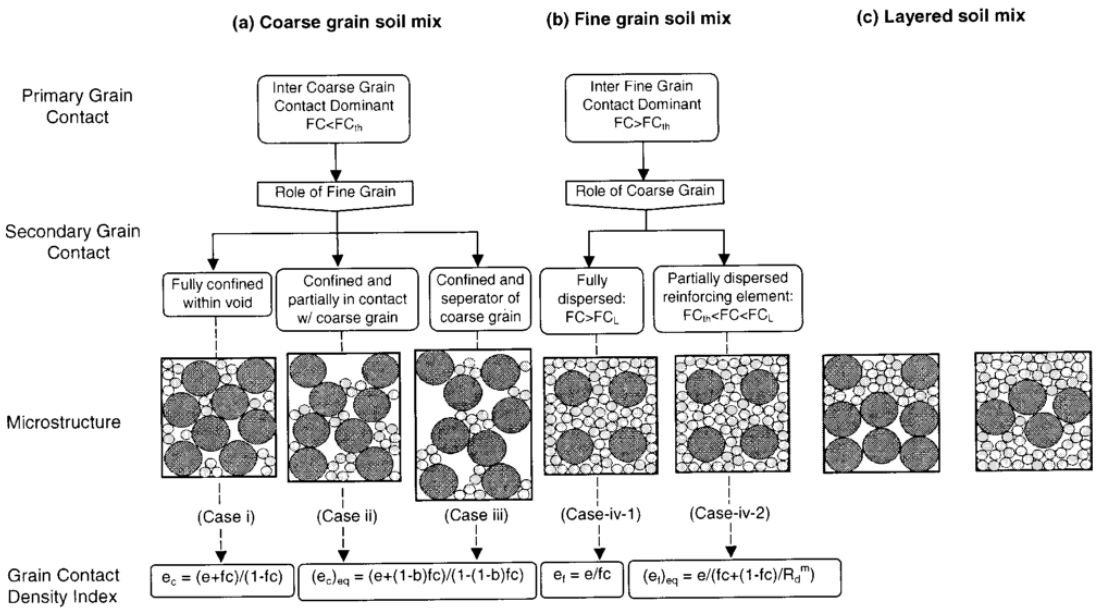


Figure 8-2: Average void ratio/porosity from the high stress CRS tests of each studied mixture at a 1 MPa, 2 MPa, 5 MPa ,10 MPa, 15 MPa, 20 MPa, 30 MPa, 40 MPa, and 50 MPa Vertical Stress. The red X indicates the interpreted critical clay fraction.



b=portion of the fine grains that contribute to the active intergrain contacts; e=global void ratio; FC=fine grains content; FC_{th}=threshhold fine grains content; FC_L=limit fines content; m: reinforcement factor; R_d=D/d=particle size disparity ratio

Figure 8-3: Flow chart for evaluating grain supported vs. clays supported or transitional material from Thevanayagam, Shenthan, Mohan, & Liang (2002)

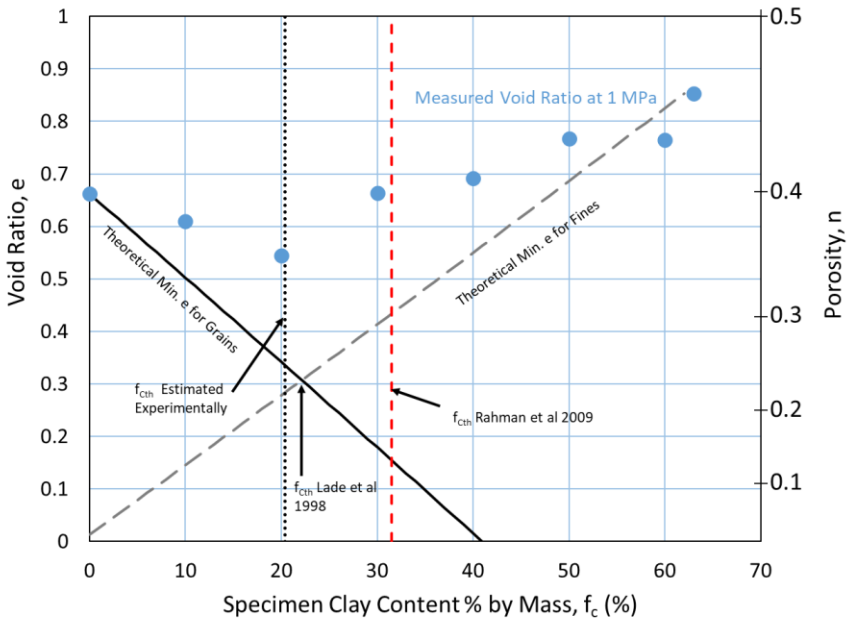


Figure 8-4: Void ratio by specimen clay content from High Stress CRS test at 1 MPA stress level. Three determinations for the threshold fines content are provided. The estimated minimum density by experimental analyses. An analytical minimum as the intersection of the theoretical minimum coarse grained and theoretical minimum fine grained void ratios per the Lade, Liggio Jr., & Yamamuro (1998) equations. And a semi-analytical analysis per the Rahman, Lo, & Gnanendran (2009) equation.

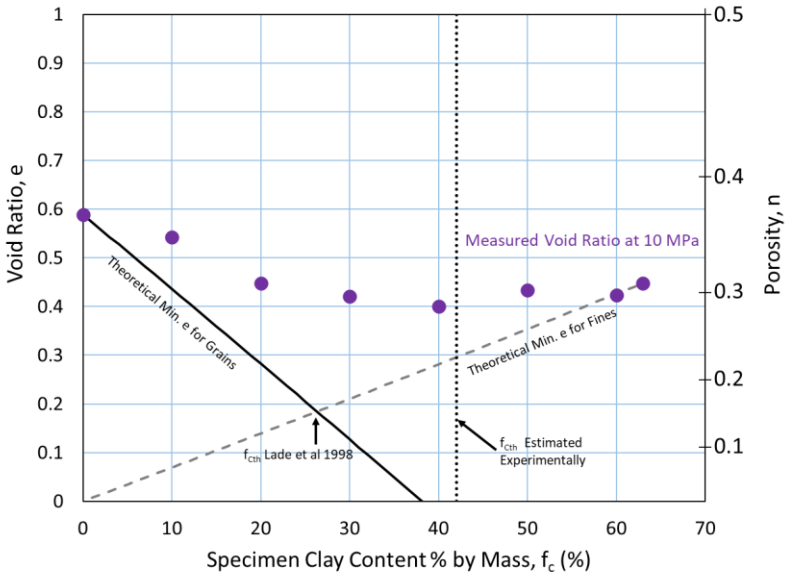


Figure 8-5: Void ratio by specimen clay content from High Stress CRS test at 10 MPA stress level. Two determinations for the threshold fines content are provided. The estimated minimum density by experimental analyses. An analytical minimum as the intersection of the theoretical minimum coarse grained and theoretical minimum fine grained void ratios per the Lade, Liggio Jr., & Yamamuro (1998) equations.

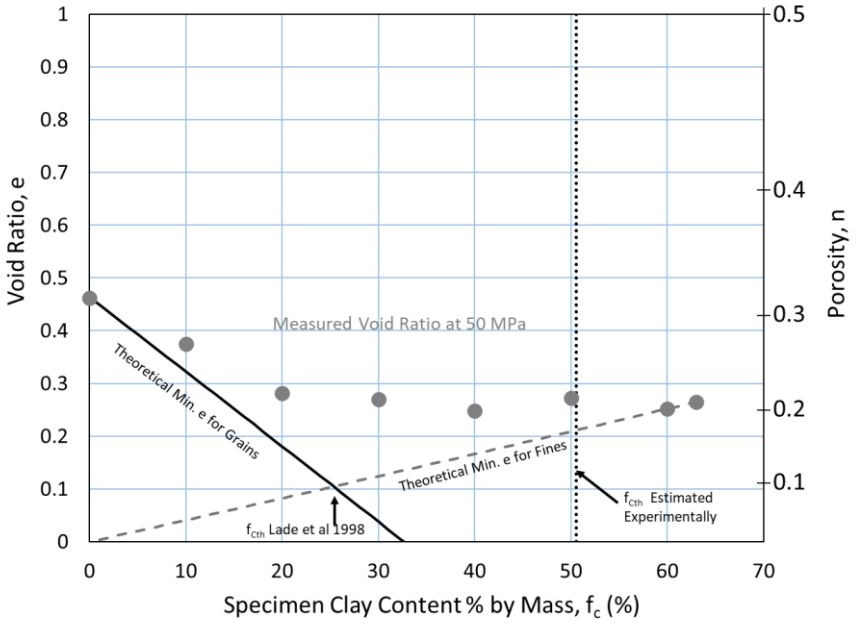


Figure 8-6: Void ratio by specimen clay content from High Stress CRS test at 50 MPA stress level. Two determinations for the threshold fines content are provided. The estimated minimum density by experimental analyses. An analytical minimum as the intersection of the theoretical minimum coarse grained and theoretical minimum fine grained void ratios per the Lade, Liggio Jr., & Yamamuro (1998) equations.

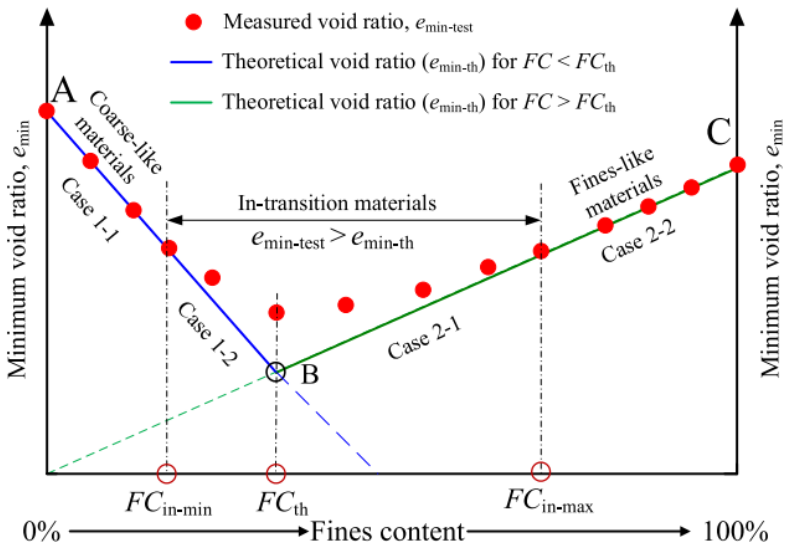


Figure 8-7: Theoretical and measured minimum void ratio for non-plastic fines in sand from Hang, Wu, Cheng, Li, & Chen (2024).

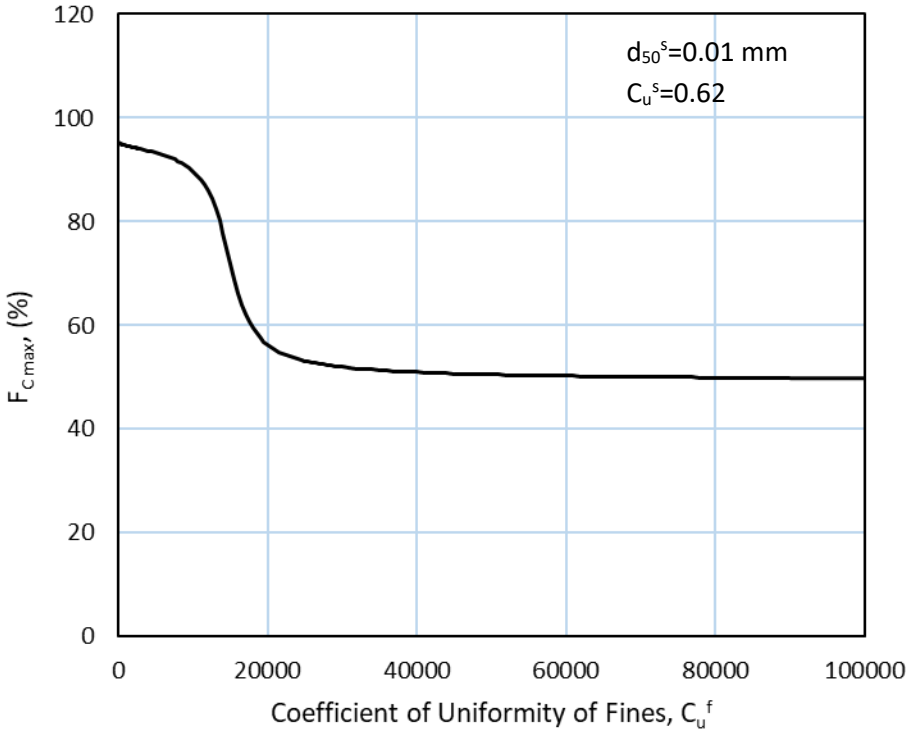


Figure 8-8: Variation in $F_{C\,max}$ by Coefficient of Uniformity for the fines using Equation 8-10 Hang, Wu, Cheng, Li, & Chen (2024). $FC_{in\text{-}max}$ varies between 49.9% and 95.4%, decreasing with and increasing C_u^{f}.

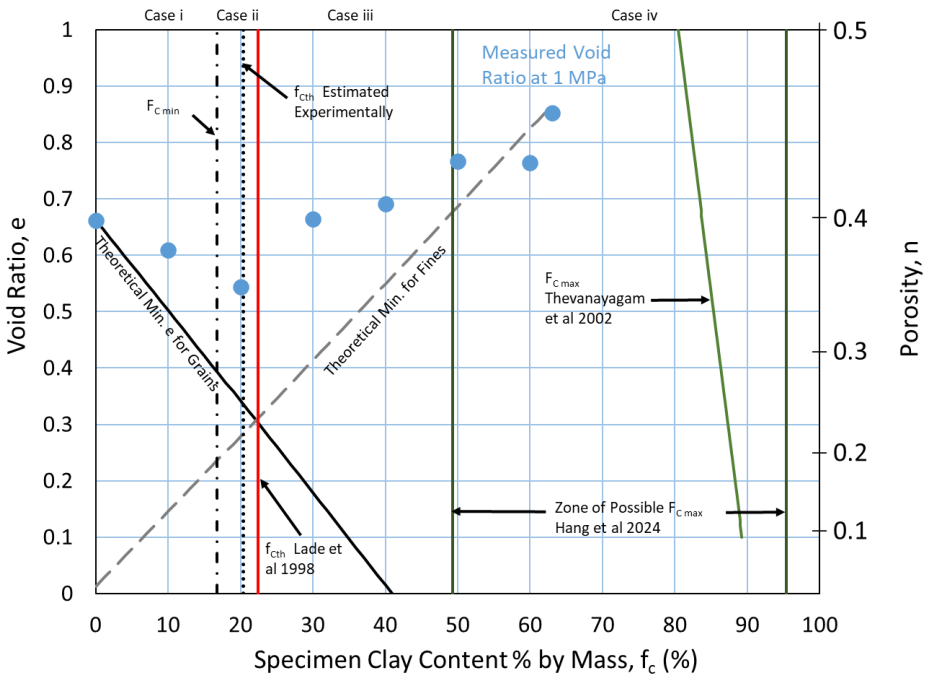


Figure 8-9: Void ratio by specimen clay content from High Stress CRS test at a 1 MPA stress level. Estimates of $FC_{in\ min}$, FC_{th} and $FC_{in\ max}$ are provided to illustrate the different Cases for grain supported or fines supported materials.

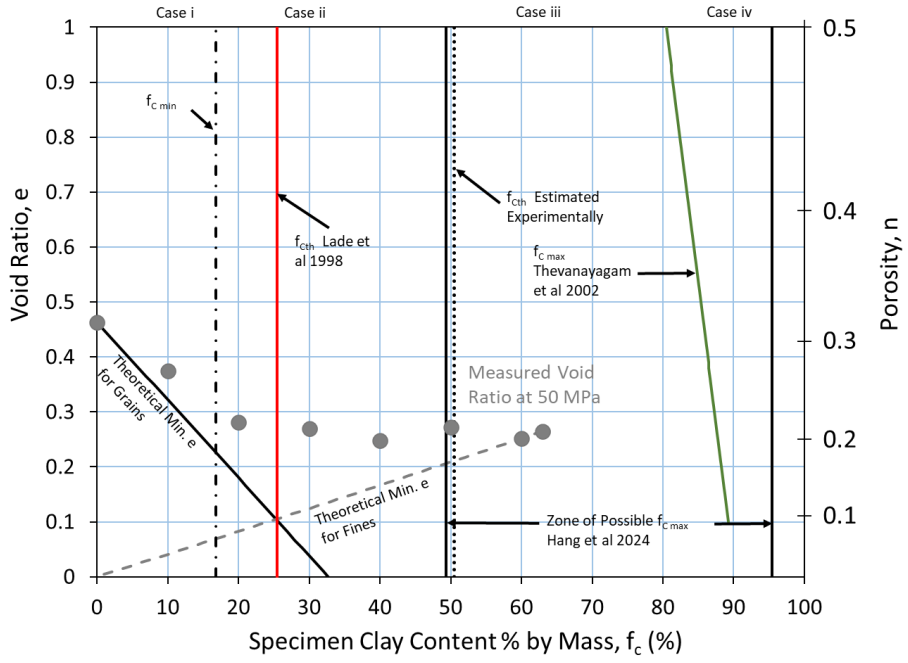


Figure 8-10: Void ratio by specimen clay content from High Stress CRS test at a 50 MPA stress level. Estimates of $FC_{in\ min}$, FC_{th} and $FC_{in\ max}$ are provided to illustrate the different Cases for grain supported or fines supported materials.

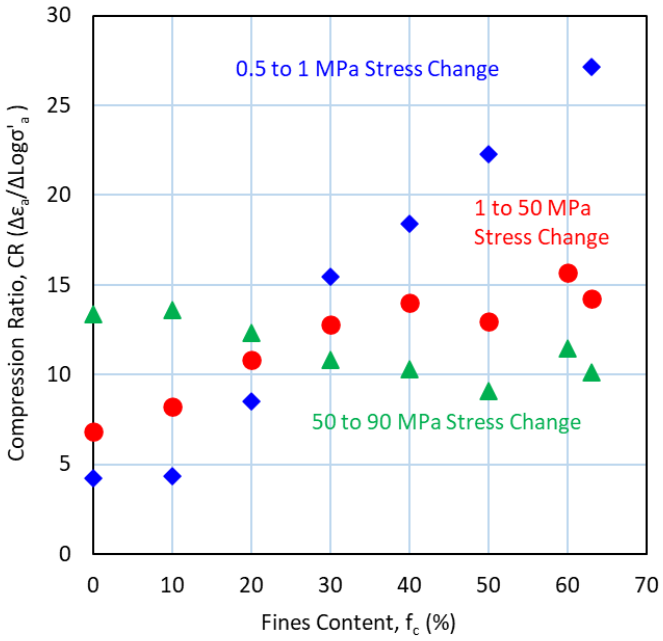


Figure 8-11: Variation in the compression ratio (CR) by specimen clay content. The blue points present CR between 0.5 to 1 MPA, the red points present CR between 1 to 50 MPa, and the green present CR between 50 to 90 MPa.

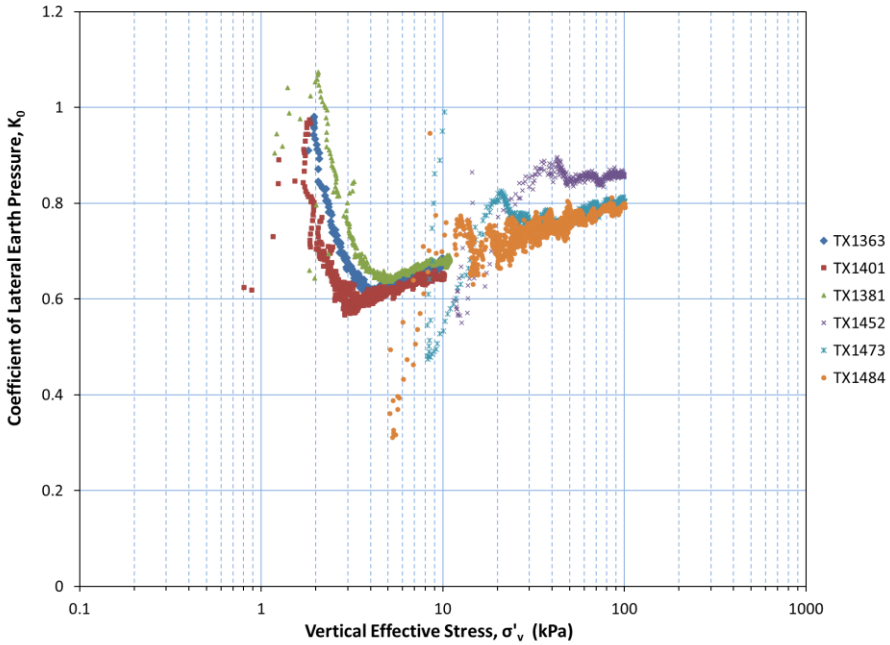


Figure 8-12: K_0 measurements during the triaxial consolidation stage for the RGoM_EI specimens.

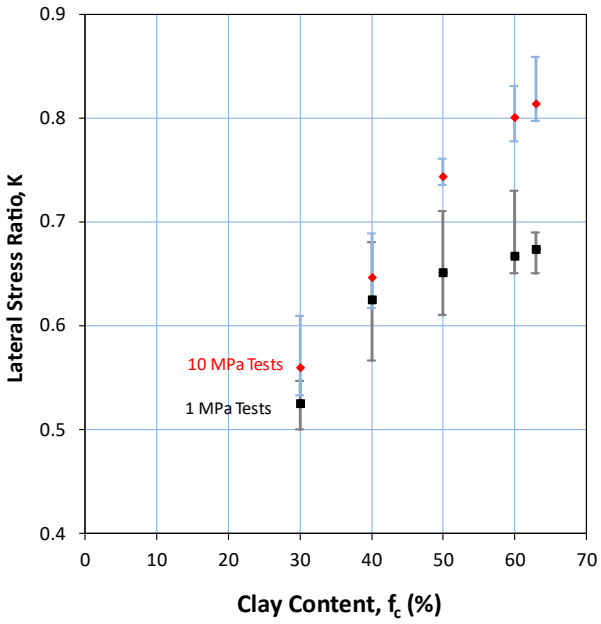


Figure 8-13: K_0 values by specimen clay content measured during consolidation phase of the triaxial tests. The black points present the average K_0 at a 1 MPa stress level with corresponding gray error bars for the minimum and maximum K_0 values. The red points present the average K_0 at a 10 MPa stress level with corresponding blue error bars for the minimum and maximum K_0 values.

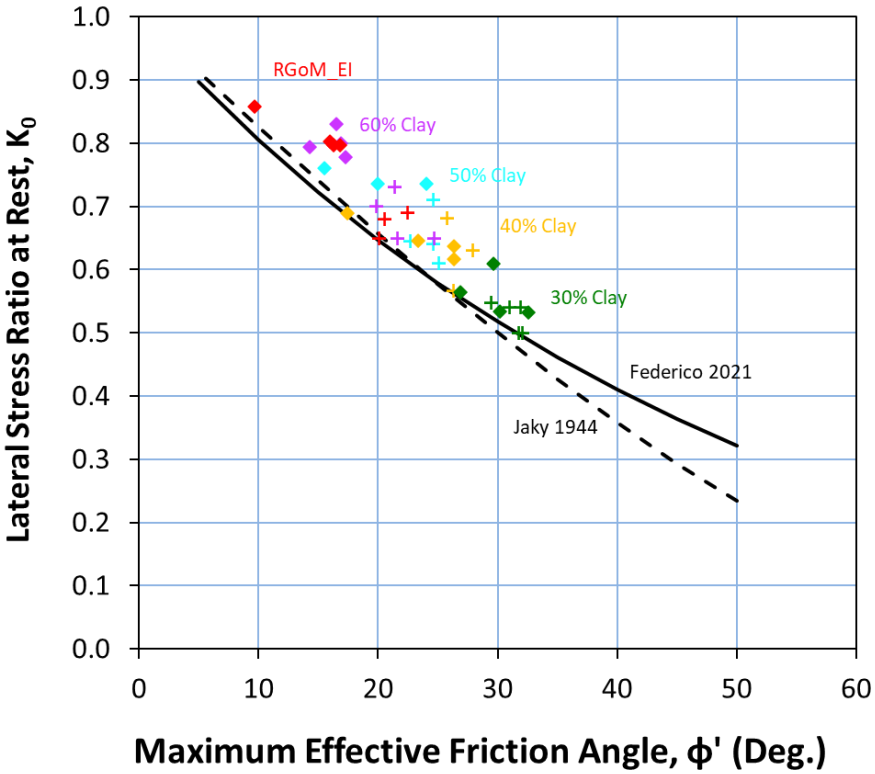


Figure 8-14: Lateral stress ratio at rest (K_0) by maximum friction angles measured during shearing. The dashed line represents the Jaky (1944) correlation, and the Solid line represents the Federico (2008) correlation.

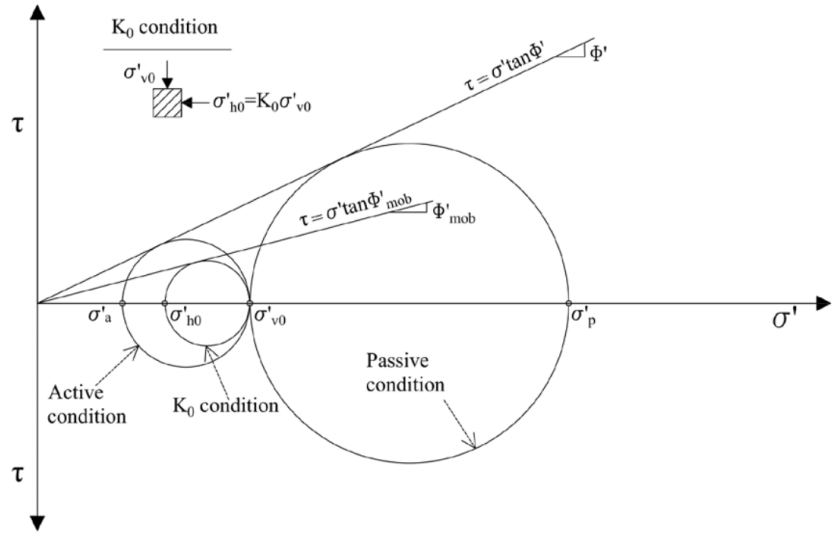


Figure 8-15: Mohr's circles of stress for K_0 condition (mobilized friction angle) and failure friction angle from (Federico, 2021).

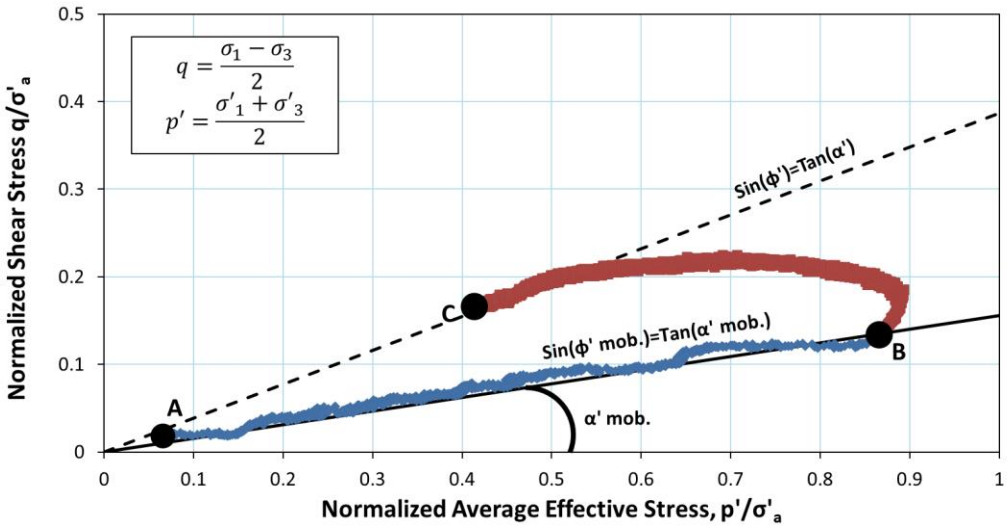


Figure 8-16: Example calculation of mobilized friction angle at maximum consolidation stress from triaxial consolidation phase. The mobilized friction angle (α' mob.) is the angle from the origin through the maximum consolidation stress (Point B) represented by the solid line. The effective failure angle is the dashed line from the origin through Point C. The stress path presents is TX1475 a 50% clay material.

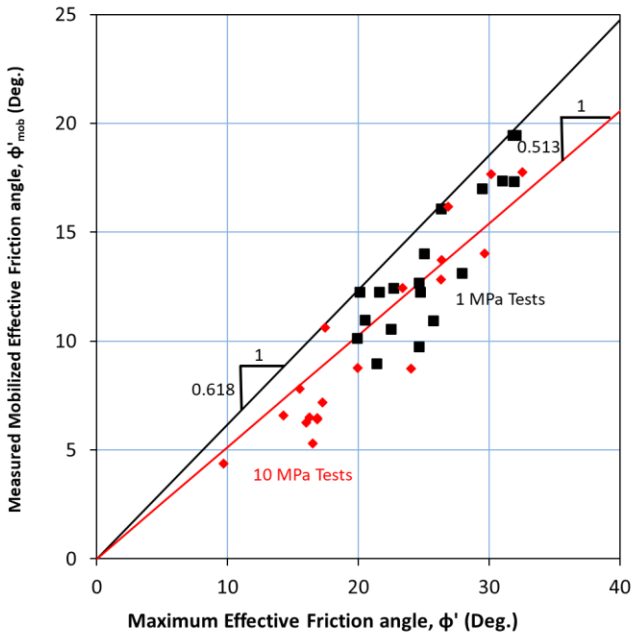


Figure 8-17: Measured mobilized friction angle during consolidation phase by maximum friction angle measured during shear phase. The black line indicates the 0.618 mobilization ratio in Equation 8-13 from (Federico, 2021) for reference. The red line provides the best fit linear correlation of a slope of 0.513 from the triaxial tests.

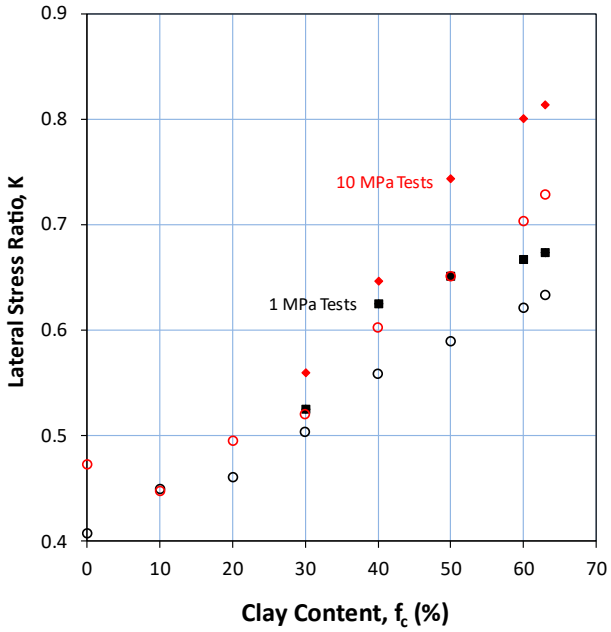


Figure 8-18: K_0 values by specimen clay content measured during the consolidation phase of the triaxial tests and predicted using Equation 8-13. The open points represent the predicted values using Equation 8-13.

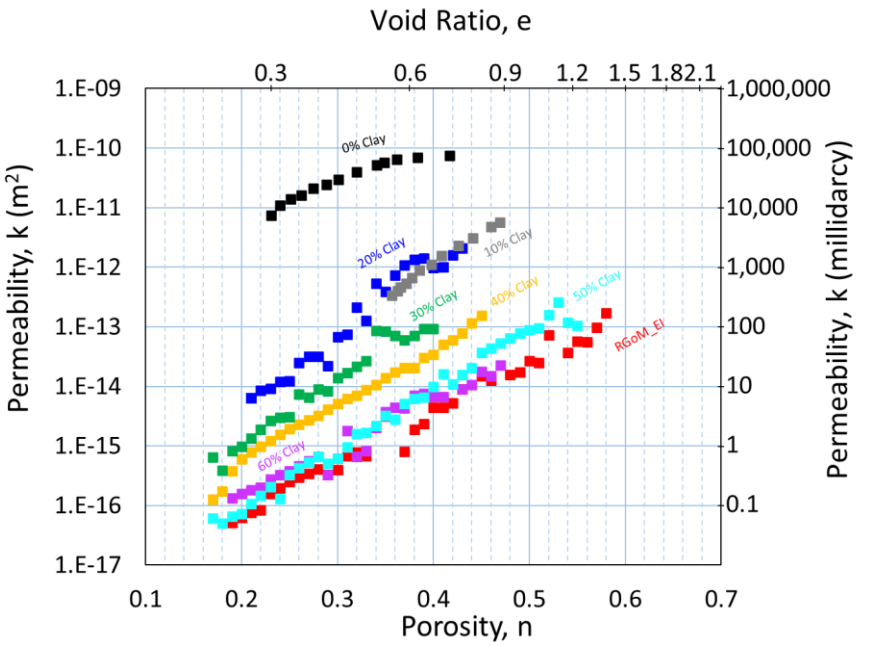


Figure 8-19: Permeability by porosity measured during high stress CRS testing.

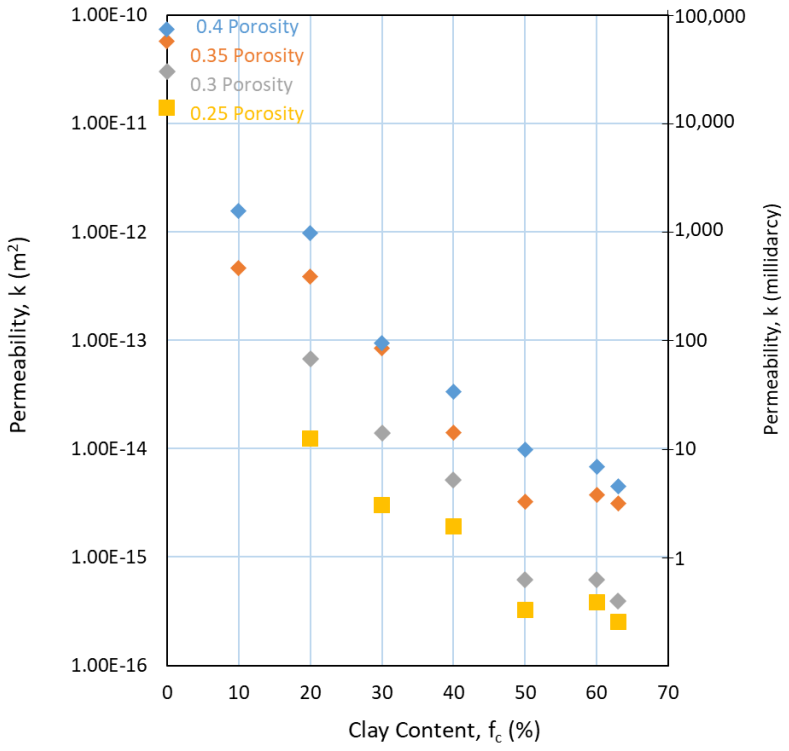


Figure 8-20: Permeability by specimen clay content at equivalent porosities of 0.4, 0.35, 0.3, and 0.25.

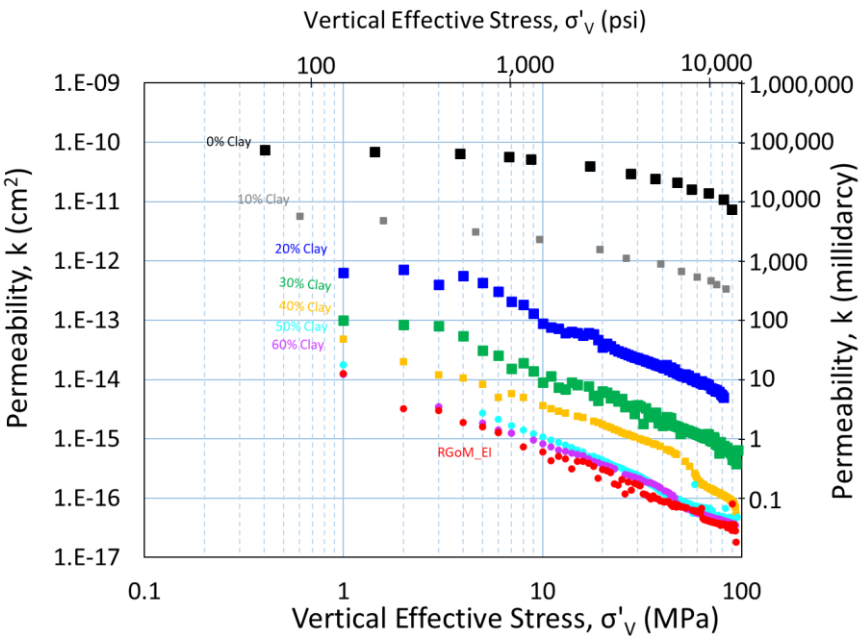


Figure 8-21: Permeability by vertical effective stress measured during high stress CRS testing.

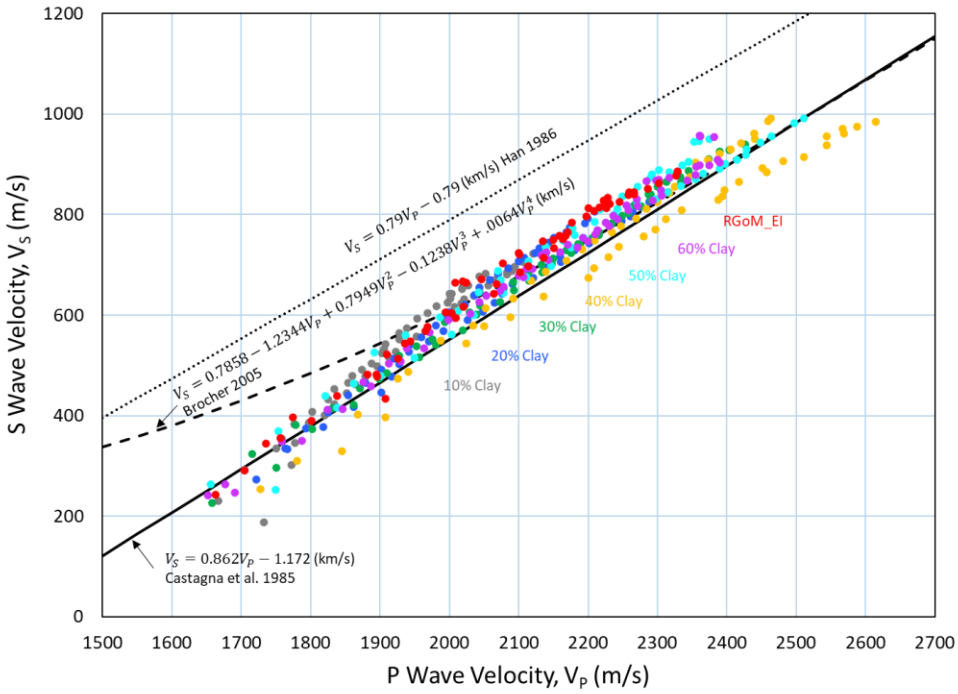


Figure 8-22: Shear wave velocity by pressure wave velocity from the TCRS tests. Three shear wave velocity correlations are presented from Castagna, Batzle, & Eastwood (1985), Han (1986), and Brocher (2005).

Figure 8-26:
tested; ca

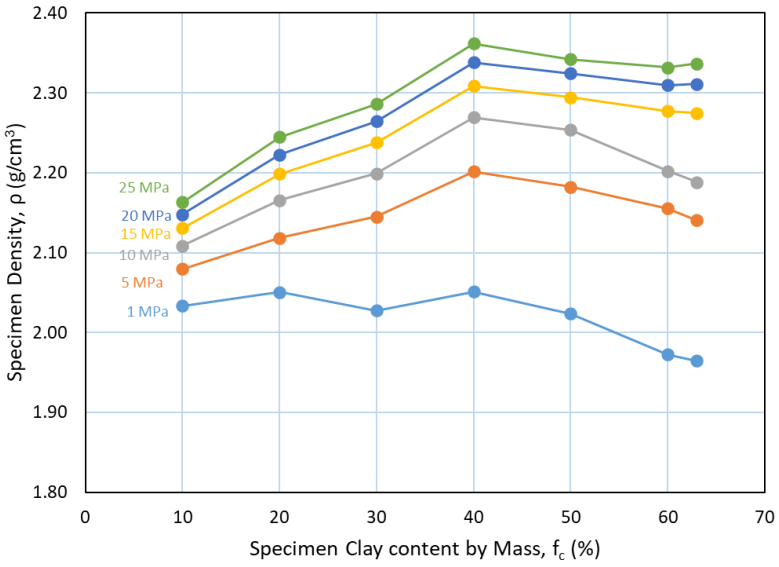


Figure 8-23: Average specimen density by clay content based on phase relations and measured volumetric strain at 6 axial stress from the TCRS tests.

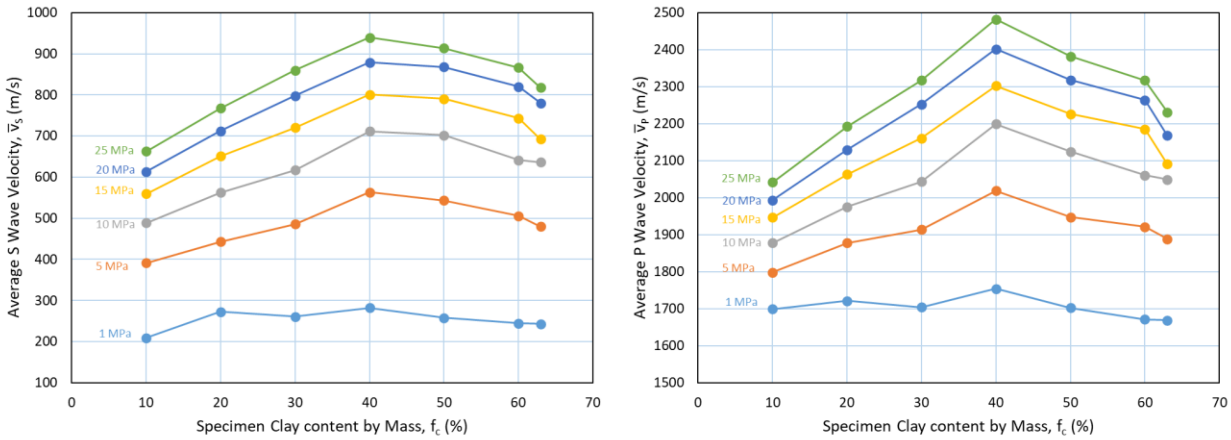


Figure 8-24: Average S wave velocity and P wave velocity by clay content from the TCRS tests.

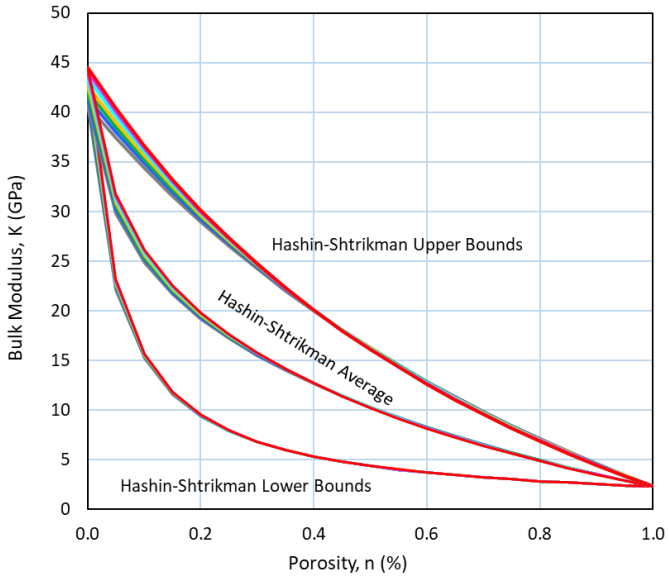


Figure 8-25: Hashin-Shtrikman bounds and average for the bulk modulus of the silt-clay mixtures tested; calculated from the mixture bulk modulus and shear modulus provided in Table 8-3.

Figure 8-27: H
calcula

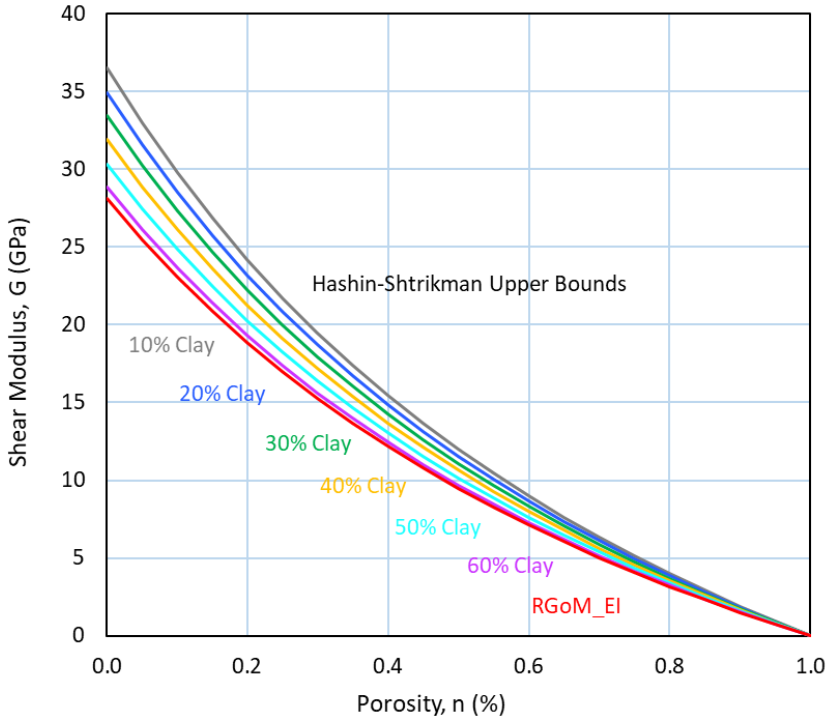


Figure 8-26: Hashin-Shtrikman upper bounds for the shear modulus of the silt-clay mixtures tested; calculated from the mixture bulk modulus and shear modulus provided in Table 8-3.

Figure 8-
measurements

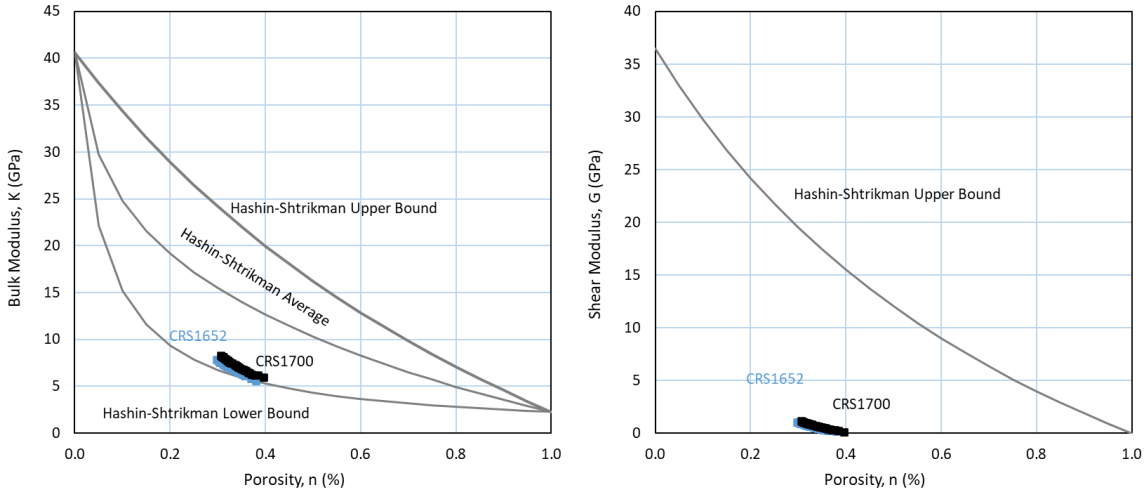


Figure 8-27: Bulk modulus and shear modulus for 10% clay mixtures calculated from wave measurements from Tall CRS testing. The Hashin-Shtrikman bounds, and average are calculated from the mixture bulk modulus and shear modulus provided in Table 8-3.

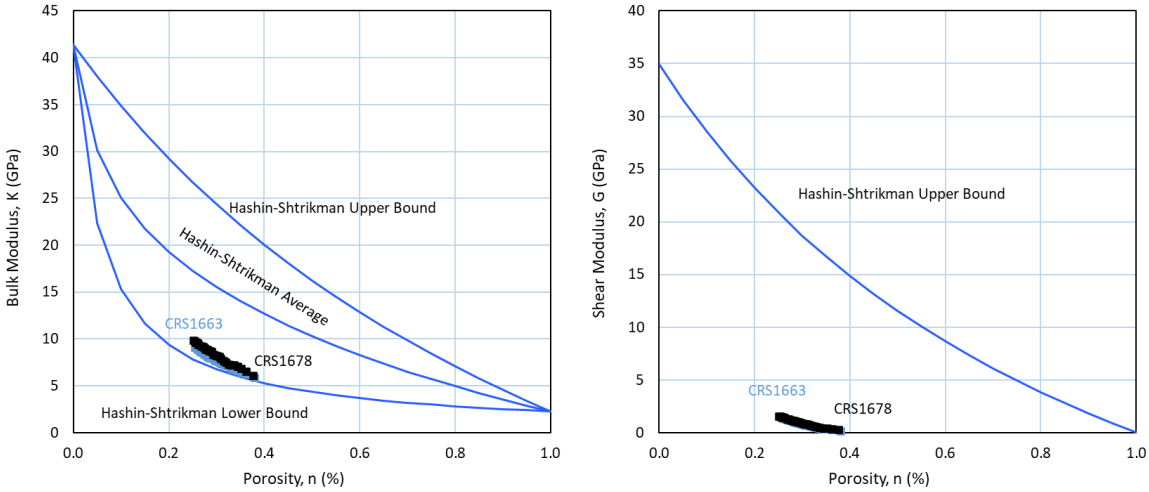


Figure 8-28: Bulk modulus and shear modulus for 20% clay mixtures calculated from wave measurements from Tall CRS testing. The Hashin-Shtrikman bounds, and average are calculated from the mixture bulk modulus and shear modulus provided in Table 8-3.

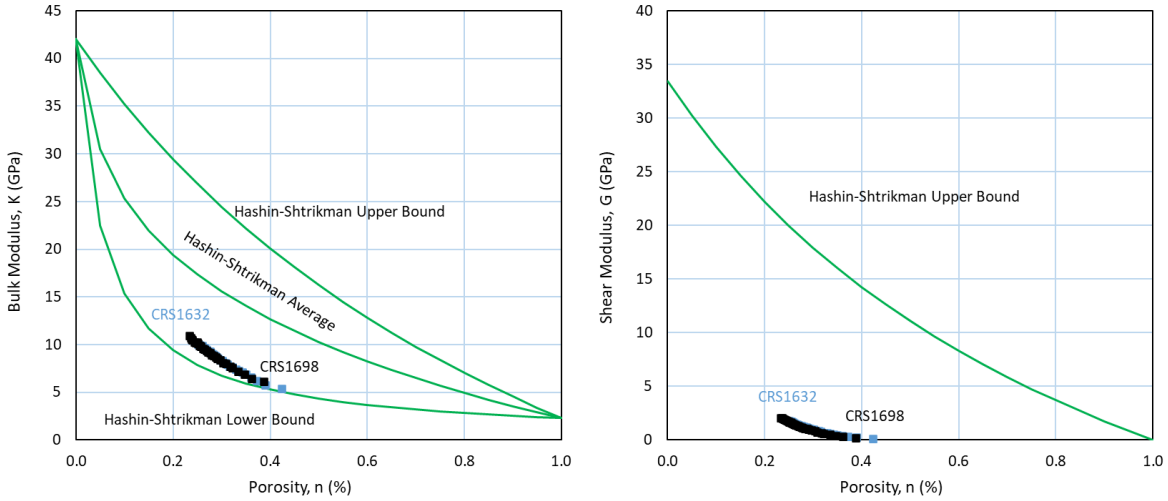


Figure 8-29: Bulk modulus and shear modulus for 30% clay mixtures calculated from wave measurements from Tall CRS testing. The Hashin-Shtrikman bounds, and average are calculated from the mixture bulk modulus and shear modulus provided in Table 8-3.

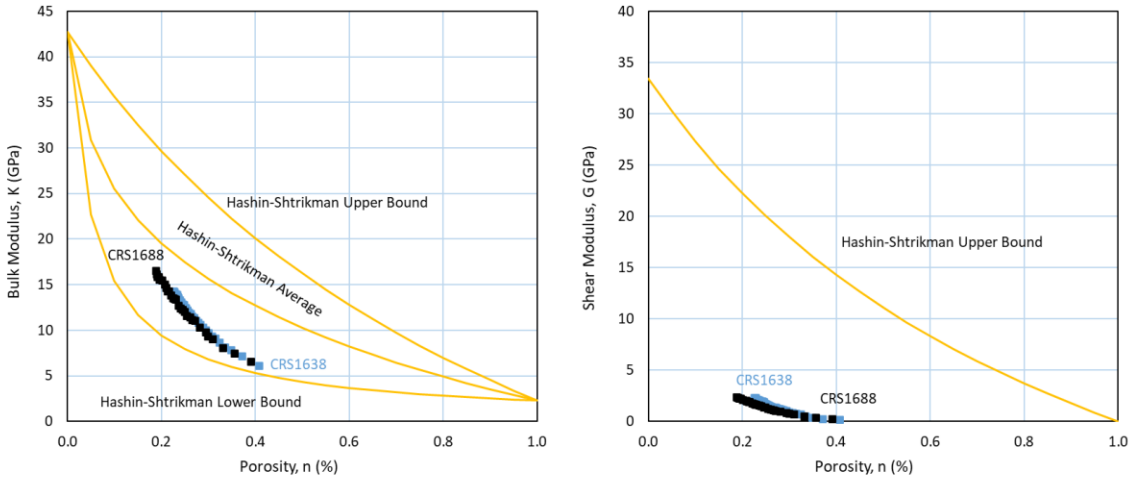


Figure 8-30: Bulk modulus and shear modulus for 40% clay mixtures calculated from wave measurements from Tall CRS testing. The Hashin-Shtrikman bounds, and average are calculated from the mixture bulk modulus and shear modulus provided in Table 8-3.

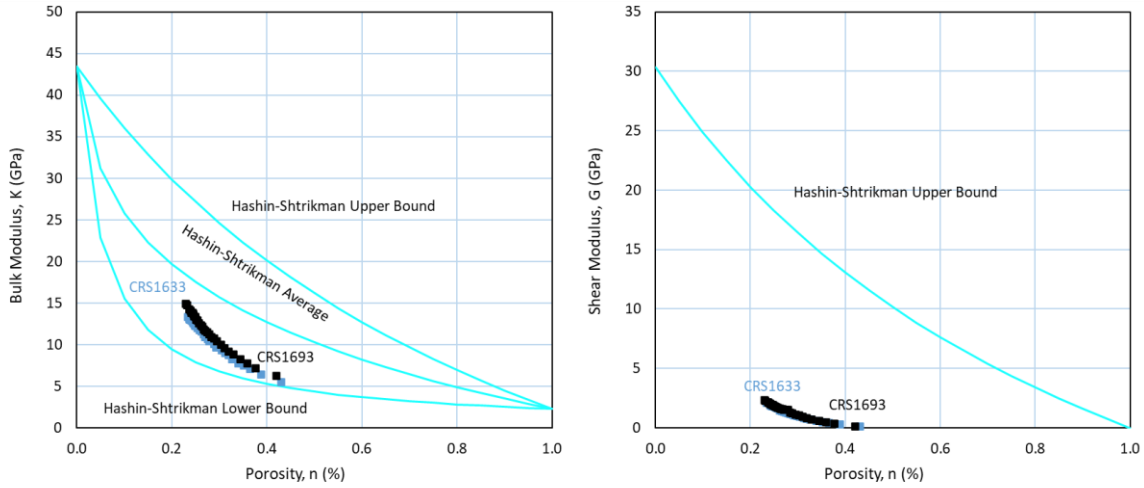


Figure 8-31: Bulk modulus and shear modulus for 50% clay mixtures calculated from wave measurements from Tall CRS testing. The Hashin-Shtrikman bounds, and average are calculated from the mixture bulk modulus and shear modulus provided in Table 8-3.

Figure 8-
measurements

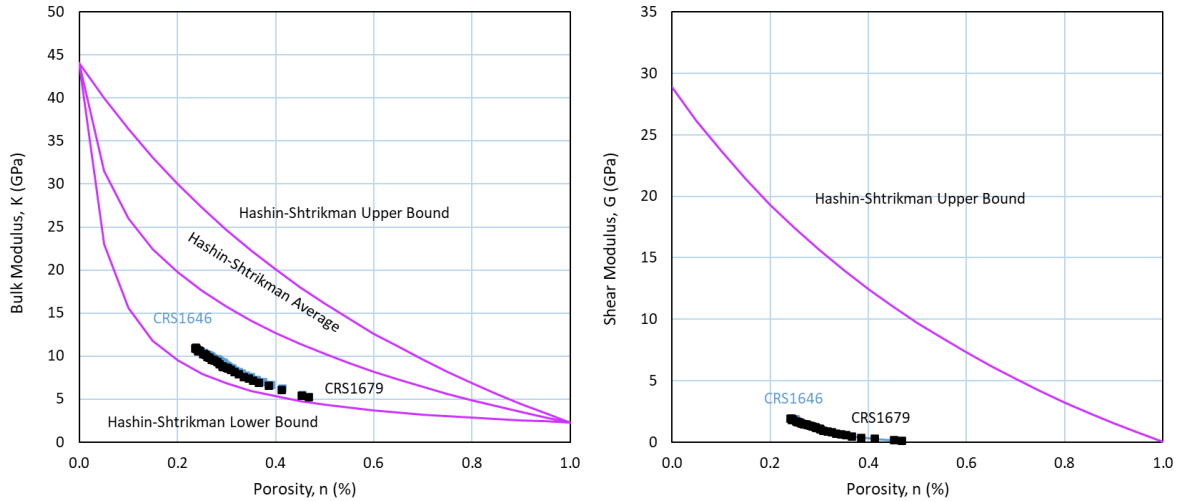


Figure 8-32: Bulk modulus and shear modulus for 60% clay mixtures calculated from wave measurements from Tall CRS testing. The Hashin-Shtrikman bounds, and average are calculated from the mixture bulk modulus and shear modulus provided in Table 8-3.

Figure 8-34
measurements

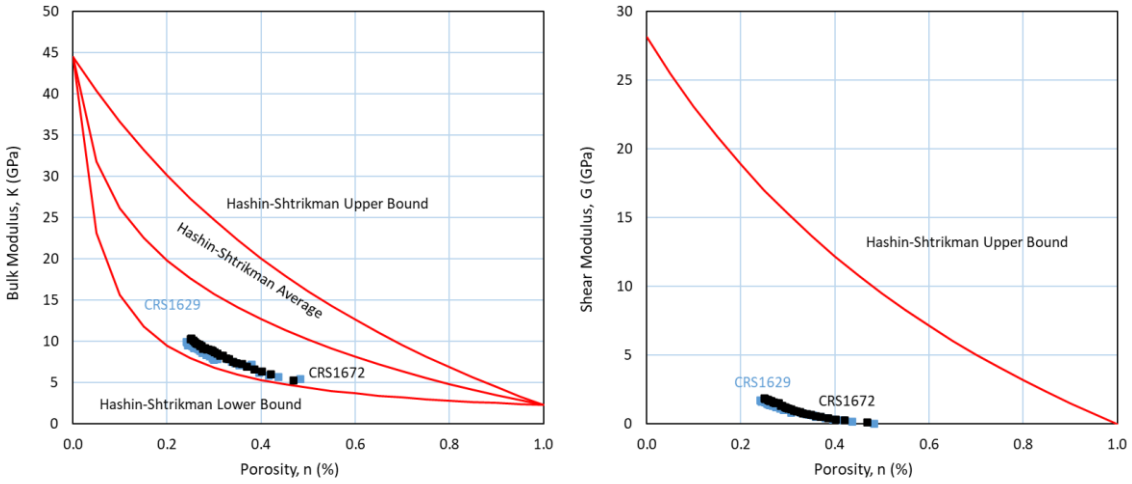


Figure 8-33: Bulk modulus and shear modulus for RGoM_EI clay mixtures calculated from wave measurements from Tall CRS testing. The Hashin-Shtrikman bounds, and average are calculated from the mixture bulk modulus and shear modulus provided in Table 8-3.

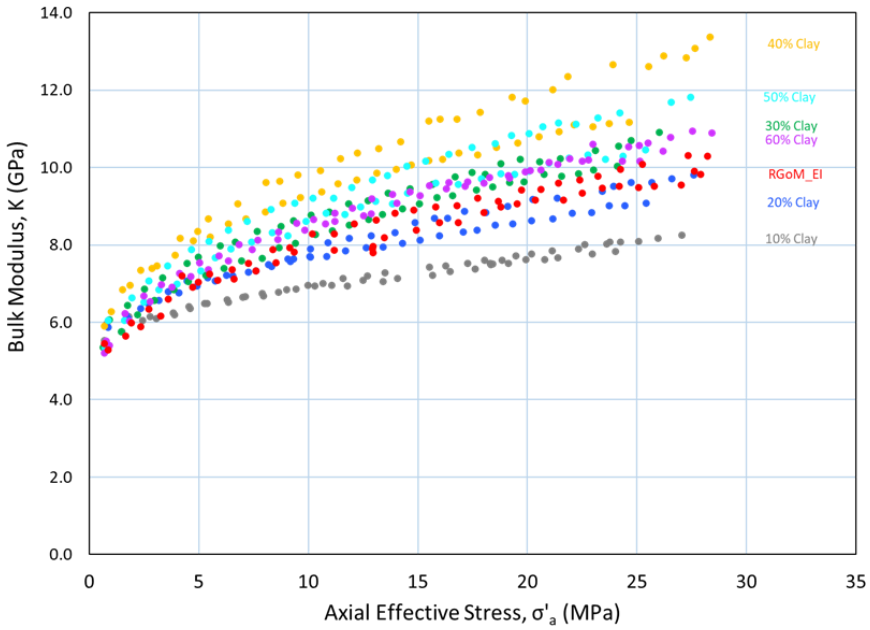


Figure 8-34: Bulk Modulus by axial effective stress (Figure 6-26).

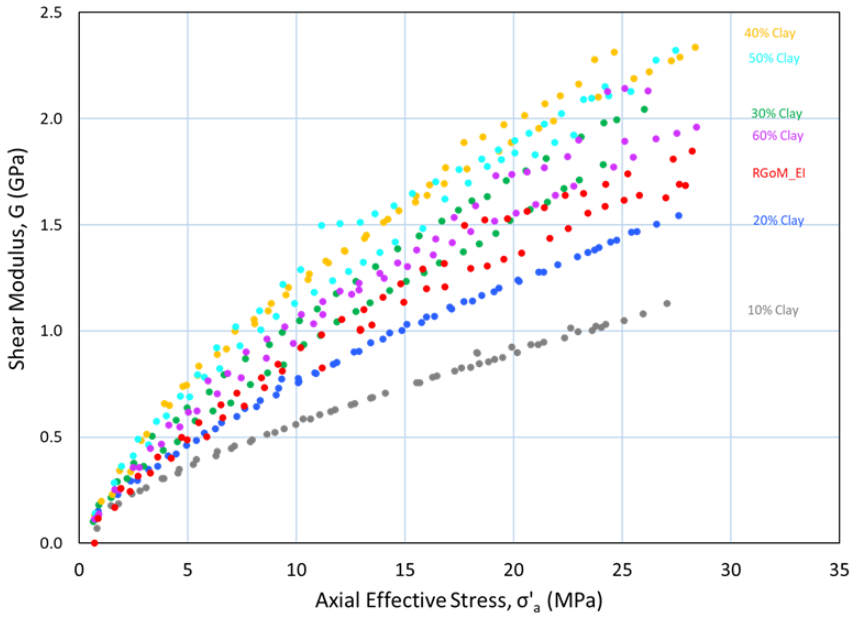


Figure 8-35: Shear modulus by axial effective stress (Figure 6-24).

Figure 8-37: S
velocity correla

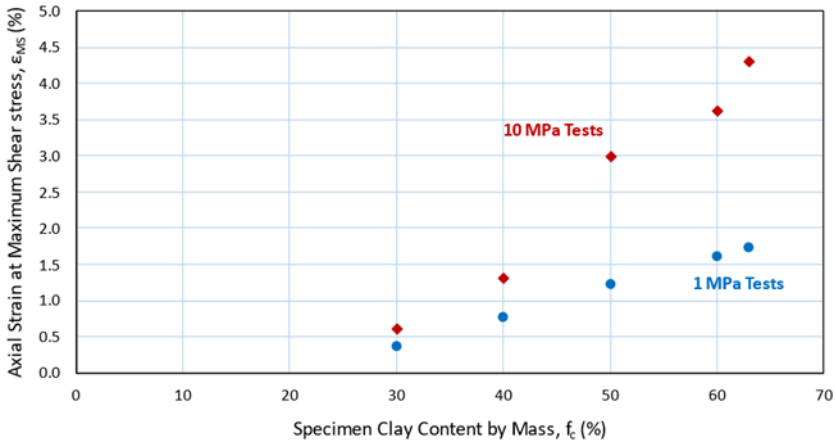


Figure 8-36: Average axial strain corresponding with the measured maximum shear stress by specimen clay content from undrained shear phase of triaxial tests at two consolidation stress levels 1 MPa and 10 MPa. (Figure 7-28).

Figure 8-38
presented from
& East

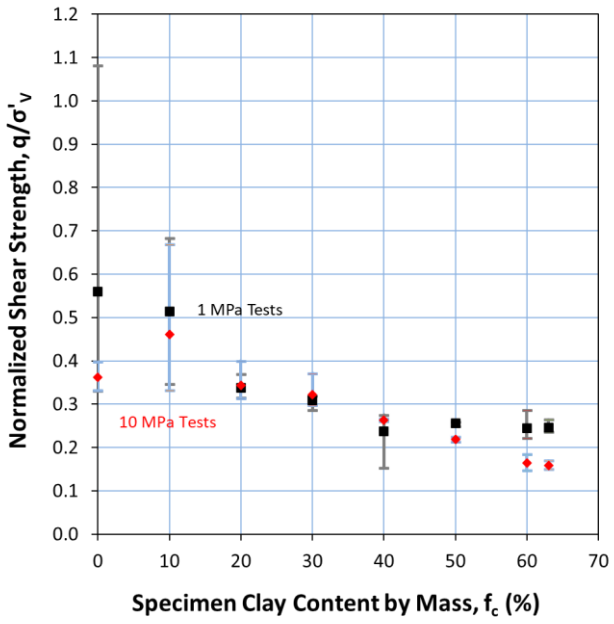


Figure 8-37: Average normalized shear strength by specimen clay content measured during the shear phase of the triaxial tests. The black points present the average q/σ'_V at a 1 MPa stress level with corresponding gray error bars for the minimum and maximum q/σ'_V values. The red points present the average q/σ'_V at a 10 MPa stress level with corresponding blue error bars for the minimum and maximum q/σ'_V values.

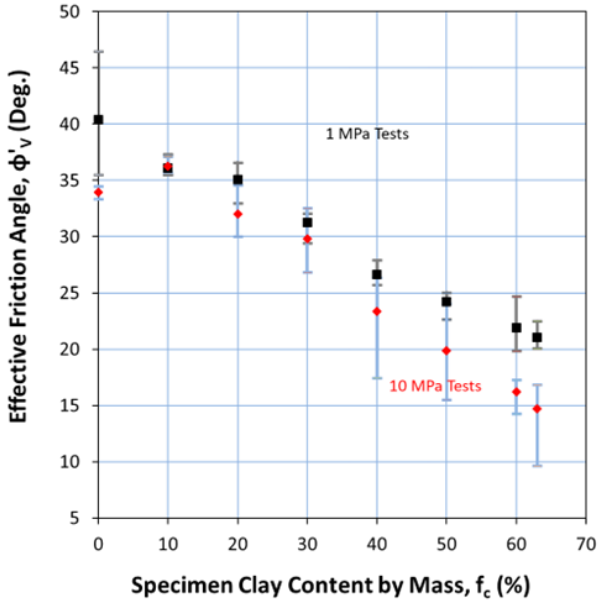


Figure 8-38: Average effective friction angle by specimen clay content measured during the shear phase of the triaxial tests. The black points present the average ϕ' at a 1 MPa stress level with corresponding gray error bars for the minimum and maximum ϕ' values. The red points present the average ϕ' at a 10 MPa stress level with corresponding blue error bars for the minimum and maximum ϕ' values.

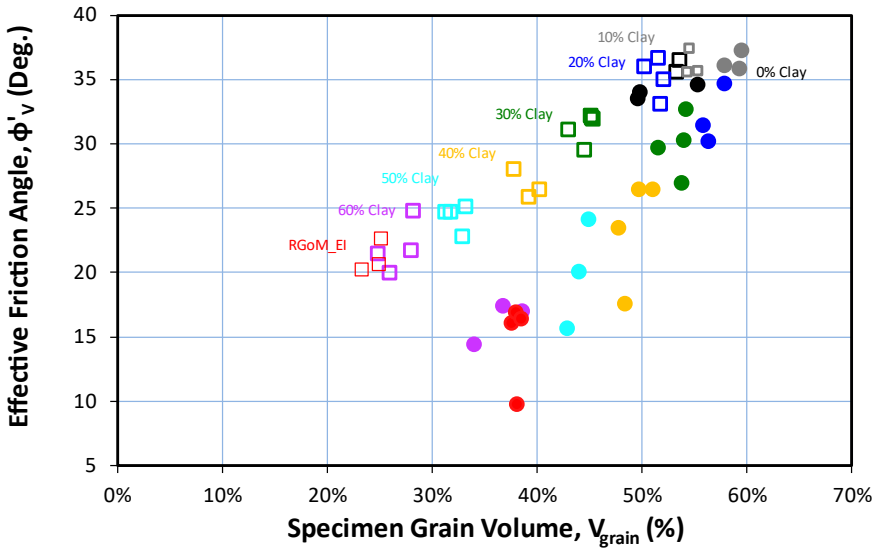


Figure 8-39: Effective friction angle by V_{grain} (1-(Porosity+V_{clay})). The open symbols are the 1 MPa tests and the closed symbols are the 10 MPa tests.

Figure 8-38
presented from
& East

CHAPTER 9. Evaluation of Clay Dependent Soil Parameter Correlations

9-1 Introduction

This chapter presents a discussion on the definition of clay content, evaluations of empirical correlations for soil engineering parameters, and field applications from results of the experimental geotechnical testing program presented in Chapters 5, 6, and 7. This chapter is divided into five sections. Section 9.2 discusses three methods of establishing specimen clay contents. These methods vary by defining the clay content by particle size, mineralogy, or a combination of particle size and mineralogy. Section 9.3 discusses variations of soil compressibility with clay content, provides a comparison of compression models for specimens of varying clay content, and provides an example of accounting for clay content in estimating overburden pressures. Section 9.4 discusses variations of soil permeability with clay content and provides a comparison of permeability models for specimens of varying clay content. Section 9.5 discusses the variations of the isotropic elastic parameters derived from velocity measurements by clay content and provides a comparison of shear modulus correlations, and an example of accounting for clay content when estimating shear modulus using the correlations. Section 9.6 discusses variations of strength parameters with clay content and provides a comparison of methods used to establish the fracture gradient during drilling that consider clay content.

9-2 Evaluating Clay Content

The first method of establishing the clay content is to assume that 63% natural clay content by mass as classified by particle for RGoM_EI fraction of a specimen is the clay content for the specimen. This classification is presented in Chapter 3 and serves as the base assumption for the laboratory testing program. Under this classification scheme the Min-U-Sil (MUS) powder is assumed to be all silt sized particles. Method 2 for determining clay content used to evaluate the test results, accounts for the percentage of clay sized particles in MUS by adjusting Equation 3-1 to Equation 9-1.

$$f_s = \frac{M_{cl} f_{sn} + M_s f_{sm}}{M_t}$$ Equation 9-1

Where:

f_s = Silt fraction of test specimen

M_{cl} = Mass of clay powder (mass)

f_{sn} = Silt fraction of clay powder

M_s = Mass of added MUS (mass)

f_{sm} = Silt fraction of added MUS

M_t = Total mass of specimen calculated from the final volume (mass)

The third method of determining clay content is to consider the mineralogical clay content of the GOM_EI powder. Within Betts (2014) X-ray powder diffraction results are provided for the GOM_EI powder that indicates clay minerals comprise 53.9% of the powder. Method three of establishing clay contents uses Equation 3-1 and assumes the natural silt content of GOM_EI is 46% and MUS is 100% mineral quartz. The experimental test results are evaluated against the clay contents established by these three methods to evaluate the importance of particle size definition of clay to the mineralogical definition of clay.

9-3 Soil Compressibility and Clay Content

Links between soil composition and compressibility are well established and reported as discussed within Chapter 2. This work intends to advance on historic works, by analyzing the clay dependency over large stress ranges for controlled synthetic specimens eliminating some variations inherent to natural materials. To evaluate the link between soil compressibility and clay content the compression curves from the High Stress CRS tests are fit with a compression model. The compression model includes inputs that are a function of the specimen clay content. The modeled clay contents are varied to accommodate the methods of establishing clay content. Based on the analyses presented in Casey, Reece, & Germaine (2019), two compression models are evaluated. The first model is a log linear

relationship between σ'_a and void ratio that is recommended for soils with liquid limits less than 50 percent. The second model is a log linear relationship between σ'_a and porosity recommended for soils with liquid limits greater than 50 percent. Figure 9-1 reproduces the High Stress CRS test compression curves presented in Figure 5-9 that are modeled to evaluate the dependency of soil compressibility on clay content. The two models evaluated are very similar, with the major difference being the variable used to represent changes in volume, either void ratio or porosity as illustrated in Equation 9-2 and Equation 9-3.

$$e - e_{ref} = -C_c Log_{10}\left(\frac{\sigma'_a}{\sigma'_{aref}}\right) \qquad \text{Equation 9-2}$$

$$\phi - \phi_{ref} = -C_{C\phi} Log_{10}\left(\frac{\sigma'_a}{\sigma'_{aref}}\right) \qquad \text{Equation 9-3}$$

Where:

e = Void Ratio

e_{ref} = Void Ratio at Reference Effective Stress

C_C = Compression Index

σ'_a = Axial Effective Stress (Force/Area)

σ'_{aref} = Reference Axial Effective Stress (Force/Area) 1 MPa used for this study.

ϕ = Porosity (percent)

ϕ_{ref} = Porosity at Reference Effective Stress (percent)

$C_{C\phi}$ = Empirical Constant

The measured High Stress CRS compression curves were fit with Equations 9-2 and 9-3, with a reference σ'_a of 0.5 MPa. Figure 9-2 and Figure 9-3 illustrate the approximated compression curves in log linear σ'_a void ratio and porosity space respectively. The clay dependency is evaluated by plotting the reference void ratios or porosity at 0.5 MPa and compression indices C_C and $C_{C\phi}$ by specimen clay content as determined by the three methods outlined in Section 9-2. The reference void ratio or porosity are adequately fit with a second order polynomial equation due to the coefficient of determination (R^2)

values exceeding 0.9 as illustrated in Figure 9-4 and Figure 9-6. The compression indices C_C and $C_{C\phi}$ are adequately fit with a linear equation due to the R^2 values exceeding 0.9 as illustrated in Figure 9-5 and 9.7.

The models are evaluated by comparing the modeled compression curves for specimens of 0% clay, 30% clay, and 65% clay (RGoM_EI) to the measured compression curves. These clay contents were chosen to evaluate a grain supported material (0% clay) a transitional material (30% clay) and a clay support material (RGoM_EI). Figure 9-8 to Figure 9-10 show the comparison of the modeled compression curves to the test compression curves. The volumetric strain of the specimens between 0.5 MPa and 60 MPa is 34% for 0% clay, 67% for 30% clay, and 73% for RGoM_EI, illustrating the link between clay content and compressibility.

The coefficient of determination (R^2) adjusted coefficient of determination ($\bar{R}^2$), and root mean squared error (RMSE) values from the comparison are presented in Table 9-1. For the 0% clay content specimen the void ratio models are a significantly better fit than the porosity models. With the best fit being the method 2 void ratio model that includes the clay sized particles of the Min-U-Sil. For the 30% clay content specimen the porosity models are a slightly better fit than the void ratio models, but both the void ratio and porosity models indicate a good correlation. With the best fit being the method 1 porosity model that does not include the clay sized particles of the Min-U-Sil. For RGoM_EI specimen the porosity models are a significantly better fit than the void ratio models. With the best fit being the method 1 porosity model that does not include the clay sized particles of the Min-U-Sil. The concave downwards nature of compression curves for grain supported materials are not properly modeled by the two equations evaluated. As such, the 0% clay models had the worst correlation overall to the test data. The 30% clay specimen had the overall best fit to the modeled data due to the general log-linear nature of the compression curve for the transitional soil. The RGoM_EI material had very good

correlation porosity models as they can follow the concave upwards compression curve typical of high plasticity clays. The void ratio models are linear in the log stress space and had a significantly worse correlation with RGoM_EI. These findings agree with the conclusions from Casey, Reece, & Germaine (2019)

To illustrate the ramifications of the dependence of soil compressibility on clay content, the vertical effective stress at Site U1324 of expedition 308 by the Integrated Ocean Drilling Program is estimated from models developed from compression testing on the silt and clay mixtures. Site U1324 from expedition 308 was selected for the availability of porosity measurements from logging while drilling as well as from moisture and density testing on core samples provided in Flemings, Behrmann, & John (2006), a robust laboratory testing program to determine particles sizes for clay content in Sawyer, Jacoby, Flemings, & Germaine (2008), and due to the general proximity of site U1324 to the RGoM_EI source. Figure 9-11 provides borehole caliper, bulk density, and porosity measurements by depth below mudline (DBML) from adnVISION logging while drilling measurements. The caliper measurements were used to create a filter to exclude data from a borehole with a measured diameter greater than 10 inches. Figure 9-11 also provides bulk density and porosity from moisture and density measurements on core samples, and clay content from a laboratory testing program documented in Sawyer, Jacoby, Flemings, & Germaine (2008). The porosity data shows decreasing porosity with increasing depth consistent with normally consolidated sediments. The bulk density and porosity from moisture and density measurements performed on core samples is used for the effective stress calculations, the logging while drilling data is provided for reference. The top 1,000 feet of sediment have an average clay content around 62% similar to the clay content of RGoM_EI. There is a sand layer around 1,000 foot DBML that has a clay contents less than 5%. Below an approximate 1,250 foot DBML the clay content varies wildly between 12% and 74% clay, indicating many layers of varying lithology.

The in situ effective stresses are calculated from compression models discussed by Casey, Reece, & Germaine (2019).

$$\sigma'_V = \sigma'_{Vref} 10^{\left(\frac{e-e_{ref}}{-C_{ce}}\right)} \qquad \text{Equation 9-4}$$

$$\sigma'_V = \sigma'_{Vref} 10^{\left(\frac{n-n_{ref}}{-C_{cn}}\right)} \qquad \text{Equation 9-5}$$

Where:

e = Void Ratio

e_{ref} = Void Ratio at Reference Effective Stress

C_{Ce} = Compression Index Void Ratio

n = Porosity (percent)

n_{ref} = Porosity at Reference Effective Stress (percent)

C_{Cn} = Compression Index Porosity

σ'_V = Vertical Effective Stress (Force/Area)

σ'_{Vref} = Reference Vertical Effective Stress (Force/Area) 1 MPa used for this study.

Figure 9-12 shows the compression curves for the models of the tested mixtures where the reference void ratio or porosity is taken at a 1 MPa stress, and the compression indices were fit over a 0.1 to 20 MPa stress range. Table 9-1 provides a summary of the compression model parameters. A void ratio model (Equation 9-4) is used for clay contents between 0% and 20% clay while a porosity model (Equation 9-5) is used for clay content of 30% or greater based on the previous evaluation of compression models and recommendations within Casey, Reece, & Germaine (2019). A void ratio and porosity model is used to capture the variation in compression curve concavity to limit error due to the model form.

Figure 9-13 presents a plot of pressures at the U1324 site. Lithostatic stress is calculated by integrating the density measurements from core samples. Hydrostatic pressure is shown on Figure 9-13 for

reference. Pore pressure measurements from Long, Flemings, Dugan, Germaine, & Ferrell (2008), and a pore pressure gradient fit through those measurements is provided. The pore pressure measurements indicate pressures above hydrostatic pressure. A pore pressure gradient fit to those measurements is used for effective stress calculations.

Figure 9-14 presents a plot of the porosity and clay content by feet DBML at site U1324. Figure 9-14 also provides estimates of the vertical effective stress at the site. Four estimates of vertical effective stress are presented in Figure 9-14, an estimate from integrating the logging while drilling density logs and subtracting the pore pressure gradient, an estimate that assumes the entire profile follows the compression behavior of the Min-U-Sil 40 silt, a similar estimate using the compression behavior of the RGoM_EI material, and an estimate where the compression behavior is dependent on the clay content using the variable compression models presented in Figure 9-12 and Table 9-2.

Due to the trend of decreasing porosity with increasing depth the Min-U-Sil 40 compression trend generally shows negligible vertical stress from the mudline to an approximate 1,200 foot depth DBML. This is attributed to the high porosity measured in the top 1,000 feet of the basin. The Min-U-Sil 40 compression model has a porosity around 0.43 at a 0.1 MPa stress projecting that behavior back to an average porosity around 0.47 as shown in the porosity plot leads to very low stress levels for Min-U-Sil 40 due to the smaller slope of the compression line (stiffness) observed for the material. The Min-U-Sil 40 material due to being grain supported has an upper bound porosity based on loose grain contacts and would not be stable at some of the high porosities measured. Min-U-Sil 40 is sensitive to the porosity with large increase in effective stress for small decreases in porosity due to the stiffness of the material. This behavior is observed at approximate depths of 1,000 feet, 1,200 feet, 1,700 feet, and 1,800 feet DBML. In between these spikes the Min-U-Sil 40 behavior predicts low vertical effective stresses relative to the other estimates.

The RGoM_EI reflects an effective stress at the mudline, as it can exist at very low stresses in a stable fabric due to the physio-chemical forces from the clay particles. The RGoM_EI material also shows increases in effective stress with decrease in porosity as it is insensitive to clay content. There are spikes in the estimated vertical effective stress at approximate depths of 1,000 feet, 1,200 feet, 1,700 feet, and 1,800 feet DBML like the 0% clay estimate. The increase in vertical effective stress for the RGoM_EI material is less significant than the 0% clay material due to the higher compressibility of RGoM_EI over this stress range.

The variable clay stress estimate shows some interesting behaviors from accounting for variations of clay content. Over the top 1,000 feet DBML, the variable clay stress estimate accounts for the high porosity measurements and predicts a similar stress to the RGoM_EI estimate. At a 1,000 foot depth DBML, where the clean sand is observed, the variable clay stress estimate shows a large spike in the estimated stress due to the low clay content. Between a 1,200 foot depth and 1,400 depth, where a decrease in both porosity and clay content is observed, the variable clay estimate tends to have a lower predicted stress than the 0% clay and RGoM_EI based predictions. This is attributed to the porosity effects counteracting the clay content effects within this model.

Figure 9-14 includes effective vertical stress calculated from integrating bulk density measurements on core samples collected from site U1324 and accounting for the pore pressure gradient. The effective stress from the RGoM_EI and variable clay models estimate are near the effective vertical stress from bulk density measurements over the top 300 feet of the bore hole but then deviate at deeper depths. This deviation is attributed to two potential process issues. First computing the vertical effective stress from compression models assumes that at site U1324 soils are normally consolidated and have equivalent density properties of the laboratory experiments. The method of predicting stress used does not account for variations in stress history. Previously loaded soils, that have been unloaded exist at

denser states and have a stiffer mechanical behavior under new loads than the compression depth trend of a normally consolidated soil. Second, this method assumes that the RGoM_EI and Min-U-Sil materials from the laboratory program have similar mechanical properties of the naturally deposited sediments at the U1324 site.

9-4 Permeability and Clay Content

Permeability and Porosity

The permeability of soil is influenced by particle grain size, pore size distribution, grain shape, tortuosity, clay content and temperature. This study evaluated the sensitivity of permeability to clay content over a large range of effective stresses. The evaluation compares predicted permeability models to the measured data. Three models were selected to evaluate the permeability by porosity relationship. Permeability measured in the High Stress CRS tests are presented in Figure 9-15 and are the control data for this evaluation. Chapter 5 and Chapter 8 provide permeability test data and an interpretation of the data. The key observations from the experimental results include a large variation in permeability between the 0% and 10% clay tests. A systematic decrease in permeability with increasing clay content. A larger decrease in permeability with increasing stress, for higher clay contents. The permeability models will be evaluated on both a goodness of fit to the test data but also qualitatively to evaluate how the models represent the key observations from testing.

The first model evaluated is a geometric mean permeability model presented in Schneider (2011), and Reece (2021). This model assumes that the material is composed of randomly distributed clay domains with clay particles and small pores and silt domains with silt grains and large pores; therefore, both the clay and silt fractions have porosity and contribute to flow Reece (2021). This model is an end member model that adjusts the contributions of the grain and clay permeabilities based on the volumetric clay fraction of the soil. The model is based on a log permeability by porosity relationship consistent with

permeability measurements over large ranges in permeability. Equation 9-6 provides the relationship between permeability and porosity.

$$\log(k) = \gamma n + k_0 \qquad \text{Equation 9-6}$$

Where:

k = Permeability (Area)

n = Porosity (Percent)

γ = Slope of log permeability by porosity

k_0 = Y intercept

The assumption of randomly distributed clay domains and silt domains with their own unique permeability-porosity relationship allows for the estimation of an effective permeability as calculated by Equation 9-7. Where the effective permeability is a function of the unique clay and silt permeabilities on the constitutive clay and silt fractions of the specimen.

$$k_{eff} = k_{cl}^{cf_v} \cdot k_{si}^{(1-cf_v)} \qquad \text{Equation 9-7}$$

Where:

k_{eff} = Effective permeability (Area)

k_{cl} = Clay domain permeability (Area)

k_{si} = Silt domain permeability (Area)

cf_v = Volume fraction of solids composed of clay

Combining Equations 9-6 and 9-7 results in Equation 9-8 that provides an estimation of permeability by porosity for mixed silts and clays assuming that silt and clay porosity within the mixture are equivalent.

$$\log(k_{eff}) = [cf_v\gamma_{cl} + (1 - cf_v)\gamma_{cl}]n + \left[cf_v k_0^{cl} + (1 - cf_v)k_0^{si}\right] \quad \text{Equation 9-8}$$

Where:

k_{eff} = Effective permeability (Area)

k_{cl} = Clay domain permeability (Area)

k_{si} = Silt domain permeability (Area)

cf_v = Volume fraction of solids composed of clay

γ_{cl} = Slope of log permeability by porosity for clay domain

k_0^{cl} = Y intercept for clay domain

γ_{si} = Slope of log permeability by porosity for silt domain

k_0^{si} = Y intercept for silt domain

Figure 9-16 provides a comparison of the measured permeabilities from the High Stress CRS tests to the modeled permeability for the mixtures estimated by the geometric mean permeability model (Equation 9-8). The modeled permeabilities indicate good agreement with the end members of 0% clay and RGoM_EI. The correlation with the intermediary mixtures is poor with the model tending to overpredict the permeability by around one to two orders of magnitude. The largest variance is for the 20% clay model at low porosity. As the end member model is a geometric mean model, the intermediary clay content predictions are equally distributed between the end members predictions. The high stress CRS test measurements do not reflect an equal distribution of permeability by clay content between the end members. A geometric mean model between a pure silt and a high clay content material does not adequately capture the stress and clay dependence of permeability and introduces a systematic error in the predictions. The systematic error is largely attributed to the initial larger difference in permeability between 0% clay and 10% clay.

A statistical evaluation comparing the modeled data to the measurements at 0% clay, 30% clay, 50% clay, and RGoM_EI is presented in Table 9-3. The coefficient of determination (R^2) adjusted coefficient of determination ($\bar{R}^2$), and absolute average percent error are provided. Where the absolute average

percent error is the absolute percent error from the model compared to the measurement at 0.01 porosity intervals average over the range of measurements. An average error over the range of measurement is provided for a more intuitive understanding of the differences between the modeled and measured data as due to the permeability being measured at very small magnitudes. As expected, the end members of 0% clay and RGoM_EI have the best correlations with R^2 values of 0.719 and 0.991 respectively, adjusted $\bar{R}^2$ values of 0.694 and 0.990 respectively, and average percent errors under 100%. The intermediary mixtures of 30% and 50% have significantly worse correlations that are not considered statistically relevant. This is attributed to the systematic shift in y intercept caused by using the 0% clay material as an end member.

Figure 9-17 provides a comparison of the measured permeabilities from the High Stress CRS tests to the modeled permeability for the mixtures estimated by a shifted geometric mean permeability model (Equation 9-8). Where the shift denotes that the 0% clay content data has been omitted from the model and the 10% clay material represents the silt fraction and lower bound for clay contents. This model is evaluated as an illustration of the improved prediction relative to the geometric mean permeability model that considers 0% clay as an end member. The modeled permeabilities indicate excellent agreement with the end members 10% and RGoM_EI. The correlation with the intermediary mixtures is much improved to be within better than an order of magnitude with the measured values. The largest variance is for the 20% clay model at higher porosity where the model tends to underpredict the permeability. Removing the large difference between 0% and 10% clay, by using 10% clay as end member, limits some of the systematic errors propagated when 0% clay is considered.

A statistical evaluation comparing the modeled data to the measurements at 0% clay, 30% clay, 50% clay, and RGoM_EI is presented in Table 9-3. The coefficient of determination (R^2) adjusted coefficient of determination ($\bar{R}^2$), and absolute average percent error are provided. As expected, the end member

RGoM_EI has the best correlation with no change in R^2, $\bar{R}^2$, or absolute average percent error from the geometric mean model. The intermediary mixtures of 30% and 50% clay have significantly improved correlations over the geometric mean model that considers 0% clay as an end member. The R^2 and $\bar{R}^2$ values now indicate statistical significance, and the absolute average percent error is under 100% for all three mixtures evaluated. Figure 9-17 shows the adjusted end member to the geometric mean model omitting the 0% clay data, best captures the significant impact clay has on the permeability of soil.

The second model evaluated is a correlation between permeability, porosity, and liquid limit discussed within Casey (2014). The model uses a similar permeability-porosity relationship as the geometric mean model but with slight modification as shown in Equation 9-9.

$$Log_{10}(k) = \gamma(n - 0.5) + Log_{10}(k_{0.5}) \qquad \text{Equation 9-9}$$

Where:

k = Permeability (Area)

n = Porosity (Percent)

γ = Slope of log permeability by porosity

$k_{0.5}$ = Permeability at a porosity of 0.5

The modification shifts the reference permeability value from a theoretical point of a permeability corresponding with a porosity of 0, to a measurable point of a permeability corresponding with 50% porosity. The intercept $Log_{10}(k_{0.5})$ and slope γ are estimated from correlations with the soil's liquid limit. Equation 9-10 provides the correlation for the intercept and Figure 9-18 provides the basis of the correlation adapted from Casey (2014). Equation 9-11 provides the correlation for the slope and Figure **9-19** provides the basis of the correlation adapted from (Casey (2014).

$$Log_{10}(k_{0.5}) = -7.55Log_{10}(W_{L(\%)}) - 3.4 \quad \text{Equation 9-10}$$

$$\gamma = 0.067W_{L(\%)} + 5.1 \quad \text{Equation 9-11}$$

Where:

$W_{L(\%)}$ = Liquid Limit (Percent)

γ = Slope of log permeability by porosity

$k_{0.5}$ = Permeability at a porosity of 0.5

Figure 9-20 provides a comparison of the measured permeabilities from the High Stress CRS tests to the modeled permeability by the liquid limit correlation model (Equations 9-9 to 9-11). The liquid limit correlation model indicates that the estimate is fair, being generally within an order of magnitude of the measured values. The modeled values vary between under and over predicting the permeabilities. For the 20% clay mixture the liquid limit model underpredicts the permeability at higher porosities and over predicts the permeability at lower porosities. This is due to the predicted slope from the liquid limit correlation being flatter than the slope in the measured permeabilities. The liquid limit correlation does an excellent job between clay contents of 40% to 50% clay. The liquid limit correlations were established from materials typically within a 40% to 60% range of clay contents, with a few outliers outside of this range. Further addition of outlier materials to the correlations will likely improve the predictions over a wider range of clay contents. This model does a poor job at estimating permeability for the low clay content, low plasticity materials of 0% clay and 10%. The model underestimates the permeability of 0% clay and overestimates the permeability of 10% clay.

A statistical evaluation comparing the modeled data to the measurements at 0% clay, 30% clay, 50% clay, and RGoM_EI is presented in Table 9-3. The coefficient of determination (R^2), the adjusted coefficient of determination ($\bar{R}^2$), and absolute average percent error are provided. The higher liquid limit and clay content mixtures of 50% clay and RGoM_EI have the best correlations with R^2 values of 0.975 and 0.951 respectively, adjusted $\bar{R}^2$ values of 0.975 and 0.947 respectively, and average percent

errors under 100%. The lower clay content mixture of 30% has a moderate correlation but is statistically relevant with an R^2 value of 0.741, an $\bar{R}^2$ value of 0.731 and average percent error of 111%. The poor fit is attributed to the low clay content of the soil and the lack of low clay materials in the data set used to establish the correlations. The 0% clay model has a very poor fit with an R^2 value of 0.099, an $\bar{R}^2$ value of 0.016 and average percent error of 92% and is not considered statistically significant. The liquid limit correlation model has similar issues to the geometric mean model when evaluating materials with lower clay contents, 30% or lower. Even with the poor fit of the low clay content data, the modeled permeabilities by the liquid limit correlation is still generally within an order of magnitude which is within normal tolerances of hydrogeologic calculations. The liquid limit correlation model is appealing as a first order approximation due to the simplicity of measuring a soils liquid limit.

The third model evaluated is the correlation between permeability, void ratio, and clay content discussed within Yang & Aplin (2010). This model uses a similar permeability-porosity relationship as the geometric mean and liquid limit models but with a more complex polynomial form as shown in Equation 9-12.

$$ln(k) = -69.59 - 26.79 \cdot CF + 44.07 \cdot CF^{0.5} + (-53.61 - 90.03 \cdot CF + 132.79 \cdot CF^{0.5}) \cdot e + (96.61 + 91.91 \cdot CF + 163.62 \cdot CF^{0.5}) \cdot e^{0.5} \qquad \text{Equation 9-12}$$

Where:

k = Permeability (Area)

e = void ratio

CF = Clay Content mass fraction of particle sizes of 2 micron in diameter

Figure 9-21 provides a comparison of the measured permeabilities from the High Stress CRS tests to the modeled permeability by the Yang & Aplin model (Equation 9-12). The mode predictions are fair, with the results being generally within an order of magnitude of the measured values. Due to the complex polynomial form the modeled values mimic the curvature trends in the measured values of a concave

downwards log permeability-porosity relationship for low clay content materials and a concave upwards log permeability porosity relationship for higher clay content materials. This behavior was not captured in the previously presented geometric mean and liquid limit models.

Yang & Aplin used the geotechnical definition of clay content defined by particle size, which is method 2 as described in Section 9.2. To evaluate the sensitivity of the Yang & Aplin permeability equation to the input clay fraction permeability was estimated using the three different methods proposed for evaluating clay fraction in Section 9-2. Figure 9-21 provides the permeability estimate from method 1 considering the clay sized particles of the RGoM_EI, Figure 9-22 provides the permeability estimate using method 2 considering the clay sized particles of both Min-U-Sil and RGoM_EI, and Figure 9-23 provides the permeability estimate using method 3 considering the mineralogical clay content. The addition of the Min-U-Sil fines content included in method 2 results in general decrease in permeability for a given porosity when compared to method. The effect is most pronounced for mixtures with lower clay contents <30% clay where the modeled permeability value is one eight to one half of the value modeled from method 1. This significant decrease is due to the sensitivity of the Yang & Aplin equation to clay content, and the relatively large increase of added clay sized particles within the Min-U-Sil material (7% clay sized particles). As the specimen clay content increases the effect of including the Min-U-Sil clay sized particles decreases due to the decreasing amount of added Min-U-Sil and increasing amount of added GoM_EI diluting the effect of the added Min-U-Sil clay particles. Method 3 considers the mineralogical clay content of the specimens. The Yang & Aplin predictions with the method 3 clay contents bound the range of measured permeability well. With the RGoM_EI prediction being very close to the measured values and the 0% clay prediction being fair, within an order of magnitude of the measured values. The method 3 clay contents tended to overpredict the permeability between specimens of 30% to 60% clay. The over prediction is attributed to the overall decrease in clay contents cause by using method 3 for establishing clay content.

The Yang & Aplin equation provides a relatively accurate prediction of permeability with each of the three methods evaluated for establishing the specimen clay content. A statistical evaluation comparing the modeled data to the measurements at 0% clay, 30% clay, 50% clay, and RGoM_EI for all three methods is presented in Table 9-3. The coefficient of determination (R^2), the adjusted coefficient of determination ($\bar{R}^2$), and absolute average percent error are provided. Method 1 for determining specimen clay contents had the highest R^2 and $\bar{R}^2$ values and the lowest absolute average percent error values. Method 2 including the added clay sized particles of Min-U-Sil leads to an overall decrease of the R^2 and $\bar{R}^2$ values and an increase in absolute average percent error values. Method 3 considering the mineralogical clay fraction leads to a general decrease of the R^2 and $\bar{R}^2$ values and an increase in absolute average percent error values. Except for RGoM_EI, which indicates an increase in R^2 and $\bar{R}^2$ values and a decrease in absolute average percent error. These results indicate that both the mineralogical clay fraction and the clay sized particles both contribute to the permeability behavior of a soil with the clay sized particles having a more significant impact to permeability behavior.

When comparing the 6 different predictions of permeability with porosity the best correlation is the adjusted end member model with the lower bound at 10% clay. The adjusted end member model requires more advanced laboratory testing to measure the permeability-porosity relationship for the end members. The liquid limit model and the Yang & Aplin equation both provide an excellent first order predictor of permeability and requires relatively simple soil index testing to determine the liquid limit or clay fraction of the soil and an estimate of the in situ porosity or void ratio. The Yang & Aplin equation with method 1 for establishing clay content provided a statistically better fit of the high stress CRS measurements. All three of the models had difficulty with the 0% clay content behavior and the all tended to underpredict the permeability of the 0% clay material.

Permeability and Stress

This study also evaluated the observed trends in permeability with effective stress. Figure 9-24 presents the log permeability by log effective stress for the tested mixtures. Figure 9-24 shows overall trends of decreasing permeability with increasing clay content and decreasing permeability with increasing effective stress. Figure 9-24 also indicates that changes in permeability due to changes in clay content are more significant for lower clay materials and increasing clay content trends to a limiting lowest permeability boundary. Figure 9-24 also confirms that changes in permeability with effective stress are directly related to the compressibility of the material. The more compressible clay rich materials have a faster decrease in permeability than the less compressible silt rich materials.

Loading effects on permeability behavior are discussed within Mueth, Jaeger, & Nagel (1998), Shafiee (2008), and Schneider (2011), who state that the silt rich specimens are supported by force chains through silt grain contacts which leave large pore spaces protected from consolidation caused by loading. The protected particles within the large pore spaces tend not to align with the direction of loading leaving a less tortuous path for flow. As the clay content increases the silt content decreases leaving less protected pore spaces resulting in a decrease in permeability. As the stress increases the clay fraction compresses limiting flow through the clay resulting in a decrease in permeability. Figure **9-24** indicates that above a clay content of 50% or greater there is negligible variation in the permeability at a stress of 1 MPa or greater. Discussed within Chapter 5, 50% clay is at a clay content equal to or greater than the critical clay content through a 50 MPa effective stress for these test mixtures. Figure 9-24 indicates that the critical clay fraction may represent the lowest permeability boundary limit.

9-5 Dynamic Properties and Clay Content

This study evaluated the sensitivity of the small strain shear modulus (G_{max}) to clay content over a large range of effective stresses. The evaluation compares G_{max} prediction models to the measured data. An evaluation of G_{max} was performed as correlations for approximating wave velocities in soils (P and S) are generally limited to correlations with field exploration measurements (SPT N, or CPT tip resistance). G_{max} has been generally correlated with the compression characteristics Jamiolkowski, Lancelotta, & Lo Presti (1995), Shibuya, Hwang, & Mitachi (1997), Rampello, Viggiani, & Amorosi (1997) and Likitlersuang, et al. (2013). Equation 9-13 provides the form for estimating G_{max} from Likitlersuang, et al. (2013)

$$\frac{G_{max}}{P_a} = Sf(e)\left(\frac{P'}{p_a}\right)^n \qquad \text{Equation 9-13}$$

Where:

G_{max}	=	Small strain modulus (~0.0001% strain)
S	=	Material constant reflecting the current soil structure
$f(e)$	=	Void ratio function to capture compression behavior
p'	=	Mean effective stress (Force/Area)
p_a	=	Reference stress, (Force/Area)
n	=	Fitting exponent

Within Likitlersuang, et al. (2013) the void ratio functions and experimentally determined fitting parameters of S and n are provided from several different researchers. Three of these empirical relationships are evaluated with the TCRS test data for the silt and clay mixtures. The three correlations are from Kim & Novak (1981), Shibuya & Tanaka (1996), and Shibuya, Hwang, & Mitachi (1997). These correlations were developed over a lower range in stress than the range in stress for the tall CRS measurements. The tall CRS experiments are within the calibrated void ratio range for the three correlations up to an approximate 3 MPa effective stress. Table 9-4 provides the void ratio function and

fitting parameters. It is important to note that the Kim & Novak (1981) correlation includes the mean effective stress, p', while the Shibuya & Tanaka (1996), and Shibuya, Hwang, & Mitachi (1997) correlations replace mean effective stress with axial effective stress, σ'_a. This simplification is due to the researcher's observation that the effects of the horizontal and vertical principal stresses on G_{max} are more or less equal Shibuya, Hwang, & Mitachi (1997).

The three empirical correlations were fit to the TCRs data. To evaluate the Kim & Novak (1981), correlation the mean effective stress, p', was approximated. Within the TCRs experiments the radial stress is not measured but the specimen is confined in a steel ring that prohibits radial deformation maintaining the K_0 condition. To estimate the radial stress the K_0 value is estimated from the Jaky equation, (Equation 2-4), where the effective friction angle is estimated based on a correlation with liquid limit presented in Figure 9-25 and Casey (2014). Figure 9-26 and Figure 9-27 provide the correlations for the effective friction angle with the soil's liquid limit. When evaluating the TCRS data for correlations with G_{max}, the friction angle, K_0, radial stress, and mean effective stress were calculated at each velocity measurement.

The empirical correlations were fit to the TCRs data in two steps. First the measured G_{max} values normalized to the void ratio function used in the correlation is plotted by an effective stress parameter (σ'_a or p') in a log-log plot. This data is fit with a power equation to determine the n exponent parameter for Equation 9-13, as shown in Figure 9-28. Second, a linear regression is performed on the measured G_{max} values and the product of the void ratio function and effective stress parameters to determine the S slope fitting parameter from Equation 9-13 shown in Figure 9-29. Table 9-5 provides the fitting parameters and the coefficient of determination (R^2) for the TCRS tests for three empirical correlations. Atmospheric pressure 0.1013 MPa was used as the reference pressure to evaluate the correlations and determine the values presented in Table 9-5. All three correlations indicate statistical significance,

based on the average R^2 values. The Kim & Novak (1981) method has the best fit, followed by Shibuya, Hwang, & Mitachi (1997) and the worst fit is Shibuya & Tanaka, (1996). The Shibuya & Tanaka (1996) void ratio function is not a reasonable function to use for soils of void ratios less than 0.5 as the function is asymptotic to a void ratio of 0. Figure 9-30 presents the average S fitting parameter for each method, multiplied by the void ratio function by void ratio to illustrate the valid range of void ratios for the correlations.

Figure 9-31 and Figure 9-32 provide plots of the S and n fitting parameters by specimen clay content and liquid limit for the Kim & Novak (1981) void ratio function. The S fitting parameters indicate a concave downwards parabolic curve with clay content and liquid limit. The S fitting parameter is between a range of 122 to 266, which is within the recommended range of 74 to 288 from Likitlersuang et al. (2013). The n fitting parameters are relatively constant value of 0.55, which is within the recommend range of 0.46 to 0.61 from Likitlersuang et al. (2013).

Figure 9-33 and Figure 9-34 provide plots of the S and n fitting parameters by specimen clay content and liquid limit for the Shibuya & Tanaka, (1996) void ratio function. The S fitting parameters indicates a trend of increasing with increasing clay content or liquid limit. The S fitting parameter is between 200 and 798. Which brackets the recommended value of 500 from Likitlersuang et al. (2013). The n fitting parameters show a slight decreasing trend with increasing clay content or liquid limit. The n fitting parameter is within a range of 0.28 to 0.5, which at or below the recommended value of 0.5 from Likitlersuang et al. (2013).

Figure 9-35 and Figure 9-36 provides plots of the S and n fitting parameters by specimen clay content and liquid limit for the Shibuya, Hwang, & Mitachi (1997) void ratio function. The S fitting parameters indicate a concave downwards parabolic curve with clay content and liquid limit. The S fitting parameter is between a range of 1,110 to 2,274. Which is within the recommend range of 1,070 to 3,080

from Likitlersuang et al. (2013). The n fitting parameters are relatively constant around a value of 0.55. Which is around the recommend value of 0.5 from Likitlersuang et al. (2013).

Figure 9-37 to Figure 9-40 show the calculated shear modulus from the wave measurements by effective stress or mean effective stress for the 10% clay, 30% clay, 50% clay and RGoM_EI specimens. The calculated shear moduli from the TCRS tests fit with the estimations of shear using the three compared empirical correlations. Although the experiments exceeded the stress range for the calibrations of the empirical correlations, the correlations are considered valid as the slope S and exponent n fitting parameters for the TCRS experiments are within or near the recommended values from Likitlersuang et al. (2013). Figure 9-37 to Figure 9-40 show the estimated shear moduli from the correlations are in good agreement with the measured shear moduli from the TCRS tests.

To evaluate the quality of the three compared void ratio functions, the functions are applied to downhole measurements from IODP Site 308 hole U1324 for comparison. Site U1324 is the same site used in the compression study presented in Section 9.3, selected for its robust measurement of particle size with depth. At site U1324 wireline shear wave velocity measurements were collected over the top approximate 1,600 feet below the mudline using a Dipole Sonic Imager. Figure 9-41 presents the borehole diameter, and shear wave velocity from wireline measurements, and bulk density from in situ measurement and core measurements by depth below mudline in feet for site U1324. The caliper measurements indicate two sets of points, blue points for borehole diameters measured less than 10 inches and orange points for borehole diameters exceeding 10 inches. The measurements made in borehole diameters exceeding 10 inches have been removed from the evaluation for being out of tolerance. The shear wave velocity and density plots have been filtered for borehole diameter tolerance. Figure 9-42 provides lithostatic stress and hydrostatic stress, and void ratio by depth below mudline in feet. The lithostatic stress is calculated by integrating the density logs and the void ratio is

from logging while drilling thermal neutron porosity measurements. Figure 9-43 shows the calculated shear modulus for Site U1324 from the shear wave velocity and density logs, filtered for borehole size tolerances.

The Shibuya & Tanaka (1996) void ratio function when used to fit the TCRS data was found to have a monotonically increasing slope S fitting parameter and monotonically decreasing n exponent fitting parameter with clay content or liquid limit. Figure 9-44 provides the basis for an alteration of the Equation 9-13 to include clay dependency for estimating G_{max}. The slope S and exponent n fitting parameters for the Shibuya & Tanaka (1996) are varied in Equation 9-13 using a linear best fit lines of the data, as presented in Figure 9-44.

Figure 9-45 provides the calculated shear modulus from the shear wave velocity measurements and density logs as well as the estimated shear modulus from the three different empirical correlations using Equation 9-13 and the average S and n from the recommended ranges and atmospheric reference pressure (0.101325 MPa). The estimated shear modulus from the modified form of Equation 9-13 for the Shibuya & Tanaka (1996) void ratio function that includes the dependence on clay content is provided in Figure 9-45. The coefficient of determination (R^2) for the estimated shear moduli are provided in Figure 9-45. The unmodified Shibuya & Tanaka, 1996 void ratio function has the worst correlation with an R^2 of 0.45, followed by Shibuya et al. (1997) an R^2 of 0.60, the Kim and Novak (1981) correlation has the best fit with an R^2 of 0.75. The vertical effective stress instead of the mean effective stress was used for all methods due to the unknown horizontal stress state. The Kim and Novak (1981) method is intended to be used with mean effective stress so using vertical effective stress may have likely reduces to effectiveness of the correlation. The modified Shibuya & Tanaka (1996) void ratio function that includes clay dependent S and n fitting parameters has the best correlation with and R^2 of 0.83.

Figure 9-46 provides the clay content from laboratory testing at Site U1324 presented in Sawyer, Jacoby, Flemings, & Germaine (2008) and the modified Shibuya & Tanaka (1996) shear wave modulus estimate overlaid on the shear modulus calculated from velocity and density measurements by depth below mudline. The estimated shear wave values are generally within the range of the calculated values from velocity measurements and are of the same magnitude. The calculated shear modulus tends to have larger extremes both lower and higher than the estimated value. In general, the estimated values show similar trends in lithology dependence as the measured values. There are some outliers to this such as at around 1,000 foot depth where a low fines material has an estimated shear modulus significantly lower than the calculated shear modulus, and around a 1,250 foot depth where the estimated shear modulus is significantly higher than the calculated shear modulus. These are attributed to using non-site specific laboratory testing to evaluate the U1324 site.

9-6 Strength Properties and Clay Content

To evaluate the dependence of the strength properties on clay content the fracture gradient at IODP site U1324 is evaluated. Where the fracture gradient is the upper bound of the drilling mud weight and larger pressures will induce fractures in the bore hole causing mud loss. The lower bound of the mud weight is the pore pressure gradient as the mud needs to prohibit fluid flow into the borehole. A comparison of the fracture gradient is evaluated by two different methods; the Matthews & Kelly (1967) method Equation 9-14 and the Eaton (1975) method Equation 9-15.

$$FG = K_0(OBG - u) + u \qquad \text{Equation 9-14}$$

$$FG = \frac{\upsilon}{1-\upsilon}(OBG - u) + u \qquad \text{Equation 9-15}$$

Where:

FG = Fracture Gradient (Force/Area per length)

K_0 = Lateral Stress Ratio

υ = Dynamic Poisson's Ratio from Wave Velocity Measurements

OBG = Overburden Gradient (Force/Area per length)

u = Pore Pressure Gradient (Force/Area per length)

The two methods have been selected as they are commonly used for borehole stability evaluations. The Eaton (1975) method has the influence of lithology built in through the inclusion of Poisson's ratio which varies by rock. Figure 9-47 provides Poisson's Ratio from the TCRS tests by P wave velocity as well as the Poisson's Ratio calculated from the Castagna, Batzle, & Eastwood (1985)**.** "mudrock" line for VP-VS relationships and a correlation of Poisson's Ratio by VP from Brocher (2005). Figure 9-47 shows that Poisson's Ratio decreases with increasing P wave velocity (which is an analog for depth due to the increase in density with consolidation) and that the TCRS measurements are around the expected measurements of Poisson's Ratio by P wave velocity. In equation 9-15 $\frac{\upsilon}{1-\upsilon}$ for a one dimensional consolidation (no lateral strain) case can be shown to be analogous to K_0 In equation 9-14 but with different physical implications. The dynamic Poisson's Ratio calculated from wave velocities decreases with depth as shown in Figure 9-47, which leads to a decreasing $\frac{\upsilon}{1-\upsilon}$ term in Equation 9-15. This is at odds with the K_0 value from the triaxial tests where K_0 is shown to be related to a soils effective friction angle and stress level Abdulhadi (2009), Casey (2014) and others. Figure 9-48 provides K_0 by Poisson's ratio and effective friction angle calculated using the Federico (2021) formula (Equation 8-13). Figure **9-48** shows the K_0 decreases with increasing friction and with decreasing Poisson's ratio.

Figure 9-49 presents the borehole diameter from wireline caliper measurements, the lithostatic stress from integrating density measurements on core samples, and pore pressures calibrated to the pore pressure measurements provided in Figure 9-13 by depth below mudline in feet at site U1324 of IODP expedition 308. The caliper measurements indicate two sets of points, blue points for borehole diameters measured less than 10 inches and orange points for borehole diameters exceeding 10 inches. The measurements made in borehole diameters exceeding 10 inches have been removed from the evaluation for being out of tolerance. Figure 9-50 presents the clay fraction by depth below mudline measured in a laboratory testing program from Sawyer, Jacoby, Flemings, & Germaine (2008), as well as the S wave and P Wave velocity wireline measurements from a dipole sonic imager at site U1324. The clay fraction is used to assign an effective friction angle to the soil based on the closest measured friction angle from the 1 MPa triaxial compression shear tests. A clay content less than 5% is assigned the 0% clay content effective friction angle, a clay content between 5% clay and 15% clay is assigned the 10% clay content effective friction angle, and so on, for each 10% change in clay until 63% clay which if exceeded is assigned the RGoM_EI effective friction angle. The effective stress at site U1324 over the top 1,600 feet ranges up to 6 MPa but does not get as high as 10 MPa. As such the 1 MPa triaxial tests were used as the basis for evaluating strength behavior. Figure 9-51 presents the effective friction angle, the dynamic Posson's ratio, and the K_0 calculated from friction angle and Poisson's ratio for comparison by depth below mudline. Figure 9-51 shows that the K_0 value calculated from Poisson's ratio is significantly larger than the K_0 value calculated from the effective friction angle. Figure 9-52 shows that this difference translates to a large variation in the safe drilling window bounded by the pore pressure gradient calibrated to pore pressure measurements and the fracture gradient calculated by either the K0 value from friction angle or from Poisson's ratio. The fraction gradient calculated by the friction angle has a much narrower safe drilling window than the fracture gradient calculated with Poisson's ratio. As the Poisson ratio calculated fracture gradient is near the overburden pressure and is

likely to be unrealistically high for the top ~2,000 feet of unlithified material. Figure 9-52 also shows the importance of accounting for lithology due to rapid changes in the safe drilling window. Around 1,000 foot there is a sand layer with minimal fines content that has a corresponding 0.5 MPa decrease in the fracture gradient. Without setting casing or careful management of mud weights such a large decrease could lead to a lost circulation event.

Table 9-1: Summary of Statistical Evaluation of Clay Content Dependency on Compressibility

		Coefficient of Determination, R^2			Adjusted Coefficient of Determination, R^2			Root Mean Squared Error		
Void Ratio (Eq. 8.1) or Porosity (Eq. 8.2)	Method of Determining Clay Content	0% Clay	30% Clay	RGoM_EI	0% Clay	30% Clay	RGoM_EI	0% Clay	30% Clay	RGoM_EI
Void Ratio	1	0.861	0.960	0.758	0.856	0.959	0.749	0.030	0.030	0.124
Void Ratio	2	0.863	0.960	0.757	0.858	0.958	0.748	0.029	0.030	0.125
Void Ratio	3	0.692	0.892	0.836	0.681	0.888	0.829	0.052	0.051	0.105
Porosity	1	0.671	0.984	0.998	0.659	0.984	0.998	0.057	0.018	0.010
Porosity	2	0.677	0.980	0.993	0.666	0.980	0.993	0.056	0.020	0.020
Porosity	3	0.541	0.958	0.985	0.525	0.957	0.984	0.078	0.030	0.033

Table 9-2: Compression Indices and Reference Densities for Modeling High Stress CRS test Results

0% Clay		10% Clay		20% Clay		30% Clay		40% Clay		50% Clay		60% Clay		RGoM_EI	
C_{ce}	e_r	C_{ce}	e_r	C_{ce}	e_r	C_{cn}	n_r	C_{cn}	n_r	C_{cn}	n_r	C_{cn}	n_r	C_{cn}	n_r
-0.078	0.684	-0.104	0.681	-0.169	0.646	-0.102	0.395	-0.120	0.409	-0.137	0.434	-0.134	0.434	-0.157	0.460

Table 9-3: Summary of Statistical Evaluation of Clay Content Dependency on Porosity and Permeability

		Coefficient of Determination, R^2				Adjusted Coefficient of Determination, R^2				Absolute Average Percent Error			
Model Evaluated	Method of Determining Clay Content	0% Clay	30% Clay	50% Clay	RGoM_EI	0% Clay	30% Clay	50% Clay	RGoM_EI	0% Clay	30% Clay	50% Clay	RGoM_EI
Geometric Mean (Reece 2021)	1	0.719	0.119	0.577	0.981	0.694	0.084	0.566	0.980	49	1903	521	4
Shifted Geometric Mean (Reece 2021)	1	N/A	0.724	0.958	0.981	N/A	0.700	0.955	0.980	N/A	59	25	4
Liquid Limit (Casey 2014)	1	0.098	0.741	0.975	0.851	-0.083	0.731	0.975	0.847	92	111	35	55
Yang + Aplin 2012	1	0.153	0.938	1.000	0.713	-0.016	0.932	1.000	0.695	92	21	3	71
Yang + Aplin 2012	2	0.070	0.800	0.940	0.713	-0.116	0.784	0.936	0.695	98	52	24	71
Yang + Aplin 2012	3	0.076	0.818	0.687	0.970	-0.108	0.803	0.670	0.968	98	153	520	29

Notes:

1. N/A = Not Applicable, 0% Clay data excluded from the shifted geometric mean model.

Table 9-4: Summary of G_{max} Correlations Evaluated with TCRS Results

	S	f(e)	n	Controlling Stress
Kim and Novak (1981)	74 -288	$\frac{(2.973 - e)^2}{1 + e}$	0.46-0.61	p'
Shibuya and Tanaka (1996)	500	$e^{-1.5}$	0.5	σ'_a
Shibuya, Hwang, and Tanaka (1997)	1070 -3080	$(1 + e)^{-2.4}$	0.5	σ'_a

Table 9-5: Summary of G_{max} Correlations Fitting Parameters and

		Kim and Novak (1981)			Shibuya and Tanaka (1996)			Shibuya, Hwang, and Tanaka (1997)		
Test Number	Percent Clay	S	n	R^2	S	n	R^2	S	n	R^2
TCRS 1652	10%	122.1	0.58	0.9989	200.5	0.50	0.9963	1110.9	0.58	0.9990
TCRS 1700	10%	137.2	0.55	0.9979	256.8	0.46	0.9976	1246.4	0.55	0.9982
TCRS 1663	20%	160.9	0.55	0.9996	313.6	0.40	0.9913	1479.0	0.54	0.9995
TCRS 1678	20%	161.3	0.55	0.9997	376.3	0.37	0.9885	1486.3	0.54	0.9991
TCRS 1632	30%	165.6	0.58	0.9992	397.9	0.39	0.9950	1530.5	0.57	0.9993
TCRS1698	30%	187.0	0.57	0.9994	407.8	0.39	0.9877	1721.5	0.56	0.9989
TCRS 1638	40%	200.8	0.57	0.9961	428.5	0.39	0.9706	2491.5	0.52	0.9918
TCRS 1688	40%	244.6	0.52	0.9936	645.1	0.31	0.9752	2361.9	0.51	0.9910
TCRS 1693	50%	266.3	0.50	0.9881	798.2	0.28	0.9768	2724.1	0.49	0.9868
TCRS 1633	50%	222.4	0.53	0.9972	512.1	0.35	0.9750	2246.3	0.52	0.9970
TCRS 1646	60%	173.4	0.57	0.9921	595.7	0.35	0.9928	2050.4	0.55	0.9919
TCRS 1679	60%	180.0	0.54	0.9915	476.3	0.34	0.9343	1845.1	0.53	0.9855
TCRS 1629	63%	150.8	0.55	0.9944	552.0	0.30	0.9705	1773.0	0.52	0.9945
TCRS 1672	63%	167.4	0.55	0.9903	651.4	0.31	0.9790	1897.5	0.53	0.9901

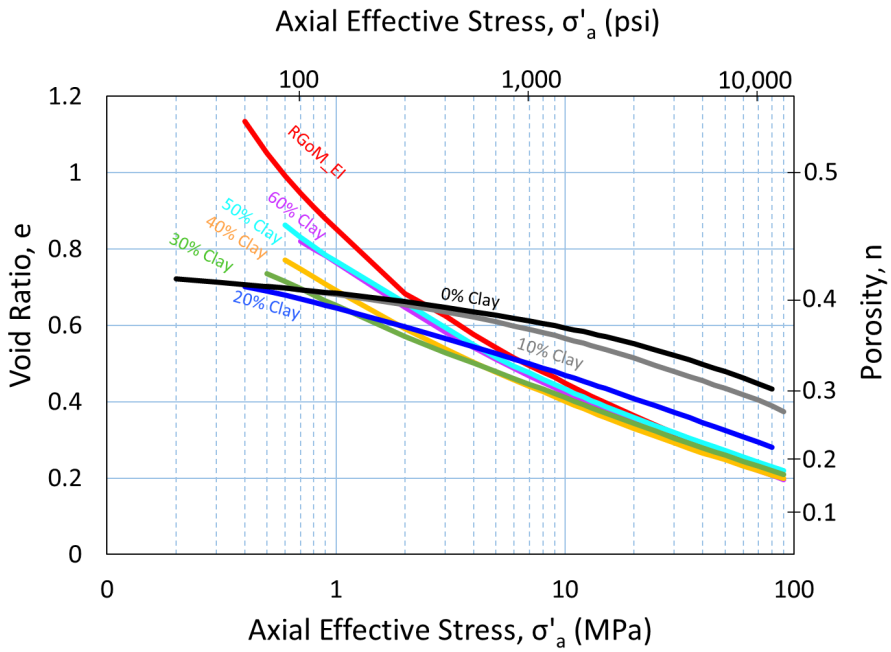


Figure 9-1: High stress CRS compression curves used to evaluate clay content effects on soil compressibility (Figure 5-9 reproduced).

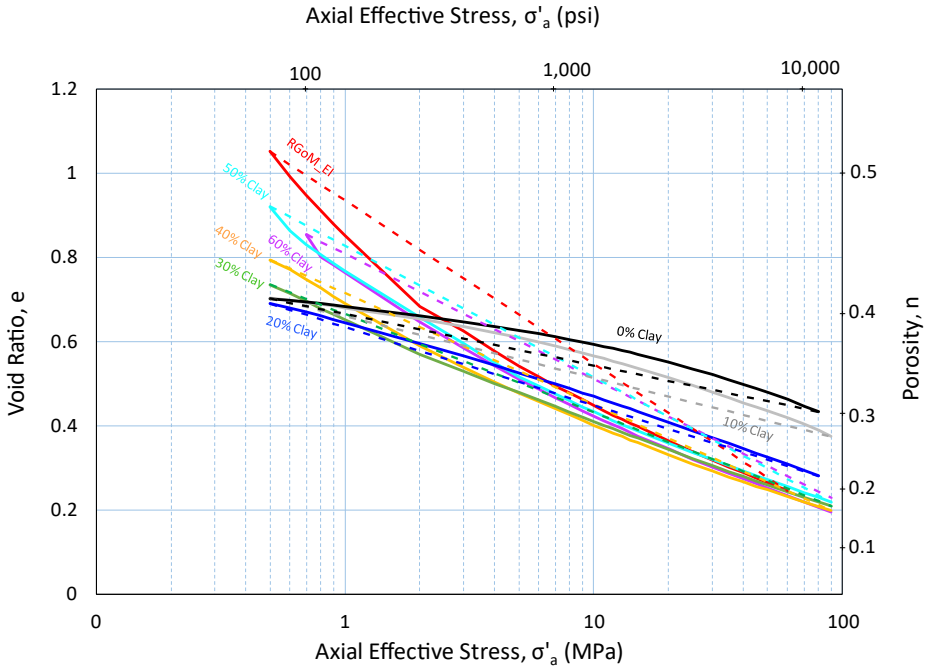


Figure 9-2: High Stress CRS compression curves (solid lines) fit with a log linear σ'_v and void ratio model (dashed lines).

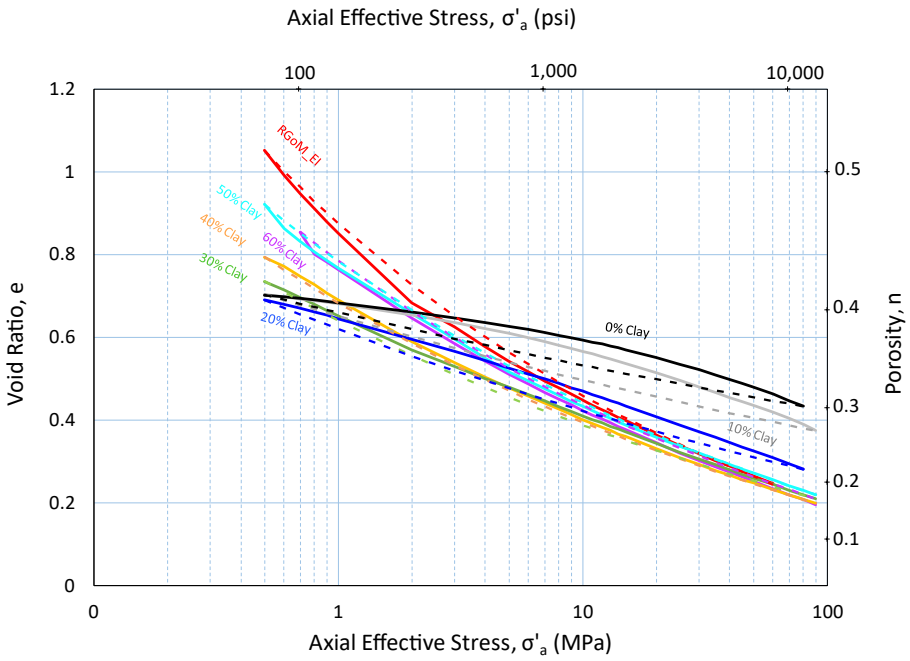


Figure 9-3: High Stress CRS compression curves (solid lines) fit with a log linear σ'_v and porosity model (dashed lines).

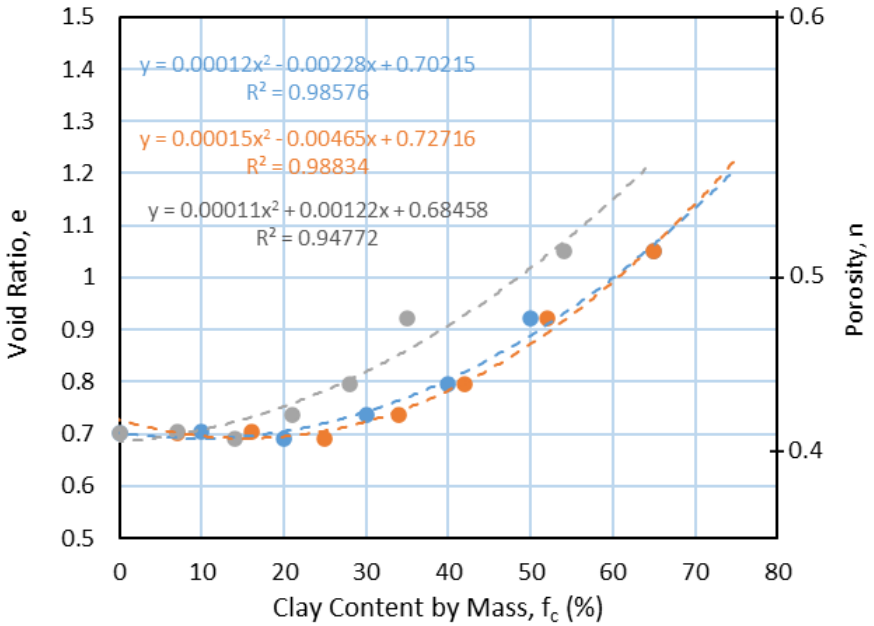


Figure 9-4: Plot of reference void ratio at σ'_v of 0.5 MPa as a function of clay content used in the compression models. The top (blue) equation corresponds to method 1 where the clay size fraction of Min-U-Sil is not accounted in the clay content. The middle equation (orange) includes the clay sized particles of Min-U-Sil material in the clay content determination. The bottom equation (grey) accounts for mineralogical clay content as discussed in Section 9-2.

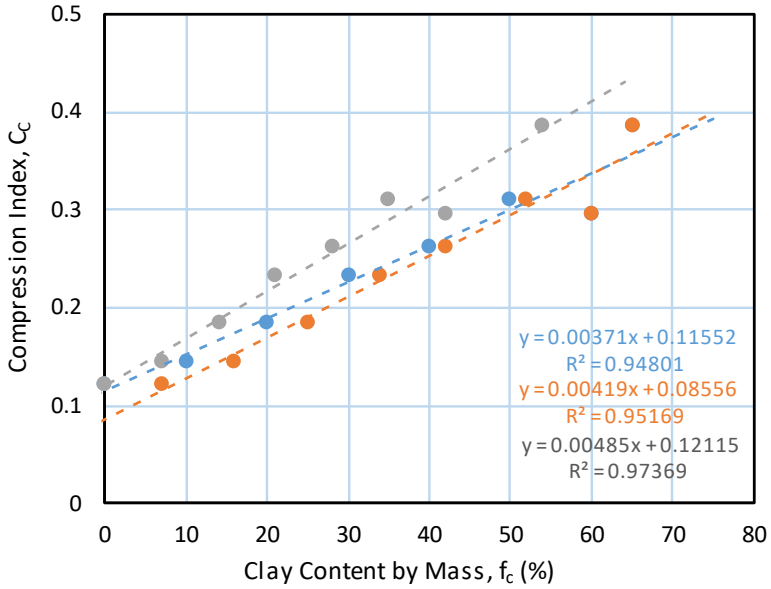


Figure 9-5: Plot of calibrated compression index (C_C) as a function of clay content used in the compression models. The top (blue) equation corresponds to method 1 where the clay size fraction of Min-U-Sil is not accounted in the clay content. The middle equation (orange) includes the clay sized particles of the added Min-U-Sil material in the clay content determination. The bottom equation (grey) accounts for mineralogical clay content as discussed in Section 9-2.

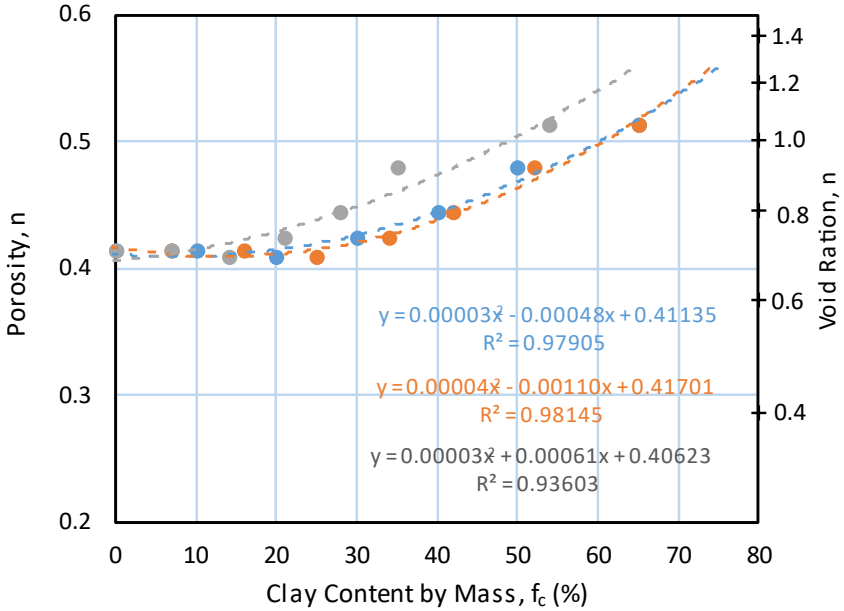


Figure 9-6: Plot of reference porosity at σ'_v of 0.5 MPa as a function of clay content used in the compression models. The top (blue) equation corresponds to method 1 where the clay size fraction of Min-U-Sil is not accounted in the clay content. The middle equation (orange) includes the clay sized particles of the added Min-U-Sil material in the clay content determination. The bottom equation (grey) accounts for mineralogical clay content as discussed in Section 9-2.

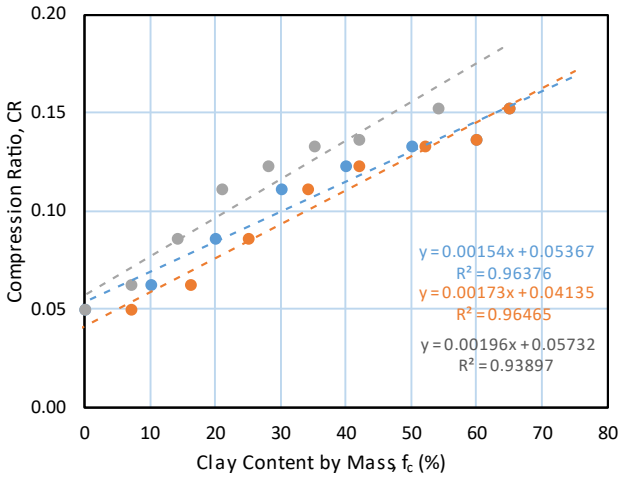


Figure 9-7: Plot of calibrated compression index ($C_{C\phi}$) as a function of clay content used in the compression models. The top (blue) equation corresponds to method 1 where the clay size fraction of Min-U-Sil is not accounted in the clay content. The middle equation (orange) includes the clay sized particles of the added Min-U-Sil material in the clay content determination. The bottom equation (grey) accounts for mineralogical clay content as discussed in Section 9-2.

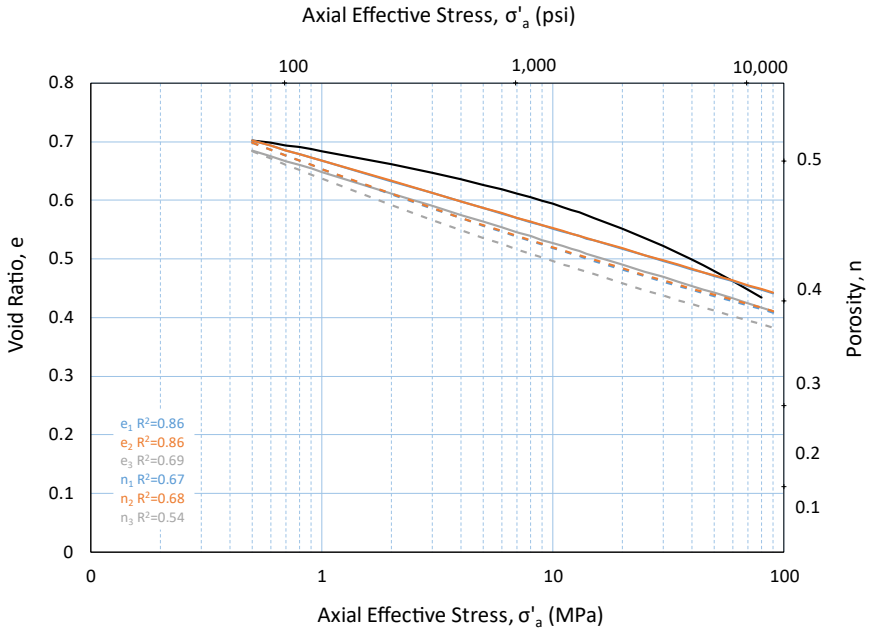


Figure 9-8: Evaluation of the 0% clay High Stress CRS compression curve by the six clay content dependent compression models. The solid black line is the 0% clay test compression curve. The solid colored lines represent the void ratio model of Equation 9-2, also denoted as e. The dashed colored lines represent the porosity model of Equation 9-3, also denoted as n. The colors denote the method used to determine clay content where blue corresponds to method 1, orange to method 2 and grey to method 3 as detailed within section 9-2.

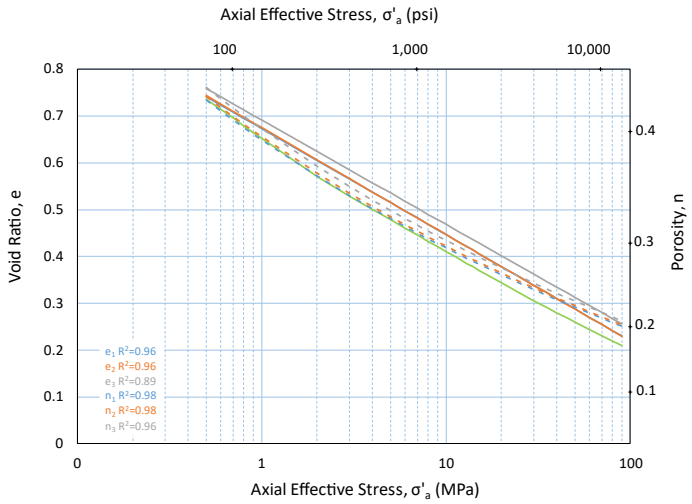


Figure 9-9: Evaluation of the 30% clay High Stress CRS compression curve by the six clay content dependent compression models. The solid green line is the 30% clay test compression curve. The solid colored lines represent the void ratio model of Equation 9-2, also denoted as e. The dashed colored lines represent the porosity model of Equation 9-3, also denoted as n. The colors denote the method used to determine clay content where blue corresponds to method 1, orange to method 2 and grey to method 3 as detailed within section 9-2

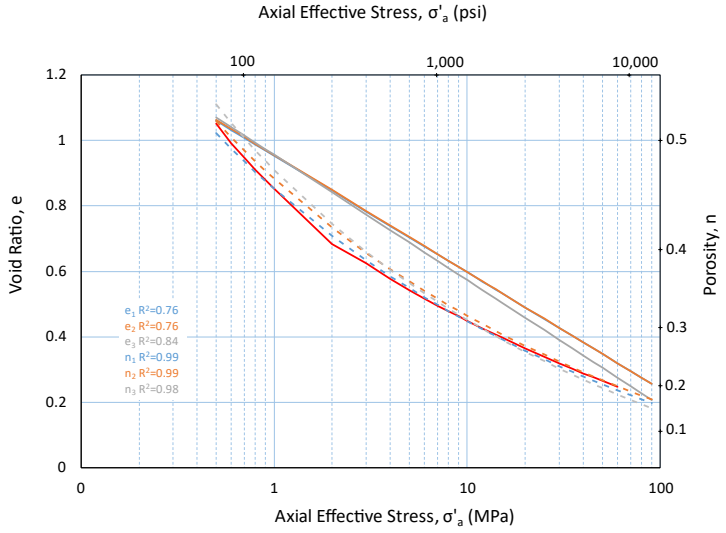


Figure 9-10: Evaluation of the RGoM_EI clay High Stress CRS compression curve by the six clay content dependent compression models. The solid red line is the RGoM_EI clay test compression curve. The solid colored lines represent the void ratio model of Equation 9-2, also denoted as e. The dashed colored lines represent the porosity model of Equation 9-3, also denoted as n. The colors denote the method used to determine clay content where blue corresponds to method 1, orange to method 2 and grey to method 3 as detailed within section 9-2

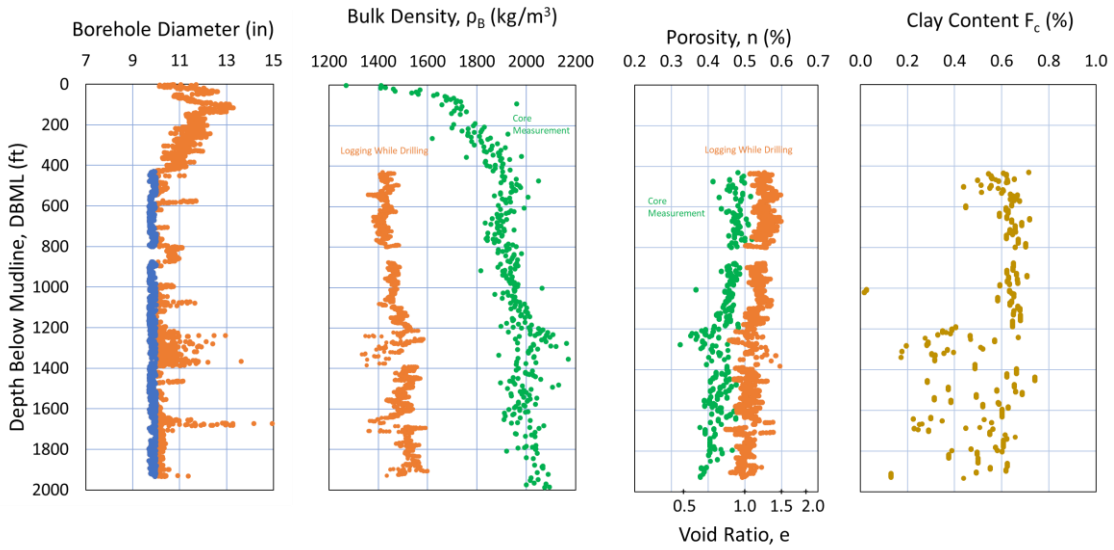


Figure 9-11: Borehole caliper measurements, and bulk density by depth below mudline in feet, from adnVISION logging while drilling measurements at IODP expedition 308 site U1324. The blue caliper data points indicate measurements less than 10 inches in diameter, the orange caliper points are greater than 10 inches and have been removed from the data processing. Porosity and bulk density are from adnVISION logging while drilling measurements (orange) and moisture and shipboard density testing (green) Flemings, Behrmann, & John (2006). Clay content from laboratory testing presented in Sawyer, Jacoby, Flemings, & Germaine (2008).

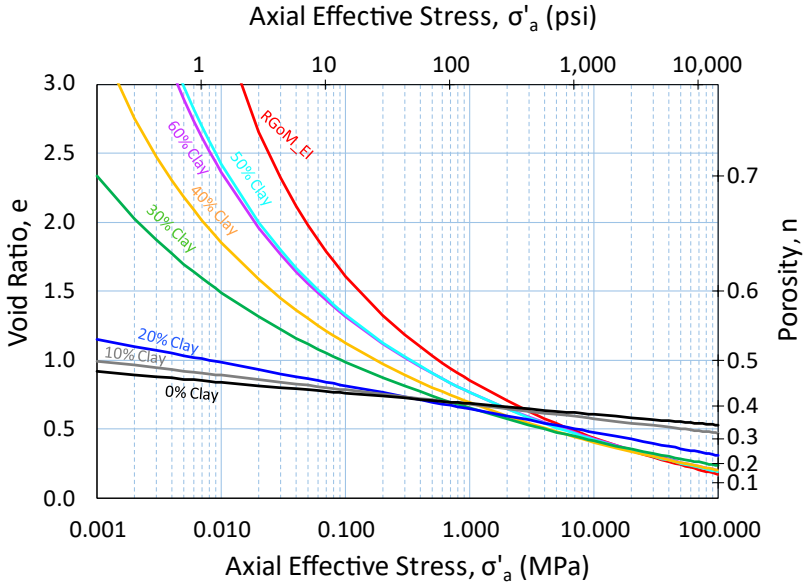


Figure 9-12: Compression models using the slope and density intercept at 1 MPa from Table 9-2 for the high stress CRS tests.

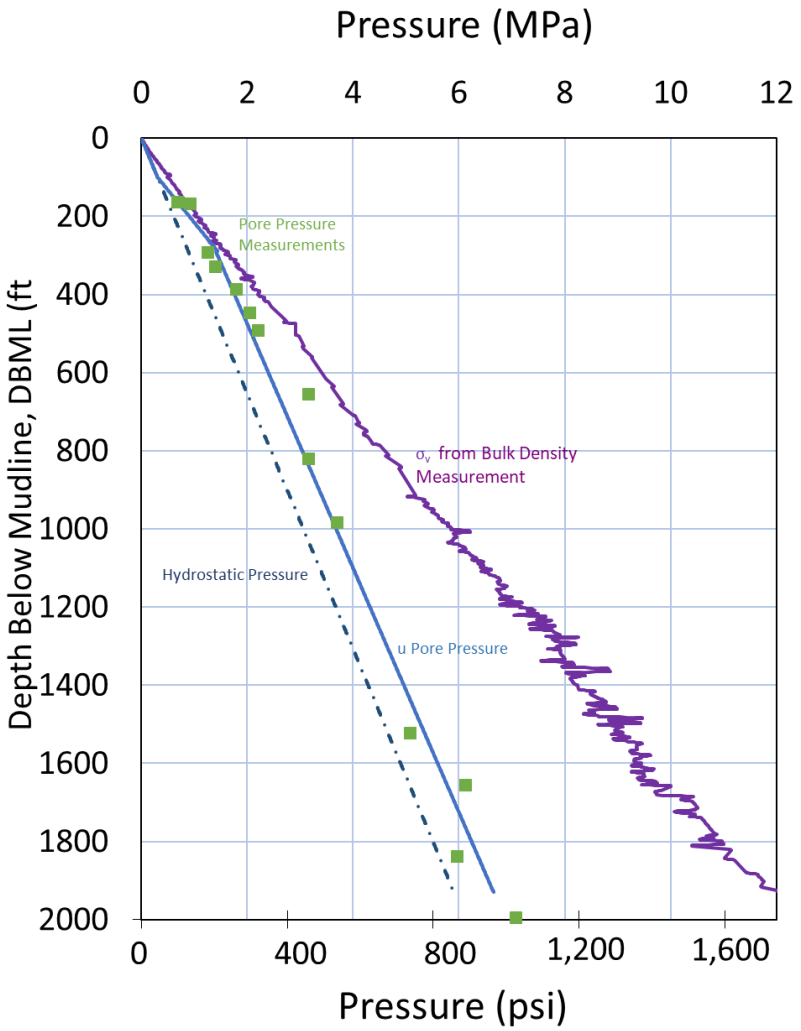


Figure 9-13: Pressure at IODP Expedition 308 Site U1324. Lithostatic pressure from integrating the bulk density measurements on core samples. Hydrostatic pressure for reference. Pore pressure measurements from Long, Flemings, Dugan, Germaine, & Ferrell (2008). Pore pressure gradient considered in calculations fit to pore pressure measurements.

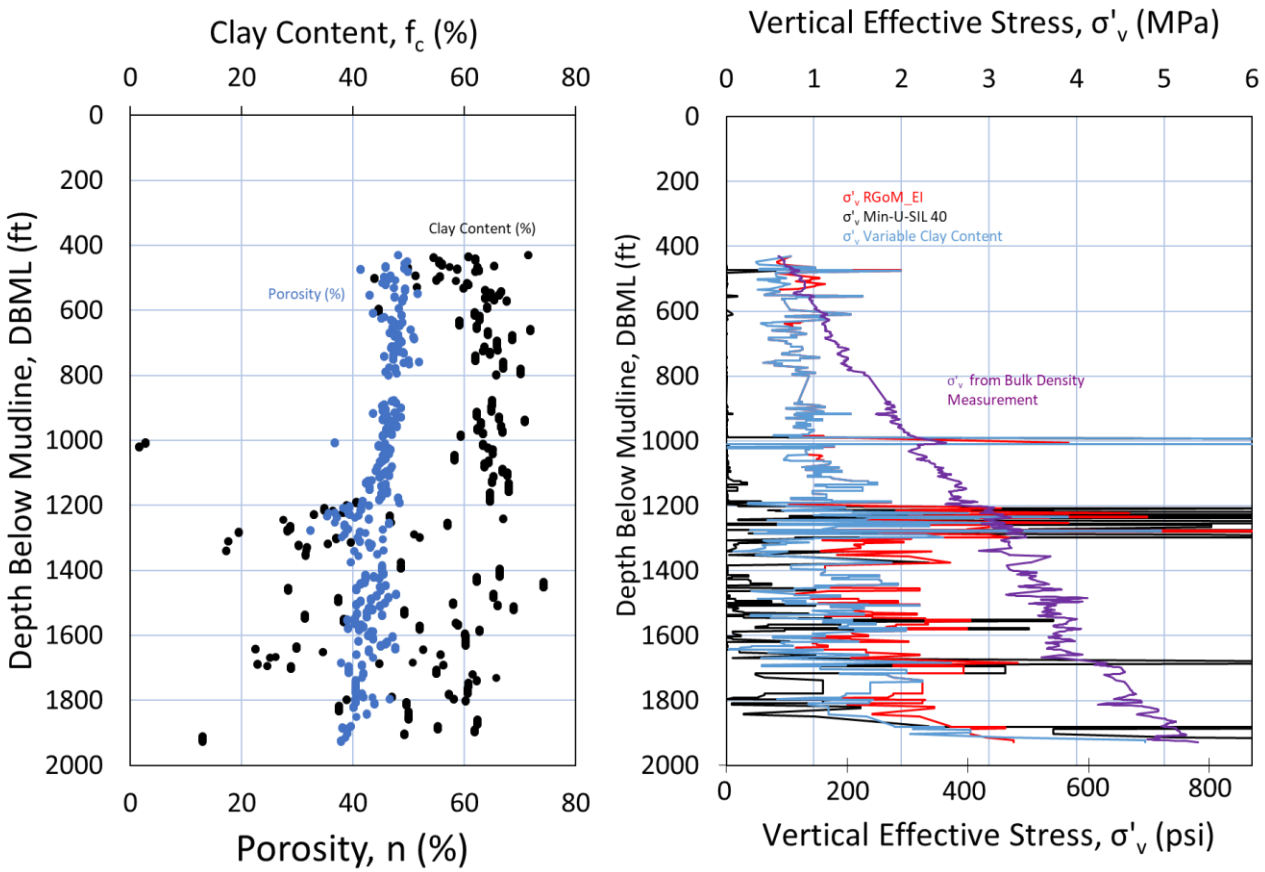


Figure 9-14: Left , porosity from moisture and shipboard density testing (blue) Flemings, Behrmann, & John (2006) and clay content from laboratory testing Sawyer, Jacoby, Flemings, & Germaine (2008). Right estimated vertical effective stress from integrating bulk density measurements and Equations 9.4 and 9.5 for RGoM_EI clay (red), Min-U-Sil 40 (black), and a variable clay content based on the compression models presented in Figure 9-13 (blue).

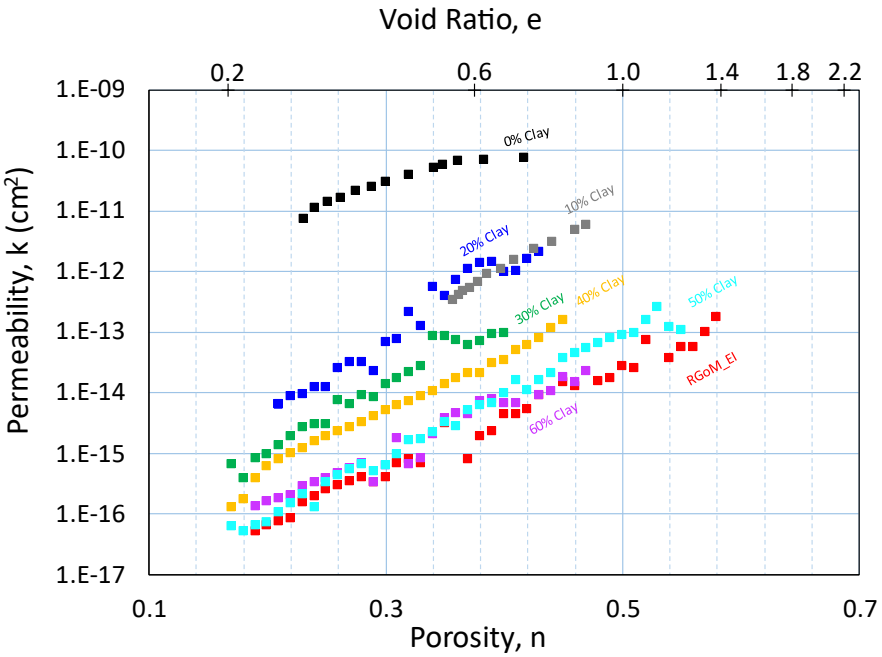


Figure 9-15: Permeability by porosity from High Stress CRS experiments.

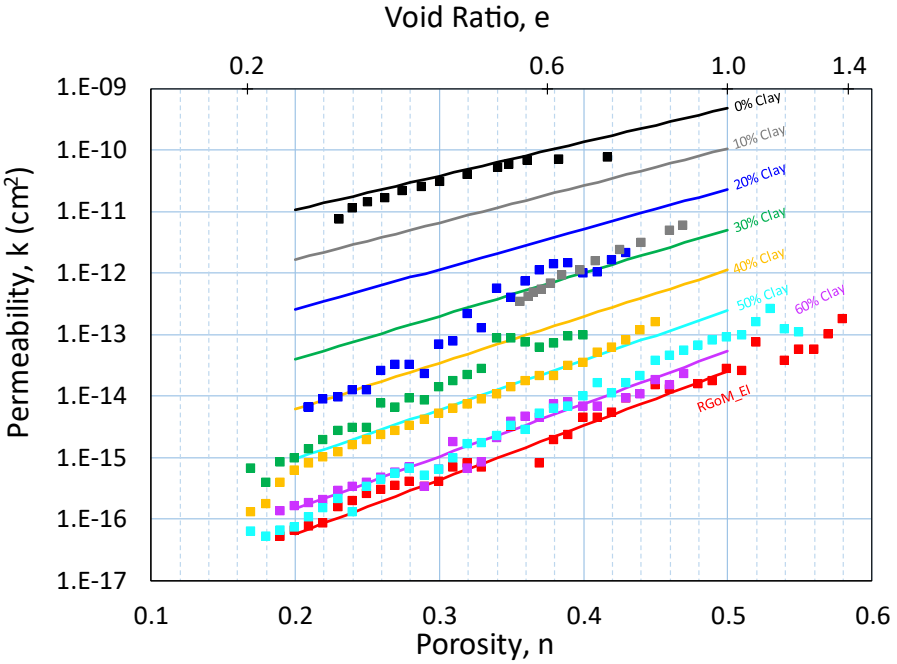


Figure 9-16: Permeability by porosity measurements from High Stress CRS measurements, solid lines indicate the geometric mean permeability by porosity model from Reece (2021).

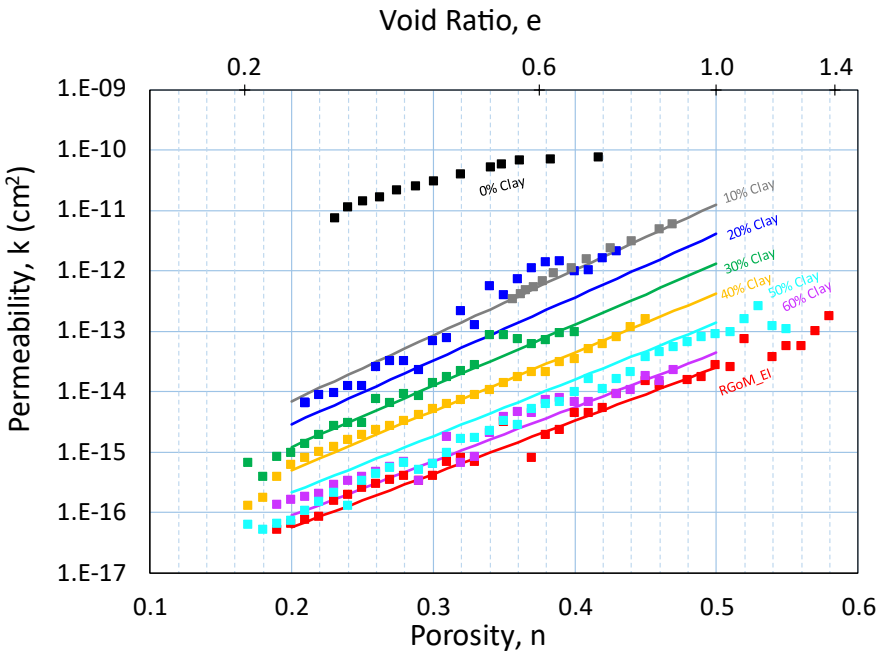


Figure 9-17: Permeability by porosity measurements from High Stress CRS measurements, solid lines indicate the shifted geometric mean permeability by porosity model from Reece (2021). The model has been shifted to omit 0% clay and use 10% clay data is the lower bound clay content.

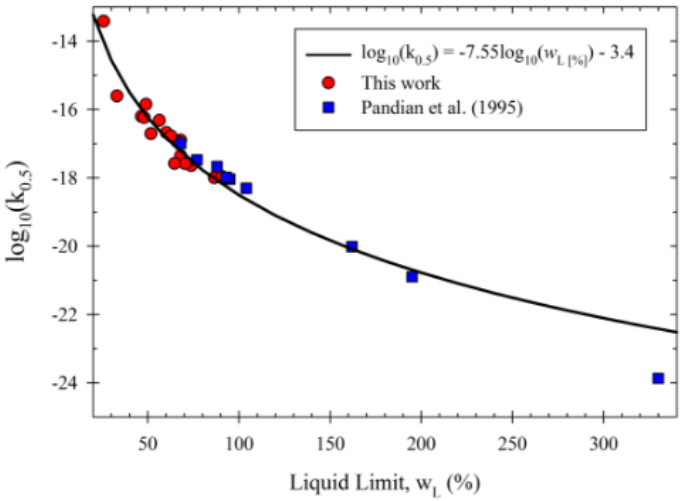


Figure 9-18: Values of $\log_{10}(k_{0.5})$ adopted from Casey (2014) plotted against liquid limit.

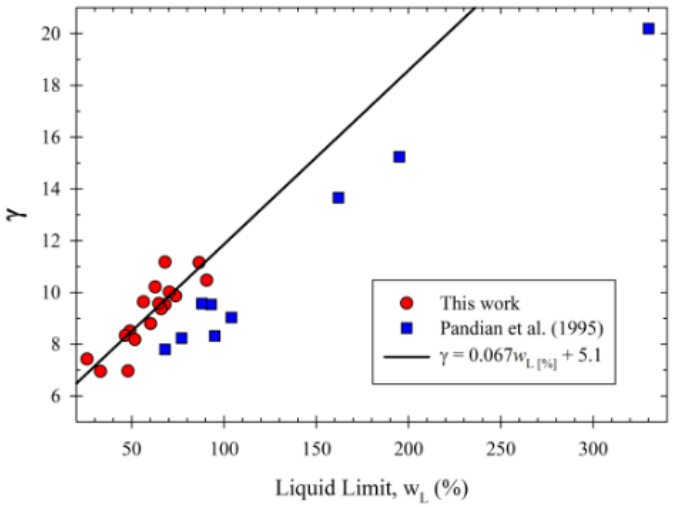


Figure 9-19: Values of γ from Casey (2014) plotted against liquid limit.

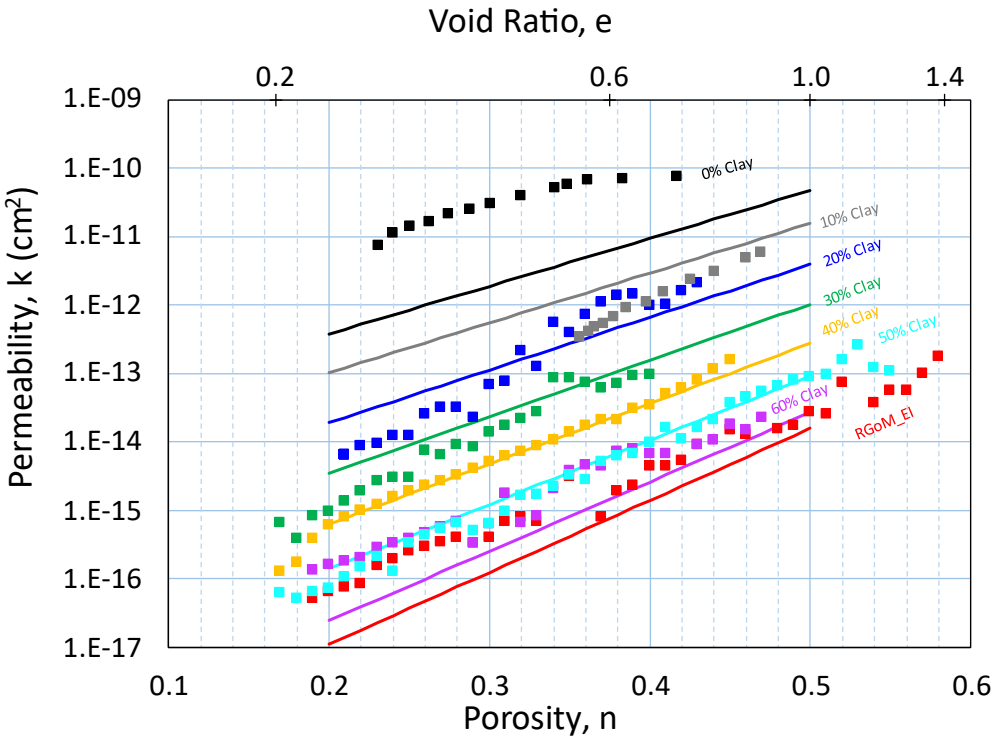


Figure 9-20: Permeability by porosity measurements from High Stress CRS measurements, solid lines indicate modeled permeability as function of the Liquid Limit from Casey (2014).

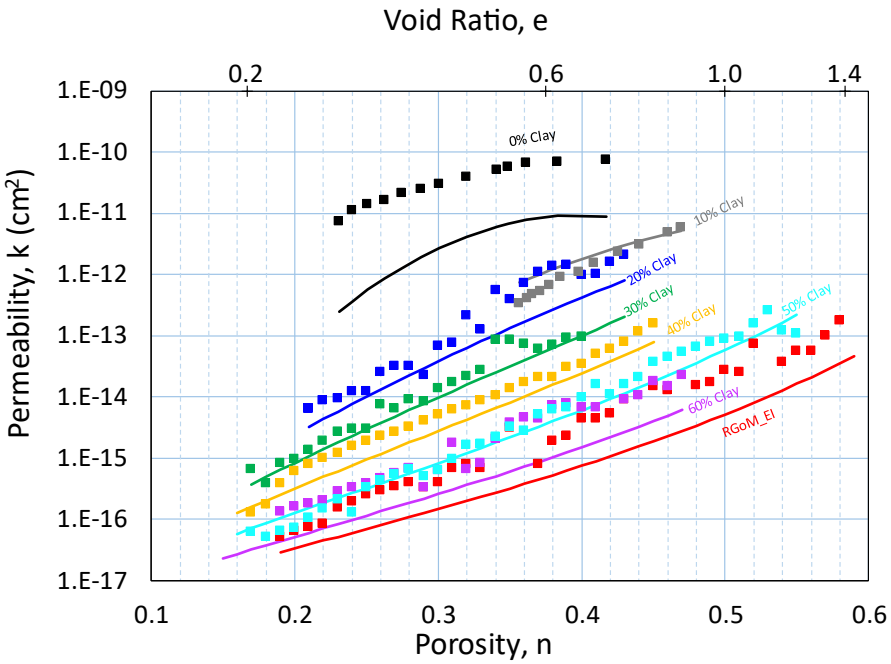


Figure 9-21: Permeability by porosity measurements from High Stress CRS measurements, solid lines indicate modeled permeability as function of clay fraction and void ratio from Yang & Aplin (2010). The clay fraction for the model is calculated using method 1, classifying clay by particle size considering the clay particle of RGoM_EI only.

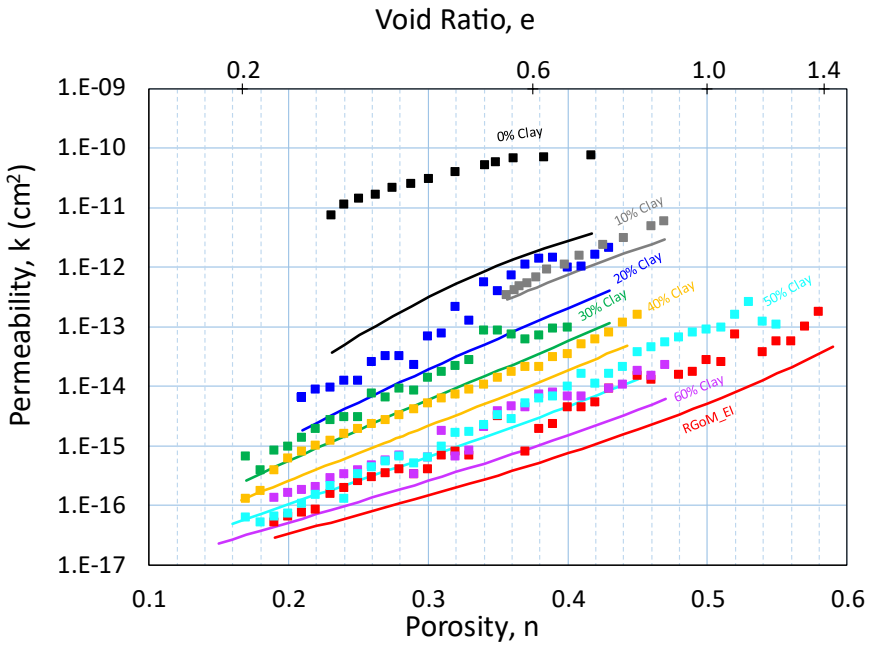


Figure 9-22: Permeability by porosity measurements from High Stress CRS measurements, solid lines indicate modeled permeability as function of clay fraction and void ratio from Yang & Aplin (2010). The clay fraction for the model is calculated using method 2, classifying clay by particle size considering both the clay particles of Min-U-Sil and RGoM_EI.

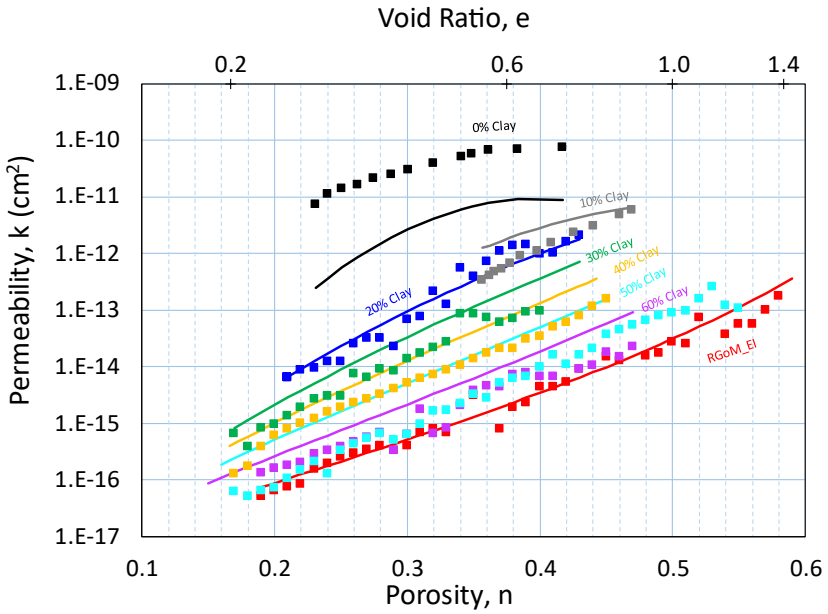


Figure 9-23: Permeability by porosity measurements from High Stress CRS measurements, solid lines indicate modeled permeability as function of clay fraction and void ratio from Yang & Aplin (2010). The clay fraction for the model in Figure 9-16 was calculated using method 3, classifying clay by mineralogy and considering the mineralogical clay fraction of RGoM_EI.

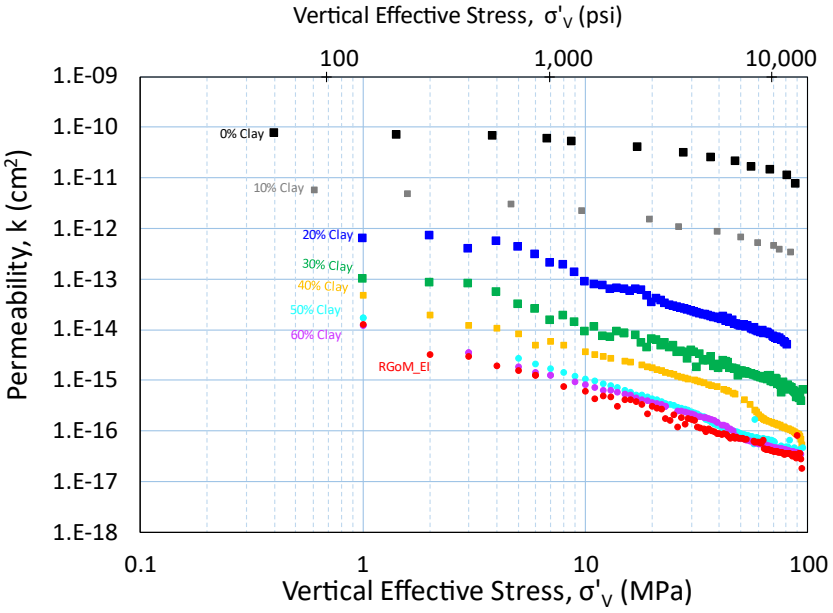


Figure 9-24: Permeability by vertical effective stress from High Stress CRS testing.

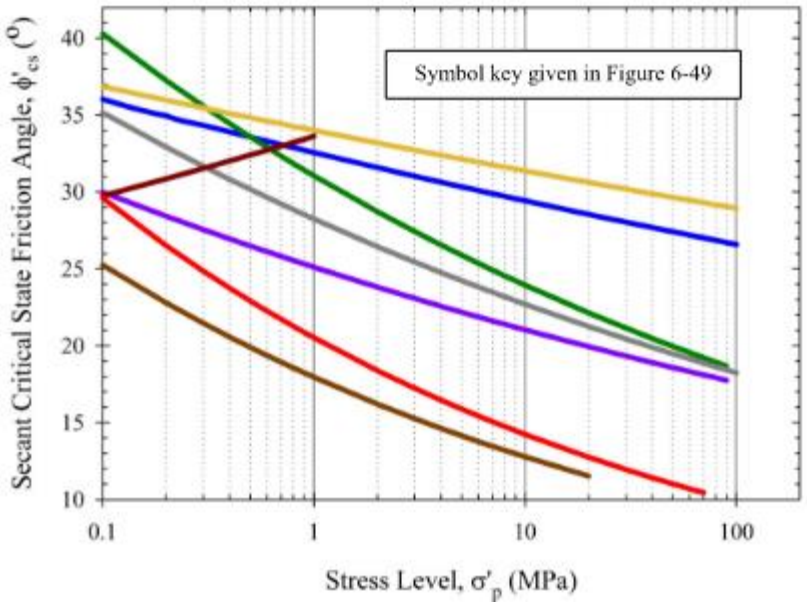


Figure 9-25: Regression lines for the critical state friction angle experimental data presented in Casey (2014) Figure 6-52. The regression lines are of the form $\phi'_{cs} = A(0.001\sigma'_V \text{ [MPa]})^B$. Figures 9-26 and 9-27 provide the correlations for A and B respectively.

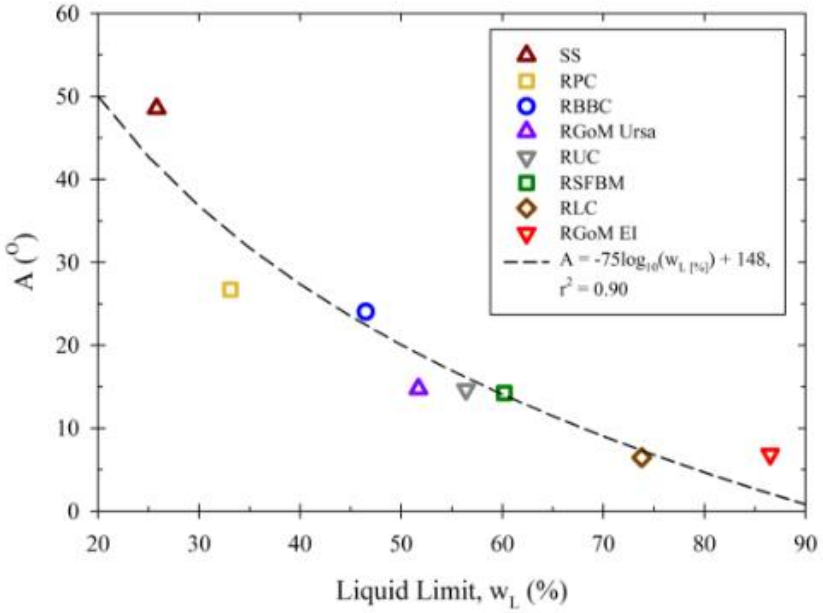


Figure 9-26: Correlation between the parameter A and liquid limit for the critical state friction angle regressions in Figure 9-21 from Casey (2014).

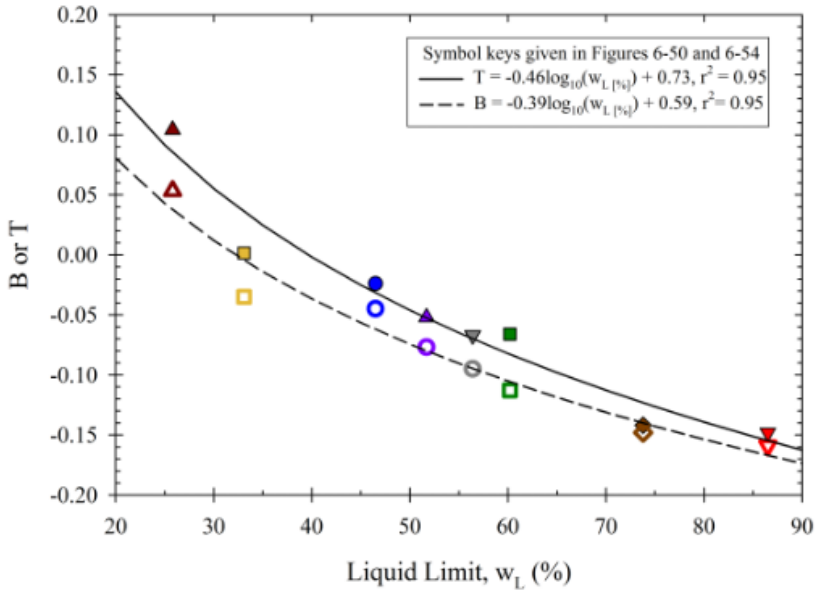


Figure 9-27: Correlation between the parameter B and liquid limit for the critical state friction angle regressions in Figure 9-21 from Casey (2014).

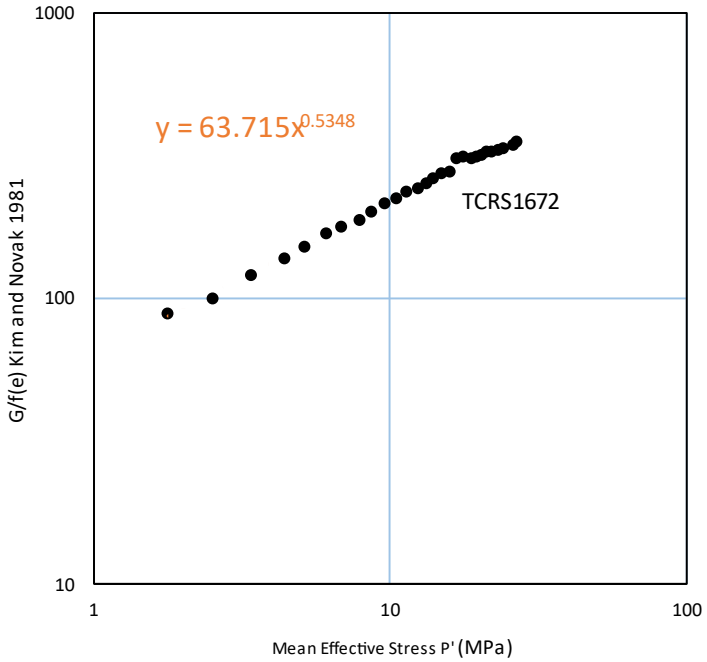


Figure 9-28: Measured small strain shear modulus G_{max}, normalized to the correlation void ratio function by effective stress state parameter. Orange line represents the power of the test data to evaluate the n value in Equation 9-13.

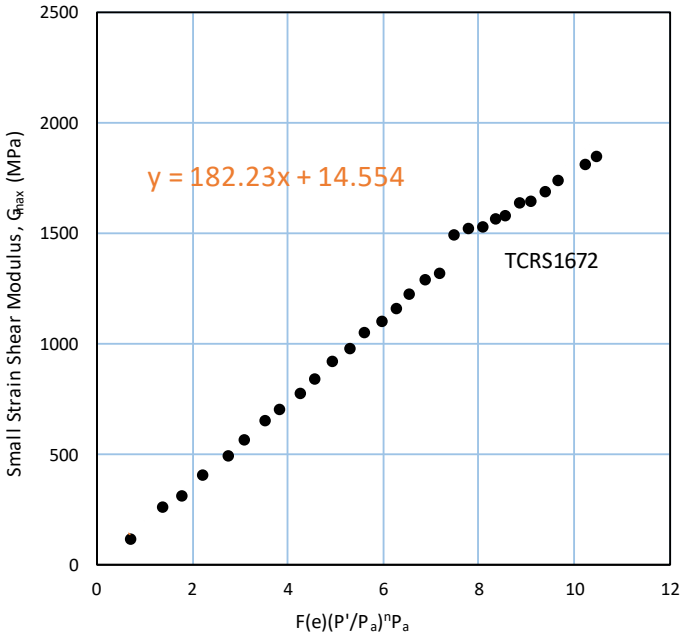


Figure 9-29: Small strain shear modulus G_{max} computed by shear wave velocity and density, by the stress components of Equation 9-13. The void ratio function is from Kim & Novak (1981) and the data are linearly fit to determine S for Equation 9-13.

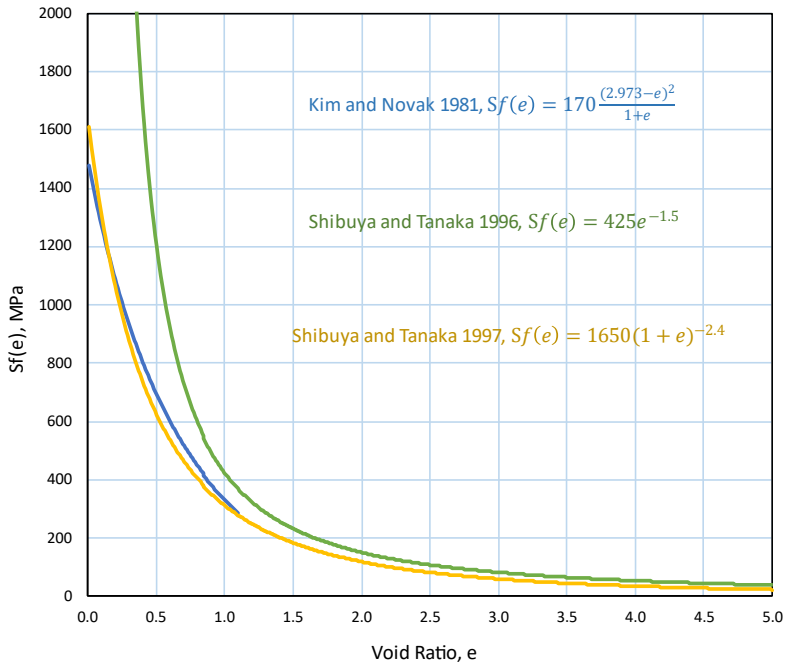


Figure 9-30: The product of the average S fitting value and void ratio function by void ratio for the three empirical correlations compared. The average S fitting values are the average of the values presented in Table 9-5 for the reference stress of 1 atmosphere 0.1013 MPa.

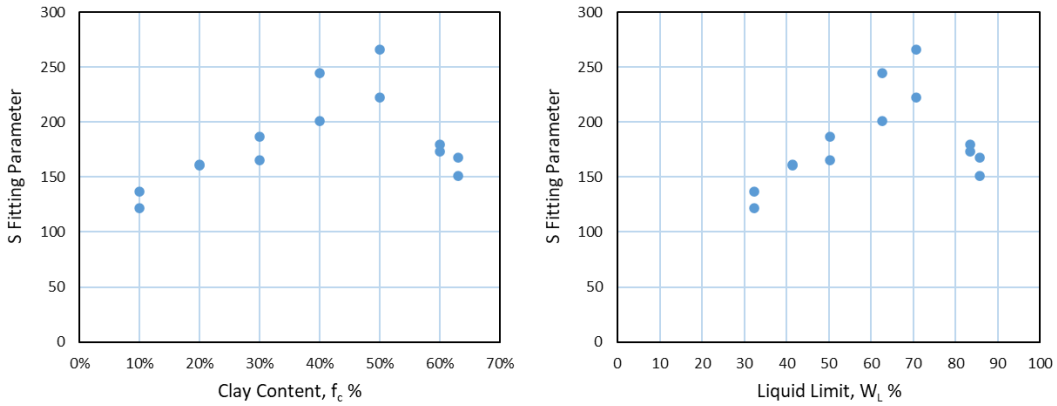


Figure 9-31: S fitting parameter for an atmospheric reference stress by clay content (left) and by liquid limit (right) for the Kim & Novak (1981) correlation.

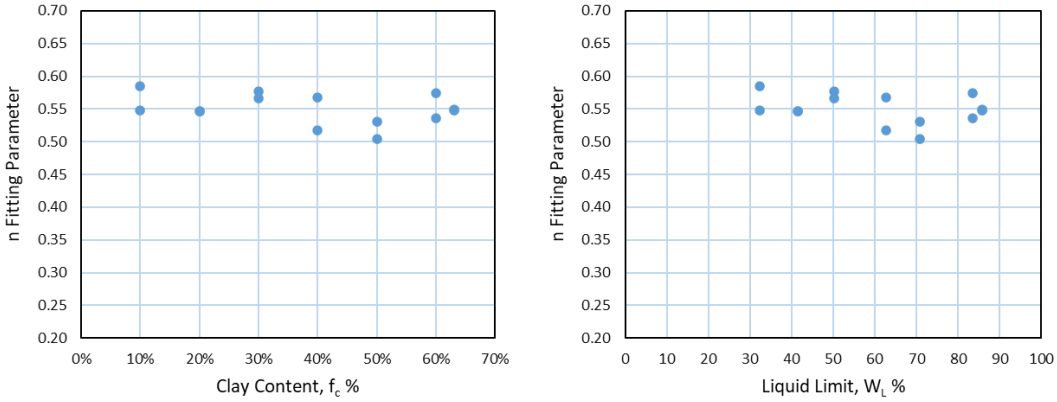


Figure 9-32: n fitting parameter for an atmospheric reference stress by clay content (left) and by liquid limit (right) for the Kim & Novak (1981) correlation.

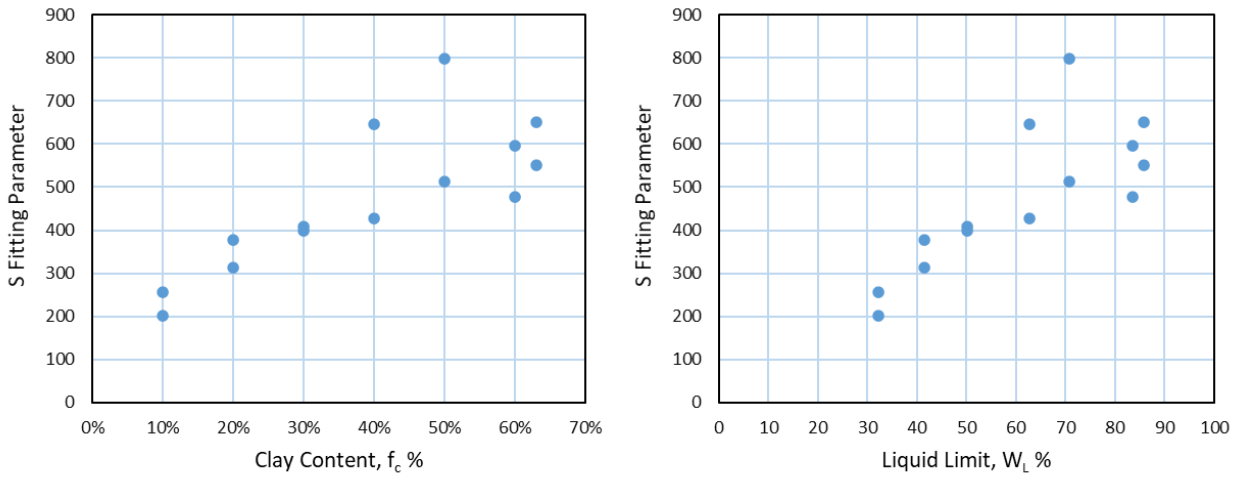


Figure 9-33: S fitting parameter for an atmospheric reference stress by clay content (left) and by liquid limit (right) for the Shibuya & Tanaka (1996) correlation.

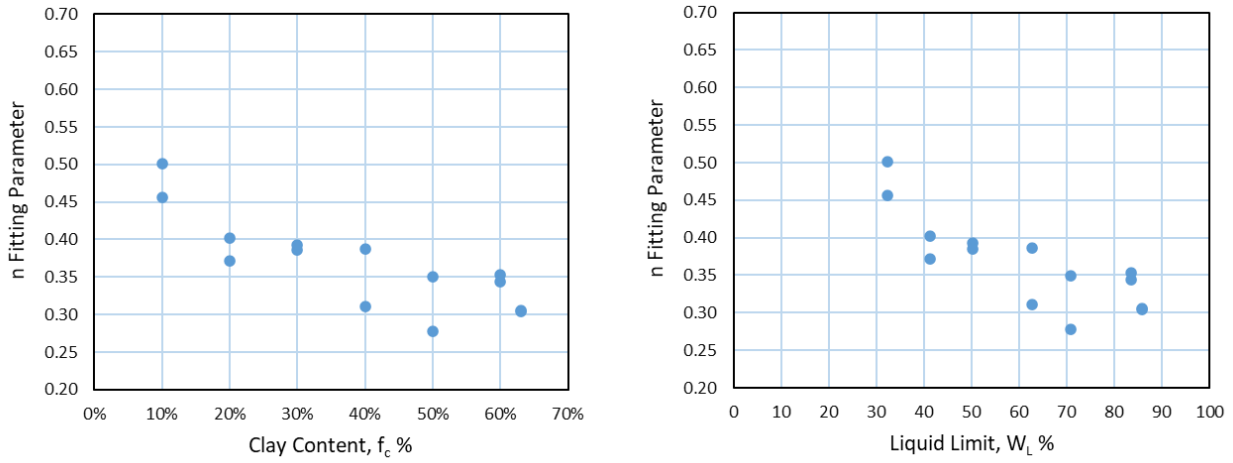


Figure 9-34: n fitting parameter for an atmospheric reference stress by clay content (left) and by liquid limit (right) for the Shibuya & Tanaka (1996) correlation.

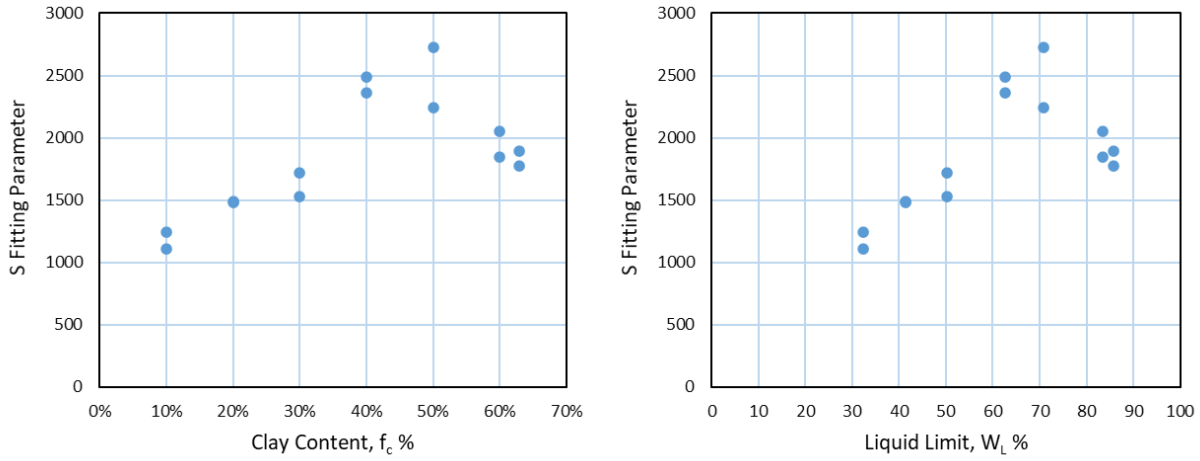


Figure 9-35: S fitting parameter for an atmospheric reference stress by clay content (left) and by liquid limit (right) for the Shibuya, Hwang, & Mitachi, (1997) correlation.

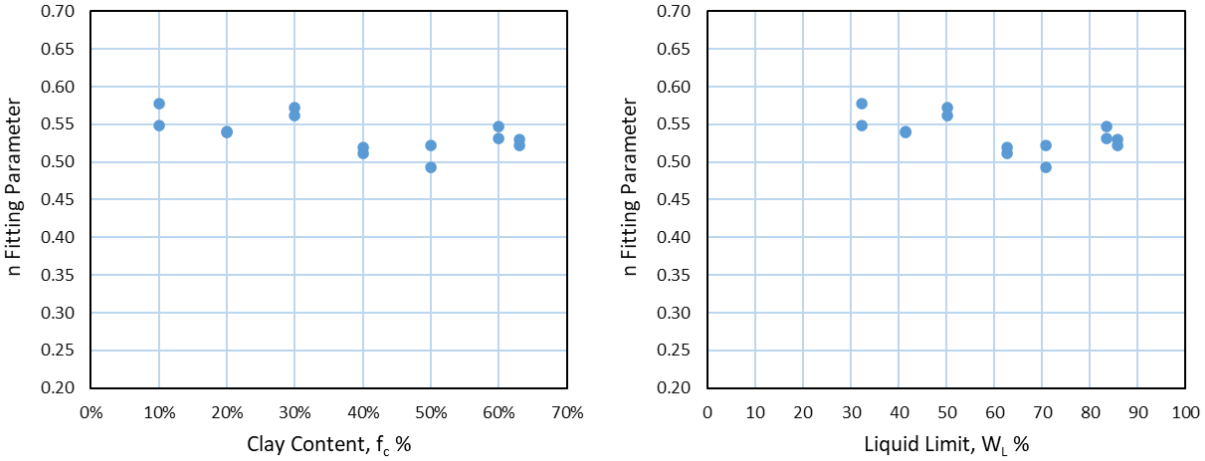


Figure 9-36: n fitting parameter for an atmospheric reference stress by clay content (left) and by liquid limit (right) for the Shibuya, Hwang, & Mitachi (1997) correlation.

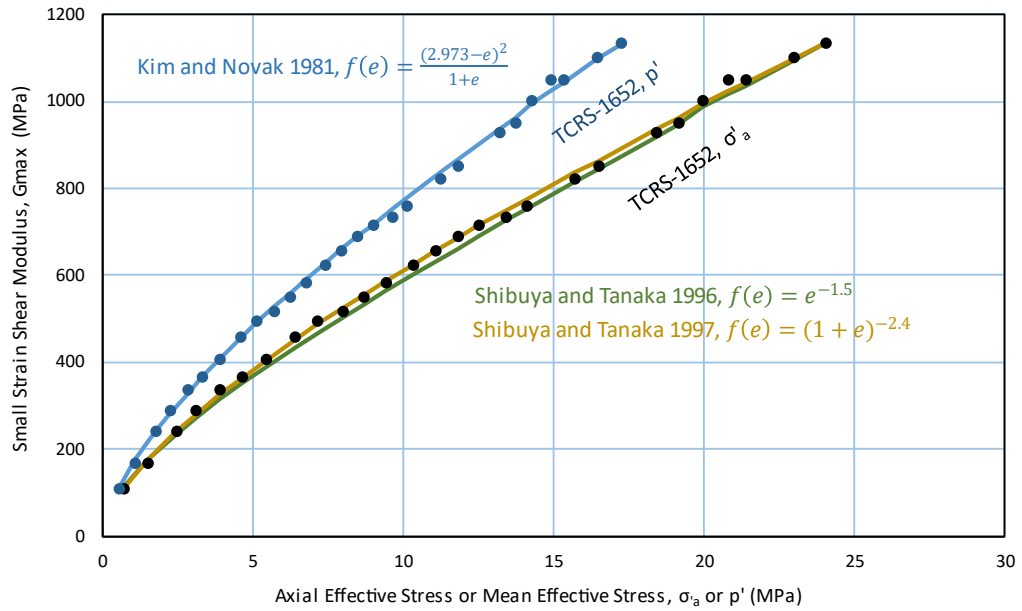


Figure 9-37: Measured G_{max} (data points) by Axial Effective Stress Shibuya & Tanaka (1996), Shibuya, Hwang, & Mitachi, (1997) or Mean Effective Stress Kim & Novak (1981), with the corresponding fit empirical correlations for TCRS 1652 a 10% clay mixture.

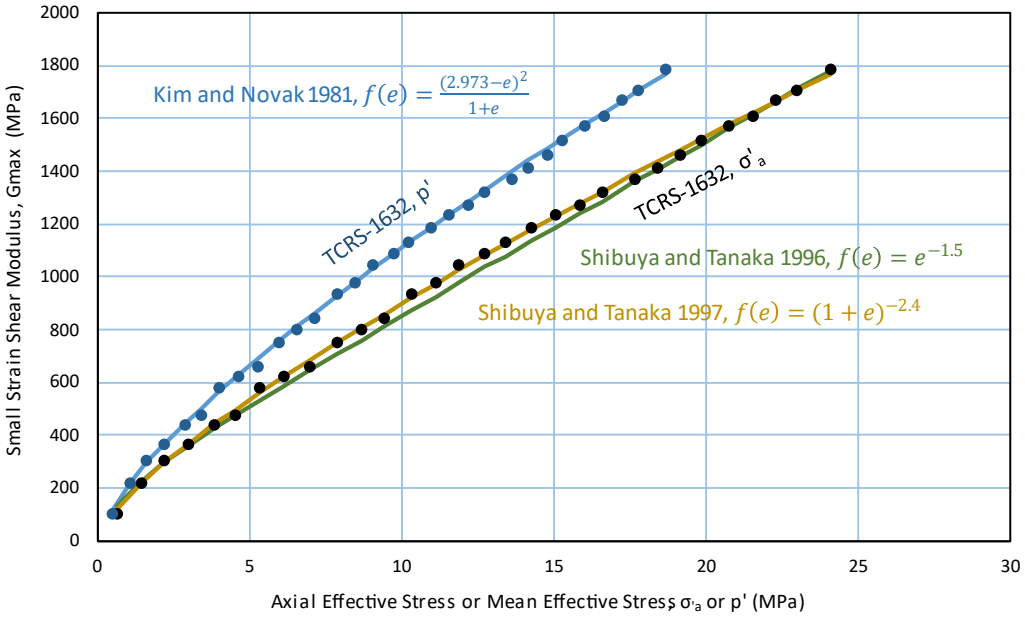


Figure 9-38: Measured G_{max} (data points) by Axial Effective Stress Shibuya & Tanaka (1996), Shibuya, Hwang, & Mitachi (1997) or Mean Effective Stress Kim & Novak (1981), with the corresponding fit empirical correlations for TCRS 1632 a 30% clay mixture.

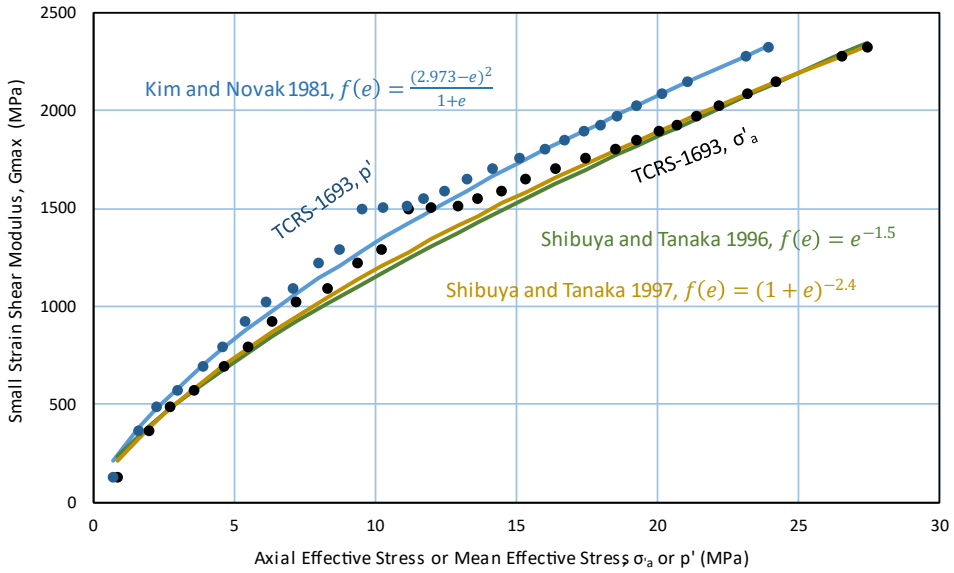


Figure 9-39: Measured G_{max} (data points) by Axial Effective Stress Shibuya & Tanaka (1996), Shibuya, Hwang, & Mitachi (1997) or Mean Effective Stress Kim & Novak, (1981), with the corresponding fit empirical correlations for TCRS 1693 a 50% clay mixture.

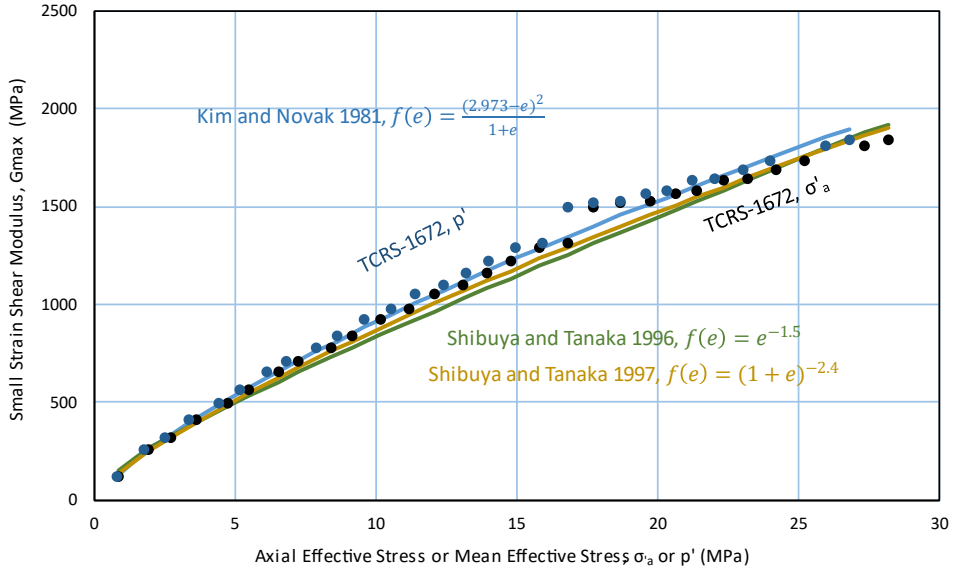


Figure 9-40: Measured G_{max} (data points) by Axial Effective Stress Shibuya & Tanaka (1996), Shibuya, Hwang, & Mitachi, (1997) or Mean Effective Stress Kim & Novak, (1981), with the corresponding fit empirical correlations for TCRS 1672 a RGoM_EI specimen.

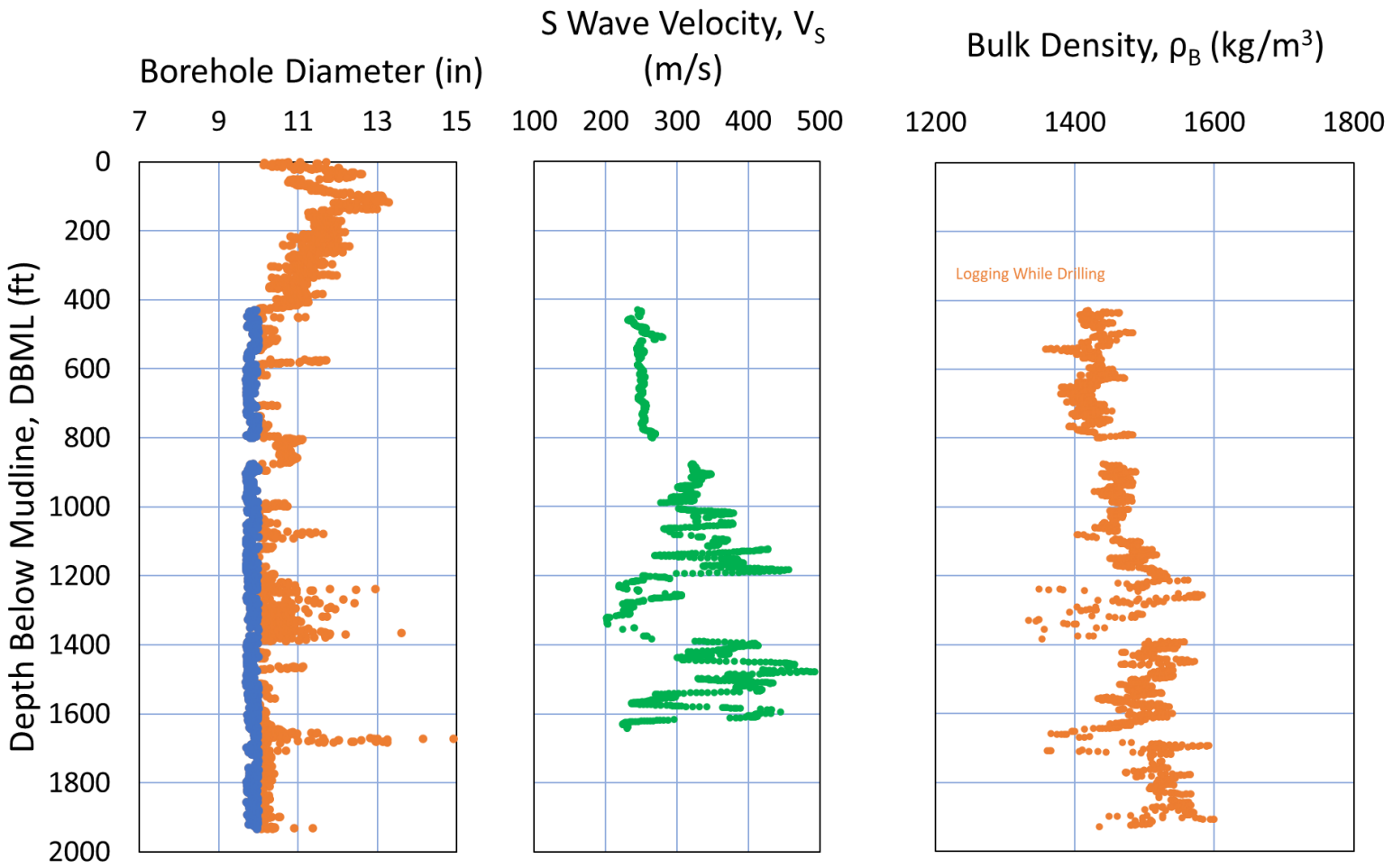


Figure 9-41: Borehole caliper and shear wave velocity from wireline measurements, and bulk density by depth below mudline in feet from logging while drilling measurements, at IODP expedition 308 site U1324. The blue caliper data points indicate measurements less than 10 inches in diameter, the orange caliper points are greater than 10 inches and have been removed from the data processing.

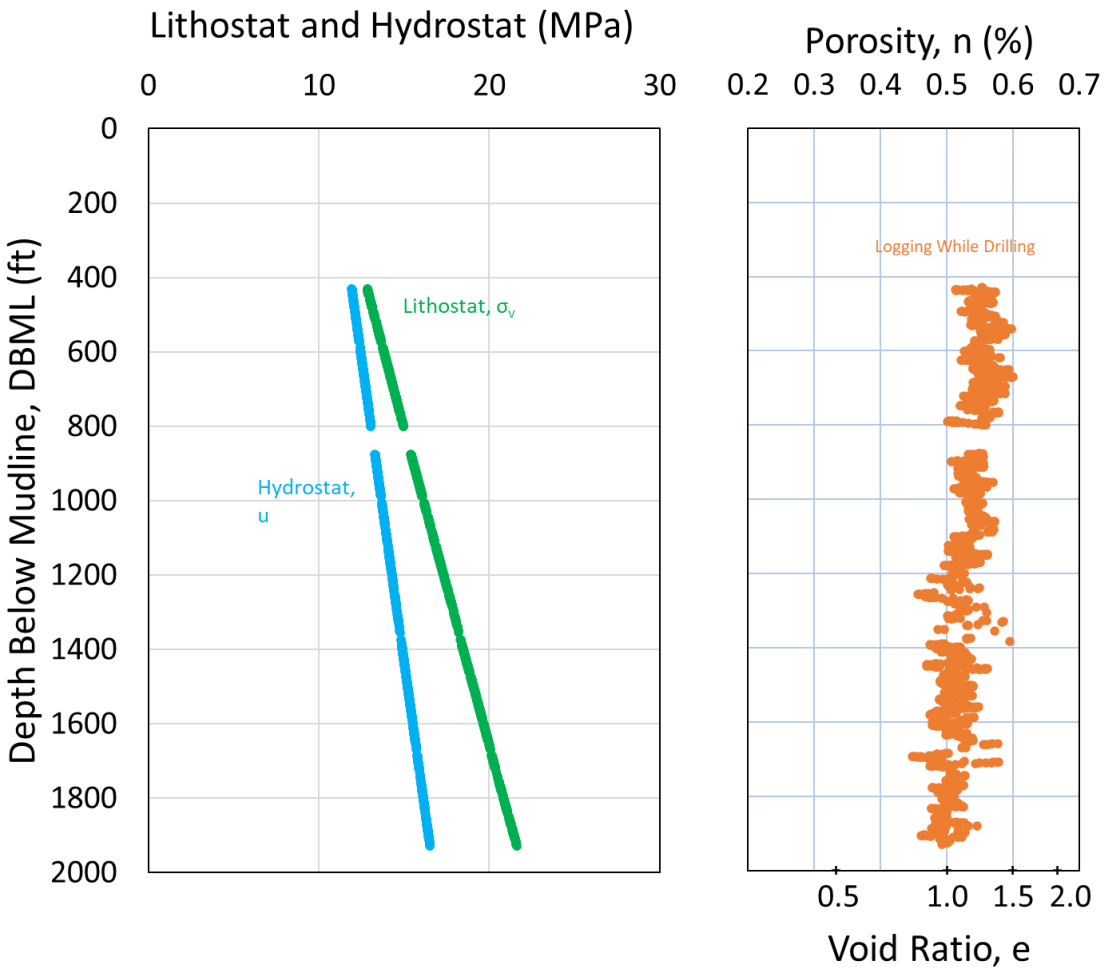


Figure 9-42: Lithostatic stress, hydrostatic stress and void ratio by depth below mudline from IODP expedition 308 site U1324. The lithostatic stress was calculated by integrating the logging while drilling density logs. Porosity is from logging while drilling neutron porosity measurements.

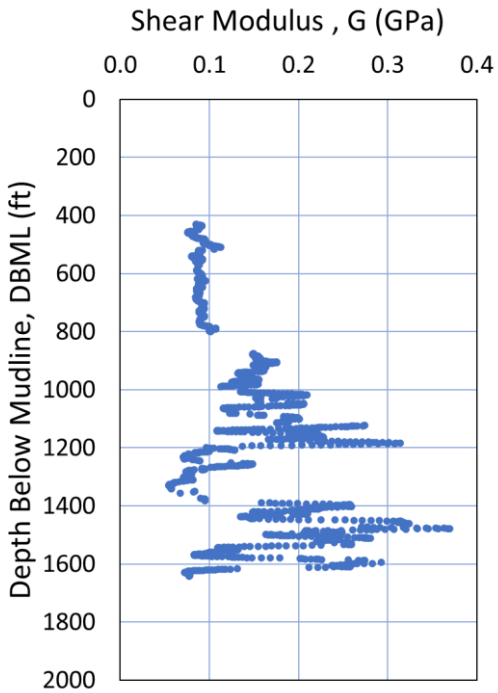


Figure 9-43: Shear modulus at site U1324 calculated from wireline dipole sonic imager velocity logs and logging while drilling density logs.

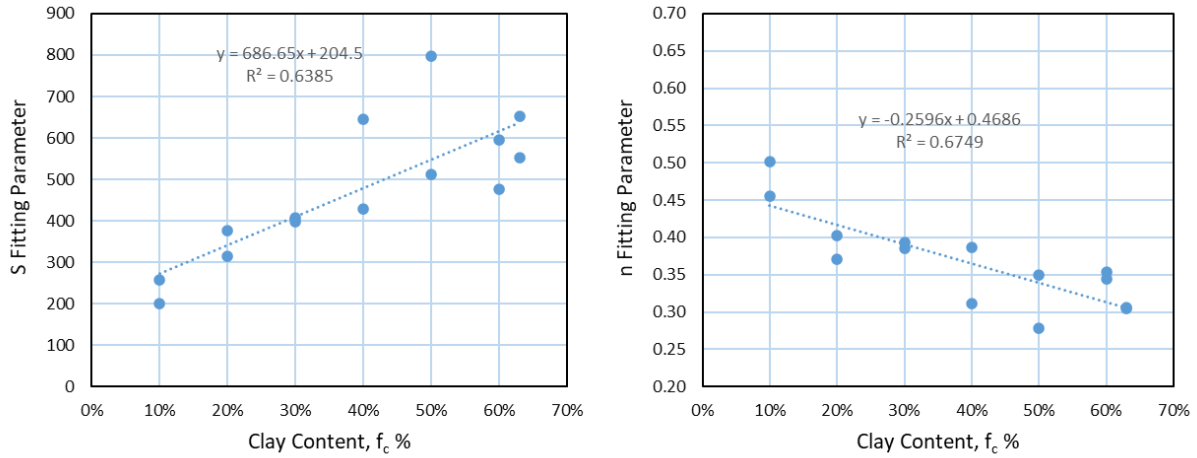


Figure 9-44: Linear best fit lines correlating the S and n parameters for the Shibuya & Tanaka (1996) void ratio function of equation 9-13 by specimen clay content.

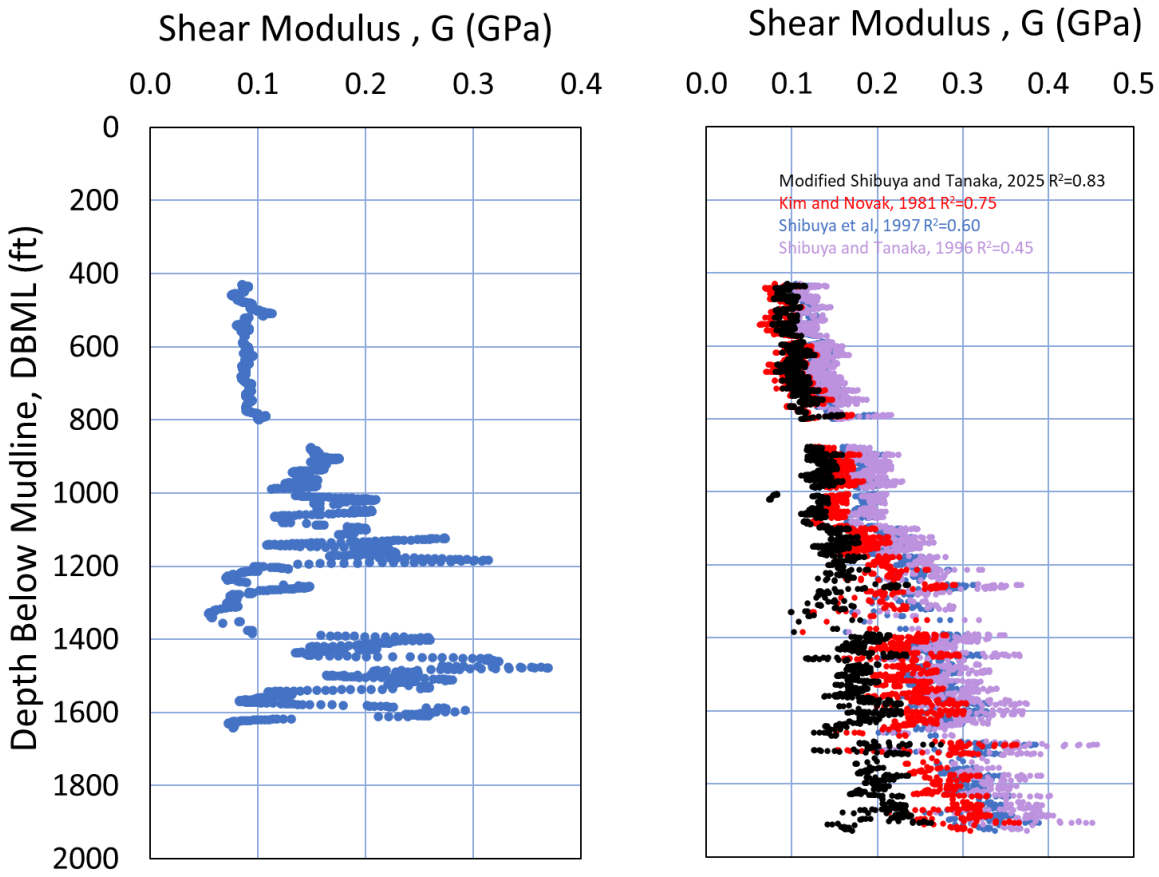


Figure 9-45: Shear modulus calculated from bulk density and wave velocity (left) and shear modulus estimated by the void ratio from Equation 9-13 by Kim & Novak (1981), Shibuya & Tanaka (1996), Shibuya, Hwang, & Mitachi (1997), and a modified version of Shibuya & Tanaka (1996) by depth below mudline. The modified version of the Shibuya & Tanaka (1996) void ratio expression adjusts the S and n fitting parameters based on clay content per the linear best fit lines provided in Figure 9-43. The coefficient of determination (R^2) is provided on the right plot.

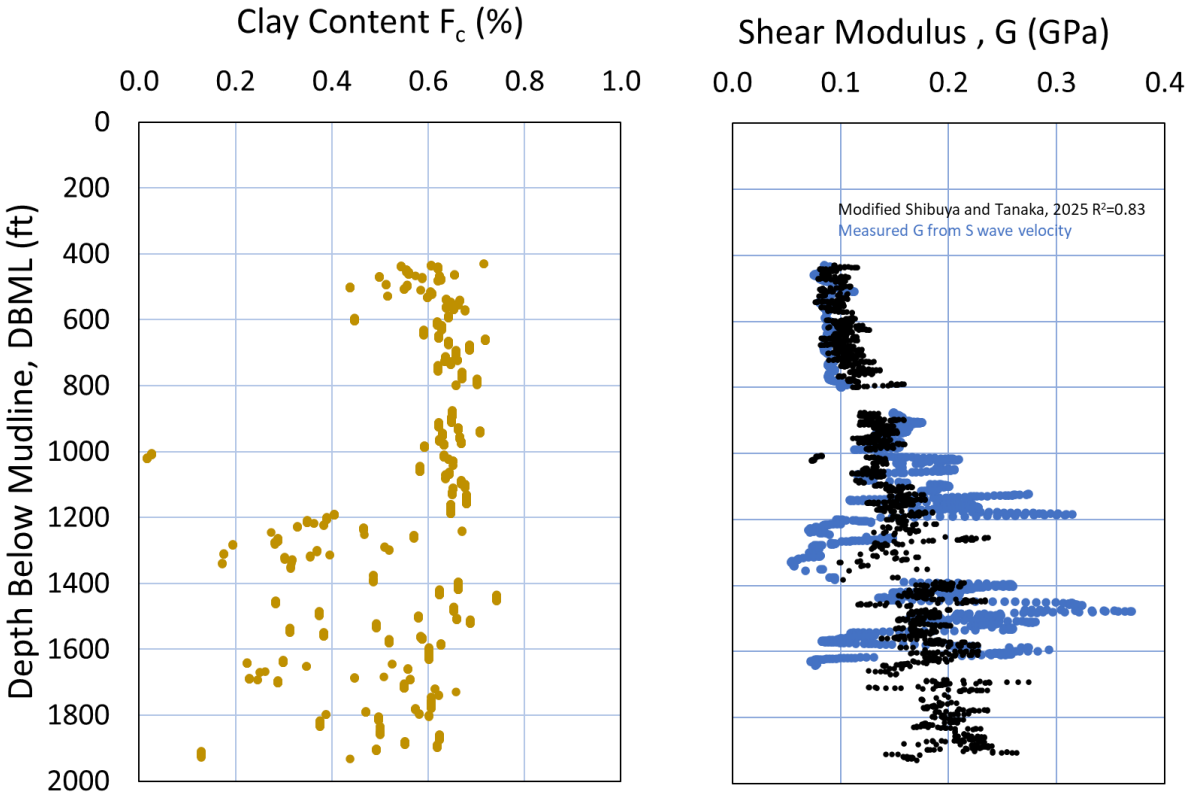


Figure 9-46: Clay content by depth below mudline in feet from Sawyer, Jacoby, Flemings, & Germaine (2008). Shear modulus calculated from bulk density from logging while drilling measurements and wave velocity from dipole sonic imager wireline measurements. An estimated shear modulus using the modified version of Shibuya & Tanaka (1996) by depth below mudline is shown for comparison to the calculated shear modules from density and velocity measurements. The modified version of the Shibuya & Tanaka (1996) void ratio expression adjusts the S and n fitting parameters based on clay content per linear best fit lines provided in Figure 9-44.

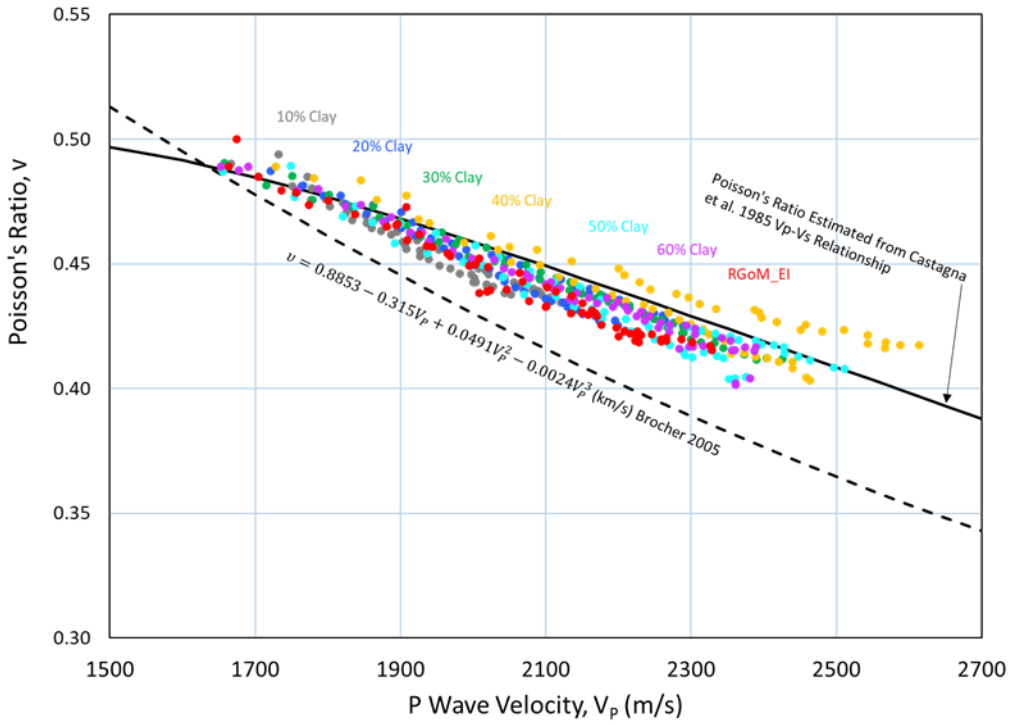


Figure 9-47: Poisson's ratio by pressure wave velocity from the TCRS tests. Two correlations are presented from calculating Poisson's ratio from the estimated shear wave using the Castagna, Batzle, & Eastwood (1985) V_P-V_S relationship, and a correlation presented in Brocher (2005).

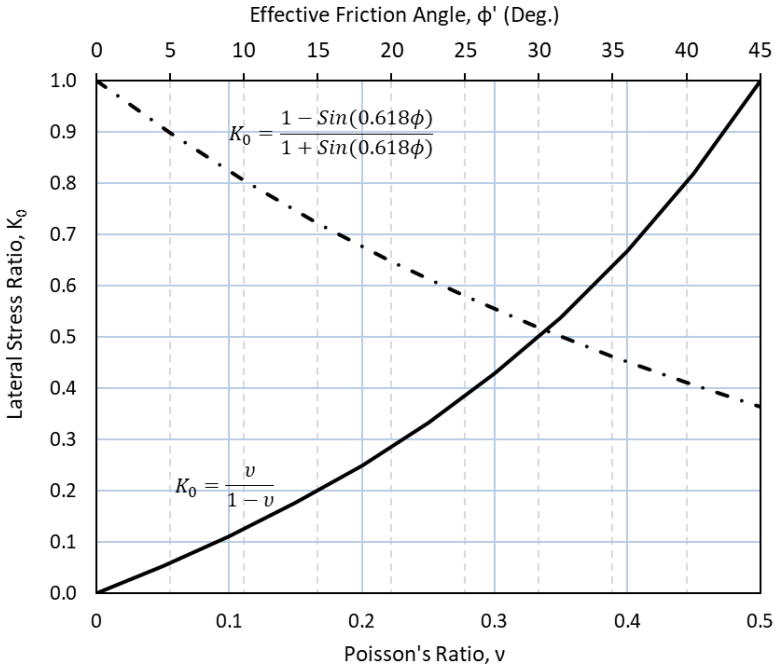


Figure 9-48: Lateral stress ratio (K_0) as a function of the dynamic Poisson's ratio solid line and as a function effective friction angle using the Federico (2021) equation (Equation 8-13).

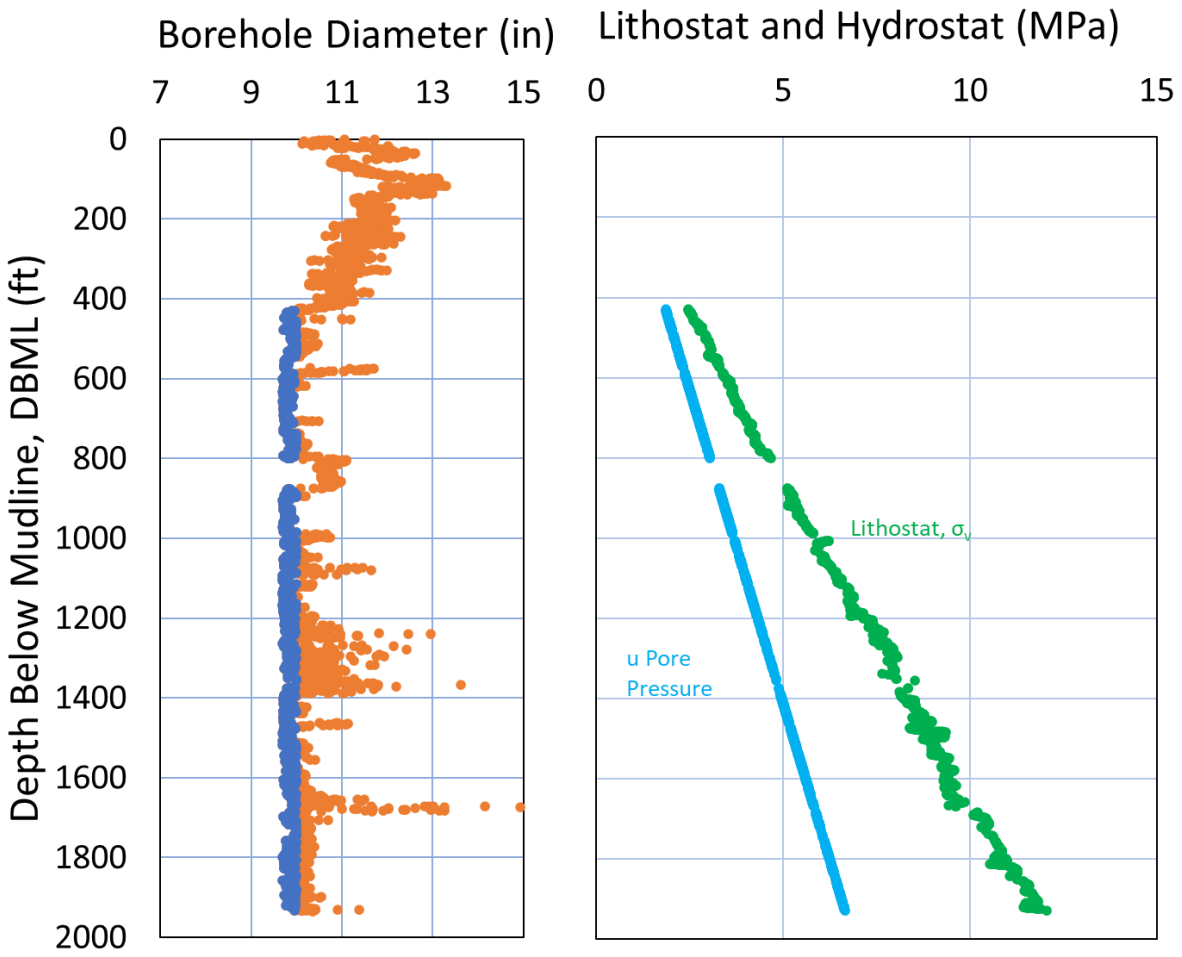


Figure 9-49: Borehole caliper wireline measurements, lithostatic stress from integrating density measurements on core samples, and pore pressure calibrated to pore pressure measurements presented in Figure 9-13 by depth below mudline at IODP expedition 308 site U1324. The blue caliper data points indicate measurements less than 10 inches in diameter, the orange caliper points are greater than 10 inches and have been removed from the data processing.

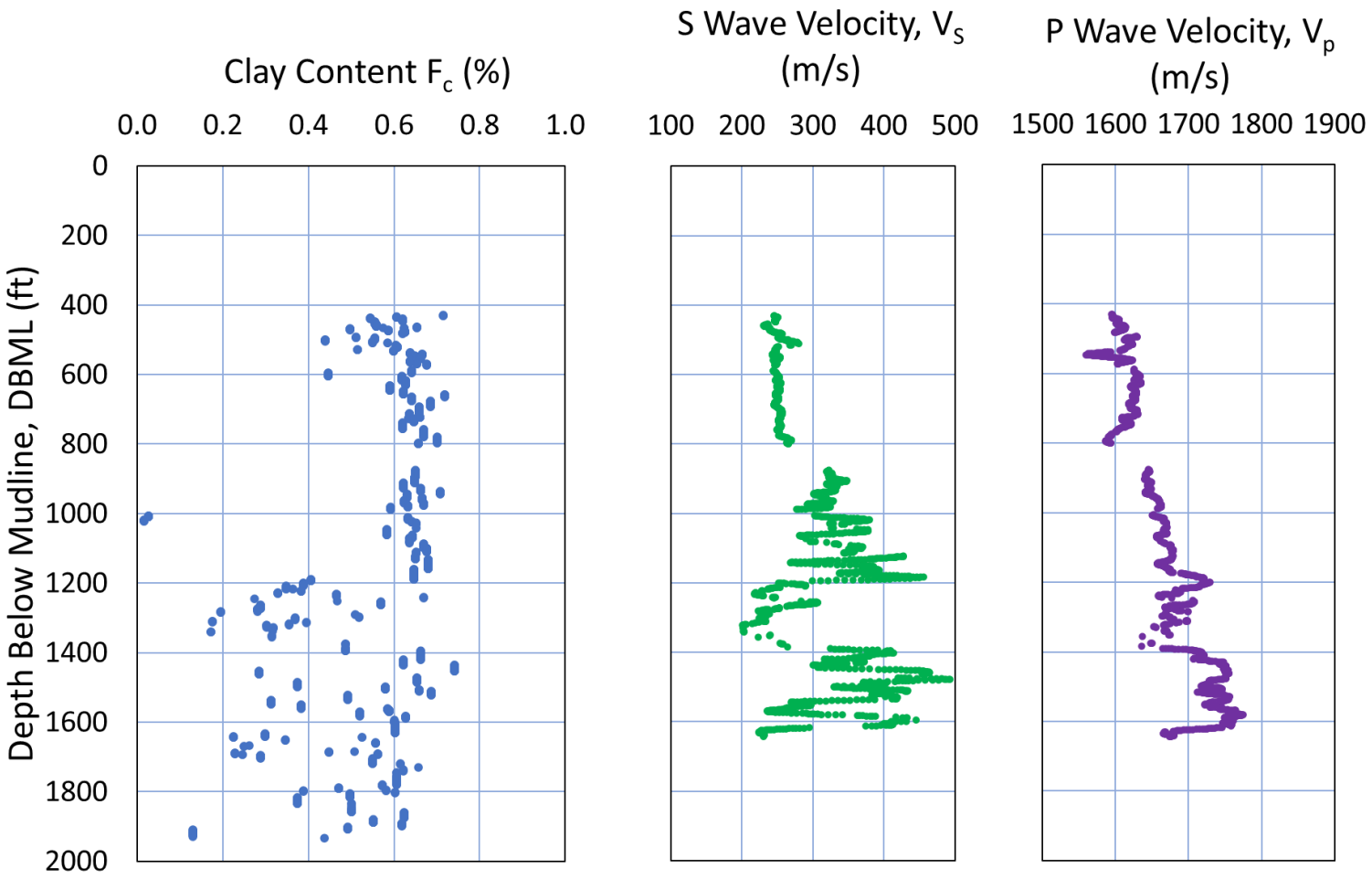


Figure 9-50: Clay content by depth below mudline in feet from Sawyer, Jacoby, Flemings, & Germaine (2008). Shear wave velocity, and pressure wave velocity by depth below mudline from dipole sonic imager wireline measurements at Site U1324. The measurements are filtered to remove measurements from a borehole diameter exceeding 10 inches.

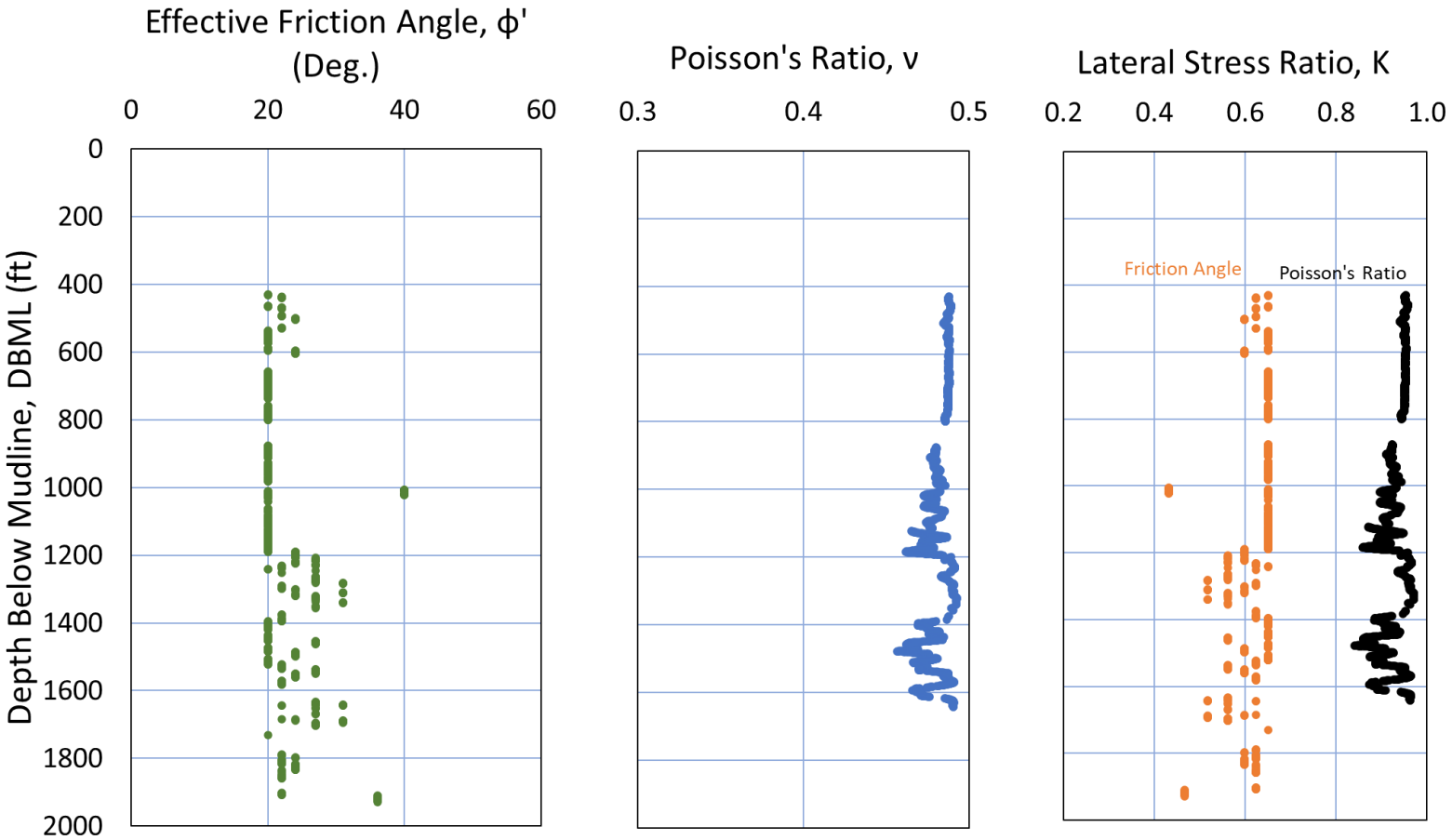


Figure 9-51: Effective friction angle from clay content, Poisson's ratio calculated from velocity wireline measurements, and lateral stress ratio from effective friction angle using Equation 8-13 and from Poisson's ratio using Equation 9-15 at Site U1324. The calculations are filtered to remove measurements from a borehole diameter exceeding 10 inches.

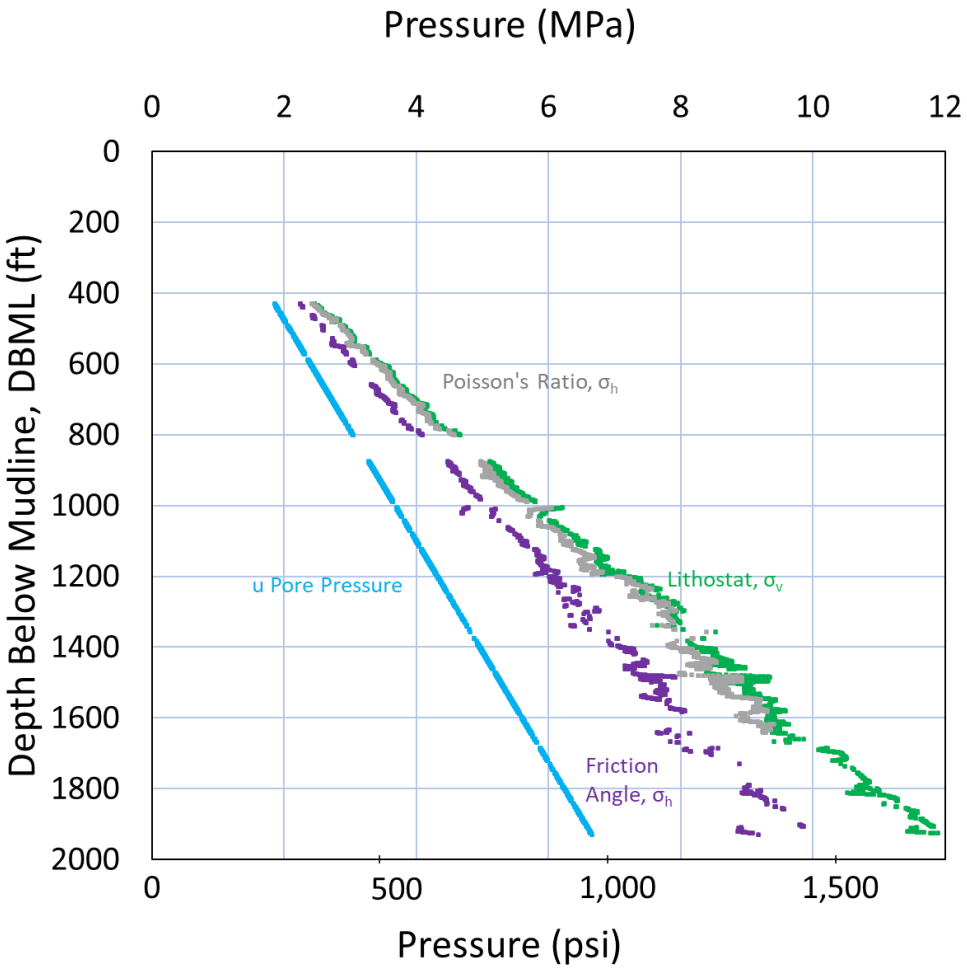


Figure 9-52: Lithostatic stress, least horizontal stress (σ_h) by the lateral stress ratio from friction angle and Poisson's Ratio, and hydrostatic stress by depth, filtered to exclude measurements from a borehole exceeding 10 inches in diameter.

CHAPTER 10. Conclusion and Recommendations

10-1 Overview

This research comprised a detailed laboratory investigation of the mechanical behavior of silt and clay mixtures over a wide range of effective axial stresses to evaluate the effects of clay content on soil behavior. The mechanical behavior of the mixtures during compression is evaluated through high stress Constant Rate of Strain (CRS) compression testing up to 100 MPa, tall CRS testing up to 30 MPa, and the consolidation phase of triaxial shear testing up to 10 MPa. Permeability behavior is evaluated through CRS testing or through measurement by constant head or falling head flow testing. The dynamic mechanical properties of the mixtures are investigated through wave velocity measurements during compression within the tall CRS apparatus. The strength of the mixtures is evaluated through K_0 consolidated undrained shear compression triaxial testing at two consolidation stress levels, 1 MPa and 10 MPa. The measured engineering parameters from the laboratory testing program are evaluated for sensitivity to clay content and comparatively to established frameworks for fabric controls on the mechanical behavior of clay supported and grain supported materials. Examples highlighting the importance of the observed trends and the impact clay content has on the behavior of soil are presented.

10-2 Key Findings and Developments

Significant observations and developments from the laboratory program, evaluations, and discussions herein are as follows:

- Resedimentation specimen creation techniques create reproducible specimens over a large range of soil lithologies allowing for the controlled study of the lithology effects in soil.

- A unified methodology of determining specimen clay content would be beneficial for organizing data. This would be especially useful in translating observations made in the field of geology to geotechnical engineering and vice versa. Geotechnical engineers tend to classify clay soils by particle size, while geologists tend to rely on both particle size and mineralogy depending on the application.
- The critical clay content or threshold fines content (f_{Cth}) provides a reasonable first order approximate limit between grain supported behaviors and clay supported behavior for mixtures of silts and high plasticity clays.
- Binary mixture theory has limited application to mixtures of grains and high plasticity fines. The theory has been developed for materials of low plasticity and does not account for high plasticity fines.
- High clay content materials and low clay content materials have distinct compression behaviors. With high clay content materials have higher initial void ratios and concave upwards compression curves in a void ratio by log effective stress space. Low clay content materials have lower initial void ratios and a concave downwards compression curve in a void ratio by log effective stress space.
- Soil compressibility increases with increasing clay content.
- Compression curves of the 30% clay content and greater specimens trended towards an intrinsic compression line at high stresses.
- Compression curves of the 20% clay content or less do not trend towards each other with increasing stress.
- Soil permeability monotonically decreases with increasing clay content and decreases with increasing stress.

- Above 50% clay content the decrease in permeability with increasing clay content is negligible, indicating a fabric controlled permeability limit.
- The decrease in permeability with increasing clay is largest between 0% clay and 10% clay. This large change is not adequately accounted for in permeability correlations.
- The change in permeability by increasing stress is most significant in high clay content materials and least significant in low clay content materials, highlighting the stress sensitivity of high clay content materials.
- Over the stress range of measurements both the shear wave velocities and specimen densities are found to be parabolic when plotted by clay content at one stress state. With the values increasing towards the critical porosity with increasing clay content and decreasing away from the critical porosity with increasing clay content. These trends are also reflected in the calculated elastic parameters.
- The lateral stress ratio at rest (K_0) is shown to increase with increasing clay content and increase with increasing stress level.
- K_0 estimated by the mobilized friction angle through the equation proposed by Federico (2021) is found to provide a reasonable lower bound for K_0 over the tested clay contents and stresses.
- Clay content has a significant impact on the strength of soil with both the undrained shear strength and effective friction angle monotonically decreasing with increasing clay content. Both the undrained shear strength and effective friction angle are shown to be sensitive to confining stress with the higher clay contents indicating larger stress sensitivities.
- Clay content also has a significant effect on the shear deformation behavior during of the materials. Ductility of the material increased with increasing clay content as observed in variations of strain to maximum shear stress by specimen clay content.

- The strain to maximum friction angle, used to approximate the critical state during undrained compressive shearing appears to be insensitive to clay content. The critical state friction angle occurs at high strains typically exceeding 8%.
- The V_{grain} parameter is strong indicator of the frictional resistance of the soil and indicates similar behavior between soils and rocks.
- The evaluation of the two different compression models by varying clay content shows the importance of selecting an appropriate compression model form for a given clay content.
- The presented example of estimating vertical effective stress at IODP expedition 308 site U1324 by applying compression models to back calculate effective stress from porosity measurements highlights the importance of lithology on the vertical effective stress. This example also shows the importance of site specific data when estimating earth stresses.
- The evaluation of the different permeability correlations showed that common correlations do not effectively estimate low clay content permeabilities and do not adequately account for variations of permeability by clay content.
- In general, the three evaluated correlations for permeability were within an order of magnitude of the measurement and can serve as a reasonable first order approximation.
- The small strain shear modulus (G_{max}) is sensitive to clay content and stress. Three common correlations for estimating G_{max} are compared illustrating the sensitivity of the parameter in a real world setting.
- An example of the clay sensitivity of the fracture gradient as estimated by the Matthews & Kelly (1967), and Eaton (1975) methods is presented. This example highlights the importance of understanding the basis of the correlations and applying the correlations appropriately. That is K_0 from friction angle is suitable for soils than K_0 derived from from Poisson's ratio which may be more appropriate for lithified rocks.

10-3 Recommendations for Future Work

Based on the results and conclusions of this work, the following are ideas for future research to expand the findings of this study.

- This study presents a systematic evaluation of the effects of clay content on strength though compression shear testing. Additional programs to quantify the effect of clay content in a normal shear mode from Direct Simple Shear (DSS) and in an extension mode though triaxial extension shearing would be beneficial for accounting for small variations in clay content in engineering and geological problems.
- All compression of the materials for the study programs was performed in a K_0 condition. Naturally deposited soil is not necessarily in K_0 conditions. It would be beneficial to understand how observed trends from this laboratory program performed in K_0 conditions deviate from testing performed along other loading paths.
- Understanding the effects of soil stress history would be very beneficial to applying these findings. It would be interesting to one could determine the minimum clay content where stress and over consolidation ratio become a significant driver of material behavior.
- The tall CRS apparatus requires in person velocity measurements. Automating the system to record wave traces at predetermined times and providing stress or deformation controls would significantly improve the testing apparatus.
- This study utilized the liquid limit correlations from Casey (2014). There would be great benefit in additional testing geologically distinct materials specifically low plasticity, low clay content materials to continue the development of those correlations.

Works Cited

Abdulhadi, N. O. (2009). *An Experimental Invistigation into the Stress-Dependant Mechanical Behavior of Cohesive Soil with Application to Wellbore Instability.* Cambridge, Massachusetts: MIT University.

Adam, L., van Wijk, K., Otheim, T., & Batzle, M. (2013). Changes in elastic wave velocity and rock microstructure due to basalt-CO2-water reactions. *Journal of Geophysical Research: Solid Earth, 118*, 4039-4047. doi:10.1002/jgrb.50302

Adams, A. (2014). *Permeability anisotropy and resistivity anisotropy of mechanically compressed mudrocks* (Vol. Ph.D. Thesis). Cambridge, Massachusetts: Massachusetts Instituted of Technology.

Addis, M., & Jones, M. (1985). Volume changes during diagenesis. *Marine Pet. Geol., 2(3)*, 241-246. doi:https://doi.org/10.1016/0264-8172(85)90013-3

Aikake, H. (1974). Markovian representation of stochastic processes and its application to the analysis of autoregressive moving average processes. *Annals of the Institute of Statistical Mathematics, 26*, 363-387. doi:https://doi.org/10.1007/BF02479833

Alberty, M., Hafle, M., Mingle, J., & Byrd, T. (1999). Mechanisms of Shallow Waterflows and Drilling Practices for Intervention. *SPE Drill & Compl, 14*, 123-129. doi:10.2118/56868-PA

Alexander, L. L., & Flemings, P. B. (1995). Geologic Evolution of a Pliocene-Pleistocene Salt-Withdrawal Minibasin: Eugene Island Block 330, Offshore Louisiana. *AAPG Bulletin*, p. 1737-1756.

Andersen, G. (1991). *Physical Mechanisms Controlling the Strength and Deformation Behavior of Frozen Sands.* Cambridge, Massachusetts: Massachusetts Institute of Technology.

Anderson, E. (1951). *The Dynamics of Faulting and Dyke Formation with Applications to Britain.* Edinburgh: Oliver and Boyd.

Aplin, A. C., Yang, Y., & Hansen, S. (1995). Assessment of B, the compression coefficient of mudstones and its relationship with detailed lithology. *Marine and Petroleum Geology, 12*(8), 955-963.

ASTM International. (2012). Standard Test Method for One-Dimensional Consolidation Properties of Saturated Cohesive Soils using Controlled-Strain Loading. *ASTM 04.08 Soil and Rock*.

ASTM International. (2014). *Standard Test Methods for Specific Gravity of Soil Solids by Water Pycnometer.*

ASTM International. (2017). *Standard Test Method for Particle-Size Distibution (Gradation) of fine-Grained Soils Using the Sedimentation (Hydrometer) Analysis.*

ASTM International. (2017). *Standard Test Methods for Liquid Limit, Plastic Limit, and Plasticity Index of Soils.*

ASTM International. (2020, April 2). Standard Practice for Classification of Soils for Engineering Purposes (Unified Soil Classification System). *ASTM D2487-17*. ASTM International. doi:10.1520/D2487-17

Athanasiou-Grivas, D., & Harr, M. (1980). Particle Contacts in Discrete Materials. *Journal of Geotechnical Engineering Division, 106*(GT5), 559-564.

Athy, L. (1930). Density, porosity, and compaction of sedimentary rocks. *Am. Assoc. Petroleum Geologists Bull., Vol. 14*, 1-30.

Ayres, A., & Theilen, F. (1991). Relationship between p-and s-wave velocities and geological properties of near-surface sediments of the continental slope of the barents sea. *Geophysical prospecting, 47*(4), 431-441.

Baldwin, B., & Butler, C. (1985). Compaction Curves. *AAPG Bull., Vol. 69*, 622-626.

Barden, L., & Berry, P. (1965). Consolidation of Normally Consolidated Clay. *J. Soil Mechanics and Foundations Division, 91*(5), 15-35.

Been, K., & Jefferies, M. (1985). A State Parameter for Sands. *Geotechnique, 35*(2), 99-112.

Behrmann, J., Flemings, P., John, C., & Scientists, a. t. (2006). Proceedings of the Integrated Ocean Drilling Program Volume 308. College Station TX. doi: doi:10.2204/iodp.proc.308.2006

Bekins, B., Mcaffrey, A., & Dreiss, S. (1995). Episodic and constant flow models for the origin of low-chloride waters in a modern accretionary complex. *Water Resources Research, 31*, 3205-3215.

Bell, A. (1915). The lateral pressure and resistance of clay and the supporting power of clay foundations. *Minutes. Proc. Inst. Civ. Eng.*, 233-272.

Betts, W. S. (2014, May). Compressibility and Permeability of Gulf of Mexico Mudrocks, Resedimented and In-situ. Austin, Texas, Texas: The University of Texas at Austin.

Birch, F., & Bancroft, D. (1938). The effect of pressures on the rigidty of rocks. *Journal of Geology, 46*, 59-87, 113-141.

Bishop, A., & Henkel, D. (1962). *The measurement of soil properties in the Triaxial test.* London, UK: E. Arnold.

Bowden, F., & Tabor, D. (1964). *The Friction and Lubrication of Solids, Part II.* London: Oxford University Press.

Bowers, G. (1995). Pore Pressure Estimation From Velocity Data: Accounting for Overpressure Mechanisms Besides Undercompaction. *SPE Drill & Compl, 10*, 85-95. doi:10.2118/27488-PA

Breckels, I., & van Eekelen, H. (1982). Relationship Between Horizontal Stress and Depth in Sedimentary Basins. *J. Pet. Technol.*, 2191-2199.

Brocher, T. (2005). Relations between elastic wavespeeds and density in the Earth's crust. *Bulletin of the Seismological Society of America, 95*(6), 83-91.

Broichhausen, H., Littke, R., & Hantschel, T. (2005). Mudstone compaction and its influence on overpressure generation, elucidated by a 3D case study in the North Sea. *Int. J. Earth Sci., 94*, 956-978.

Brooker, E., & Ireland, H. (1965). Earth pressures at rest related. *Can. Geotech. J., 2*(1), 1-15.

Bryant, W., Bennet, R., Burkett, P., & Rack, F. (1990). The Fabric of a Consolidating Clayey Sediment Column, ODP Site 697. *Proceedings of the Ocean Drilling Program, Scientific Results, 113*, 225-237.

Burland, J. (1990). On the Compressibility and Shear Strength of Natural Clays. *Geotechnique, 3*, 329-378.

Butterfield, R. (1979). A natural compression law for soils (an advance of e-log p'). *Geotechnique, 29*, 469-480.

Cabalar, A., & Hasan, R. (2013). Compressional behaviour of various size/shape sand–clay mixtures. *Engineering Geology, 164*, 36-49.

Cai, G., Liu, S., Puppala, A., & Tong, L. (2011). Assessment of the Coefficient of Lateral Earth Pressure at Rest (K0) from In Situ Seismic Tests. *GeotechnicalTesting Journal, 34*(4), 310-320.

Carman, P. (1956). *Flow of Gases through Porous Media.* London, UK: Butterworths Scientific Publications.

Carman, P. C. (1937). Fluid flow through granular beds. *Transactions of the Institution of Chemical Engineers, 15*, 150-166.

Carrier III, W. (2003). Goodbye Hazen, Hello Kozeny-Carman. *Journal of Geotechnical and Geoenvironmental Engineering, 129*(11), 1054-1056.

Casey, B. (2014). *The Consolidation and Strength Behavior of Mechanically Compressed Fine-Grained Sediments* (Vol. Phd Thesis). Cambridge, Massachusetts: MIT.

Casey, B., Germaine, J., Flemings, P., & Fahy, B. (2015). Estimating horizontal stresses for mudrocks under one-dimensional compression. *Marine and Petroleum Geology, 65*, 178-186.

Casey, B., Reece, J., & Germaine, J. (2019). One-dimensional normal compression laws for resedimented mudrocks. *Marine and Petroleum Geology, 103*, 397-403. doi:https://doi.org/10.1016/j.marpetgeo.2019.02.023

Cassagrande, A., & Rendon, F. (1978). *Gyratory shear apparatus design, testing procedures.* Vicksburg, Mississippi: Corps of Engineer Waterways Experiment Station.

Castagna, J., Batzle, M., & Eastwood, R. (1985). Relationship Between Compressional-wave and Shear-wave Velocities in Clastic Silicate Rocks. *Geophysics, 50*(4), 571-581.

Chang, C., Meidani, M., & Deng, Y. (2017). A compression model for sand–silt mixtures based on the concept of active and inactive voids. *Acta Geotechnica, 12*, 1301-1317.

Chang, C., Meidani, M., & Deng, Y. (2017). A compression model for sand–silt mixtures based on the concept of active and inactive voids. *Acta Geotechnica, 12*, 1301-1317.

Cheng, C., & Meidani, M. (2013). Dominant grains network and behavior of sand–silt mixtures: stress-strain modeling. *International Journal for Numerical and Analytical Methods in Geomechanics, 37*, 2563-2589.

Cheng, K., Wu, H., Fang, Y., & Wu, Q. (2023). Experimental study on shear wave velocity of sand-gravel mixtures considering the effect of gravel content. *Frontiers in Earth Science*, 1-8. doi:10.3389/feart.2022.1076098

Chong, S.-H., & Santamarina, J. (2016). Soil Compressibility Models for a Wide Stress Range. *J. Geotech. Geoenviron. Eng., 142*(6). doi:https://doi.org/10.1061/(ASCE)GT.1943-5606.0001482

Choo, H., & Burns, S. (2015). S.E. Shear wave velocity of granular mixtures of silica particles as a function of finer fraction, size ratios and void ratios. *Granular Matter, 17*, 567-578. doi:https://doi.org/10.1007/s10035-015-0580-2

Columbia University. (2005, August). *Data File Summary, IODP Expedition 308 - Hole U1324A*. Retrieved December 2024, from https://mlp.ldeo.columbia.edu/data/iodp-usio/exp308/U1324A/

Coulomb, C. (1776). Essai sur une application des regles des maximis et minimis a quelques problemes de statique relatifs a l'architecture. *Memoires de l'Academie Royale pres Divers Savants, 7*.

Cundall, P., Drescher, A., & Stack, O. (1982). Numerical Experiments on Granular Assemblies; Measurements and Observations. *IUTAM Conference on Deformation and Failure of Granular Materials,*, (pp. 355-370). Delft, Netherlands.

Dallmus, K. (1958). Mechanics of basin evolution and its relation to the habitat of oil in the basin. *Habitat of Oil, V1: A Symposium Conducted by the American Association of Petroleum Geologists* (pp. 883-931). New York: Am. Assoc. Pet. Geol.

Darcy, H. (1856). *Les Fontaines Publiques de la Ville de Dijon.* Paris, France: Victor Dalmont.

Das, M. (2010). *Principles of Geotechnical Engineering.* Stamford: Cengage Learning.

Deng, J., Wang, C., Zhao, Q., Guo, W., Tang, G., & Zhao, J. (2021). Depositional and Diagenetic Controls on Macroscopic Acoustic and Geomechanical Behaviors in Wufeng-Longmaxi Formation Shale. *Frontiers in Earth Science, 9*. doi:10.3389/feart.2021.617831

Dewhurst, D. N., Aplin, A. C., Sarda, J.-P., & Yang, Y. (1998). Compaction-driven evolution of porosity and permeability in natural mudstones: An experimental study. *Journal of Geophysical Researhc, 103*, 651-661.

Dewhurst, D., Aplin, A., & Sarda, J. (1999). Influence of clay fraction on pore-scale properties and hydraulic conductivity of experimentally compacted mudstones. *JJournal of Geophysical Research, 104*(B12), 29,261-29,274.

Dewhurst, D., Brown, K., Clennell, M., & Westbrook, G. (1996). A comparison of the fabric and permeability anisotropy of consolidated and sheared silty clay. *Engineering Geology, 42*, 253-267.

Dickinson, G. (1953). Geological Aspects of Abnormal Reservoir Pressures in Gulf Coast Louisiana. *Am. Assoc. Petroleum Geologists Bull., Vol. 37*, P 410-432.

Domenico, S. (1977). Elastic Properties of Unconsolidated Porous Sand Reservoirs. *Geophysics, 42*(7), 1339-1368.

Donaghe, R. T., & Townsend, F. C. (1975). *Effects of Anisotropic Versus Isotropic Consolidation in Consolidation-Undrained Triaxial Compression Tests of Cohesive Soils.* Vicksburg, MS: Soils and Pavement Laboratory, U.S. Army Engineer Waterways Experiment Station.

Du, G., Liu, N., Xia, Z., & Kang, X. (2021). Laboratory Investigation on the Stress-Dependent Anisotropic Shear Wave Velocity (Vs) and Coefficient of Lateral Earth Pressure at Rest (K0) of Granular Materials. *Advances in Civil Engineering, 2021*, 0-13. doi:10.1155/2021/6639178

Duffault, K. (2011). *Stress sensitivity of elastic wave velocities in granular media.* Trondheim: Norwegian University of Science and Technology.

Duffy, J., & Mindlin, R. (1957). Stress-strain relations and vibrations of a granular medium. *Journal of Applied Mechanics, 24*, 585-593.

Eaton, B. (1969). Fracture Gradient Prediction and Its Application in Oilfield Operations. *Journal of Petroleum Technology, No. 21*(No. 10), 1353-1360. doi:https://doi.org/10.2118/2163-PA.

Eaton, B. (1975, September). The Equation for Geopressure Prediction from Well Logs. *Paper presented at the Fall Meeting of the Society of Petroleum Engineers of AIME*. Dallas, Texas. doi:https://doi.org/10.2118/5544-MS

Eberhart-Phillips, D., Han, D., & Zoback, M. (1989). Empirical Relationships Among Seismic Velocity, Effective Pressure, Porosity, and Clay Content in Sandstone. *Geophysics, 54*(1), 82-89.

Eissa, E., & Kazi, A. (1988). Relation Between Static and Dynamice Young's Modulus of Rocks. *Int. J. Rock Mech. Min. Sci. & Geomech., 25*(6), 479-482.

Federico, A. (2021). POTENTIAL LINK BETWEEN THE GOLDEN RATIO AND THE AT-REST EARTH PRESSURE IN NORMALLY CONSOLIDATED SOILS. *Italian Journal of Engineering Geology and Environment, 2*, 17-27. doi:10.4408/IJEGE.2021-02.O-02

Federico, A., & Elia, G. (2009). At-rest earth pressure coefficient and Poisson's ratio in normally consolidated soils. In M. H. al. (Ed.), *Proceedings of the 17th International Conference on Soil Mechanics and Geotechnical Engineering* (pp. 7-10). Alexandria, Egypt: IOS Press . doi:10.3233/978-1-60750-031-5-7

Federico, A., & Elia, G. (2009). At-rest earth pressure coefficient and Poisson's ratio in normally consolidated soils. *Proceedings of the 17th International Conference on Soil Mechanics and Geotechnical Engineering* (pp. 7-10). Alexandria, Egypt: ISSMGE. doi:0.3233/978-1-60750-031-5-7

Finnegan, J. (2020). *Comparison of Resedimented with Intact Mudrock Behavior* (Vol. MS Thesis). Medford, Massachusetts: Tufts University.

Fioravante, V., Jamiolkowski, M., Lo Presti, D., Manfredini, G., & Pedroni, S. (1998). Assessment of the coeffcient of the earth pressure at rest from shear wave velocity measurements. *Geotechnique, 48*(5), 657-666.

Fjaer, E. (2008). *Petroleum Related Rock Mechanics* (Second ed.). Amsterdam: Elsevier.

Flemings, P. B. (2021). *a Concise Guiude to Geopressure, Origin, Prediction and Applications.* Cambridge: Cambridge University Press. doi:10.1017/9781107326309

Flemings, P., Behrmann, J., & John, C. (2006). *Site U1324.* College Station TX: Proceedings of The Integrated Ocean Drilling Program. doi:10.2204/iodp.proc.308.108.2006

Freeze, R., & Cherry, J. (1979). *Groundwater* (Vol. 7632). Prentice-Hall Inc.: Englewood Cliffs.

Georgiannou, V., Burland, J., & Hight, D. (1990). The Undrained Behavior of Clayey Sands in Triaxial Compression and Extension. *Geotechnique, 40*(3), 431-449.

Han, D.-H. (1986). *Effects of Porosity and Clay Content on Acoustic Properties of Sandstones and Unconsolidated Sediments.* Stanford, California: Stanford University.

Han, D.-h., Nur, A., & Morgan, D. (2011). Effects of porosity and clay content on wave velocities in sandstones. *Geophysics, 51*(11), 2093-2107.

Han, F., Ganju, E., Salgado, R., & Prezzi, M. (2018). Effects of Interface Roughness, Particle Geometry, and Gradation on the Sand–Steel Interface Friction Angle. *Journal of Geotechnical and*

Geoenvironmental Engineering, 144(12), 04018096-1 to -12. doi:10.1061/(ASCE)GT.1943-5606.0001990

Hang, T., Wu, Q., Cheng, K., Li, L., & Chen, G. (2024). A new procedure for characterizing the critical intergranular contact state of non-plastic sand – fines mixed materials. *Case Studies in Construction Materials, 20*(e02881).

Hardin, B. (1985). Crushing of Soil Particles. *Journal of Geotechnical Engineering, 111*(10), 1177-1192.

Hardin, B., & Music, J. (1963). Elastic wave velocities in Granular Soils. *Journal of Soil Mechanics, Foundations Division, 89*(SM1), 33-63.

Hart, B. S., Flemings, P. B., & Deshpande, A. (1995). Porosity and Pressure - Role of Compaction Disequilibrium in the Development of Geopressures in a Gulf-Coast Pleistocene Basin. *Geology, v. 23*, p. 45-48.

Hazen, A. (1930). Water Supply. In *American Civil Engineering Handbook.* New York: Wiley.

Hedberg, H. (1926). The Effect of Gravitational Compaction on the Structure of Sedimentary Rocks. *Bull. Amer. Assoc. Petrol. Geol., Vol. 10*, 1035-1073.

Hicher, P.-Y. (1996). Elastic Properties of Soil. *Journal of Geotechnical Engineering*, 122(8): 641-648.

Holbrook, P., Maggiori, D., & et al. (1993). Real-time pore pressure and fracture gradient evalua-tion in all sedimentary lithologies. *SPE 26791. Offshore European Conference.* Aberdeen, scotland: Society of Petroleum Engineers.

Horne, M. (1965). The Behavior of an Assembly of Rotund, Rigid, Cohesionless Particles. *Proceedings of the Royal Society of London, 286*(A), 62-78.

Hubbert, K. M. (1956). Darcy's Law and the Field Equations of the Flow of Underground Fluids. *Transaction of the AIME*, 222-239. doi:https://doi.org/10.2118/749-G

Hubbert, M., & Rubey, W. (1959). Role of Fluid Pressure in Mechanics Of Overthrust Faulting: I. Mechanics of Fluid-Filled Porous Solids and Its Apllication to Overthrust Faulting. *Bull. of the Geol. Soc. of Am., Vol. 70*, 115-166.

Hubbert, M., & Willis, D. (1957). Mechanics of hydraulic fracturing. *Petr. Trans. AIME, 210*, 153-163.

Hughes, D., & Cross, J. (1951). Elastic wave velocities in rock at high pressures and temperatures. *Geophysics, 16*, 577-593.

Hughes, D., & Jones, H. (1950). Variation of elastic moduli of igneous rocks with pressure and temperature. *Bulletin of the geological society of America, 61*, 843-856.

Hughes, D., & Kelly, J. (1952). Variation of elastic wave velocity with saturation in sandstone. *Geophysics, 17*, 739-752.

Hughes, D., Pondrom, W., & Mims, R. (1949). Transmission of elastic pulses in metal rods. *Physical Review, 75*, 1552-1556.

Ishihara, K., & Yasuda, S. (1975). Sand liquefaction in hollow cylinder torsion under irregular excitation. *Soils and Foundations, 15*(1), 29-45.

Jaky, J. (1944). The coefficient of earth pressure at rest. *Journal of the Society of Hungarian Architects and Engineers*, 355-358 (in Hungarian).

Jamiolkowski, M., Lancelotta, R., & Lo Presti, D. (1995). Remarks on the stiffness at small strains of six Italian clays. *Pre-failure Deformation of Geomaterials* (pp. 817-836). Rotterdam: Balkema.

Jana, A., Donaldson, A., Stuedlein, A., & Evans, T. (2021). Deep, in-situ nonlinear dynamic testing of soil with controlled blasting: Instrumentation, calibration, and example application to a plastic silt deposit. *Geotechnical Testing Journal, 44*(5), 1301-1326. doi:10.1520/GTJ20190426.

Jizba, D. (1991). *Mechanical and Acoustical Properties of Sandstones and Shales.* Stanford, California: Stanford University.

Jones, M., Bedford, J., & Clayton, C. (1984). On natural deformation mechanisms in the Chalk. *Journal of the Geological Society of London, 141*, 675-683.

Katahara, K. (1996). Clay Mineral Elastic Propertie. *Presented at the 1996 SEG Annual Meeting* (pp. Paper No. 1996-1691.). Denver, Colorado: SEG.

Kim, T., & Novak, M. (1981). Dynamic properties of some cohesive soils of Ontario. *Canadian Geotechnical Journal, 18*(3), 371-389.

King, M. (1983). Static and Dynamic Elastic Properties of Rocks from the Canadian Shield. *Int. J. Rock Mech. Min. Sci. & Geomech., 20*(5), 273-241.

Klimentos, T. (1991). The effects of porosity-permeability-clay content on the velocity of compressional waves. *Geophysics, 56*(12), 1930-1939.

Kozeny, J. (1927). Über kapillare Leitung der Wasser in Böden. *Royal Academy of Science, 136*, 271-306.

Ladd, C. (1960). *Stress-Strain Behavior of Saturated Clay and Basic Strength Principles.* Cambridge, MA: Research on Earth Physics, Department of Civil Engineering, MIT.

Ladd, C., & Foott, R. (1974). New Design Procedure for Stability of Soft Clays. *Journal of Geotechnical Engineering Division, 100*(7), 763-786.

Ladd, R. S. (1978). Preparing Test Specimens Using Undercompaction. *Geotechnical testing journal, 1*, p.16-23. doi:10.1520/GTJ10364J

Lade, P., & de Boer, R. (1997). The Concept of Effective Stress for Soil, Concrete and Rock. *Géotechnique, 47*(1), 61-78. doi:https://doi.org/10.1680/geot.1997.47.1.61

Lade, P., Liggio Jr., C., & Yamamuro, J. (1998). ffects of Non-Plastic Fines on Minimum and Maximum Void Ratios of Sand. *ASTM International. Geotech. Test. J., 21*(4), 336–347.

Lambe, T., & Whitman, R. (1969). *Soil Mechanics.* Massachusetts Institute of Technology: John Wiley & Sons, Inc.

Lapierre, C., Lerouil, S., & Locat, J. (1990). Mercury intrusion and permeability of Louiseville clay. *Canadian Geotech Journal, 27*, 761-773.

Lawrence, F. (1965). *Ultrasonic Shear Wave Velocities in Sand and Clay.* Cambridge, Massachusetts, USA: Massachusetts Institute of Technology Department of Civil Engineering.

Lecampion, B., Constantinescu, A., & Malinsky, L. (2006). Identification of poroelastic constants of "tight" rocks from laboratory tests. *International Journal of Geomechanics, 6*, 201-208.

Lee, J., Lee, D., & Park, D. (2014). Experimental Investigation on the Coefficient of Lateral Earth Pressure at Rest of Silty Sands: Effect of Fines. *Geotechnical Testing Journal, 37*(6), 967-979.

Lee, K. (1977). Adhesion Bonds in Sands at High Pressures. *Journal Geotechnical Engineering Division, 103*(GT8), 908-913.

Li, L., Dai, Z., Liu, R., & Jian, F. (2023). Experimental Study on the Coefficient of Earth Pressure at Rest for Sand. *Buildings, 13*(1276), 1-14. doi:10.3390/buildings13051276

Likitlersuang, S., Teachavorasinskun, S., Surarak, C., Oh, E., & Balasubramaniam, A. (2013). Small strain stiffness and stiffness degradation curve of Bangkok Clays. *Soils and Foundations, 53*(4), 498-509. doi:10.1016/j.sandf.2013.06.003

Lin, C., Lin, C., & Chang, T. (2004). The use of MASW method in the assessment of soil liquefaction potential. *Soil Dynamic Earthquake Engineering, 24*, 689-698.

Long, H., Flemings, P., Dugan, B., Germaine, J., & Ferrell, D. (2008). *Data report: penetrometer measurements of in situ temperature and pressure, IODP Expedition 308.* College Station, Texas: Integrated Ocean Drilling Program. doi:10.2204/iodp.proc.308.203.2008

Losh, S., Eglinton, L., & Wood, J. (1994). Coring and Inorganic Geochemistry in the Pathfinder Well, Results of the Pathfinder drilling program into a major growth fault. Palisades, New York, United States: LDEO Press.

Lovisa, J., & Sivakugan, N. (2015). Tall oedometer testing: method to account for wall friction. *International Journal of Geomechanics, 15*, p. 04014045.

Lowe, J., Jonas, E., & Obrican, V. (1969). Controlled gradient consolidation test. *Journal of Soil Mechanics & Foundations Div*, 92(SM5, Proc Paper 490).

Maeda, N. (1985). A Method for Reading and Checking Phase Time in Auto-Processing System of Seismic Wave Data. *Journal of the Seismological Society of Japan, 38*, 365-379.

Marion, D., Nur, A., Yin, H., & Han, D. (1992). Compressional Velocity and Porosity in Sand Clay Mixtures. *Geophysics, 57*, 554-563.

Marjanovic, J. (2016). *Stiffness characterization of mechanically-compressed co-hesive soils using wave propagation.* Cambridge, Massachusetts: Ph.D. Thesis, Massachusetts Institute of Technology.

Matthews, M., Hope, V., & Clayton, C. (1996). The use of surface waves in the determination of ground stiffness profiles. *ICE Geotechnical Engineering, 119*, 84-95.

Matthews, W., & Kelly, J. (1967). How to Predict Formation Pressure and Fracture Gradient. *Oil and Gas Journal, 65*, 92-106.

Mavko, G., Mukerji, T., & Dvorkin, J. (2020). *The Rock Physics Handbook* (3rd ed.). Cambridge: Cambridge University Press. doi:10.1017/9781108333016

Mayne, P., & Kulhawy, F. (1982). K0-OCR Relationship in Soil. *J. Geotech. Eng. Div., 108*(6), 851-869.

McCulloh, T. (1967). *Mass Properties of Sedimentary Rocks and Gravimetric Effects of Pertroleum and Natural-Gas Reservoirs.* Washington, District of Columbia: U.S. Department of the Interior.

Meade, R. (1964). *emoval of Water and Rearrangement of Particles During the Compaction of Clayey Sediments : Review.* Washington D.C.: United States Department of the Interior, Geological Survey,.

Mesri, G., & Castro, A. (1987). Ca/Ccc Concept and K0 During Secondary Compression. *Journal of Geotechnical Engineering, 113*(3), 230-247.

Mesri, G., & Vardhanabhuti, B. (2009). Compression of granular materials. *Canadian Geotechnical Journal*, 46(4): 369-392. doi:https://doi.org/10.1139/T08-123

Mitchell, J. (1976). *Fundamentals of Soil Behavior.* University of California, Berkeley: John Wiley & Sons, Inc.

Mondol, N. (2009). Porosity and permeability development in mechanically compacted silt-kaolinite mixtures. *SEG Houston 2009 International Exposition and Annual Meeting*, 2139-2143.

Mondol, N. H., Bjorlykke, K., & Jahren, J. (2008). Experimental compaction of clays: relationship between permeability and petrophysical properties in mudstones. *Petroleum Geoscience, 14*, 319-337. doi:10.1144/1354-079308-773

Mondol, N., Bjorlykke, K., Jahren, J., & Hoeg, K. (2007). Experimental Mechanical Compaction of Clay Mineral Aggregates; Changes in Physical Properties of Mudstones during Burial. *Marine and petroleum geology, 24*(5), 289-311.

Mondol, N., Bjorlykke, K., Jahren, J., & Hoeg, K. (2007). Experimental mechanical compaction of clay mineral aggregates—Changes in physical properties of mudstones during burial. *Marine and Petroleum Geology, 24*, 289-311.

Mondol, N., Jahren, J., Berre, T., Grande, L., & Bjørlykke, K. (2010). Permeability Anisotropy in Mudstones - An Experimental Study. *Search and Discovery Article #40649. Poster Session.* New Orleans, Louisiana: AAPG Annual Convention.

Monkul, M. M., & Ozden, G. (2007). Compressional behavior of clayey sand and transition fines content. *Engineering Geology, 89*, 195-205.

Mueth, D., Jaeger, H., & Nagel, S. (1998). Force distribution in a granular Medium. *Phys. Rev. E, 57*, 3164-3169. doi:10.1103/PhysRevE.57.3164

Murphy III, W. (1982). *Effects of Microstructure and Pore Fluids on the Acoustic Properties of Granular Sedimentary Materials.* Stanford, California: Stanford University.

Nagaraj, H. (2016). Influence of gradation and proportion of sand on stress–strain behavior of clay–sand mixtures. *Geo-Engineering, 7*(19). doi:10.1186/s40703-016-0033-8

Nakayama, K., & Van Siclen, D. (1981). Simulation Model for Petroleum Rxploration. *AAPG Bull., 65*, 1230-1255.

Nazarian, S., & Stokoe II, K. (1984). In situ shear wave velocities from spectral analysis of surface waves. *Proceedings of the World Conference on Earthquake Engineering 8.* San Francisco, California.

Neuzil, C. E. (2019). Permeability of Clays and Shales. *Annual review of earth and planetary sciences, 47*(1), 247-273.

Nordquist, T. (2015). *Permeability Anisotropy of Resedimented Mudrocks* (Vol. Ph.D. Thesis). Cambridge, Massachusetts: Massachusetts Institute of Technology.

Nur, A., & Simmons, G. (1969). The Effect of Saturation on Velocity in Low Porosity Rocks. *Earth and Planetary Science Letters*, 183-193.

Oda, M., & Konishi, J. (1974). Microscopic Deformation Mechanism of Granular Material in Simple Shear. *Soils and Foundations, 14*(4), 25-38.

Pandian, N., Nagaraj, T., & Raju, P. (1995). Permeability and Compressibility Behavior of Bentonite-Sand/Soil Mixes. *Geotechnical Testing Journal, 18*(1), 86-93.

Pantelidis, L. (2019). The Generalized Coeffcients of Earth Pressure: A Unified Approach. *Applied Sciences, 9*(5291), 1-42. doi:10.3390 /app9245291

Pestana-Nascimento, J. (1994, May 4). A Unified Constitutive Model for Clays and Sands. *Ph.D. Thesis*. Cambridge, Massachusetts: MAssachusetts Institute of Technology.

Pickett, G. (1963). Acoustic Character Logs and Their Applications in Formation Evaluation. *Journal of Petroleum Technology, 15*(6), 659-667.

Plumb, R. (1994). Influence of composition and texture of the failure properties of clastic rocks. *Petroluem Engineering Conference* (pp. 13-20). Delft, Netherlands: Society of Petroleum Engineers.

Plumb, R., Herron, S., & Olsen, M. (1992, October). Influence of Composition and Texture on Compressive Strength Variations in the Travis Peak Formation. *67th Annual Technical Conference and Exhibition of the Society of Petroleum Engineers* (pp. 985-998). Washington: Society of Petroleum Engineers.

Potts, D. M. (1986). A numerical study of the effects of wall deformation on earth pressures. *In. J, Numer. Analyt. Meth. in Geomech., 10*, 383-405.

Poulos, S. (1981). The Steady State of Deformation. *J. Geotech. Engng Am. Soc. Civ. Engrs, G75*, 553-562.

Prakasha, K. S., & Chandrasekaran, V. S. (2005). Behavior of Marine Sand-Clay Mixtures under Static and Cyclic Triaxial Shear. *Journal of Geotechnical and Geoenvironmental Engineering, 131*(2), 213-222.

Prasad, M. (2002). Acoustic measurements in unconsolidated sands at low effective pressure and overpressure detection. *GEOPHYSICS, 67*, 405-412. doi:10.1190/1.1468600

Prasad, M., & Meissner, R. (1992). Attenuation mechanisms in sands: Laboratory versus theoretical (Biot) data. *Geophysics, 57*(5), 710-719.

Prasad, M., Kopycinska, M., Rabe, U., & Arnold, W. (2002). Measurement of Young's modulus of clay minerals using atomicforce acoustic microscopy. *Geophysical Research Letters, 29*(8), 13-0 to 13-4. doi:10.1029/2001GL014054

Rahman, M., Lo, S., & Gnanendran, C. (2009). Reply to the discussion by Wanatowski and Chu on On equivalent granular void ratio and steady state behaviour of loose sand with fines. *(appeared in: Can. Geotech. J. J. 46(4):482) Can. Geotech. J., 46*, 483–486.

Rampello, S., Viggiani, G., & Amorosi, A. (1997). Small-strain stiffness of reconstituted clay compressed along constant triaxial effective stress ratio paths. *Géotechnique, 47*(3), 475–489.

Ranjpour, D. (2020). *Stiffness and Anisotropy Characterization of Mechanically-Compressed Cohesive Soils Using Directional Wave Propagation.* Medford, Massachusetts: Tufts University.

Rankine, W. (1856). On the stability of loose earth. *Philosophical Transactions of the Royal Society of London, 147*.

Reece, J. S. (2021). The Impact of Grain Size on the Hydromechanical Behavior of Mudstones. *Geochemistry, Geophysics, Geosystems*(22), 1-23. doi:https://doi.org/10.1029/2021GC009732

Rieke, H., & Chilingar, G. (1974). *Compaction of Argillaceous Sediments.* Amsterdam: Elsevier Scientific Pub. Co.

Robertson, D., Bolton, M., & McDowell, G. (1997). A Numerical Representation of Fracturing Granular Materials. *Internation Journal for Numerical and Analytical Methods in Geomechanics, 21*, 825-843.

Robertson, P., Campanella, R., Gillespie, D., & Rice, A. (1986). Seismic CPT to Measure in Situ Shear Wave Velocity. *Journal of Geotechnical Engineering, 112*(8), 791-803.

Rowe, P. (1954). A stress-strain theory for cohesionless soil with applications to earth pressures at rest and moving walls. *Géotechnique, 4*(2), 70-88.

Rowe, P. (1962). The stress-dilatancy relation for static equilibrium of an assembly of particles in contact. *Proceedings of the Royal Society of London, Series A, Mathematical and Physical Sciences, 269*(1339), 500-527.

Rowe, P. (1971). Theoretical Meaning and Observed Values of Deformation Parameters for Soil. In R. H. Parry (Ed.), *Stress-Strain Behavior of Soils* (pp. 143-194). Henley-on-Thames, Oxfordshire: G.T. Foulis & Co.

Santagata, M. (1998). *Factors Affecting the Initial Stiffness and Stiffness Degradation of Cohesive Soils.* Cambridge, Massachusetts, USA: Massachusetts Institute of Technology.

Santagata, M., Germaine, J. T., & Ladd, C. C. (2005). Factors Affecting the Initial Stiffness of Cohesive Soils. *Journal of Geotechnical and Geoenvironmental Engineering, 131(4)*, 430-441. doi:https://doi.org/10.1061/(ASCE)1090-0241(2005)131:4(430)

Sawyer, D., Jacoby, R., Flemings, P., & Germaine, J. (2008). *Data report: particle size analysis of sediments in the Ursa Basin, IODP Expedition 308 Sites U1324 and U1322, northern Gulf of Mexico.* Cambridge, Masssachusetts: Integrated Ocean Drilling Program. doi:10.2204/iodp.proc.308.205.2008

Schiffman, R., & Gibson, R. (1964). Consolidation of Non-homogenous Clay Layers. *J. Soil Mechanics and Foundations Division, 90*, 1-30.

Schmidt, B. (1966). a discussion of Earth Pressures at Rest Related to stress History. *Canadian Geotechnical Journal, 3*(4), 239-242.

Schneider, J. (2011). *Compression and Permeability Behavior of Natural Mudstones.* Austin: The University of Texas at Austin.

Shafiee, A. (2008). Permeability of compacted granule - clay mixtures. *Engineering Geology, 97*, 199-208. doi:10.1016/j.enggeo.2008.01.002

Shafiee, A. (2008). Permeability of compacted granule–clay mixtures. *Engineering Geology, 97*, 199-208.

Shen, J., Wang, X., Wang, X., Yao, T., Wei, H., & Zhu, C. (2021). Effect and mechanism of fines content on the shear strength of calcareous sand. *Bulletin of Engineering Geology and the Environment, 80*, 7899-7919. doi:10.1007/s10064-021-02398-w

Shibuya, S., & Tanaka, H. (1996). Estimate of elastic shear modulus in Holocene soil deposits. *Soils and Foundations, 36*(4), 45-55.

Shibuya, S., Hwang, S., & Mitachi, T. (1997). Elastic shear modulus of soft clays from shear wave velocity measurement. *Geotechnique, 47*(3), 593-601.

Shipton, B., & Coop, M. (2012). On the compression behaviour of reconstituted soils. *Soils and Foundations, 52*(4), 668-681.

Shirley, D., & Hampton, L. (1978). Shear-wave measurements in laboratory sediments. *J. Acoust. Soc. Am., 63*(2), 607-613.

Simpson, B. (1992). Retaining structures: displacement and design. *Geotechnique, 42*(4), 541-576.

Simpson, D. C. (2014). *Behavioral thresholds in mixtures of sand and clay.* Corvallis, Oregon, U.S.A.: Masters Thesis, Oregon State University. Retrieved from https://ir.library.oregonstate.edu/concern/graduate_thesis_or_dissertations/bg257j16m

Simpson, D., & Evans, T. (2016). Behavioral Thresholds in Mixtures of Sand and Kaolinite Clay. *Journal of Geotechnical and Geoenvironmental Engineering, 142*(2), 1-10. doi:10.1061/(ASCE)GT.1943-5606.0001391

Skeels, D. (1943). *The Density of Shales as a Function of Depth, a Compilation of Data - Unpublished.* New Jersey: Standard Oil Company.

Skempton, A. (1948). The Phi = 0 Analysis of Stability and Theoretical Basis. *Proc. 2nd Int. Conf. Soil Mech. and Found. Eng.*, *Vol. I*, pp. 72 - 78. Rotterdam.

Skempton, A. (1954). The Pore Pressure Coefficients A and B. *Geotechnique, 4*, 143-147.

Skempton, A. (1961). Effective Stress in Soil, Concrete and Rocks. *Pore Pressure and Suction in Soils*, 4-16.

Skinner, A. (1969). A Note on the Influence of Interparticle Friction on the hearing Strength of a Random Assembly of Spherical Particles. *Geotechnique, 69*(1), 150-157.

Spinelli, G., Giambalvo, E., & Fisher, A. (2004). Sediment permeability, distribution, and influence on fluxes in oceanic basement. (E. Davis, & H. Elderfield, Eds.) *Hydrogeology of the Oceanic Lithosphere*, 151-188.

Stokoe, K., Hwang, S., & Lee, J.-K. (1994). Effects of various parameters on the stiffness and damping of soils at small to medium strains. In S. Shibuya (Ed.), *Prefailure deformation of geomaterials. 2*, pp. 785-816. Rotterdam: Balkema.

Storer, D. (1959). Costipamento dei sedimenti argillosi nel Bacino Padano. *I Giacement Gassiferi dell'Europa Occidentale*, 519-536.

Stump, B. B. (1998). Illuminating basinal fluid flow in Eugene Island 330 (Gulf of Mexico) through in situ observations, deformation experiments, and hydrodynamic modeling. The Pennsylvania State University.

Summers, G., & Broding, R. (1952). Continuous Velocity Logging. *Geophysics, 17*(3), 598-614.

Swan, C. (1994). *Physical Mechanisms Controlling the Strength and Deformation Behavior of Unfrozen and Frozen Manchester Fine Sand.* Cambridge, Massachusetts: Massachusetts Institute of Technology.

Talesnick, M., Nachum, S., & Frydman, S. (2021). K0 determination using improved experimental technique. *Geotechnique, 71*(6), 509-520. doi:10.1680/jgeot.19.P.019

Taylor, D. (1942). *Research on Consolidation of Clays.* Cambridge, Massachusetts: Department of Civil Engineering and Sanitary Engineering, Massachusetts Institute of Technology.

Taylor, D., & Merchant, W. (1940). A Theory of Clay Consolidation Accounting for Secondary Compression. *J. Math. Physics, 19*(3), 167-185.

Taylor, E., & Leonard, J. (1990). Sediment Consolidation and Permeability at the Barbados Forearc. *Proceedings of the Ocean Drilling Program, Scientific Results, 110*, 289-308.

Terzaghi, K. (1923). Discussion of lateral earth pressure: the accurate experimental determination of the lateral earth pressure, together with a resume of previous experiments. *Trans. Am. Soc. Civ. Engrs., 86*, 1525-1543.

Terzhagi, K. (1923). Die Berechnung der Durchlässigkeits-Ziffer des Tones aus dem Verlauf. *Sitzungber Akad. Wissen Wien Math-naturw, Kl 132*, 105-124.

Terzhagi, K. (1925). *Erdbaumechanik auf bodenphysikalischer Grundlage.* Leipzig-Wien: Franz Deuticke.

Thevanayagam, S., Shenthan, T., Mohan, S., & Liang, J. (2002). Undrained fragility of clean sands, silty sands and sandy silts. *Journal of Geotechnical and Geoenvironmental Engineering, 128*(10), 849-859.

Tosoya, C. (1982). *Acoustical Properties of Clay bearing Rocks.* Stanford, California: Stanford University.

US Silica. (2017). *Western Reserve Chemicals.* Retrieved from WRChem.com: https://www.wrchem.com/wp-content/uploads/2015/11/MIN-U-SIL-BERKELEY-Tech-Data.pdf

Van Olphen, H. (1963). *An Introduction to Colloid Chemistry.* New York: John Wiley and Sons Inc.

Vanorio, T., Prasad, M., & Nur, A. (2003). Elastic Properties of Clay Dry Mineral Aggregates, Suspension and Sandstones. *Geophysical Journal International, 155*(1), 319-326. doi:0.1046/j.1365-246X.2003.02046.x

Varsamis, G., Wisniewski, L., Arian, A., & Althoff, G. (1999). A New MWD Full Wave Dual Mode Sonic Tool Design and Case Histories. *SPWLA 40th Annual Logging Symposium.*

Velde, B. (1996). Compaction Trends of Clay-rich Deep Sea Sediments. *Marine Geology, 133*, 193-201.

Vernik, L. (1993). Predicting lithology and reservoir quality from acoustic velocities based on petrophysical classification of siliciclastics. *SEG Technical Program Expanded Abstracts*, 707-710. doi:doi:10.1190/1.1822595

Vogel, C. (1952). A Seismic Velocity Logging Method. *Geophysics, 17*(3), 586-597.

Wang, L., Chu, J., & Wu, S. (2024). Mechanical Behavior of Cemented Sand under Plane Strain Condition. *International Journal of Geomechanics, 24*(9), 04024191-1 to 04024191-16. doi:10.1061/IJGNAI.GMENG-10368

Wang, Z., Wang, H., & Cates, M. (n.d.). Elastic Properties of Solid Clays. *Presented at the 1998 SEG Annual Meeting* (pp. Paper No. 1998-1045.). New Orleans: SEG.

Wijeyesekera, D., & De Freitas, M. (1976). High Pressure Consolidation of Kaolinitic Clay. *AAPG Bulletin, 60*, 293-298.

Winkler, K., & Nur, A. (1982). Seismic attenuation: effects of pore fluid and frictional sliding. *Geophysics, 47*, 1-15.

Wissa, A. E., Davis, E. H., Christian, J. T., & Heiberg, S. (1971). Consolidation at Constant Rate of Strain. *Journal of the Soil Mechanics and Foundations Division*, 1393-1413.

Woeber, A., Katz, S., & Ahrens, T. (1963). Elasticity of Selected Rocks and Minerals. *Geophysics, 28*(4), 658-663.

Wu, Y., Yamamoto, H., Cui, J., & Cheng, H. (2020). Influence of Load Mode on Particle Crushing Characteristics of Silica Sand at High Stresses. *International Journal of Geomechanics, 20*(3), 1-14. doi:10.1061/(ASCE)GM.1943-5622.0001600

Wyllie, M., Gregory, A., & Gardner, L. (1956). Elastic Wave Velocities in Heterogeneous and Porous Media. *Geophysics, 21*(1), 41-70.

Xu, D.-s., Huang, M., & Zhou, Y. (2020). One-Dimensional Compression Behavior of Calcareous Sand and Marine Clay Mixtures. *Internationl Journal Geomechanics, 20*(9), 1-9.

Yang, Y., & Aplin, A. (1998). Influence of lithology and compaction on the pore size distribution and modelled permeability of some mudstones from the Norwegian margin. *Marine and Petroleum Geology, 15*, 163-175.

Yang, Y., & Aplin, A. (2007). Permeability and petrophysical properties of 30 natural mudstones. *Journal Geophysical Research, 112*(B03206), 1-14. doi:10.1029/2005JB004243.

Yang, Y., & Aplin, A. C. (2004). Definition and practical application of mudstone porosity–effective stress relationships. *Petroleum Geoscience, 10*, 153-162.

Yang, Y., & Aplin, A. C. (2010). A Permeability–Porosity Relationship for Mudstones. *Marine and Petroleum Geology, 27*, 1692-1697.

Yin, H. (1992). *Acoustic Velocity and Attenuation of Rocks: Isotropy, Intrinsic Anisotropy, and Stress Induced Anisotropy.* Stanford, California: Stanford University.

Yu, F. (2017). Particle breakage and the critical state of sands. *Géotechnique, 67*(8), 713-719. doi:10.1680/jgeot.15.P.250

Zeng, Z., Cui, Y.-J., Conil, N., & Talandier, J. (2020). Experimental Investigation and Modeling of the Hydraulic Conductivity of Saturated Bentonite–Claystone Mixture. *International Journal of Geomechanics*, 04020184-1 to 04020184-10. doi:0.1061/(ASCE)GM.1943-5622.0001817

Zhang, J., & Shang-Xian, Y. (2017). Fracture gradient prediction: an overview and an improved method. *Petroleum Science*, 720-730. doi:10.1007/s12182-017-0182-1

Zhang, M., Takahashi, M., Morin, R., Endo, H., & Esaki, T. (2002). Determining the hydraulic properties of saturated, low-permeability geological materials in the laboratory: advances in theory and practice. In M. Sara, & L. Everett (Ed.), *ASTM STP 1415* (pp. 83-98). West Conshohocken, PA,: ASTM International,.

Zhou, Z., Chen, R., Rui, Y., & Wang, H. (2019). An Improved Automatic Picking Method for Arrival Time of Acoustic Emission Signals. *IEEE Access, 7*, 75568-75576. doi:10.1109/ACCESS.2019.2921650

Zimmer, M. (2003). *Seismic velocities in unconsolidated sands: Measurements of pressure, sorting, and compaction effects.* Stanford, California: Stanford University, Ph.D Dissertation.

Zimmer, M., Prasad, M., Mavko, G., & Nur, A. (2007). Seismic velocities of unconsolidated sands: Part 2 — Influence of sorting- and compaction-induced porosity variation. *Geophysics, 72*(1), E15-E25. doi:10.1190/1.1452609

Zoback, M. (2007). *Reservoir Geomechanics.* Cambridge: Cambridge University Press.

Zoback, M., & Healy, J. (1984). Friction, faulting, and “in situ” stresses. *Annales Geophysicae, 2*, 689-698.

Zuo, L., & Baudet, A. (2014). etermination of the transitional fines content of sand-non plastic fines mixtures. *The Japanese Geotechnical Society Soils and Foundations, 55*(1), 213-219. doi:https://doi.org/10.1016/j.sandf.2014.12.017

Appendix A – Shear Wave Processing Matlab code

```
function [UFT FT] = swaveall2(fileloc,npointavg,freqcut)
cd(fileloc)
[status, list] = system( 'dir /B /S *.csv' );
result = textscan( list, '%s', 'delimiter', '\n' );
fileList = result{1};
[Num_Files ~] = size(fileList);
a = dir('*.csv');
File_Name = {a.name};

%The above scans the directory and sub directories in the file path for
%.CSV files.  These are the oscilloscope out put files.  These names are
%inserted into a structure called a.

CH1ind = contains(fileList, 'CH1');
CH1list= fileList(CH1ind);
[Num_CH1 ~] = size(CH1list);

CH2ind = contains(fileList, 'CH2');
CH2list= fileList(CH2ind);
[Num_CH2 ~] = size(CH2list);
LFCH2=length(CH2list);

%The above searches the list of filenames found for "CH1" the oscilloscope
%input channel file and "CH2" the oscilloscope output channel file.
%Individual channel file lists are created and the overall count of each
%file type is performed.

CH2Files=split(CH2list,'\');
CH2Files=CH2Files(:,9);
CH2Files=repelem(CH2Files,3);
CH2Files=string(CH2Files);


% The above splits the oscilloscope out put file paths at the \ delimiter
% and then saves the segment containing the directory name containing the
% files in an array.  This array duplicates the file name 3 times for
% future use in an output table.

%% Setup the Import Options and import the data
opts = delimitedTextImportOptions("NumVariables", 5);

% Specify range and delimiter
opts.DataLines = [1, Inf];
opts.Delimiter = ",";

% Specify column names and types
opts.VariableNames = ["Var1", "Var2", "Var3", "VarName4", "VarName5"];
opts.SelectedVariableNames = ["VarName4", "VarName5"];
```

```
opts.VariableTypes = ["string", "string", "string", "double", "double"];

% Specify file level properties
opts.ExtraColumnsRule = "ignore";
opts.EmptyLineRule = "read";

% Specify variable properties
opts = setvaropts(opts, ["Var1", "Var2", "Var3"], "WhitespaceRule", "preserve");
opts = setvaropts(opts, ["Var1", "Var2", "Var3"], "EmptyFieldRule", "auto");

%The above sets up the options for importing data from the oscilloscope
%file types.

% Import the data
for i=1:Num_CH1
   DataCH1{i} = readtable(string(CH1list(i)), opts);
end

for i=1:Num_CH2
   DataCH2{i} = readtable(string(CH2list(i)), opts);
end

%the above completes the data import to a table.

%% Convert to output type
for i=1:Num_CH1
   dataCH1{i}=table2array(DataCH1{i});
end

for i=1:Num_CH2
   dataCH2{i}=table2array(DataCH2{i});
end

%the above converts the data import table to an array for easier mnanipulation.

%% Remove Pre-trigger Times
for i=1:Num_CH1
   ZCH1=find(dataCH1{1,i}(:,1)==0,1,'first')-1;
   dataCH1{1,i}(1:ZCH1,:)=[];
   dataCH1{1,i}(2049:end,:)=[];
   LCH1(i)=length(dataCH1{1,i}(:,1));
end

for i=1:Num_CH2
   ZCH2=find(dataCH2{1,i}(:,1)==0,1,'first')-1;
   dataCH2{1,i}(1:ZCH2,:)=[];
   dataCH2{1,i}(2049:end,:)=[];
   LCH2(i)=length(dataCH2{1,i}(:,1));
end

%The above loops remove the pre-trigger times from the input an output files
```

```
%as well as cuts the total length down to 2048 samples for expedited fft.

for i=1:Num_CH1
   if dataCH1{1,i}<2048;
   dataCH1{1,i}(end:2048,:)=[0];
   end
end

for i=1:Num_CH2
   if dataCH2{1,i}<2048;
   dataCH2{1,i}(end:2048,:)=[0];
   end
end

%The above adds zeros to the end of the input and output signals to meet a
%2048 sample length this is to maintain the correct number of datapoints
%for combining matrices

dataCH1=cell2mat(dataCH1);
dataCH2=cell2mat(dataCH2);

%the above converts the data import table to an array for easier manipulation.

time=dataCH2(:,1:2:end);
trace=dataCH2(:,2:2:end);

for i=1:Num_CH2
trace(:,i)=smooth(trace(:,i),npointavg);
end

%Lines 53 to 57 finds the the trigger time and removes the pretrigger data
%from the accelogram trims each accelogram to 2048 data points
%converts the cell area to a matrix.

%%
% Plot Initial Accelerograms

figure(1)
for i=1:Num_CH2
subplot(LFCH2,1,i)
plot(time(:,i),trace(:,i),'LineWidth',0.2)
xlim([0 0.0005])
end

%%
for i=1:Num_CH2
L1(i)=length(time(:,i));
fs(i)=1/time(2,i);
fnyq(i)=fs(i)/2;
df(i)=1/time(end,i);
f(:,i)=fs(i)*(0:(L1(i)/2))/L1(i);
```

```
end

%the above calculate the frequency vector for plotting the fft of each signal.


for i=1:Num_CH2
sfft(:,i)=fft(trace(:,i));
sfft(1,i)=0;
[mf v]=max(abs(sfft));
maxf=f(v,i);
end

%the above perform the fft of each signal.

figure(2)
for i=1:Num_CH2
hold on
plot(f(:,i),abs(sfft(1:length(f(:,i)),i)),'LineWidth',0.2)
ylabel('Amp')
xlim([0 200000])
end

%Calculate the frequency vector, Plot the initial accelerogram and compute the
%fft, set the DC component to 0 (first term of fft)


%%

for i=1:Num_CH2
   b = fir1(512,freqcut/fnyq(i),'high');
   fswave = filter(b,1,trace(:,i));
   delay=mean(grpdelay(b));
   fswave(1:delay)=[];
   LFS(i)=length(fswave);
   ftrace(:,i)= fswave;
end

LFS=min(LFS);

%the above filters the signal using a high pass digital filter of input
%frequency  then the added delay is removed to match the input time and the
%length of each filtered signal is calculated for the final output table

figure(3)
for i=1:Num_CH2
subplot(LFCH2,1,i)
plot(time(1:length(ftrace(:,i)),i),ftrace(:,i),'LineWidth',0.2)
xlim([0 0.0005])
end

%the above plots the filtered signals
```

```
%% Generate the out put table

maxF=repelem(maxf,3);

FT=zeros(LFS,length(CH2Files));

for i=1:Num_CH2
   FT(:,(i*3)-2)=time(1:LFS,i);
   FT(:,(i*3)-1)=dataCH1(1:LFS,i*2);
   FT(:,i*3)=ftrace(:,i);
end

FT=[CH2Files';maxF';FT];

UFT=zeros(2048,length(CH2Files));

for i=1:Num_CH2
   UFT(:,(i*3)-2)=time(1:2048,i);
   UFT(:,(i*3)-1)=dataCH1(1:2048,i*2);
   UFT(:,i*3)=trace(:,i);
end

UFT=[CH2Files';maxF';UFT];

%the creates an output table where the top row is the directory name of
%each trace, the second row is the dominant frequency and the following
%rows are the trace data.  The first column of each stress is the time, the
%second column is the input signal and the third column is the filtered
%output signal.
```

Appendix B – Pressure Wave Processing Matlab code

```
function [tableout] = pwaveall2(fileloc,npointavg)
cd(fileloc)


[status, list] = system( 'dir /B /S *.csv' );
result = textscan( list, '%s', 'delimiter', '\n' );
fileList = result{1};
[Num_Files ~] = size(fileList);
a = dir('*.csv');
File_Name = {a.name};

%The above scans the directory and sub directories in the file path for
%.CSV files.  These are the oscilloscope out put files.  These names are
%inserted into a structure called a.

CH1ind = contains(fileList, 'CH1');
CH1list= fileList(CH1ind);
[Num_CH1 ~] = size(CH1list);

CH2ind = contains(fileList, 'CH2');
CH2list= fileList(CH2ind);
[Num_CH2 ~] = size(CH2list);
LFCH2=length(CH2list);

%The above searches the list of filenames found for "CH1" the oscilloscope
%input channel file and "CH2" the oscilloscope output channel file.
%Individual channel file lists are created and the overall count of each
%file type is performed.

CH2Files=split(CH2list,'\');
CH2Files=CH2Files(:,9);
CH2Files=repelem(CH2Files,3);
CH2Files=string(CH2Files);


% The above splits the oscilloscope out put file paths at the \ delimiter
% and then saves the segment containing the directory name containing the
% files in an array.  This array duplicates the file name 3 times for
% future use in an output table.

%% Setup the Import Options and import the data
```

```
opts = delimitedTextImportOptions("NumVariables", 5);

% Specify range and delimiter
opts.DataLines = [1, Inf];
opts.Delimiter = ",";

% Specify column names and types
opts.VariableNames = ["Var1", "Var2", "Var3", "VarName4", "VarName5"];
opts.SelectedVariableNames = ["VarName4", "VarName5"];
opts.VariableTypes = ["string", "string", "string", "double", "double"];

% Specify file level properties
opts.ExtraColumnsRule = "ignore";
opts.EmptyLineRule = "read";

% Specify variable properties
opts = setvaropts(opts, ["Var1", "Var2", "Var3"], "WhitespaceRule", "preserve");
opts = setvaropts(opts, ["Var1", "Var2", "Var3"], "EmptyFieldRule", "auto");

%The above sets up the options for importing data from the oscilloscope
%file types.

% Import the data
for i=1:Num_CH1
   DataCH1{i} = readtable(string(CH1list(i)), opts);
end

for i=1:Num_CH2
   DataCH2{i} = readtable(string(CH2list(i)), opts);
end

%the above completes the data import to a table.

%% Convert to output type
for i=1:Num_CH1
   dataCH1{i}=table2array(DataCH1{i});
end

for i=1:Num_CH2
   dataCH2{i}=table2array(DataCH2{i});
end

%the above converts the data import table to an array for easier manipulation.
```

```
%% Remove Pre-trigger Times
for i=1:Num_CH1
   ZCH1=find(dataCH1{1,i}(:,1)==0,1,'first')-1;
   dataCH1{1,i}(1:ZCH1,:)=[];
   dataCH1{1,i}(2049:end,:)=[];
   LCH1(i)=length(dataCH1{1,i}(:,1));
end

for i=1:Num_CH2
   ZCH2=find(dataCH2{1,i}(:,1)==0,1,'first')-1;
   dataCH2{1,i}(1:ZCH2,:)=[];
   dataCH2{1,i}(2049:end,:)=[];
   LCH2(i)=length(dataCH2{1,i}(:,1));
end

%The above loops remove the pre-trigger times from the input an output files
%as well as cuts the total length down to 2048 samples for expedited fft.

for i=1:Num_CH1
   if dataCH1{1,i}<2048;
   dataCH1{1,i}(end:2048,:)=[0];
   end
end

for i=1:Num_CH2
   if dataCH2{1,i}<2048;
   dataCH2{1,i}(end:2048,:)=[0];
   end
end
%The above adds zeros to the end of the input and output signals to meet a
%2048 sample length this is to maintain the correct number of datapoints
%for combining matrices

dataCH1=cell2mat(dataCH1);
dataCH2=cell2mat(dataCH2);

%the above converts the data import table to an array for easier manipulation.

time=dataCH2(:,1:2:end);
trace=dataCH2(:,2:2:end);

for i=1:Num_CH2
```

```
trace(:,i)=smooth(trace(:,i),npointavg);
end

%Lines 53 to 57 finds the trigger time and removes the pre-trigger data
%from the Accelerogram trims each Accelerogram to 2048 data points
%converts the cell area to a matrix.

%%
% Plot Initial Accelerograms

figure(1)
for i=1:Num_CH2
subplot(LFCH2,1,i)
plot(time(:,i),trace(:,i),'LineWidth',0.2)
xlim([0 0.00005])
end

%%
for i=1:Num_CH2
L1(i)=length(time(:,i));
fs(i)=1/time(2,i);
fnyq(i)=fs(i)/2;
df(i)=1/time(end,i);
f(:,i)=fs(i)*(0:(L1(i)/2))/L1(i);
end

%the above calculate the frequency vector for plotting the fft of each signal.


for i=1:Num_CH2
sfft(:,i)=fft(trace(:,i));
sfft(1,i)=0;
[mf v]=max(abs(sfft));
maxf=f(v,i);
end

%the above performs the fft of each signal.

figure(2)
for i=1:Num_CH2
hold on
plot(f(:,i),abs(sfft(1:length(f(:,i)),i)),'LineWidth',0.2)
ylabel('Amp')
```

```
xlim([0 200000])
end

%Calculate the frequency vector, Plot the initial Accelerogram and compute the
%fft, set the DC component to 0 (first term of fft)


%% Generate the out put table

maxF=repelem(maxf,3);

tableout=zeros(2048,length(CH2Files));

for i=1:Num_CH2;
   tableout(:,(i*3)-2)=time(:,i);
   tableout(:,(i*3)-1)=dataCH1(:,i*2);
   tableout(:,i*3)=trace(:,i);
end

tableout=[CH2Files';maxF';tableout];
%the creates an output table where the top row is the directory name of
%each trace, the second row is the dominant frequency and the following
%rows are the trace data.  The first column of each stress is the time, the
%second column is the input signal and the third column is the filtered
%output signal.
```